



The
University
Of
Sheffield.

**Uranium, Plutonium and Technetium Interactions with Cement
Minerals for Radioactive Waste Management**

Antonia Sarah Yorkshire

A thesis submitted in partial fulfilment of the requirements for the degree of Doctor of Philosophy

The University of Sheffield
Faculty of Engineering
Department of Materials Science and Engineering

April 2020

Abstract

Cement materials are ubiquitous in the safe management, storage and disposal of wastes arising from the UK's nuclear industry. Within intermediate level waste (ILW) containers, and the environment of a geological disposal facility, cement materials will come into contact with a range of radionuclide species. These materials are highly complex and their interaction with radionuclides is not straightforward to understand. An alternative, simplified approach is to investigate the individual minerals that are present within cement. In this Thesis, the interactions of the cement minerals, C-S-H, ettringite and hydrotalcite with the radionuclides uranium, plutonium and technetium have been investigated.

The actinides uranium and plutonium were found to display differing behaviour when in contact with cement materials. The use of X-ray absorption spectroscopy and nuclear magnetic resonance spectroscopy have given new insights into the structure of U(VI) coordinated to C-S-H, ettringite and hydrotalcite phases and by comparison to natural uranium mineral analogues. In the case of Pu(VI), this oxidation state was shown to be unstable and radiolytically-induced reduction to hydrous Pu(IV)O₂ occurred, which did not display either incorporation into C-S-H phases or analogous coordination with U(VI) in C-S-H phases.

Re(VII) was shown to be an effective surrogate for Tc(VII), which both displayed Ca²⁺-facilitated sorption onto C-S-H phases. The coordination environment was likened to the novel synthesised calcium perrhenate or pertechnetate phases, respectively. It has been shown, for the first time, that the pertechnetate anion can be sorbed to cement minerals, such as ettringite that has been de-stabilised by carbonation effects, which may have implications for the use of cement as an immobilisation matrix for this radionuclide in the future.

Acknowledgements

There are numerous people that I need to thank for supporting me throughout the last few years.

Firstly, I would like to say a huge thank you to my supervisors, Dr. Claire Corkhill and Prof. John Provis, for giving me this opportunity. Claire, you believed in me at times when I didn't even believe in myself - thank you for your patience and resilience.

Thank you to my family for being the solid rock that always brought me back to normality, with your love, silliness and laughter.

I have made some forever friends during my time at the University of Sheffield. To the ISL, you were the guys who kept me going right till the end. Thank you for the much-needed lunch time nonsense natters and Friday (or any day) beers. You're all great scientists, but a great bunch of friends first. Thank you especially to Hannah, Rita, Sarah, Colleen, Seb and Clem for getting me through the tough times with your kind friendship.

Thanks also go to Martin Stennett for so much of your time spent teaching me the dark art that is EXAFS, as well as Dan Bailey for his continued contributions to the synthesis of technetium samples and to S. O'Sullivan, N. Hyatt, W. Lukens and S. Szenknect for the provision of samples and data.

To my good friend Lucy, who also 'made it' - you understood so well my struggles more than anybody else. Thank you for the Sheffield visits and the space to vent.

To the Unicorns, the best netball team anyone could ask for - thank you for the laughs, prosecco and love, always.

Finally, to Damon. Thank you for being the safe home to come back to after a long day. Your support has been unwavering, especially in the last few months, and for that I am forever grateful.

"All flowers, in time, bend towards the Sun"

- J.B. & E.F.

Peer Reviewed Journal Publications:

- 1) S.A. Kearney, B. McLuckie, K. Webb, R. Orr, I.A. Vatter, A.S. Yorkshire, C.L. Corkhill, M. Hayes, M.J. Angus, & J.P. Provis, Effects of plutonium dioxide encapsulation on the physico-chemical development of Portland cement blended grouts, *J. Nucl. Mater.*, 530, 151960 (2020).
- 2) S.A. Saslow, S.N. Kerisit, T. Varga, S.T. Mergelsberg, C.L. Corkhill, M. Snyder, N. Avalos, A.S. Yorkshire, D.J. Bailey, J. Crum, & R.M. Asmussen, Immobilizing Pertechnetate in Ettringite via Sulfate Substitution (Just Accepted), *Environ. Sci. Technol.* (2020).
- 3) A.S. Yorkshire, J.W. Bridge, L.J. Gardner, S.A. Walling, P. Hillel, D.E. Crean, D.J. Bailey, M.C. Stennett, R.V. Tappero, S.A. Saslow, N.C. Hyatt & C.L. Corkhill, Application of spatially-resolved X-ray and gamma spectroscopy to evaluate the interaction of technetium-99 with blended Portland cements, (IN DRAFT).

Conference Publications:

- 1) A.S. Yorkshire, J.L. Provis, M.C. Stennett, D.J. Bailey, B. Walkley, S. van Meurs, S. Parry, L. Martel, O. Walters, N.C. Hyatt & C.L. Corkhill, Understanding cement-[U,Pu,Tc] mineral systems for radioactive waste management, NUWCEM, Avignon, France, 24th - 26th October 2018. (*Extended abstract and oral presentation.*)
- 2) A.S. Yorkshire, J.L. Provis, M.C. Stennett, N.C. Hyatt and C.L. Corkhill, Understanding Radionuclide Interactions with Cementitious Materials for Radioactive Waste Management, Waste Management Conference, Phoenix, Arizona, USA, 18th - 22nd March 2018. (*Poster presentation.*)
- 3) A.S. Yorkshire, S.A. Kearney, J.L. Provis, M. Angus, R. Orr, N.C. Hyatt & Claire L. Corkhill, Understanding radionuclide interactions with cementitious materials for UK radioactive waste management, PETRUS-ANNETTE, Lisbon, Portugal, 26th - 30th June 2017. (*Extended abstract and oral presentation.*)

Abbreviations and Definitions

ACW	Artificial cement water
AFm-X	$\text{Ca}_4(\text{Al}_2\text{O}_6)(\text{X})12\text{H}_2\text{O}$, where X = anion
AIMD	Ab initio molecular dynamics
B₀	External magnetic field (NMR)
B	Bond valence parameter
BFS	Blast-furnace slag
C (as a suffix)	Carbonated / pre-carbonated
C-S-H	Calcium-silicate-hydrate(s)
CSH(X)	C-S-H phase with Ca/Si ratio = X
DLS	Diamond Light Source
E	Energy
Ett	Ettringite ($\text{Ca}_6\text{Al}_2(\text{SO}_4)_3(\text{OH})_{12}\cdot 26\text{H}_2\text{O}$), also AFt
EXAFS	Extended X-ray absorption fine structure (spectroscopy)
FA	Fly ash
GDF	Geological disposal facility
GGBS	Ground-granulated blast-furnace slag
HT	Hydrotalcite ($\text{Mg}_6\text{Al}_2\text{CO}_3(\text{OH})_{16}\cdot 4\text{H}_2\text{O}$)
I₀	Incident beam
I	Ionic strength
IAP	Ion activity product
ICP	Inductively-coupled plasma
IPA	Isopropanol alcohol
I_t	Transmitted beam
JRC	Joint Research Centre
LSC	Liquid scintillation counting
LCF	Linear combination fitting
LDH	Layered double hydroxide
LLW	Low-level waste
MAS	Magic angle spinning (at 54.74°)
MS	Mass spectrometry
MWCO	Molecular weight cut-off
N	Coordination number
NMR	Nuclear magnetic resonance

NNL	National Nuclear Laboratory
NRVB	Nirex reference vault backfill
NSLS-II	National Synchrotron Light Source II
OES	Optical emission spectroscopy
OPC	Ordinary Portland cement
ORNL	Oak Ridge National Laboratory
PC	Portland cement
PCM	Plutonium contaminated material
PFA	Pulverised fuel ash / fly ash
PMMA	Polymethyl methacrylate
PNNL	Pacific Northwest National Laboratory
PSD	Particle size distribution
pzc	Point of zero charge
R	Bond length / interatomic distance (Å)
R_d	Ratio of a sorbate partitioned onto a sorbent (L kg ⁻¹) K _d refers to the equilibrium value
S₀²	Amplitude reduction factor
SI	Saturation index
σ²	Sigma-squared (mean-square thermal disorder parameter)
SIT	Specific ion interaction theory
SPFT	Single pass flow-through
SS-NMR	Solid-state NMR
SEM/EDX	Scanning electron microscopy / energy dispersive X-ray
ThORP	Thermal Oxide Reprocessing Plant
TUoS	The University of Sheffield
XAFS	X-ray absorption / fluorescence spectroscopy
XANES	X-ray absorption near edge structure (spectroscopy)
XRF	X-ray fluorescence
XRD	X-ray diffraction
ζ	Symbol for zeta potential (mV); the electrical potential of a surface at the slipping plane (the interface between bulk fluid ions and fluid ions attached to a surface)

Contents

Chapter 1 – Introduction	1
Chapter 2 – Literature review	5
2.1 Introduction and Background	5
2.1.1 Portland cement	5
2.1.2 Cement hydration	5
2.1.3 Major hydration products	6
2.1.3.1 <i>Calcium-silicate-hydrates (C-S-H)</i>	6
2.1.3.2 <i>Portlandite (CH)</i>	7
2.1.4 Minor Hydration Products	7
2.1.4.1 <i>AFm phases</i>	7
2.1.4.2 <i>AFt phases</i>	7
2.1.5 Supplementary cementitious materials	8
2.1.5.1 <i>Fly ash (FA)</i>	8
2.1.5.2 <i>Blast-furnace slag (BFS)</i>	9
2.1.5.3 <i>Silica fume (SF)</i>	9
2.1.6 Geological disposal	9
2.1.6.1 <i>Cementitious repository conditions</i>	10
2.2 Uranium	11
2.2.1 Solubility and speciation of uranium	11
2.2.1.1 <i>U(IV) solubility / speciation in alkaline conditions</i>	11
2.2.1.2 <i>Oxidative dissolution</i>	13
2.2.1.3 <i>U(VI) solubility / speciation in alkaline conditions</i>	13
2.2.1.4 <i>Hydrous alkali / alkali-earth uranates</i>	13
2.2.1.5 <i>Uranium speciation in cementitious environments</i>	14
2.2.1.6 <i>Hydrous calcium uranate</i>	14
2.2.1.7 <i>Uranyl carbonates</i>	15
2.2.2 Uranium uptake by Portland cement and C-S-H	16
2.2.2.1 <i>Natural uranium minerals as analogues for cementitious speciation</i>	19
2.2.3 Uranium uptake by other cement phases	20
2.2.3.1 <i>Silica</i>	20
2.2.3.2 <i>Carbonate layered double hydroxides (LDH-CO₃)</i>	21
2.3 Plutonium	22
2.3.1 Solubility and speciation of plutonium	22
2.3.1.1 <i>Alkaline media</i>	23
2.3.1.2 <i>Pu(IV) colloids</i>	26

2.3.1.3 Acidic media	26
2.3.1.4 Plutonium solubility and speciation in cementitious environments	27
2.3.2 Plutonium immobilisation in cement matrices and cement phases	30
2.3.2.1 Plutonium uptake by cement matrices	30
2.3.2.2 The role of C-S-H and proposed mechanisms of uptake	30
2.3.2.3 Plutonium sorption by C-S-H: A study by Haußler et al.....	33
2.3.2.4 PuO ₂ encapsulation in cement matrices: A study by Kearney et al.	34
2.3.2.5 Plutonium leaching from cement matrices	35
2.3.3 Plutonium interactions with other related cementitious phases.....	36
2.3.3.1 Minor cement hydrate phases	36
2.3.3.2 Calcite	36
2.4 Technetium	37
2.4.1 Solubility and speciation of technetium	37
2.4.1.1 Tc(IV) solubility in alkaline solution	38
2.4.1.2 Tc(VII) solubility in alkaline solution	39
2.4.1.3 Technetium solubility in cement equilibrated solution: A study by Pilkington.	39
2.4.2 Technetium immobilisation in cement matrices	40
2.4.2.1 Reductive immobilisation	40
2.4.2.2 Speciation of “grout-reduced” technetium	41
2.4.2.3 Non-reductive immobilisation.....	42
2.4.2.4 Technetium immobilisation in ettringite: A study by Saslow et al.....	44
2.5 Summary and Research Scope	45
2.5.1 Summary of literature findings.....	45
2.5.1.1 Uranium.....	45
2.5.1.2 Plutonium	45
2.5.1.3 Technetium	45
2.5.2 Scope of the research in this Thesis	45
Chapter 3 – Experimental methods	47
3.1 Cement phase syntheses	47
3.1.1 Materials	47
3.1.2 C-S-H synthesis	47
3.1.3 Hydrotalcite synthesis	48
3.1.4 Ettringite synthesis.....	48
3.1.5 Pre-carbonation of phases	49
3.2 Characterisation methods	49
3.2.1 X-ray diffraction (XRD)	49
3.2.1.1 Experimental XRD methods used in this Thesis:	50

3.2.1.2 Rietveld refinement and crystallite size	51
3.2.2 Particle size distribution (PSD)	51
3.2.2.1 Experimental PSD method used in this Thesis:.....	51
3.2.3 Zeta (ζ) potential measurements	52
3.2.3.1 Experimental ζ -potential method used in this Thesis:.....	52
3.2.4 Solid-state nuclear magnetic resonance spectroscopy (SS-NMR).....	52
3.2.4.1 Experimental MAS SS-NMR methods used in this Thesis:.....	53
3.2.5 Synchrotron X-ray absorption/fluorescence spectroscopy (XAFS).....	53
3.2.5.1 Experimental XAS methods used in this Thesis:.....	55
3.2.5.2 Beamline set-up.....	55
3.2.5.3 Data processing: XANES.....	56
3.2.5.4 Data processing: EXAFS	57
3.2.6 Scanning electron microscopy / energy dispersive X-ray (SEM/EDX) spectroscopy	59
3.2.6.1 Experimental SEM/EDX methods used in this Thesis:	59
3.3 Solution analyses	60
3.3.1 pH measurements	60
3.3.2 Inductively coupled plasma techniques (ICP-OES/MS)	60
3.3.2.1 Experimental ICP-OES/MS methods used in this Thesis:	60
3.3.3 Liquid scintillation counting.....	61
3.3.3.1 Experimental LSC methods used in this Thesis:	61
3.3.4 Alpha spectrometry	62
3.3.4.1 Experimental Alpha spectrometry methods used in this Thesis:.....	62
3.4 Thermodynamic modelling	62
3.4.1 Phreeqc.....	62
3.4.1.1 Experimental Phreeqc methods used in this Thesis:.....	63
Chapter 4 – Characterisation of precursor cement minerals and X-ray absorption spectroscopy standards	65
4.1 Introduction.....	65
4.2 Experimental	65
4.2.1 Cement minerals	65
4.2.2 X-ray absorption / fluorescence spectroscopy standards.....	65
4.3 Results I: Cement minerals	67
4.3.1 C-S-H.....	67
4.3.1.1 Pre-carbonated C-S-H phases.....	71
4.3.2 Hydrotalcite	73
4.3.3 Ettringite.....	74

4.3 Results II: XAFS standards	76
4.3.1 Uranium compounds	76
4.3.1.1 <i>Uranium oxides and uranyl nitrate: XAFS</i>	77
4.3.2 Uranium minerals	81
4.3.2.1 <i>XRD</i>	81
4.3.2.2 <i>XAFS</i>	85
4.3.2.3 <i>EXAFS fitting of uranyl silicate models</i>	91
4.3.2.4 <i>EXAFS fitting of other uranium mineral phases</i>	92
4.3.2.5 <i>EXAFS fitting of uranophane (B)</i>	92
4.3.3 Rhenium compounds	93
4.3.3.1 <i>XAFS</i>	94
4.3.3.2 <i>EXAFS fitting of Re compounds</i>	97
4.3.4 Technetium compounds.....	97
4.3.4.1 <i>XAFS</i>	98
4.3.4.2 <i>EXAFS fitting of Tc compounds</i>	100
4.4 Discussion	100
4.4.1 Cement hydrate phases	100
4.4.1.1 <i>C-S-H</i>	100
4.4.1.2 <i>Minor cement hydrate phases</i>	101
4.4.2 X-ray absorption / fluorescence standards	102
4.4.2.1 <i>Uranium standards</i>	102
4.4.2.2 <i>Rhenium and technetium standards</i>	103
4.5 Conclusions	105
Chapter 5 – Identification and characterisation of secondary uranium phases in cementitious systems	107
5.1 Introduction	107
5.2 Experimental Methods	107
5.2.1 Uranium contact experiments.....	107
5.2.1.1 <i>C-S-H phases</i>	107
5.2.1.2 <i>Minor cement hydrate phases</i>	108
5.2.1.3 <i>Solution and solid-state analyses</i>	108
5.2.2 X-ray absorption spectroscopy.....	108
5.2.3 Nuclear magnetic resonance spectroscopy.....	110
5.2.4 Geochemical modelling.....	111
5.3 Results	111
5.3.1 U(VI)-contacted C-S-H phases: <i>Preliminary analysis</i>	111
5.3.1.1 <i>Mineral ageing</i>	112

5.3.2 U(VI)-contacted C-S-H phases: <i>All Ca/Si ratios with 0.5 mM U(VI)</i>	114
5.3.2.1 <i>Ca and Si release, non-carbonated</i>	114
5.3.2.2 <i>Ca and Si release, pre-carbonated</i>	116
5.3.2.3 <i>X-ray diffraction</i>	119
5.3.3 U(VI)-contacted C-S-H phases: <i>All Ca/Si ratios with 10 mM U(VI)</i>	122
5.3.3.1 <i>Ca and Si release, non-carbonated</i>	122
5.3.3.2 <i>Ca and Si release, pre-carbonated</i>	124
5.3.3.3 <i>X-ray diffraction</i>	126
5.3.4 U(VI)-contacted minor cement phases	129
5.3.4.1 <i>Elemental release</i>	129
5.3.4.2 <i>X-ray diffraction</i>	132
5.3.5 Geochemical modelling results.....	134
5.3.6 X-ray absorption spectroscopy: XANES	137
5.3.6.1 <i>Linear combination fitting</i>	137
5.3.6.2 <i>U(VI)-CSH(X) linear combination fitting</i>	139
5.3.6.3 <i>U(VI)-hydrotalcite linear combination fitting</i>	144
5.3.7 X-ray absorption spectroscopy: EXAFS.....	145
5.3.7.1 <i>EXAFS fitting of U(VI)-contacted C-S-H phases</i>	145
5.3.7.2 <i>Fitting of 0.5 mM U(VI)-contacted C-S-H phases</i>	149
5.3.7.3 <i>Fitting of 10 mM U(VI)-contacted C-S-H phases</i>	150
5.3.7.4 <i>Fitting of pre-carbonated U(VI)-contacted C-S-H phases</i>	151
5.3.7.5 <i>EXAFS fitting of U(VI)-contacted hydrotalcite phases</i>	155
5.3.8 ²⁹ Si Nuclear magnetic resonance spectroscopy.....	157
5.3.8.1 <i>C-S-H with Ca/Si = 0.6</i>	157
5.3.8.2 <i>C-S-H with Ca/Si = 1.2</i>	161
5.3.9 ²⁷ Al Nuclear magnetic resonance spectroscopy	164
5.3.9.1 <i>Ettringite</i>	164
5.3.9.2 <i>Hydrotalcite</i>	166
5.4 Discussion	167
5.4.1 U(VI)-C-S-H systems.....	167
5.4.1.1 ²⁹ Si NMR.....	168
5.4.1.2 <i>EXAFS: 0.5 mM U(VI)-contacted C-S-H</i>	171
5.4.1.3 <i>EXAFS: 10 mM U(VI)-contacted C-S-H phases</i>	172
5.4.1.4 <i>Formation of calcium uranates</i>	173
5.4.1.5 <i>Mineral ageing</i>	175
5.4.2 U(VI)-ettringite systems	176
5.4.3 U(VI)-hydrotalcite systems	177

5.5 Conclusions and further work	178
5.5.1 Conclusions	178
5.5.2 Further work.....	179
Chapter 6 – Effect of high plutonium loading on C-S-H phases	181
6.1 Introduction	181
6.2 Experimental Methods	181
6.2.1 Part 1 – U(VI) as a Pu(VI) surrogate	181
6.2.1.1 U(VI) / C-S-H hydrothermal ageing.....	181
6.2.1.2 Pu(VI) / C-S-H contact studies.....	183
6.2.2 Part 2 – U(IV) as a Pu(IV) surrogate: a lower concentration study	185
6.2.3 Geochemical modelling.....	187
6.2.4 PuO ₂ encapsulation in Portland cement blends.....	187
6.3 Results	188
6.3.1 Plutonium (VI) contacted with C-S-H.....	188
6.3.1.1 Plutonium contacted C-S-H(0.6).....	189
6.3.1.2 Plutonium contacted CSH(0.6): pre-carbonated	190
6.3.1.3 Plutonium contacted CSH(1.2)	190
6.3.1.4 Plutonium contacted CSH (1.2): pre-carbonated	191
6.3.2 Uranium(IV) contacted with C-S-H	192
6.3.2.1 Uranium contacted CSH(0.6).....	193
6.3.2.2 Uranium contacted CSH(0.6): pre-carbonated.....	194
6.3.2.3 Uranium contacted CSH(1.2).....	194
6.3.2.4 Uranium contacted CSH(1.2): pre-carbonated.....	196
6.3.3 Geochemical modelling results	197
6.3.4 PuO ₂ encapsulation in Portland cement blends.....	201
6.3.4.1 Solid-phase analyses	201
6.3.4.2 Solution analyses	203
6.4 Discussion	206
6.4.1 Pu(VI)/(VI) behaviour in C-S-H suspension	206
6.4.1.1 Effect of carbonation.....	208
6.4.2 Origin of PuO ₂ ·xH ₂ O.....	208
6.4.2.1 PuO ₂ ·xH ₂ O crystallite size	209
6.4.3 PuO ₂ encapsulated in cement matrices.....	211
6.4.3 U(IV) behaviour in C-S-H suspension	211
6.5 Conclusions and further work	212
6.5.1 Conclusions	212
6.5.2 Further work.....	213

Chapter 7 – Rhenium and technetium uptake and coordination in cementitious environments.....	215
7.1 Introduction.....	215
7.2 Experimental	215
7.2.1 Rhenium sorption experiments	215
7.2.1.1 C-S-H phases	215
7.2.1.2 Minor cement phases.....	216
7.2.1.3 Solution and solid phase analyses.....	217
7.2.2 Technetium sorption experiments.....	217
7.2.2.1 C-S-H phases	217
7.2.2.2 Minor cement phases.....	218
7.2.2.3 Solution and solid phase analyses.....	218
7.2.3 Calculation of mass changes.....	219
7.2.3.1 R_d values	219
7.2.3.2 Percentage mass loss of Re-contacted minor phases and controls	219
7.2.4 X-ray absorption / fluorescence measurements.....	220
7.2.4.1 Preparation of Re L_{III} -edge XAFS samples.....	220
7.2.4.2 Preparation of Tc K-edge XAFS samples.....	220
7.3 Results I: Sorption / Uptake	223
7.3.1 Rhenium uptake by C-S-H phases	223
7.3.1.1 X-ray diffraction.....	224
7.3.2 Rhenium uptake by minor cement phases.....	226
7.3.2.1 Percentage mass change	227
7.3.2.2 X-ray diffraction.....	232
7.3.3 Technetium uptake by C-S-H phases	235
7.3.3.1 X-ray diffraction.....	236
7.3.4 Technetium uptake by minor cement phases	238
7.3.4.1 Percentage mass loss of controls	238
7.3.4.2 X-ray diffraction.....	243
7.4 Results II: X-ray absorption spectroscopy	243
7.4.1 XANES.....	243
7.4.1.1 Linear combination fitting	246
7.4.1.2 Re-contacted phases.....	252
7.4.1.3 Tc-contacted phases.....	253
7.4.2 EXAFS	254
7.4.2.1 EXAFS fitting of Re-contacted phases	258
7.4.2.2 EXAFS fitting of Tc-contacted phases.....	259

7.5 Discussion	264
7.5.1 Rhenium uptake and coordination in cement phases	265
7.5.1.1 <i>C-S-H, portlandite and calcite</i>	265
7.5.1.2 <i>Ettringite and calcium sulfate</i>	266
7.5.1.3 <i>Ettringite and Re-sulfate formation</i>	267
7.5.1.4 <i>Hydrotalcite</i>	268
7.5.2 Technetium uptake and coordination with cement phases	268
7.5.2.1 <i>C-S-H, portlandite and calcite</i>	268
7.5.2.2 <i>Ettringite and calcium sulfate</i>	269
7.5.2.3 <i>Hydrotalcite</i>	269
7.6 Conclusions and further work	269
7.6.1 Rhenium as a technetium surrogate	269
7.6.2 Implications for waste disposal	271
7.6.3 Further work	271
Chapter 8 – Concluding remarks	273
Appendix 1	277
Appendix 2	279
References	281

Chapter 1 – Introduction

Nuclear power generation is currently a reliable energy source world-wide and, in the UK, provides between 16 to 20% of electricity to the national grid [1]. The production of radioactive wastes arises from a wide range of operations throughout the civil nuclear power industry, as well as from military, research and medical operations [2]. The types of waste streams produced from nuclear activities in the UK can be generally sub-categorised into three main areas of low-level waste (LLW), intermediate-level waste (ILW) and high-level waste (HLW) which vary by their measure of radioactivity and whether or not they are heat generating [3,4].

Cement materials are ubiquitous in their use in the nuclear industry. These uses range from structural applications in nuclear plant and processing buildings, to encapsulation of LLW and ILW waste streams [5–8]. In all of these environments, cement materials will come into contact with uranium, minor actinides and a range of radionuclide fission products. Due to the long-lived nature of many of these radioactive isotopes, the materials that come into contact with them require long-term management (>100,000 years) to ensure the safety of the environment and future populations. The accepted management plan is disposal in a geological repository, itself constructed using cementitious materials [9]. Therefore, understanding the interaction of relevant radionuclides with cement materials is of particular importance to understand the long-term safety of disposal.

Portland cement grouts are the most common type of cement used in the nuclear industry applications outlined above [5,8]. On addition of water, anhydrous Portland cement clinker undergoes hydration to form cement hydrate phases that form a composite mineral matrix. The main binder phase of Portland cements is calcium-silicate-hydrate (C-S-H), which is intermixed with portlandite ($\text{Ca}(\text{OH})_2$) and other minor cement hydrate phases [10]. These minor cement hydrate phases may further contain sulfur, aluminium, magnesium, carbon or iron present in the initial cement clinker or additives, and examples include, but are not limited to, ettringite ($\text{Ca}_6\text{Al}_2(\text{SO}_2)_3(\text{OH})_{12}\cdot 26\text{H}_2\text{O}$) and layered double hydroxides (e.g. hydrotalcite, $(\text{Mg}_6\text{Al}_2(\text{CO}_3)(\text{OH})_{16}\cdot 4\text{H}_2\text{O})$ minerals [11–13].

Portland cement grouts used in nuclear waste immobilisation are amended by substitution of a portion of the anhydrous clinker with supplementary cementitious materials, such as blast-furnace slag (BFS), pulverised fuel ash / fly ash (PFA), silica fume (SF) and, in the case of geological disposal backfill, limestone [5,6,14]. These supplementary materials are by-products of industrial processes, e.g. iron ore smelting and coal burning, therefore they are chemically complex, and often highly variable in their composition. As such, the resulting cement systems are highly heterogeneous and the mechanisms that govern interactions between cement and radionuclide species can be difficult to ascertain. The use of the single

cement mineral phases C-S-H, ettringite and hydrotalcite, offers a simplified alternative to underpin the specific interactions of radionuclides with cement materials.

The interaction between cement minerals and three selected radionuclides were considered as the subject of this Thesis:

Uranium (U) - This actinide is at the centre of the nuclear industry due to its use as nuclear fuel. A significant range of wastes containing uranium isotopes will therefore be generated throughout the nuclear fuel cycle, which may be cemented [15]. In the UK, until the recent closure of the ThORP facility at Sellafield [3], spent nuclear fuel was reprocessed to remove the usable uranium. This required removal of fuel cladding from the fuel, which contains uranium contamination and is disposed of in cement grout and classified as ILW [16–18].

Plutonium (Pu) - A high yield neutron capture product of uranium, plutonium was separated from spent nuclear fuel during reprocessing operations at ThORP [19]. The resulting plutonium dioxide (PuO_2 , 140 tonnes) is stored at the Sellafield site until a decision is made about its re-use, until which time it requires periodic treatment and repackaging. These operations generate materials contaminated with plutonium (e.g. gloves, filters, metal containers etc.), known as plutonium contaminated material (PCM). PCM is super-compacted into “pucks” which are placed in a standard 500 L stainless steel nuclear waste drum and the surrounding annulus infilled with a PFA-substituted Portland cement grout [16,17,20–22].

Technetium (Tc) - Technetium-99 (^{99}Tc) is a beta-emitting fission product of uranium-235 (^{235}U) or plutonium-239 (^{239}Pu) [23]. Generated during reprocessing, this radionuclide is immobilised with other fission products in a vitreous wasteform, however, the relatively low volatilisation temperature makes heat treatment challenging [24]. An alternative wasteform for ^{99}Tc -bearing reprocessing wastes is cement grout, which is currently being investigated for the immobilisation of historic military reprocessing wastes generated in the USA. These grouts typically contain a reducing component, such as sulfur-rich slag, to reduce pertechnetate (Tc(VII)O_4^-) to less soluble reduced Tc(IV) species [25]. However, the retention of pertechnetate by cement minerals is not well understood.

The objectives of this Thesis are to:

- 1) Understand how the actinides U(VI) and Pu(VI) behave when in contact with individual cement mineral phases, in terms of their chemical coordination and local environment, and to determine how their behaviour compares, considering the hypotheses;

In contact with low Ca/Si ratio (< 0.8) C-S-H phases, will uranium adopt the same coordination environment as established for intermediate and high Ca/S ratios (> 0.8) C-S-H phases?

Can ^{29}Si and ^{27}Al solid state NMR be used to infer the coordination of uranium in contact with C-S-H, hydrotalcite and ettringite minerals?

Is uranium(VI) a useful chemical surrogate for aqueous plutonium(VI), under pseudo-simulated analogous conditions, in contact with C-S-H phases?

- 2) Understand the sorption and uptake behaviour of Re(VII) and Tc(VII) in cementitious environments and evaluate the usefulness of rhenium as a surrogate for ^{99}Tc , considering the hypotheses;

Is rhenium(VII) a useful chemical surrogate for technetium(VII), under non-reducing conditions, in contact with major and minor cement hydrate phases?

Will technetium(VII) sorption onto C-S-H phases change as function of Ca/Si ratios?

Can the role of sulfate in minor hydrate phases (e.g. ettringite) on technetium(VII) uptake be ascertained using sorption experiments?

The background literature, experiments and investigations performed to meet these objectives are presented in a series of Chapters in this Thesis, as follows:

Chapter 2 is a discussion of relevant literature on the solubility and speciation behaviour of uranium, plutonium and technetium under cementitious and highly alkaline conditions, and details studies to date that investigate the interactions of these radionuclides with cement materials.

Chapter 3 details the experimental methodologies adopted throughout this Thesis. The experimental work was performed using ^{238}U and ^{99}Tc isotopes at the HADES facility at The University of Sheffield and plutonium at the National Nuclear Laboratory and the Joint Research Centre (^{240}Pu and ^{239}Pu). The use of X-ray absorption / fluorescence spectroscopy (XAFS) and solid-state nuclear magnetic resonance (SS-NMR) spectroscopy were key techniques utilised in these investigations, and these experiments performed at the Diamond Light Source, KEK and The University of Sheffield are detailed herein.

Chapter 4 describes the synthesis and characterisation of the cement hydrate phases C-S-H, ettringite ($\text{Ca}_6\text{Al}_2(\text{SO}_2)_3(\text{OH})_{12}\cdot 26\text{H}_2\text{O}$) and hydrotalcite ($\text{Mg}_6\text{Al}_2(\text{CO}_3)(\text{OH})_{16}\cdot 4\text{H}_2\text{O}$) used in the Thesis as 'simplified' models of the related intermixed phases that form in composite Portland cement grouts. Also described is the characterisation of uranium-, rhenium- and technetium-bearing standard phases that could be considered relevant for the respective coordination environments and speciation of these nuclides in cement matrices.

Chapter 5 describes experiments whereby the speciation of U(VI) was investigated after aqueous contact with C-S-H, ettringite and hydrotalcite phases. Studies already published in

the literature have shown that U(VI) will sorb to C-S-H phases, however, this Chapter presents the first consideration of the uranyl silicate phases haiweeite ($\text{Ca}(\text{UO}_2)_2(\text{Si}_5\text{O}_{12})(\text{OH})_2 \cdot 6\text{H}_2\text{O}$) and weeksite ($\text{K}_2(\text{UO}_2)_2(\text{Si}_5\text{O}_{12})(\text{OH})_4\text{H}_2\text{O}$) as natural mineral analogues to determine the speciation of U(VI) in cement matrices.

Chapter 6 describes experiments conducted with aqueous Pu(VI) in an attempt to understand plutonium speciation after aqueous contact with C-S-H, and how its behaviour differs from that of U(VI). The aqueous solution behaviour of plutonium has been demonstrated to be very complex due to alpha-radiolysis effects and complicated redox chemistry. Also detailed in this Chapter is a study of the effects of encapsulated PuO_2 solids on the microstructural development of the surrounding cement matrix.

Chapter 7 is an evaluation of Re(VII) as a surrogate for the uptake and sorption of $^{99}\text{Tc}(\text{VII})$ by C-S-H, ettringite, hydrotalcite and other minor cement phases. Experiments were conducted with both rhenium and technetium, however the relative safety of rhenium, comparative to beta-emitting ^{99}Tc , allowed more versatile handling and a wider range of solution analyses.

Finally, **Chapter 8** is a summary of the experimental findings and concluding remarks.

Chapter 2 – Literature review

2.1 Introduction and Background

This Chapter includes a discussion of the hydrate phase assemblage of Portland cement and cement blends, used in the long-term management and potentially geological disposal of intermediate level waste (ILW). Further to this, the solubility and speciation of the radionuclides uranium, plutonium and technetium, which are studied throughout this Thesis, is described in detail (**Sections 2.2, 2.3 and 2.4**). The review also includes a discussion on the behaviour of the radionuclides relevant to a cementitious repository and in contact with particular cement hydrate phases, as well as other conditions used in this Thesis. Finally, the importance of the research detailed herein is outlined in **Section 2.5**.

2.1.1 Portland cement

Portland cement clinker, the precursor to hydrated Portland cement, is made-up of the raw materials calcium oxide (lime; CaO) from limestone and silica (SiO₂), alumina (Al₂O₃) and iron oxide (Fe₂O₃) from clays, shale and sand. The raw materials are heated to 1400-1450 °C in a kiln which results in the formation of agglomerated nodules which are then ground and mixed with calcium sulfate (usually in the form of gypsum; CaSO₄·2H₂O) to create anhydrous cement powder. The four main mineral constituents of cement powder are outlined in **Table 2.1.1** with a minor percentage of cement powder comprised of unreacted lime, a small amount of gypsum and other minor impurities such as alkali sulfates [11,26,27].

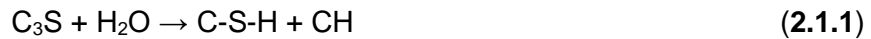
Table 2.1.1: A summary of the four main mineral species found in Portland cement clinker, where C = CaO, S = SiO₂, A = Al₂O₃ and F = Fe₂O₃.

	Ideal oxide composition	Cement notation	Percentage composition (approx.)
Alite	3CaO·SiO ₂	C ₃ S	60
Belite	2CaO·SiO ₂	C ₂ S	20
Aluminate	3CaO·Al ₂ O ₃	C ₃ A	10
Ferrite	4CaO·Al ₂ O ₃ ·Fe ₂ O ₃	C ₄ AF	10

2.1.2 Cement hydration

On addition of water to cement powder, the mineral components react with water and undergo dissolution, subsequently precipitating hydrated minerals; termed hydration reactions [11]. Hydration reactions allow water to be incorporated into the structure of newly precipitated cement products, which overtime form a hardened cement paste with a complex structure. The calcium silicates are first to react and produce portlandite (Ca(OH)₂) and the C-S-H gel

phase (calcium silicate hydrate); the main components that lead to early setting strength (see **Section 2.1.3**) [11]:



Equation 2.1.1 is non-stoichiometric as C-S-H forms with varying amounts of calcium and silicon to give variations in the Ca/Si ratio [27]. Portlandite may not form as separate phase but can be interspersed in the C-S-H phase. C₂S is less soluble than C₃S and so the hydration reaction in this case is slower, with C₂S hydration products tending to contribute to the strength of mature cement paste [11]. C₃A and C₄AF phases also hydrate to form additional minor phases (see **Section 2.1.4**).

2.1.3 Major hydration products

2.1.3.1 Calcium-silicate-hydrates (C-S-H)

C-S-H gel is the bulk amorphous component of hardened cement paste and forms ~50 wt% of the cement matrix [11,28]. Two morphological forms of C-S-H are able to form in a cement; C-S-H(I) and C-S-H(II). The former forms a ‘crumpled foil’ type morphology which tends to elongate into a fibrous morphology at the highest Ca/Si, more akin to the mineral 14 Å tobermorite (Ca₅Si₆O₁₆(OH)₂·4H₂O). The latter, however, consists of bundles of fibres that are more ordered than C-S-H(I), and is not dissimilar to the mineral jennite (Ca₉Si₆O₁₈(OH)₆·8H₂O) [11]. The layered structure of C-S-H is depicted in **Figure 2.1.1** as the 14 Å tobermorite sublattice structure [29].

The XRD pattern of a bulk cement does not show defined diffraction peaks for a C-S-H phase but its presence is indicated by a diffuse scattering region [10]. C-A-S-H phases also form on incorporation of aluminium into the C-S-H structure, usually sourced from supplementary cementitious materials (SCMs) that contain high Al₂O₃ content (see **Section 2.1.5**). Aluminium is thought to substitute primarily into silicon sites of the “dreierketten unit” of the C-S-H phase, also shown in **Figure 2.1.1** [29,30].

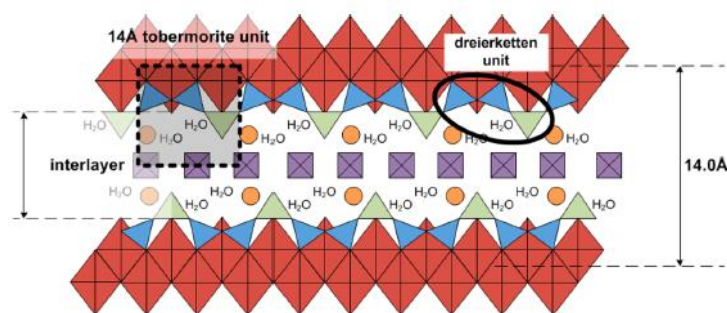


Figure 2.1.1: Schematic sublattice representation of 14 Å tobermorite (i.e. C-S-H(I)) (from [29]). Red diamonds = octahedral intralayer calcium; blue triangles = paired silicon tetrahedra; green triangles = bridging silicon tetrahedra; orange circles = charge balancing alkali cations; purple squares = interlayer protons and/or calcium cations.

2.1.3.2 Portlandite (CH)

Portlandite is the crystalline mineral form of calcium hydroxide which can be detected in an XRD pattern of a bulk cement by prominent diffraction peaks [10]. Although portlandite forms discrete crystals, it has already been established that this phase can be interspersed in the C-S-H phase. As portlandite is readily carbonated in air, this phase is partly responsible for the carbonation (CaCO_3 formation) of cements [11].

2.1.4 Minor hydration products

The remainder of the cement structure is made up of crystallites of minor hydration products [10,11,28]. Some minor phases arise from the cement clinker composition, however the type of SCM present can also dictate the formation of other minor phases (see **Section 2.1.5**) [12].

2.1.4.1 AFm phases

AFm phases have a layered-double hydroxide-type (LDH) structure and form on hydration of calcium aluminate in the presence of anionic species [11]. LDHs are a class of anionic clay, in contrast to more commonly encountered cationic clays, with a structure that is defined by stacked layers of edge-sharing octahedral hydroxides consisting of divalent and trivalent metal cations (**Figure 2.1.2**). Charge balancing is achieved through intercalation of interlayer anions [31]. Sulfate and carbonate are common anionic components dissolved in cement pore water and form monosulfate ($\text{Ca}_4(\text{Al}_2\text{O}_6)(\text{SO}_4)\cdot x\text{H}_2\text{O}$) and monocarbonate ($\text{Ca}_4(\text{Al}_2\text{O}_6)(\text{CO}_2)\cdot x\text{H}_2\text{O}$) phases, respectively. In the case of these phases, calcium and aluminium / iron are the hydroxides which form hexagonal lamellar plates, with water and anionic species filling the interlayer spaces [32].

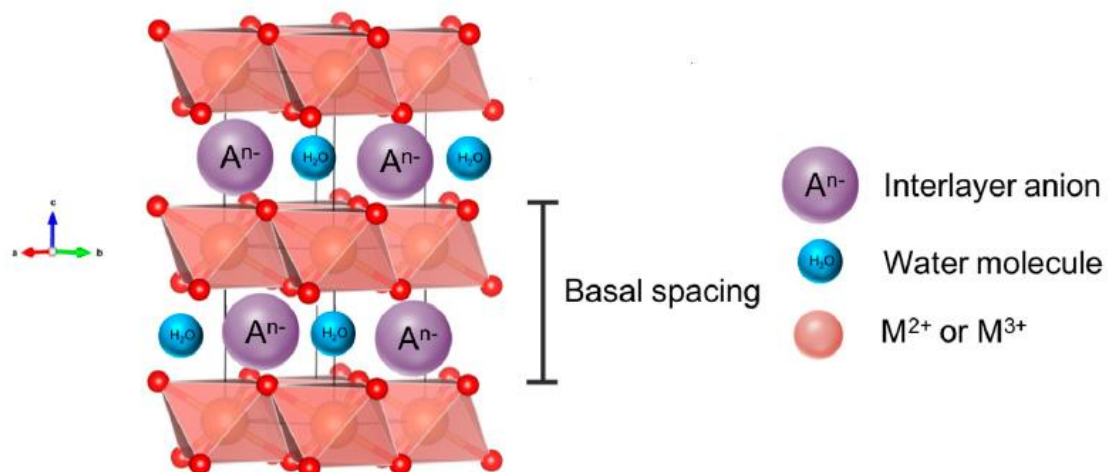


Figure 2.1.2: A schematic structure of a layered double hydroxide (from [33]). For AFm phases, M^{2+} = calcium, M^{3+} = aluminium (or iron), interlayer anions = sulfate, carbonate (or chloride).

2.1.4.2 AFt phases

Ettringite ($\text{Ca}_6(\text{Al}_2\text{O}_6)(\text{SO}_4)_3\cdot 32\text{H}_2\text{O}$), the AFt phase, contains three times the stoichiometric amount of sulfate as the monosulfate counterpart [11,34]. Ettringite is composed of calcium

and aluminium / iron hydroxide polyhedra that form channels, or a column-like structure, with water and sulfate anions filling the channel interlayers (**Figure 2.1.3**) [35]. The abundance of ettringite is dependent on the ratio of available aluminium and sulfate; as the Al/S ratio increases with increased hydration of C₃A in the cement paste, less sulfate is available for incorporation into ettringite crystals, which are then readily converted into monosulfate [11].

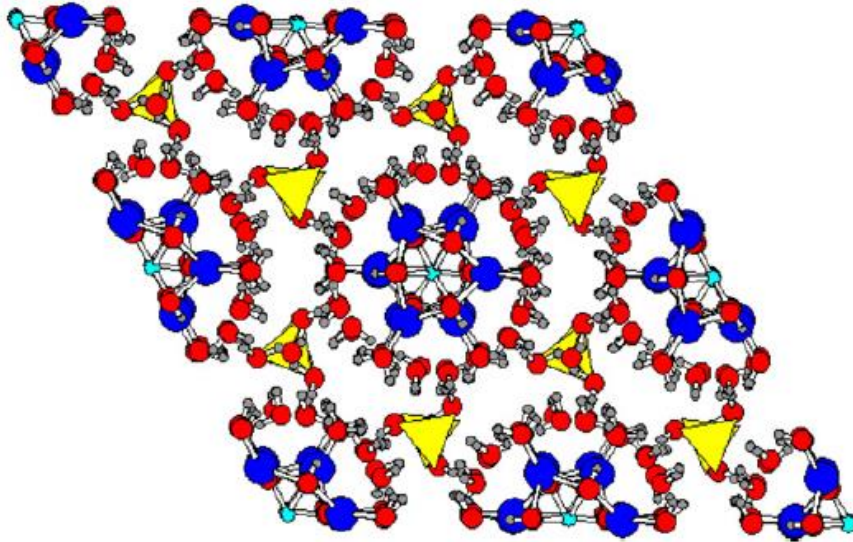


Figure 2.1.3: Crystal structure of ettringite projected along the (0001) plane (from [35]). $\text{Ca}_6[\text{Al}_2(\text{OH})_{12}\cdot 24\text{H}_2\text{O}]^{6+}$ columns lie parallel to the c-axis with sulfate and water molecules in the inter-column channels. Blue circles = calcium atoms, red circles = oxygen atoms, cyan circles, aluminium atoms, yellow triangles = sulfate tetrahedra, grey circles = hydrogen atoms.

2.1.5 Supplementary cementitious materials

Supplementary cementitious materials (SCMs) can be blended with PC, reducing the heat of hydration of cement clinker to discourage cracking of the wasteform, that may occur as a result of large thermal outputs [7,36]. The elements within these additives (including calcium, aluminium, magnesium, sulfate) in the anhydrous phase can be carried through during hydration reactions and form products in hardened cement paste [12]. This occurs via pozzolanic (e.g. in fly ash or silica fume) or latent (e.g. in blast-furnace slag) reaction of the additives in the presence of portlandite and / or water, to form minor secondary hydrate phases [37,38]. High amounts of additives will likely be used in cements for a geological repository (see **Section 2.1.6** on “Geological disposal”) [6].

2.1.5.1 Fly ash (FA)

Fly ash is a by-product of coal burning at temperatures exceeding 1000 °C. When the residual ash from inorganic aluminosilicate impurities cools, it forms spherical particles with a high silica content. During hydration of a cement blend, the addition of this extra silica reduces the

Ca/Si ratio of the C-(A)-S-H phase [37,38]. FA/PC blends have historically been, and are currently used to infill compacted pucks of plutonium contaminated material (PCM) waste streams into 500 litre steel drums [16,17,20–22].

2.1.5.2 Blast-furnace slag (BFS)

Blast-furnace slag arises from the quenching of molten iron during ore-smelting processes, which is generally an alumina-calcium glass containing a wide range of other elements such as silicon, magnesium and sulfur. Upon hydration of slag, calcium and silicon migrate outwards (to form C-(A)-S-H) and leave a concentrated pool of magnesium and aluminium which are incorporated into hydrotalcite-type LDH phases $[(M^{2+}_{1-x}M^{3+}_x)(OH)_2]^{x+}$. With reference to **Figure 2.1.2**, the hydrotalcite structure $(Mg_6Al_2CO_3(OH)_{16}\cdot 4H_2O)$ can be represented with magnesium and aluminium as M^{2+} and M^{3+} , respectively, and partial replacement of hydroxyl interlayer anions with carbonate anions [13,37]. Further to this, sulfide species (S^{2-} , S_2^{2-}) from slags are beneficial for the immobilisation of redox active contaminants. Although they do not themselves form hydration products, the imposed reducing conditions can act to reductively precipitate highly mobile, oxidised contaminants [5,26,39].

Ground granulated blast-furnace slag (GGBS) is a very fine powdered form of slag that is used to encapsulate a range of ILW streams [19]. Spent Magnox fuel cladding (a.k.a. swarf) and Magnox sludges, contaminated with uranium isotopes and fission products, are encapsulated / immobilised using GGBS/PC grouts [16–18].

2.1.5.3 Silica fume (SF)

Silica fume is a by-product of silicon metal / alloy production. When quartz is heated to high temperatures of up to 2000 °C, SiO_2 vapour oxidises and condenses to form nano-crystalline silica. The SiO_2 content of silica fume is >85 wt %, primarily vitreous (with small crystalline inclusions), resulting in a C-S-H phase whereby the Ca/Si ratio is significantly reduced in SF/PC blends [12,37,38]. Silica fume may be used at high replacement levels of Portland cement in the construction of a geological disposal vault backfill [6].

2.1.6 Geological disposal

In the long-term management of radioactive waste, a geological disposal facility (GDF) is proposed for the UK and is, generally, internationally agreed upon as one of the best practicable options for radioactive waste disposal [40,41]. A GDF will be constructed deep underground and will consist of a multi-barrier system to mitigate the release of radioactivity, over hundreds of thousands of years (**Figure 2.1.4**) [2,9];

- In the case of an ILW repository, wasteforms will likely be fabricated using cementation techniques, often Portland cements and SCMs, as described in **Section 2.1.5**;

- These wasteforms will be contained within waste packages, typically steel canisters, which will be placed at 200-1000 metres below ground;
- Waste packages will then be surrounded by a backfill or buffer material, which may consist of a clay or cement, to provide chemical conditioning;
- The host rock will then act as the final physical barrier surrounding and containing the engineered facility [2,14,15,42,43].

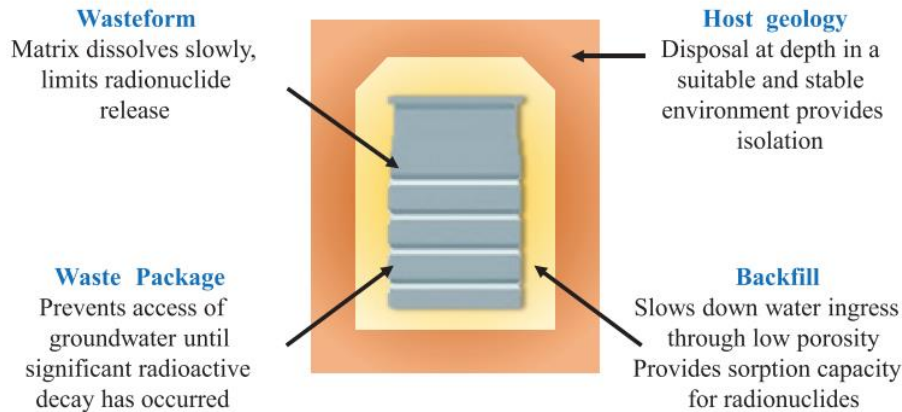


Figure 2.1.4: The multi-barrier concept (from [2]).

The final structure and design of an GDF in the UK is yet to be determined, as it requires the ongoing selection of an appropriate site [41,42]. However, it is conceivable that cement materials will be used in abundance at various stages in the construction of a GDF, as has already been established for similar facilities in other European countries and the USA [42]. For an ILW repository, this will likely be inclusive of waste package design, backfill for chemical conditioning, and construction purposes, such as fracture grouting, shotcrete and tunnel plugs for mechanical stabilisation [6,44].

2.1.6.1 Cementitious repository conditions

The local, early conditions in a cementitious repository will be imposed predominantly by the surrounding cementitious backfill. Cement equilibrated pore waters will result in a high pH, due to dissolution of alkali hydroxides, calcium hydroxides and calcium-silicate-hydrates [44]. This high alkalinity is beneficial in that it 1) promotes a high, selective sorption capacity of cement mineral and geological surfaces and 2) decreases the solubility of radionuclides [16,44] to retard their release, from the site of disposal, into the geosphere. Furthermore, while it is expected that redox conditions in a repository will be primarily be reducing, post-closure, the eventual ingress of oxygenated ground and surface waters will impose oxidising conditions to some extent [44]. It is therefore important to gain a fundamental understanding of the solubility, speciation and behaviour of radionuclides under alkaline and repository relevant

conditions, to understand how they will interact with cementitious materials. This is addressed for uranium, plutonium and technetium in the following sections.

2.2 Uranium

Uranium (U) is an actinide at the centre of the nuclear fuel cycle; natural uranium ore, uraninite (UO_2), is mined for its use as nuclear fuel. The two most naturally abundant isotopes of uranium are uranium-238 (^{238}U) and uranium-235 (^{235}U) which make up ~99.3 and ~0.7 % of the total isotopic abundance. In Magnox reactors, natural uranium was used as the nuclear fuel source but in more recent advanced-gas cooled reactors, ^{235}U enrichment is required. Until recently in the UK, once UO_2 fuel had been used within a nuclear reactor, it was reprocessed to remove the usable uranium and plutonium (to recycle into new fuel) and highly active fission products, which are immobilised in a borosilicate glass matrix. Prior to reprocessing, the used nuclear fuel is removed from its cladding, which is disposed of in cement grout and classified as an intermediate level waste (ILW) [3,4]. The cement grout will come into contact with uranium fuel fragments that remain attached to the cladding (particularly for earlier Magnox-type cladding). Cement grout is also used to immobilise plutonium-contaminated materials (PCM), and the primary decay product of plutonium is uranium. Therefore, cements encapsulating PCM will, in the future, also contain uranium isotopes.

2.2.1 Solubility and speciation of uranium

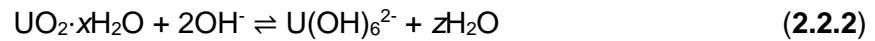
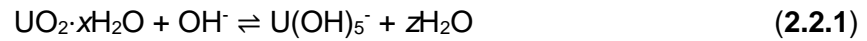
Uranium has the electronic configuration $[\text{Rn}] 5f^3 6d^1 7s^2$ and predominantly resides in the +4 or +6 oxidation state. The +5 oxidation state of uranium has a strong preference for disproportionation to +4 and +6 states, as well as being readily oxidised to U(VI) [45]. Although U(V) compounds will therefore be intermediately observable, U(IV) and U(VI) will be considered as the dominant oxidation states of uranium under aqueous reducing and oxidising conditions, respectively. In aqueous solution the +6 oxidation state is considered soluble and mobile, whereas the +4 oxidation state is considered insoluble and limits the mobility of uranium. The speciation of uranium at higher pH values is most relevant for the conditions that will be present in a cementitious repository for ILW.

2.2.1.1 U(IV) solubility / speciation in alkaline conditions

The solubility of U(IV) in the alkaline region has been studied to some extent. *Fujiwara et al.* investigated the solubility of $\text{UO}_2 \cdot x\text{H}_2\text{O}$ at pH 12-14 (0.5 to 2 M NaClO_4) under reducing conditions ($\text{Na}_2\text{S}_2\text{O}_4$, $E_h = -700$ mV), in the absence of carbonate [46]. The total uranium concentration was shown to increase with increasing pH (**Figure 2.2.1**), with less than 10^{-8} M established as U(VI). *Ryan & Rai* (pH ~13, ~0.1 - 10 M NaOH) and *Tremaine et al.* (pH 11.5

and 12.5, LiOH) also noted an increase in UO_2 solubility with pH under reducing conditions [47,48].

Fujiwara et al. determined that below pH 13.5, the $\text{U}(\text{OH})_5^-$ (aq) hydrolysis product would dominate aqueous speciation and above pH 13.5, the $\text{U}(\text{OH})_6^{2-}$ (aq) species would dominate, according to Equations 2.2.1 and 2.2.2:



where $z = (x-2)$. The formation of colloids of less than 1 μm in size was also identified as a fraction of the U(IV) speciation, but was shown to decrease with increasing pH.

However, there has also been debate whether the observation of these particular U(VI) hydrolysis species are real. *Çevirim-Papaioannou et al.* stated that U(VI) (aq) equilibrated in reducing conditions (various reducing agents, 0.1 and 5 M NaCl) resulted instead in $\text{U}(\text{OH})_4$ (aq) as the dominant U(IV) aqueous species [49,50]. Nevertheless, the prevalence of all U(VI) (aq) species under alkaline conditions in a repository would require reducing conditions to be maintained, which is not sustainable over the timescale of hundreds of years wherein groundwater and oxygen will eventually ingress.

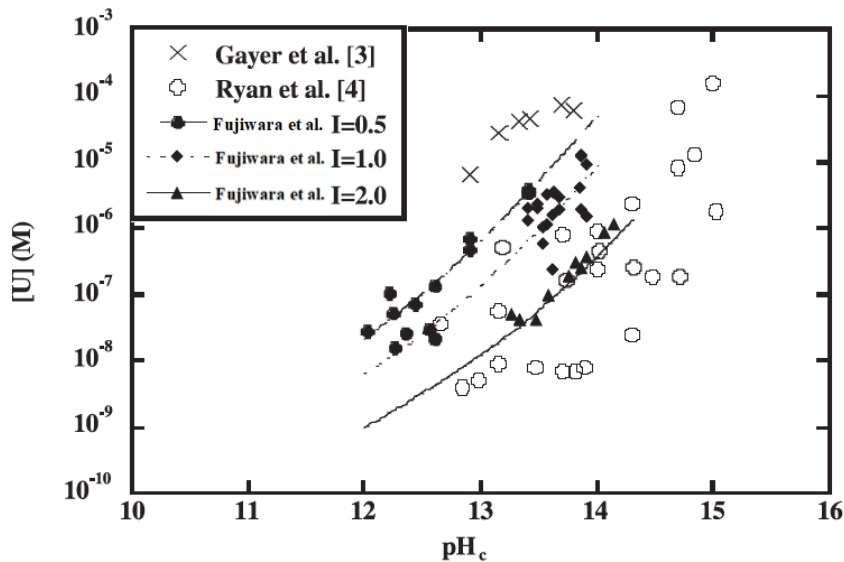
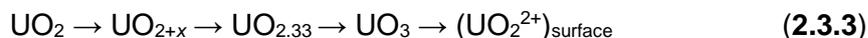


Figure 2.2.1: Solubility of U(IV). Points are experimental and curves are calculated (from [46]).

2.2.1.2 Oxidative dissolution

In the absence of reducing conditions and in the presence of trace oxygen, U(IV) will undergo partial oxidation with the effect of increasing the uranium solubility [51]. The general process of UO_2 surface oxidative dissolution was summarised by *Kim et al.* in **Equation 2.2.3** [52]:



2.2.1.3 U(VI) solubility / speciation in alkaline conditions

In general, at low pH the U(VI) speciation is dominated by the uranyl ion, UO_2^{2+} , but at high pH, complexes of hydroxides (e.g. $\text{UO}_2(\text{OH})_x^{y-}$) and / or carbonates will dominate (**Figure 2.2.2**).

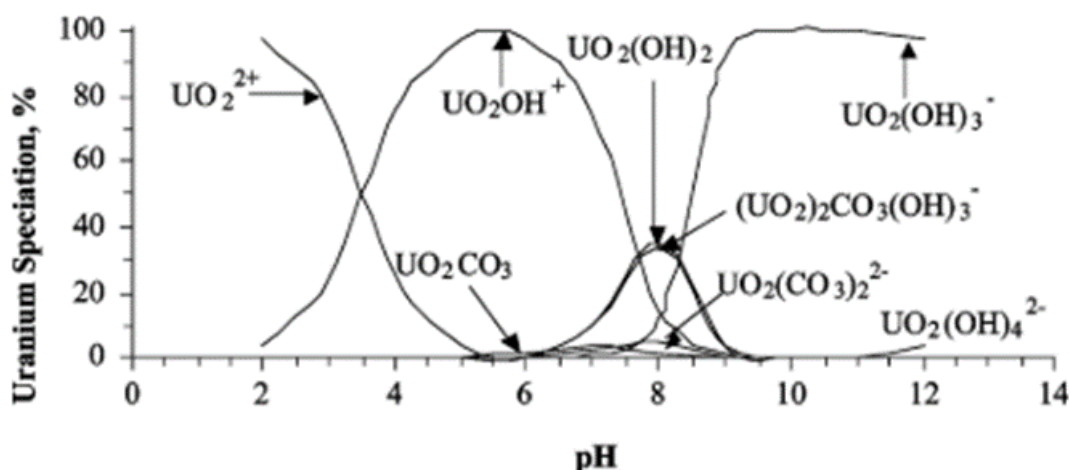


Figure 2.2.2: Effect of pH on modelled uranium speciation (from [53]) for the +6 oxidation state at $[\text{U}] = 2 \mu\text{M}$ and $[\text{TIC}] = 0.125 \text{ mM}$.

Martinez-Torrents et al. determined that at pH 11, 12 and 13 (in 0.01 and 0.1 M TMACl) the U(VI) speciation at a concentration of $4.5 \times 10^{-6} \text{ M}$ progressed from $\text{UO}_2(\text{OH})_3^-$ and $(\text{UO}_2)_3(\text{OH})_7^-$, to $\text{UO}_2(\text{OH})_3^-$, to $\text{UO}_2(\text{OH})_4^{2-}$ as a result of increased hydrolysis with increasing pH [54,55]. The formation of polynuclear species, such as $(\text{UO}_2)_3(\text{OH})_7^-$, will only prevail at higher concentrations; exceeding $\sim 10^{-8} \text{ M U(VI)}$ [53,56].

2.2.1.4 Hydrous alkali / alkali-earth uranates

Altmaier and colleagues described the solubility of U(VI) in a series of sodium, potassium or magnesium chloride solutions ($\sim 0.03 - 5 \text{ M}$) from undersaturation conditions in the alkaline pH range [57–59]. The clarkeite phase $((\text{Na,K})_2\text{U}_2\text{O}_7 \cdot \text{H}_2\text{O}_{(cr)})$ was shown to be solubility limiting above pH ~ 8 and pH ~ 9.5 in NaCl and KCl solutions, respectively. Further to this, *Endrizzi et al.* concluded that $\text{UO}_2(\text{OH})_3^-$ (aq) dominated U(VI) aqueous speciation at moderately alkaline pH ($\sim 7-9$) when U(VI) exhibited the lowest solubility ($10^{-8}-10^{-9} \text{ M}$), and $\text{UO}_2(\text{OH})_4^{2-}$ (aq)

dominated at alkaline / hyper-alkaline pH (>9) when [U(VI)] was $\sim 10^{-6}$ M at pH 13, in NaCl solutions ($\sim 0.1 - 5$ M, 25 ° C) [60]. For the MgCl₂ system however, the formation of a ternary Mg-U(VI)-OH_(s) phase was not observed over the timescale of the experiment (≤ 200 days, up to pH 9.7) and metaschoepite (UO₃·2H₂O_(cr)) was shown to be the U(VI) solubility limiting phase, with Mg(OH)₂ formation limiting the solubility of Mg above pH ~ 9 . However, these studies still highlight the importance of considering metal uranate formation under cementitious conditions.

2.2.1.5 Uranium speciation in cementitious environments

Sutton *et al.* characterised a 3:1 PFA:OPC grout leachate solution with reference to U(VI) speciation [53]. Potassium and sodium had a high initial release from the grout (73 % and 99 %, respectively) after two sequential leachings in deionised water, however the calcium release was only 7 % at this same stage (**Table 2.2.1**). The author postulated that potassium and sodium uranate formation would therefore be important at early stages in a repository, at pH 12-13, for limiting the solubility of U(VI). Calcium uranate formation would therefore become more prevalent at later stages of cement degradation, when the pH is ~ 11 , however the availability of calcium will be limited by sulfate (due to ettringite (Ca₆Al₂(SO₄)₃(OH)₁₂·26H₂O) formation, with aluminate) and carbonate (due to calcium carbonate formation) concentrations.

Table 2.2.1: Analysis of cementitious grout leachate, primary and secondary washings (from [53]).

Component	Concentration in leachate/mM		Amount leached from repository grout (%)	
	Wash 1	Wash 2	Wash 1	Wash 2
K	91.2	3.14	70.6	2.43
Na	41.1	8.70	81.7	17.3
Ca	19.2	7.84	4.74	1.93
Mg	0.099	—	0.111	—
Si	0.217	0.047	0.010	0.002
Al	0.033	0.024	0.002	0.001
Fe	0.003	0.001	0.002	0.001
TIC	0.125	0.092	0.012	0.010
SO ₄ ²⁻	0.305	0.079	—	—
Cl ⁻	0.035	0.014	—	—
pH	11.8	11.1		

^aErrors reported within 5% of the analytical result. ^bTIC: total inorganic carbon.

2.2.1.6 Hydrous calcium uranate

The formation of hydrous calcium uranates has been identified in several studies. *Valsami-Jones et al.* reported that the mixing of uranyl nitrate and calcium hydroxide solutions resulted in the formation of a poorly crystalline precipitate with an approximate formula of

$\text{CaU}_{1.6}\text{O}_{5.8}\cdot 2.5\text{H}_2\text{O}$ (water content varied between 6-8 %) [61]. *Ding et al.* also synthesised calcium uranate particles using aqueous hydroxylation reactions [62]. In this study, the orange hydrous uranate was prepared by alkalisation of a 1:1 molar U(VI):Ca(II) nitrate solution by addition of saturated calcium hydroxide, until pH 12 was reached. Between pH 5-7 uranium showed nucleation into calcium deficient, poorly-ordered nanoparticles which continued to take up calcium until a general formula of $\text{Ca}_2(\text{UO}_2)_3\text{O}_{3.75}(\text{OH})_{2.5}\cdot 3.5\text{H}_2\text{O}$ was attained. Further to this, in the Thesis of *Sutton* (1999), the precipitates formed on addition of calcium hydroxide at pH 9 to uranyl nitrate solutions (10 mM) resembled schoepite and a higher pH of 11 was required to identify calcium uranate precipitates [63].

With relevance to cementitious surfaces, *Felipe-Sotelo et al.* discussed the speciation of U(VI) (10^{-4} M, as uranyl nitrate) in water equilibrated with Nirex Reference Vault Backfill (NRVB) cement (462 ppm Ca^{2+}) in contact with NRVB surfaces [64]. Using SEM/EDX elemental mapping of the NRVB surface, the Si:Ca:U:O ratio was given as 0.1:0.9:1:4 which was considered indicative of the formation of a calcium uranate (CaUO_4 -type) phase (**Figure 2.2.3**). However, fitting of the EXAFS spectrum of this region eluded to a uranyl oxy-hydroxide species, possibly becquerelite. Given that becquerelite has the general formula $\text{Ca}(\text{UO}_2)_6\text{O}_4(\text{OH})_6\cdot 8\text{H}_2\text{O}$, the association of U(VI) with Ca is still significant to the effect of secondary phase formation in cementitious systems.

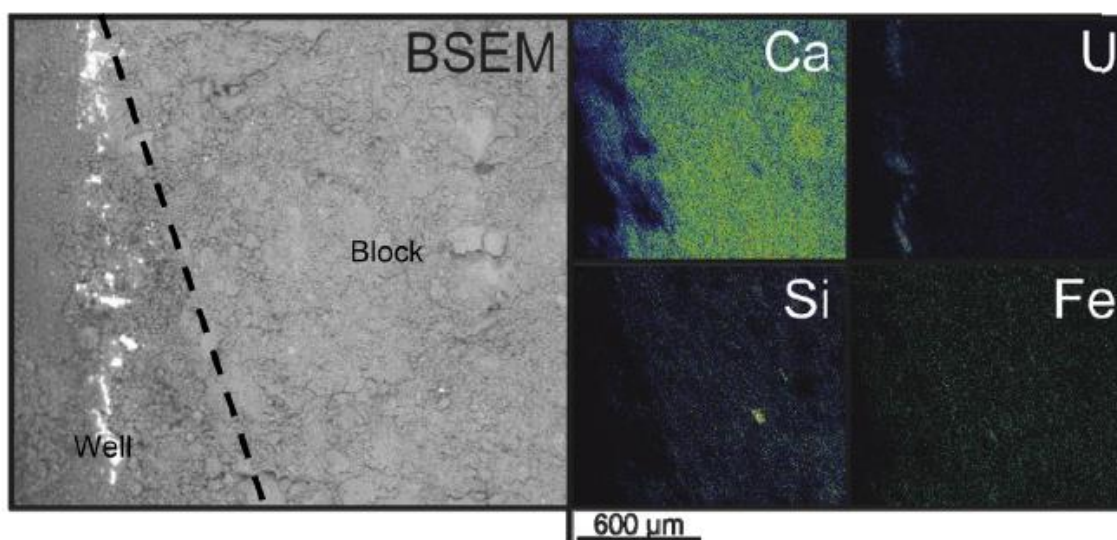


Figure 2.2.3: Backscattering images and EDXA elemental mapping of the edge of the central well of the NRVB block used in the diffusion of U(VI) (from [64]).

2.2.1.7 Uranyl carbonates

As discussed in *Section 2.2.1.3*, U(VI) speciation is dominated by uranyl hydroxide or carbonate complexes at higher pH values; uranyl carbonate complexes in particular are very stable and their formation is important to consider in cementitious environments where calcium

carbonate solids and dissolved carbonate species will be present. *Sutton et al.* identified that $\text{UO}_2(\text{CO}_3)_2^{2-}$ and $(\text{UO}_2)_2\text{CO}_3(\text{OH})_3^-$ would be the dominant aqueous uranyl carbonate species present in an alkaline 3:1 PFA:OPC leachate solution, with the latter being dominant at pH 8 ($[\text{C}] = 0.125 \text{ mM}$ and $[\text{U}] = 2 \text{ }\mu\text{M}$) (**Figure 2.2.2**). The uranyl carbonate species considered most stable, $\text{UO}_2(\text{CO}_3)_3^{4-}$, was not identified as it requires higher concentrations of carbonate in order to form.

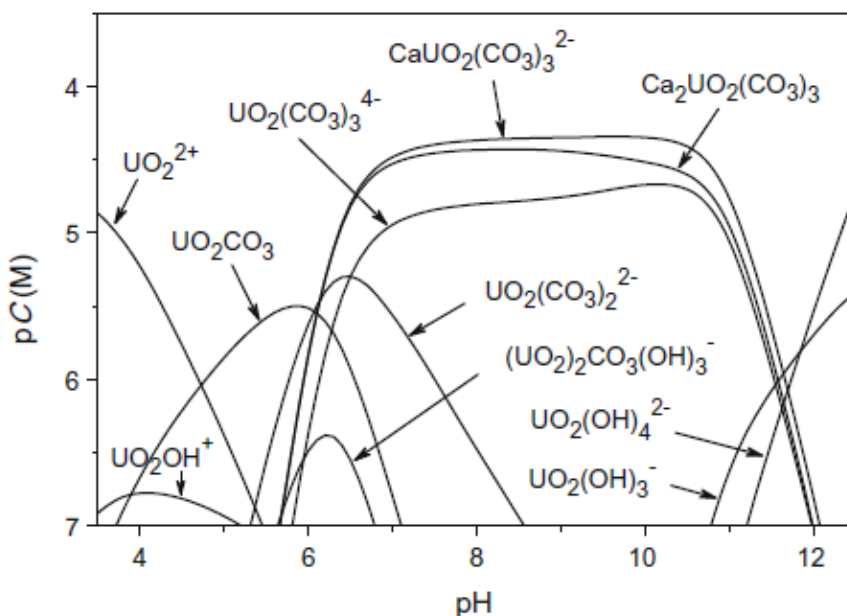


Figure 2.2.4: Aqueous U(VI) speciation, expressed as the negative logarithm of U(VI) concentration (pC), versus pH; $[\text{U(VI)}]_{\text{total}} = 10^{-4} \text{ M}$, $[\text{Ca(NO}_3)_2] = 10^{-3} \text{ M}$, $[\text{NaHCO}_3] = 5 \times 10^{-3} \text{ M}$, atmospheric CO_2 ($p\text{CO}_2 = 10^{-3.5} \text{ atm}$). Speciation was calculated using PHREEQC (without ionic strength corrections) (from [65]).

Saleh et al. identified that at $[\text{HCO}_3^-] = 5 \text{ mM}$, $\text{UO}_2(\text{CO}_3)_3^{4-}$ formation was in fact favourable [65]. The formation of Ca-bearing uranyl carbonate complexes were also identified in this system with $[\text{Ca}] = 1 \text{ mM}$ and $[\text{U}] = 0.01 \text{ mM}$. Although *Sutton et al.* measured a Ca concentration the order of 10s of mM in the grout leachate (**Figure 2.2.4**), the carbonate and uranium concentrations were probably not high enough to predict such phases with a U:C(:Ca) ratio of 1:3(:1,2). These studies highlight the importance of the aqueous solution composition on the speciation of U(VI).

2.2.2 Uranium uptake by Portland cement and C-S-H

C-S-H is largely considered to be the bulk binder phase in Portland cement matrices, and therein dictates much of the reactivity of cement surfaces. Studies of U(VI) uptake by cement and C-S-H have been particularly prevalent to underpin the mechanisms by which U(VI)

associates with cementitious materials. The results from several experimental studies are displayed in **Table 2.2.2**.

In summary, the mode of U(VI) uptake by C-S-H phases at trace concentrations is largely considered to be controlled by surface complexation, with the potential to transition into an interlayer species that may or may not be chemisorbed. The coordination environment is similar to a uranyl silicate, and specifically uranophane-type $(\text{Ca}(\text{UO}_2)_2\text{SiO}_3(\text{OH})_2 \cdot 5\text{H}_2\text{O})$ moieties have been identified. At higher concentrations of U(VI), Ca-uranate precipitates can form and limit the solubility of U(VI) in the alkaline region, as already discussed previously.

Table 2.2.2: Summary of literature for U(VI) sorption on Portland cements and C-S-H.

Reference	Surface(s)	Comments	Proposed uptake mechanism(s)
<i>Sutton et al.</i> [53]	3:1 PFA:PC blend	- Sorption studies using ~2 μM U(VI).	- Sorption of UO_2^{2+} occurs at low pH (~20%), but increases with pH as monohydroxide species dominate. - The grout surface was negatively charged, and therefore uptake was rationalised by chemi-sorption through an OH ligand exchange mechanism with silanol groups and surface complex formation.
<i>Pointeau et al.</i> [66]	PC and BFS/PFA/PC blends (Ca/Si = 0.7, 1.0, 1.3) C-S-H (Ca/Si = 0.8, 1.3)	- Sorption studies using nM to sub-nM U(VI).	- For Ca/Si ratios > 1, the zeta potential (i.e. surface charge) was positive due to adsorbed Ca^{2+} , suggesting uptake of anionic U(VI) hydroxide species through favourable electrostatic interactions. - For Ca/Si ratios < 1, the zeta potential was negative and surface complexation of anionic U(VI) hydroxide species was proposed (as in <i>Sutton et al.</i>).
<i>Harfouche et al.</i> [67]	C-S-H (Ca/Si = 0.65, 0.75, 1.07, 1.1, 1.29)	- Sorption and co-precipitation samples with 1100 - 3400 ppm U(VI) loading (μM - mM). - EXAFS measured.	- The linear $[\text{O}=\text{U}=\text{O}]^{2+}$ structure is preserved upon sorption or incorporation by CSH. - EXAFS indicates a uranophane type coordination in all sorption samples due to Ca scatterers, regardless of loading or Ca/Si ratio. - For coprecipitated samples, at 3400 ppm U(VI) and Ca/Si = 1.29 a uranophane or U(VI) solid phase was indicated by U-U backscatters. At 1000 ppm and Ca/Si = 0.65, 1.1 an identified uranyl silicate moiety was identified. - Uptake mechanism is still relatively unknown as the results differ depending on the C-S-H synthesis method and U(VI) addition method / loading.
<i>Wieland et al.</i> [68]	Portland cement C-S-H (Ca/Si - 1.8)	- U(VI) sorption studies (0.5 μM) and higher loading samples (>2000 ppm). - EXAFS and XRF mapping measured.	- XRF mapping of cement sorption samples showed an association of U with Ca. - EXAFS showed that the coordination environment around U(VI) was similar in both cement and C-S-H, similar to uranophane. - Ca-uranate formation was not conclusive by EXAFS.
<i>Tits et al.</i> [69]	C-S-H (Ca/Si = 0.75, 1.07, 1.65)	- U(VI) sorption at sub- μM and higher loading samples (~70 ppm - ~200 000 ppm). - Time-resolved laser fluorescence measured.	- U(VI) sorption on C-S-H samples in artificial cement water (ACW) is weaker than in alkali-free conditions, and decreases with Ca/Si ratio - U(VI) interlayer incorporated species identified in C-S-H at low Ca/Si ratio (and probably present at higher Ca/Si) exhibits silanol coordination and exchange with Ca - uranophane or soddyite type moiety. - At low Ca/Si only sorbed U(VI)-silanol surface complex (possibly inner-sphere) was identified. Could also be incorporated but with a lower Si coordination number than the previous species. - A Ca-uranate phase was only observed for C-S-H with very high U(VI) loading (~200 000 ppm) in alkali free solutions due to oversaturation of this phase.
<i>Macé et al.</i> [70]	Portland cement with high silica content, C-S-H (Ca/Si = 0.7, 1.07 and 1.8)	- Samples from sorption, hydration or diffusion with low (1000s ppm) and high (10 000s ppm) U(VI) loading. - EXAFS measured.	- At low loading, U(VI) had the same coordination environment in C-S-H and PC, regardless of preparation method, with a U-O _{ax} distance similar to uranophane. - At high loading the spectra were comprised of two different components: a species similar to that at low loading and a species with a Ca-uranate type coordination.

Gaona *et al.* adopted the experimental data from [67–70] to develop a thermodynamic model of U(VI) interactions with C-S-H, by adaptation of the CSH3T model for C-S-H by Kulik [71,72]. The approach used was the formation a C-S-H-U(VI) aqueous solid solution series under alkaline free conditions in the pH range 10.1 to 12.5 and Ca/Si range 0.6 to 1.6, taking into account U(VI) uptake into the C-S-H interlayer, only (**Figure 2.2.5**). From a consideration of nine U(VI)-containing end members, model refinement resulted in the identification of three phases that would predominantly form under the given conditions: $(\text{CaO})_2(\text{UO}_3)(\text{SiO}_2)_{2.5}(\text{H}_2\text{O})_5$; $(\text{CaO})_2(\text{UO}_3)_{1.5}(\text{SiO}_2)_2(\text{H}_2\text{O})_5$; and $(\text{CaO})_3(\text{UO}_3)_{1.5}(\text{SiO}_2)_2(\text{H}_2\text{O})_{5.5}$, with Ca/Si = 0.8, 1 and 1.5, respectively. The predictions were able to correctly map the trends of U(VI) sorption on C-S-H which indicate that U(VI) uptake increases with decreasing Ca/Si ratio [69], likely due to formation of the $(\text{CaO})_2(\text{UO}_3)(\text{SiO}_2)_{2.5}(\text{H}_2\text{O})_5$ end member with Ca/Si = 0.8. This trend is important to consider for degraded, decalcified cement systems where Ca/Si ratios will be low.

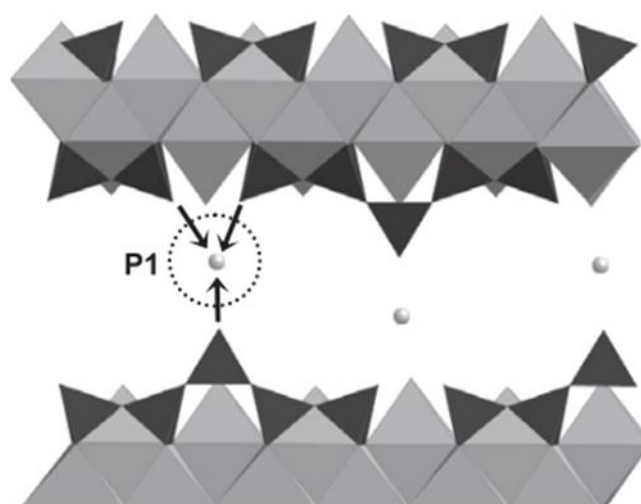


Figure 2.2.5: Site proposed for the incorporation of U(VI) into the C-S-H interlayer (P1) providing a molecular environment consistent with soddyite (3 Si atoms coordinated to U(VI) in the first Si-shell). Grey: Ca-octahedra; black: Si-tetrahedra (from [71]).

2.2.2.1 Natural uranium minerals as analogues for cementitious speciation

Natural mineral analogues can be used to help identify the speciation of U(VI) phases in cement matrices, particularly using XRD, XAS and SEM/EDX analyses. Such U(VI) minerals have been discussed above and include the uranyl silicates uranophane $(\text{Ca}(\text{UO}_2)_2(\text{SiO}_3\text{OH})_2 \cdot 5\text{H}_2\text{O})$ and soddyite $((\text{UO}_2)_2\text{SiO}_4 \cdot 2\text{H}_2\text{O})$, and Ca-bearing minerals such as becquerelite (uranyl oxy-hydroxide; $\text{Ca}(\text{UO}_2)_6\text{O}_4(\text{OH})_6 \cdot 8\text{H}_2\text{O}$) and clarkeite (calcium uranate; $(\text{Na,Ca})(\text{UO}_2)\text{O}(\text{OH}) \cdot 0-1\text{H}_2\text{O}$). These are secondary mineral phases that form from the paragenesis of uraninite in silicon or calcium rich groundwaters [73,74].

2.2.3 Uranium uptake by other cement phases

2.2.3.1 Silica

The uptake of U(VI) by silica surfaces is considered to occur through surface complexation [75–77]. *Prikryl et al.* showed that U(VI) sorption to quartz was dependent on pH and the concentration of carbonate ions in solution ($[U] = 2 \times 10^{-7}$ M in 0.1 M NaNO₃) [78]. Over the pH range studied (2.5 to 9.5) the quartz surface maintained a negative charge, however the U(VI) speciation was shown to dictate the percentage of U(VI) uptake. In the presence of atmospheric CO₂ (**Figure 2.2.6.A**), U(VI) uptake increased from pH ~2.5 and reached a maximum at pH 6 to 6.5 before decreasing again at higher pH values. At low levels of CO₂ (**Figure 2.2.6.C**), U(VI) uptake also increased from pH ~2.5 up to pH 6 but remained relatively constant at higher pH values. With reference to the relative U(VI) speciation (**Figure 2.2.6.B** and **2.6.6.D**) sorption therefore occurs when U(VI) hydroxy complexes dominate and the presence of U(VI) carbonate complexes decreases the sorption selectivity of U(VI). Similar behaviour was also reported by *Stamberg et al.* ($[U] = 8.4 \times 10^{-5}$ M in 0.01 M NaNO₃ or 0.005 M Na₂CO₃ on mesoporous silica), *Fox et al.* ($[U] = 10^{-6}$ M at 430 ppm CO₂ or 2 % CO₂ on quartz) and *Saleh et al.* ($[U] = 10^{-4}$ M in 0.005 M NaHCO₃ on silica nanoparticles) [65,75,77,79]. Further to this, studies have also shown that Ca²⁺ ions in solution will also form uranyl carbonate complexes such as CaUO₂(CO₃)₃²⁻ and Ca₂UO₂(CO₃)_{3(aq)} (**Figure 2.2.4**), to the effect of decreasing U(VI) sorption, rather than through Ca²⁺ and U(VI) competition for sorption sites [77,80].

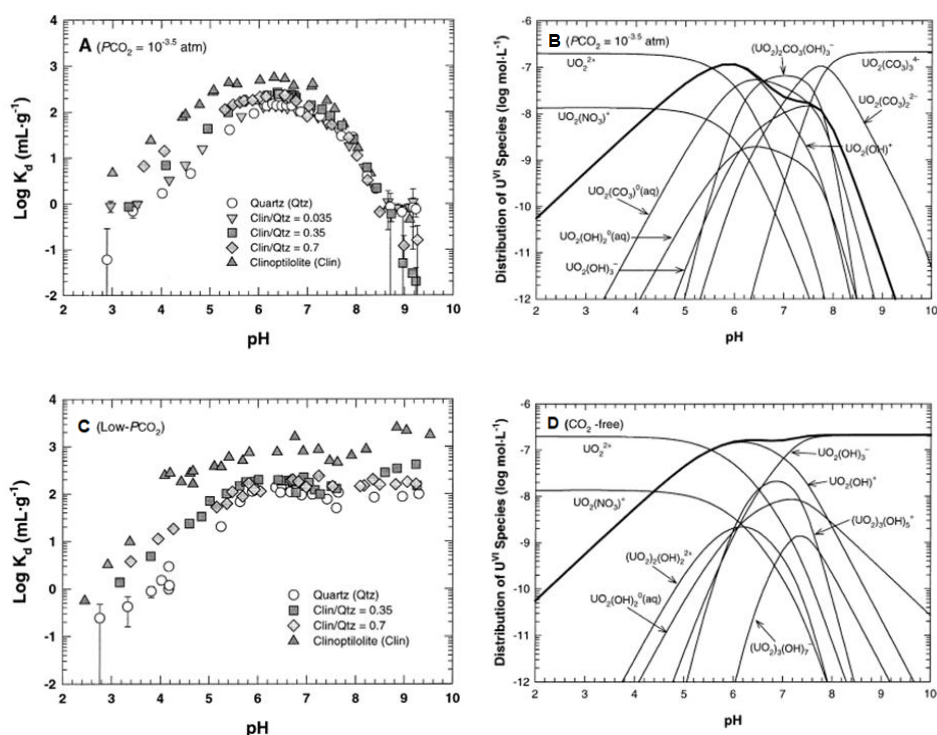


Figure 2.2.6: A and C: U(VI) sorption as a function of pH on quartz (white circles, other sorbents not discussed here). B and D: U(VI) aqueous speciation as function of pH at atmospheric CO₂ (relevant to A) and low CO₂ (relevant to C) levels (from [78]).

2.2.3.2 Carbonate layered double hydroxides (LDH-CO₃)

Pshinko et al. determined that U(VI) uptake by LDH-CO₃ phases was hindered at alkaline pH by the formation of stable aqueous uranyl carbonate complexes, UO₂(CO₃)₂²⁻ and UO₂(CO₃)₃⁴⁻ (species discussed in *Section 2.2.1.7*) [81,82]. A release of carbonate anions at pH values above ~7 corresponded to a decrease in U(VI) uptake for a Zn,Al-CO₃ LDH phase in 0.01 M NaClO₄ (S/L = 1 to 2 g L⁻¹) (**Figure 2.2.7**, grey circles). The exchange of carbonate anions for uranyl carbonate anions was therefore not considered as the mechanism of uptake. The authors concluded that LDH-CO₃ phases are good sorbents for uranium cations (UO₂²⁺) at acidic pH values, however, become less effective for uranium hydroxide anions at alkaline pH values. *Kulyukhin & Krasavina* showed that hydrotalcite (Mg₆Al₂CO₃(OH)₁₆·4H₂O) will sorb UO₂²⁺ from aqueous nitrate solutions at pH values of ~4 and ~5, at a capacity of >99 % for [U] = 10 mM and ~20-30 % for [U] = 100 mM (20 g L⁻¹) [83]. There was no discussion about the mechanism of uptake, but given that hydrotalcite will display a positive surface charge in this pH range [84], negatively charged nitrate anions in solution may act to facilitate the uptake of UO₂²⁺ through electrostatic means. However, uranium secondary phase formation also cannot be ruled out at the concentrations of uranyl nitrate used, which is a process described in more detail in **Chapter 5** of this Thesis, for alkaline pH values.

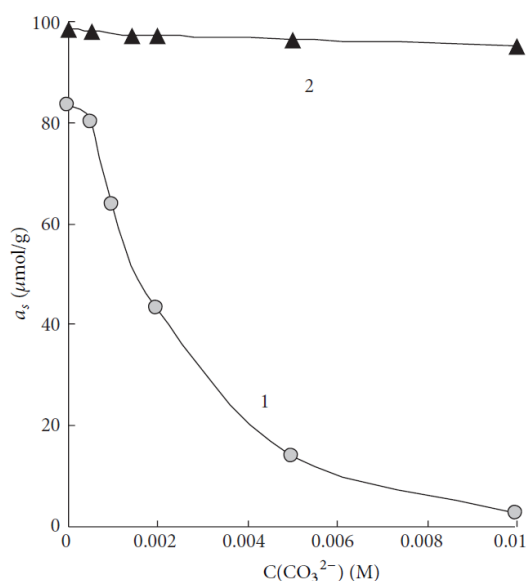


Figure 2.2.7: Effect of carbonate ion concentration on U(VI) sorption with different forms of adsorbents: (1) Zn,Al-CO₃ and (2) Zn,Al-EDTA (not discussed here). [U] = 1 × 10⁻⁴ M and S/L = 1 g L⁻¹ (from [81]).

Heat treated LDH-CO₃ phases, however, do show promise for the uptake of uranium at alkaline pH. Calcination of hydrotalcite (above the decomposition temperature of CO₂, 850 °C) forms a mixed Mg,Al oxide. *Timoshenko et al.* showed that heat treated hydrotalcite (500 °C) even demonstrated a high capacity for U(VI) uptake (>99 %) in aqueous solutions of 0.01 M NaClO₄ up until pH 12 for [U] = 0.1 mM (S/L = 2 g L⁻¹) [85]. The uptake process could therefore

be a result of recombination of the mixed oxide phase with $\text{UO}_2(\text{CO}_3)_3^{4-}$ anions to form a LDH- $\text{UO}_2(\text{CO}_3)_3$ phase, however there is little structural characterisation in the literature to confirm this [86].

There is little evidence in the literature for studies concerning the uptake of U(VI) by other LDH phases relevant to cements, such as AFm phases (calcium aluminates), or related phases e.g. ettringite ($\text{Ca}_6\text{Al}_2(\text{SO}_4)_3(\text{OH})_{12}\cdot 26\text{H}_2\text{O}$) [87]. **Chapter 5** includes a discussion on the first recorded ^{27}Al NMR spectra for U(VI)-contacted ettringite phases.

2.3 Plutonium

Plutonium contaminated materials (PCM) are intermediate level wastes (ILW) in the UK generated from fuel processing operations; currently encapsulated in Portland cement grouts for disposal. Although categorised as ILW, PCM waste streams can still contain significant radioactivity of up to 5 GBq g^{-1} [88]. Understanding the robustness of cemented PCM wastefoms and the behaviour of plutonium in contact with cement hydrate phases will contribute to the safety case for continued above-ground storage and proposed final geological disposal of these materials. There has been increasing discussion that plutonium residues, currently stored at the Sellafield Ltd. site, may also require cementitious immobilisation in the future [89].

2.3.1 Solubility and speciation of plutonium

Plutonium has an electronic configuration of $[\text{Rn}] 5f^6 7s^2$ and the accessible oxidation states of plutonium (+3, +4, +5, +6, +7, +8) display complicated redox chemistry in aqueous solution, much more so than uranium, controlled heavily by pH and redox potential (**Figure 2.3.1**) [90,91]. The work in this Thesis is primarily concerned with plutonium solubility and speciation under alkaline conditions and, more importantly, under cementitious conditions relevant to geological disposal. $\text{Pu(IV)O}_2(\text{s})$ is generally considered as the sparingly soluble solid phase that determines aqueous plutonium concentrations [92]; the solubility of $\text{PuO}_2(\text{s})$ in aqueous solution has been widely studied concerning the aqueous plutonium species that are in equilibrium with the solid phase.

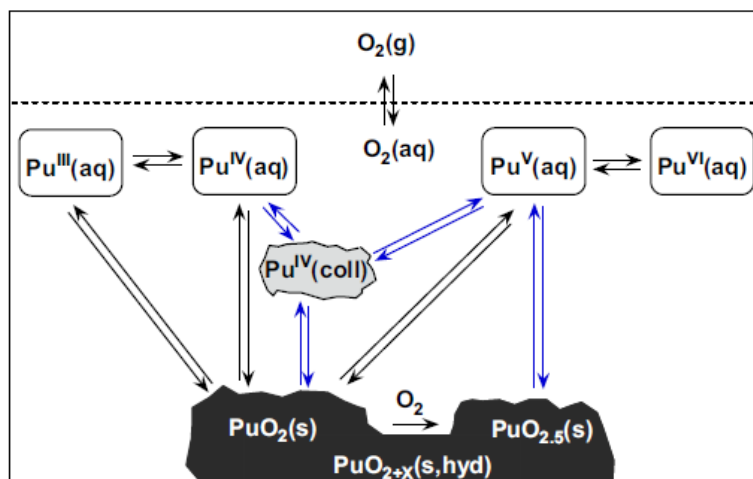


Figure 2.3.1: Solid-liquid and redox equilibria of plutonium under reducing conditions, in redox-neutral solutions and in the presence of oxygen (from [90]).

2.3.1.1 Alkaline media

The +3 oxidation state of plutonium is observable in alkaline, aqueous solutions but only under reducing conditions [90,93–96]. As Pu(IV)O₂ is the solubility limiting phase for aqueous plutonium concentrations, it has been observed that Pu³⁺_(aq) is generated primarily via reductive dissolution of PuO_{2(s)} according **Equation 2.3.1** summarised in [90,96].



Tasi et al. observed Pu³⁺_(aq) between pH ~8-13 under highly reducing conditions (pe+pH = 2 achieved using SnCl₂) in 0.1 M NaCl (**Figure 2.3.2**), however, also found that at pH 9 and 12 the solid Pu(OH)_{3(am)} phase was also in coexistence with PuO_{2(am,hyd)} (30 ± 5 % Pu(III)_(s)) [94]. In non-reducing conditions Pu(III) will undergo oxidation to Pu(IV/V) in alkaline media in the presence of oxygen [90,97].

Although Pu³⁺_(aq) hydrolysis is not considered significant in acidic media [95] (see *Section 2.3.1.3*) it should be considered above pH 5 [92]; *Odoh et al.* calculated that the pK_a of Pu³⁺ hydrolysis was 6.65 [98].

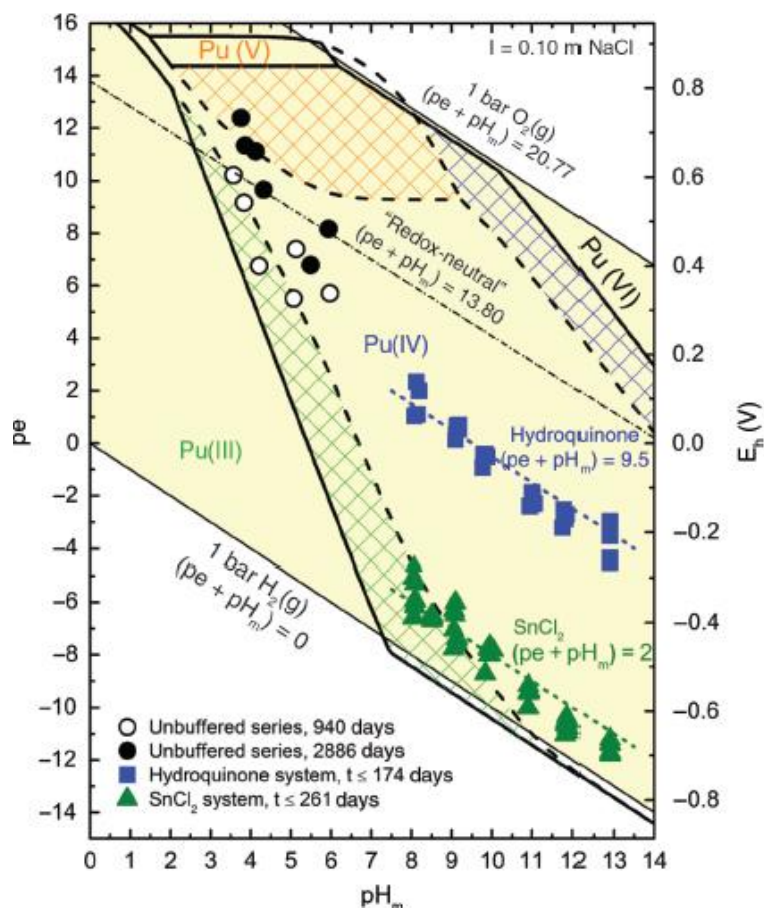
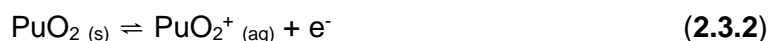


Figure 2.3.2: Pourbaix diagram of plutonium calculated for $[\text{Pu}] = 10^{-5} \text{ M}$ and $I = 0.10 \text{ m NaCl}$ using thermodynamic and (SIT) activity models (from [94]).

Given that Pu(IV)O_2 is established as the plutonium solubility limiting phase, $\text{Pu}^{4+}_{(\text{aq})}$ is in direct equilibrium with $\text{PuO}_2_{(\text{s})}$ under redox neutral conditions. However, it has been shown that the +5 oxidation state of plutonium dominates in aqueous solution above $\text{pH } 3$, under redox neutral conditions (in the presence of oxygen), as $\text{PuO}_2^+_{(\text{aq})}$, in coexistence with $\text{Pu(IV/VI)}_{(\text{aq})}$ [94,99,100]. This is due primarily to oxidative dissolution of $\text{PuO}_2_{(\text{s})}$, as described by **Equation 2.3.2** summarised in [99].



Delegard et al. determined that the aqueous plutonium concentration increased with increasing hydroxide activity ($[\text{NaOH}] = 1\text{-}15 \text{ M}$) and was predominantly present as Pu(V) [100]. However, *Neck et al.* also noted that above $\text{pH } \sim 5$ in 0.1 M NaCl solution, Pu(V) concentrations in solution started to decrease with increasing pH, up to $\text{pH } 10$ (**Figure 2.3.3**) [99]. This latter observation was attributed to the formation of a mixed valent plutonium oxide, $\text{PuO}_{2+x(\text{s})}$, resulting from oxygen scavenging by the initial solid PuO_2 phase. In the presence of water and oxygen, $\text{PuO}_2_{(\text{s})}$ is therefore partially oxidised and resides in equilibrium with

Pu(V)_(aq) and Pu(IV)_(aq) (**Figure 2.3.1**) [99,101–103]. The +6 oxidation state of plutonium can also coexist in solution with Pu(IV/V)_(aq) under alkaline conditions, as PuO₂²⁺, however it is quickly reduced to Pu(V) above pH ~5 and between pH 3-9, Pu(V)_(aq) is the dominant species [99].

Pu⁴⁺_(aq) hydrolyses more readily than Pu³⁺_(aq), with a calculated pK_a of 0.17, attributed to a higher effective charge at the plutonium centre which lowers the free energy of hydrolysis and in turn the pK_a value [98].

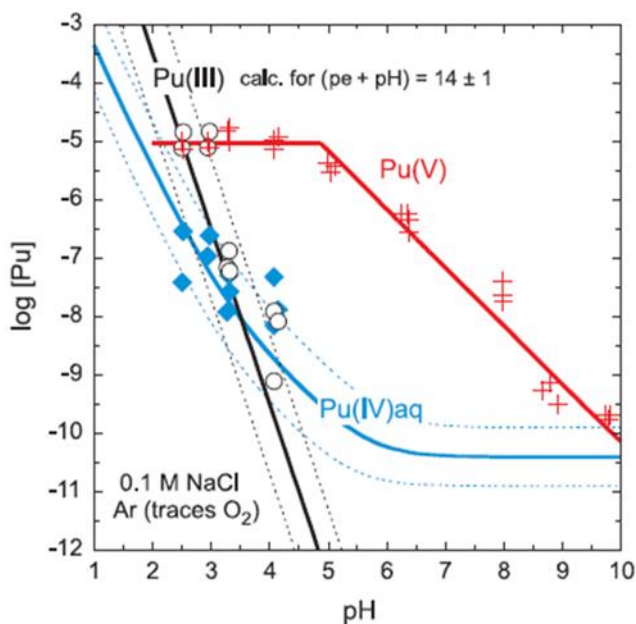


Figure 2.3.3: Equilibrium concentrations (and calculated concentrations from [50]) of Pu(III), Pu(IV) and Pu(V) (from [99]).

The +7 oxidation state of plutonium can only be isolated by electrochemical or ozonisation methods in alkaline solutions (1 M up to 15 M NaOH) [104–110] and Pu(VII)_(aq) is short-lived. *Antonio et al.* determined that Pu(VII)_(aq) has a half-life of 3.7 h before it is auto-reduced back to Pu(VI)_(aq) in 2 M NaOH [104]. There is also debate about the coexistence of Pu(VIII)_(aq) with Pu(VII)_(aq) in these hyperalkaline NaOH solutions. *Nikonov* and colleagues maintain that the oxidative ozonisation process of Pu(VI) solutions ([NaOH] = 1-10 M) can yield up to 15 ± 5 % Pu(VIII)_(aq) as PuO₄, in correspondence with Pu(VII)_(aq) [106,110], indicated by a blue-black colouration of the solution. However, *Antonio et al.* did not corroborate this observation, rather observed only an opaque green solution after ozonisation, indicative of Pu(VII)_(aq) [104]. Similarly, *Gogolev et al.* indicated that the half-life of PuO₄ was on the order of 10⁻² s and was unobservable in 1-16 M NaOH [111]. Given that the early conditions in a repository are likely to be anoxic and reducing, the higher oxidation states of plutonium formed under highly oxidising conditions are not relevant for this Thesis.

2.3.1.2 Pu(IV) colloids

Colloidal clusters of plutonium, on the order of nm, can also form in acidic to alkaline conditions [90,112,113]. The study by *Ekberg et al.* determined that plutonium colloids were produced instantly by addition of 0.19 M NaOH to a 0.19 M Pu(IV) solution in 1 M HCl (pH not stated but considered to be alkaline). EXAFS measurements confirmed that the colloidal particles were formed in the cubic space group Fm-3m as Pu(IV)O₂. Nano-particulate Pu(IV)O₂ with a mean particle size of 2.5 nm was also determined by *Romanchuk et al.* in 3 M NH₃H₂O (pH ~ 11), regardless of whether the starting plutonium oxidation state was +3, +4, +5, or +6. The nature of these colloidal particles and the complex dissolution-precipitation equilibria of PuO₂ is often the reason in the literature that PuO_{2(s)}, in equilibrium with aqueous solution, is referred to as “(am)”, “(am, hyd)”, “(coll)” or similar, and the colloids themselves should be considered in equilibrium with the aqueous media (refer to **Figure 2.3.1**).

2.3.1.3 Acidic media

The chemistry of plutonium in acidic media is fairly well established, as nitrate solutions are used extensively in the nuclear industry for fuel reprocessing [91]. They are considered here due to the methodology employed in **Chapter 6**, which used an acidic Pu-containing solution. Plutonium solubility is generally higher under acidic than alkaline conditions, with aqueous concentrations on the order of ~10⁻⁴ to 10⁻³ M at pH ~3.5 compared to ~10⁻⁹ M at pH ~9, as shown by *Fujiwara et al.* in **Figure 2.3.4** (NaClO₄ solution, in the presence of a Na₂S₂O₄ reducing agent) [114]. Pu(III)_(aq) is much more prevalent under reducing conditions when the pH is in the acidic region [92,95,114].

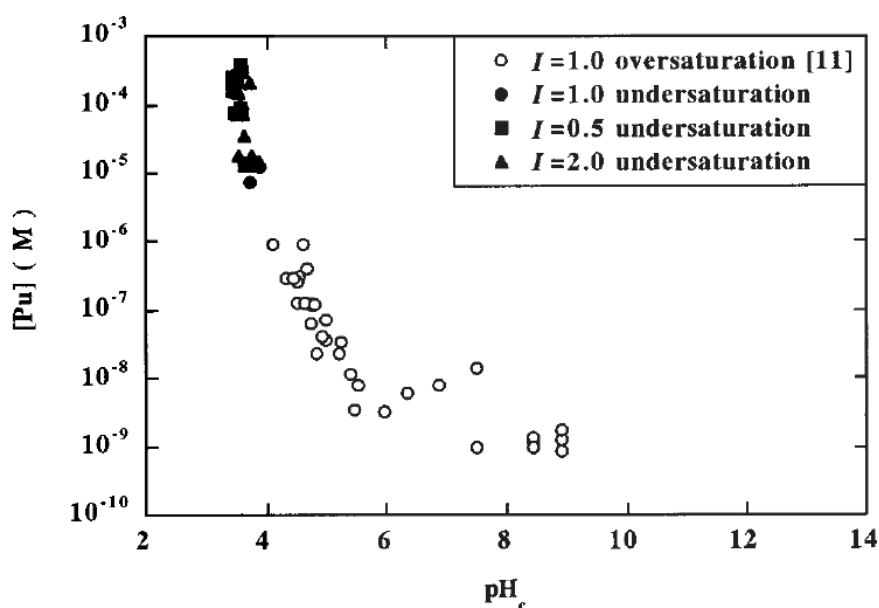


Figure 2.3.4: PuO₂·xH₂O solubility (as Pu(III)_(aq)) in NaClO₄ with Na₂S₂O₄ (from [114]).

Rai et al. observed plutonium concentrations ranging from 10^{-3} to 10^{-7} M within the pH range 1.5 to 6 for crystalline $\text{PuO}_{2(s)}$ in distilled water and, likewise, *Fujiwara et al.* observed concentrations ranging from 10^{-3} to 10^{-6} M at pH ~4 to 5 (NaClO_4) [115–117].

The solubility studies by *Neck et al.* discussed in *Section 2.3.1.1* that extend their datasets to the acidic region also confirm that plutonium solubility is on the order of $\sim 10^{-5}$ to 10^{-3} M in the absence of a reducing agent [90,101].

2.3.1.4 Plutonium solubility and speciation in cementitious environments

Given the harsh oxidative and hyperalkaline conditions required to form and maintain the +7 and +8 oxidation states of plutonium described above, it seems unlikely that they will prevail under repository conditions. It is generally agreed that $\text{Pu(III)}_{(aq)}$ and $\text{Pu(IV)}_{(aq)}$ will be the dominant species in a closed cementitious repository; the former prevailing early on when reducing conditions dominate and the latter establishing overtime with oxygen ingress [97,118]. However, it is plausible that Pu(VI) salts (e.g. nitrates, carbonates) will be present to some extent, if only transiently [91], as a result of disposal of cemented ILW streams, namely PCM [20].

Pryke et al. determined the solubility of Pu(IV) under oxidising conditions in cement equilibrated waters ($S/L = 100 \text{ g L}^{-1}$) from a 9:1 BFS/OPC blend ($\text{pH} = 12.5$) and a 10:1 PFA/OPC blend ($\text{pH} = 11.5$) [119]. The cement waters were filtered and spiked with Pu(IV) nitrate to exceed the solubility of plutonium (as previously reported by the author [120]). The pH of the solutions was readjusted to the starting pH (12.5 or 11.5) using NaOH, where required. After a minimum of 24-hour equilibration, the solutions were centrifuged (4 000 g, 10 min) and ultrafiltered (1.7 nm). The plutonium concentrations determined in each of the cement waters is shown in **Table 2.3.1**, accompanied by the concentration determined using an undefined “simple” model, as stated by the authors.

The theoretically determined concentrations of plutonium were slightly lower than those measured in the centrifuged and ultrafiltered samples; the authors did not give any suggestion as to why this was but stated that the modelling results agreed well with the experimental data. The experimentally determined concentrations did not vary significantly between the two different cement waters, however there was a slight decrease in the measured plutonium concentration after ultrafiltration, for both. It is likely that this could be a result of the formation of Pu-bearing colloids or polynuclear species, larger than 17 \AA in size. Modelling results also determined that the solution species in both cases were likely to be $\text{Pu(OH)}_{4(aq)}$ and $\text{PuO}_2(\text{OH})_{2(aq)}$ and that solubility was limited by the formation of a $\text{PuO}_2\text{-hyd}_{(s)}$ phase. The authors did not explore the possibility of plutonium sorption onto dissolved cement species.

Table 2.3.1: Plutonium concentrations (M) determined experimentally and theoretically (using an undefined model) in cement equilibrated waters by *Pryke et al.* [119].

	Centrifugation	Ultrafiltration	Modelled	Predicted phases
9:1 BFS/OPC	9×10^{-8}	1×10^{-8}	4×10^{-9}	Aqueous: Pu(OH) ₄ , PuO ₂ (OH) ₂ Solid: PuO ₂ -hyd
10:1 PFA/OPC	8×10^{-8}	2×10^{-8}	4×10^{-9}	Aqueous: Pu(OH) ₄ , PuO ₂ (OH) ₂ Solid: PuO ₂ -hyd
9:1 BFS/OPC + carbonate	-	3×10^{-9}	-	-
10:1 PFA/OPC + carbonate	-	1×10^{-9}	-	-
9:1 BFS/OPC + sulfate	-	7×10^{-9}	-	-
10:1 PFA/OPC + sulfate	-	7×10^{-9}	-	-

The solubility of plutonium in the cement waters, with CaSO₄ and CaCO₃ added to saturation, was also determined after ultrafiltration (**Table 2.3.1**). The plutonium solubility was reduced from 10⁻⁸ to 10⁻⁹ M in the presence of carbonate or sulfate. No sulfate complexes were predicted to form under the given conditions, rather, the observed behaviour was hypothesised to be the result of kinetics, where sulfate ions stabilise small actinide species, slowing the rate of agglomeration and allowing them to pass through the ultrafilter. Similarly, modelling studies did not predict the formation of carbonate species, and a similar mechanism was proposed for the lower solubility. However, this kinetic argument was not well formulated a later study by *Krot et al.* determined that SO₄²⁻ and CO₃²⁻ anions (0.5 M) did not affect the composition or rate of precipitation of PuO₂.xH₂O precipitation from solutions of 0.2 M NaOH (room temperature) or 1 M NaOH (60 °C), compared to pure NaOH solutions [121].

The results from this study varied from those in a study by *Ewart et al.* [118,122] which show lower plutonium concentrations by at least one order of magnitude for the corresponding pH values of 11.5 and 12.5. This study describes the solubility of Pu(III) in a deoxygenated concrete equilibrated water, as a function of pH, using aged concrete from the Harwell site [122]. The rationale for using Pu(III), even though it only prevails under reducing conditions ((pe+pH) = 2 [94]), was the assumption that it would undergo rapid oxidation to Pu(IV) in water at high pH values, and that Pu(IV) will be the persistent oxidation state of plutonium under repository conditions. Pu(III)_(aq) was added to concrete-equilibrated water and the pH was adjusted to pH 7-13 using NaOH or HCl. The solutions were filtered at 2-4 nm (an approximate MWCO of 25 000 - 30 000). Between pH values of 7 and 9, the concentration decreased from ~10⁻⁵ to ~10⁻¹⁰ M, but above pH 9 the concentration did not deviate significantly from 10⁻¹⁰ M

(Figure 2.3.5). Furthermore, the solid phase predicted by modelling (HARPHRQ code, HATCHES database) was expected to be $\text{Pu}(\text{OH})_{4(s)}$ in equilibrium with $\text{Pu}(\text{OH})_{4(aq)}$, in contrast with the $\text{PuO}_2\cdot\text{hyd}$ phase predicted by *Pryke et al.* The formation of the $\text{Pu}(\text{OH})_5^-$ hydrolysis product was disregarded, as an associated increase in solubility at high pH values was not observed.

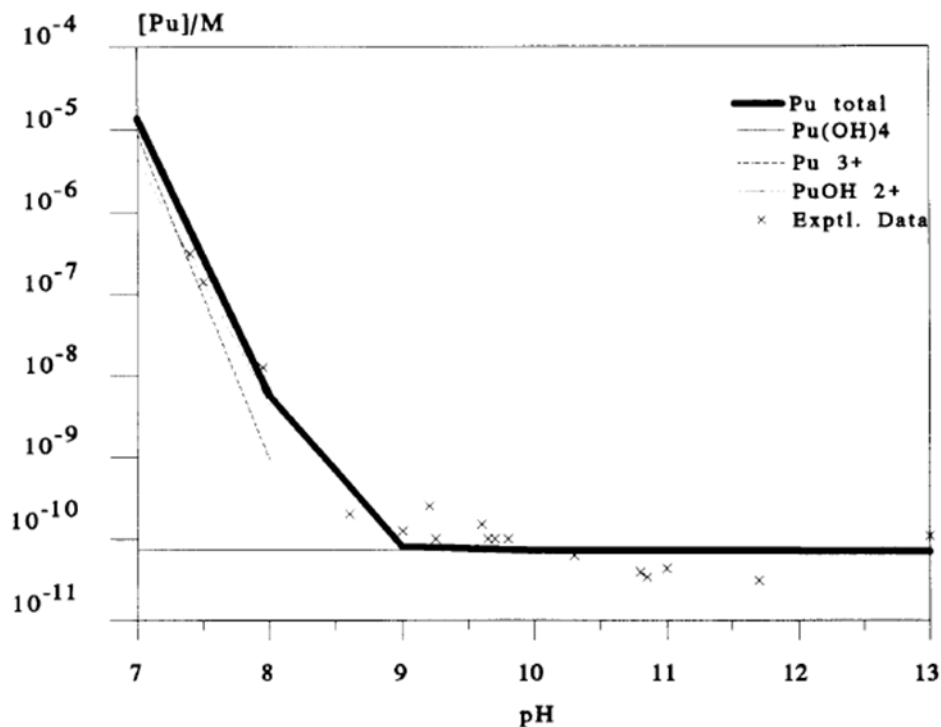


Figure 2.3.5: Plutonium solubility, experimental and simulated with HARPHRQ (from [122])

Krot et al. also studied the influence of other various anions on $\text{PuO}_2\cdot x\text{H}_2\text{O}$ precipitation in NaOH solutions. As with sulfate and carbonate, anions such as NO_2^- (2 M) and various organic anions (0.1 M) were not shown to significantly alter the rate of $\text{PuO}_2\cdot x\text{H}_2\text{O}$ formation. In the presence of SiO_3^{2-} (0.05 M in 0.2 M NaOH) or PO_4^{3-} (~0.05 M in 0.2 - 12 M NaOH), however, the 'usual' green precipitate formed showed a grey colouration. Significant deflocculation (i.e. conversion of the precipitate to the colloid phase) of the precipitates was also observed on washing with water. The silicate- and phosphate-induced precipitates were therefore analysed by IR spectroscopy. Absorption bands at 1000 cm^{-1} and 1020 cm^{-1} signified the presence of silicate and phosphate vibrations, respectively, indicating that both were present in the respective precipitates. The authors concluded that single phase $\text{PuO}_2\cdot x\text{H}_2\text{O}$ was therefore not present, and the precipitates were more akin to $\text{PuO}_2\cdot y\text{SiO}_2\cdot x\text{H}_2\text{O}$ or $\text{PuO}_2\cdot y\text{P}_2\text{O}_5\cdot x\text{H}_2\text{O}$ phases. In the case of the former phase, this could have implications for the co-precipitation of plutonium with low Ca/Si ratio C-S-H phases, relating to the work carried out in **Chapter 6**.

2.3.2 Plutonium immobilisation in cement matrices and cement phases

2.3.2.1 Plutonium uptake by cement matrices

The findings from several studies investigating batch plutonium sorption onto cements are summarised in **Table 2.3.2**; *Ochs et al.* also further summarises the results from plutonium sorption onto concrete, cement and cement phases (**Figure 2.3.6**) [123].

Table 2.3.2: Summary of literature for plutonium sorption on Portland cements.

Reference	Cement surface(s)	General comments and conclusions
<i>Hoglund et al.</i> [124]	Portland cements including fly ash and silica blends	<ul style="list-style-type: none"> - R_d values were $\sim 10^3$-10^4 L kg⁻¹. - Cement composition had little effect on R_d value. - Sorption behaviour resembled that of U or Np.
<i>Heimann</i> [125]	Portland cement with 20 vol% silica fume	<ul style="list-style-type: none"> - Sorption of Pu (and Am, Cs, Sr) leached from used fuel and waste glasses performed at 200 °C. - Cement showed a 'higher' selectivity for Pu than Am, in the same study. - High sorption capacity for actinides theorised due to presence of apatite phases or high pH.
<i>Aggarwal et al.</i> [126]	Various Portland cement blends, C-S-H and various minor phases	<ul style="list-style-type: none"> - R_d values were $\sim 10^3$-10^5 L kg⁻¹ for all surfaces. - Tendency towards higher sorption in blends containing more PC suggest sorption was mainly onto hydration products. - C-S-H was considered to be the most important phase for sorption.

Portland cement surfaces have been shown to exhibit R_d values for plutonium on the order of $\sim 10^3$ - 10^5 L kg⁻¹ [123,124,126], where the general formula for the R_d value of a sorbate is given in **Equation 2.3.3**, and is defined as the ratio of a sorbate partitioned onto / into a sorbent, compared to the solution phase [127]:

$$R_d = \frac{\text{concentration in the solid phase}}{\text{concentration in the solution phase}} \quad (2.3.3)$$

These early reported studies of plutonium sorption onto cement surfaces do not widely explore the mechanisms of uptake or plutonium speciation, but are in general agreement that C-S-H phases likely play the most important role in the uptake process. It is generally reported that the surface chemistry of C-S-H phases dictates the sorption of plutonium (and other actinides) onto Portland cements [128,129].

2.3.2.2 The role of C-S-H and proposed mechanisms of uptake

The surface of C-S-H phases are made up of silicon (>SiOH) and calcium (>CaOH) sites. At a low Ca/Si ratio, silanol (SiO⁻) sites will dominate and result in an overall negative surface

potential. When the Ca/Si ratio is increased, increased calcium ions in solution will sorb to silanol sites, increasing the positivity of the surface potential [128,130]. A negative surface potential is electrostatically favourable for the uptake of positively charge plutonium (and other actinide) species. It could therefore be assumed that plutonium sorption will occur onto C-S-H via silanol sites, but in competition with Ca^{2+} ions. The uptake of plutonium by C-S-H phases was described in detail by *Haußler et al.*

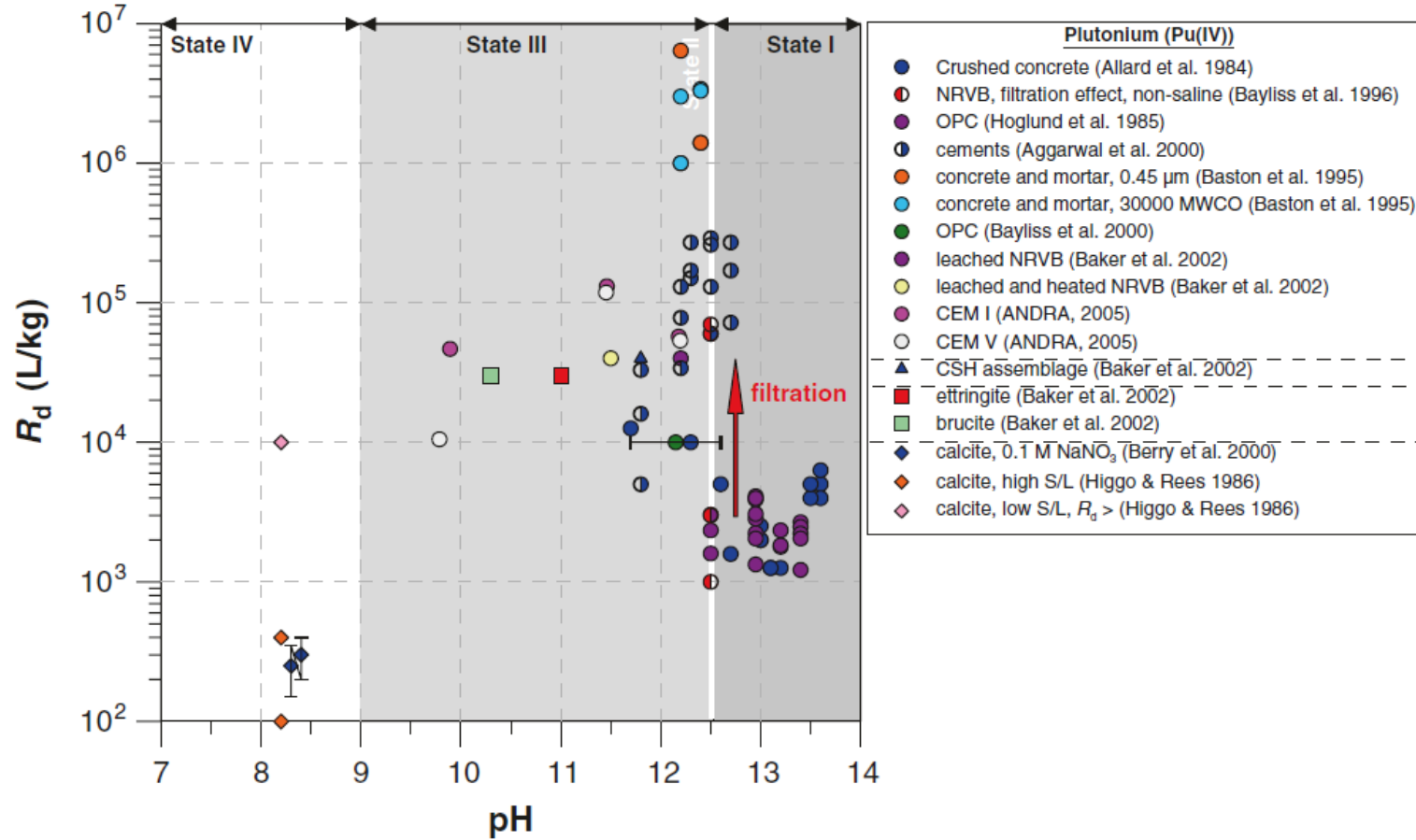


Figure 2.3.6: R_d values of plutonium in cementitious systems (from [123])

2.3.2.3 Plutonium sorption by C-S-H: A study by Haußler et al.

More recently (published towards the completion of this PhD Thesis), *Haußler et al.* described the mechanisms of actinide sorption onto C-S-H phases, and is the first study of its kind to investigate in plutonium uptake in detail [97]. C-S-H phases were synthesised at Ca/Si ratios of 0.75, 1.07 and 1.65 using the direct synthesis method (i.e. solid starting materials of SiO₂ and CaO, similar procedure described already in **Chapter 3**), with S/L ratios between 0.5 to 20 g L⁻¹. Pu(III) was added on the order of 10 nM to the C-S-H phase suspensions which were then equilibrated for 72 hours. ICP-MS measurements confirmed that ≥ 99 % of the plutonium was removed from solution at all Ca/Si ratios. Phreeqc modelling (using the PSI database) calculated that Pu(III)_(aq) oxidised to form a “hydrous, aged” PuO₂ phase within the measured E_h range of the experiment, indicating that Pu(III) uptake could be attributed to the precipitation of this phase rather than sorption by C-S-H (**Figure 2.3.7**).

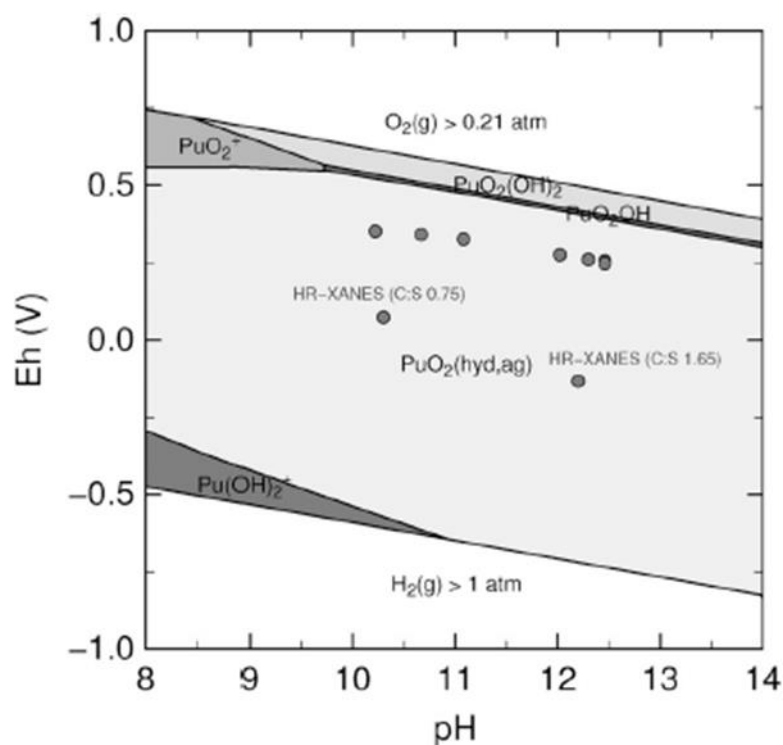


Figure 2.3.7: Predominance diagram for an equilibrium concentration of 1×10^{-10} M Pu(III) in the system C-S-H/MilliQ water for C/S ratios between 0.7 and 1.8. The grey dots mark the measured E_h and pH values of the sorption samples with different C/S ratios and the samples for HR-XANES with C/S 0.75 and 1.65 (from [97]).

In addition to the aforementioned sorption suspensions, C-S-H samples with a higher Pu(III) loading (10 μM concentration) were measured by high resolution (HR) XANES. The HR-XANES measurements determined that plutonium was predominantly in the +4 oxidation state, but this was confirmed for the Ca/Si ratios of 0.75 and 1.65 only (**Figure 2.3.8**). The authors also speculated about the possibility of a plutonium +5 state co-existing as a hydroxide

species, attributed to a post-edge shoulder in the XANES spectra, which was not observed in the Pu(IV)O₂ standard. This, again, is evidence of formation of a mixed valent PuO_{2+x} phase described above by [99] and is consistent with results obtained in the present Thesis (see **Chapter 6**). There was no conclusion made about possible uptake modes of plutonium by C-S-H relating to the theory described in *Section 2.3.2.2*; it seems likely that the authors assumed the precipitation of the hydrous PuO₂ phase was the only reason for plutonium uptake.

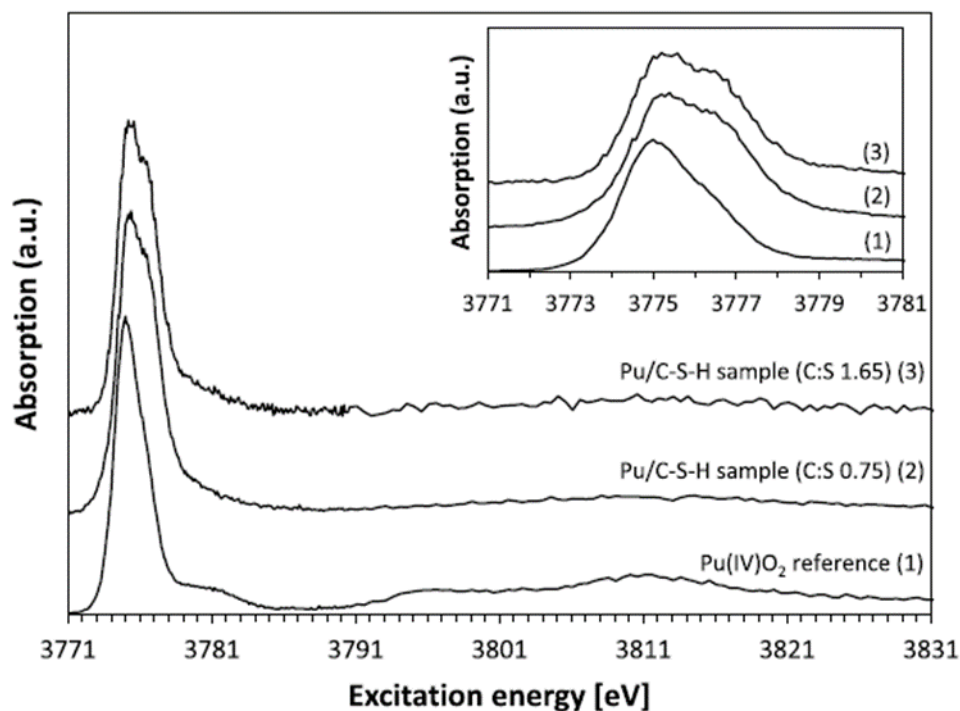


Figure 2.3.8: Pu M_v-edge HR-XANES spectra of the Pu/C-S-H samples with C/S 0.75 and C/S 1.65 and the corresponding Pu(IV)O₂ reference (from [97]).

2.3.2.4 PuO₂ encapsulation in cement matrices: A study by Kearney *et al.*

Characterisation of cement encapsulated PuO₂ particles by *Kearney et al.* considered the effect of localised alpha radiation damage on the physico-chemical development of the cement matrix (see **Appendix 1**, co-authored by A. S. Yorkshire) [131]. Magnox PuO₂ particles were encapsulated in Sellafield Ltd UK nuclear specification Portland cement grouts of 3.44:1 BFS/PC and 3:1 PFA/PC, respectively, which were cured for over 1 year in Ca(OH)₂ solution, before characterisation and comparison to control, non PuO₂-containing samples. By SEM and optical imaging, it was not possible to observe any interaction between PuO₂ and cement hydrate phases formed in both cement formulations, suggesting that PuO₂ was relatively undisturbed by the surrounding alkaline media. Additional XRD measurements of the cement blends did, however, present observable changes, attributed to radiation damage: in the BFS

blend, there was an increase in intensity of the (100) reflection of ettringite for the PuO₂-containing sample when compared to the blank. This was hypothesised to be the result of radiolytically-induced oxidation of sulfide leading to an increase in available sulfate for ettringite formation, at the expense of monosulfoaluminate [132]. However, the authors stated that there was little conclusive evidence for this and further investigation of this hypothesis is beyond the scope of this current study. The main conclusion to draw from this study was the apparent chemical stability of the encapsulated PuO₂ surrounded by an alkaline cement matrix, consistent with the low solubility of PuO₂ observed under alkaline conditions (see Section 2.3.1.1). This observation is also described in more detail in **Chapter 6** in this Thesis.

2.3.2.5 Plutonium leaching from cement matrices

Bernard et al. and *Law et al.* described leaching of plutonium from cement matrices in water [133,134]. The former demonstrated that over the course of 435 days, 2.8×10^{-6} (2.8×10^{-4} %) and 5×10^{-8} (5×10^{-6} %) weight fractions of plutonium were leached from full scale cement blocks containing liquid NaNO₃ waste (containing Pu, in addition to Am, Cs, Sr and Co) and solid metallic waste (Pu and Cs containing), respectively. Similarly, *Law et al.* also observed plutonium release from cementitious matrices over the course of 322 days at a long-term rate of $\sim 10^{-5}$ %, per day.

Law et al. described an initial plutonium release rate of $\sim 10^{-3}$ - 10^{-4} %. Given that the dissolution media was deionised water, this initial high leaching rate is not surprising. A decrease in the plutonium leaching rate overtime was attributed to the formation of secondary phases acting as a diffusion barrier, namely plutonium co-precipitating with calcite. However, later μ -XRF mapping and μ -XAS results did not appear to corroborate the formation of such a phase and showed evidence for Pu-oxide type coordination only. Further to this, XANES data showed that plutonium was present as a mixture of Pu(VI) and Pu(V); with between 45-56 % \pm 3 % conversion to Pu(V), suggesting that Pu(IV) underwent slight oxidation during sample preparation which continued with curing of the cement (**Figure 2.3.9**). This is consistent with the formation of a mixed valent oxide proposed by *Neck et al.* [99].

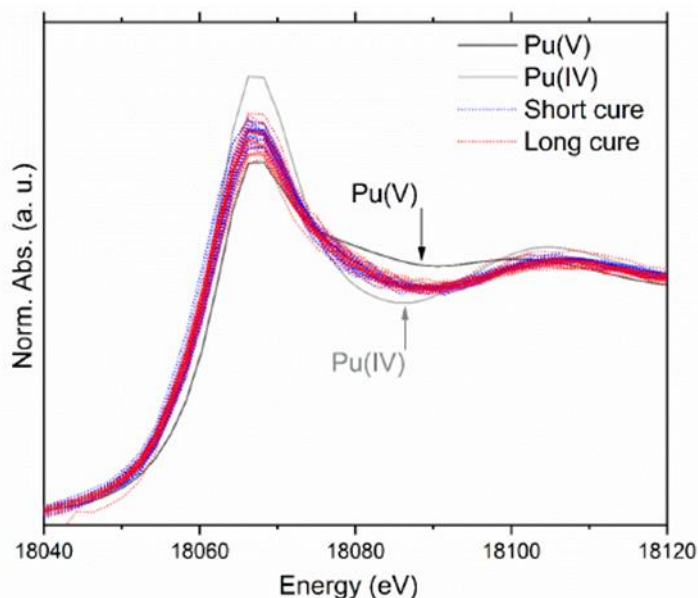


Figure 2.3.9: Pu L_{III}-edge XANES from all sampling points with comparative standards of Pu(IV)_(aq) and Pu(V)_(aq) (from [134]).

2.3.3 Plutonium interactions with other related cementitious phases

2.3.3.1 Minor cement hydrate phases

The uptake of plutonium onto minor cement phases is not widely reported. As mentioned in Section 2.3.2.1, Aggarwal *et al.* trialed plutonium batch sorption onto minor phases including chloride- and carbonate-interlayer hydrotalcite phases as well as chloroaluminate (Ca₂Al(OH)₆(Cl)·xH₂O). The authors only concluded that hydrotalcites gave an R_d value of ~10⁴ L kg⁻¹ and chloroaluminates a value of ~10³-10⁴ L kg⁻¹, with no further discussion on the mechanism of uptake. This was within the same range as the R_d values calculated for the Portland cements and C-S-H phases in the same study.

2.3.3.2 Calcite

Plutonium association with calcite was eluded to by Law *et al.* (see above). Ochs *et al.* also reported an R_d value of plutonium on calcite on the order of ~10² (0.1 M NaNO₃, pH ~8), determined by Berry *et al.* who described that plutonium uptake by calcite-containing rocks occurred by sorption directly to calcite [135].

Higgo and Rees determined the influence of different S/L ratios on plutonium uptake in marine sediments that contained 45-80 % calcite [136]. Above 40 g L⁻¹ (0.04 kg L⁻¹) the R_d values obtained were of the order 100-400 L kg⁻¹, but at 3 g L⁻¹ (0.003 kg L⁻¹) the R_d values were significantly enhanced to above 10⁴ L kg⁻¹. The former values were attributed to formation of Pu-carbonate complexes in solution that sorbed less effectively to the sediments, thus decreasing the R_d values. Although these values were obtained in solutions of sea water, on

natural sediments, the formation of Pu-carbonate complexes are also important to consider for solubility limitations of plutonium in cementitious environments (**Chapter 6**).

2.4 Technetium

Technetium-99 (^{99}Tc) is a radionuclide of high prominence when considering immobilisation techniques for radioactive waste disposal, due to its high solubility as the pertechnetate (Tc(VII)O_4^-) anion, which renders it highly mobile in the subsurface under oxidising conditions, and its long half-life of 210 000 years, which means it will be a dominant contributor to the radiological inventory in the post-closure safety case for any geological repository [23]. Generated as a fission product of uranium-235 or plutonium-239, ^{99}Tc is a low energy beta-emitter ($E_{\text{max}} = 0.29 \text{ MeV}$) with a specific activity of 0.017 Ci g^{-1} (629 MBq g^{-1}). Approximately 97 % of technetium is removed from the void spaces of fuel rods during spent fuel reprocessing operations [137]. In the USA, a significant amount of ^{99}Tc -bearing waste was generated during early reprocessing efforts to produce plutonium for military purposes; these wastes are currently stored in failing underground storage tanks at the Hanford site and further wastes at the Savannah River site [138]. Due to the volatility of some technetium compounds (e.g Tc_2O_7 boiling point at $311 \text{ }^\circ\text{C}$), the vitrification of ^{99}Tc is problematic at operational temperatures typical of a low-activity glass melt ($1150 \text{ }^\circ\text{C}$) [24]. As such, significant effort has been made to understand whether cement grouts can be used as an alternative.

2.4.1 Solubility and speciation of technetium

Technetium is a transition metal with electronic configuration $[\text{Kr}] 4d^5 5s^2$ and primarily resides in the +4 or +7 oxidation states [137]. The solubility of technetium is controlled by the oxidation state and the relative redox conditions of the solution (**Figure 2.4.1**). The following is a discussion on the implications of the oxidation state on the technetium aqueous speciation, relative to alkaline solutions relevant for studying cementitious environments.

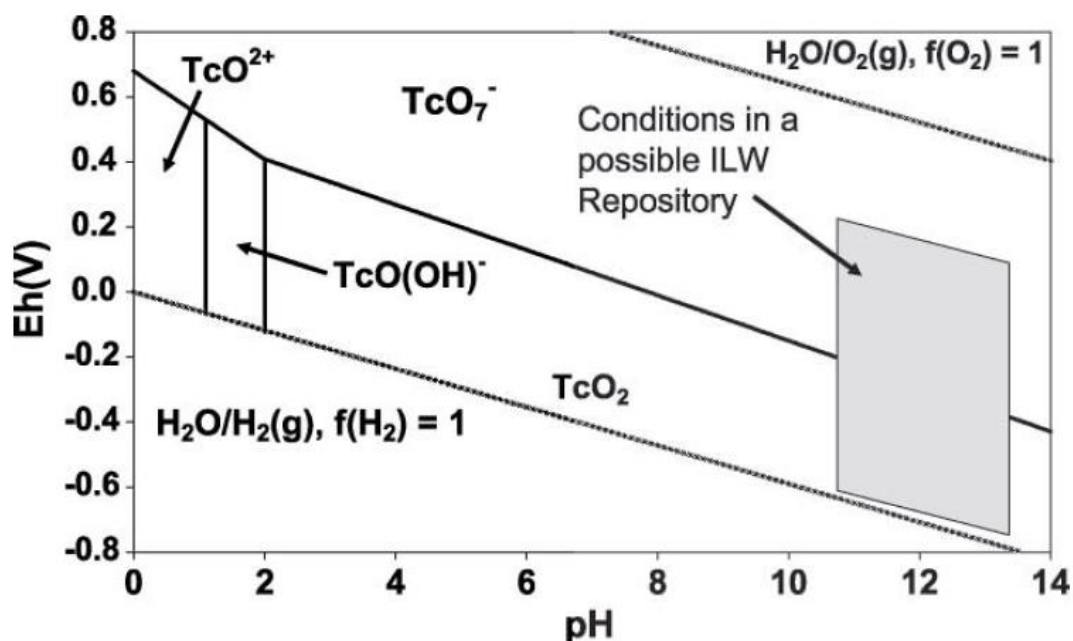


Figure 2.4.1: Pourbaix diagram for technetium (from [139]).

2.4.1.1 Tc(IV) solubility in alkaline solution

Studies conducted in the alkaline region have shown that Tc(IV) solubility displays pH dependency and that $TcO_2 \cdot xH_2O$ will be the solubility limiting phase if reducing conditions are maintained. *Yağcintaş et al.* used $Na_2S_2O_4$, $SnCl_2$ and Fe powder to maintain reducing conditions ($pe+pH \leq 2$) in solutions of NaCl (0.1 - 5 M), $MgCl_2$ and $CaCl_2$ (0.25 - 4.5 M) [140,141]. From neutral pH to pH ~9, Tc(IV) solubility generally showed no pH (or ionic strength) dependency, which was attributed to the lack of H^+ exchange to control the technetium solubility in this region. Above pH 9 in NaCl, Tc(IV) solubility increased and, above pH 11, the solubility showed a definitive linear increase as result of dominant anionic hydrolysis species, $TcO(OH)_3^-$ (aq). The behaviour observed was different for $MgCl_2$ and $CaCl_2$ solutions. Tc(IV) solubility showed a much sharper increase in the alkaline pH region and the authors proposed the formation of ternary complexes, namely $M[TcO(OH)O_5]^{3+}$ (aq), where M = Mg or Ca. Similarly, *Eriksen et al.* theorised the formation of Tc(IV)-hydroxo-carbonato complexes in Na_2CO_3 solutions exposed to various partial pressures of CO_2 [142]. Such complexes could therefore have implications for the increased mobility of Tc(VI) in Mg, Ca or carbonate rich alkaline solutions.

The pH dependence of Tc(IV) solubility in the alkaline region is further corroborated in studies by *Meyer et al.* (0.01 to 2.6 M NaCl; pH 7-10) [143,144] and *Eriksen et al.* (Na_2CO_3 ; pH 7-12), however, in the study by *Warwick et al.* the measured Tc(IV) solubility was slightly lower [139]. In 0.3 M NaOH solutions at pH >13, the values for Tc(IV) concentration in solution were

obtained on the order of 10^{-9} to 10^{-8} M, compared to $\sim 10^{-7}$ M for *Yalçintaş et al.* Nevertheless, the same general trend of increased Tc(IV) solubility at high pH values was observed and concluded by the authors.

2.4.1.2 Tc(VII) solubility in alkaline solution

If reducing conditions are not maintained and oxidative conditions prevail, Tc_(aq) will predominantly reside in the +7 oxidation state as the mobile pertechnetate anion (Tc(VII)O₄⁻). The work carried out in this Thesis concerns the interactions of the pertechnetate anion with cement hydrate phases (**Chapter 7**).

2.4.1.3 Technetium solubility in cement equilibrated solution: A study by Pilkington

Pilkington also investigated the solubility of technetium in cement waters between pH 11-13 [145]. Cement grouts of 10:1 PFA:OPC, 6:1 CaO:OPC and 3:1 BFS:OPC were equilibrated in deionised water. Technetium was added as either NH₄TcO₄ ranging from 10^{-7} to 10^{-5} M or solid TcO₂·xH₂O (with an equivalent concentration of 2.5×10^{-4} M) and Na₂S₂O₄-containing variants were also prepared to induce reducing conditions. In summary, after equilibration for 6-7 weeks it was found that:

- (i) under non-reducing conditions the final concentration of Tc_(aq) in the NH₄TcO₄ solutions was not significantly different.
- (ii) for NH₄TcO₄ under reducing conditions, the solutions with a higher initial Tc_(aq) concentration ($\sim 10^{-5}$ M) had the highest redox potentials (Eh = -70 - +60 mV), corresponding to the oxidation of Na₂S₂O₄ and, in turn, the reduction of pertechnetate. A black solid was also observed in these solutions, likely to be TcO_{2(hyd)}.
- (iii) when NH₄TcO₄ was added at a lower initial Tc_(aq) concentration ($\sim 10^{-7}$), and under reducing conditions, there was a decrease in concentration by ~ 1 order of magnitude.
- (iv) solid TcO₂·xH₂O was still present in all solutions. Under non-reducing conditions, Tc_(aq) concentrations ranged from $\sim 10^{-6}$ to 10^{-5} M compared to lower $\sim 10^{-8}$ to 10^{-7} M concentrations under reducing conditions. This was attributed to some oxidation of TcO₂·xH₂O to pertechnetate under non-reducing conditions.
- (v) relatively no differences were observed between the concentrations in the different cement waters and the pH range studied.

These findings are agreement that technetium will prevail as the mobile pertechnetate species in a cementitious repository in the absence of reducing conditions (see *Section 2.4.2.3*)

2.4.2 Technetium immobilisation in cement matrices

2.4.2.1 Reductive immobilisation

An early leaching study by *Brodda* indicated that BFS-containing cement blends showed an increased retention for pertechnetate (99.9 % retention) compared to that of pure Portland cements and calcium aluminate cements (~80-90 % retention) in both water and quinary brine solutions (NaCl-KCl-MgCl₂-MgSO₄) [146]. The author theorised that this was due to a mineral fixation process, sequestering technetium, that was more prominent in slag-containing systems. More recent studies have deduced that BFS and other soluble sulfide species act to reductively precipitate pertechnetate species and immobilise technetium in a lower oxidation state [39,137,147]. In particular, cementitious formulations are being developed by the Savannah River Laboratory and the Pacific Northwest National Laboratory specifically for the treatment of radionuclide-containing salt solutions as a bi-product of HLW processing, referred to as Saltstone (or Cast Stone) [25]. High volume replacement of PC by BFS is used to maintain reducing conditions in order to retain pertechnetate (and chromate) species through reductive immobilisation [39]. The typical composition of a BFS-containing Saltstone formulation was outlined by *Cantrell et al.* and is given in **Table 2.4.1** [148].

Table 2.4.1: Dry composition of Saltstone blend by weight (from [148]).

Blast-furnace slag	Fly ash	Portland cement
45 %	45 %	10 %

Leaching studies have been carried out to observe the retention of technetium in Saltstone grouts. *Cantrell et al.* adopted a modified SPFT test (static conditions other than for sampling periods of 3 mL min⁻¹) for Saltstone cured with 10 ppm technetium, in 5 mM Ca(OH)₂ solutions (pH 12.5 - 12.9). Technetium release was initially reported to be 30 times higher at an Eh value below -100 mV, compared to after ~40 days when the Eh dropped below -400 mV. This was also in general agreement with the results from *Pabalan et al.* who showed a dependency of technetium release with Eh [149]. A Saltstone (cured with packed column subject to an effluent flow (0.0066 mL min⁻¹, 0.5 mL min⁻¹ for sampling periods) showed an initial spike in technetium release (8.8 % of total Tc) when the Eh was measured at +414 mV (attributed to partial oxidation of the grout during preparation of the column, in turn reducing its initial effectiveness). Subsequent early stage technetium release was then low as the system became quickly reducing (Eh = -453 mV), followed by a gradual increase coinciding with more positive Eh values. This is in line with the redox stability fields of Tc(VII) and Tc(IV) relating to lower retention and higher retention, respectively [150,151].

Although solid-phase characterisation was not carried out in these studies, *Cantrell et al.*, used thermodynamic modelling of the Saltstone system to conclude that Tc-sulfide phases were present but that Tc release was controlled by the higher solubility $\text{TcO}_2 \cdot x\text{H}_2\text{O}$ phase (**Figure 2.4.2**). It seems likely that hydrous Tc-oxide and -sulfide phases are in coexistence in the cement matrix (see *Section 2.4.2.2*).

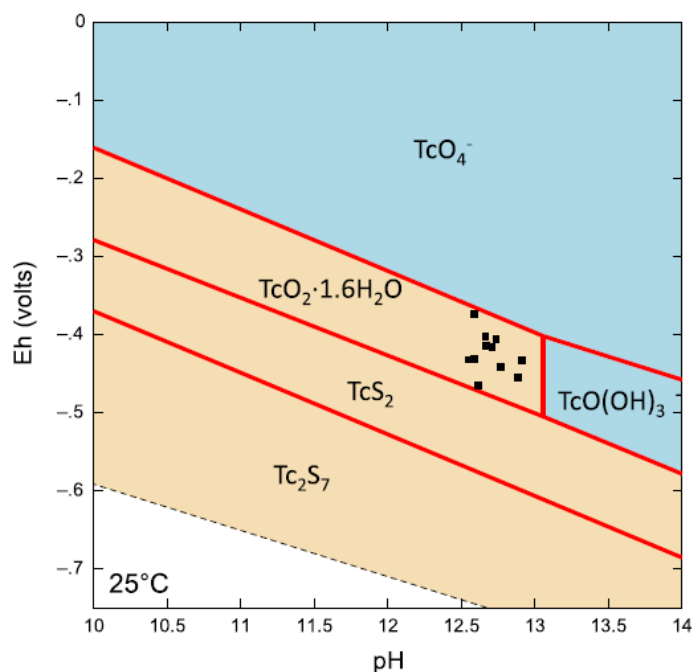


Figure 2.4.2: Eh-pH diagram for Tc constructed using a porewater composition that approximates the Saltstone system (10^{-6} M Tc, 0.4 M NaNO_3 , 0.01 M Na_2SO_4). Points represent approximate measured Eh values. (from [148])

2.4.2.2 Speciation of “grout-reduced” technetium

Several X-ray absorption spectroscopy studies have been adopted to determine the speciation of technetium sequestered in reducing grouts (Tc K-edge = 21 044 eV). *Allen* used EXAFS to determine the local and extended coordination of technetium in BFS-containing Portland cement grouts with and without Na_2S , FeS and NaH_2PO_2 additives. The study concluded that BFS-only grouts showed partial reduction of pertechnetate, with the formation of Tc clusters revealed to have a S first shell coordination. In the case of FeS and Na_2S additives, further Tc-Tc interactions suggested a structure similar to TcS_2 ; and for the NaH_2PO_2 additive, Tc-O and Tc-Tc interactions pertained to a TcO_2 -type phase. XANES was also used to interpret to extent of pertechnetate reduction indicated by the negative edge shift in E_0 and the presence of FeS was shown to reduce Tc almost to the same extent as TcO_2 . In addition, ferrous-only FeO, mixed ferrous/ferric Fe_3O_4 and Mn_3O_4 additives did not prove to be reactive towards Tc immobilisation.

Later studies have shown that the Tc-sulfide species reported by *Allen* can have variations in local coordination. *Lukens et al.* identified a TcS_x phase in Saltstone-based Portland cements to be akin to a Tc_3S_{10} phase (or Tc_2S_7 phase) which has a structure composed of triangular Tc(IV) clusters linked by disulfide and sulfide chains (**Figure 2.4.3**) [152].

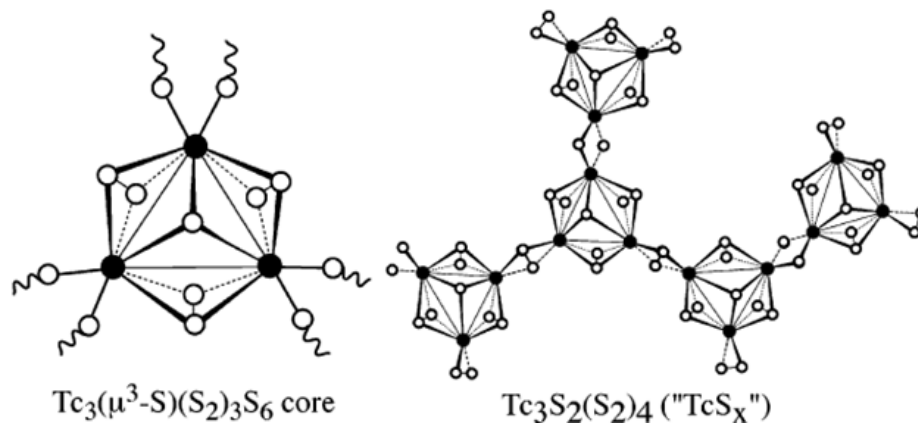


Figure 2.4.3: The $Tc_3(\mu^3-S)(S_2)_3S_6$ core that forms structural building blocks of TcS_x , and a portion of the proposed structure of TcS_x . Technetium atoms are illustrated by solid circles; sulfur atoms are depicted by open circles (from [152]).

However, *Arai et al.* actively noted that the Tc-sulfide phase, also in Saltstone-based cement, was different to that shown by *Lukens et al.* Rather, the average technetium coordination number was summed to be 6, suggesting partially sulfidised Tc(IV) species [153]. The authors discussed that this could range from fully hydrolysed $Tc(IV)O(OH)_2(H_2O)_3$, to partially or fully sulfidised $Tc(IV)O(H_2O)_{5-x}S_x^{2-}$ species in coexistence throughout the cement matrix, which was consistent with fitting of oxygen shells (at ~ 1.7 Å and ~ 2.1 Å) and sulfur and technetium shells (at ~ 2.9 Å) in the EXAFS region. Similarly, *Asmussen et al.* determined technetium speciation in Cast Stone by XANES linear combination fitting to be 13% $Tc(IV)_2S_7$ and 28% $Tc(IV)O_2$ [154]. The remainder of the technetium speciation was still attributed to $Tc(VII)O_4$, showing that sulfide phases were not 100 % effective at reductively precipitating technetium. Nevertheless, these studies still highlight the importance of sulfide-containing species for technetium immobilisation, but they also highlight that cement hydrate phases, such as AFm and Aft phases, which also contain sulfur, have been overlooked as potential sorbents of technetium.

2.4.2.3 Non-reductive immobilisation

The above studies have shown reductive immobilisation to be an important practice for technetium retention in cementitious wastefoms. If a geological repository is chosen for the final disposal of ILW, after several years groundwater will ingress, eventually inducing O_2 diffusion through the cement. *Lukens et al.* showed that O_2 diffusion induced significant re-

oxidation of technetium to pertechnetate, much more so than the purposeful addition of NO_3^- oxidants. Retrospectively, there is little information about the behaviour of pertechnetate species interacting with non-reducing cement hydrate phases and how these can be utilised or modified to allow for higher pertechnetate retention.

Studies have shown that non-reducing cements do not retain Tc(VII) well. *Corkhill et al.* considered the migration of pertechnetate through quartz sand and cement grout (Nirex Reference Vault Backfill; NRVB) columns, in the absence of reducing agents [155]. More than 98 % of the technetium ($^{99\text{m}}\text{Tc}$, ~ 20 MBq aqueous injections) was eluted through the water-saturated columns. Technetium displayed conservative transport behaviour through the quartz column whereas the NRVB induced more longitudinal dispersivity through the column (**Figure 2.4.5**). This behaviour was attributed to the negative surface charge of the quartz at the experimental pH (~ 5.7), leading to repulsive electrostatic interactions between the quartz surface and TcO_4^- . In the case of NRVB, the slower transport of technetium through the column was attributed to high internal porosity of NRVB leading to regions where the flow was decreased or immobile, rather than an active sorption mechanism. *Druteikiene et al.* also concluded that pertechnetate sorption to hardened Portland cement paste was low ($R_d = \sim 1.5 \times 10^{-3} \text{ L g}^{-1}$) over the course of 42 days, corroborating the hypothesis that cement will not retain pertechnetate via chemi-sorption onto silanol predominant surfaces [156]. Further investigation is required to establish which cement phases are capable of sequestering technetium through non-reductive means.

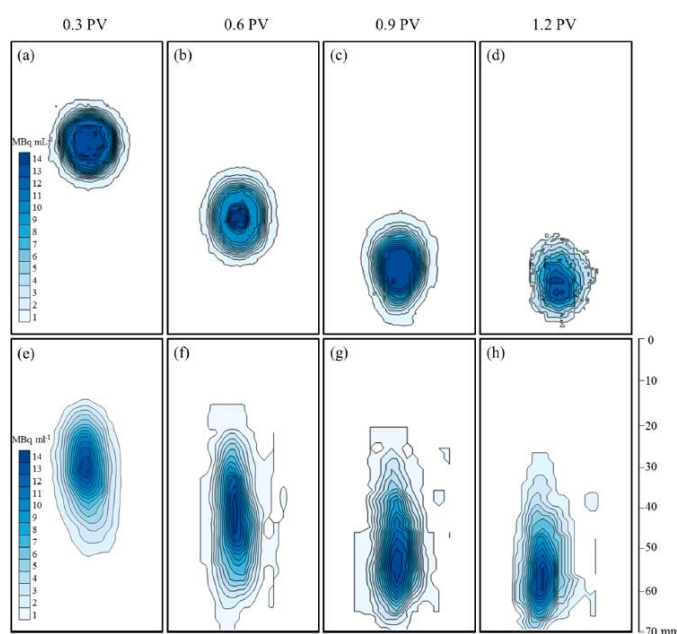


Figure 2.4.6: Calibrated concentration distribution from gamma camera images of $^{99\text{m}}\text{Tc}$ activity in Ottawa quartz sand in a pH 5.7 solution at (a) 0.29 pore volumes (PV) (8 min), (b) 0.58 PV (16 min), (c) 0.87 PV (24 min), and (d) 1.16 PV (32 min) and in Nirex Reference Vault Backfill at (e) 0.3 PV (20 min), (f) 0.6PV (40 min), (g) 0.9 PV (60 min), and (h) 1.2 PV (80 min) (from [155]).

2.4.2.4 Technetium immobilisation in ettringite: A study by Saslow et al.

As noted previously, the role of cement hydrate phases in the sorption of technetium to cement grouts has not been widely considered, despite the fact that mechanisms of uptake for other anionic radionuclide species (e.g. selenite / selenate, iodate) have been postulated, for example, by AFm phases and ettringite [157,158]. During the course of this Thesis, discussions with collaborators at the Pacific Northwest National Laboratory led to the development of a co-authored study on the uptake of pertechnetate by ettringite phases (Saslow et al., see **Appendix 2**, co-authored by A. S. Yorkshire) [159]. In this study, NaTcO_4 was coprecipitated with ettringite (using stoichiometric amounts of $\text{Ca}(\text{OH})_2$ and $\text{Al}_2(\text{SO}_4)_3$) to achieve a TcO_4^- loading of between 0.9 to 166 ppm. XRD refinement revealed an increase in the ettringite unit cell volume and lattice a parameter, compared to ettringite precipitated in the absence of technetium. This was attributed to the larger size of the TcO_4^- anion (2.52 Å [160]), compared to SO_4^{2-} (2.42 Å [161]), being accommodated and thus increasing the size of the intracolumn channel in ettringite.

Using EXAFS measurements and *ab initio* molecular dynamics (AIMD) calculations the authors proposed mechanisms for anion exchange to account for the charge balance deficiency between TcO_4^- and SO_4^{2-} . The uptake mechanism was rationalised by the simultaneous incorporation of an OH^- anion with TcO_4^- , in place of ($\text{SO}_4^{2-} + \text{H}_2\text{O}$), given that this AIMD calculation provided the best fit for the experimental EXAFS spectrum for 100 ppm and 160 ppm containing ettringite (**Figure 2.4.6**).

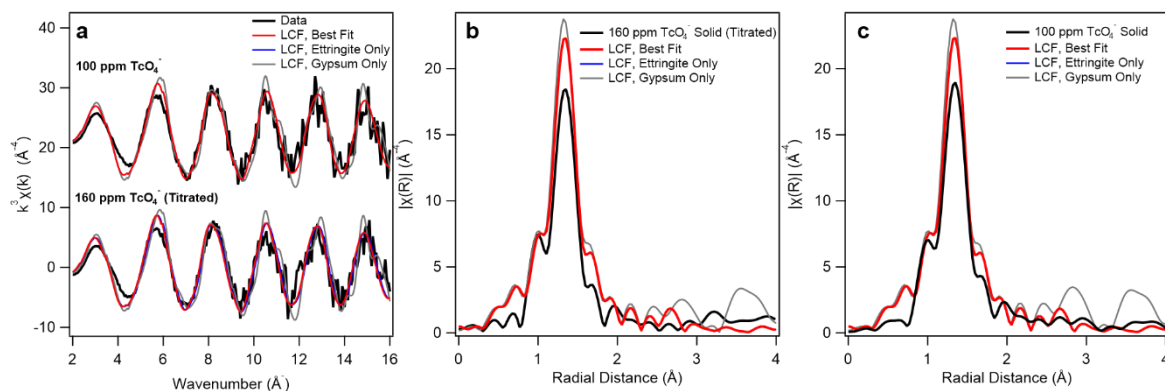


Figure 2.4.6: Structural environment of TcO_4^- and proposed incorporation modes by EXAFS and AIMD spectra. (from [159], note that gypsum samples are also shown to indicate the role of gypsum impurities).

This study confirms the importance of considering minor cement hydrate phases for pertechnetate immobilisation without the need for reduction to Tc(IV). Samples of $\text{NH}_4\text{TcO}_4^-$ contacted ettringite phases synthesised at TUoS that were supplementary to this study are also discussed in **Chapter 7** of this Thesis.

2.5 Summary and Research Scope

2.5.1 Summary of literature findings

2.5.1.1 Uranium

Uranium has been studied extensively with regards to sorption and uptake of U(VI) onto cement and C-S-H phases. Natural mineral analogues can be significant in understanding the long-term capability of cement materials to retain uranium.

2.5.1.2 Plutonium

Due to the complex solution behaviour exhibited by plutonium, the +4 oxidation state will limit the mobility of plutonium in cementitious environments. There has been little investigation into the uptake mechanism of plutonium by cement phases in comparison to uranium.

2.5.1.3 Technetium

Immobilisation of technetium in cementitious materials has been studied extensively with regard to reductive precipitation as Tc(IV)-sulfide phases. Thus far there has been little consideration for the role of other sulfur-containing cement minerals and their capacity for enhanced technetium sequestration, such as ettringite or AFm-SO₄ phases, particularly in the case of the mobile pertechnetate anion.

2.5.2 Scope of the research in this Thesis

Although the previous studies detailed were conducted to begin understanding the importance of particular cementitious conditions and cement hydrate phases in sorbing and retaining radionuclides, there is the ongoing need for further investigation to explore the fundamental interactions of uranium, plutonium and technetium with cement materials, given the complexity of cementitious systems. In particular:

- For uranium(VI), use of specialised spectroscopic techniques such as X-ray absorption spectroscopy have been used to understand the coordination environment of uranium(VI) in contact with C-S-H. However, further investigation is still needed to understand the coordination environment and / or mineralogy of uranium in calcium deficient, blended cement systems (i.e. low Ca/Si ratios), resulting from high replacement levels of Portland cement. Furthermore, use of additional spectroscopic techniques, such as nuclear magnetic resonance (NMR), have not been used to the same extent, if at all, to investigate the coordination environment of uranium in contact with C-S-H, hydrotalcite or ettringite. These may be used to underpin the extent of uranium incorporation into cements, also using uncommonly studied mineral analogues as a comparison.

- Given the complexity of plutonium solubility and speciation in solution, as well its high toxicity and radiotoxicity, this radionuclide is studied to a much lesser extent than uranium. There is a lack of understanding of how plutonium will behave, especially over long time periods, if encapsulated in or sequestered by cement minerals. This can be addressed by focusing, to begin with, on the interaction of plutonium with C-S-H phases, as a simplified system.
- It has been established that technetium(VII) is not well retained by cements. However, it is important to gain an understanding of which cement hydrate phases may, specifically, be responsible for precipitating, sorbing and retarding technetium(VII) release from cement matrices. This understanding may be instigated by carrying out fundamental sorption experiments with a range of major and minor cement mineral phases. Such information could be used more effectively to tailor cement formulations for technetium wasteforms, in addition to using additives that impose reducing conditions for reductive precipitation of technetium.

The experimental Chapters, **5**, **6** and **7**, therefore aim to address these disparities in the literature, also based on the objectives and hypotheses outlined in **Chapter 1**.

Chapter 3 – Experimental methods

This Chapter describes all of the synthesis methods, characterisation techniques and specialist techniques used throughout the experimental parts of this Thesis. Experiments involving contact of synthesised cement phases with the radionuclides uranium, plutonium and technetium (and the surrogate rhenium) are not described here but are detailed individually in **Chapters 5, 6 and 7**, respectively.

3.1 Cement phase syntheses

The syntheses described below for calcium-silicate-hydrates (C-S-H), hydrotalcite ($\text{Mg}_6\text{Al}_2(\text{CO}_3)(\text{OH})_{16}\cdot x(\text{H}_2\text{O})$) and ettringite ($\text{Ca}_6\text{Al}_2(\text{SO}_4)_3(\text{OH})_{12}\cdot x(\text{H}_2\text{O})$) are used throughout this Thesis. The characterisation of these phases is detailed in **Chapter 4**.

3.1.1 Materials

All materials for synthesis were supplied by Sigma Aldrich, unless otherwise stated. For the synthesis of C-S-H, CaO of general-purpose grade (Fisher Scientific) and fumed AEROSIL 200 SiO_2 were used. CaO was calcined at 900 °C for 10 hours prior to use to eliminate any CO_2 impurities or pre-hydration products. ACS grade NaOH ($\geq 97.0\%$), Na_2CO_3 (99%), $\text{Al}(\text{NO}_3)_3\cdot 9\text{H}_2\text{O}$ ($\geq 98\%$), $\text{Mg}(\text{NO}_3)_2\cdot 6\text{H}_2\text{O}$ (99%), $\text{Ca}(\text{OH})_2$ ($\geq 97.0\%$) and $\text{Al}_2(\text{SO}_4)_3\cdot 16\text{H}_2\text{O}$ ($\geq 98\%$) were used for the synthesis of hydrotalcite and ettringite. Ultra High-Quality deionised water (referred to as UHQ hereafter) was used for all aqueous solutions and suspensions, which was generated by filtration to achieve a resistivity measurement of $18.18\ \text{M}\Omega\ \text{cm}^{-1}$; the requirement to ensure no ionic impurities (e.g. salts) are present. All weighing of pre-cursors was carried out under ambient conditions on the benchtop, but mixing, filtration and storage was carried out under an N_2 atmosphere unless otherwise stated.

3.1.2 C-S-H synthesis

C-S-H was synthesised using two methods; both were “direct” synthesis methods using solid CaO and SiO_2 as starting materials. The first method required weighing separate stoichiometric amounts of CaO and SiO_2 to achieve theoretical C-S-H Ca/Si ratios of 0.6, 0.8, 1.0, 1.2, 1.4 and 1.6, respectively. The weighed powders were added to Ar-degassed UHQ at a S/L mass ratio of 15. The resulting suspensions were mixed for a minimum of 7 days at 40 rpm on a rotary shaker under a N_2 atmosphere, before being filtered gravitationally through a Whatman-542-ashless filter paper. The solids were left to dry at ambient temperature for at least 24 hrs, before grinding into a fine powder for characterisation (see **Section 3.2**) and thereafter stored under N_2 .

The second method differed in that a stock suspension of SiO₂ in Ar-degassed UHQ was prepared. The AERSOIL SiO₂ particles dispersed well within UHQ with vigorous shaking without the need for ultra-sonication. Aliquots of the 7.1 g L⁻¹ stock suspension of SiO₂ were removed and added to pre-weighed amounts of CaO to achieve the same theoretical Ca/Si ratios as in the first method. These C-S-H suspensions were mixed for a minimum of 46 days under N₂, and aliquots were taken directly for use in rhenium sorption experiments described in **Chapter 7**. A sample of each C-S-H suspension was also filtered gravitationally through a Whatman-542-ashless filter paper and left to dry at ambient temperature for at least 24 hrs, before grinding into a fine powder for X-ray diffraction measurements (see **Section 3.2.1**).

Solutions of the reaction mixtures were removed for ICP-OES analysis to determine the resulting Ca/Si ratio of the phases (see **Section 3.3.2**), detailed in **Chapter 4**.

3.1.3 Hydrotalcite synthesis

A pH-controlled solution mixing method was used to precipitate a Mg,Al-containing layered double hydroxide with a “carbonate interlayer”, similar to the method used by Aimoz et al. [157]. A solution of 1 M Mg(NO₃)₃ / 1 M Al(NO₃)₃ was added dropwise to a 1 M Na₂CO₃ solution, and the pH was maintained >11.0 with additions of 0.5 M NaOH where necessary. The precipitated solid was filtered gravitationally using a Whatman-542-ashless filter paper and washed with a minimum of 10 mL UHQ to ensure removal of residual salts and carbonates. The powder was dried under ambient atmosphere at 35 °C for ~24 hours before being ground into a fine powder for characterisation (see **Section 3.2**) and stored under N₂.

3.1.4 Ettringite synthesis

A new synthesis method was developed for producing ettringite, based on the reaction outlined in **Equation 3.1** and the methods previously reported by Goetz-Neunhoeffler et al. and Yang et al. [34,162]:



Ca(OH)₂ was added to an aqueous solution of Al₂(SO₄)₃ in Ar-degassed UHQ in stoichiometric amounts and the solution / suspension was mixed well before pouring into Teflon lined Parr vessels which were sealed and tightened and placed into a heating block for 1 week at 180 °C (not under N₂ atmosphere).

After reaction, the resulting solids were removed from the Parr vessels and dried at 35 °C for ~24 hours before being ground to a fine powder for characterisation (see **Section 3.2**) and subsequently stored under N₂.

3.1.5 Pre-carbonation of phases

A proportion of each of the synthetic phases was pre-carbonated for use in radionuclide contact experiments. The synthetic powders were weighed into vials (~1.8 g for C-S-H phases and hydrotalcite, and ~0.5 g for ettringite) and placed into a desiccator. The desiccator was placed under vacuum for ~30 minutes and purged with a 1 % CO₂ / N₂ gas mix to oversaturate the phases with CO₂ (an equivalent of 10 000 ppm CO₂ compared to atmospheric levels of ~400 ppm CO₂). Such high levels of CO₂ were required to allow distinction between natural carbonation effects and experimentally induced carbonation effects for analysis of phases after radionuclide contact (**Chapters 5, 6 and 7**). The desiccator was then sealed and monitored using a CO₂ monitor for 48 hours to ensure that high levels of CO₂ were maintained. The phases were analysed by X-ray diffraction (see Section **3.2.1**) after this time.

3.2 Characterisation methods

3.2.1 X-ray diffraction (XRD)

X-ray diffraction is used to generate information about the crystallinity and structure of a material. When an incident X-ray beam is focused on a material and the wavelength (λ) is similar to the distance characteristic of the atomic spacings in the material, the X-rays are diffracted. In the case of a crystalline material, the X-rays are scattered off lattice planes that are spaced at a given distance, d . When the diffracted waves give rise to constructive interference, a diffraction pattern can be generated by measuring the intensity of the diffracted waves as a function of the scattering angle, θ . Peaks will arise in the diffraction pattern at points where the θ value satisfies Bragg's Law (**Equation 3.2**):

$$n\lambda = 2d.\sin(\theta) \quad (3.2)$$

where d is the lattice spacing, θ is the angle between the incident X-ray beam and the lattice planes, and n is a positive integer. The width and intensity of the Bragg peaks are related to the crystallinity of the material [163]. Bragg diffraction is shown schematically in **Figure 3.1**.

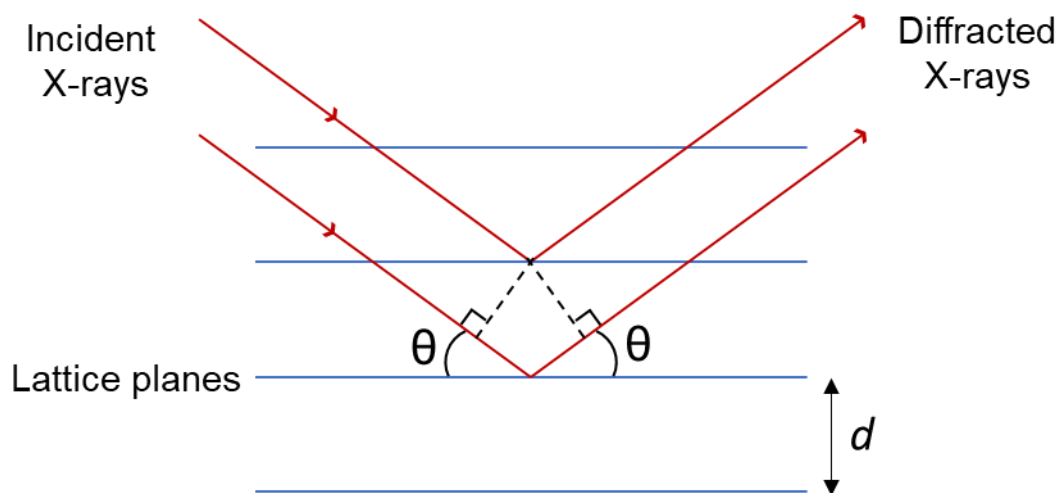


Figure 3.1: Bragg diffraction.

3.2.1.1 Experimental XRD methods used in this Thesis:

Chapter 4, 5, and 7: A Bruker D2 Desktop instrument was used for measurement of X-ray diffraction patterns. Samples were measured between $5-70^\circ 2\theta$ for C-S-H and hydrotalcite, and between $5-50^\circ 2\theta$ for all other phases. The counting time was 1 s per step in increments of $0.02^\circ 2\theta$ with a 1 mm divergence slit. The full specifications of the instrument are shown in **Table 3.1**. Whilst it is acknowledged that angles below 5° provide information on interlayer d-spacing, the diffractometer used and sample preparation methods required to measure radioactive samples gave large background interference at these lower angles, and so 5° was the minimum angle used.

Table 3.1: Bruker D2 Desktop instrumental parameters.

Wavelength:	Cu K-alpha, 1.5406 Å
Geometry:	Theta/Theta
Detector:	1-dimensional LYNXEYE
Goniometer radius:	141.0 mm
Standard apertures:	2.5 ° Soller slits 2.5 and 0.5 Ni filters to suppress 99.99+% K-beta radiation

Non-radioactive powdered samples, and rhenium-containing samples, were pressed into a 10 mm diameter recess on a low background Si(111) plate within into a PMMA holder (**Chapter 4 and 7**). For uranium-containing samples the compressed powder was covered with an acetate film, held in place with PVA glue, to prevent dispersion of radioactive material (**Chapter 5**). In the case of technetium-containing samples, a polymethyl methacrylate (PMMA) sample holder allowed containment with a screw-on dome; powders were suspended

in isopropanol alcohol (IPA) and dropped on a flat Si(111) plate and allowed to dry before being contained in the holder. Measurement parameters used were the same as described above, however the divergence slit was removed in this case to accommodate for the containment dome on the sample platform (**Chapter 7**). For plutonium-containing samples, which required additional shielding, the preparation method is outlined specifically in **Chapter 6**.

For samples with large background interference resulting from radioactive containment measures, the background was minimised by subtraction during data processing using the Bruker DIFFRAC.EVA software.

3.2.1.2 Rietveld refinement and crystallite size

Rietveld refinement was also performed to determine the quantity of phases present in synthesised materials (for C-S-H and ettringite, **Chapter 4**) and to determine lattice parameter shifts for phases subjected to sorption experiments (**Chapter 7**) using the Topas 4.2 software. This refinement process uses least squares refinement to minimise differences between an experimentally measured diffraction pattern and a theoretically generated diffraction pattern for the phases of interest [164]. Crystallite sizes for nano-crystalline phases were also determined using the Topas 4.2 software (C-S-H and PuO₂, **Chapter 4** and **6**).

3.2.2 Particle size distribution (PSD)

Particle size distribution of synthesised cement phases was approximated using the Fraunhofer model, whereby particles are assumed to be spherical, non-transparent and have a low scattering angle (< 30°) [165]. This model allowed for measurement of particle sizes without considering the absorptive or refractive properties of the material, which is ideal in this case given that these properties were unknown for the synthesised cement phases. However, one drawback of using the Fraunhofer model is the large errors that can be associated with the measurements [166].

3.2.2.1 Experimental PSD method used in this Thesis:

Chapter 4: A Malvern Mastersizer 2000 instrument with laser diffraction (LAS) measurement technique was used. A liquid dispersion method was used for analysis of synthesised cement phases with an isopropanol dispersant. The powders were well ground in a pestle and mortar and sonicated for ~10 minutes prior to measurement to prevent agglomeration. Given that particle sizes were above ~600 nm, blue light ($\lambda = 450-490$ nm) was used to measure the particle size distribution.

3.2.3 Zeta (ζ) potential measurements

The zeta potential of a material is defined as the potential difference between a bulk fluid and the stationary layer of fluid surrounding a particle of that material [167]. The potential difference around a particle will determine how a material will interact with ions in solution. In this case, the zeta potentials of cement phase particles in aqueous solution were measured.

3.2.3.1 Experimental ζ -potential method used in this Thesis:

Chapters 4 and 7: The surface zeta potentials of the cement phases in solution (at varying pH) were measured using a Zetasizer Nano instrument at 25 °C in UHQ. In the first instance, powder samples of minor cement hydrate phases were sieved to <63 μm before addition to UHQ and nitric acid solutions (pH 4.8) at 0.1 wt %, respectively. The samples were shaken well and left to equilibrate overnight before being sealed with Parafilm and removed from the N_2 atmosphere for measurements. Prior to measurement, the samples were shaken again and left aside for 10 minutes to allow for larger particles to settle. Supernatant from the top of each suspension was removed, added to a folded capillary zeta cell, and measured straight away to minimise ambient exposure. The cell was equilibrated at temperature for 120 s before being measured in triplicate for 10 measurements. Additional measurements were made for C-S-H phases, that were synthesised using the second method (see **Section 3.1.2**), in their respective equilibrated synthesis solutions.

3.2.4 Solid-state nuclear magnetic resonance spectroscopy (SS-NMR)

Nuclear magnetic resonance (NMR) spectroscopy can be used to determine chemical environments of specific nuclei (spin $\neq 0$) within liquid or solid phases. For poorly crystalline or amorphous materials lacking long range order, NMR is particularly useful as it is one of the only techniques that can probe local structure in disordered environments. In an NMR experiment the sample is subject to a magnetic field (B_0) which splits the energy levels of the nuclei's spin states. The nuclei are perturbed by applying a pulse of radio frequency radiation, causing absorption or emission of energy to allow the nuclei to relax back to their equilibrium state. The electromagnetic response that is produced from this is then recorded as a free induction decay and a Fourier transform is applied to the recorded signal to generate a resonance spectrum. Nuclei in different chemical environments can experience slightly different magnetic fields due to shielding from surrounding electrons, thus producing slightly different resonance responses. The resonance frequencies are reported as a chemical shift (δ) which is relative to the known chemical shift of an external standard [168,169].

In solid materials, the NMR spectrum recorded will often appear broadened due to effects such as dipolar interactions, anisotropy due to chemical shielding and quadrupolar interactions. These effects can be reduced by using magic angle spinning (MAS), whereby the sample is spun at an angle of 54.74 ° relative to B_0 [168]. MAS experiments suppress

dipolar interactions and remove anisotropy and first-order quadrupolar interactions (for nuclei with spin = $\frac{1}{2}$, such as ^{29}Si).

3.2.4.1 Experimental MAS SS-NMR methods used in this Thesis:

Chapter 5: NMR experiments were carried out in the Department of Chemistry at The University of Sheffield. Spectra were collected using a Bruker Avance III HD 500 spectrometer at 11.4 T, using 4 mm ZrO_2 sample rotors, resulting in a Larmor frequency of 130.32 MHz for ^{27}Al and 99.35 MHz for ^{29}Si . For samples containing uranium, the associated radiological hazard required the samples to be packed in the Department of Materials Science and Engineering prior to transport to and measurement in Chemistry.

Ettringite and Hydrotalcite (^{27}Al): ^{27}Al chemical shifts were referenced to $\text{Al}(\text{NO}_3)_3$ (aq). A MAS rate of 12.5 kHz was applied. Conventional single pulse experiments were carried out using an optimised pulse length of 1.4 μs and recycle delays of 35 and 25 s for ettringite and hydrotalcite, respectively. 256 scans were acquired for each sample.

C-S-H (^{29}Si): ^{29}Si chemical shifts were referenced to neat tetramethylsilane (TMS). A MAS rate of 12.5 kHz was applied. Conventional single pulse experiments were carried out using an optimised pulse length of 1.4 μs and a recycle delay of 45 s. 256 scans were acquired for each sample.

3.2.5 Synchrotron X-ray absorption/fluorescence spectroscopy (XAFS)

X-ray absorption/fluorescence spectroscopy (XAFS) can be used to interpret information on the oxidation state and local coordination environment of a given element in a material. During an XAFS experiment the material is subjected to a beam of X-rays over a given energy range, specific to the element of interest, allowing for absorption of the X-rays and in turn ejection of electrons and ionisation of the atom. The energy range is windowed around the value of E_0 – “the energy required to cause ejection of a core electron from an atom” – specific to the atom and atomic shell being measured, in order to record an absorption energy spectrum. These spectra can be collected in two ways; using 1) transmission, by measuring the transmitted beam, or 2) fluorescence, by measuring subsequent fluorescent X-rays or Auger electrons [163,170].

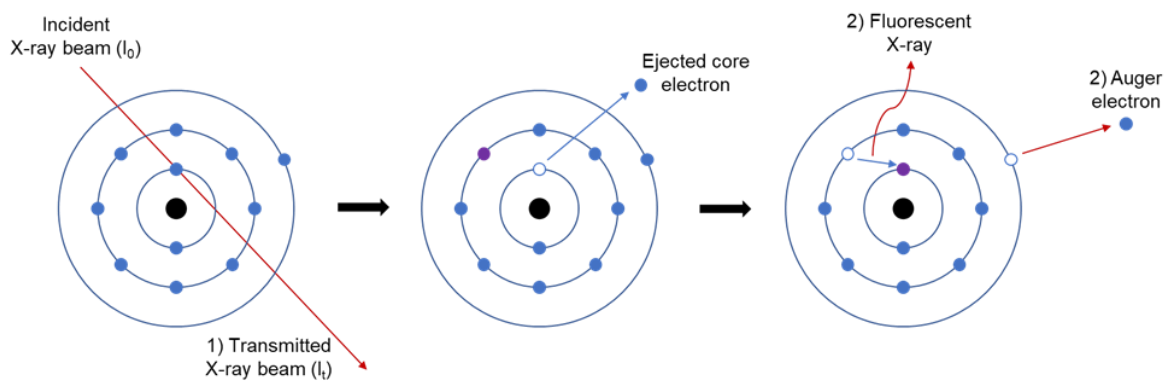


Figure 3.2: X-ray absorption and fluorescence of a theoretical atom.

Figure 3.2 shows the basic principles of XAFS on the atomic level, whereby an incident X-ray beam (I_0) causes the ejection of a core electron to generate a core hole. The core hole is filled by an electron dropping down from an outer shell which is also accompanied by the ejection of an Auger electron. In measuring transmission, the intensity of I_t is measured and compared to the intensity of I_0 – the difference is the absorption. In measuring fluorescence, the energy released as the outer electron drops to fill the core hole, or the “electron yield” (ejection of Auger electrons) is measured. An example of an energy spectrum generated from these measurements is shown in **Figure 3.3** [163,170].

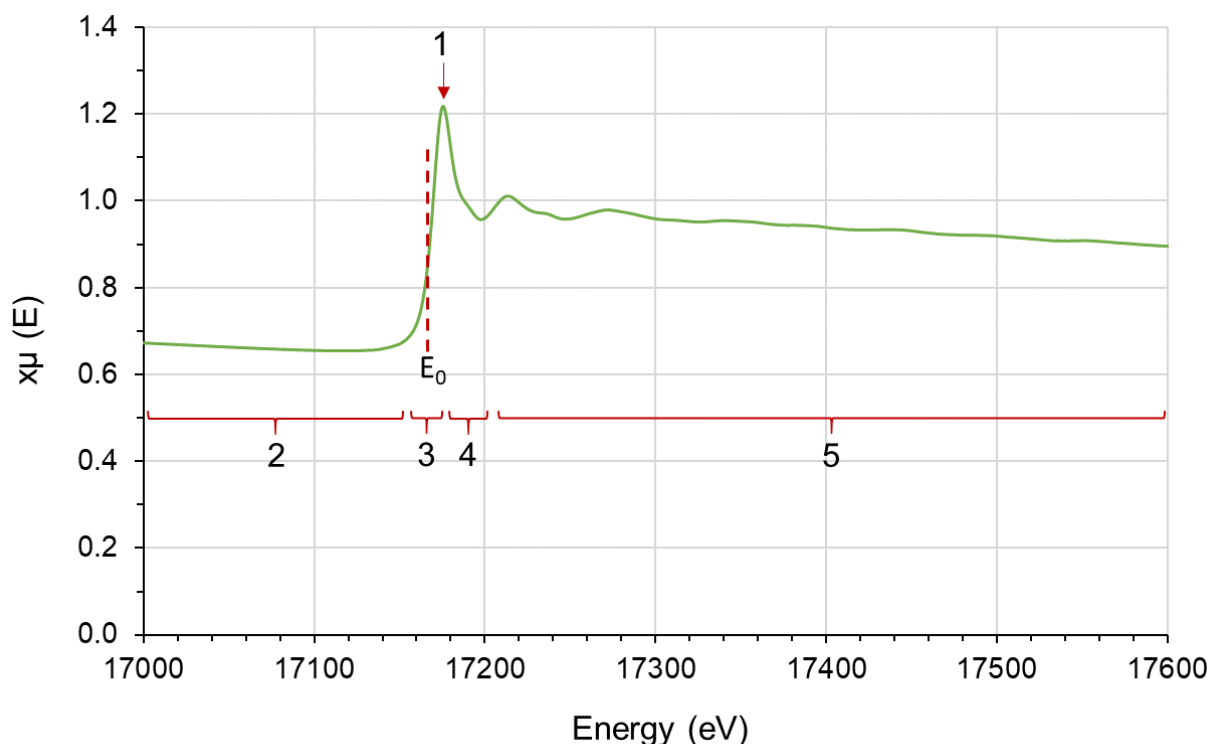


Figure 3.3: XAS spectrum of UO_2 measured across the L_{III} -edge of uranium (17166 eV), shown in green. Labeled regions of interest include E_0 , the white line (1), the pre-edge (2), the edge (3), XANES (4) and EXAFS (5). $x\mu(E)$ is related to the ratio of the incident (I_0) and transmitted (I_t) beam intensities.

The XAFS spectrum can be broken down into the following regions:

- 1) *Pre-edge*: this refers to the region of the spectrum before the edge where photon absorption steadily decreases with increasing energy, as a general rule.
- 2) *Edge*: the region where absorption rises as a result of the incidence X-rays' energy matching the required energy to excite electrons for a given orbital. In the case of Figure 3.3 this corresponds to the outer 2p (or L_{III}) orbital of uranium. The white line is the region at the top of the edge, where absorption is much higher than the rest of the spectrum.
- 3) *X-ray absorption near edge structure (XANES)*: the region of features on, or just after the edge, extending to approximately 50 eV beyond the edge.
- 4) *Extended X-ray absorption fine structure (EXAFS)*: the region of oscillations extending far beyond the edge and XANES region.

3.2.5.1 Experimental XAS methods used in this Thesis:

The Hephaestus application from the Demeter 0.9.26 software package [171] was used to calculate the optimal mass for one absorption length of standards, so that transmission measurements could be collected. Pellets of the standards were pressed using a stainless-steel die under ~0.5 tonne of pressure using the weighed sample material mixed with a polyethylene glycol (PEG) binder, to achieve a mass of ~25-50 mg of either 3 mm or 6 mm diameter pellets. Preparation of uranium, technetium and rhenium-containing samples is detailed in the relevant **Chapters; 5 and 7**.

3.2.5.2 Beamline set-up

1) Diamond Light Source (DLS): B18

Beamline B18 has a Si(111) monochromator to allow measurement within the 2.05-20 keV range. Beam collimation was achieved using a Cr and Pt coated Si mirror [172].

2) National Synchrotron Light Source II (NSLS-II): BMM

The BMM beamline is fitted with a Si(111) monochromator to allow measurement within the 4.5-21 keV range. An unfocused beam with dimensions 0.5 mm x 6 mm was used, and beam collimation was achieved using a parabolic mirror of 30 nm Pt coated with 5 nm Rh [173].

3) Photon factory (at KEK): BL-27B

The BL27B beamline at the Photon factory, KEK uses a Si(111) monochromator to allow measurements in the 4-20 keV range. An unfocused beam with dimensions 0.5 mm x 6 mm was used [174].

Chapter 5: The U L_{III} -edge (171 66 eV) was measured on beamlines B18 (DLS) and BMM (NSLS-II). Monochromator calibration was performed on B18 by use of yttrium (Y) foil,

assigning the first inflection point of the Y K-edge as 17 038 keV. For beamline BMM, a UO₂ standard was measured at the L_{III}-edge to allow alignment of the sample data. Samples were measured simultaneously in transmission and fluorescence mode, with samples orientated at 45 ° with respect to both the incoming X-ray beam and fluorescence detector.

Chapter 7: The Tc K-edge (21 044 eV) was measured at the B18 beamline (DLS) with monochromator calibration performed using a molybdenum (Mo) foil to assign the first inflection point of the Mo K-edge as 20 000 eV; samples were measured in fluorescence mode. Rhenium-containing samples were measured at the L_{III}-edge (10 535 eV) using both BL-27B (KEK) and B18 (DLS). For beamline BL-27B, monochromator calibration was performed using a Re metal standard to assign the first inflection point of the Re L_{III}-edge as 10 535 eV. A hafnium oxide (HfO₂) external standard was measured in fluorescence mode after the sample to allow alignment of the data sets. The samples were measured in transmission and fluorescence mode simultaneously.

The Athena and Artemis applications also from the Demeter 0.9.26 software package were used for post processing of data [171]. Data normalisation and linear combination fitting of XANES profiles was performed using the Athena application and EXAFS fitting was achieved using the Artemis application.

3.2.5.3 Data processing: XANES

The Athena application was used for post processing of XANES data as follows;

- 1) Data were imported by selecting the $\ln(I_0)$ and $\ln(I_t)$ channels as the numerator and denominator values, respectively. At this point, reference data was also imported, where applicable.
- 2) Multiple scans per sample were merged.
- 3) The value of E_0 was assigned to the first inflection point (maximum) of the energy derivative.
- 4) E_0 values were calibrated using either the align function (for U samples, aligning the Y references) or the calibrate function (for Re and Tc samples, assigning the relevant metal standard to the correct value of E_0 and applying the associated edge shift to sample data).
- 5) Data normalisation and background subtraction were performed by selecting appropriate pre- and post-edge ranges, allowing the edge jump to be set at 1.
- 6) Truncation of data was performed in the event of an “impurity” edge being present and encroaching on the data.
- 7) Linear combination fitting of XANES spectra was also performed in Athena using relevant standards (**Chapter 4**), with fitting procedures reported individually in

Chapters 5, 6 and 7. As a general rule, no more than four standards were applied at any one time and the value of E_0 was allowed to refine.

3.2.5.4 Data processing: EXAFS

The normalised, modelled EXAFS signal, $\chi(k)$, is given by **Equation 3.3**:

$$\chi(k) = S_0^2 \sum_i N_i \frac{f_i(k)}{kD_i^2} e^{-\frac{2D_i}{\lambda(k)}} e^{-2k^2\sigma^2} \sin(2kD_i + \delta_i(k)) \quad (3.3)$$

where k is the wavenumber, S_0^2 is the amplitude reduction factor, N is the coordination number, D is the interatomic distance (also R), λ is the inelastic mean free path, f is the (back-)scattering amplitude, δ is the (back-)scattering phase and σ^2 is the mean-square (thermal) disorder in the distance for the i^{th} shell, where i represents the number of shells over which the equation is summed [170,175].

Fitting of EXAFS scattering paths / shells was performed as follows;

- 1) In Athena, the Rbkg (background) value was set. A value of 1 was generally used, however in instances where the data had large artefacts or background noise at low R values, the Rbkg value was adjusting accordingly, to no less than 0.8 or no more than 1.2.
- 2) The values of dk and dR for the Hanning windows to which the EXAFS models were fitted were set at 0 and 1, respectively.
- 3) Data was imported from Athena into the Artemis application.
- 4) Scattering paths were generated by importing a relevant CIF file and running a FEFF calculation; an automated program for calculating theoretical *ab initio* multiple scattering pathways [176,177].
- 5) Scattering pathways were then fitted sequentially, taking into account the following steps (see also **Figure 3.4**):
 - The amplitude reduction factor, S_0^2 , was obtained for each absorber on a given beamline, by fitting the first scattering pathway for a standard (usually an oxide or metal) with a known, fixed coordination number, N , allowing S_0^2 to refine; given the converse correlation between N and S_0^2 (see **Equation 3.3**). The value of S_0^2 was then fixed in the model for the fitting of subsequent samples.
 - Scattering (interatomic) distances, R , were pre-set according to the value generated for given pathways in the FEFF calculation. The values were allowed to refine, to within ~10 % of the original distance. Large variations were generally omitted as false scattering paths, unless reasonable justification could be made.
 - Thermal disorder parameters, σ^2 , were set as guess parameters at a value of 0.003 and allowed to refine. Negative or very large values were generally rejected and

resolved by fixing the value in the model as low as reasonably practical, determined by trial and error.

- Coordination numbers, N, were initially set according to the values generated in the FEFF calculation, for a given CIF file structure. Refinement of the first shell coordination number was generally achieved due to previously fixing the value of the amplitude.
- For refinement of subsequent coordination numbers, a trial and error approach was used to refine the values to the nearest whole number.
- The deviation from the value of E_0 , ΔE , was allowed to vary as a global parameter in the model.
- At each stage, the R-factor was used to determine whether the fit was reasonable, with a baseline value of <0.05 (5 %) generally accepted as a good fit.
- In cases where there was not a single appropriate CIF file structure on which to model the data, pathways were generated using FEFF calculations from multiple CIF files and fitted using some prior knowledge of the systems and scientific reasoning.

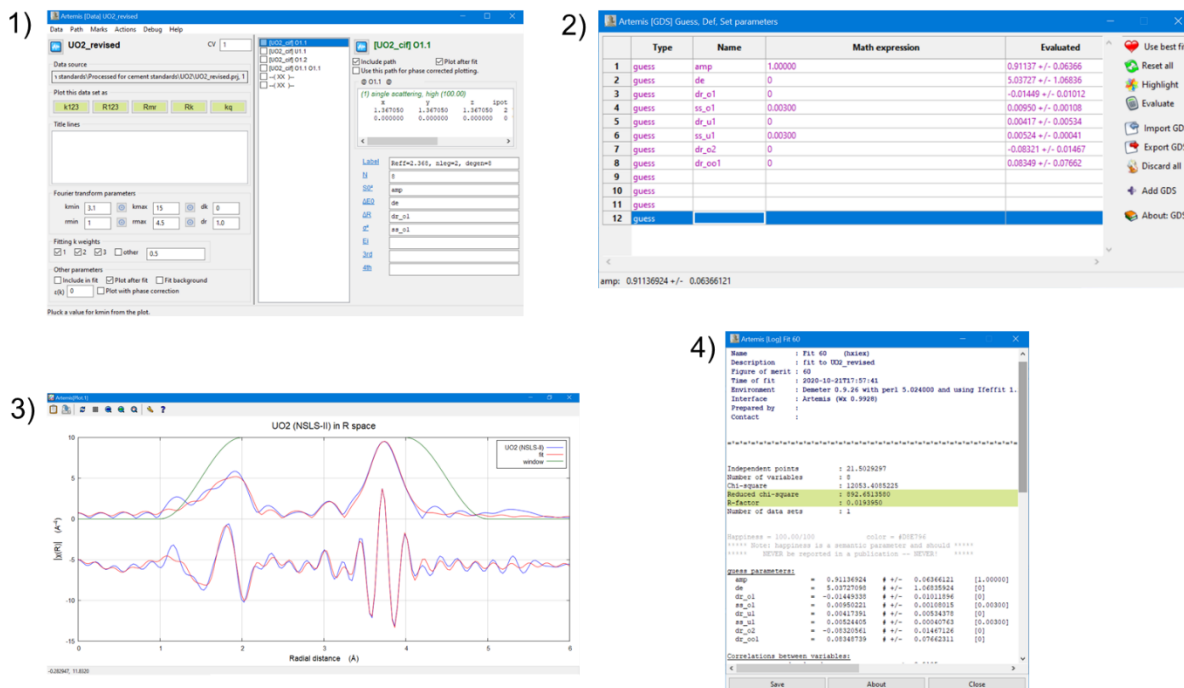


Figure 3.4: Screenshots of various fitting stages of EXAFS models in the Artemis software (example is for a UO_2 standard). 1) Scattering pathways from FEFF calculations of a UO_2 CIF file are added to the pathway list. The parameters N , S_0^2 , ΔE , ΔR and σ^2 are defined in code, for each pathway. 2) The defined codes are assigned as guess parameters, with an approximated value, so the parameters can be refined. 3) The chosen pathways, with given parameters, are fitted by the software. Once executed, the fit is displayed in the plot window. 4) The refined parameter values and R-factor value of the fit are outputted into a script.

3.2.6 Scanning electron microscopy / energy dispersive X-ray (SEM/EDX) spectroscopy

Scanning electron microscopy can be used to study the microstructure of a material. An SEM instrument generates a collimated beam of electrons that are focused at a sample surface; the electrons hit the surface and scatter elastically (i.e. backscattered electrons, BSEs) or inelastically (i.e. secondary electrons, SEs) off atoms within the material, generating a signal which is detected to produce an image of the surface. BSEs are generated with an energy similar to that of the incidence beam, making them able to escape from greater depth of the sample surface, with moderate resolution. SEs have a much lower energy than the incident beam, and so can only escape if generated from near the surface of the material, but the limited escape depth of SEs enables imaging with a higher resolution than BSEs. **Figure 3.5** shows the SEM process and interaction volume of a material [10].

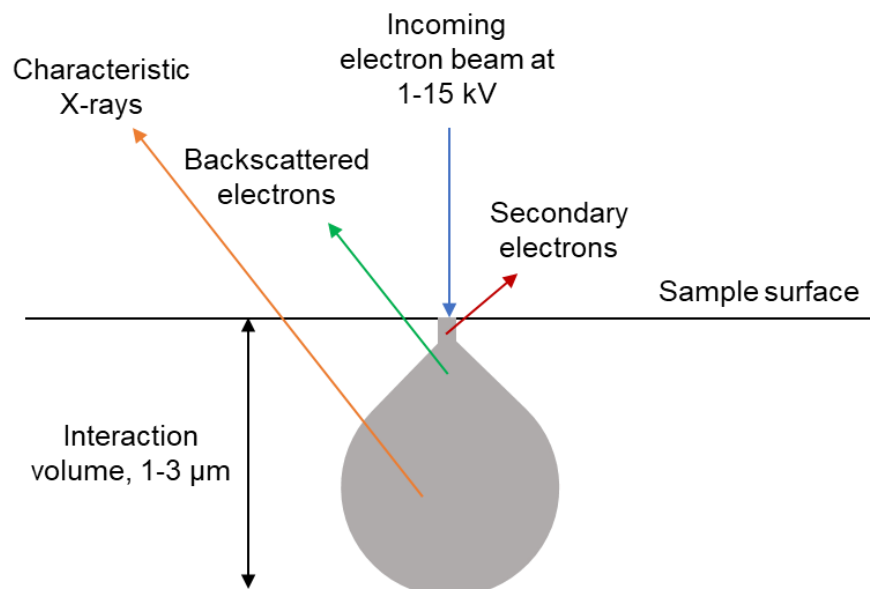


Figure 3.5: Electron interactions with the surface of a sample during SEM imaging [10].

SEM imaging can be coupled with energy dispersive X-ray analysis. Characteristic X-rays, that are generated when an incident electron knocks out an electron from the inner shell of an atom, can be detected in the imaging process to allow elemental mapping of the surface.

3.2.6.1 Experimental SEM/EDX methods used in this Thesis:

Chapter 7: Samples were mounted in epoxy resin and ground using 240-1200 SiC grit paper followed by polishing from 6 mm down to 0.25 mm using diamond suspension, before being carbon coated. A Hitachi TM303 desktop SEM/EDX instrument with an accelerating voltage of 15 kV was used and semi-quantitative EDX map counting was performed using a Bruker

Quantax 70 detector for 10 minutes. The full procedure is outlined by *Kearney, Yorkshire et al.* [131] (see **Appendix 1**).

3.3 Solution analyses

All solutions sampled over the course of this Thesis were analysed for composition and pH, unless otherwise stated in individual chapters.

3.3.1 pH measurements

The pH of solutions was measured before further analysis, using a Mettler Toledo meter and probe at ambient temperature. The meter and probe were calibrated using pH 4, 7 and 10 buffer solutions prior to measurements.

3.3.2 Inductively coupled plasma techniques (ICP-OES/MS)

Inductively coupled plasmas can be used to ionise solutions and, coupled with a detection technique, to measure cation concentrations. The plasma is generated by ionisation of argon gas using a high frequency electric field. When a solution is passed through the plasma, energy is transferred from the plasma to the solution in order to ionise and excite the elements present. Spectroscopic or spectrometric techniques (i.e. optical emission or mass spectrometry), can be used to detect the ionised cations in the solution. The spark generated from ionisation of the cations generates a discharge plasma that is characteristic to the cation(s) of interest, which is detected, and allows determination of the cation concentration, compared to a known external standard [178].

3.3.2.1 Experimental ICP-OES/MS methods used in this Thesis:

Analyses were performed using a Thermofisher Scientific iCAP Duo 6300 ICP-OES and a Thermofisher Scientific iCAP RQ ICP-MS. All solutions were filtered to 0.22 µm and acidified with 20 µL concentrated HNO₃ (99.99 % purity) to prevent precipitation and agglomeration prior to analysis.

Chapter 4: Ca and Si concentrations in C-S-H reactions solutions were measured. Dilutions were performed in UHQ and ranged from 1:2 to 1:6 depending on Ca/Si ratio.

Chapter 5 and 7: The concentrations of U, Re, Ca, Si, Al, Mg and S were measured in solution after radionuclide contact experiments with cement phases. Dilutions were performed in UHQ and ranged from 1:2 to 1:10 depending on the sample. Additional Re measurements were carried out using ICP-MS where necessary and are detailed in **Chapter 7**.

3.3.3 Liquid scintillation counting

Liquid scintillation counting allows determination of the concentration of a radionuclide based on the interaction of its alpha or beta decay with scintillant molecules (scintillators). The scintillators are typically organic molecules with π -cloud aromaticity, allowing ionising radiation from the radionuclide to be absorbed. **Figure 3.6** demonstrates the liquid scintillation counting process and depicts a radioactive nucleus surrounded by solvating scintillators. Of the organic scintillators, some are primary phosphors which absorb the initial alpha or beta radiation. The absorbed energy is then released as a photon from this primary phosphor which can be transferred between other primary phosphors, as well as secondary phosphors. The secondary phosphors release the energy at a different wavelength that allows the energy to be detected by a photomultiplier tube (PMT). The photon energy can be transferred between many primary scintillators before reaching a secondary phosphor. Using knowledge of the specific activity of the radionuclide being measured, the outputted decays per second (DPS) can be converted into an amount of radionuclide per sample [179].

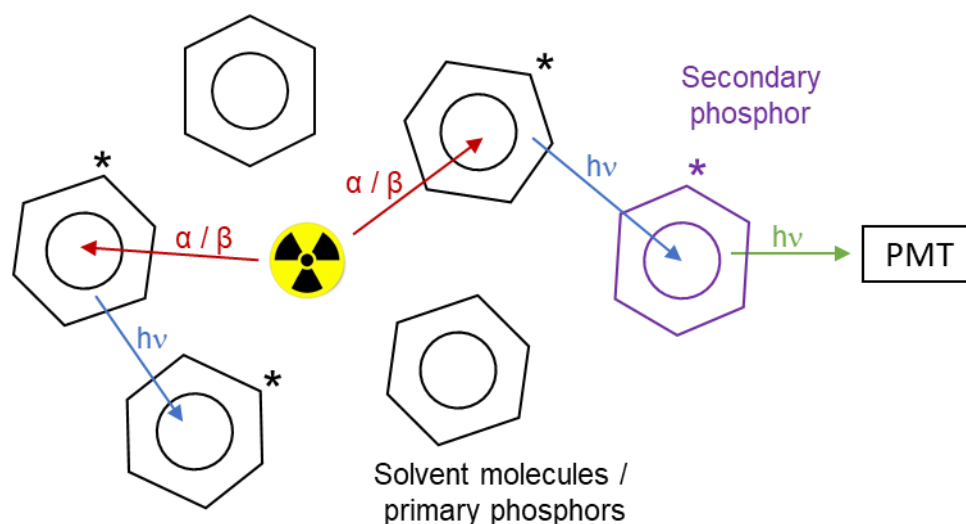


Figure 3.6: Schematic of the liquid scintillation counting process. Radioactive atom is shown by the trefoil symbol and the asterisk represents an energetically excited molecule.

3.3.3.1 Experimental LSC methods used in this Thesis:

Chapter 7: A HIDEX 300 SL instrument was used with an Ecoscint A scintillation cocktail to determine the concentration of ^{99}Tc in solution. Sample solutions were filtered through a $0.22\ \mu\text{m}$ filter before a 2 mL aliquot was removed and dispensed into a frosted scintillation vial with 18 mL of scintillation cocktail added. Vial lids were double sealed with Parafilm to reduce the risk of spillage of radioactive material, before being shaken well and placed in the measurement rack in darkness for a minimum of 15 hours before being measured, to minimise

effects from light exposure of the scintillation cocktail. Each vial was measured for 60 seconds, as further counting times did not improve the results obtained. ^{99}Tc standards were also made from dilution of a 0.1 mM stock solution of aqueous NaTcO_4 to obtain concentrations of 0.01 mM, 0.02 mM, 0.05 mM and 0.1 mM for comparison to samples.

3.3.4 Alpha spectrometry

As an alternative to liquid scintillation counting, alpha spectrometry can be used to determine concentrations of alpha-decaying radionuclides in solution without the requirement of a scintillator [180]. Analysis was performed at the central lab facility at NNL and the instrument used for alpha spectrometry was an ORTEC Alpha Ensemble for Pu-containing cement storage solutions.

3.3.4.1 Experimental Alpha spectrometry methods used in this Thesis:

Chapter 6: A measured aliquot of cement storage solution was placed onto a pre-flamed and pre-weighed planchet. The sample was heated to complete dryness then re-flamed to fix all material onto the surface of the planchet before being re-weighed to ensure <4 mg of solids were present on the tray. A high voltage setting of 50 V and a vacuum of 0.1 Torr was applied to every chamber in the instrument. The activity for the Pu isotopes per mL of solution were calculated from peak ratios which were subsequently converted into a concentration of Pu.

3.4 Thermodynamic modelling

3.4.1 Phreeqc

Geochemical modelling was used as a guide to estimate the mineral phases that were thermodynamically favourable to form in the experimental systems used. The Phreeqc Interactive 3.3.12-12704 software was used to model the systems using the Lawrence Livermore National Laboratory (LNLL), ThermoChimie and HATCHES databases, as a function of concentration and pH. This software can be used to simulate equilibrium and non-equilibrium reactions between water and a wide range of minerals [181].

The saturation index (SI) of a phase determines whether a phase will tend to be deposited from aqueous solution ($\text{SI} > 0$), remain in solution ($\text{SI} < 0$), or is in equilibrium ($\text{SI} = 0$). The term is defined in **Equation 3.4**:

$$\text{SI} = \log_{10} (\text{IAP}/K_{\text{sp}}) \quad (3.4)$$

where IAP is the ion activation product and K_{sp} is the solubility product [182].

3.4.1.1 Experimental Phreeqc methods used in this Thesis:

SI values for mineral phases were calculated by inputting the concentrations of relevant elements in solution. This was achieved by using a “solution spread” table (Figure 3.7), whereby the concentrations measured by ICP analyses (see Section 3.3.2) and the relevant measured or approximated experimental pH values (see Section 3.3.1) were inputted. The resulting SI values calculated using the inputs compared against the chosen databases where then plotted for each mineral phase, as a function of pH. The modelled concentrations and pH values used specifically for uranium and plutonium systems in this Thesis are defined individually in Chapters 5 and 7.

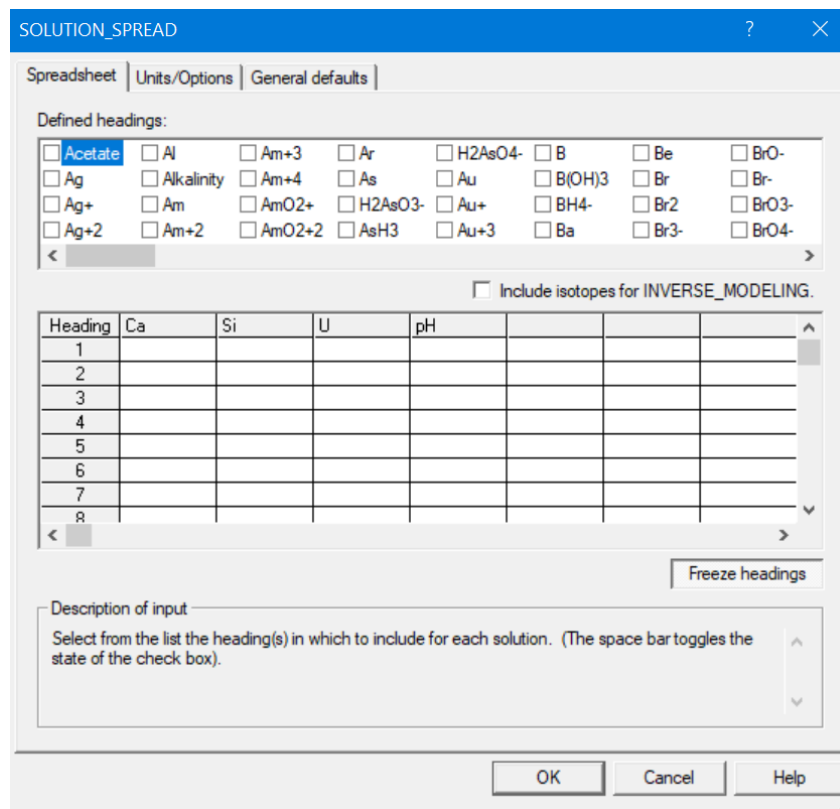


Figure 3.7: Example of a solution spread table in the Phreeqc software.

Chapter 4 – Characterisation of precursor cement minerals and X-ray absorption spectroscopy standards

4.1 Introduction

This Chapter describes the characterisation of:

- (i) the cement hydrate phases used for radionuclide-contact experiments in **Chapters 5, 6 and 7**. This includes C-S-H, hydrotalcite ($\text{Mg}_6\text{Al}_2(\text{CO}_3)(\text{OH})_{16}\cdot 4\text{H}_2\text{O}$) and ettringite ($\text{Ca}_6\text{Al}_2(\text{SO}_4)_3(\text{OH})_{12}\cdot 26\text{H}_2\text{O}$).
- (ii) the standards used for uranium, rhenium and technetium X-ray absorption / fluorescence spectroscopy (XAFS) analysis in **Chapters 5 and 7**.

Also included in the results are some of the first reported models of EXAFS fitting of the uranyl silicate minerals haiweeite ($\text{Ca}(\text{UO}_2)_2(\text{Si}_5\text{O}_{12})(\text{OH})_2\cdot 6\text{H}_2\text{O}$) and weeksite ($\text{K}_2(\text{UO}_2)_2(\text{Si}_5\text{O}_{12})(\text{OH})_4\text{H}_2\text{O}$) as well as novel Ca-bearing perrhenate and pertechnetate phases.

4.2 Experimental methods

4.2.1 Cement minerals

C-S-H, hydrotalcite and ettringite phases were synthesised according to the procedures already outlined in **Chapter 3**. The synthetic powders were ground finely using a pestle and mortar before analysis using X-ray diffraction, particle size distribution (where applicable) and zeta potential measurements, as described by the procedures also outlined in **Chapter 3**.

Additional analysis to calculate the molar Ca/Si ratio of C-S-H phases was carried out using ICP-OES of the C-S-H synthesis reaction solutions.

4.2.2 X-ray absorption / fluorescence spectroscopy standards

The uranium, rhenium and technetium X-ray absorption / fluorescence spectroscopy standards referenced throughout this Thesis, which were considered important for understanding the coordination of radionuclides in cementitious systems, are listed in **Tables 4.1 to 4.3**, along with information from where they were sourced.

For the synthesis of technetium standards, the NH_4TcO_4 sourced from ORNL had to be purified before use (**Table 4.3**). ^{99}Tc is a beta emitter and must only be handled with a radiation protection adviser (RPA) approved protocol.

Impure NH_4TcO_4 was dissolved in a basic solution of NH_4OH / H_2O_2 and gently heated. The solution became lighter in colour as impure pertechnetate was oxidised and dissolved, after

which the solution volume was gradually reduced by evaporation, to the point of supersaturation, to re-precipitate NH_4TcO_4 . The solution was further reduced in volume and the remaining 1-2 mL was removed and taken as waste. The re-precipitated NH_4TcO_4 solid was washed with ethanol and dried overnight in an oven.

A Ca-pertechnetate phase was synthesised as a standard. Later determined to be $\text{Ca}_{x/2}(\text{TcO}_4)_2 \cdot z\text{H}_2\text{O}$ (see **Section 4.3.4**), this phase has not previously been reported in the literature. A novel synthesis method was used whereby NH_4TcO_4 was mixed with CaO and sealed under vacuum in a fused quartz ampoule, which was then heat treated in a tube furnace under N_2 for 2 hours at 450 °C. The sample was retrieved from the ampoule after heat treatment. It should also be noted that the analogous $\text{Ca}_{x/2}(\text{ReO}_4)_2 \cdot z\text{H}_2\text{O}$ phase (**Table 4.2**) was also synthesised using NH_4ReO_4 and CaO precursors using the same method. These synthesis procedures were performed, with thanks, by Dr. D. Bailey in the MIDAS facility at The University of Sheffield.

Table 4.1: U XAFS standards.

Standard	Source
Uranium dioxide (UO_2)	Synthesised at The University of Sheffield (TUoS)
Uranium trioxide (UO_3)	Synthesised at TUoS
Uranyl nitrate ($\text{UO}_2(\text{NO}_3)_2 \cdot 6\text{H}_2\text{O}$)	TUoS stock
Calcium uranate (CaUO_4)	Synthesised at TUoS by S. O'Sullivan
Tricalcium uranate (Ca_3UO_6)	Synthesised at TUoS
Magnesium uranate (MgUO_4)	Synthesised at TUoS by S. O'Sullivan
Uranophane ($\text{Ca}(\text{UO}_2)_2\text{SiO}_3(\text{OH})_2 \cdot 5\text{H}_2\text{O}$)	Raistrick Collection - Rhodesia, South Africa
Haiweeite ($\text{Ca}(\text{UO}_2)_2(\text{Si}_5\text{O}_{12})(\text{OH})_2 \cdot 6\text{H}_2\text{O}$)	Excalibur mineral Co. - Teofilo Otoni, Minas Gerais, Brazil
Weeksite ($\text{K}_2(\text{UO}_2)_2(\text{Si}_5\text{O}_{12})(\text{OH})_4\text{H}_2\text{O}$)	Excalibur mineral Co. - Claim, Juab Co., Utah
Bayleyite ($\text{Mg}_2(\text{CO}_3)_3 \cdot 18\text{H}_2\text{O}$) / Andersonite ($\text{Na}_2\text{Ca}(\text{UO}_2)(\text{CO}_3)_3 \cdot 6\text{H}_2\text{O}$)	Excalibur mineral Co. - Ambrosia Lake District, McKinley Co., New Mexico
Soddyite ($(\text{UO}_2)_2\text{SiO}_4 \cdot 2\text{H}_2\text{O}$)	Excalibur mineral Co. - Musonoi, Shaba Province, Zaire
Coffinite ($\text{U}(\text{SiO}_4)_{1-x}(\text{OH})_{4x}$)	Sample courtesy of S. Szenknect [183]

Table 4.2: Re XAFS standards.

Standard	Source
Ammonium perrhenate (NH_4ReO_4)	Sigma Aldrich
Re metal (for energy alignment)	Synthesised at TUoS by D. Bailey
Calcium perrhenate ($\text{Ca}_{x/2}(\text{ReO}_4)_2 \cdot z\text{H}_2\text{O}$)	Synthesised at TUoS by D. Bailey
Rhenium disulfide (ReS_2)	Synthesised at TUoS by D. Bailey

Table 4.3: Tc XAFS standards.

Standard	Source
Ammonium pertechnetate (NH_4TcO_4)	Oak Ridge National Laboratory (ORNL)
Tc metal (for energy alignment)	Synthesised at TUoS by D. Bailey
Calcium pertechnetate ($\text{Ca}_{x/2}(\text{TcO}_4)_2 \cdot z\text{H}_2\text{O}$)	Synthesised at TUoS by D. Bailey
Technetium sulfide (TcS_x)	Data courtesy of W. Lukens [152]

All the standards were analysed to verify their composition, where possible, prior to measurement by XAFS. After measurement, the standards were fitted to EXAFS models using FEFF calculations to generate scattering pathways using appropriately selected CIF files. All fitting was performed using a Hanning window with $dk = 0$ and $dR = 1$. It should be noted that all EXAFS spectra were k^3 -weighted, allowing for a fairly uniform amplitude to be displayed in k -space given that signal contributions were largely dominated by oxygen nearest neighbours throughout [170].

4.3 Results I: Cement minerals

4.3.1 C-S-H

Figure 4.1 displays the XRD patterns of C-S-H phases synthesised from $\text{Ca/Si} = 0.6$ to 1.6 using the direct reaction method (**Chapter 3**), hereafter labelled “CSH(X)”, where X is the theoretical Ca/Si ratio. The peaks identified correspond with those for C-S-H(I) (tobermorite, PDF card no. 00-045-1480 [184]) and are in good agreement with the diffraction patterns obtained by *Rodriguez et al.* [185]. The main C-S-H(I) peak at (220) was observed at $\sim 29^\circ 2\theta$ in all of the C-S-H diffraction patterns. The (002) basal reflection was identified from $\text{Ca/Si} = 1.0$ onwards at $\sim 7^\circ$, however, due to high background interference at low 2θ values this reflection was not readily identifiable at lower Ca/Si ratios. There is a decrease in 2θ value for

the identified basal reflection peak from CSH(1.6) to CSH(1.0) which is consistent with a decrease of the basal spacing (i.e. interlayer) with increasing Ca/Si ratio. The emergence of the (222) peak from Ca/Si = 1.4 indicates the increased crystallinity of the CSH(1.4) and CSH(1.6) phases [185].

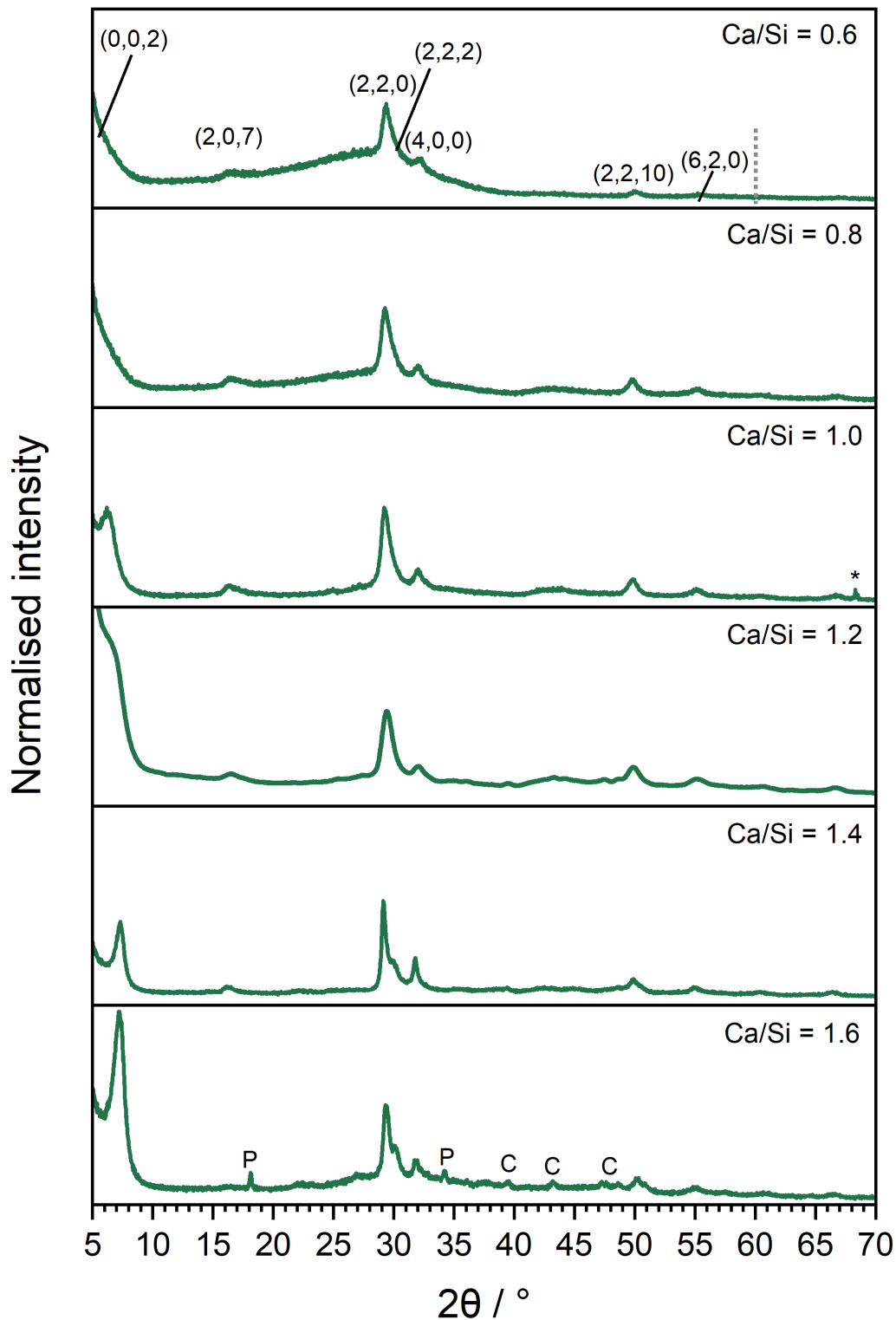


Figure 4.1: XRD patterns of C-S-H(I) phases (tobermorite, PDF card no 00-045-1480 [184]) and given Miller indices, synthesised at theoretical Ca/Si ratios of 0.6, 0.8, 1.0, 1.2, 1.4 and 1.6. The grey dashed line indicates where Miller indexing from the PDF card ceases. The presence of multiple phases is indicated by the presence of portlandite (P) (PDF card no 00-044-1481 [186]) and, subsequently, calcite (C) (PDF card no. 01-078-4614 [187]).

The presence of portlandite (PDF card no 00-044-1481 [186]) at Ca/Si = 1.6 indicates phase separation as a result of maximum incorporation of calcium into the C-S-H phase [188]. Although the CaO starting material for synthesis was heat treated prior to use and every attempt was made to exclude CO₂ during the synthesis, there is still the observation of calcite at Ca/Si = 1.6 (PDF card no. 01-078-4614 [187]). The C-S-H phase at the higher Ca/Si ratio therefore appears to be more susceptible to carbonation due to the presence of portlandite [189].

The effective molar Ca/Si ratio of the C-S-H phases was determined by ICP-OES analysis of the C-S-H reaction solutions. The remaining, unreacted concentrations of calcium and silicon were determined and subsequently subtracted from the initial amount of calcium and silicon reacted, according to **Equation 4.1**:

$$\frac{\text{Ca}}{\text{Si}} \text{ ratio} = \frac{([\text{Ca}]_{\text{initial}} - [\text{Ca}]_{\text{remaining}}) \div M_{\text{rCa}}}{([\text{Si}]_{\text{initial}} - [\text{Si}]_{\text{remaining}}) \div M_{\text{rSi}}} \quad (4.1)$$

where concentrations are in ppm and the M_r of calcium and silicon are 40.078 g mol⁻¹ and 28.085 g mol⁻¹, respectively.

Table 4.4 gives the average calculated Ca/Si ratios for the C-S-H phases used throughout this Thesis. The direct synthesis method appears to reproduce the theoretical Ca/Si ratio well, with a maximum deviation of 0.06 for Ca/Si = 1.6 (calculated Ca/Si = 1.54 ± 0.03). At Ca/Si 1.4 and 1.6, the calculated ratio is slightly lower than expected even within error. This further corroborates the idea that the C-S-H phase is approaching the maximum incorporation of calcium into the C-S-H phase, for this particular synthesis method.

Table 4.4: Molar Ca/Si ratios of synthesised C-S-H phases. Errors are based on standard deviation of triplicate measurements.

CSH(X)	Average calculated Ca/Si ratio of C-S-H phase
CSH(0.6)	0.61 ± 0.02
CSH(0.8)	0.82 ± 0.03
CSH(1.0)	1.00 ± 0.04
CSH(1.2)	1.18 ± 0.05
CSH(1.4)	1.35 ± 0.04
CSH(1.6)	1.54 ± 0.03

The particle size distribution of the of the CSH(1.0) phase is shown in **Figure 4.2**. Particle sizes were shown to be less than ~100 µm with the highest volume density of particles in the

~10 - 100 μm region. For the remaining C-S-H phases the particle size was not shown to vary significantly.

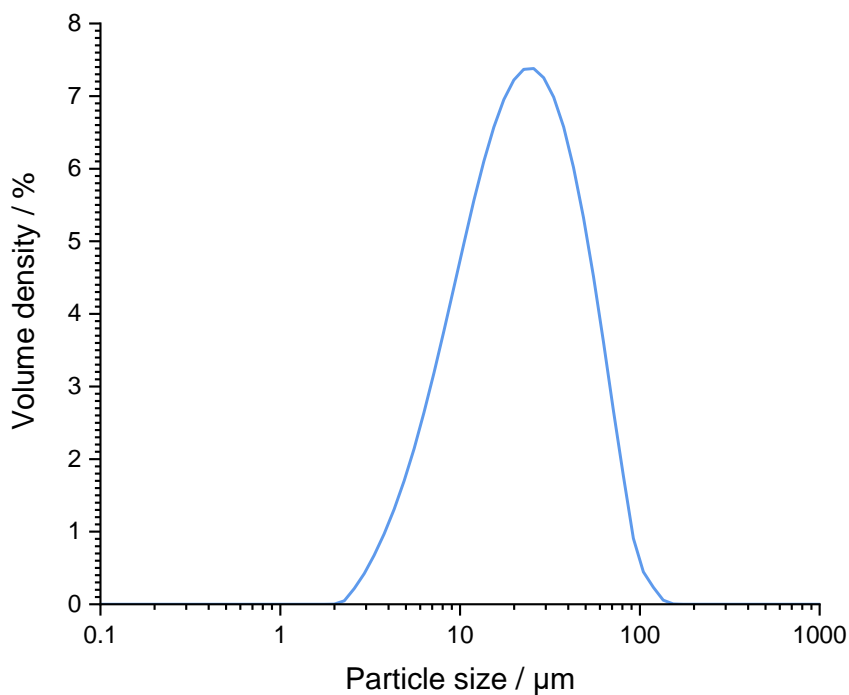


Figure 4.2: Particle size distribution of C-S-H powder (Ca/Si = 1.0).

The surface zeta potentials, as a function of calculated Ca/Si ratio, for C-S-H phases dispersed in both fresh UHQ and their respective C-S-H equilibrated synthesis solutions are displayed in **Figure 4.3**. Measurements of the zeta potential in C-S-H equilibrated solution were shown to be more positive than measurements taken after the C-S-H phases were in re-suspended UHQ. The surface zeta potential of the C-S-H phases was therefore dependent on the amount of Ca^{2+} present in solution [130]. For both data sets, the general trend of increasing positivity of the C-S-H surface was also observed with increasing Ca/Si ratio.

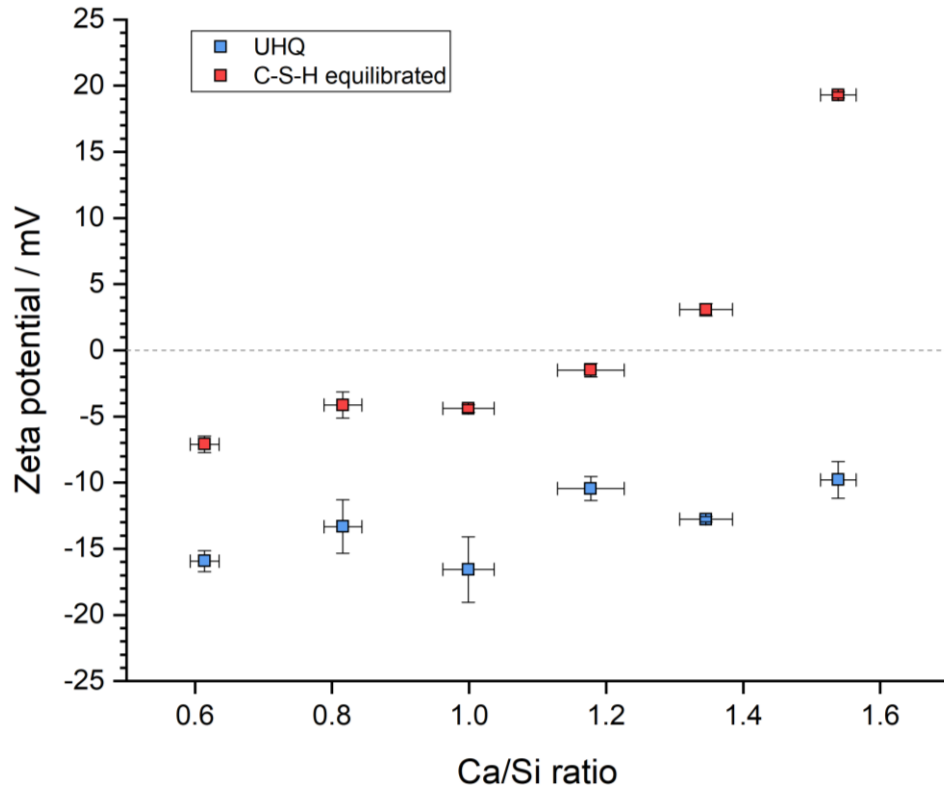


Figure 4.3: Zeta potential measurements of C-S-H phases dispersed in UHQ and C-S-H equilibrated water, plotted as a function of Ca/Si ratio. Errors are based on standard deviation of triplicate measurements.

4.3.1.1 Pre-carbonated C-S-H phases

The C-S-H phases were subject to a 1 % CO₂ atmosphere to introduce carbon into the system and induce calcium carbonate formation. The XRD patterns of the pre-carbonated C-S-H phases are displayed in **Figure 4.4**. The peaks for C-S-H(I) were still indexed, but additionally all three polymorphs of calcium carbonate (calcite, aragonite and vaterite) were identified after carbonation of most of the C-S-H phases. Only aragonite was not identified in the CSH(1.0) and CSH(1.4) phases.

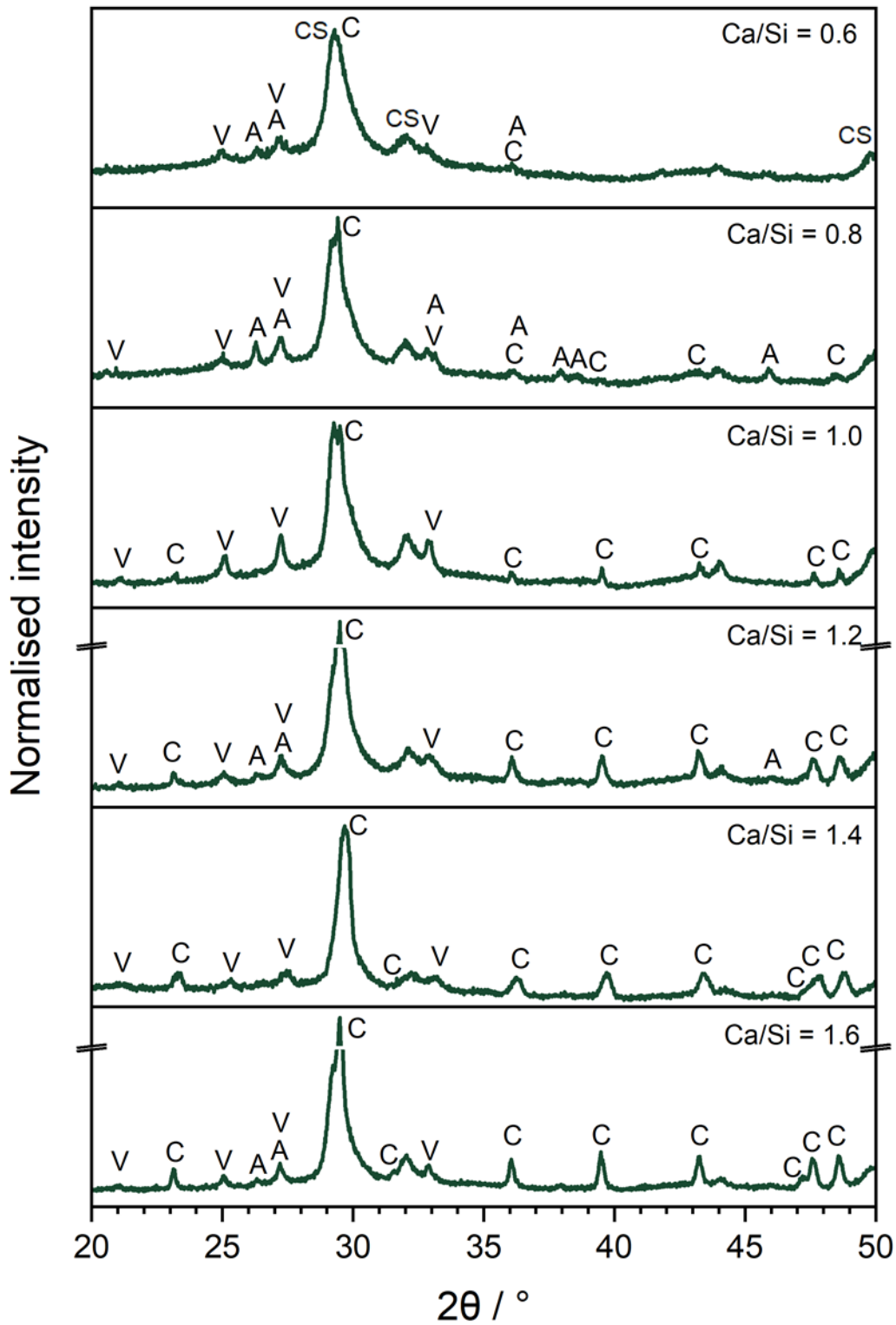


Figure 4.4: XRD patterns of pre-carbonated C-S-H phases. The peaks for C-S-H(I) can still be indexed (tobermorite, PDF card no 00-045-1480 [184]) and the positions are denoted by “CS” on the top pattern. A = aragonite (PDF card no. 01-085-6703 [190]); C = calcite (PDF card no. 01-078-4614 [187]); V = vaterite (PDF card no. 04-017-8634 [191]).

4.3.2 Hydrotalcite

A Mg/Al-hydrotalcite phase with a carbonate anion interlayer was synthesised by pH controlled mixing of 1 M $\text{Mg}(\text{NO}_3)_3$ / 1 M $\text{Al}(\text{NO}_3)_3$ in 1 M Na_2CO_3 solution (described in **Chapter 3**). **Figure 4.5** displays the XRD patterns for the synthesised phase and the “carbonated” phase (PDF card no. 01-082-8041 [192]). The crystallite size of hydrotalcite was calculated to be 5.1 ± 0.1 nm using Rietveld refinement ($R_{\text{wp}} = 9.028$).

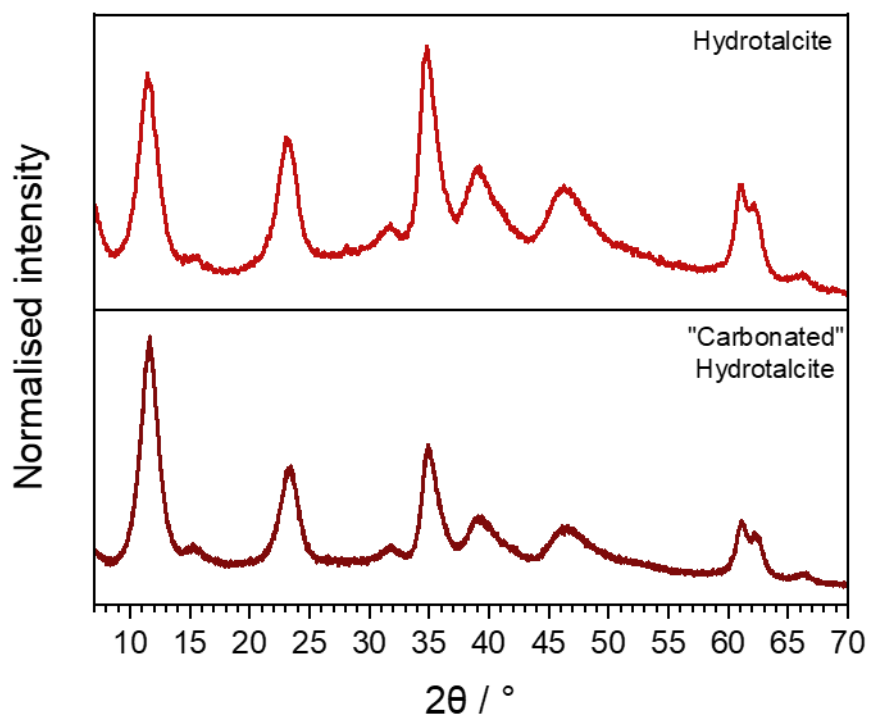


Figure 4.5: XRD patterns of hydrotalcite and “carbonated” hydrotalcite (PDF card no. 01-082-8041 [192]).

Exposure of the hydrotalcite phase to a 1 % CO_2 atmosphere did not result in a significant change in the XRD pattern. This is not unexpected given that the hydrotalcite phase was already stabilised with a carbonate interlayer [193]. The hydrotalcite phase was still identifiable (PDF card no. 01-082-8041 [192]) with a calculated crystal size of 5.5 ± 0.1 nm by Rietveld refinement ($R_{\text{wp}} = 10.257$). The slight increase in crystallite size is attributed to improved drying overtime, rather than any carbonation effects.

Hydrotalcite particle size distribution was shown to be less than ~ 100 μm with the highest volume density of particles in the $\sim 2 - 100$ μm region (**Figure 4.6**). The hydrotalcite phase also had a measured surface zeta potential of -16.3 ± 1.7 mV in UHQ water ($\text{pH} = 9.7 \pm 0.5$).

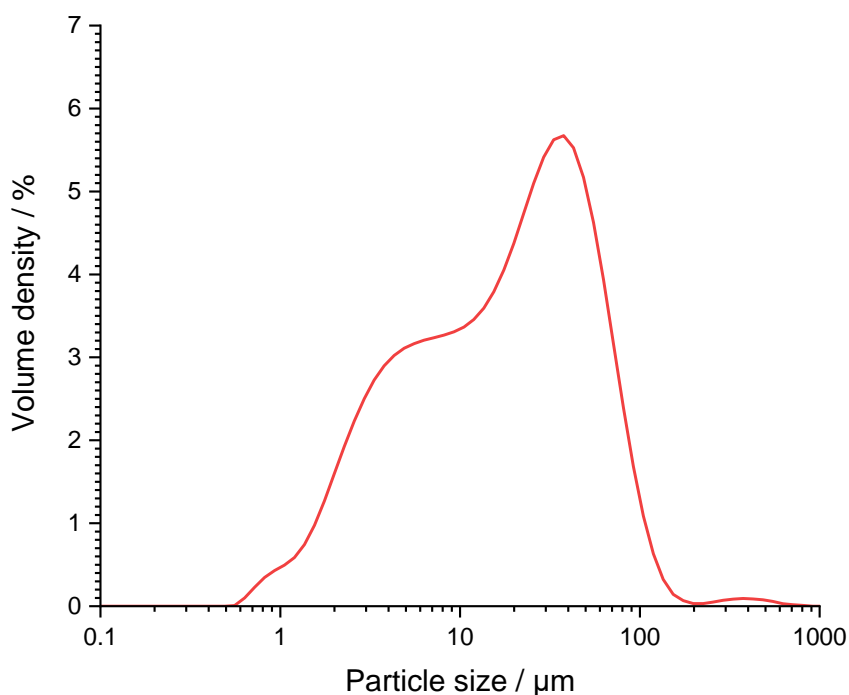


Figure 4.6: Particle size distribution of synthetic hydrotalcite powder.

4.3.3 Ettringite

The ettringite phases produced by hydrothermal synthesis (described in **Chapter 3**) were shown by XRD to be crystalline, with a crystal size of $\sim 130 \text{ \AA}$ calculated by Rietveld refinement. **Figure 4.7** displays the XRD diffraction patterns of two selected ettringite samples.

Pure phase ettringite was difficult to achieve and the phases generally displayed some calcium sulfate impurities of anhydrite or gypsum in XRD analyses (**Table 4.5**). This is important to note as such impurity phases, also including trace levels of AFm-SO_4 , may have different sorption / uptake capacities for radionuclides. This is taken into consideration during the discussion of relevant results in **Chapters 5** and **7**. Exposure of the ettringite phases to a 1 % CO_2 atmosphere did not result in a significant change in the XRD pattern resulting from destabilisation of the ettringite structure due to carbonation.

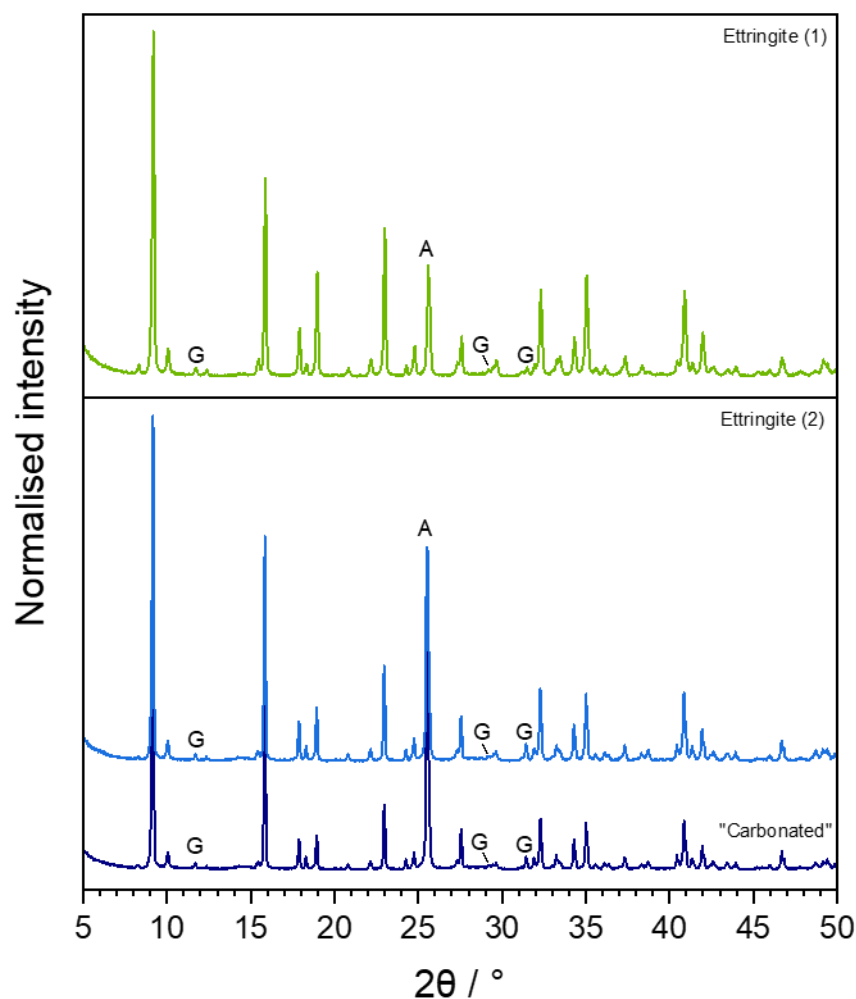


Figure 4.7: XRD patterns of two ettringite phases (PDF card no. 04-013-3691 [194]) with differing amounts of calcium sulfate impurities, ettringite (1) and ettringite (2). "Carbonated" ettringite (2) is also shown. A = anhydrite (PDF card no. 00-037-1496 [195]); G = gypsum (PDF card no. 00-033-0311 [196])

Due to the small amount of ettringite that could be produced at any one time, the particle size distribution of the synthetic ettringite phases could not be measured as a result of the relatively large volume of powder required for use in the PSD measurements, which is a destructive technique. All ettringite powders were sieved to $<60 \mu\text{m}$ before use in further experiments and the percentage of calcium sulfate impurities for each specific phase used are stated in the relevant Chapters. The zeta potential of the ettringite phases was measured to be $+1.8 \pm 0.1 \text{ mV}$ in UHQ ($\text{pH} = 9.6 \pm 0.1$).

Table 4.5: Percentage composition of ettringite phases determined by Rietveld refinement using CIF files for ettringite, anhydrite (orthorhombic) and gypsum [194,197,198].

	Rwp	GOF	Ettringite / %	Anhydrite / %	Gypsum / %
Ettringite (1)	14.36	3.91	93.4 ±0.6	4.6 ±0.5	2.0 ±0.3
Ettringite (2)	24.23	6.63	86.0 ±1.7	12.4 ±1.5	1.6 ±0.4

4.3 Results II: XAFS standards

4.3.1 Uranium compounds

The XANES spectra of all the uranium compounds and minerals used as standards, measured at the U L_{III}-edge (17 166 eV), are given in **Figure 4.8**.

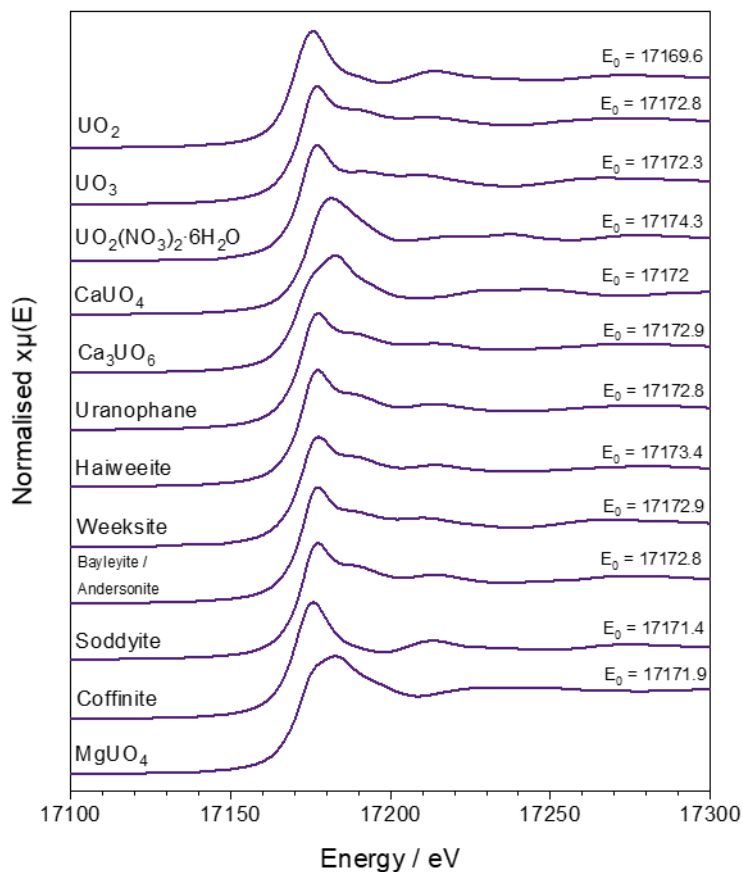


Figure 4.8: U L_{III}-edge measurements of all U standards.

4.3.1.1 Uranium oxides and uranyl nitrate: XAFS

The k^3 -weighted XAFS spectra and corresponding Fourier transforms to R-space of synthesised oxides / ternary oxides and uranyl nitrate are given in **Figures 4.9** and **4.10**.

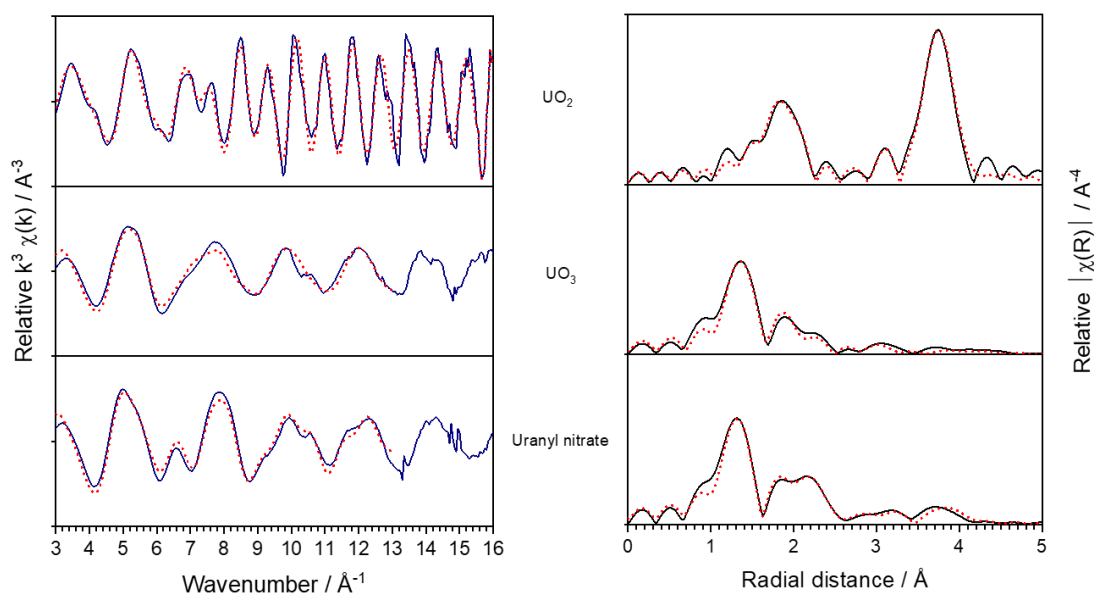


Figure 4.9: k^3 -weighted XAFS spectra of UO_2 , UO_3 and uranyl nitrate with corresponding Fourier transforms to R-space. Included on the plots are the EXAFS fits (red, dashed).

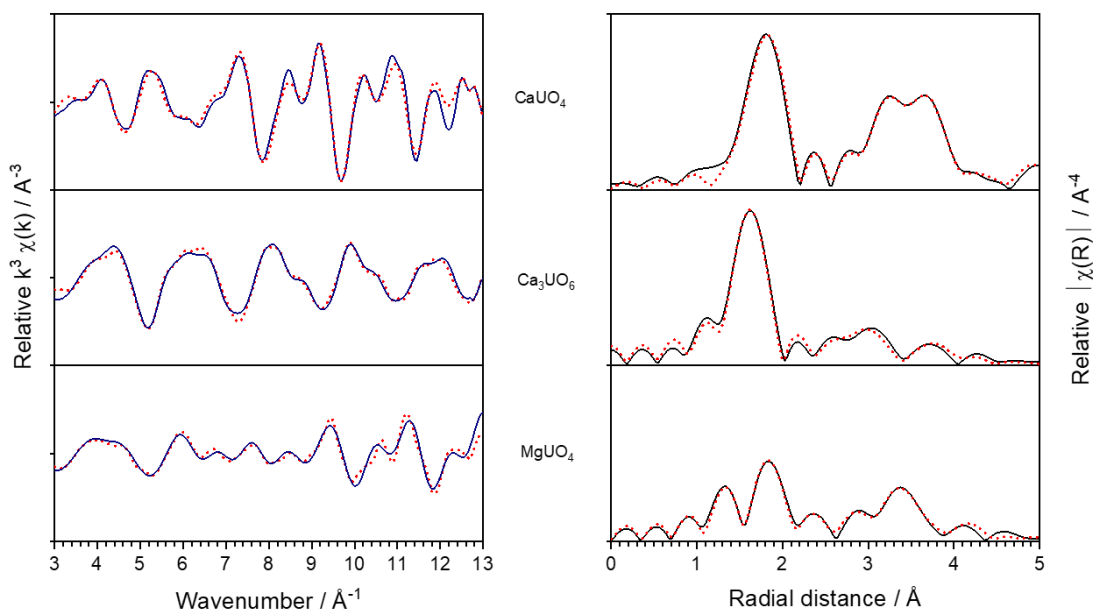


Figure 4.10: k^3 -weighted XAFS spectra of CaUO_4 , Ca_3UO_6 and MgUO_4 with corresponding Fourier transforms to R-space. Included on the plots are the EXAFS fits (red, dashed).

The uranium compounds were fitted to EXAFS models generated using FEFF calculations of appropriately selected CIF files. In the first instance, a model for UO_2 was generated in order to refine a value for the amplitude reduction factor (S_0^2) for uranium measured on beamline B18 at DLS. The value of S_0^2 for uranium was then set in the model for the fitting of subsequent standards. The results of the fits for the synthesised oxides / ternary oxides and uranyl nitrate are given in **Tables 4.6** to **4.11**. Axial and equatorial oxygens of U(VI) compounds are denoted by (ax) and (eq), respectively, where applicable.

4.3.1.2 EXAFS fitting of uranium oxides and nitrate

UO_2 (**Table 4.6**): The CIF file for UO_2 was taken from *Greaux et al.* [199] (space group = Fm-3m) to fit oxygen and uranium single pathways. An additional multi-scattering pathway was also required to improve the R-factor of the fit, at a distance of 3.82 ± 0.07 Å. The value of S_0^2 was refined at 0.859 ± 0.048 .

UO_3 (**Table 4.7**): The CIF file for UO_3 was taken from *Loopstra et al.* [200] (γ - UO_3 , space group = Fddd) to fit oxygen and uranium pathways. The first oxygen (ax) distance was refined at 1.791 ± 0.010 Å with $N_{O1} = 2.0 \pm 0.3$.

Uranyl nitrate (**Table 4.8**): The CIF file for $\text{UO}_2(\text{NO}_3)_2 \cdot 6\text{H}_2\text{O}$ fitting was taken from *Taylor et al.* [201] (space group = Cmc21). The first oxygen (ax) distance was refined at 1.764 ± 0.006 Å with $N_{O1} = 2.4 \pm 0.20$.

4.3.1.3 EXAFS fitting of uranates

CaUO_4 (**Table 4.9**): The CIF file used for CaUO_4 fitting was courtesy of S. O'Sullivan (space group = R-3m). The first oxygen distance (ax) was refined at 1.953 ± 0.006 Å with $N_{O1} = 2.2 \pm 0.2$.

Ca_3UO_6 (**Table 4.10**): The CIF file used for Ca_3UO_6 fitting was taken from *Holc et al.* [202] (space group = R-3). The first oxygen distance was refined at 2.069 ± 0.064 Å with $N_{O1} = 4.5 \pm 0.2$.

MgUO_4 (**Table 4.11**): the CIF file used for MgUO_4 fitting was taken from *Zachariassen et al.* [203] (space group = Imam). The first oxygen (ax) distance was refined at 1.948 ± 0.006 Å with $N_{O1} = 1.8 \pm 0.1$.

Table 4.6: EXAFS fit of UO₂ performed between k-range 3.1 - 15 Å⁻¹ and R-range 1 - 4.5 Å.

UO ₂	ΔE	R _{U-o} (1)	N _o (1)	σ ² _o (1,2)	R _{O-U-o}	N _{oo}	σ ² _{oo}	R _{U-U}	N _U	σ ² _U	R _{U-o} (2)	N _o (2)
R-factor = 0.019 S _o ² = 0.859(48) CIF file from [199]	5.38(99)	2.349(10)	8	0.0090(1)	3.82(7)	24	as σ ² _o	3.87(1)	12	0.0050(4)	4.46(1)	24

Table 4.7: EXAFS fit of UO₃ performed between k-range 3.6 - 12.5 Å⁻¹ and R-range 0.9 - 4 Å.

UO ₃	ΔE	R _{U-o}	N _o	σ ² _o	R _{U-U}	N _U	σ ² _U
R-factor = 0.021 CIF file from [200]	8.48(1.90)	1.791(10) (ax)	2.03(30)	0.003(1)	4.14(7)	4	0.02(1)
		2.339(1) (eq)	2	-	-	-	-
		2.49(3) (eq)	2	-	-	-	-
		3.4 (eq)	1	-	-	-	-

Table 4.8: EXAFS fit of UO₂(NO₃)₂·6H₂O performed between k-range 3.6 - 12.7 Å⁻¹ and R-range 1 - 4.5 Å.

UO ₂ (NO ₃) ₂ ·6H ₂ O	ΔE	R _{U-o} (1)	N _o (1)	σ ² _o (1,2)	R _{U-N}	N _N	σ ² _N	R _{O-U-o}	N _{oo}	σ ² _{oo}	R _{U-o} (2)	N _o (2)
R-factor = 0.009 CIF file from [201]	8.74(1.21)	1.764(6) (ax)	2.41(20)	0.0028(7)	2.95(2)	2	0.0010(21)	3.60(4)	2	0.001	3.75(8)	1
		2.37(2) (eq)	2	-	-	-	-	-	-	-	4.30(2)	6
		2.49(2) (eq)	2	-	-	-	-	-	-	-	-	-
		2.55(2) (eq)	2	-	-	-	-	-	-	-	-	-

Table 4.9: EXAFS fit of CaUO₄ performed between k-range 3.4 - 12 Å⁻¹ and R-range 1.2 - 5 Å.

CaUO ₄	ΔE	R _{U-o} (1)	N _O (1)	σ ² _O (1,2)	R _{U-ca} (1)	N _{Ca} (1)	σ ² _{Ca} (1,2)	R _{U-U}	N _U	σ ² _U	R _{U-o} (2)	N _O (2)	R _{U-ca} (2)	N _{Ca} (2)
R-factor = 0.009 CIF file courtesy of S. O'Sullivan	4.79(68)	1.953(6) (ax)	2.15(15)	0.0034(3)	3.68(1)	6	0.0052(7)	3.88(1)	6	0.005(1)	4.29(3)	12	5.34(2)	6
		2.28(4) (eq)	6	-	-	-	-	-	-	-	4.45(2)	12	-	-

Table 4.10: EXAFS fit of Ca₃UO₆ performed between k-range 3.6 - 12.3 Å⁻¹ and R-range 1.1 - 5 Å.

Ca ₃ UO ₆	ΔE	R _{U-o} (1)	N _O (1)	σ ² _O (1,2)	R _{U-ca} (1)	N _{Ca} (1)	σ ² _{Ca} (1,2)	R _{U-o} (2)	N _O (2)	R _{U-U}	N _U	σ ² _U	R _{U-ca} (2)	N _{Ca} (2)
R-factor = 0.009 CIF file from [202]	3.08(67)	2.069(64)	4.50(22)	0.0029(5)	3.46(1)	6	0.013(1)	4.33(2)	6	5.54(12)	2	0.012(3)	5.78(6)	6
		-	-	-	4.18(2)	6	-	-	5.85(4)	6	-	-	-	-

Table 4.11: EXAFS fit of MgUO₄ performed between k-range 3.5 - 12.75 Å⁻¹ and R-range 1.1 - 4.7 Å.

MgUO ₄	ΔE	R _{U-o} (1)	N _O (1)	σ ² _O (1,2)	R _{U-U} (1)	N _U (1)	σ ² _U (1,2)	R _{U-o} (2)	N _O (2)	R _{U-Mg}	N _{Mg}	σ ² _{Mg}	R _{U-U} (2)	N _{Ca} (2)
R-factor = 0.016 CIF file from [203]	3.33(1.31)	1.948(6) (ax)	1.77(13)	0.0017(4)	3.51(3)	3	0.009(3)	3.83(4)	4	4.00(2)	4	0.0001	4.30(3)	2
		2.16(1) (eq)	3	-	-	-	-	4.24(4)	4	-	-	-	-	-
		3.17(2) (eq)	2	-	-	-	-	-	-	-	-	-	-	-

4.3.2 Uranium minerals

4.3.2.1 XRD

Given that the uranium mineral phases analysed by XAFS were generally naturally occurring, the co-existence of other mineral phases was highly probable. The powders extracted from the minerals named as uranophane ($\text{Ca}(\text{UO}_2)_2\text{SiO}_3(\text{OH})_2 \cdot 5\text{H}_2\text{O}$), haiweeite ($\text{Ca}(\text{UO}_2)_2(\text{Si}_5\text{O}_{12})(\text{OH})_2 \cdot 6\text{H}_2\text{O}$), weeksite ($\text{K}_2(\text{UO}_2)_2(\text{Si}_5\text{O}_{12})(\text{OH})_4\text{H}_2\text{O}$), soddyite ($(\text{UO}_2)_2\text{SiO}_4 \cdot 2\text{H}_2\text{O}$) and bayleyite ($\text{Mg}_2(\text{UO}_2)(\text{CO}_3)_3 \cdot 18\text{H}_2\text{O}$) / andersonite ($\text{Na}_2\text{Ca}(\text{UO}_2)(\text{CO}_3)_3 \cdot 6\text{H}_2\text{O}$) were therefore analysed by XRD to attempt identification of the U-bearing minerals and other impurities (**Figures 4.11 to 15**). It should be noted that the coffinite phase was a pure-phase, synthetic sample obtained from the work carried out in [183].

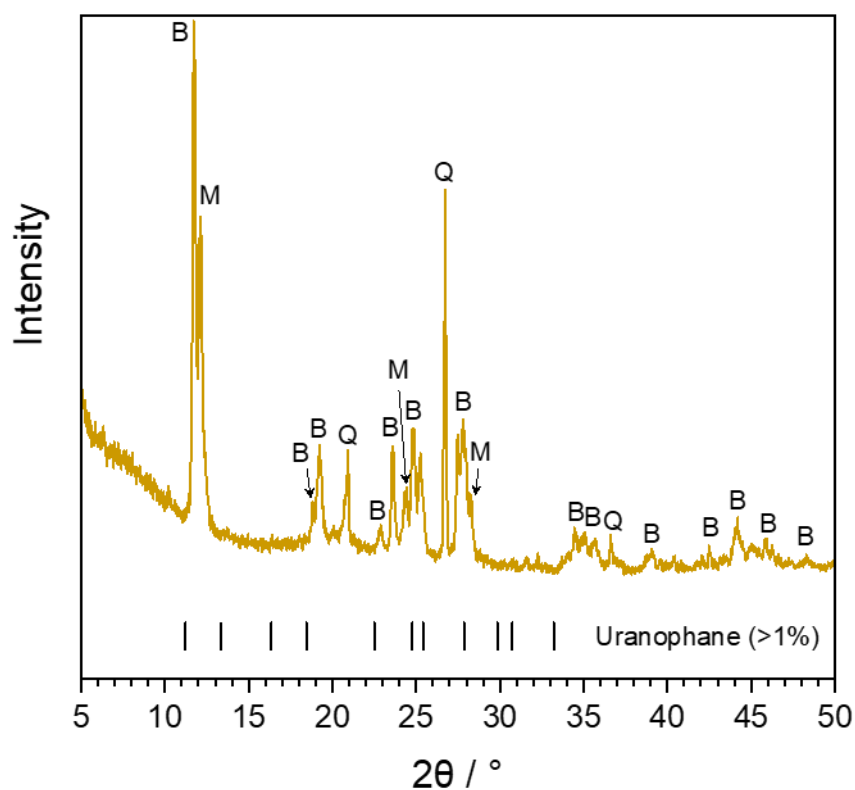


Figure 4.11: XRD pattern of mineral phase named as uranophane (PDF card no. 00-039-1360 [204], ICSD no. 250001 [205]). B = billietite ($\text{Ba}(\text{UO}_2)_6\text{O}_4(\text{OH})_6 \cdot 8\text{H}_2\text{O}$, COD no. 9010599, ICSD no. 156226 [206]); M = metaschoepite / “sodium-substituted” ($(\text{UO}_2)_4\text{O}(\text{OH})_6(\text{H}_2\text{O})_5$, ICSD no. 156714 / $\text{Na}(\text{UO}_2)_4\text{O}_2(\text{OH})_5(\text{H}_2\text{O})_5$, COD no. 9010195, ICSD no. 156715 [207]); Q = quartz (PDF card no. 01-089-8940 [208]). Peak positions for uranophane with intensity >1 % are also shown.

The mineral powder that was named as uranophane only showed U-bearing phases that could be identified as billietite (general formula $\text{Ba}(\text{UO}_2)_6\text{O}_4(\text{OH})_6 \cdot 8\text{H}_2\text{O}$) [206] and a “sodium-substituted” metaschoepite phase (general formula $(\text{UO}_2)_4\text{O}(\text{OH})_6 \cdot 5\text{H}_2\text{O}$) [207]. These are secondary minerals that occur as an alteration product of uraninite, as is the case with uranophane. As billietite is an uncommon secondary mineral, it could also be likely the phase occurs as the Ca-bearing analogue of billietite, becquerelite ($\text{Ca}(\text{UO}_2)_6\text{O}_4(\text{OH})_6 \cdot 8(\text{H}_2\text{O})$), in this system, given that the XRD patterns are similar [209]. The mineral sample is hereafter denoted as “uranophane (B)”.

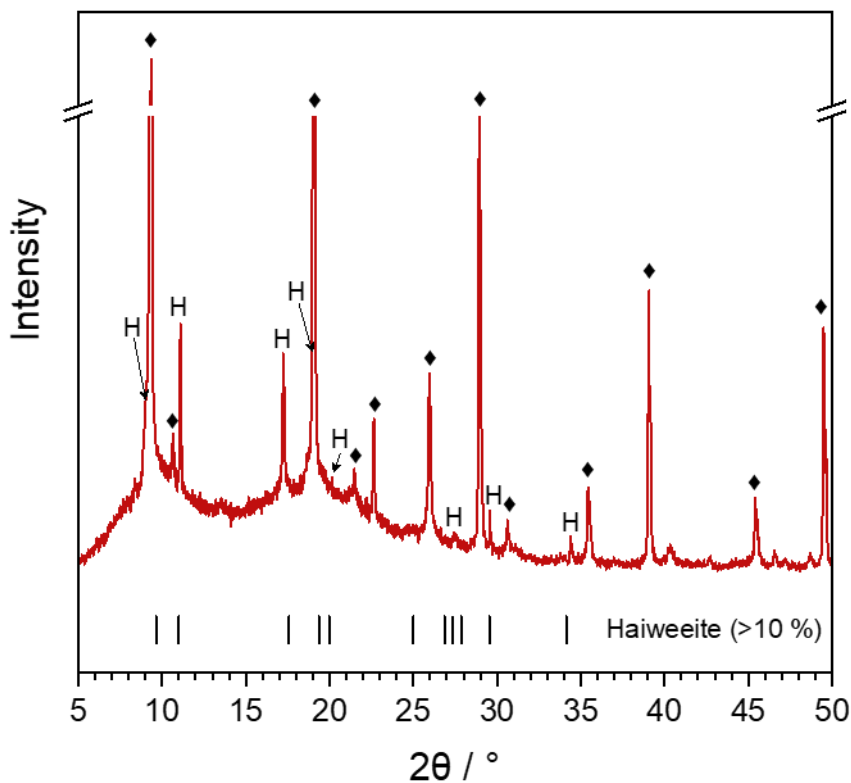


Figure 4.12: XRD pattern of mineral phase named as haiweeite (PDF card no. 00-012-0721 [210], ICSD no. 187584 [211]). H = haiweeite (peak positions for intensity >10% are also shown); ◆ = unidentified peaks.

Peaks for the haiweeite mineral ($\text{Ca}(\text{UO}_2)_2(\text{Si}_5\text{O}_{12})(\text{OH})_2 \cdot 6\text{H}_2\text{O}$) were identified in the XRD pattern for the powder sample of the same name [210,211]. Additional peaks that could not be identified as U-bearing phases were attributed to other phases from the haiweeite-bearing pegmatite matrix, but which were not identified as either quartz (SiO_2), feldspar (various aluminosilicates) or mica (various sheet silicates) phases.

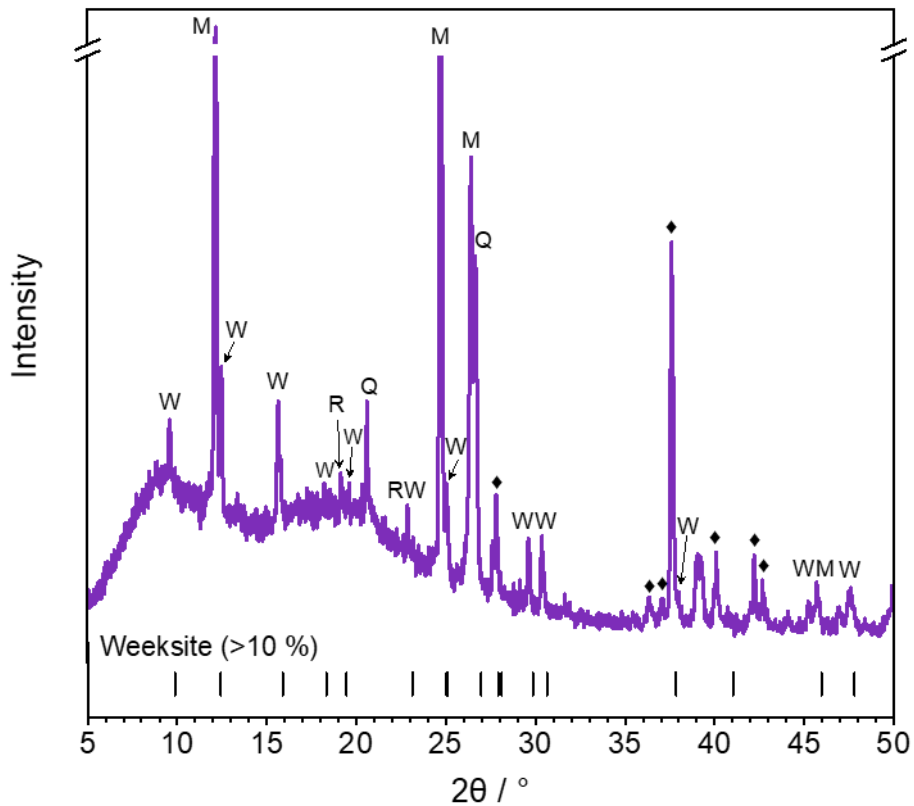


Figure 4.13: XRD pattern of mineral phase named as weeksite (PDF card no. 00-050-1660 [212], ICSD no. 63515 [213]). W = weeksite (peak positions for intensity >10 % are also shown); M = metaschoepite ($(\text{UO}_2)_4\text{O}(\text{OH})_6 \cdot 5\text{H}_2\text{O}$, ICSD no. 156714 [207]); R = rutherfordine (UO_2CO_3 , COD 9004535, ICSD 27053 [214]) Q = quartz (PDF card no. 01-089-8940 [208]). ♦ = unidentified peaks.

The weeksite mineral ($\text{K}_2(\text{UO}_2)_2(\text{Si}_5\text{O}_{12})(\text{OH})_4\text{H}_2\text{O}$) was identified in the XRD pattern of the powder of the same name [212,213], along with metaschoepite (general formula $(\text{UO}_2)_4\text{O}(\text{OH})_6 \cdot 5\text{H}_2\text{O}$) and a partial correlation with rutherfordine (UO_2CO_3). Some additional peaks could not be identified as U-bearing phases and were attributed to other phases in the rhyolite matrix, but were not identified as any feldspar phases.

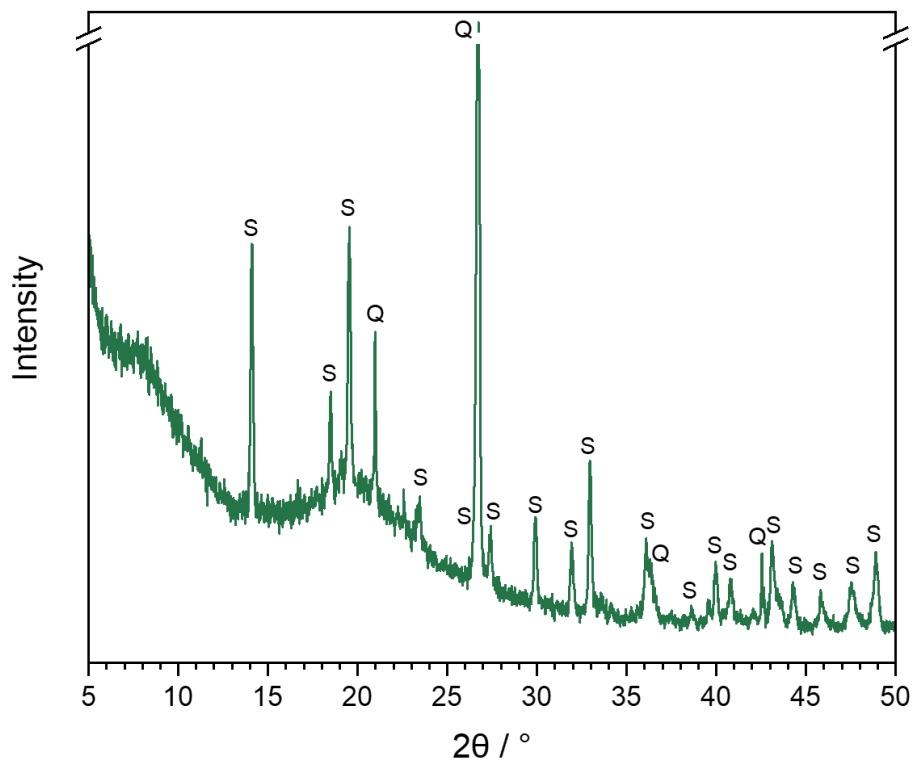


Figure 4.14: XRD pattern of the mineral phase named as soddyite (PDF card no. 04-011-3340 [215]).
 S = soddyite; Q = quartz (PDF card no. 01-089-8940 [208]).

The only U-bearing phase identified in the soddyite mineral phase was that of the uranyl silicate, soddyite $((\text{UO}_2)_2\text{SiO}_4 \cdot 2\text{H}_2\text{O})$ [215]. Only quartz (SiO_2) was identified as an additional phase.

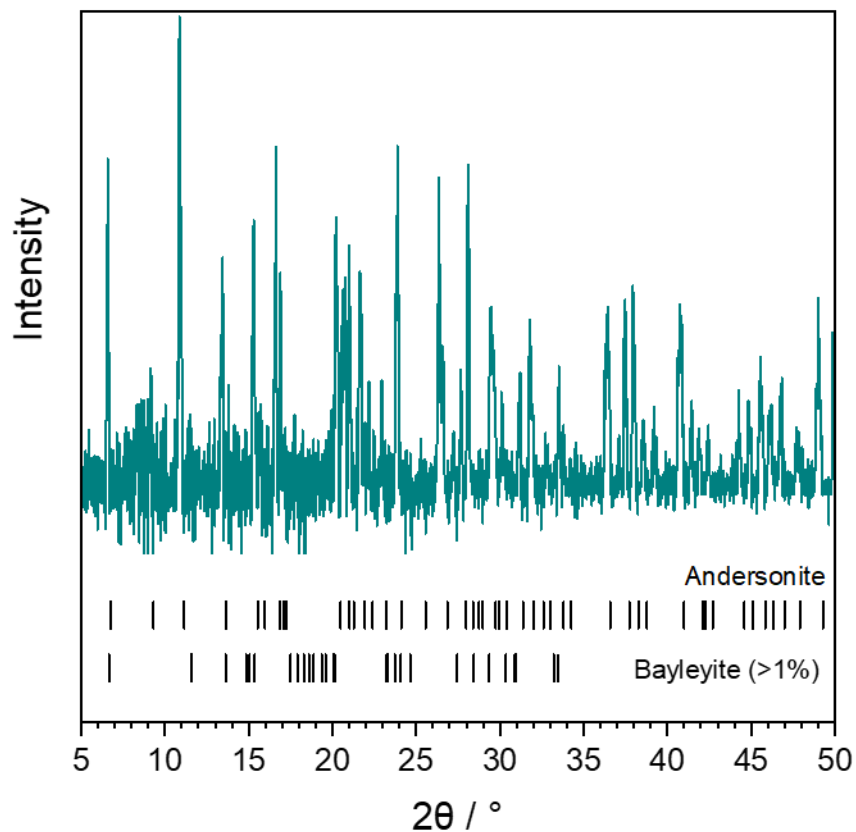


Figure 4.15: XRD pattern of the mineral named as bayleyite / andersonite (ICSD no. 32101 [216] / PDF card no. 00-045-1434 [217]) [218]. Peak positions for andersonite and bayleyite (> 1% intensity) are given.

The X-ray diffraction pattern for the bayleyite / andersonite mineral displayed significant background noise, however the andersonite ($\text{Na}_2\text{Ca}(\text{UO}_2)(\text{CO}_3)_3 \cdot 6\text{H}_2\text{O}$) [217,218] and bayleyite ($\text{Mg}_2(\text{UO}_2(\text{CO}_3)_3 \cdot 18\text{H}_2\text{O})$) [216] mineral phases were identified.

4.3.2.2 XAFS

The k^3 -weighted XAFS spectra and corresponding Fourier transforms to R-space of the uranium minerals are given in **Figures 4.16** and **4.17**. For uranophane ($\text{Ca}(\text{UO}_2)_2\text{SiO}_3(\text{OH})_2 \cdot 5\text{H}_2\text{O}$), haiweeite ($\text{Ca}(\text{UO}_2)_2(\text{Si}_5\text{O}_{12})(\text{OH})_2 \cdot 6\text{H}_2\text{O}$), weeksite ($\text{K}_2(\text{UO}_2)_2(\text{Si}_5\text{O}_{12})(\text{OH})_4\text{H}_2\text{O}$), soddyite ($(\text{UO}_2)_2\text{SiO}_4 \cdot 2\text{H}_2\text{O}$) and bayleyite ($\text{Mg}_2(\text{UO}_2)(\text{CO}_3)_3 \cdot 18\text{H}_2\text{O}$) / andersonite ($\text{Na}_2\text{Ca}(\text{UO}_2)(\text{CO}_3)_3 \cdot 6\text{H}_2\text{O}$) and coffinite ($\text{U}(\text{SiO}_4)_{1-x}(\text{OH})_{4x}$), EXAFS scatterers were fitted with pathways generated by using appropriately selected CIF files for the corresponding mineral phases. In the case of uranophane (B), given that the uranophane mineral was not identified in the sample of the powder analysed by XRD, several fits were performed using CIF files for each uranophane,

metaschoepite $((\text{UO}_2)_4\text{O}(\text{OH})_6 \cdot 5\text{H}_2\text{O})$, billietite $(\text{Ba}(\text{UO}_2)_6\text{O}_4(\text{OH})_6 \cdot 8\text{H}_2\text{O})$ and becquerelite $(\text{Ca}(\text{UO}_2)_6\text{O}_4(\text{OH})_6 \cdot 8(\text{H}_2\text{O}))$, respectively. The results of the uranium mineral EXAFS fits are given in **Tables 4.12 to 17**. Axial and equatorial oxygens are indicated by (ax) and (eq), respectively.

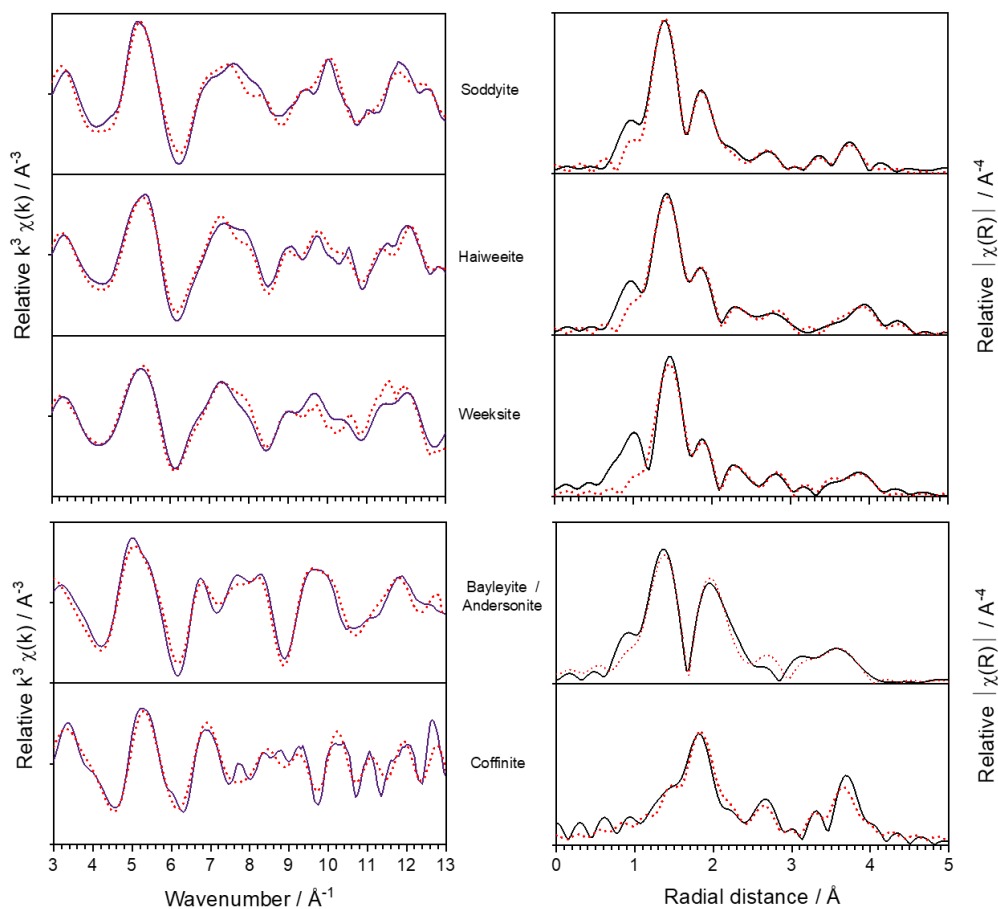


Figure 4.16: k^3 -weighted XAFS spectra of haiweeite, weeksite, soddyite, bayleyite / andersonite and coffinite with corresponding Fourier transforms to R-space. Included on the plots are the EXAFS fits (red, dashed).

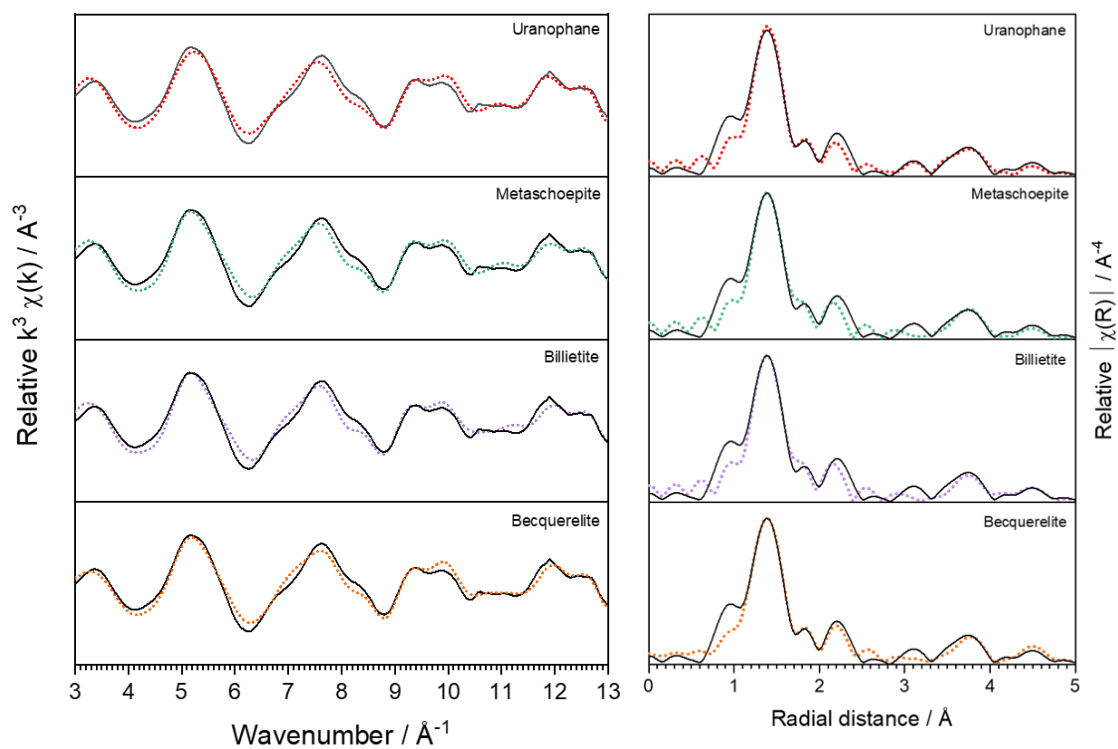


Figure 4.17: k^3 -weighted XAFS spectrum of uranophane (B) with corresponding Fourier transform to R-space. Included on the plots are EXAFS fits corresponding to uranophane, metaschoepite, billietite and becquerelite (colour, dashed).

Table 4.12: EXAFS fits of uranyl silicate minerals, haiweeite (k-range: 3.6 - 13.4 Å⁻¹; R-range: 1 - 5 Å), weeksite (k-range: 3.65 - 13.31 Å⁻¹; R-range: 1.1 - 5 Å) and soddyite (k-range: 3.66 - 13.37 Å⁻¹; R-range: 1 - 4.7 Å). The hydrogen pathway in soddyite is treated tentatively due to being a light element.

Uranyl silicates	ΔE	R _{U-o} (1)	N _o (1)	σ^2_{o} (1,2)	R _{U-si}	N _{si}	σ^2_{si}	R _{U-U}	N _U	σ^2_U	R _{U-o} (2)	N _o (2)
Haiweeite R-factor = 0.017 CIF file from [211]	7.06(1.08)	1.803(11) (ax)	2.13(26)	0.003(1)	3.17(2)	1	0.004(2)	4.02(2)	2	0.005(2)	4.08(6)	2
		2.20(3) (eq)	1		3.62(6)	1		-	-	-	-	-
		2.31(2) (eq)	3		3.79(4)	2		-	-	-	-	-
		2.46(3) (eq)	2		-	-	-	-	-	-	-	-
Weeksite R-factor = 0.019 CIF file from [213]	8.32(1.67)	1.825(8) (ax)	1.75(22)	0.0024(1)	3.21(3)	1	0.005(2)	4.06(3)	2	0.007(3)	-	-
		2.21(2) (eq)	1		3.72(3)	2		-	-	-	-	-
		2.35(2) (eq)	3		3.90(4)	2		-	-	-	-	-
		2.52(2) (eq)	2		-	-	-	-	-	-	-	-
Soddyite R-factor = 0.016 CIF file from [215]	7.65(1.79)	1.791(9) (ax)	2.24(34)	0.003(1)	3.17(5)	1	0.007(3)	3.90(3)	2	0.004(2)	4.10(5)	4
		2.27(2) (eq)	2		3.74(4)	2		-	-	-	-	-
		2.41(2) (eq)	3		-	-	-	-	-	-	-	-
	H scatterer:	2.77(14)	2	0.0001	-	-	-	-	-	-	-	-

Table 4.13: EXAFS fit of bayleyite / andersonite performed between k-range 3.6 - 12.4 Å⁻¹ and R-range 1 - 4.7 Å.

Bayleyite / Andersonite	ΔE	R _{U-o} (1)	N _o (1)	σ^2_{o} (1,2)	R _{U-C}	N _C	σ^2_C	R _{U-Na}	N _{Na}	σ^2_{Na}	R _{U-Ca}	N _{Ca}	σ^2_{Ca}	R _{U-o} (2)	N _o (2)
R-factor = 0.023 CIF file from [218]	8.60(1.61)	1.796(9) (ax)	2.52(26)	0.0031(7)	2.91(2)	3	0.001(2)	3.71(5)	1	0.0001	3.98(2)	2	0.002(2)	4.31(9)	2
		2.43(12) (eq)	4		-	-	-	-	-	-	-	-	-	-	-

Table 4.14: EXAFS fit of coffinite performed between k-range 3 - 13.8 Å⁻¹ and R-range 1.2 - 4 Å

Coffinite	ΔE	R _{U-o}	N _o	σ ² _o	R _{U-si}	N _{si}	σ ² _{si}	R _{U-U}	N _U	σ ² _U
R-factor = 0.029 CIF files from [219,220]	5.62(1.65)	2.26(1)	4	0.004(1)	3.11(2)	2	0.004(1)	3.81(1)	2	0.0028(7)
		2.38(1)	4		3.81(3)	2		-	-	-

Tables 4.15-4.18: EXAFS fit of uranophane (B) performed between k-range 3.6 - 13.6 Å⁻¹ and R-range 1 - 5 Å.

Table 4.15: Uranophane.

Uranophane (B)	ΔE	R _{U-o} (1)	N _o (1)	σ ² _o (1,2)	R _{U-si}	N _{si}	σ ² _{si}	R _{U-U}	N _U	σ ² _U	R _{U-o} (2)	N _o (2)	
Uranophane R-factor = 0.017 CIF file from [205]	7.47(1.41)	1.796(7) (ax)	2.01(22)	0.003(1)	3.65(4)	1	0.003(5)	3.88(2)	1	0.005(2)	4.92(7)	2	
		2.19(2) (eq)	1		3.82(5)	1		-	-	-	-	-	
		2.32(2) (eq)	2		-	-	-	-	-	-	-	-	-
		2.48(2) (eq)	2		-	-	-	-	-	-	-	-	-

Table 4.16: Metaschoepite.

Uranophane (B)	ΔE	R _{U-o}	N _o	σ ² _o	R _{U-U}	N _U	σ ² _U
Metaschoepite R-factor = 0.026 CIF file from [207]	8.24(1.62)	1.799(9) (ax)	2.04(24)	0.003(1)	3.88(2)	2	0.007(2)
		2.25(2) (eq)	2		4.60(6)	1	
		2.41(2) (eq)	2		-	-	-
		2.53(3) (eq)	1		-	-	-

Table 4.17: Billietite.

Uranophane (B)	ΔE	R_{U-o}	N_o	σ^2_o	R_{U-U}	N_U	σ^2_U	R_{U-Ba}	N_{Ba}	σ^2_{Ba}
Billietite R-factor = 0.027 CIF file from [206]	7.47(1.66)	1.798(9) (ax)	2.00(24)	0.003(1)	3.88(3)	3	0.010(2)	4.72(4)	1	0.005(4)
		2.25(2) (eq)	2		-	-	-	-	-	-
		2.42(2) (eq)	2		-	-	-	-	-	-
		2.53(3) (eq)	1		-	-	-	-	-	-

Table 4.18: Becquerelite.

Uranophane (B)	ΔE	R_{U-o}	N_o	σ^2_o	R_{U-U}	N_U	σ^2_U
Becquerelite R-factor = 0.017 CIF file from [221]	8.61(2.34)†	1.765(2)† (ax)	1.40(41)	0.0002(19)	3.89(2)	1	0.004(1)
		1.89(3) (ax)	1		4.60(3)	1	
		2.14(1) (eq)	1		-	-	-
		2.30(1) (eq)	2		-	-	-
		2.44(2) (eq)	1		-	-	-
		2.51(2) (eq)	1		-	-	-

† correlation between variables.

4.3.2.3 EXAFS fitting of uranyl silicate models

For the uranyl silicates haiweeite, weeksite and soddyite, a first oxygen shell, second silicon shell and a third uranium shell (with $N_U = 2$) were fitted, and the scattering distances, in Å, were refined in each case (**Table 4.12**). Only the coordination number for the first oxygen path was refined and subsequent coordination numbers were set in the model using values generated by the FEFF calculations as a starting point, but were sequentially refined using trial and error where necessary, to achieve the best fit.

Haiweeite: The CIF file for haiweeite taken from *Plasil et al.* [211] was used as the model basis (space group = Pbcn). The first oxygen (ax) distance was refined at 1.803 ± 0.011 Å with a N_{O1} value of 2.1 ± 0.3 . Subsequent oxygen (eq) distances were refined at 2.20 ± 0.03 Å ($N_{O2} = 1$), 2.31 ± 0.02 Å ($N_{O3} = 3$) and 2.46 ± 0.03 Å ($N_{O4} = 2$). Various silicon scatterers were fitted with a total N_{Si-tot} value of 4, between ~ 3.17 and 3.79 Å. The uranium distance was refined at 4.02 ± 0.02 Å. An additional oxygen distances was also refined at 4.08 ± 0.06 Å $N_{O5} = 2$.

Weeksite: The CIF file for haiweeite taken from *Baturin et al.* [213] was used as the model basis (space group = Cmmm). The first oxygen (ax) distance was refined at 1.825 ± 0.008 Å with a N_{O1} value of 1.8 ± 0.2 . Subsequent oxygen (eq) distances were refined at 2.21 ± 0.02 Å ($N_{O2} = 1$), 2.35 ± 0.02 Å ($N_{O3} = 3$) and 2.52 ± 0.02 Å ($N_{O4} = 2$). Silicon scatterers were fitted with a total N_{Si-tot} value of 5, between ~ 3.21 and 3.90 Å. The uranium distance was refined at 4.06 ± 0.03 Å.

Soddyite: The CIF file for soddyite taken from *Demartin et al.* [215] was used as the model basis (space group = Fddd). The first oxygen (ax) distance was refined at 1.791 ± 0.009 Å with a N_{O1} value of 2.2 ± 0.3 . Two subsequent oxygen (eq) distances were refined at 2.27 ± 0.02 Å ($N_{O2} = 2$) and 2.41 ± 0.02 Å ($N_{O3} = 3$) and a tentative hydrogen distance at 2.77 ± 0.14 Å ($N_{H1} = 2$). Two silicon scatterers were fitted with a total N_{Si-tot} value of 3 at ~ 3.17 and ~ 3.74 Å. The uranium distance was refined at 3.90 ± 0.03 Å. One additional oxygen distance was refined at 4.10 ± 0.05 Å with $N_{O4} = 4$.

The main differences to note between the different fits of the uranyl silicates are:

- (i) The distances and N_{O1} value refined for the first oxygen pathway.
- (ii) The number of oxygen (eq) pathways fitted (3 for haiweeite and weeksite and 2 for soddyite).
- (iii) The total number of silicon pathways fitted (3 for haiweeite and weeksite and 2 for soddyite).
- (iv) The uranium scatterer distance (~ 4.0 Å for haiweeite and weeksite and ~ 3.9 Å for soddyite).

No calcium and / or potassium scatterers could be fitted in the haiweeite or weeksite fits despite them being Ca- and / or K-containing minerals.

4.3.2.4 EXAFS fitting of other uranium mineral phases

Bayleyite / andersonite (Table 4.13): The bayleyite / andersonite containing mineral could only be fitted with EXAFS scatters related to the structure of andersonite. Fitting with a CIF file for bayleyite [216] did not allow for fitting of magnesium scatterers at a reasonable distance. The CIF file for andersonite taken from *Coda et al.* [218] was used as the model basis (space group = R-3m). The first oxygen (ax) distance was refined at 1.796 ± 0.009 Å with a N_{O1} value of 2.5 ± 0.3 and the second oxygen (eq) distance at 2.4 ± 0.01 with $N_{O2} = 4$, as well as a subsequent carbon distance at 2.91 ± 0.02 with $N_{C1} = 3$. Sodium and calcium paths were fit at 3.71 ± 0.05 Å ($N_{Na1} = 1$) and 3.98 ± 0.02 Å ($N_{Ca1} = 2$), respectively. An additional oxygen scatterer was refined at 4.31 ± 0.09 Å with $N_{O2} = 2$.

Coffinite (Table 4.14): The CIF files for coffinite were taken from *Fuchs et al.* and *Bauer et al.* [219,220] and used as the model basis (space group = I41/amd). The first oxygen and second distances were refined at 2.26 ± 0.01 Å and 2.38 ± 0.01 Å both with $N_{O(1,2)} = 4$. Subsequent silicon distances were refined at 3.11 ± 0.02 Å and 3.81 ± 0.03 Å ($N_{Si(1,2)} = 2$). A uranium distance was refined at 3.81 ± 0.01 Å with $N_{U1} = 2$.

4.3.2.5 EXAFS fitting of uranophane (B)

Uranophane / uranyl silicate (Table 4.15): The CIF file for uranophane taken from *Barinova et al.* [205] was used as the model basis (space group = P21/a). The first oxygen (ax) distance was refined at 1.796 ± 0.007 Å with a N_{O1} value of 2.0 ± 0.2 . Subsequent oxygen (eq) distances were refined at 2.19 ± 0.02 Å ($N_{O2} = 1$), 2.32 ± 0.02 Å ($N_{O3} = 2$), 2.48 ± 0.02 Å ($N_{O4} = 2$). Two silicon scatterers were fitted with a total N_{Si-tot} value of 2 at ~ 3.65 and ~ 3.82 Å. A uranium distance was refined at 3.88 ± 0.02 Å with $N_{U1} = 1$. One additional oxygen distance was refined at 4.92 ± 0.07 Å with $N_{O5} = 2$.

Metaschoepite (Table 4.16): The CIF file for metaschoepite taken from *Klingensmith et al.* [207] was used as the model basis (space group = Pbcn). The first oxygen (ax) distance was refined at 1.799 ± 0.009 Å with a N_{O1} value of 2.0 ± 0.2 . Subsequent oxygen (eq) distances were refined at 2.25 ± 0.02 Å ($N_{O2} = 2$), 2.41 ± 0.02 Å ($N_{O3} = 2$), 2.53 ± 0.03 Å ($N_{O4} = 1$). Two uranium scatterers were fitted at 3.88 ± 0.02 Å ($N_{U1} = 2$) and 4.60 ± 0.06 Å ($N_{U2} = 1$).

Billietite (Table 4.17): The CIF file for billietite taken from *Finch et al.* [206] was used as the model basis (space group = Pbn21). The first oxygen (ax) distance was refined at 1.798 ± 0.009 Å with a N_{O1} value of 2.0 ± 0.2 . Subsequent oxygen (eq) distances were refined at 2.25

$\pm 0.02 \text{ \AA}$ ($N_{O2} = 2$), $2.42 \pm 0.02 \text{ \AA}$ ($N_{O3} = 2$) and $2.53 \pm 0.03 \text{ \AA}$ ($N_{O4} = 1$). A uranium scatterer was fitted at $3.88 \pm 0.03 \text{ \AA}$ with $N_{U1} = 3$. An additional barium scatterer could also be fitted at a distance of 4.72 ± 0.04 with $N_{Ba1} = 1$.

Becquerelite (Table 4.18): The CIF file for becquerelite taken from *Pagoaga et al.* [221] was used as the model basis (space group = Pn21a). The first oxygen (ax) distance was refined at $1.765 \pm 0.002 \text{ \AA}$ with a N_{O1} value of 1.4 ± 0.4 . Subsequent oxygen (eq) distances were refined at $1.89 \pm 0.03 \text{ \AA}$ ($N_{O2} = 1$), $2.14 \pm 0.01 \text{ \AA}$ ($N_{O3} = 1$), $2.30 \pm 0.01 \text{ \AA}$ ($N_{O4} = 2$), $2.44 \pm 0.02 \text{ \AA}$ ($N_{O5} = 1$) and $2.51 \pm 0.02 \text{ \AA}$ ($N_{O6} = 1$). Two uranium scatterers were fitted at $3.89 \pm 0.02 \text{ \AA}$ ($N_{U1} = 1$) and $4.60 \pm 0.03 \text{ \AA}$ ($N_{U2} = 1$). An additional calcium path was not generated and / or fitted.

The fits for uranophane and becquerelite both achieved an R-factor of 0.017, whereas for metaschoepite and billietite the R-factor was above 0.025. Just by observation of the fits by eye in **Figure 4.17**, the fit for becquerelite appears closest to the Fourier transform profile at early radial distances (i.e. for U- O_{ax} and U- O_{eq} distances with uranyl coordination) whereas at later radial distances the fit for uranophane is favourable (i.e. above $\sim 3 \text{ \AA}$, potentially relating to U-Si distances).

4.3.3 Rhenium compounds

The XANES spectra of the rhenium compounds used as standards, measured at the Re L_{III} -edge (10 535 eV), are given in **Figure 4.18**.

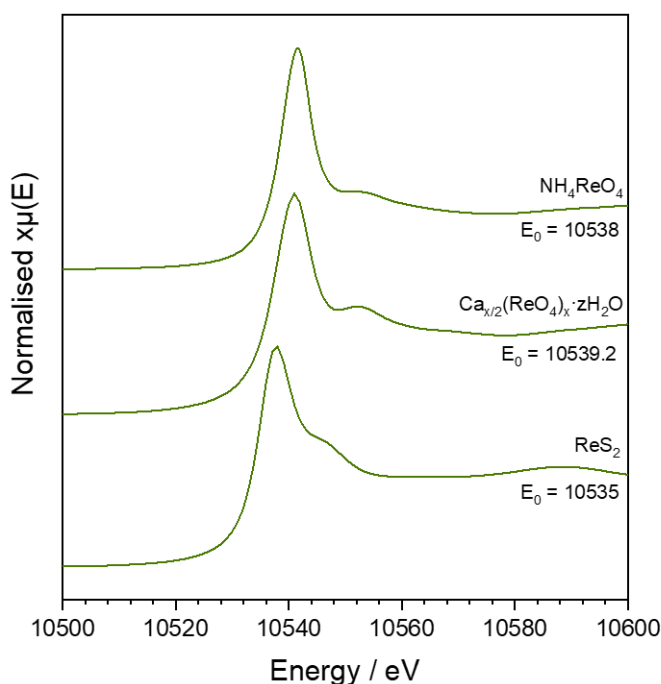


Figure 4.18: Re L_{III} -edge measurements of all Re standards.

4.3.3.1 XAFS

The k^3 -weighted XAFS spectra and corresponding Fourier transforms to R-space of rhenium compounds are given in **Figure 4.19**. Given that the $\text{Ca}_{x/2}(\text{ReO}_4)_x \cdot z\text{H}_2\text{O}$ phase has scarcely been reported in the literature as the $\text{Ca}(\text{ReO}_4)_2 \cdot 2\text{H}_2\text{O}$ phase [222–224], XRD was also measured on the synthesised phase to verify that the NH_4ReO_4 and CaO starting materials were not the only phases present (**Figure 4.20**).

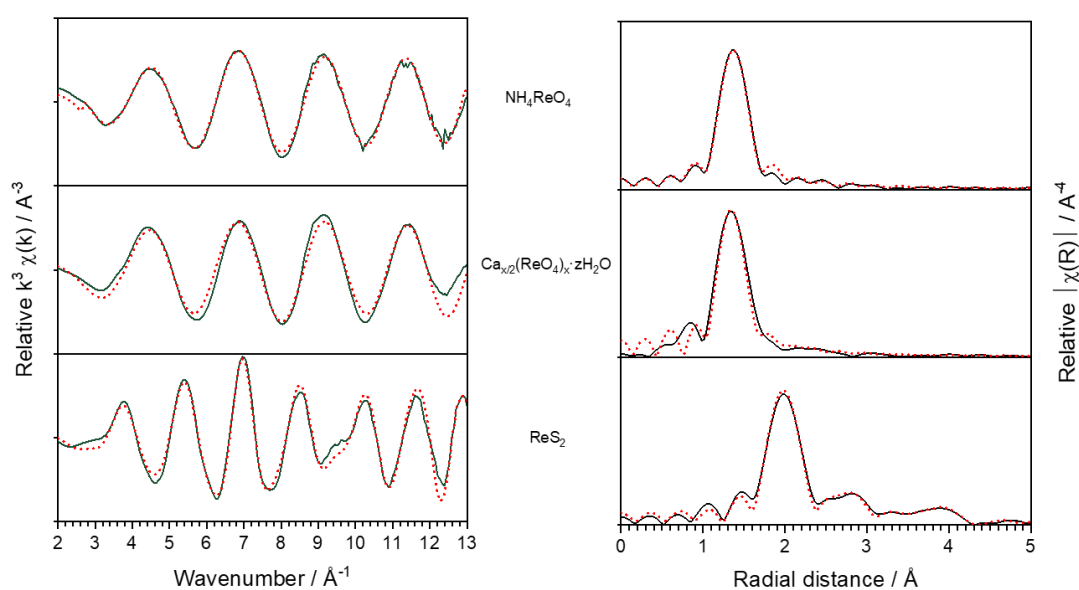


Figure 4.19: k^3 -weighted XAFS spectra of NH_4ReO_4 , $\text{Ca}_{x/2}(\text{ReO}_4)_x \cdot z\text{H}_2\text{O}$ and ReS_2 with corresponding Fourier transforms to R-space. Included on the radial plots are the EXAFS fits (red, dashed).

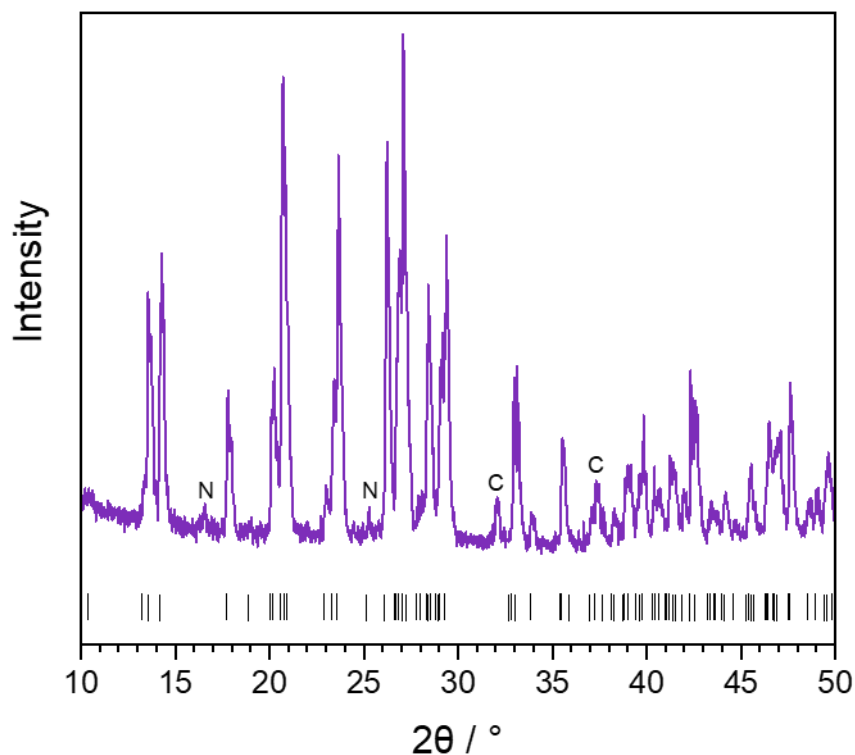


Figure 4.20: XRD pattern of synthesised $\text{Ca}_{x/2}(\text{ReO}_4)_x \cdot z\text{H}_2\text{O}$ phase and peak positions for $\text{Ca}(\text{ReO}_4)_2 \cdot 2\text{H}_2\text{O}$ (>1 % intensity) from [223] (ICSD no. 41049). N = NH_4ReO_4 (ICSD no. 1395 [225]); C = CaO (COD no. 1000044). Data courtesy of D. Bailey.

The XRD pattern of the synthesised $\text{Ca}_{x/2}(\text{ReO}_4)_x \cdot z\text{H}_2\text{O}$ phase is in good agreement with the simulated XRD pattern generated from the $\text{Ca}(\text{ReO}_4)_2 \cdot 2\text{H}_2\text{O}$ structure outlined by *Baur et al.* [223]. This is a good indication that a Ca-bearing perrhenate was successfully synthesised, which contained some small CaO and NH_4ReO_4 impurities.

The radial Fourier transforms of the perrhenate compounds and ReS_2 were fitted to EXAFS models generated using FEFF calculations of appropriately selected CIF files. The value of S_0^2 for rhenium was refined for each of the perrhenate phases. The results of the fits are given in **Tables 4.19** and **4.20**.

Table 4.19: EXAFS fits of perrhenate phases, ammonium perrhenate (k-range: 2.7 - 13 Å⁻¹; R-range: 0.9 - 4 Å) and calcium perrhenate (k-range: 2.2 - 12.9 Å⁻¹; R-range: 0.9 - 4 Å).

Perrhenates	ΔE	$R_{\text{Re-O}} (1)$	$N_{\text{O}} (1)$	$\sigma^2_{\text{O}} (1,2)$
NH₄ReO₄ R-factor = 0.005 $S_0^2 = 0.68(3)$ CIF file from [225]	9.95(46)	1.732(2)	4	0.0005(3)
Ca_{x/2}(ReO₄)_x·zH₂O R-factor = 0.022 $S_0^2 = 0.69(4)$ CIF files from [223]	7.85(90)	1.723(4)	4	0.0005(5)

Table 4.20: EXAFS fit of ReS₂ performed between k-range 3.2 - 12 Å⁻¹ and R-range 1 - 4.5 Å. The value of S_0^2 was set at 0.68.

ReS ₂	ΔE	$R_{\text{Re-S}} (1)$	$N_{\text{S}} (1)$	$\sigma^2_{\text{S}} (1-5)$	$R_{\text{Re-Re}} (1)$	$N_{\text{Re}} (1)$	$\sigma^2_{\text{Re}} (1,2)$	$R_{\text{Re-S}} (2)$	$N_{\text{S}} (2)$	$R_{\text{Re-Re}} (2)$	$N_{\text{Re}} (2)$	$R_{\text{Re-S}} (3-5)$	$N_{\text{S}} (3-5)$
R-factor = 0.013 CIF file from [226]	8.16(93)	2.383(7)	6	0.0050(4)	2.79(1)	3	0.0044(9)	3.77(9)	1	3.79(5)	3	4.09(5)	3
												4.22(8)	2
												4.65(26)	2

4.3.3.2 EXAFS fitting of Re compounds

NH_4ReO_4 (Table 4.19): The CIF file from *Kruger et al.* [225] (space group = I41/a) was used to fit an oxygen path refined at distance of $1.732 \pm 0.002 \text{ \AA}$ with $N_{\text{O}_1} = 4$. No further pathways improved the fit and the Fourier transform profile appears to be only the result of oscillations arising from the first oxygen shell (Figure 4.17). The value of S_0^2 was refined at 0.68 ± 0.03 .

$\text{Ca}_{x/2}(\text{ReO}_4)_x \cdot z\text{H}_2\text{O}$ (Table 4.19): The CIF file for $\text{Ca}(\text{ReO}_4)_2 \cdot 2\text{H}_2\text{O}$ from *Baur et al.* [223] (space group = C2/c) was used to fit an oxygen path refined at a distance of $1.723 \pm 0.004 \text{ \AA}$ with $N_{\text{O}_1} = 4$. The value of S_0^2 was refined at 0.69 ± 0.04 .

ReS_2 (Table 4.20): The CIF file taken from *Murray et al.* [226] was used to fit ReS_2 . A first sulfur shell was fit with $N_{\text{S}_1} = 6$ and refined at a distance of $2.384 \pm 0.005 \text{ \AA}$. Subsequent rhenium and sulfur paths were fit according to the FEFF calculation. The value of S_0^2 was set equal to 0.68; the value refined for rhenium measured on the same beamline.

4.3.4 Technetium compounds

The XANES spectra of the technetium compounds used as standards, measured at the Tc K-edge (21 044 eV), are given in Figure 4.21. The pertechnetate compounds display a pre-edge feature which is attributed to the allowed $1s \rightarrow 4d$ transition due to lack of an inversion centre in tetrahedral TcO_4^- [227].

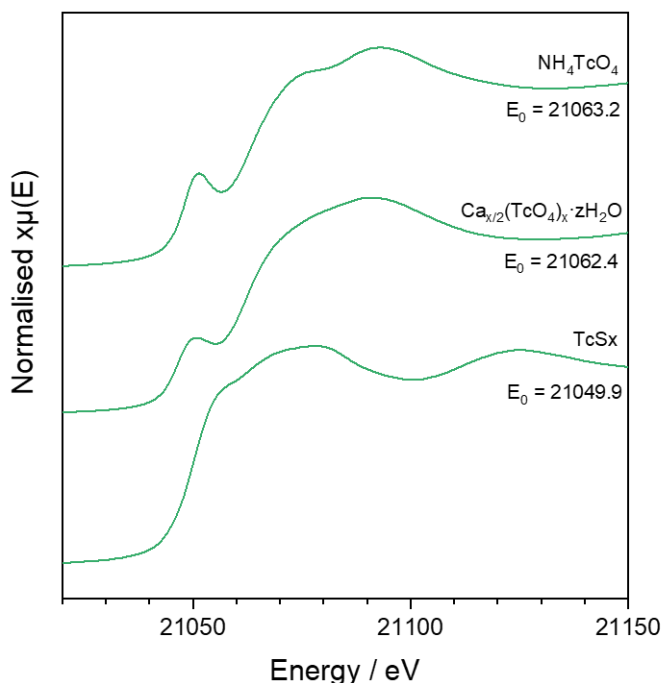


Figure 4.21: Tc K-edge measurements of all Tc standards.

4.3.4.1 XAFS

The k^3 -weighted XAFS spectra and corresponding Fourier transforms to R-space of pertechnetate compounds are given in **Figure 4.22**. Given that the $\text{Ca}_{x/2}(\text{TcO}_2)_x \cdot z\text{H}_2\text{O}$ phase has not been reported in the literature, XRD was also measured on the synthesised phase to verify that the NH_4TcO_4 and CaO starting materials were not the only phases present (**Figure 4.23**).

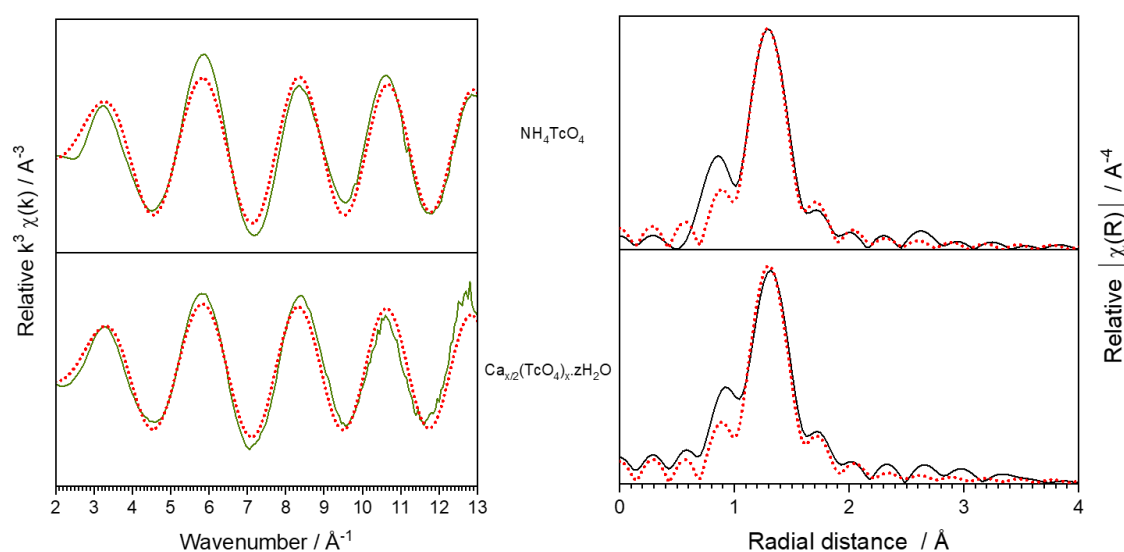


Figure 4.22: k^3 -weighted XAFS spectra of NH_4TcO_4 and $\text{Ca}_{x/2}(\text{TcO}_4)_x \cdot z\text{H}_2\text{O}$ with corresponding Fourier transforms to R-space. Included on the radial plots are the EXAFS fits (red, dashed), where applicable.

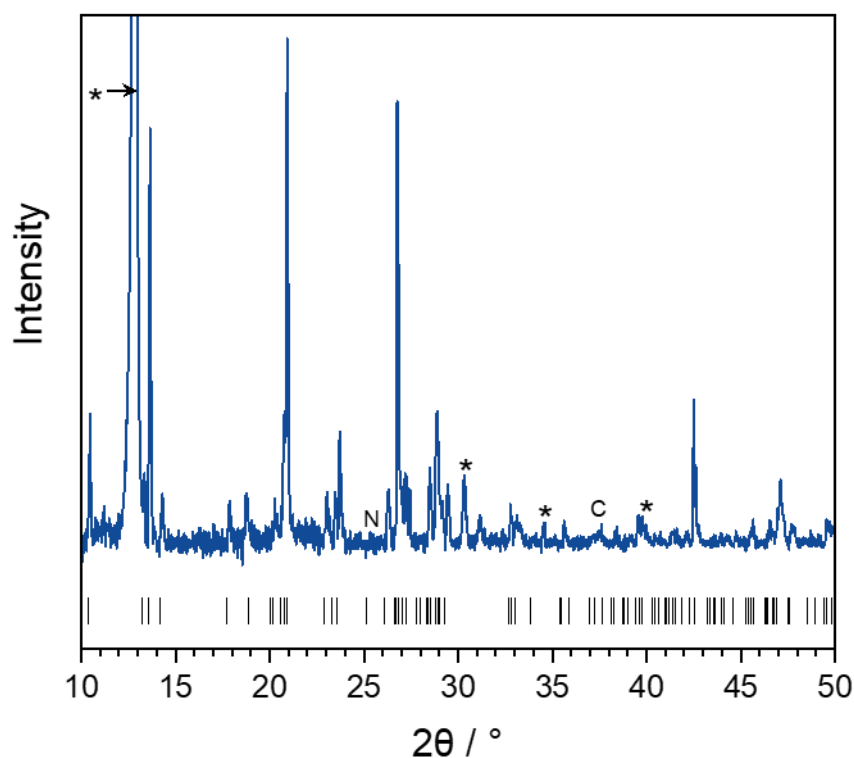


Figure 4.23: XRD pattern of synthesised $\text{Ca}_{x/2}(\text{TcO}_4)_x \cdot z\text{H}_2\text{O}$ phase and peak positions for theoretical $\text{Ca}(\text{TcO}_4)_2 \cdot 2\text{H}_2\text{O}$ (all intensities) based on data from [223] (ICSD no. 41049). N = NH_4TcO_4 (PDF card no. 04-008-8709, ICSD no. 1395 [228]); C = CaO (COD no. 1000044); * = sample holder interference. Data courtesy of D. Bailey.

A theoretical XRD pattern for $\text{Ca}(\text{TcO}_4)_2 \cdot 2\text{H}_2\text{O}$ was generated by substitution of rhenium for technetium in the CIF file from [223], under the assumption that the same structure would be adopted in the technetium analogue of the Ca-bearing phase. The XRD pattern of the synthesised $\text{Ca}_{x/2}(\text{TcO}_4)_x \cdot z\text{H}_2\text{O}$ phase was in good agreement with the generated XRD pattern. Only very low intensity peaks were observed for potential NHTcO_4 and CaO starting materials. This is again a good indication that a Ca-bearing pertechnetate phase was successfully synthesised.

The radial Fourier transforms of the pertechnetate compounds were fitted to EXAFS models generated using FEFF calculations of appropriately selected CIF files. The value of S_0^2 for technetium was refined in the NH_4TcO_4 model and subsequently set in the model for $\text{Ca}_{x/2}(\text{TcO}_4)_x \cdot z\text{H}_2\text{O}$. The results of the fits are given in **Table 4.21**. Note that EXAFS fitting of the TcS_x phase has previously been reported by *Lukens et al.* [152].

Table 4.21: EXAFS fits of perrhenate phases, ammonium perrhenate (k-range: 2.8 - 13.4 Å⁻¹; R-range: 0.9 - 4 Å) and calcium perrhenate (k-range: 2.7 - 13.3 Å⁻¹; R-range: 0.9 - 4 Å).

Pertechnetates	ΔE	R_{Re-O} (1)	N_o (1)	σ^2_o (1)
NH₄TcO₄ R-factor = 0.016 $S_0^2 = 0.80(4)$ CIF file from [228]	1(1)	1.721(4)	4	0.0011(4)
Ca_{x/2}(TcO₄)_x·zH₂O R-factor = 0.029 $S_0^2 = 0.73(5)$ CIF file amended from [223]	2.6(1.1)	1.728(6)	4	0.0008(7)

4.3.4.2 EXAFS fitting of Tc compounds

NH₄TcO₄ (Table 4.21): The CIF file from *Faggiani et al.* [228] (space group = I41/a) was used to fit an oxygen path refined at a distance of 1.721 ± 0.004 Å with $N_{O1} = 4$. No further pathways improved the fit and the Fourier transform profile appears to be only the result of oscillations arising from the first oxygen shell (Figure 4.22). This is consistent with previous fits of pertechnetate compounds [227]. The value of S_0^2 was refined at 0.80 ± 0.04 .

Ca_{x/2}(TcO₄)_x·zH₂O (Table 4.21): The Tc-amended CIF file for Ca(ReO₄)₂·2H₂O from *Baur et al.* [223] (space group = C2/c) was used to fit a first shell oxygen of $N_{O1} = 4$ at 1.728 ± 0.006 Å. The value of S_0^2 was refined at 0.73 ± 0.05 .

4.4 Discussion

4.4.1 Cement hydrate phases

4.4.1.1 C-S-H

C-S-H phases with varying Ca/Si ratios were successfully synthesised with reference to XRD data reported in the literature [184,185]. Above a Ca/Si ratio of approximately 1.5, the presence of portlandite was observed which has commonly been reported at this Ca/Si range [185,229,230].

The trend of increasing positivity of the zeta potential of the C-S-H surfaces with increasing Ca/Si ratio is a result of the decreased availability of negatively charged silanol sites (Si-O⁻) [231] with increasing availability of Ca²⁺. The dissolved Ca²⁺ content in solution acts as an electrical double layer to the effect of creating a more positive zeta potential, which explains why the C-S-H equilibrated solutions inherently increased the positivity of the C-S-H surfaces [130,232]. Above Ca/Si = 1.2 the C-S-H equilibrated solution surpassed the Ca²⁺ concentration required for a surface charge of zero i.e. the Ca²⁺ concentration of potential zero

charge ($[Ca^{2+}]_{pzc}$) which could have important implications for the uptake of negatively charge species by C-S-H surfaces (see **Chapter 7**).

Carbonation of the C-S-H phases under accelerated conditions (1 % CO₂) for 48 hours resulted in the observation of all three polymorphs of calcium carbonate. A previous study by *Li et al.* also identified that the three polymorphs of calcium carbonate are able to coexist in carbonated C-S-H phases [233]. *Li et al.* further concluded that there was no preferential formation for either one of the polymorphs under accelerated carbonation conditions, but did note that vaterite would be transformed into the more thermodynamically stable polymorphs of calcite and aragonite, overtime. The absence of clear identification of aragonite in the CSH(1.0) and CSH(1.4) phases in this study indicates that the transformation of a significant amount of vaterite to the more stable polymorph had not yet occurred at time of analysis.

In comparison to ambient CO₂ levels (~400 ppm), this pre-treatment atmosphere results in a significant increase in the CO₂:Ca ratio during the carbonation reaction. According to *Han et al.* [6] and *Kinoshita et al.* [7], the vaterite polymorph forms when there is a decreased $[Ca^{2+}]/[CO_3^{2-}]$ ratio. Vaterite has also been reported to form via carbonation of C-S-H phases with Ca/Si ratios ≥ 0.67 by *Black et al.* [189] which is consistent with observation of vaterite in the pre-carbonated C-S-H phases here.

4.4.1.2 Minor cement hydrate phases

A nano-crystalline hydrotalcite phase was successfully synthesised using co-precipitation methods as reported in the literature [157], with a surface zeta potential measurement of -16.3 ± 1.7 mV in UHQ water. The zeta potential of hydrotalcite phases is dependent on the pH, as well as the influence of electrolytes in solution [84].

A study by *Ralla et al.* measured the zeta potential of a commercial carbonate-hydrotalcite, *Syntal 696*, from pH 6 to 12. It was demonstrated that the point of zero charge for this hydrotalcite phase was at pH ~11, i.e. below pH 11 the zeta potential was positive, but above pH 11 the zeta potential was negative. The authors discussed that this hydrotalcite was therefore capable of 'weak' anion exchange, depending on the extent of ionisation of the surface functional groups.

Further to this, *Wan et al.* discussed the influence of the Mg/Al atomic ratio on the interlayer spacing of carbonate-hydrotalcite phases and in turn the zeta potential; an increase in the Mg/Al ratio saw an increase in interlayer spacing / decrease in the zeta potential [234]. This is related to the effect of weaker charge density between hydrotalcite layers with lower Al³⁺ content, and therefore weaker hydrogen bonding between the layers [235]. The point of zero charge measured for hydrotalcites with Mg/Al of 2, 3, 4 and 5 was also centred around pH ~11, but was slightly decreased with increasing Mg/Al ratio. From this, it is therefore inferred that the Mg/Al ratio of the synthesised hydrotalcite phase in this current study had a high Mg/Al

ratio, given that the pH in UHQ buffered to ~10 but the zeta potential was still measured to be negative. The role of the dissolved content of carbonate in solution also cannot be overlooked; the presence of negatively charged carbonate anions next to the hydrotalcite surface in solution would also contribute to a negative zeta potential.

Crystalline ettringite phases were also successfully synthesised, albeit with anhydrite and gypsum impurities. The calcium sulfate impurities did not significantly perturb the surface charge of the ettringite phase and the zeta potential was measured at $+1.8 \pm 0.1$ mV in UHQ water. According to *Medala et al.* ettringite fundamentally always displays a positive structural charge in aqueous solution at alkaline pH [236].

4.4.2 X-ray absorption / fluorescence standards

4.4.2.1 Uranium standards

The EXAFS spectra of the U-oxides were fitted to EXAFS models using appropriate CIF files which indicates that they were sufficiently synthesised to allow fitting of oxygen, uranium and / or calcium and magnesium scatterers, where relevant. The uranyl nitrate phase that was used for the pre-cursor U(VI) solutions in **Chapter 5** was also successfully fit to an appropriate model. In the case of the minerals haiweeite, weeksite and soddyite, EXAFS models were also fitted which indicate local uranyl silicate coordination.

The weeksite group of uranyl silicate minerals includes haiweeite, and encompasses uranyl silicate minerals with a U:Si ratio of 2:5 (or 2:6) [237–240]. It is therefore not surprising that the EXAFS models of the mineral phases are so similar. The local coordination of the uranyl group was shown to have a refined O_{ax} distance of ~ 1.80 Å with $N_{O1} = \sim 2.1$ in haiweeite and ~ 1.83 Å with $N_{O1} = \sim 1.8$ in weeksite, which is the only major difference between the models. The uranium distance was also refined at ~ 4 Å in both of the fits. No calcium or potassium pathways could be fitted in the data and it is therefore not possible to use EXAFS to differentiate between these two minerals.

Soddyite belongs to a different sub-group of uranyl silicate minerals with a U:Si ratio of 2:1 [237,239,240]. The O_{ax} distance was refined at a distance of ~ 1.79 Å with $N_{O1} = \sim 2.2$. For the uranium distance, this was observed to be shorter than in haiweeite and weeksite, at ~ 3.9 Å. Given that uranium is a heavy atom and therefore a strong X-ray scatterer, the refined uranium distance is perhaps more reliable than those of silicon scatterers. This therefore indicates that EXAFS can be used to differentiate between the two different groups of uranyl silicates, at least, based on the U- O_{ax} and U-U distances.

As an aside, the XANES spectra of each of the uranyl silicates are also practically identical and, alone, cannot be used to distinguish between them, given that the local uranyl coordination is very similar (**Figure 4.24**).

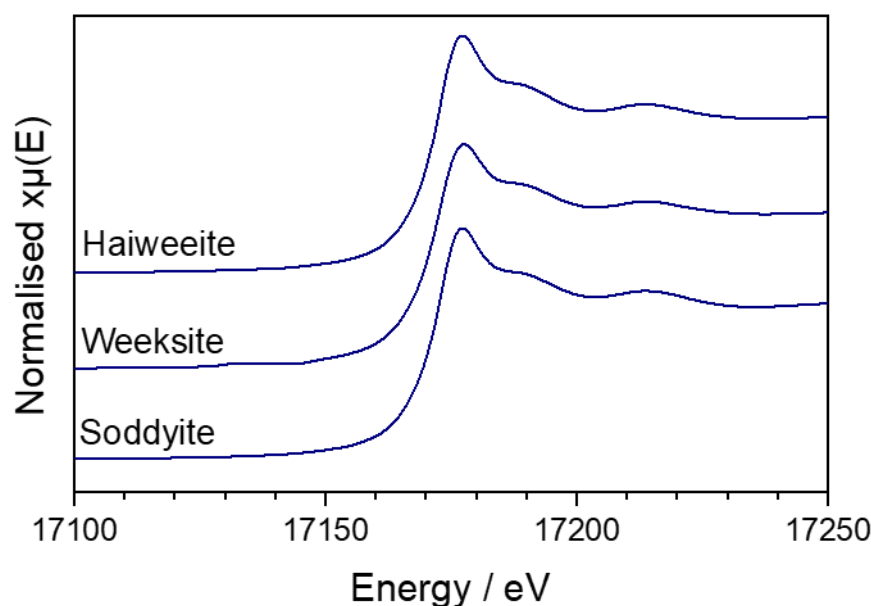


Figure 4.24: U L_{III}-edge measurements of uranyl silicates, showing a similar profile.

For uranophane (B), the situation is a little more complicated. The sample of the powder measured by XRD, although from the same mineral assemblage, was not the exact sample that was measured by XAFS. The XRD data do not show the positive identification of a uranophane phase, but it cannot be ruled out that at some location in the mineral sample there is some uranophane in coexistence with the other mineral phases [209]. The best fit for the EXAFS region appeared to be a combination of the becquerelite model, for U-O distances, and the uranophane model, for further distances. At least one uranium distance could be fitted using all four of the different models, respectively, and was consistently refined at 3.88 ± 0.03 Å.

However, with comparison to literature values for uranophane (~ 1.82 Å [241], 1.818 ± 0.04 Å [242] and 1.82 Å ± 0.2 [70,204] for O_{ax}), the value of O_{ax} refined here was consistently less than 1.8 Å, calculated at 1.796 ± 0.007 Å specifically in the uranophane fit. This could be an indication that uranium has coordination more akin to a uranyl group in a metaschopeite or becquerelite structure. The value of O_{ax} for schoepite was determined to be 1.80 ± 0.01 Å in [243] and implied for becquerelite as 1.75 ± 0.03 Å (O_{ax1}) and 1.83 ± 0.02 Å (O_{ax2}), in [64,244]. The literature values for uranophane EXAFS fitting can therefore be used to compare with the relevant data sets in **Chapter 5**, as an alternative, rather than the ambiguous values obtained here.

4.4.2.2 Rhenium and technetium standards

Although the EXAFS fits for the perrhenate and pertechnetate phases alone were not largely insightful into the long-range coordination environments for rhenium or technetium in the

compounds, the XRD diffraction data are a good indication that $\text{NH}_4\text{ReO}_4 / \text{NH}_4\text{TcO}_4$ and CaO were reacted successfully to form a Ca-bearing perrhenate or pertechnetate phase. Additionally, the synthesised ReS_2 was fit to an appropriate model of Re-S and Re-Re distances which is relevant for the work carried out in **Chapter 7** which investigates Re-ettringite interactions.

Using the refined first shell oxygen distances from the EXAFS fitting, a bond valence sum (**Equation 4.2**) was applied to indicate the average oxidation state of rhenium or technetium in the perrhenate and pertechnetate phases:

$$\text{Bond valence} = \exp((R_0 - R)/B) \quad (4.2)$$

where R is the bond length and R_0 and B are the bond valence parameters, defined as the “notional length of a bond of unit valence” (i.e. theoretical bond length) and a “measure of the softness of the interaction between atoms” (i.e. bond strength), respectively [245]. The sum of the bond valences around each atom is equal to the oxidation state of the atom.

The values of R_0 and B for a Re(VII)-O bond were used as 1.909 and 0.37, respectively, according to *Gagné et al.* [246]. The calculated oxidation state of rhenium in the perrhenate phases are given in **Table 4.22**.

Table 4.22: Oxidation state calculations for Re in perrhenates.

	E_0 / eV^*	$R_{\text{EXAFS}} / \text{Å}$	N_{EXAFS}^\dagger	Re oxidation state
NH_4ReO_4	10538	1.732(2)	4	6.7(1)
Ca-perrhenate	10539.2	1.723(4)	4	6.9(1)

* Re L_{III} -edge

† fixed in the model

The calculated oxidation states for rhenium are only ~ 0.3 and ~ 0.1 valence units lower than the expected oxidation state of +7 for NH_4ReO_4 and Ca-perrhenate, respectively.

The values of R_0 and B for a Tc(VII)-O bond were used as 1.943 and 0.406, respectively, according to *Wester et al.* [247]. The calculated oxidation state of technetium in the pertechnetate phases are given in **Table 4.23**.

Table 4.23: Oxidation state calculations for Tc in pertechnetates.

	E_0 / eV^*	$R_{\text{EXAFS}} / \text{\AA}$	N_{EXAFS}^\dagger	Calculated oxidation state at Tc atom
NH_4TcO_4	21063.2	1.721(4)	4	6.6(1)
Ca-pertechnetate	21062.4	1.728(6)	4	6.5(1)

*Tc K-edge

†fixed in the model

The calculated oxidation states for technetium are slightly lower than those for rhenium in the respective analogous compounds, and ~ 0.4 and ~ 0.5 valence units lower than the expected oxidation state of +7 for NH_4TcO_4 and Ca-pertechnetate, respectively.

4.5 Conclusions

This Chapter gives an overview of the cement hydrate phases synthesised for use in contact experiments using uranium, plutonium and rhenium / technetium detailed in **Chapters 5, 6** and **7**. Additionally, the standards used for comparison to and justification of results from XAFS data obtained for uranium, rhenium and technetium have also been presented.

Chapter 5 – Identification and characterisation of secondary uranium phases in cementitious systems

5.1 Introduction

In this Chapter the behaviour of uranium (U) in contact with cement hydrate phases was investigated. Studies to date have been focused primarily on low concentration sorption studies of U(VI) onto C-S-H phases which have demonstrated that U(VI) maintains the uranyl moiety ($O=U=O$) on sorption to C-S-H surfaces, and adopts a uranophane ($Ca(UO_2)_2SiO_3(OH)_2 \cdot x(H_2O)$)-type coordination [67,68].

The experiments described here were designed to follow on from literature findings and induce precipitation of U-bearing secondary phases in cementitious systems, to elucidate whether similar U environments were observable. C-S-H phases, as well as hydrotalcite ($Mg_6Al_2(CO_3)(OH)_{16} \cdot 4H_2O$) and ettringite ($Ca_6Al_2(SO_4)_3(OH)_{12} \cdot 26H_2O$) were contacted with U(VI) concentrations ranging from trace (0.5 mM) to elevated concentrations (> 10 mM), relative to nuclear waste encapsulation. X-ray absorption / fluorescence spectroscopy (XAFS) and X-ray diffraction (XRD) was used to analyse a suite of uranium-bearing minerals and ceramic phases using EXAFS modelling, to compare with the XAFS and XRD results obtained from U(VI)-contacting of cement phases.

To the best of the author's knowledge, this is the also the first study to adopt the use of nuclear magnetic resonance (NMR) spectroscopy to probe the ^{29}Si and ^{27}Al environments in cement phases after contact with U(VI).

5.2 Experimental methods

All experiments in this Chapter were carried out under N_2 in an anaerobic chamber unless otherwise stated. Characterisation of all pre-cursor cement hydrate phases is described in **Chapter 4**.

5.2.1 Uranium contact experiments

5.2.1.1 C-S-H phases

A preliminary experiment was conducted with C-S-H at $Ca/Si = 0.6$ (CSH(0.6)) as a scoping exercise to observe the U(VI) behaviour (see **Section 5.3.1**). CSH(0.6) was contacted with 0.5, 5, 10, 25 and 50 mM uranyl nitrate ($UO_2(NO_3)_2 \cdot 6H_2O$) at a S/L ratio of 25 g L^{-1} , over a 48 hour time period with sampling of the supernatant at 2, 4, 6, 12, 24 and 48 hours. The results from this experiment concluded that U(VI) precipitation with the cement phases was instant.

Further to this, C-S-H phases with Ca/Si ratios of 0.6, 0.8, 1.0, 1.2 and 1.6 (CSH(X), where X = Ca/Si ratio) were also contacted with uranyl nitrate at concentrations of 0.5 mM and 10 mM at a S/L ratio of 25 g L⁻¹, for 48 hours. Pre-carbonated versions of the C-S-H phases with the same Ca/Si ratios were also contacted with uranyl nitrate using the same methodology (synthesis described in **Chapter 3**); these phases are denoted with a “C” suffix hereafter. The error given for all solution analyses was calculated from the standard deviation of triplicate measurements.

5.2.1.2 Minor cement hydrate phases

In addition to U(VI) precipitation in C-S-H systems, the effect of secondary phase formation in the presence of hydrotalcite and ettringite was also investigated. Hydrotalcite and ettringite phases were contacted with uranyl nitrate at concentrations of 0.5 mM and 10 mM with a S/L ratio of 25 g L⁻¹ ratio for 48 hours using the same methodology as for C-S-H phases.

5.2.1.3 Solution and solid-state analyses

The U(VI)-contacted cement phases were mixed at 40 rpm on a rotary shaker for the given time periods, after which the suspensions were filtered through 0.22 µm cellulose filters. The solution pH values were measured before the solutions were acidified and prepared for ICP-OES analysis to measure U, Ca, Si, S, Al, and / or Mg concentrations. The remaining solids were dried at ambient temperature, under N₂, for at least 24 hours before preparation for X-ray diffraction (XRD), X-ray absorption / fluorescence spectroscopy (XAFS) and nuclear magnetic resonance spectroscopy (NMR), where applicable.

5.2.2 X-ray absorption spectroscopy

Selected samples were measured by XAFS at the U L_{III}-edge (17166 eV) on beamline B18 at DLS and beamline BMM at NSLS-II (**Table 5.1**). The U(VI)-contacted cement phases were pressed into pellets using a polyethylene-glycol (PEG) binder (~30 % PEG). For DLS, 3 mm pellets were mounted into 3.5 mm circular holes in individual rectangular Perspex® slides (~6 mm x ~12 mm x ~1 mm), using a Kapton® tape seal on either side to hold the pellets in place. The slides were fitted within 2 mL Eppendorf mini-centrifuge tubes which were then heat sealed into polypropylene bags. For NSLS-II, 6 mm pellets were mounted into a 4 x 2 array Perspex® sample holder, sealed with Kapton® tape and heat sealed into a polypropylene bag. Samples were measured in fluorescence mode with the sample orientated at 45° to the incidence X-ray beam and adjacent fluorescence detector.

Table 5.1: U(VI)-contacted cement phase samples measured by XAFS.

Phase	[U(VI)] / mM	~U(VI) loading on cement phase / ppm	Beamline used / comments
CSH(0.6)	0.5	4 800	B18 (DLS); both “young” (Y) and “aged” (A) samples
CSH(0.6) C	0.5	4 800	B18 (DLS)
CSH(0.8)	0.5	4 800	B18 (DLS)
CSH(1.2)	0.5	4 800	B18 (DLS)
CSH(1.2) C	0.5	4 800	B18 (DLS)
CSH(1.6)	0.5	4 800	B18 (DLS)
Hydrotalcite	0.5	4 800	B18 (DLS)
CSH(0.6)	10	95 000	B18 (DLS); both “young” (Y) and “aged” (A) samples
CSH(0.6) C	10	95 000	B18 (DLS)
CSH(0.8)	10	95 000	BMM (NSLS-II)
CSH(1.2)	10	95 000	BMM (NSLS-II)
CSH(1.2) C	10	95 000	BMM (NSLS-II)
CSH(1.6)	10	95 000	BMM (NSLS-II)
CaCO ₃ *	10	95 000	BMM (NSLS-II)
Hydrotalcite	10	95 000	B18 (DLS)

*for comparison to pre-carbonated C-S-H phases

A suite of uranium standards that were considered relevant to U(VI) secondary phase formation in cements were also measured, primarily on B18 at DLS (**Table 5.2**). The XRD patterns of the standards are shown in **Chapter 4**. Powders of the standards were weighed out to ensure the mass of material corresponded to one absorption length of U and pressed into pellets using PEG to allow for transmission XAFS measurements to be made.

Table 5.2: U standards measured by XAFS.

Standard (general formula)	Approximate U oxidation state
Uranium dioxide (UO ₂)	4
Uranium trioxide (UO ₃)	6
Uranyl nitrate (UO ₂ (NO ₃) ₂ ·6H ₂ O)	6
Calcium uranate (CaUO ₄)	6
Tricalcium uranate (Ca ₃ UO ₆)	6
Magnesium uranate (MgUO ₄)	6
Haiweeite (Ca(UO ₂) ₂ (Si ₅ O ₁₂)(OH) ₂ ·6H ₂ O)	6
Weeksite (K ₂ (UO ₂) ₂ (Si ₅ O ₁₂)(OH) ₄ H ₂ O)	6
Bayleyite (Mg ₂ (UO ₂)(CO ₃) ₃ ·18H ₂ O) / andersonite (Na ₂ Ca(UO ₂)(CO ₃) ₃ ·6H ₂ O)	6
Soddyite ((UO ₂) ₂ SiO ₄ ·2H ₂ O)	6
Coffinite (U(SiO ₄) _{1-x} (OH) _{4x})	4
Mixed becquerelite (Ca(UO ₂) ₆ O ₄ (OH) ₆ ·8H ₂ O) / metaschoepite (UO ₃ ·xH ₂ O (x<2)) mineral *	6

*XRD analysis in **Chapter 4** concluded that the mineral named as uranophane was a mixed becquerelite/metaschoepite mineral phase

5.2.3 Nuclear magnetic resonance spectroscopy

Samples of U(VI)-contacted CSH(0.6) and CSH(1.2) were analysed by ²⁹Si solid-state NMR spectroscopy, under the conditions of 0.5 mM U(VI), 10 mM U(VI) and pre-carbonation. Deconvolution of the spectra was performed using fitting of Gaussian peaks to the total signal to determine the contribution from individual Qⁿ Si species [168]. The Ca/Si ratio of the U(VI) / C-S-H systems was also determined using **Equation 5.1**, also outlined in [229]:

$$\text{Ca/Si} = \frac{\frac{3}{2}Q^1 + \frac{2}{3}Q^2}{Q^1 + Q^2} \quad (5.1)$$

using the Q¹ and Q² Si contributions determined using NMR spectra deconvolution.

Additional samples of 0.5 mM and 10 mM U(VI)-contacted hydrotalcite and ettringite were also measured by ²⁷Al solid-state NMR spectroscopy.

5.2.4 Geochemical modelling

Geochemical modelling was performed using the Phreeqc Interactive 3.4.0-12927 software [248] and the Lawrence Livermore National Laboratory thermodynamic database, to determine the saturation index (SI) of mineral phases likely to form in aqueous solution under experimental the experimental conditions of the U(VI)-contact studies. The saturation index (SI) of a phase determines whether an aqueous system is saturated with respect to the given phase, such that: $SI = 0$ means the phase is in equilibrium (i.e. saturated); $SI < 0$ means the phase is undersaturated and $SI > 0$ means the phase is supersaturated.

The results from ICP-OES analyses and the solution pH were used for the model input for Ca, Si, S, Al or Mg. The concentration of carbonate in solution could not be determined, therefore, the model was generated (i) in the absence of HCO_3^- and (ii) at a range of HCO_3^- concentrations from 0.1 ppm up to 1000 ppm to determine if U-carbonate complexes were thermodynamically favourable to form.

5.3 Results

5.3.1 U(VI)-contacted C-S-H phases: Preliminary analysis

The reaction between U(VI) and CSH(0.6) was rapid and an instant yellow precipitate was observed at all concentrations of U(VI) (**Figure 5.1**). The Ca, Si and U concentrations in solution showed no significant change after 2 hours contact time at all values of $[\text{U}]_{t=0}$. The uptake of U(VI) was >99 % at $[\text{U}]_{t=0} = 0.5 - 25 \text{ mM}$ but at 50 mM uptake was reduced to ~60 %. This indicated that the point of saturation for U(VI) uptake by C-S-H at S/L 25 g L^{-1} was achieved between 25 and 50 mM $[\text{U}]_{t=0}$ and further analysis determined that the point of U(VI) saturation was close to 30 mM, which is equivalent to ~285 ppt of U(VI) / C-S-H.



Figure 5.1: Yellow precipitate formed on addition of U(VI) to CSH(0.6)

The pH of the CSH(0.6) phase in UHQ was measured to be pH ~9.5, therefore it was expected that the high acidity of the uranyl nitrate solution (e.g. pH 2.5 ± 0.1 at 50 mM) would have a damaging effect on the C-S-H structure, with the effect of enhancing the release of calcium to solution. This is evident in the calcium and silicon solution data (e.g. for the 10 mM solution, see *Section 5.3.3.1*) and the XRD patterns, which indicated a breakdown of the C-S-H crystalline structure particularly from 25 mM $[U]_{t=0}$ onwards (**Figure 5.2**), potentially forming an amorphous silica gel. At the lowest uranyl nitrate concentration of 0.5 mM, the diffraction pattern still resembled C-S-H very closely and peaks pertaining to the C-S-H(I) phase were still identifiable (tobermorite, PDF card no. 00-045-1480 [184]) [185].

The diffraction pattern for the 10 mM sample displayed additional peaks between $5 - 30^\circ 2\theta$ (denoted as “♦”) as well as maintaining some characteristic peaks for C-S-H (denoted as “CS”). The additional peaks were assigned to a “calcium-uranyl-silicate-hydrate phase” (PDF card no. 47-0497 [249]) with the chemical formula $Ca_2(UO_2)_2Si_6O_{15} \cdot 10H_2O$ [249]. As this phase had a U:Si ratio of 1:3, which is the same as in the weeksite mineral group (general chemical formula $K_2(UO_2)_2(Si_5O_{12})(OH)4H_2O$ [237,249–251], see **Chapter 4**), it is hereafter denoted as “Ca-weeksite”.

5.3.1.1 Mineral ageing

A repeat measurement of the 10mM contacted CSH(0.6) sample, more than one month after the U(VI)-contact experiment, showed an increase in intensity of the diffraction peaks pertaining to the Ca-weeksite phase (**Figure 5.3**) which indicates that the mineral phase became more crystalline with time.

In the PhD Thesis of *Sutton* (1999) the same ageing process was observed for uranium precipitates formed by addition of $Ca(OH)_2$ and cement grout leachate solutions to uranyl nitrate at both pH 9 and 11. The XRD patterns obtained in the study showed an increase in peak intensity at each time point of analysis of 3, 6 and 9 weeks [63]. The precipitates in this case were identified as schoepite ($(UO_2)_8O_2(OH)_{12} \cdot 12(H_2O)$, pH 9) and calcium uranate ($CaUO_4$, pH 11) in the $Ca(OH)_2$ solutions, and calcium or potassium uranates in the grout leachate solutions.

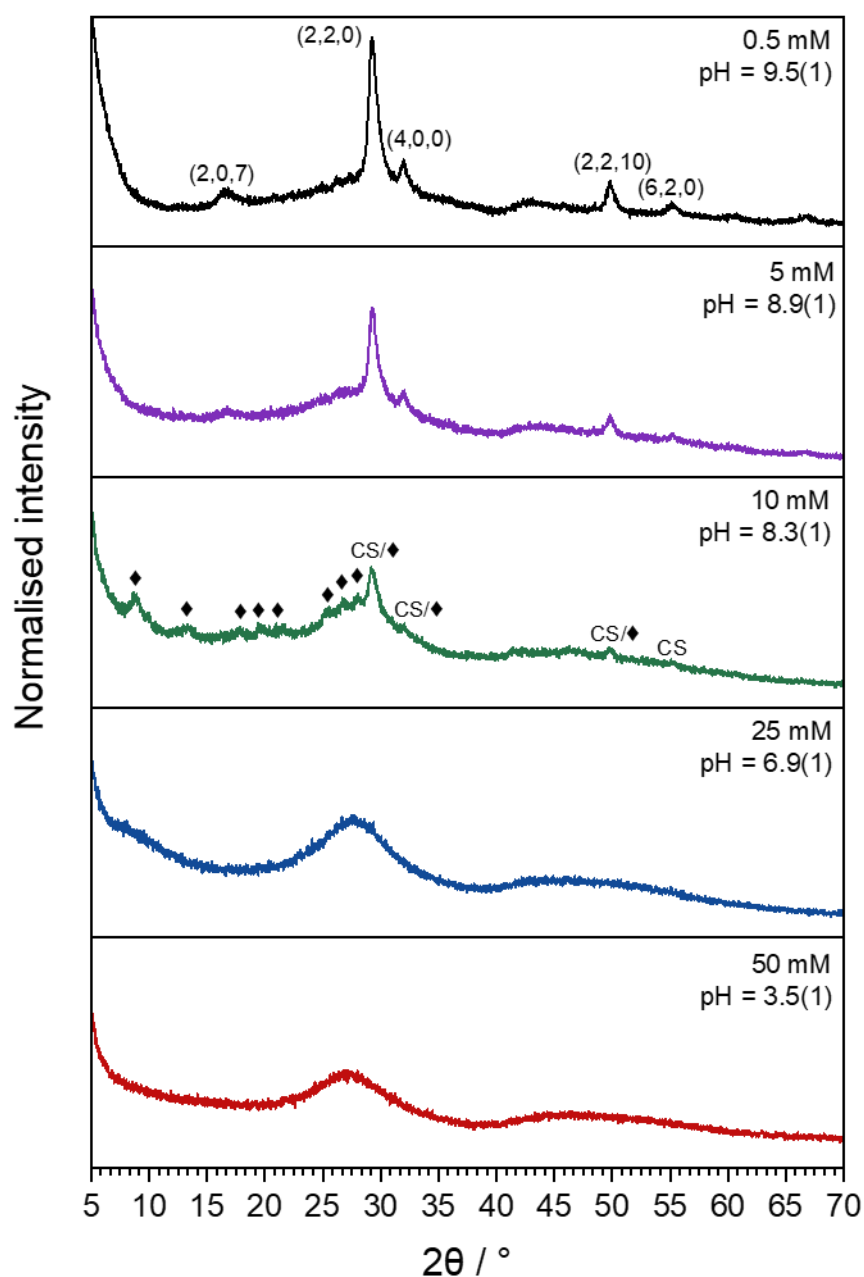


Figure 5.2: XRD patterns of CSH(0.6) “CS” (tobermorite, PDF card no. 00-045-1480 [184]) [185] contacted with varying concentrations of uranyl nitrate at 25 g L^{-1} showing the effect of decreasing pH on the C-S-H structure. The 10 mM sample shows peaks attributable to Ca-wecksite “♦” (PDF card no.00-012-0461/2 [250]) [249]. Background subtraction was performed on the diffraction patterns in this figure to highlight the effect of U(VI) addition and in particular the Ca-wecksite mineral peaks. Miller indices for tobermorite (C-S-H(I)) are also given.

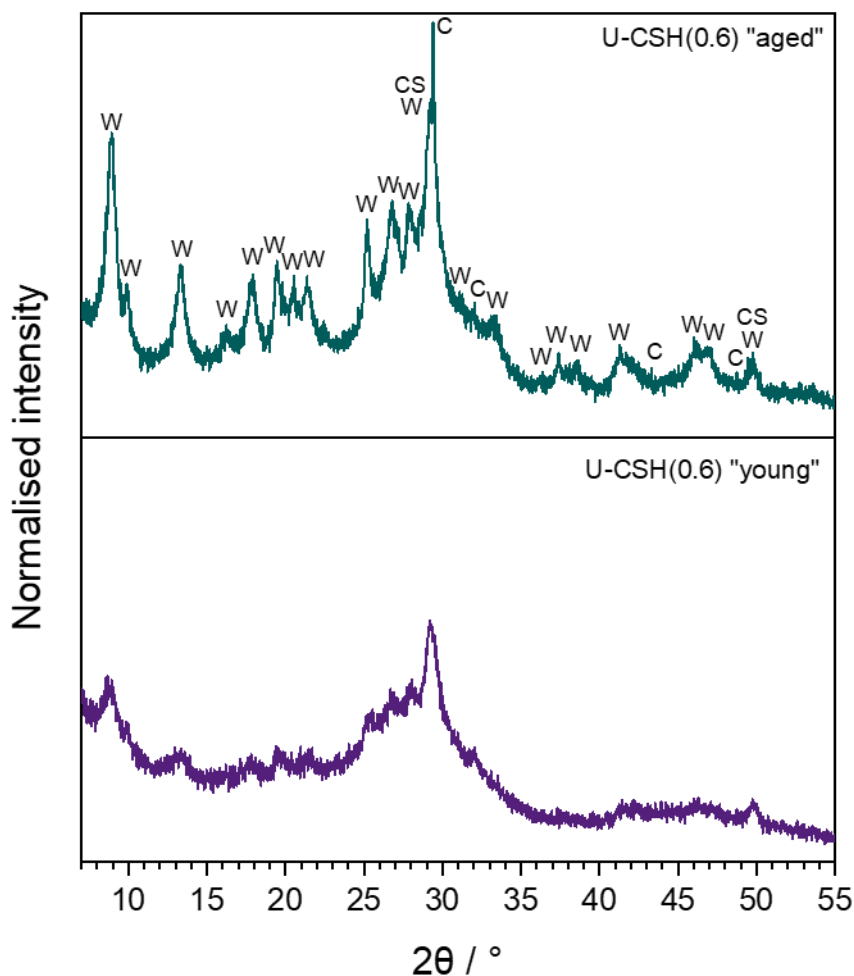


Figure 5.3: XRD patterns of CSH(0.6) contacted with 10 mM uranyl nitrate after ~24 hours drying (“young”) and after at least 1 month of ageing (“aged”). C = calcite; CS = C-S-H(I) (tobermorite, PDF card no. 00-045-1480 [184]) [185]; W = Ca-weeksite (PDF card no. 47-0497 [249]). Background subtraction was performed on the diffraction patterns in this figure to highlight the effect of U(VI) addition and in particular the Ca-weeksite mineral peaks.

5.3.2 U(VI)-contacted C-S-H phases: All Ca/Si ratios with 0.5 mM U(VI)

5.3.2.1 Ca and Si release, non-carbonated

The pH measurements for the C-S-H phases after contact with 0.5 mM uranyl nitrate (pH = 3.6 ± 0.1) are given in **Table 5.3**. As expected, the pH values increased with increasing Ca/Si ratio as a result of increased calcium content in the C-S-H and subsequently greater Ca²⁺ release into solution. This shows the buffering capacity of the C-S-H phases in acidic solution at 25 g L⁻¹.

Table 5.3: pH values of 0.5 mM U(VI) / C-S-H solutions after 48 hours.

CSH(X)	pH
CSH(0.6)	9.6 ± 0.0
CSH(0.8)	10.4 ± 0.0
CSH(1.0)	11.5 ± 0.0
CSH(1.2)	11.6 ± 0.0
CSH(1.6)	12.2 ± 0.0

Figure 5.4 displays the calcium and silicon release from the C-S-H phases into solution after contact with U(VI) for 48 hours. It should be noted that for all Ca/Si ratios no / negligible uranium was detected by ICP-OES measurements in solution, indicating >99 % uptake of U(VI) via sorption or precipitation.

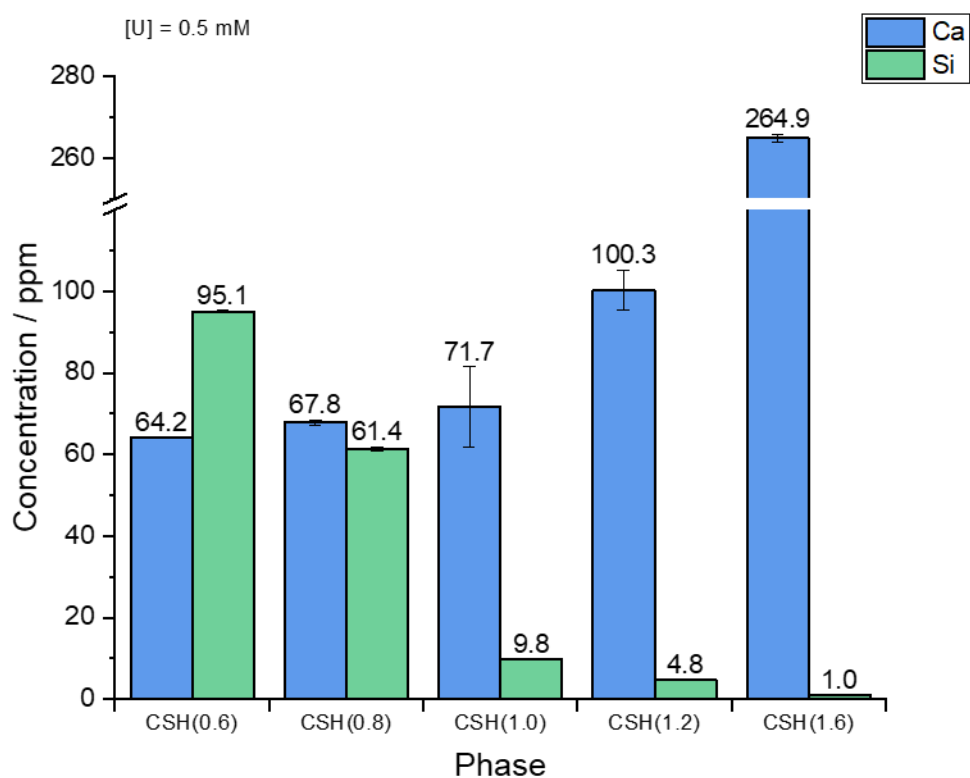


Figure 5.4: Ca and Si release from C-S-H phases in contact with 0.5 mM U(VI) (25 g L^{-1}) for 48 hours.

In the 0.5 mM U(VI) solution, calcium release increased with Ca/Si ratio of the C-S-H phase, in line with an increase in the measured pH values. The release of silicon decreased with

Ca/Si ratio, which is expected as a result of the lower amount of silicon available in the system; only in the CSH(0.6) phase did silicon release exceed that of calcium. The molar Ca/Si ratios of the U(VI) / C-S-H solutions are displayed in **Table 5.4**.

Table 5.4: Ca/Si ratio of C-S-H phases compared to the Ca/Si ratio in solution after contact with 0.5 mM U(VI), and the ratio of Ca partitioned in the solid and solution.

Ca/Si ratio of C-S-H phase	Ca/Si ratio of solution after U(VI) contact	Ca _{C-S-H} /Ca _{solution} ratio: <1 = higher Si/Ca release >1 = higher Ca/Si release
0.6	0.5	0.8
0.8	0.8	1
1.0	5.1	5.1
1.2	15	13
1.6	186	116

The Ca/Si molar ratios in the 0.5 mM U(VI)-contact solutions highlight the disparity seen between the higher Ca/Si ratios and the relative release of calcium and silicon into solution. For the CSH(0.6) and CSH(0.8) phases the corresponding solution Ca/Si ratio of 0.5 and 0.8, respectively, indicates that the relative release of Ca and Si was approximately 1:1. From the CSH(1.0) phase onwards, the Ca/Si ratios of the solution relative to the Ca/Si ratio of the initial solid phase significantly increases, from 5.1 for CSH(1.0) to 116 at CSH(1.6). This is indicative of a release of interlayer calcium from the C-S-H phases, which becomes significant above Ca/Si = 0.83 [252].

5.3.2.2 Ca and Si release, pre-carbonated

The pH measurements for the pre-carbonated C-S-H phases after contact with 0.5 mM uranyl nitrate (pH = 3.6 ± 0.1) are given in **Table 5.5**. The pH values only show a slight general increase with increasing Ca/Si ratio, but are generally lower than the values measured for the non-carbonated counterparts (**Table 5.3**), which is indicative of dissolved carbonate (HCO₃⁻) in solution [253].

Table 5.5: pH values of 0.5 mM U(VI) / pre-carbonated C-S-H solutions after 48 hours.

CSH(X) C	pH
CSH(0.6) C	10.1 ± 0.0
CSH(0.8) C	10.2 ± 0.1
CSH(1.0) C	10.4 ± 0.0
CSH(1.2) C	10.6 ± 0.0
CSH(1.6) C	10.6 ± 0.0

Figure 5.5 displays the calcium and silicon release from the pre-carbonated C-S-H phases into solution after contact with U(VI) for 48 hours. It should be noted that for all Ca/Si ratios no uranium was detected by ICP-OES measurements in solution, indicating >99 % uptake of U via sorption or precipitation.

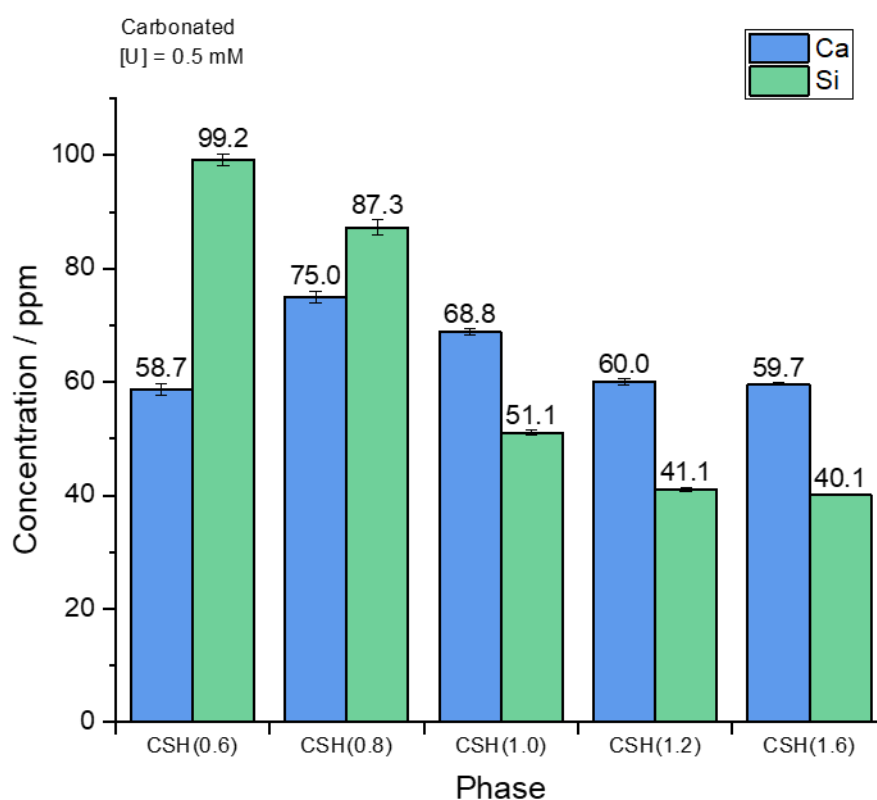


Figure 5.5: Ca and Si release from pre-carbonated C-S-H phases in contact with 0.5 mM U(VI) (25 g L⁻¹) for 48 hours.

For the pre-carbonated C-S-H phases in contact with the 0.5 mM U(VI) solution the calcium release increased from CSH(0.6) C to CSH(0.8) C but thereafter decreased with increasing

Ca/Si ratio from ~75 ppm for CSH(0.8) C to ~60 ppm for CSH(1.6) C. There was not a significant release of Ca at higher Ca/Si ratios, as observed for the non-carbonated phases (i.e. ~100 ppm and ~260 ppm for CSH(1.2) and CSH(1.6), respectively). Given that calcium carbonate solubility is lower than that of C-S-H (i.e. $\text{Ca}(\text{OH})_2$) [254,255], carbonation of interlayer calcium therefore explains the lower release of calcium from the pre-carbonated C-S-H phases, relative to the non-carbonated phases, at higher Ca/Si ratio [256].

The release of silicon decreased with increasing Ca/Si in all of the pre-carbonated C-S-H phases. However, the concentrations of silicon released were higher in comparison to the non-carbonated phases, especially at higher Ca/Si ratios (e.g. ~40 ppm for CSH(1.6) C and ~40 ppm for CSH(1.6) C). This is the opposite behaviour that would be expected for the silicon solubility at the relative pH values measured (e.g. pH ~10 for CSH(1.6) C and pH ~12 for CSH(1.6)). As silicon solubility is expected to increase at higher pH [231], this increased silicon release at lower pH values of ~10 must also be related to carbonation effects. Decalcification of the C-S-H structure would result in areas of enriched silicon cross-linking in the C-S-H structure i.e. an increase in Q^3 species. As calcium has become consumed in the formation of calcium carbonates, which are less prone to dissolution at pH 10, silicon may therefore have been preferentially leached from the structure.

The Ca/Si molar ratio of the U(VI) / C-S-H C solutions are given in **Table 5.6**.

Table 5.6: Ca/Si ratio of pre-carbonated C-S-H phases compared to the Ca/Si ratio in solution after contact with 0.5 mM U(VI), and the ratio of Ca partitioned in the solid and solution.

Ca/Si ratio of C-S-H phase	Ca/Si ratio of solution after U(VI) contact	$\text{Ca}_{\text{C-S-H}}/\text{Ca}_{\text{solution}}$ ratio: <1 = higher Si/Ca release >1 = higher Ca/Si release
0.6	0.4	0.7
0.8	0.6	0.8
1.0	0.9	0.9
1.2	1.0	0.8
1.6	1.0	0.6

The Ca/Si molar ratios of the U(VI) 0.5 mM contact solutions for the pre-carbonated C-S-H phases show that the Ca/Si ratios of the solution relative to the Ca/Si ratio of the initial solid phase were less than 1 in all cases, which indicates that silicon release was slightly higher than calcium release. This is again in agreement with carbonation of interlayer calcium to the effect of reducing calcium release into solution [256].

5.3.2.3 X-ray diffraction

The XRD patterns for the 0.5 mM U(VI)-contacted C-S-H phases from Ca/Si ratios 0.8 to 1.6 are shown in **Figure 5.6**. Peaks for C-S-H(I) were identified in all of the U(VI)-contacted phases (tobermorite, PDF card no. 00-045-1480 [184]) [185]. Carbonation during analysis and / or drying was evident in all of the phases by the identification of peaks for calcite (PDF card no. 01-078-4614 [187]). The peaks for calcite were sharper and more intense for the higher Ca/Si ratios of 1.2 and 1.6 compared to 0.8 and 1.0. There were no additional peaks observed for U-containing phases.

The XRD patterns for the pre-carbonated 0.5 mM U(VI)-contacted C-S-H phases from Ca/Si ratios 0.6 to 1.6 are also shown in **Figure 5.7**. In addition to peaks for C-S-H(I), peaks for calcium carbonate polymorphs were also identified at all Ca/Si ratios.

The presence of calcite, vaterite and aragonite (Ca/Si = 0.6, 0.8, 1.2 and 1.6 only) phases is in line with the calcium carbonate polymorphs identified from the pre-carbonation process, already discussed in **Chapter 4**. No additional peaks were observed for U-containing phases.

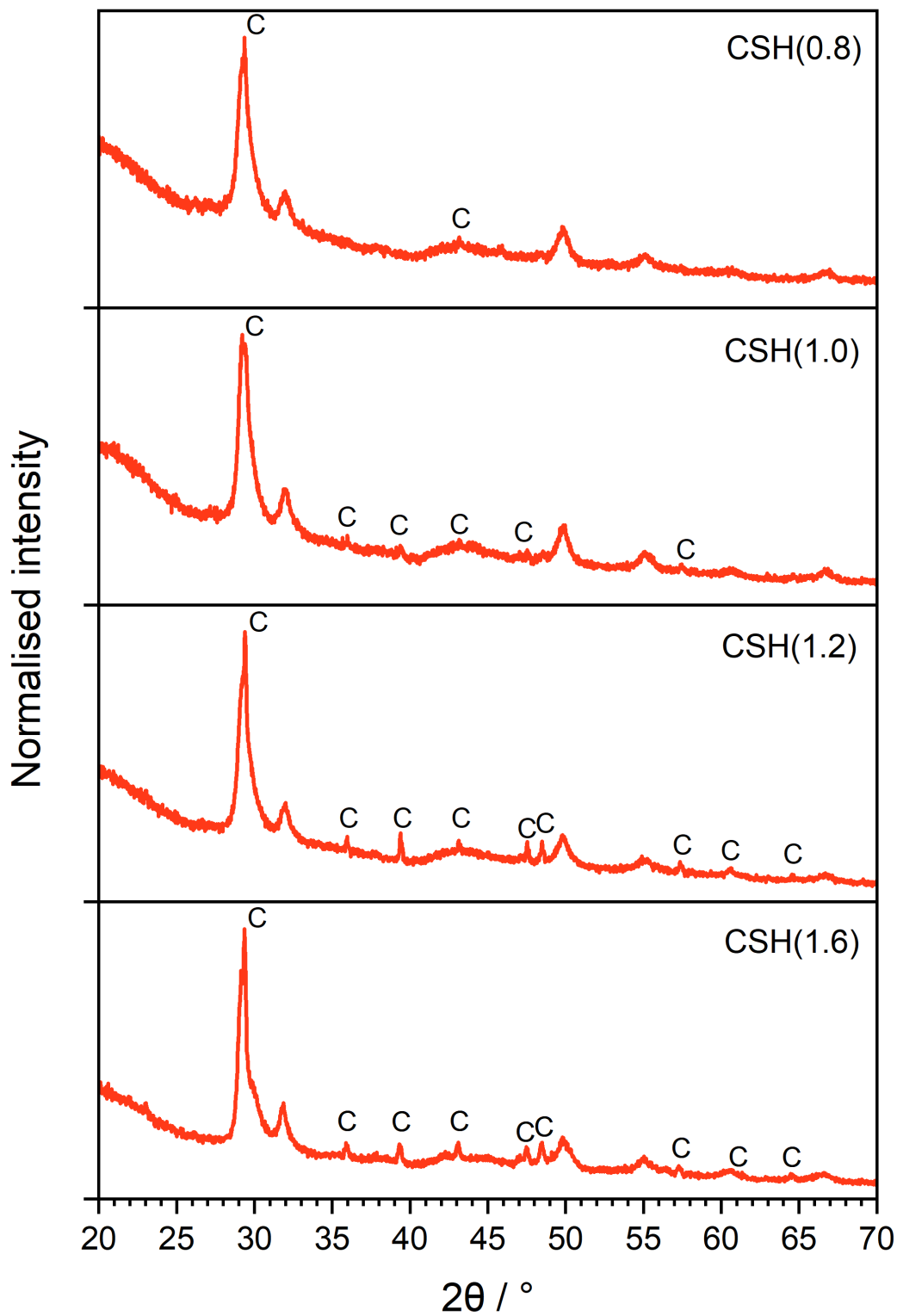


Figure 5.6: XRD patterns of C-S-H phases at Ca/Si ratios of 0.8, 1.0, 1.2 and 1.6 contacted with 0.5 mM uranyl nitrate. For the Ca/Si ratio of 0.6 see **Figure 5.2**. Peaks for C-S-H(I) were identified in all samples (tobermorite, PDF card no. 00-045-1480 [184]) [185]. C = calcite (PDF card no. 01-078-4614 [187]).

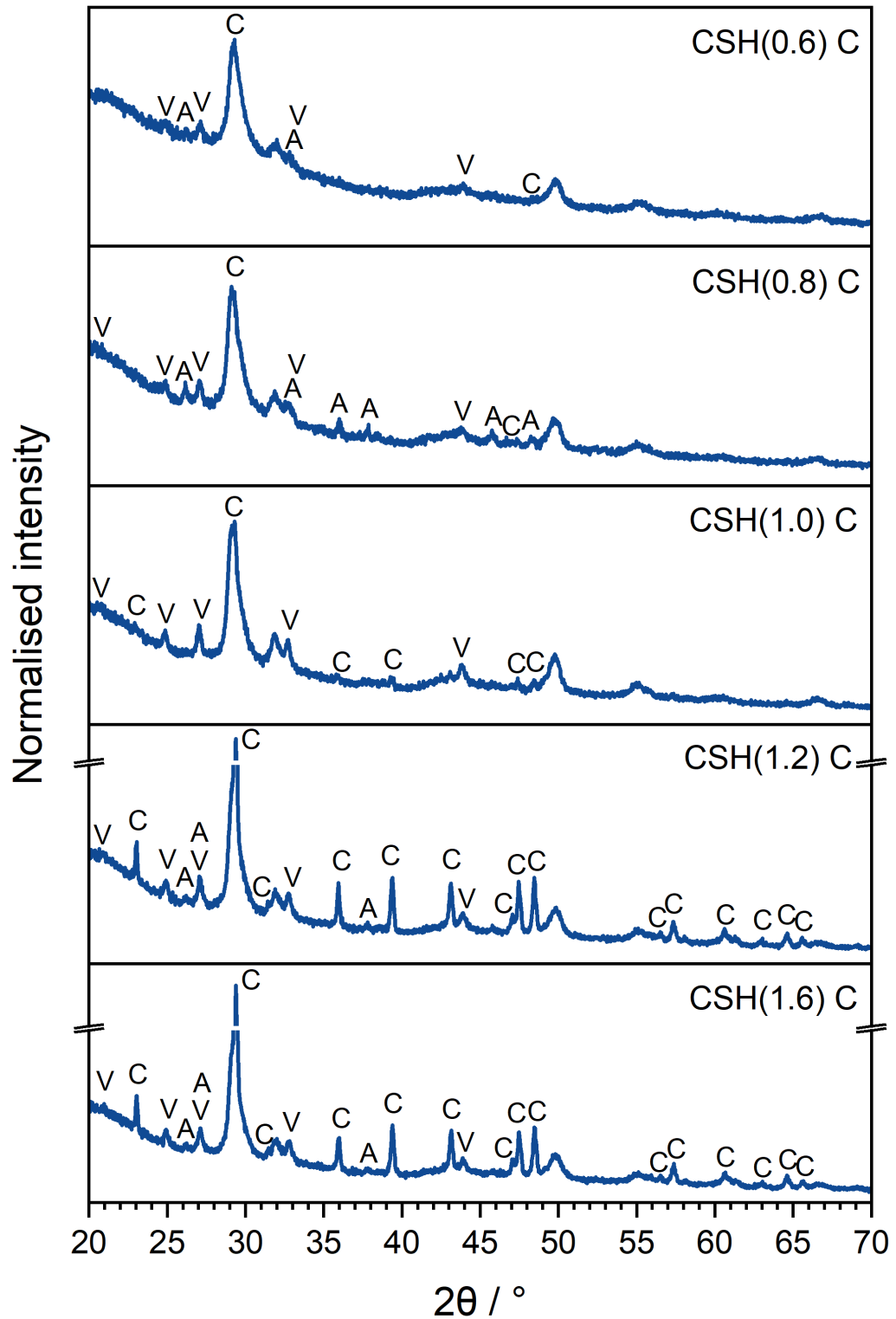


Figure 5.7: XRD patterns of pre-carbonated C-S-H phases at Ca/Si ratios of 0.6, 0.8, 1.0, 1.2 and 1.6 contacted with 0.5 mM uranyl nitrate. Peaks for C-S-H(I) were identified in all (tobermorite, PDF card no. 00-045-1480 [184]) [185]. A = aragonite (PDF card no. 01-085-6703 [190]); C = calcite (PDF card no. 01-078-4614 [187]); V = vaterite (PDF card no. 04-017-8634 [191]).

As the pH of the 0.5 mM uranyl solution did not have a significantly damaging effect on the C-S-H structure and no U-containing phases were identified in the XRD patterns for the 0.5 mM U(VI)-contacted CSH(X) and CSH(X) C phases, it was considered that XAFS would be instrumental for the identification of the U(VI) coordination environment in these systems. These results are discussed further in **Sections 5.3.6** and **5.3.7**.

5.3.3 U(VI)-contacted C-S-H phases: All Ca/Si ratios with 10 mM U(VI)

5.3.3.1 Ca and Si release, non-carbonated

The pH measurements for the C-S-H phases after contact with 10 mM uranyl nitrate ($\text{pH} = 2.8 \pm 0.0$) are given in **Table 5.7**. As expected, the pH values increase with increasing Ca/Si ratio due to increased calcium content and subsequently higher Ca^{2+} release into solution.

Table 5.7: pH values of 10 mM U(VI) / C-S-H solutions after 48 hours.

CSH(X)	pH
CSH(0.6)	9.2 ± 0.0
CSH(0.8)	9.3 ± 0.0
CSH(1.0)	9.5 ± 0.0
CSH(1.2)	10.0 ± 0.0
CSH(1.6)	11.2 ± 0.2

The pH values were only slightly lower than measured in the 0.5 mM U(VI)-contacted phases, which suggests that there was a high release of calcium into solution, to the effect of a buffer, due to the high acidity of the 10 mM U(VI) solution. This was observed in the calcium and silicon release data displayed in **Figure 5.8**. It should again be noted that for all Ca/Si ratios no / negligible uranium was detected by ICP-OES measurements in solution, indicating >99 % uptake of uranium via sorption or precipitation.

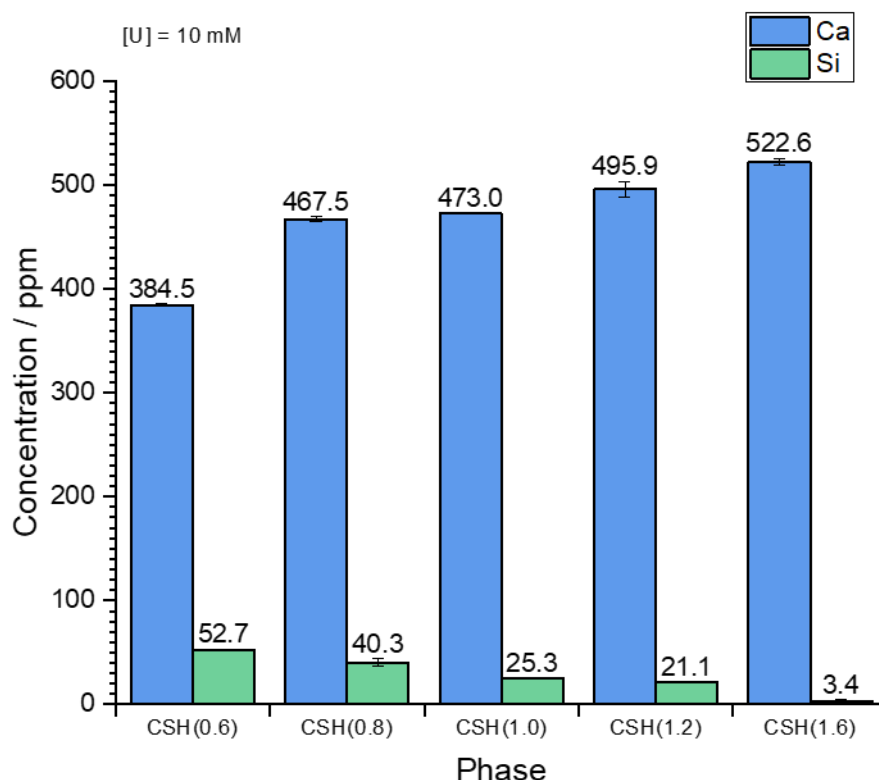


Figure 5.8: Ca and Si release from C-S-H phases in contact with 10 mM U(VI) (25 g L^{-1}) for 48 hours.

For the 10 mM U(VI)-contacted C-S-H phases there was a clear trend of elevated calcium release relative to silicon release, with the calcium release also increasing with Ca/Si ratio. The silicon release decreased with increasing Ca/Si ratio which was again attributed to the lower amount of silicon available in the system. The molar Ca/Si ratio of the 10 mM U(VI) / C-S-H solutions are shown in **Table 5.8**.

Table 5.8: Ca/Si ratio of C-S-H phases compared to the Ca/Si ratio in solution after contact with 10 mM U(VI), and the ratio of Ca partitioned in the solid and solution.

Ca/Si ratio of C-S-H phase	Ca/Si ratio of solution after U(VI) contact	$\text{Ca}_{\text{C-S-H}}/\text{Ca}_{\text{solution}}$ ratio: <1 = higher Si/Ca release >1 = higher Ca/Si release
0.6	5.1	8.5
0.8	8.1	10
1.0	13	13
1.2	17	14
1.6	108	68

In all cases, the molar calcium release compared to silicon was significantly higher than 1 which indicates elevated calcium release. Although the difference observed between the calcium and silicon concentrations in solution appear relatively large in **Figure 5.8**, at higher Ca/Si ratios the relative release of calcium to silicon was not significantly changed in comparison to the 0.5 mM contacted samples. In fact, for the CSH(1.6) phase the relative Ca/Si release was lower in the 10 mM U(VI)-contacted sample, at 68, compared to the 0.5 mM U(VI)-contacted sample, at 116.

5.3.3.2 Ca and Si release, pre-carbonated

The pH measurements for the pre-carbonated C-S-H phases after contact with 10 mM uranyl nitrate ($\text{pH} = 2.8 \pm 0.0$) are given in **Table 5.9**. The pH values do not show a particular trend with Ca/Si ratio but are lower overall than the values measured for the non-carbonated counterparts (**Table 5.7**), which is indicative of dissolved carbonate (HCO_3^-) in solution [253] in addition to the effect of the increased acidity of the 10 mM U(VI) solution.

Table 5.9: pH values of 10 mM U(VI) / pre-carbonated C-S-H solutions after 48 hours.

CSH(X) C	pH
CSH(0.6) C	9.5 ± 0.0
CSH(0.8) C	9.2 ± 0.1
CSH(1.0) C	9.7 ± 0.0
CSH(1.2) C	9.1 ± 0.0
CSH(1.6) C	9.2 ± 0.0

Figure 5.9 displays the calcium and silicon release from the pre-carbonated C-S-H phases into solution after contact with U(VI) for 48 hours. It should again be noted that for all Ca/Si ratios no / negligible uranium was detected by ICP-OES measurements in solution, indicating >99 % uptake of uranium via sorption or precipitation.

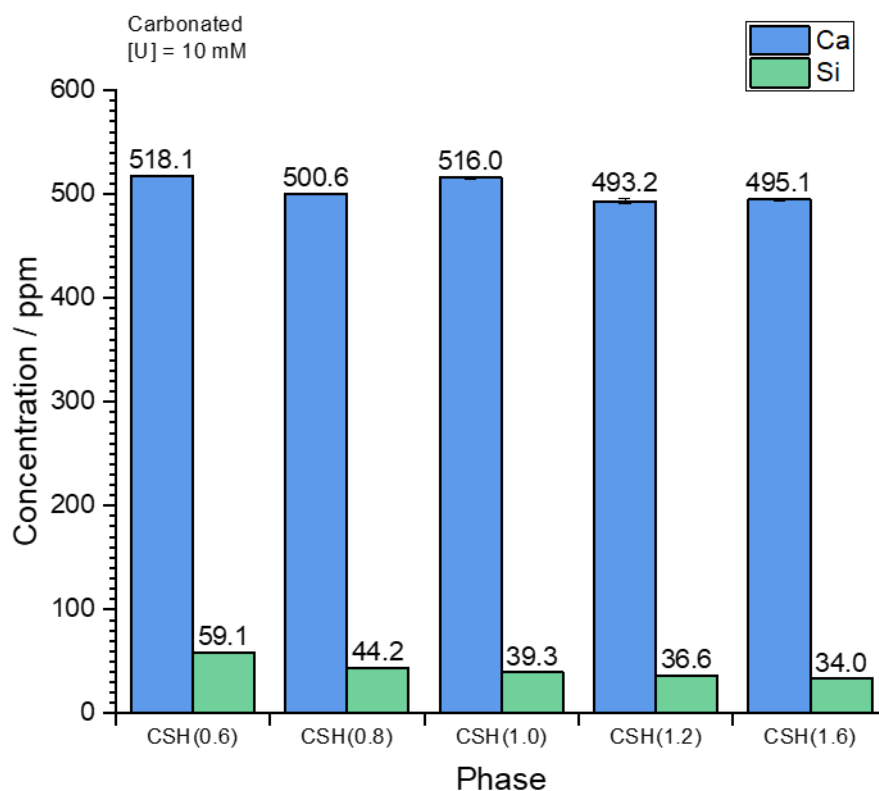


Figure 5.9: Ca and Si release from pre-carbonated C-S-H phases in contact with 10 mM U(VI) (25 g L⁻¹) for 48 hours.

In the pre-carbonated C-S-H 10 mM U(VI)-contacted phases, the calcium release showed a slight decrease with increasing Ca/Si but was consistently high at ~500 ppm. This consistency in calcium release could be a result of calcium carbonate dissolution to the effect of maintaining the pH at ~9.5 in all of the systems. The silicon release also showed a slight decrease with increasing Ca/Si ratio, as expected, due to the lower availability of silicon in the system. The molar Ca/Si ratio of the 10 mM U(VI) / C-S-H C solutions are shown in **Table 5.10**.

Table 5.10: Ca/Si ratio of pre-carbonated C-S-H phases compared to the Ca/Si ratio in solution after contact with 10 mM U(VI), and the ratio of Ca partitioned in the solid and solution.

Ca/Si ratio of C-S-H phase	Ca/Si ratio of solution after U(VI) contact	Ca _{C-S-H} /Ca _{solution} ratio: <1 = higher Si/Ca release >1 = higher Ca/Si release
0.6	6.1	10
0.8	7.9	9.9
1.0	9.2	9.2
1.2	9.4	7.9
1.6	10	6.4

In all cases, the molar calcium release compared to silicon release was higher than 1. This ratio decreased with increasing Ca/Si of the C-S-H phase, which is retrograde to the expected trend, and is attributed to the presence of increased carbonation of interlayer calcium to the effect of relatively decreased calcium release, as previously discussed.

5.3.3.3 X-ray diffraction

The XRD patterns for the 10 mM U(VI)-contacted C-S-H phases from Ca/Si ratios 0.8 to 1.6 are shown in **Figure 5.10**. The main C-S-H(I) reflection, (2,2,0), at $\sim 29^\circ$ 2θ and the (2,2,10) reflection at $\sim 50^\circ$ 2θ were the only peaks pertaining to the C-S-H phase that were identified at all Ca/Si ratios (tobermorite, PDF card no. 00-045-1480 [184]). There were no additional U-bearing phases observed by X-ray diffraction, however the loss of intensity of the C-S-H peaks and increased amorphous contribution to the signal could be indicative of the formation of an initial poorly crystalline amorphous phase, such as the Ca-weeksite phase (discussed in **Section 5.3.1**).

Calcite was also present in the phases with initial Ca/Si ratios of 1.0, 1.2 and 1.6 as a result of carbonation during analysis and / or drying. Vaterite was observed in the samples with initial Ca/Si ratios of 0.8 and 1.0; this was attributed to accelerated carbonation due to unavoidable storage of the phases outside of the anaerobic chamber during a laboratory move. The XRD patterns for the pre-carbonated 10 mM U(VI)-contacted C-S-H phases from Ca/Si ratios 0.6 to 1.6 are also shown in **Figure 5.11**. As with the non-carbonated samples, the main C-S-H(I) reflection, (2,2,0), at $\sim 29^\circ$ 2θ and the (2,2,10) reflection at $\sim 50^\circ$ 2θ were the only peaks pertaining to the C-S-H phase at all Ca/Si ratios (tobermorite, PDF card no. 00-045-1480 [184]).

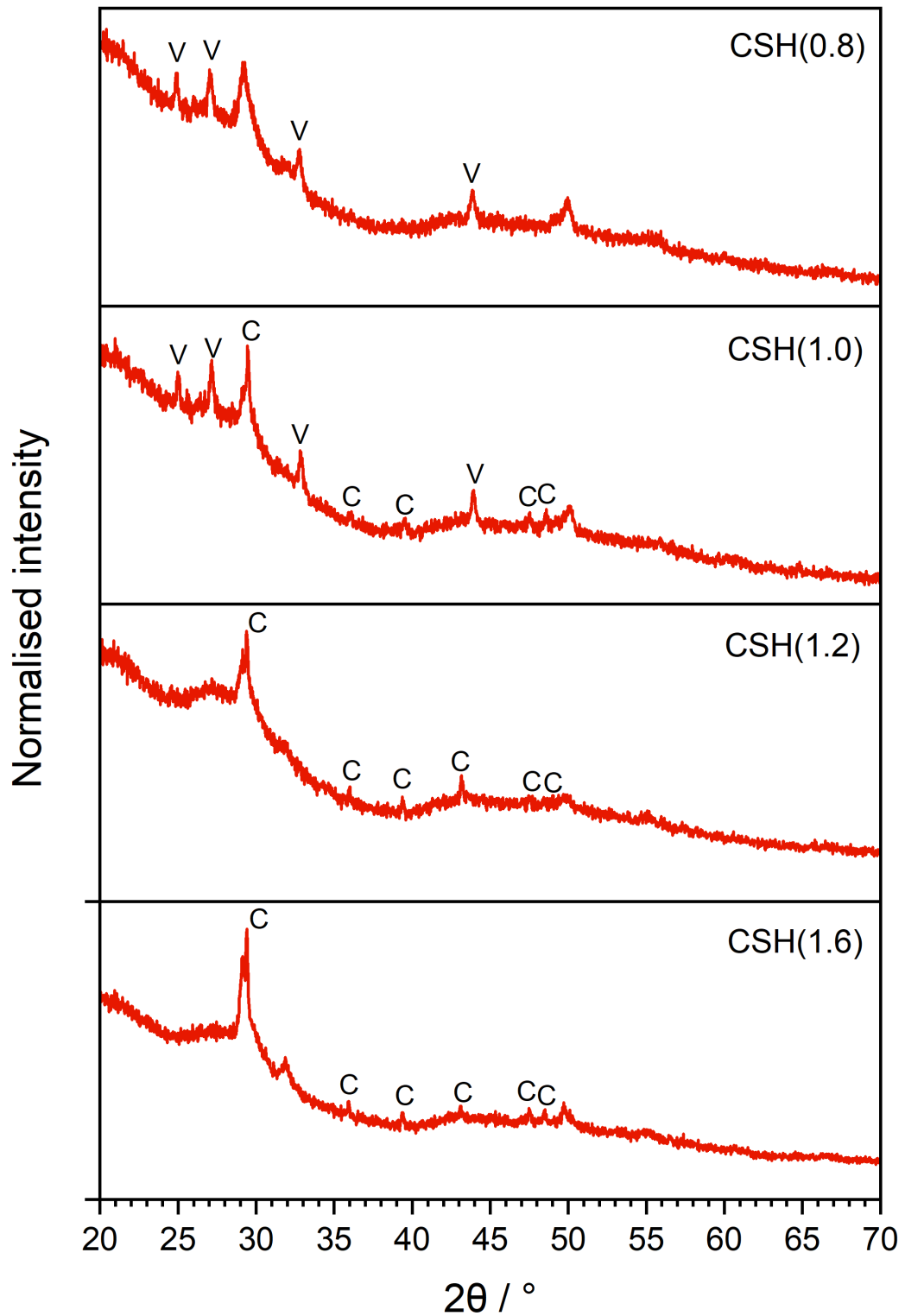


Figure 5.10: XRD patterns of C-S-H phases at Ca/Si ratios of 0.8, 1.0, 1.2 and 1.6 contacted with 10 mM uranyl nitrate. For the Ca/Si ratio of 0.6 see **Figure 5.2**. Peaks for C-S-H(I) at $\sim 29^\circ$ 2θ and $\sim 50^\circ$ 2θ only were identified in all (tobermorite, PDF card no. 00-045-1480 [184]) [185]. C = calcite (PDF card no. 01-078-4614 [187]); V = vaterite (PDF card no. 04-017-8634 [191]).

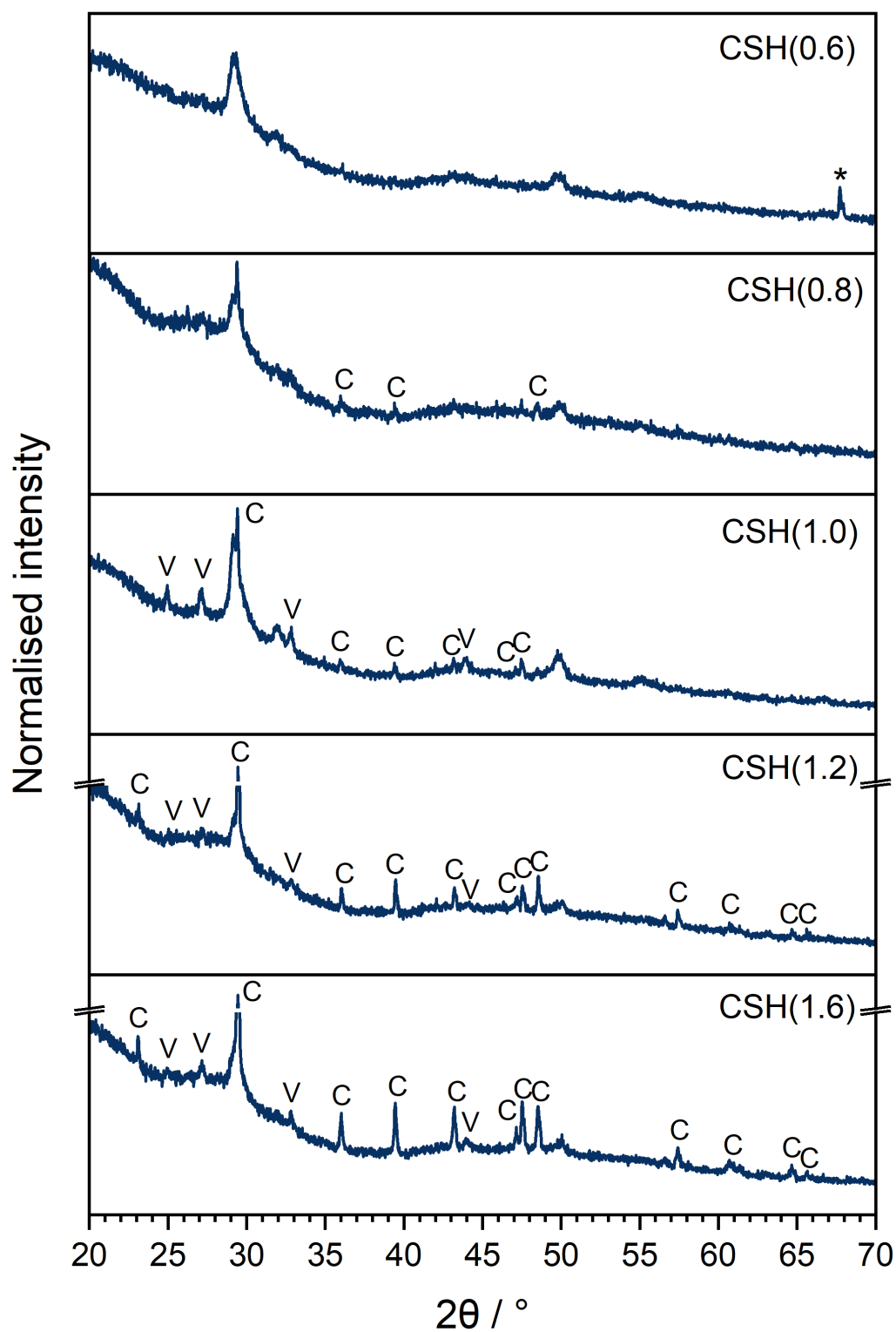


Figure 5.11: XRD patterns of pre-carbonated C-S-H phases at Ca/Si ratios of 0.6, 0.8, 1.0, 1.2 and 1.6 contacted with 10 mM uranyl nitrate. Peaks for C-S-H(I) at $\sim 29^\circ$ 2θ and $\sim 50^\circ$ 2θ only were identified in all (tobermorite, PDF card no. 00-045-1480 [184]) [185]. C = calcite (PDF card no. 01-078-4614 [187]); V = vaterite (PDF card no. 04-017-8634 [191]); * = quartz impurity from characterisation preparation.

5.3.4 U(VI)-contacted minor cement phases

5.3.4.1 Elemental release

The pH measurements for the minor cement hydrate phases ettringite and hydrotalcite after contact with 0.5 mM (pH = 3.6 ± 0.1) and 10 mM (pH = 2.8 ± 0.0) uranyl nitrate are given in **Table 5.11**.

Table 5.11: pH values of ettringite and hydrotalcite contacted with 0.5 mM and 10 mM U(VI) after 48 hours.

Phase, U(VI) concentration	pH
Ettringite, [U] = 0.5 mM	10.5 ± 0.2
Ettringite, [U] = 10 mM	9.9 ± 0.2
Hydrotalcite, [U] = 0.5 mM	10.2 ± 0.2
Hydrotalcite, [U] = 10 mM	7.8 ± 0.2

U(VI) uptake as a percentage of $[U]_{t=0}$ by both ettringite and hydrotalcite at the two concentrations of U(VI) is given in **Figure 5.12**. At both 0.5 mM and 10 mM U(VI), ettringite effectively showed complete uptake of U(VI) (>99 %) whereas hydrotalcite showed ~30 % uptake at both U(VI) concentrations. The release of Ca, Al, S or Mg from the ettringite and hydrotalcite phases after contact with U(VI), at both concentrations, are also given in **Figures 5.13** and **5.14**, respectively.

The release of calcium and sulfur from ettringite was observed to increase with increasing U(VI) concentration (and decreasing pH). The concentration of calcium was over two times higher in the 10 mM U(VI) solution than the 0.5 mM solution (~1 000 ppm vs ~450 ppm), whereas the sulfur concentration only showed a smaller increase from ~300 ppm to ~400 ppm.

For the hydrotalcite phase, the magnesium release was very low in the 0.5 mM U(VI) solution at 0.20 ± 0.02 ppm and significantly increased in the 10 mM U(VI) solution to 36.2 ± 1.8 ppm, as a result of increased dissolution at lower pH.

The aluminium release in both ettringite and hydrotalcite displayed different behaviour in that it decreased with addition of more U(VI). For hydrotalcite, this could be related to the decrease in aluminium solubility with decreasing pH. For ettringite, this could also be the case to some extent, but the explanation could be more complex and requires the justifications of XRD and NMR analyses (see *Section 5.3.4.2* and **Section 5.3.9**, respectively)

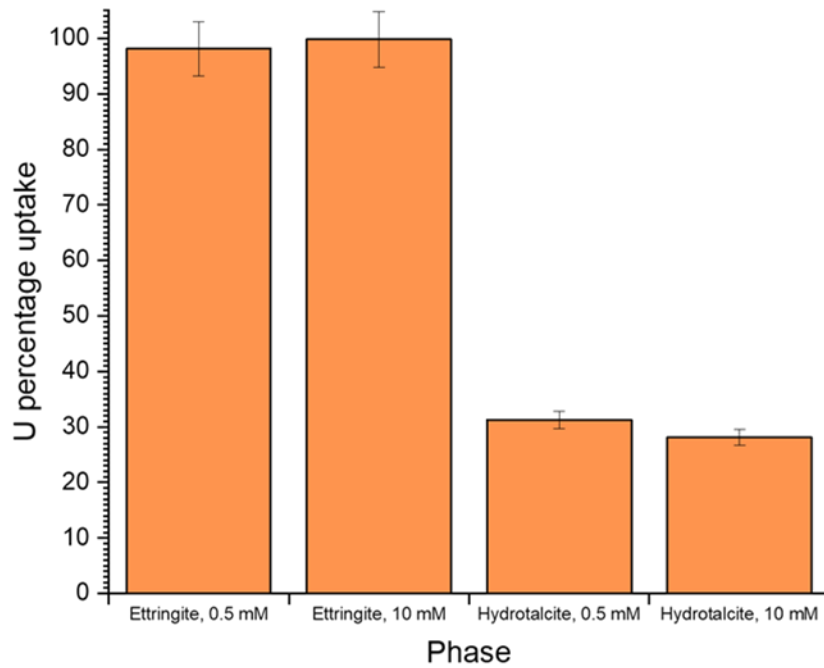


Figure 5.12: U(VI) uptake by ettringite and hydrotalcite (25 g L^{-1}) at 0.5 mM and 10 mM U(VI) as a percentage of $[U]_{t=0}$. Note that the error bars for the ettringite phases indicate there could in excess of 100 % uptake of U(VI), which is not possible, however the errors are an indication of the \pm standard deviation of triplicate sampling.

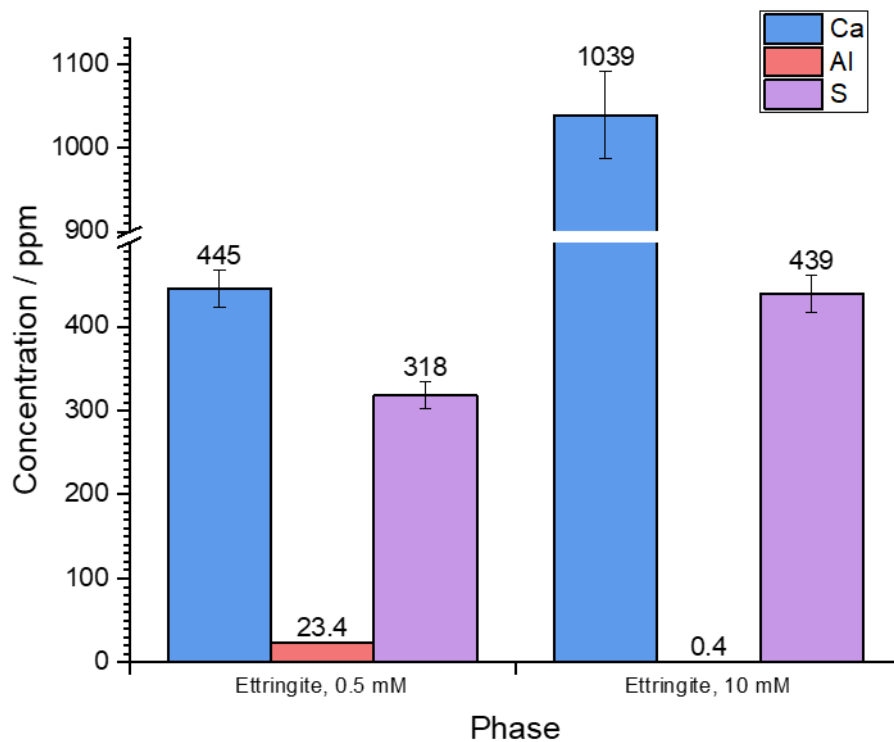


Figure 5.13: Ca, Al and S release from ettringite phases (25 g L^{-1}) in contact with 0.5 mM and 10 mM U(VI), respectively, for 48 hours

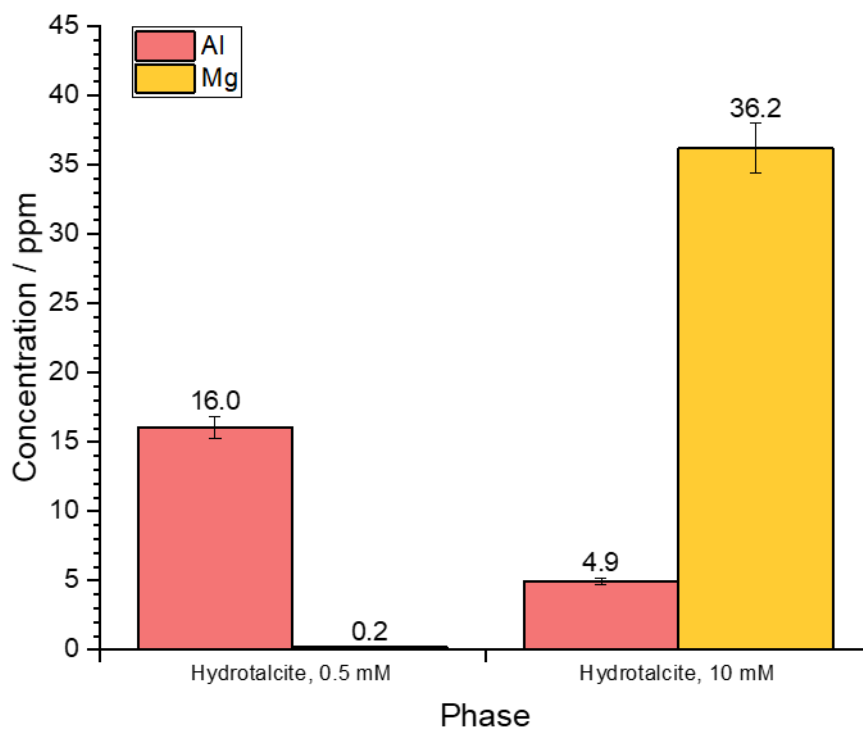


Figure 5.14: Al and Mg release from hydrotalcite phases (25 g L^{-1}) in contact with 0.5 mM and 10 mM U(VI), respectively, for 48 hours

5.3.4.2 X-ray diffraction

The XRD patterns for the U(VI)-contacted ettringite phases are shown in **Figure 5.15** along with the non-U(VI)-contacted starting phase.

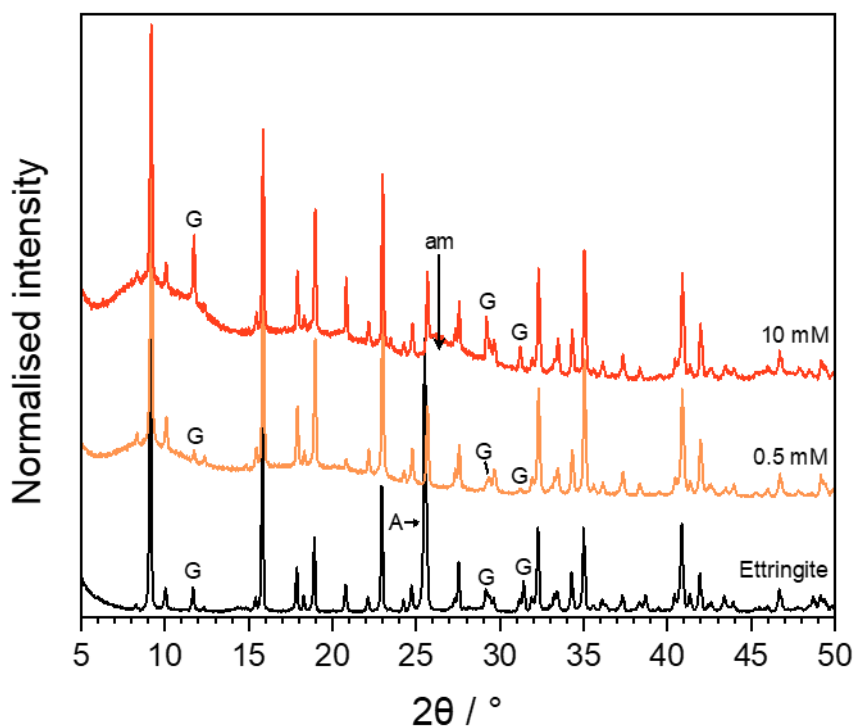


Figure 5.15: XRD patterns of ettringite (PDF card no. 04-013-3691 [194]) before and after contact with U(VI) at 0.5 mM and 10 mM. A = anhydrite (PDF card no. 00-037-1496 [195]); G = gypsum (PDF card no. 00-033-0311 [196]). Regions of diffuse scattering are a result of sample preparation methods for radioactive samples unless denoted by “am”.

The reflections assigned to the ettringite phase (PDF card no. 04-013-3691 [194]) were maintained after contact of the phase with both 0.5 mM and 10 mM U(VI). The peak attributed to the reflection of anhydrite at $\sim 25.5^\circ 2\theta$ (denoted “A”) disappears at both U(VI) concentrations due to the dissolution of anhydrite. The peaks assigned to gypsum (denoted “G”) decreased in intensity relative to ettringite after contact with 0.5 mM U(VI) but increased in intensity after contact with 10 mM U(VI), which is unexpected given the corresponding increase in calcium and silicon release. Despite the reduced aluminium release, the increased intensity of the gypsum peaks could be a result of increased ettringite dissolution in the 10 mM U(VI) solution. The lower concentration of aluminium in solution could therefore be explained by the precipitation of a poorly crystalline Al-hydroxide phase, indicated by the region of diffuse scattering observed between $\sim 26\text{--}30^\circ 2\theta$, that could also be U-, S- or Ca-containing. Given that >99 % uptake of U(VI) was observed and no other U-containing phases were observed by XRD, it is plausible that this is U-containing. The measurement of ^{27}Al NMR analysis on these phases goes some way to explaining this observation (see **Section 5.3.9**).

The XRD patterns for the U(VI)-contacted hydrotalcite phases are shown in **Figure 5.16** along with the non-U(VI)-contacted starting phase.

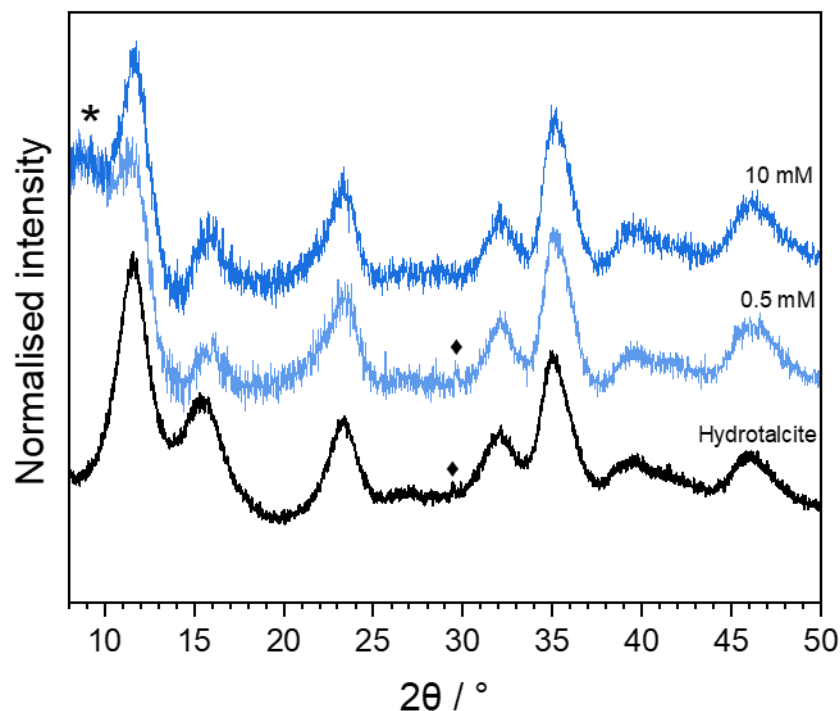


Figure 5.16: XRD patterns of hydrotalcite (PDF card no. 01-082-8041 [192]) before and after contact with U(VI) at 0.5 mM and 10 mM. Background subtraction was performed on the diffraction patterns in this figure to better highlight the diffraction peaks. The ◆ indicates an unidentified phase and the asterisk indicates the background from sample preparation methods that could not be subtracted.

The XRD pattern for nano-crystalline hydrotalcite (PDF card no. 01-082-8041 [192]) was maintained on addition of 0.5 mM and 10 mM U(VI) to the hydrotalcite phase. The diffuse nature of the diffraction patterns makes the identification of any low yield secondary phases difficult, however there appears to be little to no change in the diffraction pattern on addition of both concentrations of U(VI). In the starting phase there is a peak at $\sim 29.5^\circ 2\theta$, which shows a partial correlation with boehmite ($\text{AlO}(\text{OH})$), and is still present in the 0.5 mM U(VI)-contacted sample but not in the 10 mM U(VI)-contacted sample.

5.3.5 Geochemical modelling results

The results from geochemical modelling based on ICP-OES analyses and pH measurements are shown in **Figure 5.17** for the C-S-H systems at $[U] = 0.5$ mM and 10 mM, respectively. It should be noted that addition of HCO_3^- to the system allowed inclusion of the phase UO_2CO_3 but the saturation index was negative at all concentrations up to 1000 ppm.

The uranium phases identified to be saturated in the C-S-H systems using geochemical modelling did not vary with uranium concentration and only U(VI) phases were identified: calcium uranate (CaUO_4); haiweeite ($\text{Ca}(\text{UO}_2)_2(\text{Si}_5\text{O}_{12})(\text{OH})_2 \cdot 6\text{H}_2\text{O}$); soddyite ($(\text{UO}_2)_2(\text{SiO}_4) \cdot 2\text{H}_2\text{O}$); uranophane ($\text{Ca}(\text{UO}_2)_2\text{SiO}_3(\text{OH})_2 \cdot 5\text{H}_2\text{O}$); metaschoepite ($\text{UO}_3 \cdot 2\text{H}_2\text{O}$); and uranium hydroxide ($\text{UO}_2(\text{OH})_2$). Although the calcium uranate phase identified is a high temperature phase [257], hydrous forms of calcium uranate exist and are typically solubility limiting at high pH, as previously discussed in **Chapter 2** [61,62,249].

The results for the geochemical modelling for hydrotalcite and ettringite systems at the corresponding experimental pH values and $[U] = 0.5$ mM and 10 mM are shown in **Figures 5.18** and **5.19**, respectively, for all potential Ca-, S-, Al-, Mg- or U-containing phases that were identified to be saturated in the system. Boehmite and diaspore ($\text{AlO}(\text{OH})$ polymorphs), corundum (Al_2O_3), gibbsite ($\text{Al}(\text{OH})_3$), metaschoepite ($\text{UO}_3 \cdot 2\text{H}_2\text{O}$) and uranium hydroxide ($\text{UO}_2(\text{OH})_2$) were identified as being saturated in both hydrotalcite systems. For the ettringite systems, calcium uranate was additionally identified in both systems, however for the 10 mM U(VI) system, Al_2O_3 had a negative SI, probably due to the low concentration of aluminium measured in solution.

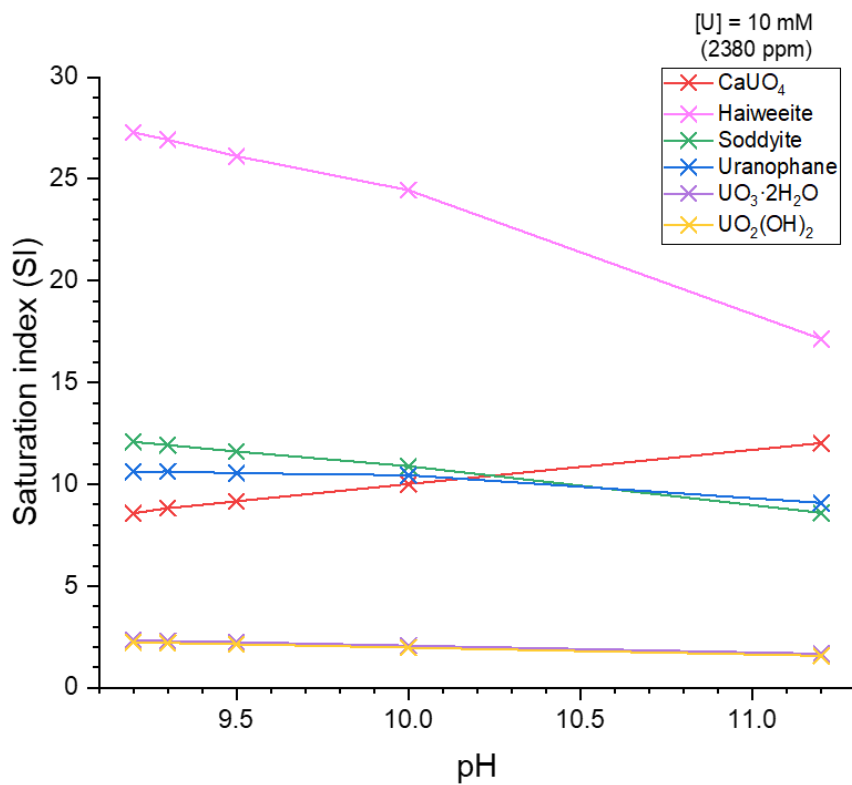
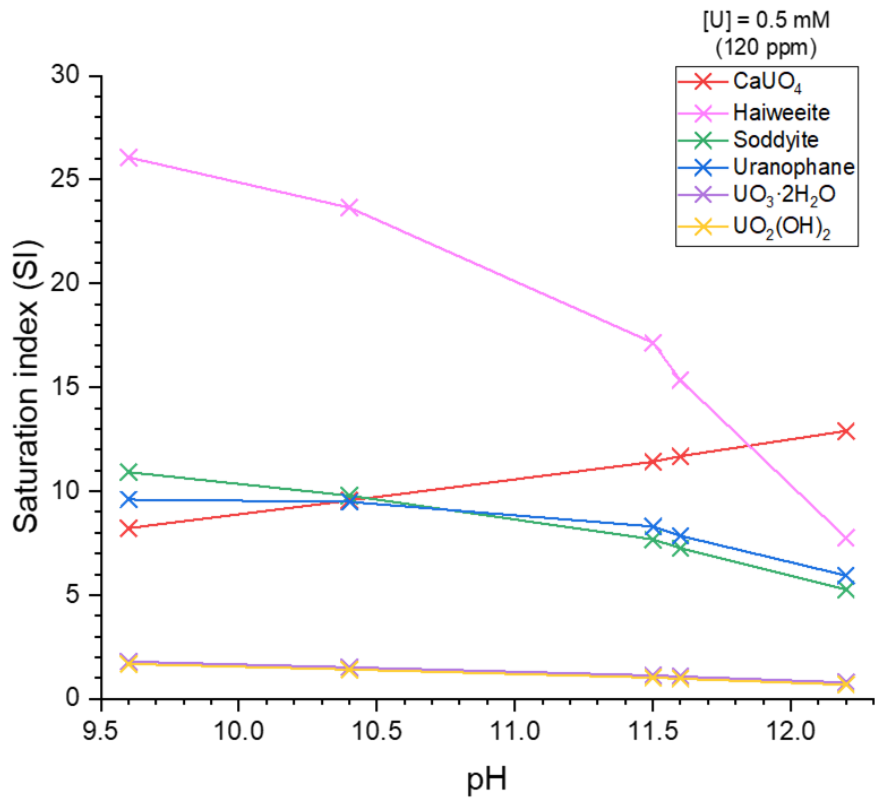


Figure 5.17: Geochemical modelling results showing saturated U(VI) phases over the experimental pH range measured for the C-S-H samples in contact with 0.5 mM U(VI) (top) and 10 mM U(VI) (bottom).

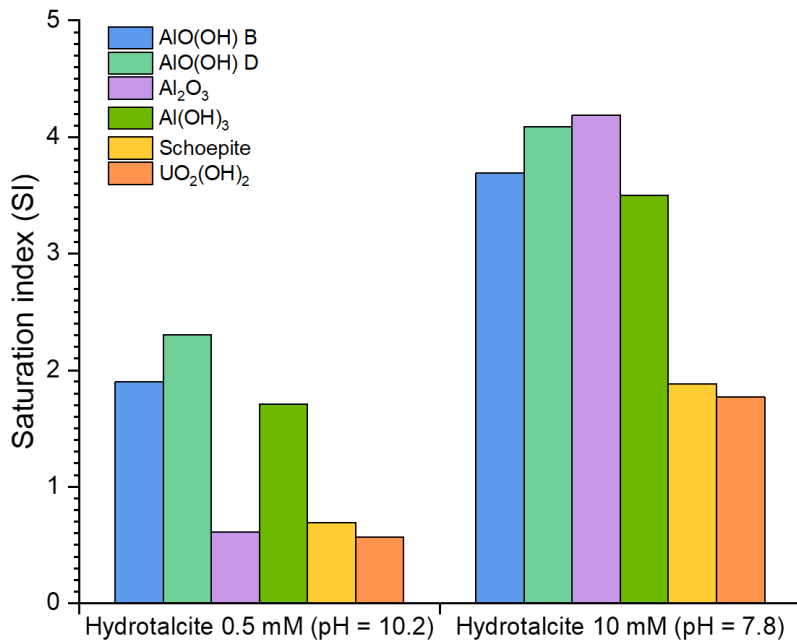


Figure 5.18: Geochemical modelling results showing all identified saturated phases over the experimental pH range measured for the hydrotalcite samples in contact with 0.5 mM U(VI) (left) and 10 mM U(VI) (right).

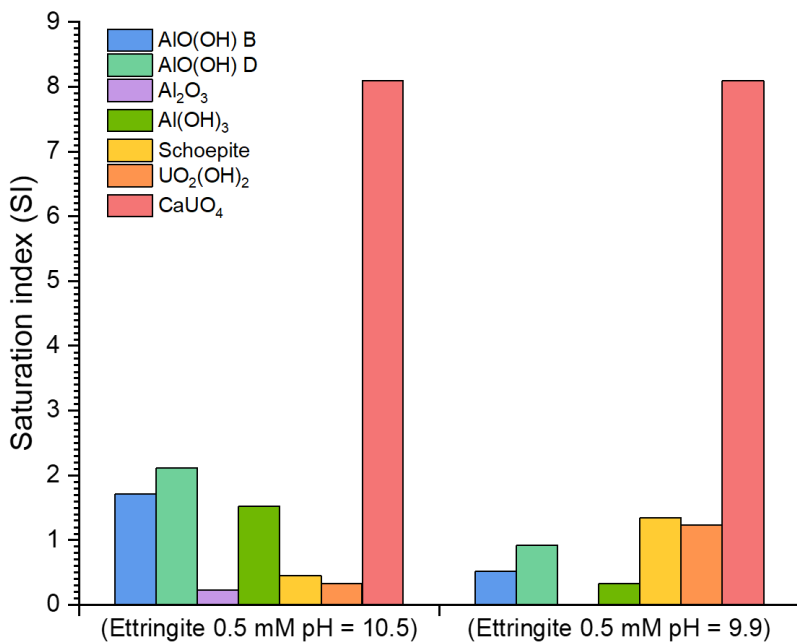


Figure 5.19: Geochemical modelling results showing all identified saturated phases over the experimental pH range measured for the ettringite samples in contact with 0.5 mM U(VI) (left) and 10 mM U(VI) (right).

5.3.6 X-ray absorption spectroscopy: XANES

The XANES spectra at the U L_{III}-edge for the selected U(VI)-contacted samples are shown in **Figure 5.20**. An additional U(VI)-contacted calcite (CaCO₃) phase was also measured for comparison to the pre-carbonated C-S-H phases, however the spectrum obtained was not well resolved. The XAFS of U(VI)-contacted ettringite was unfortunately not measured, due to constraints on available experimental time at Diamond Light Source and NSLS-II. The Athena application from the Demeter 0.9.26 software package was used for post-processing and normalisation of XAFS data. The value of E₀ was assigned to the first inflection point of the derivative of the energy spectrum.

5.3.6.1 Linear combination fitting

XANES linear combination fitting of the U(VI)-contacted phases to the XANES spectra of U-bearing phases, used as standards (described in **Table 5.2** and **Chapter 4**), was also performed in the Athena application. This was done so as to match the XANES profiles of the samples to the most likely combination of XANES profiles of the standard phases, to infer the identity of the U(VI) local coordination in contact with the cement phases. For C-S-H phases, the standards considered were as follows:

- U/(Ca,K)/Si bearing phases: haiweeite (Ca(UO₂)₂(Si₅O₁₂)(OH)₂·6H₂O) and weeksite (K₂(UO₂)₂(Si₅O₁₂)(OH)₄H₂O);
- U/Ca bearing phases: CaUO₄, Ca₃UO₆ and mixed becquerelite (Ca(UO₂)₆O₄(OH)₆·8H₂O) / metaschoepite (UO₃·xH₂O (x<2));
- U/Si bearing phases: soddyite ((UO₂)₂(SiO₄)·2H₂O) and coffinite (U(SiO₄)_{1-x}(OH)_{4x});
- U/C bearing phases: mixed bayleyite (Mg₂(UO₂)(CO₃)₃·18H₂O) / andersonite (Na₂Ca(UO₂)(CO₃)₃·6H₂O));
- U/O bearing phases: UO₂, UO₃ and UO₂(NO₃)₂·6H₂O;

and for hydrotalcite phases, the standards considered were:

- U/Mg bearing phases: MgUO₄;
- U/C bearing phases: mixed bayleyite (Mg₂(UO₂)(CO₃)₃·18H₂O) / andersonite (Na₂Ca(UO₂)(CO₃)₃·6H₂O));
- U bearing phases: UO₂, UO₃ and UO₂(NO₃)₂·6H₂O.

All fitting was performed between -20 and +30 eV from the position of E₀ and the value of ΔE for each standard fitted was recorded. Margin of error for the fits was calculated by the Athena software.

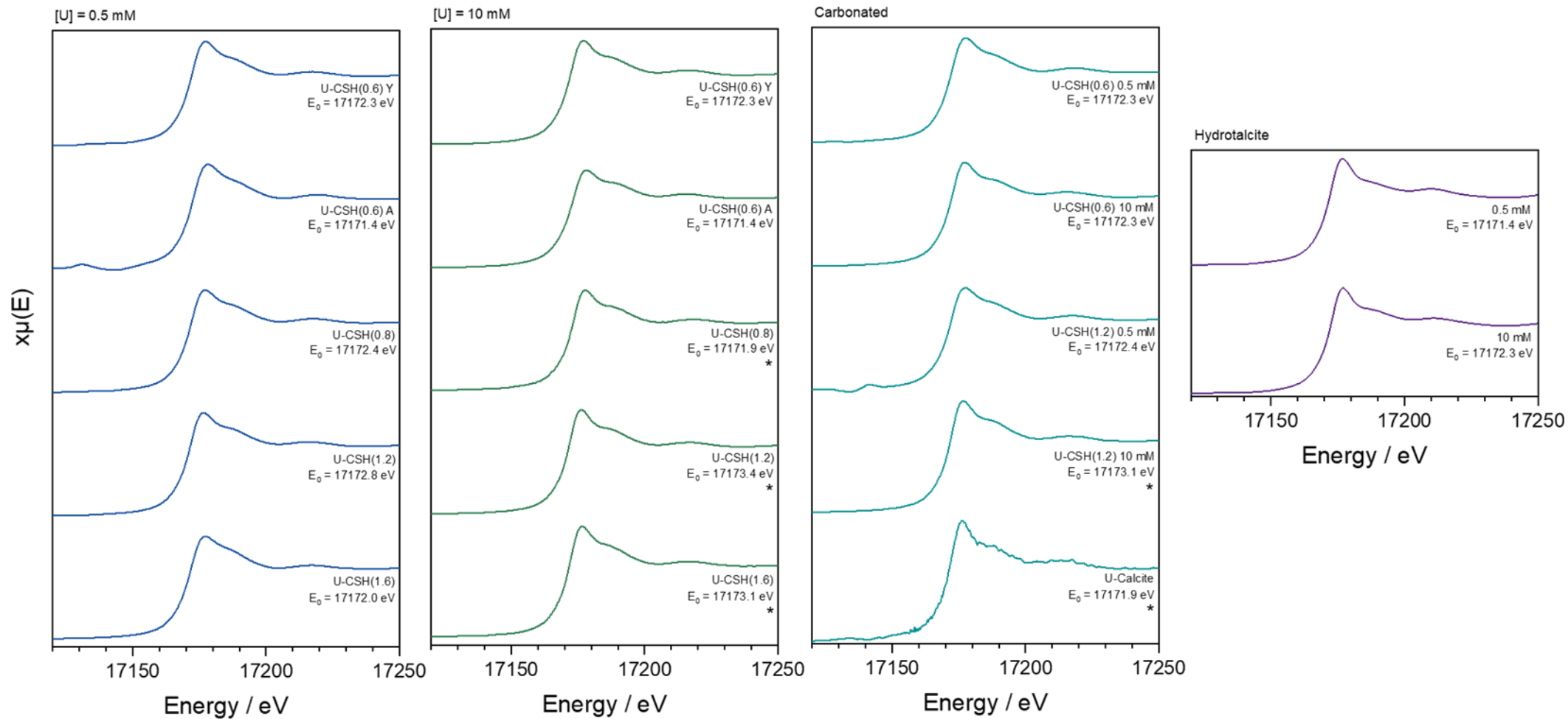


Figure 5.20: U L_{III}-edge measurements of all U(VI)-contacted phases. Asterisk indicates samples that were measured at NSLS-II rather than DLS.

5.3.6.2 U(VI)-CSH(X) linear combination fitting

A trial linear combination fit (LCF) of all possible standards (total = 11) yielded total weightings of >2, with some components also being negatively weighted. This was probably due to the large number of standards available, some with very similar XANES profiles. To address this issue, the number of possible combinations of standards was limited with the following justifications.

The results from the geochemical modelling of the U(VI) / C-S-H systems indicated that uranyl silicates (such as haiweeite ($\text{Ca}(\text{UO}_2)_2(\text{Si}_5\text{O}_{12})(\text{OH})_2 \cdot 6\text{H}_2\text{O}$), soddyite ($(\text{UO}_2)_2\text{SiO}_4 \cdot 2\text{H}_2\text{O}$), uranophane ($\text{Ca}(\text{UO}_2)_2\text{SiO}_3(\text{OH})_2 \cdot 5\text{H}_2\text{O}$)) or calcium uranate phases would be the predominate solid phases under the experimental conditions adopted, along with a possible contribution from metaschoepite ($\text{UO}_3 \cdot 2\text{H}_2\text{O}$) phases or other uranyl-oxy hydroxide phases. With reference to the literature described in **Chapter 2** the formation of a uranyl silicate phases has been documented in [67–71] for U(VI) sorbed on C-S-H phases (i.e. uranophane and / or soddyite), as well as observed for the low Ca/Si ratio CSH(0.6) phase contacted with [U] = 10 mM in this study (XRD detection of Ca-weeksite-type phase; $\text{Ca}_2(\text{UO}_2)_2\text{Si}_6\text{O}_{15} \cdot 10\text{H}_2\text{O}$, see **Section 5.3.1**). At higher concentrations of U(VI), the solubility of U(VI) was shown to be limited by the precipitation of hydrous calcium uranate phases in [53,61–63]. Additionally, becquerelite has potentially been identified on U(VI)-contacted cementitious surfaces [64].

As discussed in **Chapter 4**, the XANES spectra (in the LCF fitted region) of the uranyl silicates soddyite ($(\text{UO}_2)_2\text{SiO}_4 \cdot 2\text{H}_2\text{O}$), haiweeite ($\text{Ca}(\text{UO}_2)_2(\text{Si}_5\text{O}_{12})(\text{OH})_2 \cdot 6\text{H}_2\text{O}$) and weeksite ($\text{K}_2(\text{UO}_2)_2(\text{Si}_5\text{O}_{12})(\text{OH}) \cdot 4\text{H}_2\text{O}$) are very similar. The spectra for CaUO_4 and Ca_3UO_6 , however, are more easily distinguishable from one another.

Given these rationalisations, the maximum combination of standards allowed at any one time in the fitting of the U(VI)-CSH samples was therefore limited to a maximum of 4 or 5 of the total, for non-carbonated and pre-carbonated samples, respectively, to allow for the potential fitting of the local coordination of:

1. A uranyl silicate-type phase (e.g. soddyite, haiweeite, weeksite, uranophane);
2. A calcium uranate-type phase (i.e. CaUO_4);
3. A tri-calcium uranate-type phase (i.e. Ca_3UO_6);
4. A uranyl-oxy hydroxide- / becquerelite-type phase (e.g. UO_3 , mixed becquerelite / metaschoepite);
5. A uranyl carbonate-type phase (e.g. bayleyite / andersonite)*.

It should be noted that although calcium carbonates were also detected in the XRD patterns for the non-carbonated U(VI)-CSH phases, as well as in the pre-carbonated phases, but no

uranyl carbonate phases were identified as being saturated in the geochemical model, the different behaviour of calcium and silicon release discussed under **Sections 5.3.2** and **5.3.3** was the justification for the additional point 5 (*). Bayleyite / andersonite, however, were not identified as contributing to any of the fits for the pre-carbonated phases, therefore it was removed and the fits were repeated with a maximum of any 4 standards, as for the non-carbonated phases. It is probably more likely that the relative releases of calcium and silicon contributed to differing amounts of silicon and / or calcium containing phases in the pre-carbonated C-S-H phases.

All fits were inspected to check that reasonable numbers and errors were achieved, after which the top fit (lowest R-factor) was selected as representative. The results from the linear combination fitting for all U-CSH(X) and U-CSH(X) C samples are given in **Figures 5.21** and **Figure 5.22**, respectively (percentages), and **Table 5.12** (weighted fractions).

For the 0.5 mM U(VI)-contacted C-S-H series, haiweeite ($\text{Ca}(\text{UO}_2)_2(\text{Si}_5\text{O}_{12})(\text{OH})_2 \cdot 6\text{H}_2\text{O}$) and calcium uranate were identified in all of the fits and accounted for ~45-75 % and ~15-30 % of the XANES signal, respectively. In the CSH(0.6) phase only (both young and aged samples – Y and A, respectively) the remainder of the signal was attributed to weeksite ($\text{K}_2(\text{UO}_2)_2(\text{Si}_5\text{O}_{12})(\text{OH}) \cdot 4\text{H}_2\text{O}$) (~25-30 %). It should again be noted that haiweeite and weeksite have a similar XANES spectra (see **Chapter 4**).

For CSH(0.8) and CSH(1.2) there was also an increasing signal from the mixed becquerelite / metaschoepite (B / M) phase with increasing Ca/Si ratio (~5 % and ~12 %, respectively). The B / M signal was still present in the CSH(1.6) phase along with the emergence of a signal contribution from tricalcium uranate. These observations generally correspond with a decrease in Si-bearing phase signals and a concurrent increase in Ca-bearing phase signals as the Ca concentration of the phase increases from Ca/Si = 0.8 to 1.6.

Haiweeite ($\text{Ca}(\text{UO}_2)_2(\text{Si}_5\text{O}_{12})(\text{OH})_2 \cdot 6\text{H}_2\text{O}$) was also identified for all samples in the 10 mM U(VI)-contacted C-S-H series. For CSH(0.6) Y the remainder of the signal was attributed to ~6 % calcium uranate and ~6 % tricalcium uranate. Approximately 8 % of each of these phases also contributed to the signal in the CSH(0.6) A phase, but there was also a significant contribution from the B / M phase (~43 %). This could indicate that the ageing process observed in *Section 5.3.1.1* could also contribute to the formation of a Ca-uranyl-oxy hydroxide phases.

The CSH(0.8) and CSH(1.2) phases both had approximately >90 % signal contribution from haiweeite and the remainder of the signal contribution was fitted from tricalcium uranate. The CSH(1.6) phase displayed a haiweeite signal of >85 % and the remainder from tricalcium

uranate. This could be an indication of the higher calcium content of the latter phase compared to the former phases. With reference back to the calcium and silicon release data for the 10 mM series (*Section 5.3.3.1*), the increased signal from a uranyl silicate phase (e.g. haiweeite), compared to that of calcium uranate phases, could be a result of the increased calcium loss into solution relative to silicon.

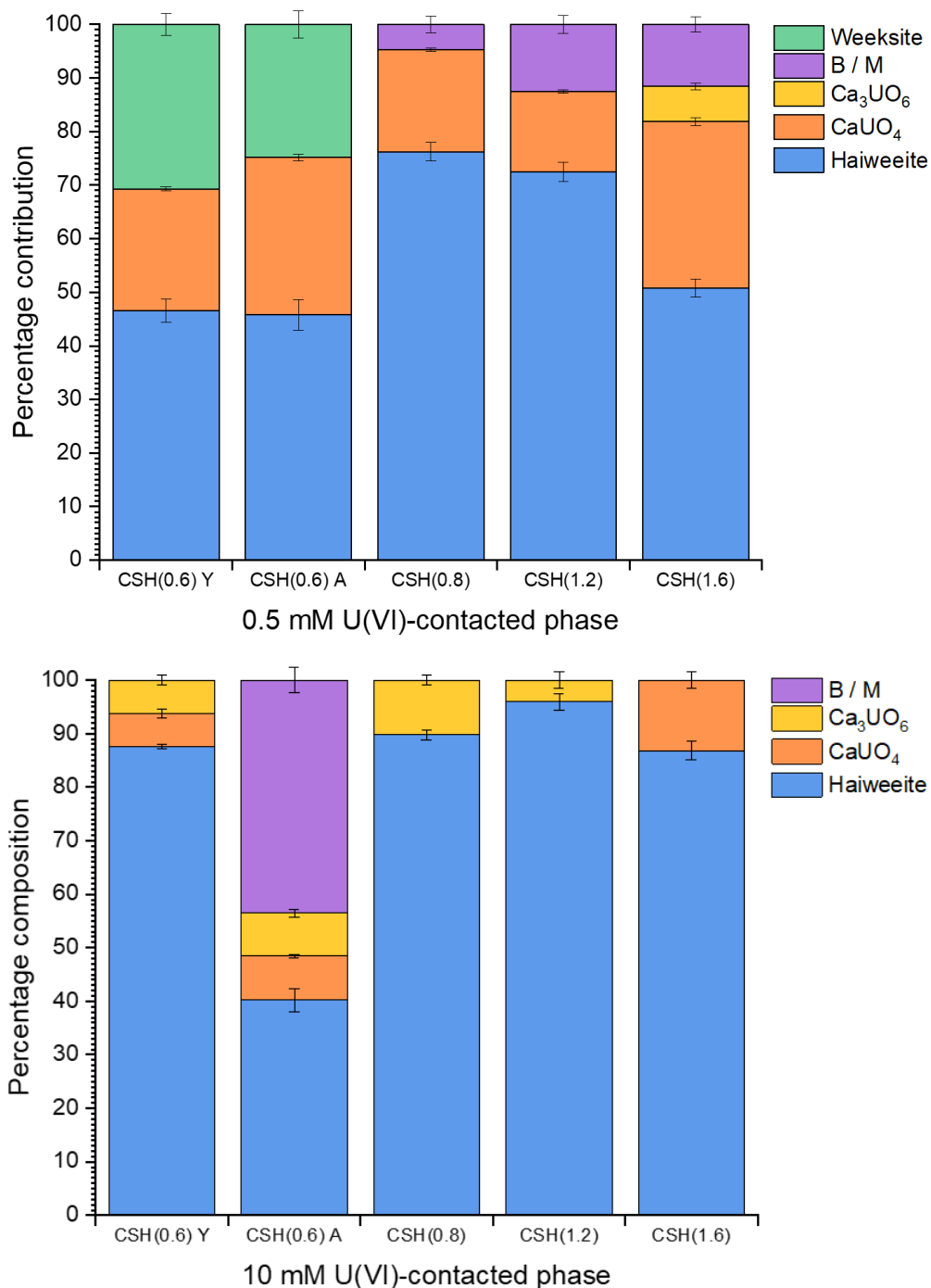


Figure 5.21: Linear combination fitting of U-contacted C-S-H phases. B / M = becquerelite / metaschoepite phase.

For the pre-carbonated 0.5 mM U(VI)-contacted C-S-H phases with initial Ca/Si = 0.6 and 1.2, the signal from haiweeite ($\text{Ca}(\text{UO}_2)_2(\text{Si}_5\text{O}_{12})(\text{OH})_2 \cdot 6\text{H}_2\text{O}$) was ~80 % and ~75 %, respectively (**Figure 5.22**). The remainder of the signal was attributed to calcium uranates (~20 %) for CSH(0.6) and to calcium uranate (~20 %) and uranyl nitrate (UN, ~6 %) for CSH(1.2). The uranyl nitrate signal could be a result of unreacted uranyl nitrate salt, however this seems unlikely given that it is highly soluble in aqueous solution and was not identified in any other systems. It is probably more likely that this is a signal contribution from some other uranyl species with a similar XANES spectra that may or may not be coordinated to nitrate.

In the fits for the pre-carbonated 10 mM U(VI)-contacted C-S-H phases, also with initial Ca/Si = 0.6 and 1.2, a contribution of ~90 % for haiweeite was fitted. For the CSH(0.6) phase, the remainder of the signal was attributed to B / M (~7 %) and tricalcium uranate (~3 %) and for CSH(1.2) it was attributed to calcium uranate.

The fit for the U(VI)-contacted calcite phase from any 2 of UO_2 , UO_3 , uranyl nitrate (UN), bayleyite / andersonite (B / A), CaUO_4 , Ca_3UO_6 and B / M is shown in **Figure 5.22** for reference. The fit yielded a total weighting of 1.125, of which 1.000 was attributed to bayleyite / andersonite and 0.125 was attributed to calcium uranate. The errors calculated by the Athena software were zero (**Table 5.12**).

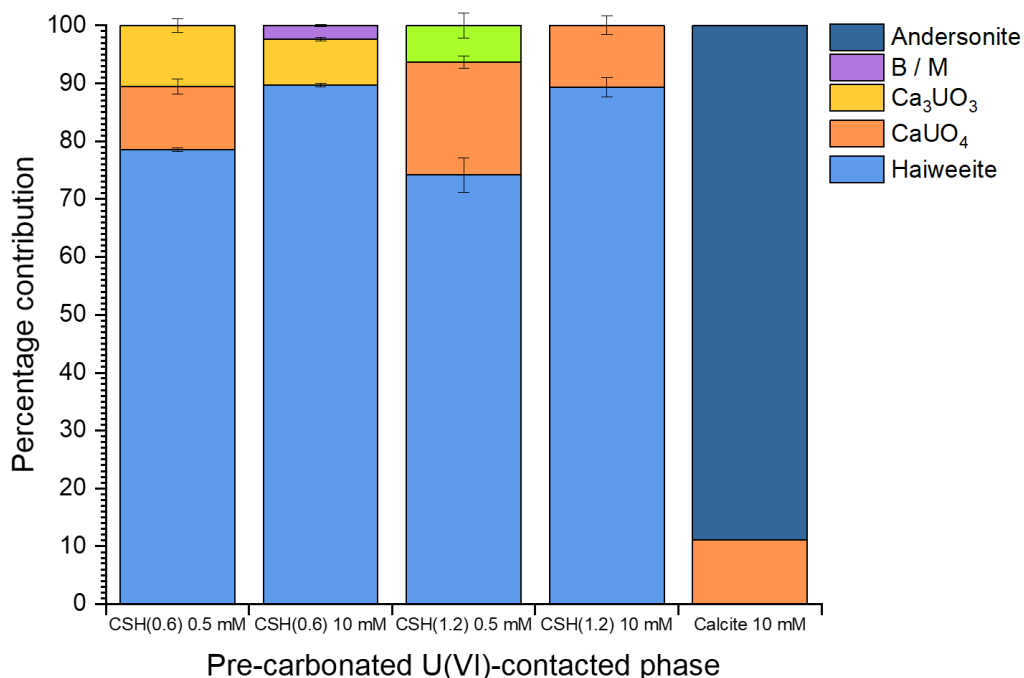


Figure 5.22: Linear combination fitting of pre-carbonated U-contacted C-S-H phases. B / M = becquerelite / metaschoepite and B / A = bayleyite / andersonite.

Table 5.12: Weighted fraction of components in XANES signal of U(VI)-contacted C-S-H phases and U(VI)-contacted calcite using LCF. B / M = becquerelite / metaschoepite and B/ A = andersonite / bayleyite.

[U] / mM	Sample	R-factor	Total weighting	CaUO ₄		Ca ₃ UO ₆		Haiweeite		Mixed B / M		Other		
				Wt.	ΔE	Wt.	ΔE	Wt.	ΔE	Wt.	ΔE	Wt.	ΔE	Phase
0.5	U-CSH(0.6) Y	2 x 10 ⁻⁵	1.014	0.230(4)	-0.70(7)			0.472(22)	-0.28(10)			0.311(21)	-0.85(19)	Weeksite
	U-CSH(0.6) A	3 x 10 ⁻⁵	1.024	0.301(6)	-1.31(6)			0.468(29)	-1.25(3)			0.254(26)	0.36(2)	Weeksite
	U-CSH(0.8)	1 x 10 ⁻⁵	1.005	0.192(3)	0.75(7)			0.767(18)	-0.36(3)	0.047(16)	-3.3(6)			
	U-CSH(1.2)	9 x 10 ⁻⁶	1.007	0.151(3)	1.10(9)			0.731(18)	-0.28(2)	0.126(17)	-0.83(19)			
	U-CSH(1.6)	6 x 10 ⁻⁶	1.008	0.313(7)	-1.4(1)	0.066(6)	3.0(2)	0.512(17)	-0.53(3)	0.117(14)	-2.6(2)			
10	U-CSH(0.6) Y	2 x 10 ⁻⁵	1.002	0.062(8)	1.7(3)	0.062(10)	2.8(3)	0.878(4)	-0.14(1)					
	U-CSH(0.6) A	2 x 10 ⁻⁵	0.994	0.082(3)	5.1(3)	0.080(7)	-3.4(2)	0.400(22)	-0.32(7)	0.433(24)	0.35(8)			
	U-CSH(0.8)	2 x 10 ⁻⁴	0.966			0.099(9)	3.0(4)	0.868(9)	0.47(2)					
	U-CSH(1.2)	5 x 10 ⁻⁴	0.985			0.040(15)	2.9(1.6)	0.945(15)	0.71(3)					
	U-CSH(1.6)	3 x 10 ⁻⁴	1.049	0.138(17)	-0.16(31)			0.911(18)	0.46(3)					
0.5	U-CSH(0.6) C	2 x 10 ⁻⁵	1.019	0.111(13)	1.7(2)	0.107(12)	-1.3(2)	0.800(3)	0.04(3)					
10	U-CSH(0.6) C	8 x 10 ⁻⁶	1.005			0.079(3)	3.37(9)	0.902(3)	0.151(8)	0.024(2)	5.9(4)			
0.5	U-CSH(1.2) C	5 x 10 ⁻⁵	0.998	0.195(10)	0.69(15)			0.740(30)	-0.57(3)			0.063(22)	-2.7(5)	Uranyl nitrate
10	U-CSH(1.2) C	3 x 10 ⁻⁴	1.058	0.113(17)	0.31(39)			0.945(18)	0.57(3)					
10	U-Calcite	2 x 10 ⁻³	1.125	0.125(0)	-1.9(0)							1.000(0)	0.35(0)	B / A

5.3.6.3 U(VI)-hydrotalcite linear combination fitting

The relatively smaller suite of U standards relevant for fitting to the U(VI)-contacted hydrotalcite systems (UO_3 , bayleyite / andersonite (B / A), uranyl nitrate, MgUO_4) meant that the combination of all standards could be fitted. The results are given in **Figure 5.23** (percentages) and **Table 5.13** (weighted fractions).

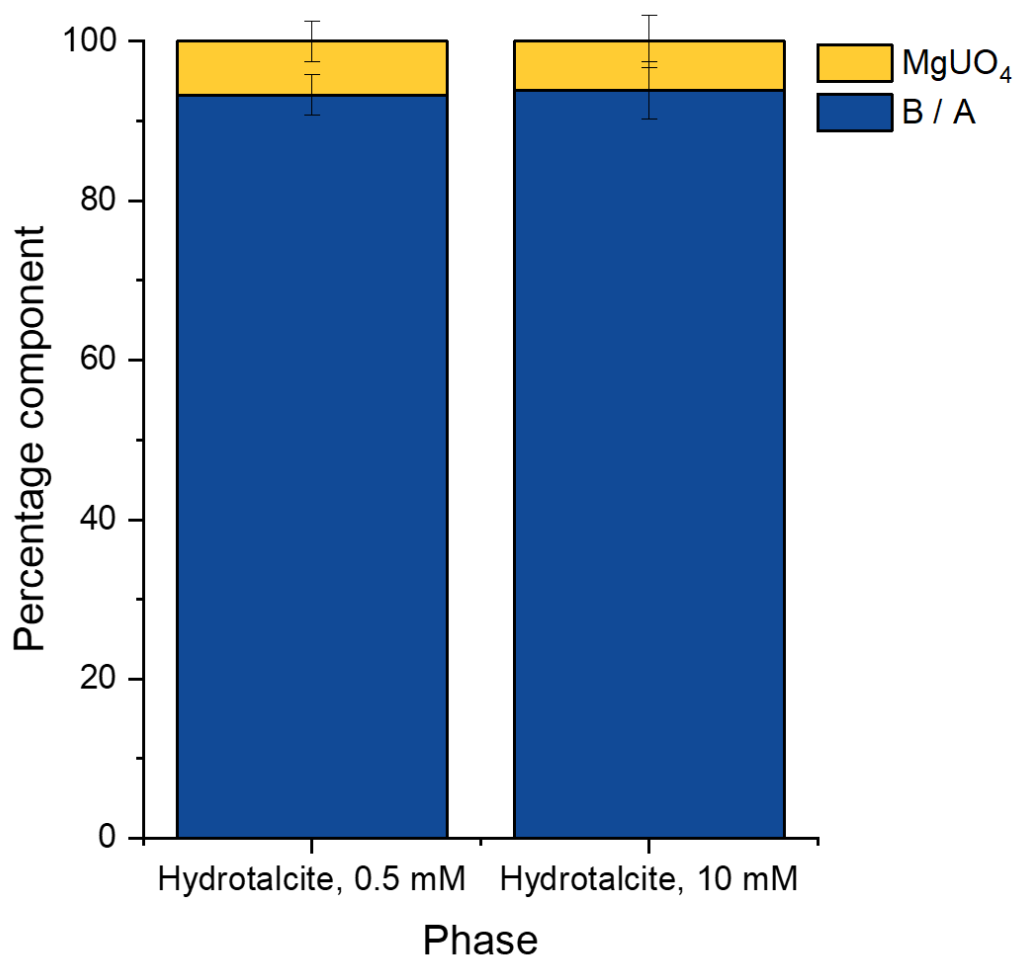


Figure 5.23: Linear combination fitting of U(VI)-contacted hydrotalcite phases. B / A = bayleyite / andersonite.

Table 5.13: Weighted fraction of components in XANES signal of U-contacted hydrotalcite phases using LCF.

Sample	R-factor	Total weighting	Andersonite		MgUO ₄	
			Wt.	ΔE	Wt.	ΔE
Hydrotalcite [U]= 0.5 mM	0.002	1.000	0.933(25)	0.90(7)	0.067(25)	-1.6(1.2)
Hydrotalcite [U= 10 mM	1×10^{-3}	1.000	0.939(18)	0.36(6)	0.061(33)	-0.8(1.1)

Bayleyite / andersonite was identified as the predominant contribution to the signal for both of the U(VI)-contacted hydrotalcite phases which could primarily be an indication that uranium was maintained as the uranyl moiety in the +6 oxidation state. However, given that bayleyite is a magnesium uranyl carbonate ($\text{Mg}_2(\text{UO}_2)(\text{CO}_3)_3 \cdot 18\text{H}_2\text{O}$) there is potential for this phase to form in this system. MgUO_4 was also identified as contributing to a small percentage of the signal (~6 %) in both phases.

5.3.7 X-ray absorption spectroscopy: EXAFS

Scattering paths for EXAFS fitting were generated from FEFF calculations using appropriately selected CIF files as the input. In the first instance, models for the fitting of X-ray scatterers to the uranium standards were devised. The value of the amplitude reduction factor (S_0^2) for a uranium absorber measured on beamline B18 (DLS) was refined in the model for UO_2 as 0.859 (see **Chapter 4**) and was thereafter set in the model for the fitting of all other uranium standards and samples. The k^3 -weighted spectra, Fourier transform radial plots and EXAFS models for all of the uranium standards have already been given in **Chapter 4**.

The k^3 -weighted spectra of the U(VI)-contacted C-S-H phases shown **Figures 5.24 to 5.26** with corresponding Fourier transform radial plots.

5.3.7.1 EXAFS fitting of U(VI)-contacted C-S-H phases

For measurements where the k-space resolution allowed, the fitting was performed between ~3.5 to ~12.5 \AA^{-1} , with the k-range selected where the signal was equal to 0 using a $dk = 0$ Hanning window. For measurements with poor resolution, the k-range was only extended to ~10 \AA^{-1} . Pathways were generated and fitted between 1 - 5 \AA in R-space using a $dR = 1$ Hanning window. ΔE was allowed to vary as a global parameter. The margin of error for all the refined parameters (S_0^2 , N, R, σ^2 , ΔE ; defined previously in **Chapter 3**) was calculated by the Artemis software for a given fit. Pathways were generally omitted if the errors were larger than the values refined for each parameter.

Each phase that was fitted exhibited a split equatorial shell (i.e. two or more O_{eq} distances), which has previously been reported for other EXAFS models of U(VI) in C-S-H environments [67,70], as well as for uranophane [70,241], soddyite [70] and schoepite [243] (**Chapter 4**), and indicates disorder [243].

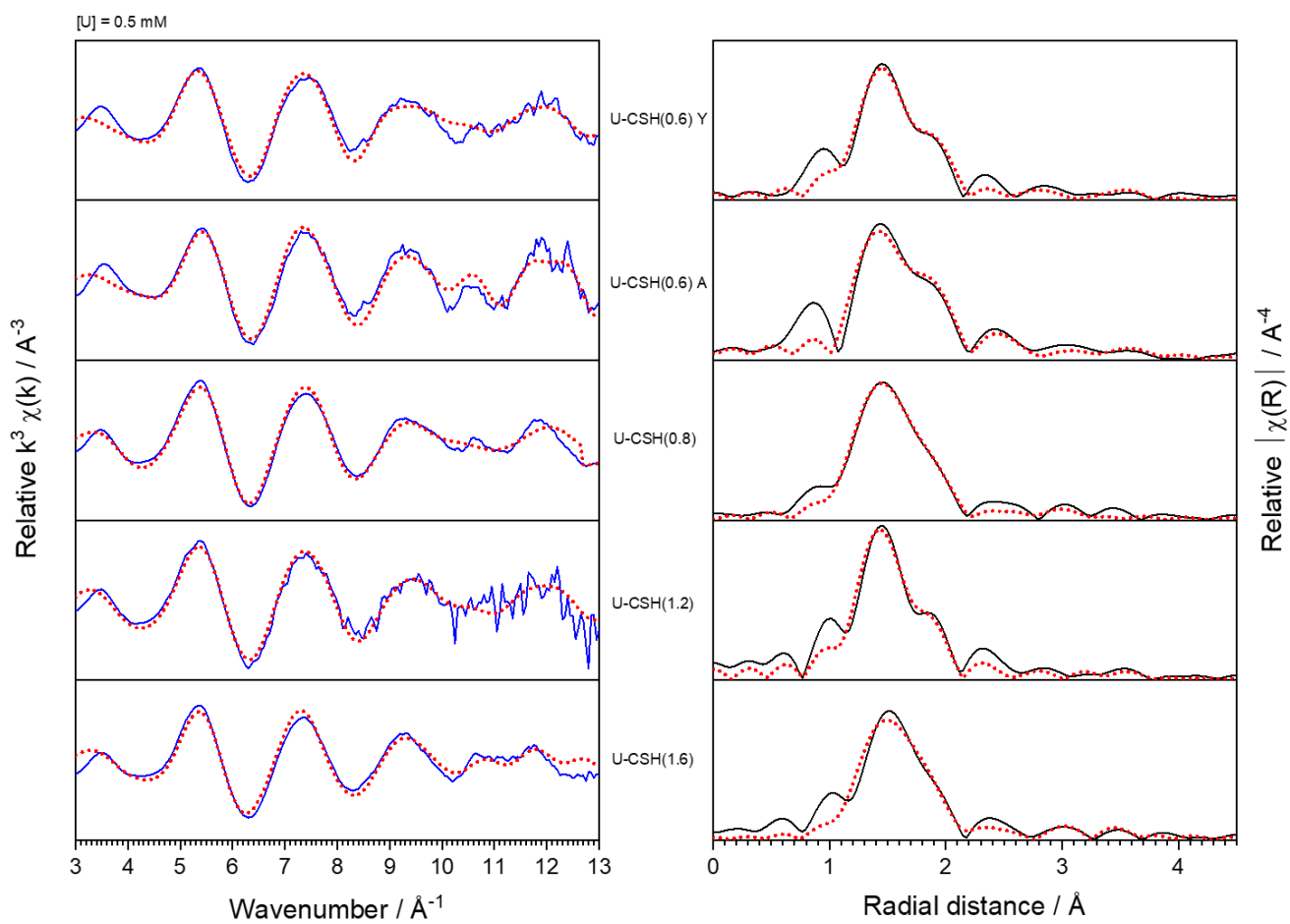


Figure 5.24: k^3 -weighted spectra and Fourier transform radial plots for 0.5 mM U(VI)-contacted C-S-H phases.

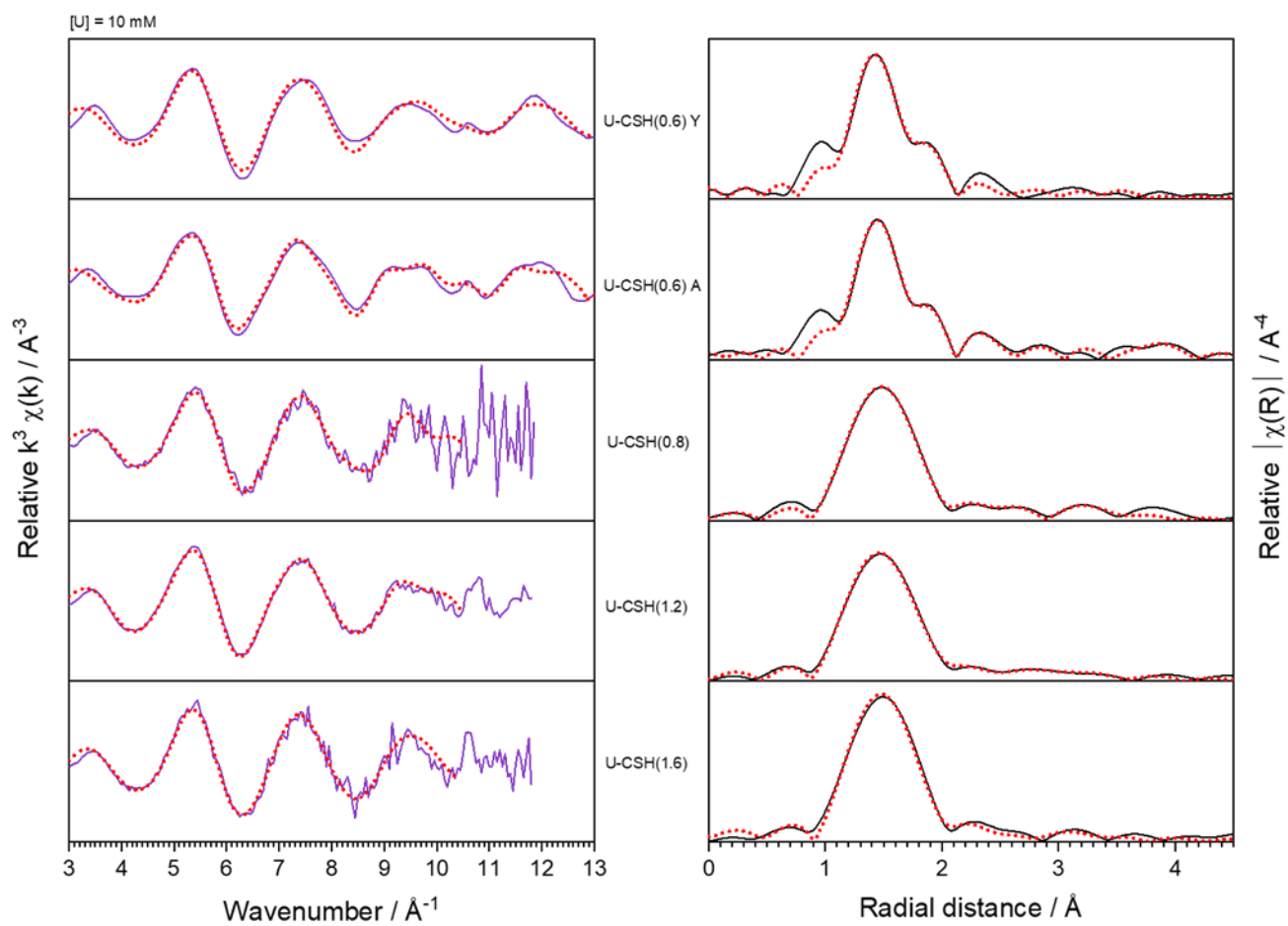


Figure 5.25: k^3 -weighted spectra and Fourier transform radial plots for 10 mM U(VI)-contacted C-S-H phases.

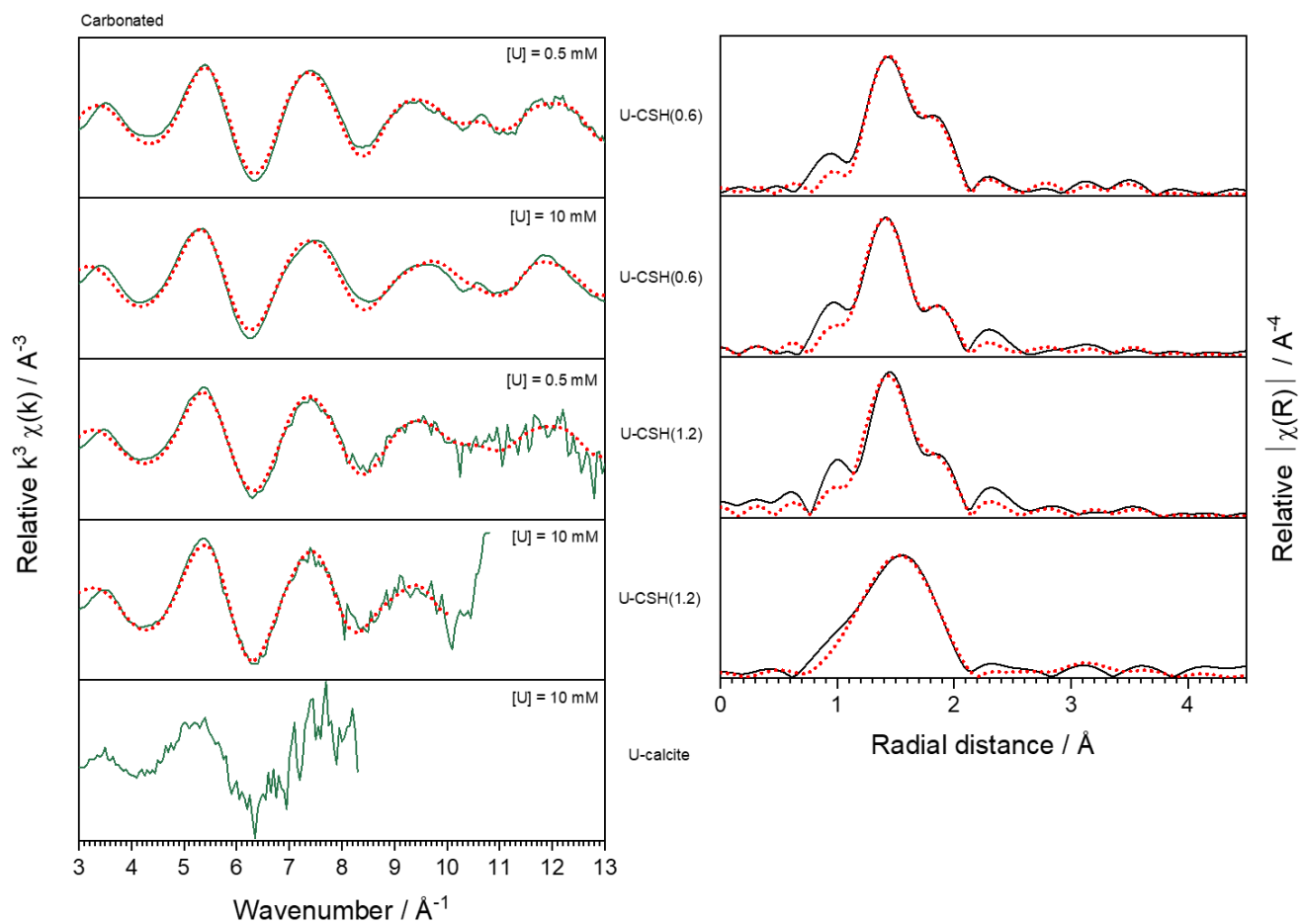


Figure 5.26: k^3 -weighted spectra and Fourier transform radial plots for pre-carbonated U(VI)-contacted C-S-H phases.

5.3.7.2 Fitting of 0.5 mM U(VI)-contacted C-S-H phases

Given that previous literature has already conceived a uranyl silicate-type coordination for U(VI) sorption whereby the uranyl moiety is retained, the phases were initially fitted as uranyl silicates using the CIF file for haiweeite ($\text{Ca}(\text{UO}_2)_2(\text{Si}_5\text{O}_{12})(\text{OH})_2 \cdot 6\text{H}_2\text{O}$) [211]. In addition to the literature findings, no additional precipitated U(VI) phases were identified by XRD for the U(VI) contacted samples and the results from linear combination fitting also indicate that the phases have significant contribution in their XANES signal from haiweeite-type coordination, i.e. a uranyl silicate.

For all 0.5 mM U(VI)-contacted C-S-H phases the first O_{ax} shell (referred to as ax), second O_{eq} shell (referred to as eq) and a silicon shell were fitted. The results are given in **Table 5.14**.

U-CSH(0.6) Y: The first oxygen (ax) distance was refined at $1.827 \pm 0.011 \text{ \AA}$ with $N_{\text{O}1} = 2.88 \pm 0.28$. Two subsequent oxygen (eq) paths were fitted with N_{O} values of 1 and 3, but a third oxygen pathway was not favourable. Two silicon pathways were also fitted both with $N_{\text{Si}} = 1$. Either addition of, or replacement of silicon scatterers with, a calcium distance of $\sim 3.5 \text{ \AA}$ (akin to a calcium uranate [258]) did not improve the fit and led to an increase of ΔE or correlation between $N_{\text{O}1}$ and σ^2_{O} , respectively.

U-CSH(0.6) A: The aged sample could be fitted to same model as the young sample. The first oxygen (ax) distance was refined at $1.802 \pm 0.008 \text{ \AA}$ with $N_{\text{O}1} = 1.85 \pm 0.19$. Either addition of, or replacement of silicon scatterers with, a calcium distance of $\sim 3.5 \text{ \AA}$ did not improve the fit and led to an increase of ΔE and an increased R-factor.

U-CSH(0.8): The first oxygen (ax) distance was refined at $1.800 \pm 0.013 \text{ \AA}$ with $N_{\text{O}1} = 2.73 \pm 0.42$. The subsequent oxygen (eq) pathways were fitted with the same N_{O} values as in the haiweeite model (see **Chapter 4**) of 1, 3 and 2. Three silicon pathways were fitted with the same N_{Si} values as in the haiweeite model of 1, 1 and 2. Either addition of, or replacement of silicon scatterers with, a calcium distance of $\sim 3.5 \text{ \AA}$ did not improve the fit and led to an increase of ΔE or a significant number of correlations between variables, respectively.

U-CSH(1.2): The first oxygen (ax) distance was refined at $1.804 \pm 0.011 \text{ \AA}$ with $N_{\text{O}1} = 2.38 \pm 0.33$. The subsequent oxygen (eq) paths were fitted with the same N_{O} values as in the haiweeite model of 1, 3 and 2. Three silicon pathways were fitted with N_{Si} values fixed at 1, 2 and 2. Either addition of, or replacement of silicon scatterers with, a calcium distance of $\sim 3.5 \text{ \AA}$ did not improve the fit and led to a large ΔR_{Ca} (and negative σ^2_{Ca}) or correlations between $N_{\text{O}1}$ and σ^2_{O} / $\Delta R_{\text{O}1}$ and ΔE , respectively.

U-CSH(1.6): The ΔE value of was correlated with $N_{\text{O}1}$ in that refining both parameters led to a ΔE value of over +10 eV. Therefore, $N_{\text{O}1}$ was set in the model as 2. The first oxygen (ax)

distance was refined at $1.812 \pm 0.008 \text{ \AA}$. Three subsequent oxygen (eq) paths were fitted with $N_{\text{O}} = 3, 2$ and 1 , respectively. Three silicon pathways were initially fitted with the same N_{Si} values as in the haiweeite model of $1, 1$ and 2 . However, the fit was significantly improved, with observation by eye and with a reduced R-factor (0.021 down to 0.017), by addition of a calcium scatterer at $3.50 \pm 0.03 \text{ \AA}$ in place of the second silicon.

The main differences to note between the fits of the 0.5 mM U(VI)-CSH phases were:

- (i) The distance refined for the axial oxygen shell (no general trend)
- (ii) The number of equatorial oxygen pathways fitted (a very general increase with Ca/Si ratio; 2 for U-CSH(0.6) Y and A, and 3 for U-CSH(0.8,1.2,1.6))
- (iii) The addition of a calcium scatterer for the U-CSH(1.6) phase.

5.3.7.3 Fitting of $10 \text{ mM U(VI)-contacted C-S-H}$ phases

The formation of the Ca-weebsite phase identified by XRD ($\text{Ca}_2(\text{UO}_2)_2\text{Si}_6\text{O}_{15} \cdot 10\text{H}_2\text{O}$) for the aged U-CSH(0.6) phase and the high release of calcium from the C-S-H solids in 10 mM U(VI) solution, relative to silicon release (see *Section 5.3.3.1*), is an indication that solid uranyl-silicate precipitates may predominantly form in the 10 mM series. The results from linear combination fitting also indicate that the phases have significant contribution in their XANES signal from haiweeite-type coordination, i.e. a uranyl silicate. The phases were therefore initially fitted as uranyl silicates using the CIF file for haiweeite ($\text{Ca}(\text{UO}_2)_2(\text{Si}_5\text{O}_{12})(\text{OH})_2 \cdot 6\text{H}_2\text{O}$) [211].

For all $10 \text{ mM U(VI)-contacted C-S-H}$ phases the first O_{ax} shell (referred to as ax), second O_{eq} shell (referred to as eq) and a silicon shell were fitted. A uranium distance could only be fitted in the CSH(0.6) A sample. The results are given in **Table 5.15**.

U-CSH(0.6) Y: The first oxygen (ax) distance was refined at $1.807 \pm 0.011 \text{ \AA}$ with $N_{\text{O}1} = 2.41 \pm 0.40$. Three subsequent oxygen (eq) paths were fitted with N_{O} values of $2, 3$ and 1 , respectively. Three silicon pathways were fitted with N_{Si} values fixed at $1, 2$ and 2 .

U-CSH(0.6) A: The aged sample was fit to the same model as the young sample and within error the refined parameters for the oxygen (ax and eq) and silicon shells were the same. Unlike in the young sample, an additional uranium pathway was also fitted at $3.99 \pm 0.04 \text{ \AA}$ with $N_{\text{U}1} = 2$.

The spectra for the remaining $10 \text{ mM U(VI)-contacted}$ phases were not as well-resolved in k space out to $\sim 12.5 \text{ \AA}^{-1}$ and could only be fitted to $\sim 10 \text{ \AA}^{-1}$. The value of $N_{\text{O}1}$ was set at 2 .

U-CSH(0.8): The first oxygen (ax) distance was refined at 1.798 ± 0.011 Å. Two subsequent oxygen (eq) paths were fitted with N_{O} values of 3 and 2, respectively. Three silicon pathways were fitted with N_{Si} values of 1, 1 and 2.

U-CSH(1.2): The same model as for CSH(0.8) was fitted, and the first oxygen (ax) distance was refined at 1.801 ± 0.006 Å.

U-CSH(1.6): The same model as for CSH(0.8) was fitted, and the first oxygen (ax) distance was refined at 1.813 ± 0.007 Å.

The main observations to note for the 10 mM U(VI)-contacted CSH phases (0.8 to 1.6, measured on beamline BMM) are a slight increase in the axial oxygen distance, equatorial oxygen distances and silicon distances with increasing Ca/Si ratio, albeit within error.

5.3.7.4 Fitting of pre-carbonated U(VI)-contacted C-S-H phases

U-CSH(0.6) C ([U] = 0.5 mM): The first oxygen (ax) distance was refined at 1.811 ± 0.009 Å with $N_{\text{O}1} = 2.18 \pm 0.27$. Three subsequent oxygen (eq) paths were fitted with N_{Ox} values of 2, 3 and 1, respectively. Three silicon pathways were fitted with N_{Si} values fixed at 1, 2 and 2.

U-CSH(0.6) C ([U] = 10 mM): The first oxygen (ax) distance was refined at 1.800 ± 0.010 Å with $N_{\text{O}1} = 2.45 \pm 0.38$. Three subsequent oxygen (eq) paths were fitted with N_{Ox} values of 2, 3 and 1, respectively. Three silicon pathways were fitted with N_{Si} values fixed at 1, 2 and 2.

U-CSH(1.2) C ([U] = 0.5 mM): The first oxygen distance was refined at 1.816 ± 0.010 Å with $N_{\text{O}1} = 2.71 \pm 0.33$. Three subsequent oxygen paths were fitted with N_{O} values of 2, 3 and 1, respectively. Three silicon pathways were fitted with N_{Si} values fixed at 1, 2 and 2.

U-CSH(1.2) C ([U] = 10 mM): The spectra was not as well-resolved in k space out to ~ 12.5 Å⁻¹ and could only be fitted up to 10.2 Å⁻¹. The value of $N_{\text{O}1}$ was set at 2. The first oxygen distance was refined at 1.798 ± 0.011 Å. Two subsequent oxygen paths were fitted with N_{O} values of 3 and 2, respectively. Three silicon pathways were fitted with N_{Si} values fixed at 1, 1 and 2.

There was no obvious trend seen for the pre-carbonated phases with increasing Ca/Si ratio or concentration of U(VI). The results are given in **Table 5.16**.

Table 5.14: EXAFS fits of 0.5 mM U(VI)-contacted C-S-H phases performed between k-range ~3.5 - ~12.5 Å⁻¹ and R-range 1 - 5 Å.

[U] = 0.5 mM	ΔE	R_{U-o}	N_o	σ^2_o	R_{U-si}	N_{Si}	σ^2_{Si}
U-CSH(0.6) Y R-factor = 0.016	7.78(2.20)	1.827(11) (ax)	2.88(28)	0.0050(8)	3.20(5)	1	0.009(4)
		2.20(2) (eq)	1		3.68(7)	1	
		2.30(1) (eq)	3		3.94(5)	2	-
U-CSH(0.6) A R-factor = 0.017	3.43(2.00)	1.802(8) (ax)	1.85(19)	0.0016(7)	3.08(2)	1	0.004(2)
		2.16(2) (eq)	1		3.65(3)	1	
		2.27(1) (eq)	3		3.86(3)	2	
U-CSH(0.8) R-factor = 0.010	1.64(3.03) [†]	1.800(13) [†] (ax)	2.73(42)	0.005(1)	3.12(5)	1	0.012(8)
		2.16(4) (eq)	1		3.52(13)	1	
		2.23(2) (eq)	3		3.66(52)	2	
		2.32(3) (eq)	2		-	-	-
U-CSH(1.2) R-factor = 0.006	4.95(2.27)	1.804(11) (ax)	2.38(33)	0.004(1)	3.10(2)	1	0.005(1)
		2.22(3) (eq)	1		3.63(3)	2	
		2.26(2) (eq)	3		3.84(3)	2	
		2.42(2) (eq)	2		-	-	-
U-CSH(1.6) R-factor = 0.017	0.4(2.0)	1.812(8) (ax)	2	0.0040(6)	3.05(2)	1	0.007(2)
		2.24(5) (eq)	1		3.50(3) (Ca)	1	(0.005(2))
		2.21(2) (eq)	3		3.78(3)	2	
		2.34(2) (eq)	2		-	-	-

[†]correlation between variables

Table 5.15: EXAFS fits of 10 mM U(VI)-contacted C-S-H phases performed between k-range ~3.5 - ~12.5 Å⁻¹ * and R-range 1 - 5 Å.

[U] = 10 mM	ΔE	R _{U-o}	N _o	σ ² _o	R _{U-Si}	N _{Si}	σ ² _{Si}	R _{U-U}	N _U	σ ² _U
U-CSH(0.6) Y R-factor = 0.011	5.46(2.76)	1.807(11) (ax)	2.41(40)	0.003(1)	3.14(5)	1	0.009(4)	-	-	-
		2.19(2) (eq)	2		3.65(6)	2		-	-	-
		2.32(2) (eq)	3		3.88(6)	2		-	-	-
		2.48(5) (eq)	1		-	-	-	-	-	-
U-CSH(0.6) A R-factor = 0.008	2.7(3.0)	1.805(11) (ax)	2.39(32)	0.004(1)	3.13(3)	1	0.005(2)	3.99(4)	2	0.009(3)
		2.19(2) (eq)	2		3.64(3)	2		-	-	-
		2.31(3) (eq)	3		3.83(4)	2		-	-	-
		2.47(5) (eq)	1		-	-	-	-	-	-
U-CSH(0.8) * R-factor = 0.009 (NSLS-II)	5.95(2.38)	1.798(11) (ax)	2	0.0021(5)	3.12(3)	1	0.005(3)	-	-	-
		2.22(2) (eq)	3		3.42(4)	1		-	-	-
		2.38(3) (eq)	2		3.69(3)	2		-	-	-
U-CSH(1.2) * R-factor = 0.004 (NSLS-II)	5.60(1.37)	1.801(6) (ax)	2	0.0010(5)	3.16(2)	1	0.002(2)	-	-	-
		2.24(1) (eq)	3		3.49(5)	1		-	-	-
		2.40(2) (eq)	2		3.71(3)	2	-	-	-	-
U-CSH(1.6) * R-factor = 0.008 (NSLS-II)	8.09(1.65)	1.813(7) (ax)	2	0.0016(4)	3.17(5)	1	0.013(7)	-	-	-
		2.25(1) (eq)	3		3.66(11)	1		-	-	-
		2.42(2) (eq)	2		3.82(6)	2		-	-	-

*poor resolution in k-space, fitted out to ~10 Å⁻¹. Samples measured at NSLS-II also had S₀² set as 0.911.

Table 5.16: EXAFS fits of pre-carbonated U(VI)-contacted C-S-H phases performed between k-range ~3.5 - ~12.5 Å⁻¹ * and R-range 1 - 5 Å.

Carbonated	ΔE	R_{U-O} (1)	N_O (1)	σ^2_O (1,2)	R_{U-Si}	N_{Si}	σ^2_{Si}
U-CSH(0.6) [U] = 0.5 mM R-factor = 0.011	6.97(2.00)	1.811(9)	2.18(27)	0.0028(9)	3.12(3)	1	0.008(2)
		2.21(1) (eq)	2		3.65(3)	2	
		2.31(1) (eq)	3		3.87(4)	2	
		2.46(3) (eq)	1		-	-	-
U-CSH(0.6) [U] = 10 mM R-factor = 0.012	4.10(2.68)	1.800(10) (aq)	2.45(38)	0.003(1)	3.14(5)	1	0.008(4)
		2.20(2) (eq)	2		3.64(5)	2	
		2.33(3) (eq)	3		3.85(6)	2	
		2.49(5) (eq)	1		-	-	-
U-CSH(1.2) [U] = 0.5 mM R-factor = 0.017	6.93(2.12)	1.816(10) (aq)	2.71(33)	0.004(1)	3.13(5)	1	0.009(3)
		2.21(1) (eq)	2		3.67(5)	2	
		2.31(2) (eq)	3		3.89(6)	2	
		2.49(4) (eq)	1		-	-	-
U-CSH(1.2) * [U] = 10 mM R-factor = 0.019 (NSLS-II)	-2(3)	1.767(16) (aq)	2	0.004(1)	3.08(5)	1	0.003(4)
		2.22(2) (eq)	3		3.33(7)	1	
		2.27(7) (eq)	2		3.59(4)	2	

* poor resolution in k-space, fitted out to ~10 Å⁻¹. Samples measured at NSLS-II also had S_0^2 set as 0.911.

The k^3 -weighted spectra of the U(VI)-contacted hydrotalcite phases are shown **Figure 5.27** with corresponding Fourier transform radial plots.

5.3.7.5 EXAFS fitting of U(VI)-contacted hydrotalcite phases

The fitting for hydrotalcite phases was performed between 3.5 to 12 \AA^{-1} (the k -range was selected where the signal was equal to 0 using a $dk = 0$ Hanning window). Pathways were generated and fitted between 1 - 5 \AA in R-space using a $dR = 1$ Hanning window. ΔE was allowed to vary as a global parameter. The CIF files for andersonite, bayleyite and MgUO_4 were used to generate different pathways [203,216,218]. The results are given in **Table 5.17**.

0.5 mM U-hydrotalcite: The first oxygen (ax) distance was refined at $1.817 \pm 0.009 \text{ \AA}$ with $N_{O1} = 2.42 \pm 0.23$. The subsequent oxygen (eq) pathway was refined at $2.44 \pm 0.01 \text{ \AA}$ with $N_{O2} = 4$. A uranium distance was fitted at $3.40 \pm 0.03 \text{ \AA}$ with $N_U = 2$, from the pathway generated for the U-U distance in MgUO_4 . A subsequent magnesium distance was also fitted at $3.83 \pm 0.03 \text{ \AA}$ with $N_{Mg} = 4$.

10 mM U-hydrotalcite: This phase was fitted with the same model as the 0.5 mM U(VI)-contacted phase, and the distances refined were the same within error. The value of N_{O1} , for the axial oxygens, was slightly increased at $2.80 \pm 0.22 \text{ \AA}$. The best value of N_{Mg} for the magnesium scatterer was also slightly increased, set at 6.

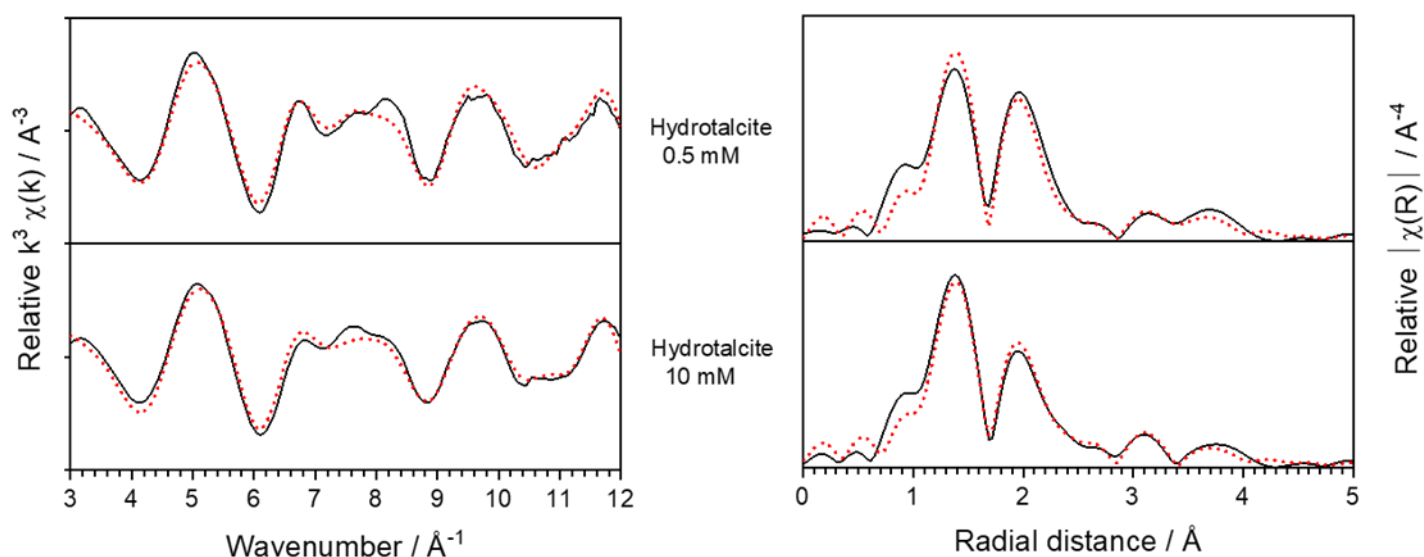


Figure 5.27: k^3 -weighted spectra and Fourier transform radial plots for U(VI)-contacted hydrotalcite phases.

Table 5.17: EXAFS fits of U(VI)-contacted hydrotalcite phases performed between k-range 3.5 - 12 Å⁻¹ and R-range 1 - 5 Å.

Hydrotalcite	ΔE	R _{U-o}	N _o	σ^2_o	R _{U-c}	N _c	σ^2_c	R _{U-U}	N _U	σ^2_U	R _{U-Mg}	N _{Mg}	σ^2_{Mg}
[U] = 0.5 mM R-factor = 0.018	8.4(1.5)	1.817(9) (ax)	2.42(23)	0.0033(8)	2.93(2)	3	0.002(2)	3.40(3)	2	0.004(2)	3.83(3)	4	0.001(2)
		2.44(1) (eq)	4										
[U] = 10 mM R-factor = 0.009	9.4(1.4)	1.819(9) (ax)	2.80(22)	0.0047(8)	2.93(1)	3	0.002(2)	3.39(2)	2	0.005(2)	3.84(2)	6	0.006(2)
		2.44(1) (eq)	4										

5.3.8 ^{29}Si Nuclear magnetic resonance spectroscopy

5.3.8.1 C-S-H with Ca/Si = 0.6

The normalised ^{29}Si NMR spectra of CSH(0.6) as (i) a pure phase, (ii) contacted with 0.5 mM U(VI) and (iii) contacted with 10 mM U(VI) are shown in **Figure 5.28**.

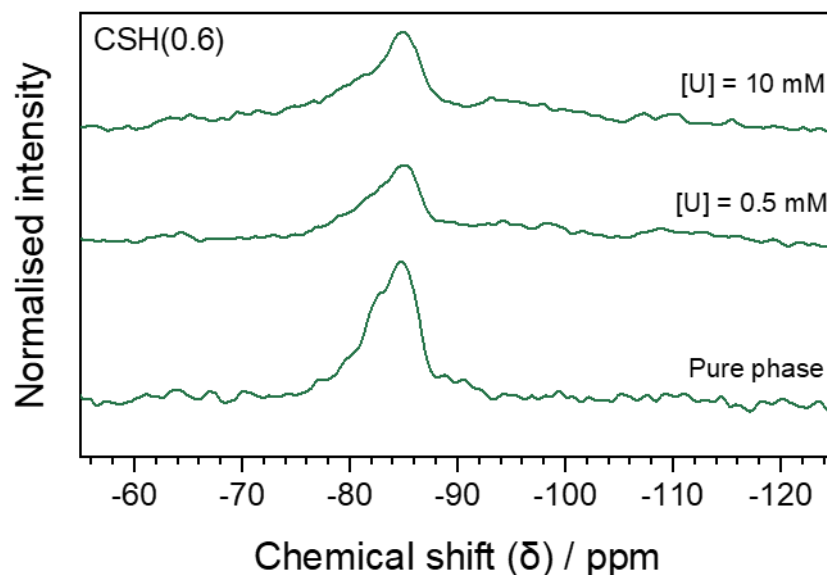


Figure 5.28: Normalised ^{29}Si spectra of CSH(0.6) under various U(VI)-contacting conditions.

The pure CSH(0.6) phase displayed a signal between $\delta = -78$ to -90 ppm that decreased in intensity with addition of U(VI). An increase in the signal at higher chemical shifts was also seen with U(VI) addition. **Figure 5.29** shows the individual spectra and the assignment of different tetrahedral silicon Q^n species [168] using deconvolution fitting of Gaussian peaks. The percentages of each Q^n species calculated for each system are given in **Table 5.18**.

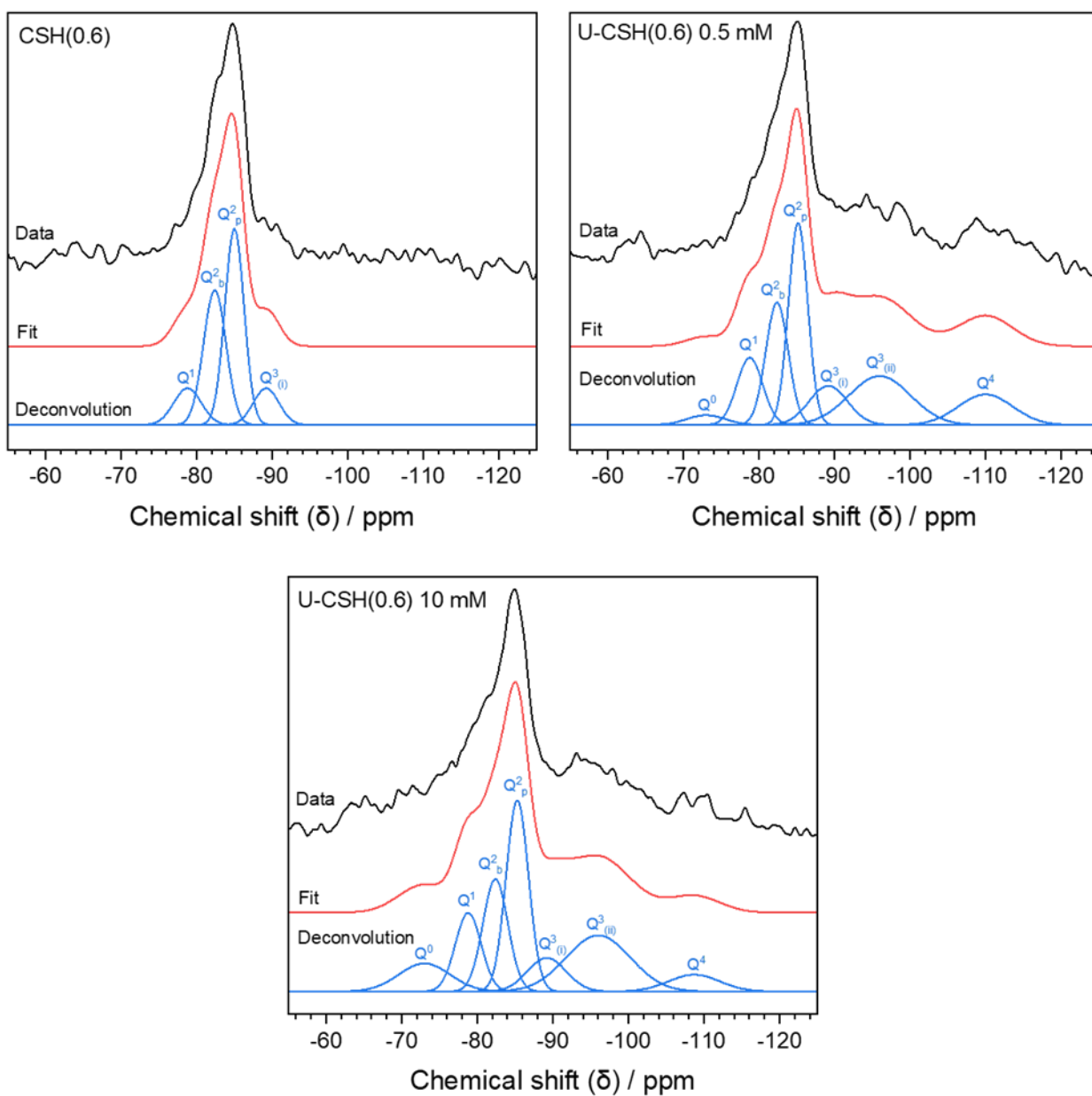


Figure 5.29: Non-normalised ^{29}Si spectra of CSH(0.6) under various U(VI)-contacting conditions and Si Q^n species deconvolution.

Table 5.18: Percentage of Si Qⁿ species in CSH(0.6) and U(VI)-contacted CSH(0.6) systems. Error calculated as a % of the noise contribution to signal.

	Ca/Si *	% contribution to signal (and chemical shift / ppm)						
		Q ⁰	Q ¹	Q ^{2_b}	Q ^{2_p}	Q ^{3_(i)}	Q ^{3_(ii)}	Q ⁴
CSH(0.6) (error ± 7.8 %)	0.67	-	12 (-78.8)	35 (-82.5)	43 (-85)	11 (-89.2)	-	-
U-CSH(0.6) 0.5 mM (error ± 7.9 %)	0.81	3 (-73)	12 (-78.7)	18 (-82.4)	26 (-85.2)	10 (-89.2)	20 (-96)	11 (-110)
U-CSH(0.6) 10 mM (error ± 5.4 %)	0.83	9 (-73)	12 (-78.8)	17 (-82.4)	26 (-85.3)	8 (-89.2)	22 (-96)	5 (-108.7)

*determined using **Equation 5.1** [229]

The silicon Qⁿ species in the CSH(0.6) phase are fairly typical of a pure phase C-S-H at lower Ca/Si ratio [259,260]. The Q¹ contribution (12 %) is the signal arising from silicon tetrahedron dimers or silicon chain termination points, the Q^{2_b} (35 %) and Q^{2_p} (43 %) contributions arise from mid-chain silicon tetrahedron (bridging and pairing, respectively) and the Q³ contribution (11 %) is the signal arising from cross-linked silicon tetrahedra. These sites are referenced in **Figure 5.30** with the regions in which they occur in the ²⁹Si NMR spectrum, taken directly from *Walkley and Provis* [168], for illustration.

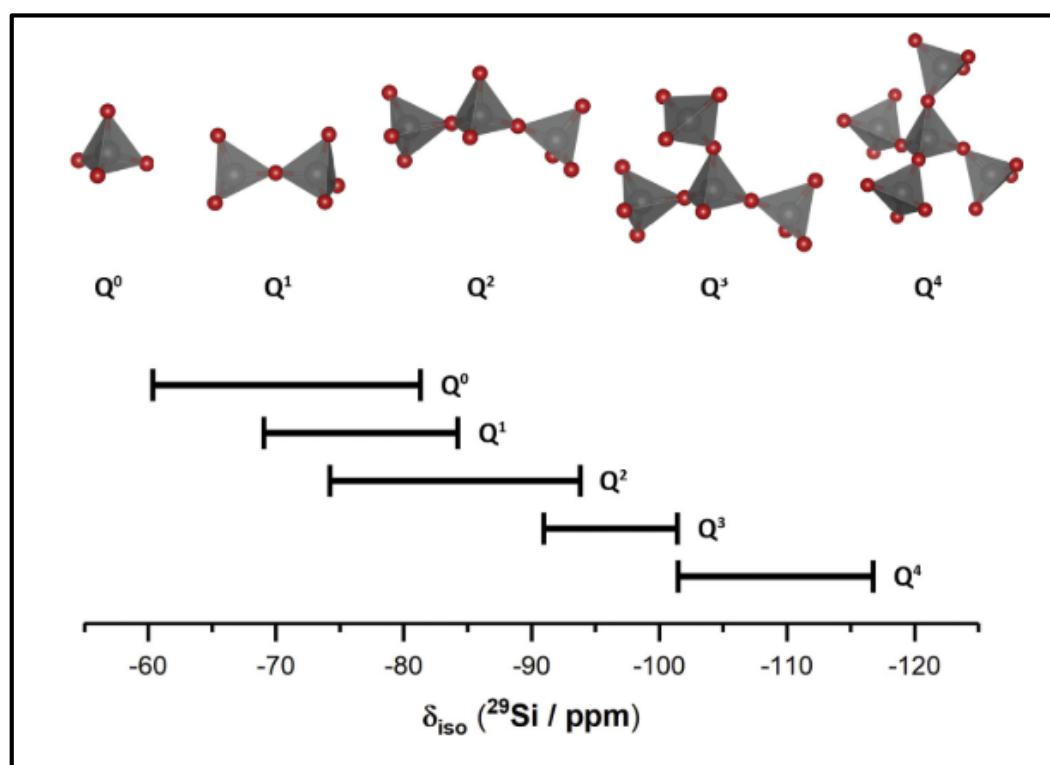


Figure 5.30: Qⁿ Si tetrahedral sites identifiable by ²⁹Si NMR, taken from *Walkley & Provis* [168].

With addition of U(VI) to the CSH(0.6) phases, it is clear that there was retention of the Q¹, Q² and Q³⁽ⁱ⁾ sites, albeit with a slight change in signal contribution, that signify retention of the original C-S-H structure. This is in good agreement with the XRD data that also displayed the presence of the C-S-H phase after contact with 0.5 mM U(VI), and (but to a lesser extent) with 10 mM U(VI). The percentage contribution of the Q¹ species remained at 12 % in both cases but there was also a small contribution from Q⁰ (hydrated silicon monomers) that was fitted at 3 % and 9 % for the 0.5 mM and 10 mM U(VI)-contacted phases, respectively, likely as a result of the acidic pH dissolving calcium from the phase and forming a silica gel. The relative signals from the Q² sites both decreased by ~17 % for bridging and pairing species, respectively, in each of the U(VI)-contacted samples, which is consistent with an increase in Ca/Si ratio as highlighted in **Table 5.18**.

The percentage signal from Q³⁽ⁱ⁾ displayed a slight decrease on moving from pure phase, to 0.5 mM U(VI)-contacted, to 10 mM U(VI)-contacted. The emergence of an additional Gaussian contribution in the Q³ region at $\delta = -96$ ppm was also significant, denoted as Q³⁽ⁱⁱ⁾, at 20 % and 22 % for the low and high concentrations of U(VI), respectively. In addition to this, a Q⁴ signal (fully polymerised silicon tetrahedron) was also observed at $\delta = \sim -110$ ppm with a contribution of 11 % and 5 %, respectively. These Qⁿ species indicate a change in the silicon environment as a result of U(VI) addition, potentially arising from the Q³ and Q⁴ species of a uranyl silicate phase, as discussed further in *Section 5.4.1.2*).

5.3.8.2 C-S-H with Ca/Si = 1.2

The normalised ^{29}Si NMR spectra of CSH(1.2) as (i) a pure phase, (ii) contacted with 0.5 mM U and (iii) contacted with 10 mM U are shown in **Figure 5.31**.

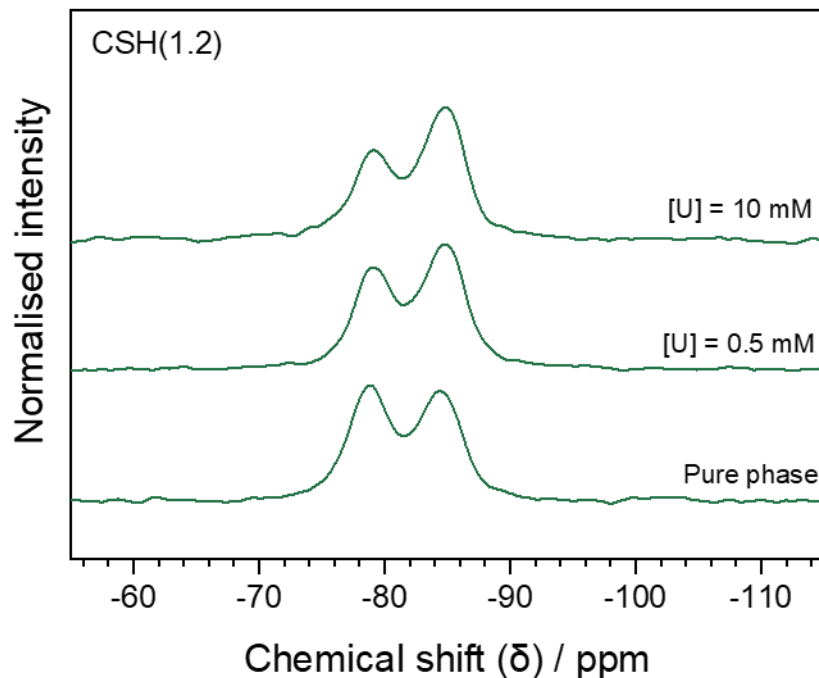


Figure 5.31: Normalised ^{29}Si spectra of CSH(1.2) under various U(VI)-contacting conditions.

The pure CSH(1.2) phase and U(VI)-contacted phases displayed a signal between $\delta = -74$ to -90 ppm. **Figure 5.32** shows the individual spectra and the assignment of different tetrahedral silicon Q^n species [168] using deconvolution fitting of Gaussian peaks, and the percentages of each Q^n species for each system are given in **Table 5.19**.

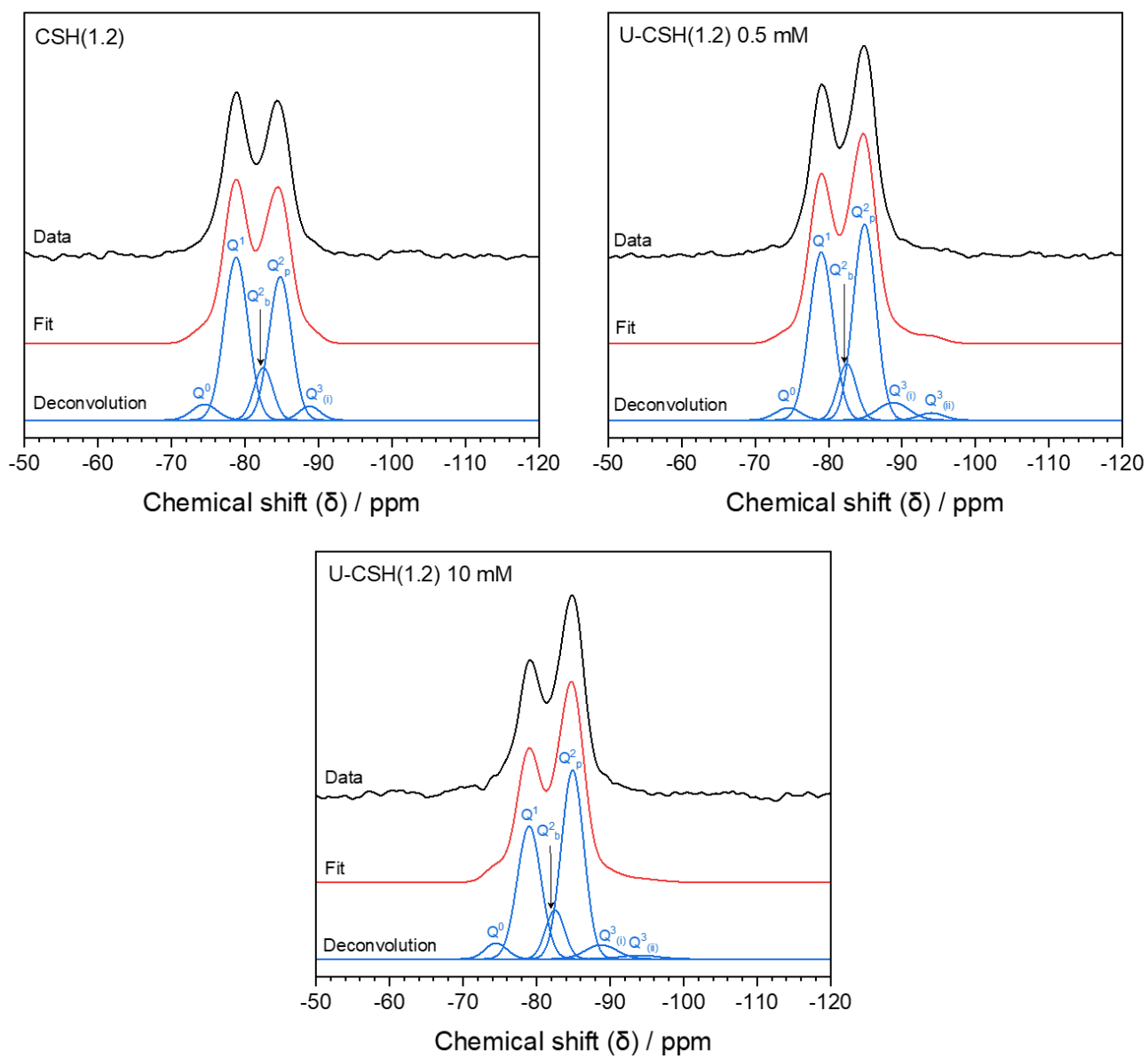


Figure 5.32: Non-normalised ^{29}Si spectra of CSH(1.2) under various U(VI)-contacting conditions and Si Q^n species deconvolution.

Table 5.19: Percentage of Si Qⁿ species in CSH(1.2) and U(VI)-contacted CSH(1.2) systems. Error calculated as a % of the noise contribution to signal.

	Ca/Si _*	% contribution to signal (and chemical shift / ppm)						
		Q ⁰	Q ¹	Q ^{2_b}	Q ^{2_p}	Q ^{3_(i)}	Q ^{3_(ii)}	Q ⁴
CSH(1.2) (noise ± 1.1 %)	1.1	4 (-74.5)	44 (-78.8)	11 (-82.5)	37 (-84.8)	3 (-88.8)	-	-
U-CSH(1.2) 0.5 mM (noise ± 2.8 %)	0.96	3 (-74.5)	38 (-79)	10 (-82.5)	42 (-84.9)	5 (-88.8)	2 (-94)	-
U-CSH(1.2) 10 mM (noise ± 1.7 %)	0.93	4 (-74.5)	34 (-79)	10 (-82.5)	46 (-84.9)	5 (-88.8)	1 (-94)	-

*determined using **Equation 5.1** [229]

The silicon Qⁿ species in the CSH(1.2) phase were typical of a pure phase C-S-H at moderate range Ca/Si ratio [259–264]. The Q¹ and Q^{2_p} species contributed to the majority of the signal, at 44 % and 37 %, respectively. There was also a small Q³ (Q^{3_(i)}) signal identified (3 %) and, unlike in the CSH(0.6) phase, a small signal from Q⁰ species (4 %) which could be a result of unreacted silica.

The addition of U(VI) to the CSH(1.2) phase at both U(VI) concentrations saw a decrease in the Q¹ signal relative to an increase in the Q^{2_p} signal, by ~5-6 % at 0.5 mM U(V) and a further 4 % at 10 mM U(VI). This is a result of the higher release of calcium from the C-S-H phases, relative to silicon, which was further increased at the higher concentration of U(VI), thus reducing the Ca/Si ratio of the C-S-H phase. The presence of these signals, however, still indicates the retention of the C-S-H structure on addition of U(VI), just with a decrease in the Ca/Si ratio, as shown in **Table 5.19**.

As observed in the U(VI)-contacted CSH(0.6) phases, the emergence of a signal from a second Q³ species (Q^{3_(ii)}) is potentially evident at -94 ppm. However, the percentage contribution of this species is very low (≤ 2 %) and less than the calculated noise of the spectra, therefore this contribution is negligible.

5.3.9 ^{27}Al Nuclear magnetic resonance spectroscopy

5.3.9.1 Ettringite

The normalised ^{27}Al spectra of ettringite is given in **Figure 5.33** along with the spectra for the 0.5 mM and 10 mM U(VI)-contacted ettringite phases. The peak at $\delta = 15$ ppm results from the two octahedrally coordinated aluminium sites in ettringite which cannot be resolved at the magnetic field used in this study (9.4 T), denoted as “Ett-Al” [265]. The small, broad peak at $\delta = \sim 10$ ppm in the initial ettringite phase, appearing as a shoulder of the main ettringite peak, was attributed to octahedrally coordinated aluminium in calcium aluminate monosulfate phases (AFm, $\text{Ca}_4(\text{Al}_2\text{O}_6)(\text{SO}_4)12\text{H}_2\text{O}$) arising from small impurities of this phase remnant from the synthesis process (denoted as “AFm-Al”) [266].

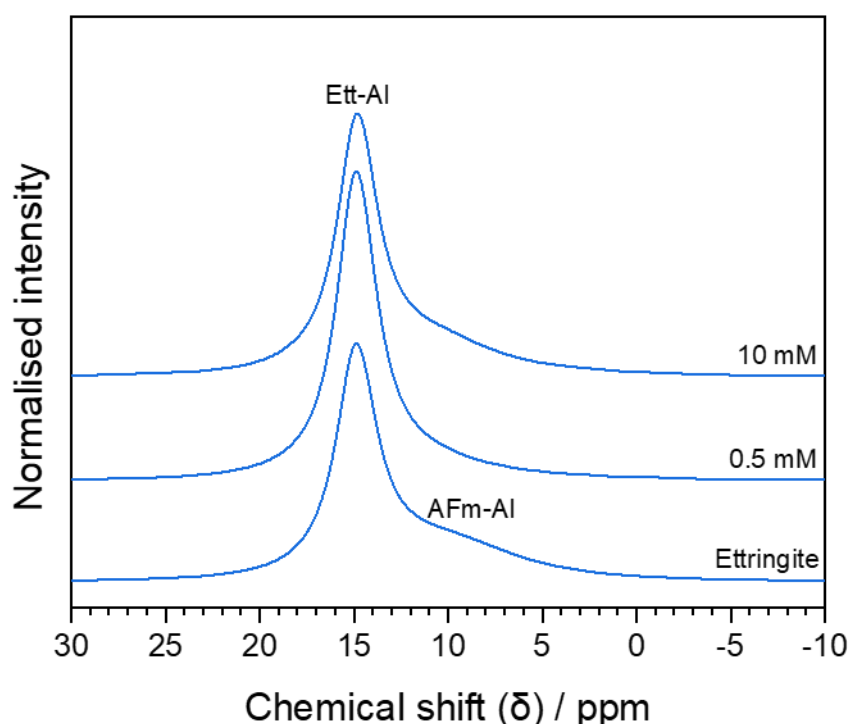


Figure 5.33: ^{27}Al NMR spectra of pure phase ettringite and ettringite contacted with 0.5 mM and 10 mM U(VI).

The peak arising from aluminium in ettringite is maintained after contacting the ettringite phase with both 0.5 mM and 10 mM U(VI) which is consistent with identification of the ettringite phase by XRD for the corresponding samples. The peak for the aluminium sites in AFm was observed to disappear after addition of 0.5 mM U(VI), however a peak in the same region was still observed, albeit at a lower intensity, after addition of 10 mM U(VI) (**Figure 5.34**).

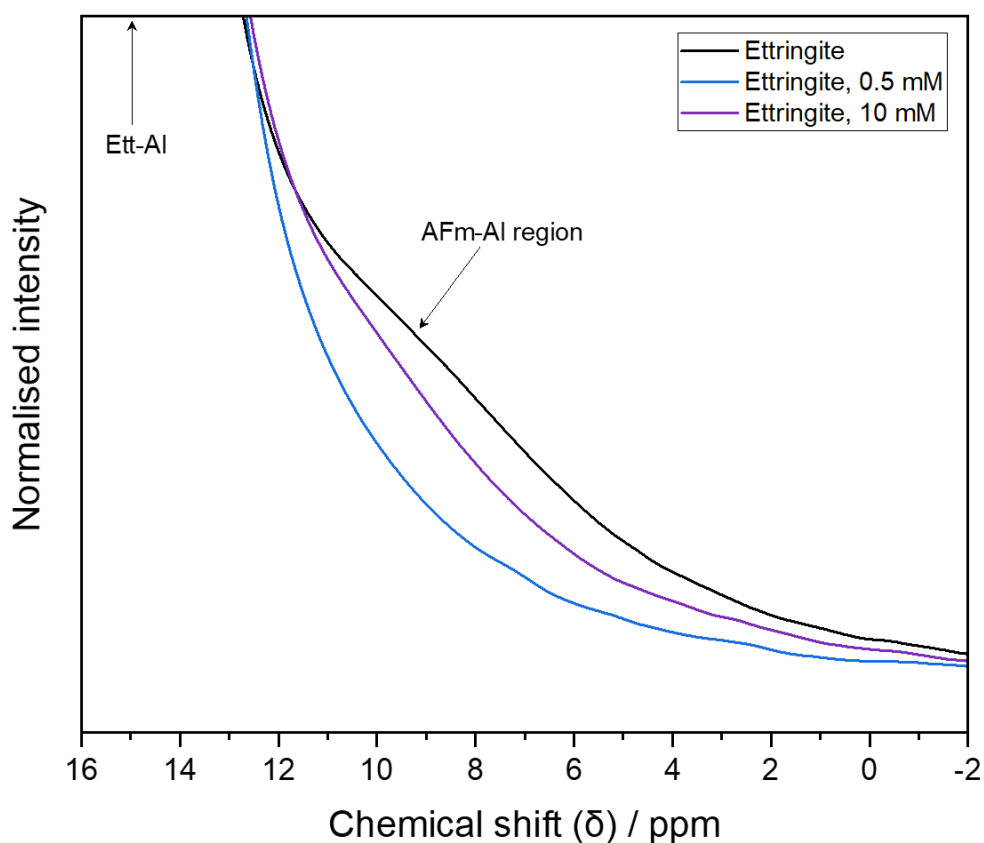


Figure 5.34: ^{27}Al NMR spectra of pure phase ettringite and ettringite contacted with 0.5 mM and 10 mM U(VI), highlighting the AFm-Al region of the spectra.

The disappearance and re-emergence of this peak in the AFm-Al region could be attributed to two possible scenarios with reference to the solution data, given that aluminium release from the ettringite phase was higher in the 0.5 mM U(VI)-contacted phase than in the 10 mM U(VI)-contacted phase (see *Section 5.3.4.1*); (i) increased dissolution of the AFm phase (at 0.5 mM U(VI)) and higher retention of the AFm phase (at 10 mM U(VI)) or (ii) the precipitation of a poorly crystalline or low yield U-substituted AFm phase in the 10 mM U(VI)-contacted sample, given that AFm is a layered double hydroxide that can display ion-exchange capabilities [82,157,267].

5.3.9.2 Hydrotalcite

The ^{27}Al spectra of hydrotalcite (**Figure 5.35**) displays a peak at $\delta = 11$ ppm which was attributed to the single octahedral aluminium environment in hydrotalcite, surrounded by octahedrally coordinated magnesium atoms (denoted as “HT-Al”). The broad shoulder at $\delta = 1-3$ ppm was observed due to the presence CO_3^{2-} interlayer anions (denoted as “int.”) [168,268]. There was no change observed in the spectra as a result of U(VI) addition at both 0.5 mM and 10 mM which suggests no solid phase structural interaction of U(VI) with aluminium from the hydrotalcite phase.

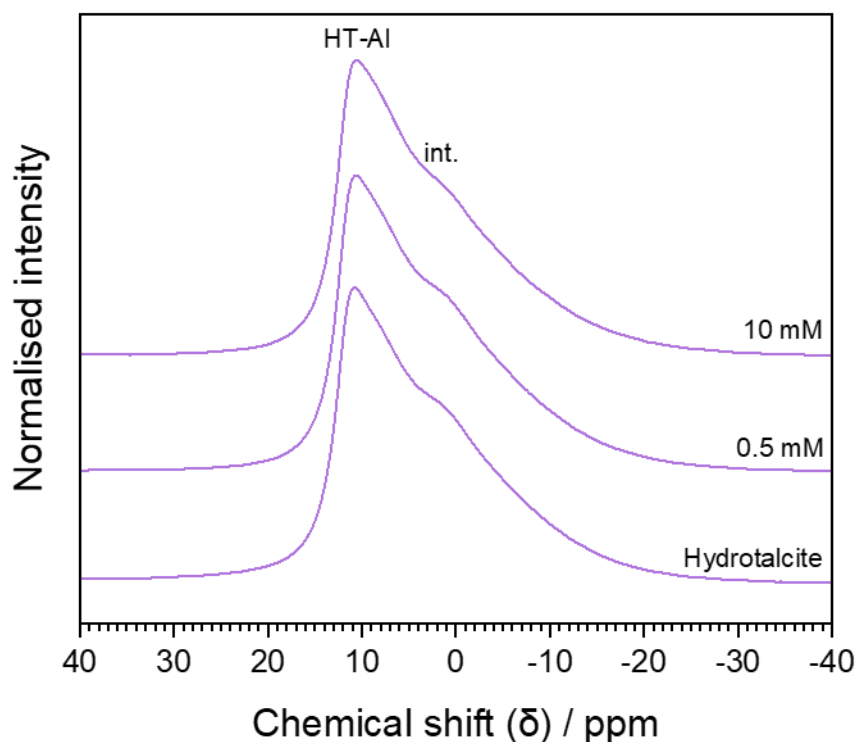


Figure 5.35: ^{27}Al NMR spectra of pure phase hydrotalcite and hydrotalcite contacted with 0.5 mM and 10 mM U(VI).

5.4 Discussion

5.4.1 U(VI)-C-S-H systems

In the U(VI)-C-S-H systems the presence of uranyl silicate-type coordination was apparent, given the availability of silicon and the results from the linear combination fitting of XANES data. EXAFS fitting of silicon distances for all the U(VI)-contacted C-S-H phases was also a good indication that uranium showed bonding to silicon in a uranyl silicate moiety. The identification of the Ca-weeksite phase by XRD for the CSH(0.6) phase was an indication that the uranyl silicate phases formed were also Ca-bearing. (See *Section 5.4.1.1* below.)

The formation of calcium uranates was also inferred, particularly at higher Ca/Si ratios, from the pH of the solutions (pH >11 at Ca/Si \geq 1.0 in 0.5 mM U(VI) solution) [62,63], availability of calcium in the system and the results from XANES linear combination fitting. (See *Section 5.4.1.5* below.)

The presence of calcium carbonates did not appear to largely effect the speciation of U(VI) in the solid phases.

5.4.1.1 Formation of uranyl silicates

Geochemical modelling of the systems indicated that the formation of the Ca-bearing uranyl silicate minerals haiweeite ($\text{Ca}(\text{UO}_2)_2(\text{Si}_5\text{O}_{12})(\text{OH})_2 \cdot 6\text{H}_2\text{O}$) and uranophane ($\text{Ca}[(\text{UO}_2)(\text{SiO}_3\text{OH})]_2 \cdot 5\text{H}_2\text{O}$) were favourable. The Ca-bearing uranyl silicate phase with formula $\text{Ca}_2(\text{UO}_2)_2\text{Si}_6\text{O}_{15} \cdot 10\text{H}_2\text{O}$ (Ca-weeksite) was identified in the 10 mM U(VI)-contacted CSH(0.6) system, by XRD. As discussed previously, *Skakle et al.* categorised this mineral in the uranyl silicate subgroup of weeksite (nominally $\text{K}_2(\text{UO}_2)_2(\text{Si}_5\text{O}_{13}) \cdot 4\text{H}_2\text{O}$) with U:Si ratio of 2:5 (or 2:6) [237–240,249] (**Table 5.20** and see also **Chapter 4**).

Table 5.20: U:Si and Ca:Si ratios of uranyl silicate minerals.

Mineral	U:Si	Ca:Si / Ca/Si
Weeksite ($\text{K}_2(\text{UO}_2)_2(\text{Si}_5\text{O}_{13})4\text{H}_2\text{O}$)	2:5	2:5 (0.4) (K/Si)
Haiweeite ($\text{Ca}(\text{UO}_2)_2(\text{Si}_5\text{O}_{12})(\text{OH})_2 \cdot 6\text{H}_2\text{O}$) [211]	2:5	1:5 (0.2)
“Ca-weeksite” / $\text{Ca}_2(\text{UO}_2)_2\text{Si}_6\text{O}_{15} \cdot 10\text{H}_2\text{O}$ [249]	2:6	2:6 (~0.3)
Soddyite ($(\text{UO}_2)_2\text{SiO}_4 \cdot 2\text{H}_2\text{O}$) [215,240]	2:1	-
Uranophane ($\text{Ca}[(\text{UO}_2)(\text{SiO}_3\text{OH})]_2 \cdot 5\text{H}_2\text{O}$) [205,269]	1:1	1:2 (0.5)

If the Ca/Si ratios of the mineral phases are also considered, uranophane might initially be the phase considered most likely to form in the C-S-H system with Ca/Si = 0.6, as it has the closest Ca/Si ratio of 0.5, if complete conversion of the C-S-H were attained. From the XRD pattern of the U-CSH(0.6) phase however, peaks for C-S-H(I) were still identified, indicating that C-S-H was still present in coexistence with the Ca-wecksite phase formed.

Further to this, ^{29}Si NMR analysis of the CSH(0.6) system indicates that the Ca/Si ratio of C-S-H phase, on addition of U(VI), actually increases from ~0.6 to ~0.8, for both the 0.5 mM and 10 mM U(VI)-contacted phase. If the presence of U(VI) is initially disregarded, with reference back to the calcium and silicon release data, the high release of calcium relative to silicon release for this phase (~380 ppm vs ~52 ppm, respectively, at 10 mM U(VI), pH = 9.2) would indicate a decrease in the Ca/Si ratio of the C-S-H phase (considering leaching into solution only). However, in the presence of U(VI), it appears that the Ca-wecksite phase is preferentially forming which requires a source of silicon, to the effect of removing silicon from the C-S-H phase and increasing the Ca/Si ratio of the initial C-S-H phase. Although the relative release of silicon exceeded the release of calcium for the 0.5 mM U(VI)-contacted phase (~95 ppm vs ~64 ppm, respectively, pH = 9.6; the opposite trend for 10 mM U(V)-contacted phase), which would support the observed increase in Ca/Si ratio, the observation of $\text{Q}^{3(\text{ii})}$ and Q^4 signals in this phase could also indicate the formation of a uranyl silicate-type phase (see **Figures 5.36** and **5.37** below).

5.4.1.2 ^{29}Si NMR

For the CSH(0.6) phase, in particular, the change in silicon Q^n species as a result of U(VI) addition was particularly prominent. Two situations were considered for the emergence of, and increase in, signals for $\text{Q}^{3(\text{ii})}$ and Q^4 species in C-S-H (~15 % and ~ 5 %, respectively):

- (i) Decalcification of the C-S-H structure due to calcium carbonate formation (calcium carbonates were identified in the XRD patterns, despite attempts to reduce the effect of this) - independent of the presence of U(VI).
- (ii) Formation of new silicon species that would be expected to form in uranyl silicate minerals (**Figures 5.36** and **5.37**) - dependent on the presence of U(VI).

In the first situation, decalcification via carbonation of the C-S-H structure would lead to an increase in cross-linking of silicon tetrahedra and therefore an increase in Q^3 species (and potentially Q^4 species if complete decalcification and fully polymerised silicon sites were attained). However, this would also lead to a relative decrease in the Q^1 to Q^2 ratio and in turn a decrease in the Ca/Si ratio of the C-S-H phase [233,270]. Given that the Ca/Si ratio was observed to increase in the CSH(0.6) system (from ~0.6 to ~0.8), the effect of carbonation can therefore be considered as negligible, relative to the effect of U(VI) addition.

In the second situation, the formation of $Q^3_{(ii)}$ and Q^4 species can be considered relative to the uranyl silicate mineral structures. These minerals are inherently sheet structured, with layers of uranyl silicates interspersed with interlayer cations and / or water molecules [237].

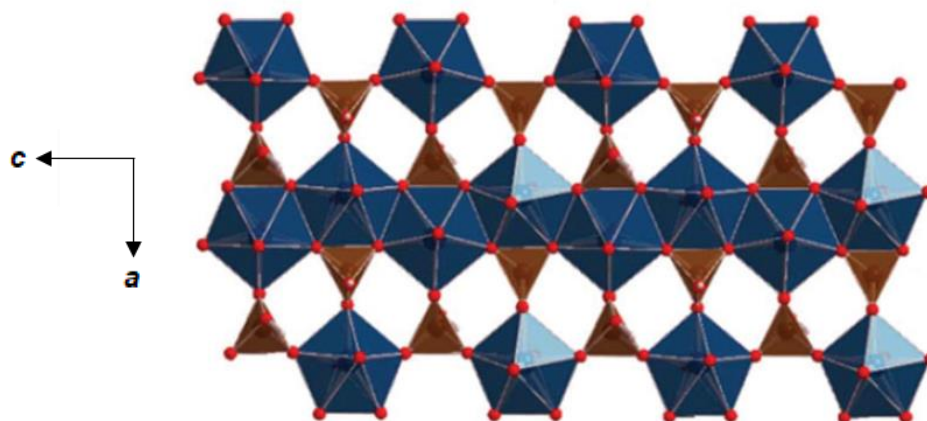


Figure 5.36: View of uranophane- β uranyl silicate layer along [010] (from [269]). Silicon tetrahedron are in brown and uranyl pentagonal bipyramids are in blue.

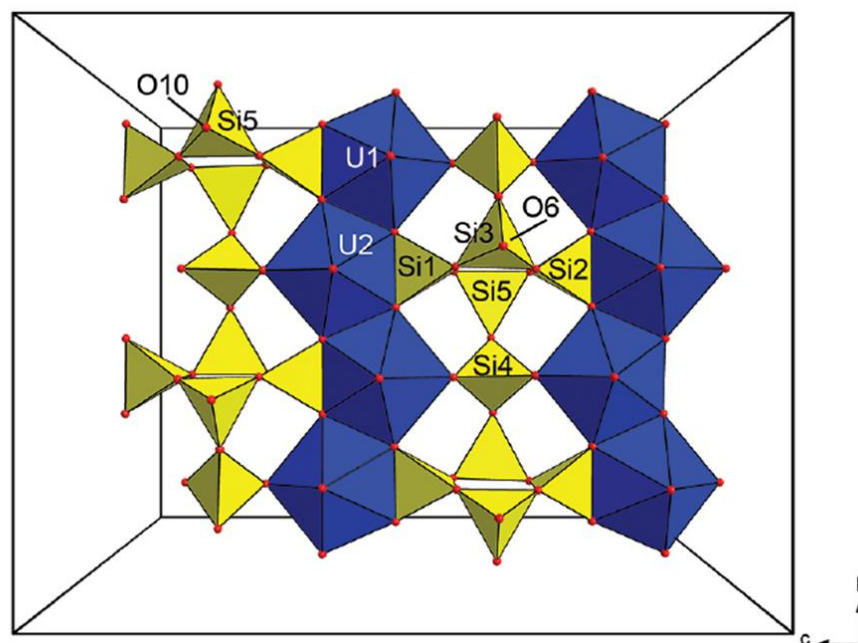


Figure 5.37: Uranyl silicate sheets in the crystal structure of haiweeite along [100] (from [211]). Silicon tetrahedra are in yellow and uranyl pentagonal bipyramids are in blue. Note that in weeksite, the Si3 Q^3 tetrahedron is a Q^4 species that connects to subsequent uranyl silicate sheets [251].

Uranophane: Exhibits only a $Q^3(3U)$ species (**Figure 5.36**). Chains of pentagonal bipyramidal uranyl polyhedral make up uranyl chains, whereby the $Q^3(3U)$ species are edge-sharing with

one pentagonal uranyl unit of one uranyl chain (2 x U) and vertex-sharing with another uranyl unit (1 x U) of the adjacent uranyl chain, to form uranyl-silicate sheets [205,269].

Weeksite & Haiweeite: Weeksite exhibits Q^4 and $Q^4(2U)$ species and demonstrates pentagonal bipyramidal uranyl chains, whereby the $Q^4(2U)$ species are edge sharing with one pentagonal uranyl unit (2 x U) to form the uranyl-silicate sheets. The sheets are connected by vertex-sharing Q^4 species (connected to three $Q^4(2U)$ species and one further Q^4 species). Haiweeite exhibits Q^3 and $Q^4(2U)$ species (**Figure 5.37**). The $Q^4(2U)$ species are also edge-sharing with pentagonal bipyramidal uranyl units (2 x U), as in weeksite. The Q^3 species are then vertex-sharing with three of the $Q^4(2U)$ species, but unlike in weeksite (and as these are Q^3 species), the sheets are not then connected [211,251].

Uranophane and weeksite would therefore account for the observations of $Q^{3(iii)}$ and Q^4 species only, respectively. Given that the haiweeite structure exhibits both Q^3 and Q^4 species, this could account for the observed signals in the ^{29}Si NMR spectra for the CSH(0.6) phases. The formula of the $\text{Ca}_2(\text{UO}_2)_2\text{Si}_6\text{O}_{15}\cdot 10\text{H}_2\text{O}$ (Ca-weeksite) phase reported by *Skakle et al.* would also indicate that the silicon environment is not only attributed to $Q^4(xU)$ species; the ratio of oxygen atoms per silicon atoms, from the Si_6O_{15} unit, is not equal to 4 (i.e. $15/6 \neq 4$) [249]. *Skakle et. al* categorised this phase in the weeksite sub-group, which encompasses haiweeite, and therefore the phase observed here with the same formula could exhibit a haiweeite-type structure. The amount of water (and OH groups) reported in the formula could therefore vary and account for the existence of the silicon $Q^{3(iii)}$ species observed by NMR.

For the CSH(1.2) phase, the emergence and increase in the $Q^{3(iii)}$ and Q^4 signals in the ^{29}Si NMR spectra after U(VI)-contact, relative to the C-S-H Q^n , species was less prominent. The Ca/Si ratio of the phase was seen to decrease from ~ 1.1 to ~ 0.9 as well as the ratio of Q^1 to Q^2 species, with addition of U(VI). The decrease in Ca/Si ratio could be a result of the amount of calcium released into solution, relative to silicon (~ 100 ppm vs ~ 5 ppm at pH = 11.6 for 0.5 mM U(VI) and ~ 500 ppm vs ~ 21 ppm at pH = 10 for 10 mM U(VI)), or from carbonation effects as discussed previously. The higher initial Ca/Si ratio of the C-S-H phase resulting in better retention of the C-S-H phase during contact with U(VI) solutions which could account for why there was no significant increase of the $Q^{3(iii)}$ and Q^4 signals ($\leq 5\%$). This could be more indicative of a U(VI) species that is physi-sorbed to the to the C-S-H surface as discussed in **Chapter 2** [53,66–71] or the formation of a calcium uranate species (see *Section 5.4.1.5*) whereby by the average silicon signal by NMR may not be greatly perturbed.

5.4.1.3 EXAFS: 0.5 mM U(VI)-contacted C-S-H

Table 5.21: O_{ax} and U-U distances obtained by EXAFS fitting of mineral phases in **Chapter 4** (and elsewhere) for reference.

Mineral	O _{ax} / Å	U-U / Å	Reference(s)
Haiweeite (Ca(UO ₂) ₂ (Si ₅ O ₁₂)(OH) ₂ ·6H ₂ O)	1.803(11)	4.02(2)	Chapter 4
Soddyite ((UO ₂) ₂ SiO ₄ ·2H ₂ O)	1.791(9)	3.90(3)	Chapter 4
Weeksite (K ₂ (UO ₂) ₂ (Si ₅ O ₁₂)(OH)4H ₂ O)	1.825(8)	4.06(3)	Chapter 4
Uranophane (Ca[(UO ₂)(SiO ₃ OH)] ₂ ·5H ₂ O)	~1.82	~3.95	[70,204,241,242]

Uranophane has predominantly been referred to in the literature as the comparative U(VI) species that forms on interaction with C-S-H phases. *Macé et al.* determined that at 'low' loadings of U(VI) (~1 000 to 3 000 ppm) on C-S-H, U(VI) was shown to have an O_{ax} distance of 1.82 ± 0.02 Å which was in line with the average value of 1.82 ± 0.02 obtained by *Ginderow et al.* for uranophane, as well as other values reported for uranophane [70,204,241,242]. Comparatively, the 0.5 mM U(VI) solution with 25 g L⁻¹ of the C-S-H phases analysed here equates to a U(VI) loading of ~4 800 ppm and the O_{ax} (and O_{eq}) distances determined by EXAFS fitting are given again in **Table 5.22**.

Table 5.22: O_{ax} and O_{eq} distances obtained by EXAFS fitting of 0.5 mM U(VI)-contacted C-S-H phases.

Ca/Si ratio	O _{ax} distance / Å	O _{eq} distances / Å
0.6 (young / aged)	1.827(11) / 1.802(8)	2.20(2), 2.30(1) / 2.16(2), 2.27(1)
0.8	1.800(13)	2.16(4), 2.23(2), 2.32(3)
1.2	1.804(11)	2.22(3), 2.26(2), 2.42(2)
1.6	1.812(8)	2.24(5), 2.21(2), 2.34(2)

For a Ca/Si ratio of 0.6, the O_{ax} distance of ~1.82 Å could potentially be indicative of a uranophane-type coordination, however this was seen to decrease to a value of ~1.80 Å with ageing. This decreased distance could be a result of increased order of the U(VI)-silicate overtime (see *Section 5.4.1.6*). However, this shorter distance is also more akin to the value obtained for the haiweeite mineral of 1.803 ± 0.011 Å in **Chapter 4 (Table 5.21)**, also in line with the observation of silicon Q³_(iii) and Q⁴ species by NMR.

At Ca/Si ratios of 0.8 and 1.2, the O_{ax} distance was $1.80 \pm 0.01 \text{ \AA}$ but for a Ca/Si ratio of 1.6 the distance was increased to $1.812 \pm 0.008 \text{ \AA}$. Although every attempt was made to analyse the samples as soon as possible after they were made (and certainly within less than a month), this disparity could also be an effect of ageing of the samples at Ca/Si ratios of 0.8 and 1.6. However, it should also be noted that the fit of the CSH(1.6) phase was improved with addition of a calcium scattering pathway in replacement of a silicon pathway. The first O_{ax} distance in the calcium uranate phase analysed in **Chapter 4** was fitted at $1.953 \pm 0.006 \text{ \AA}$, so an increased O_{ax} distance and a fitted calcium distance of $3.50 \pm 0.03 \text{ \AA}$ for the CSH(1.6) phase could be an indication of mixed uranyl silicate and calcium uranate contributions in the EXAFS region.

In addition to this, the CSH(0.6) phases displayed a split equatorial oxygen shell ($N_{O_{eq1}} = 1$ and $N_{O_{eq2}} = 3$) with distances in the young sample of ~ 2.20 and $\sim 2.30 \text{ \AA}$, respectively, and in the aged sample of $\sim 2.16 \text{ \AA}$ and $\sim 2.27 \text{ \AA}$, respectively. These decreasing distances could again be a result of increasing order of the sample over time. Furthermore, the equatorial oxygen shells of the CSH(0.8), CSH(1.2) and CSH(1.6) phases were further split with three equatorial distances fitted ($N_{O_{eq1}} = 1$ and $N_{O_{eq2}} = 3$ and $N_{O_{eq3}} = 2$) which is an indication of increased disorder in these systems, relative to the CSH(0.6) phases [241].

5.4.1.4 EXAFS: 10 mM U(VI)-contacted C-S-H phases

Macé *et al.* further reported an O_{ax} distance for U(VI)-silicate moieties, on C-S-H phases with 'high' U(VI) loadings ($\sim 13\ 000$ to $\sim 45\ 000$ ppm), of $1.80 \pm 0.02 \text{ \AA}$. This is consistent with the generally lower values of O_{ax} obtained here for 25 g L^{-1} of the C-S-H phases in 10 mM U(VI) solution, equating to U(VI) loadings of $\sim 95\ 000$ ppm (**Table 5.23**). In the former study, the O_{ax} distance of soddyite was also referenced (in addition to uranophane) as $1.79 \pm 0.01 \text{ \AA}$ (determined by DeMartin *et al.* [215]) to further indicate the possible O_{ax} distances that could form for U(VI) coordinated in C-S-H systems. This was also determined as $1.791 \pm 0.009 \text{ \AA}$ for the soddyite mineral (**Table 5.21**).

Table 5.23: O_{ax} and O_{eq} distances obtained by EXAFS fitting of 10 mM U(VI) -contacted C-S-H phases.

Ca/Si ratio	O_{ax} distance / \AA	O_{eq} distances / \AA
0.6 (young / aged)	1.807(11) / 1.805(11)	2.19(2), 2.32(1), 2.48(5) / 2.19(2), 2.31(3), 2.47(5)
0.8 *	1.798(11)	2.22(2), 2.38(3)
1.2 *	1.801(6)	2.24(1), 2.40(2)
1.6 *	1.813(7)	2.25(1), 2.42(2)

*k-space resolved up to $\sim 10 \text{ \AA}^{-1}$

For the CSH(0.6) sample, the O_{ax} and O_{eq} distances did not change, within error, as a result of the age of the sample, indicating that the local average U(VI)-silicate coordination was not changed over time. However, the addition of a U-U backscattering distance for the aged phase is perhaps an indication of the increased order over a longer range and is in agreement with an increase in crystallinity as observed by X-ray diffraction. The split equatorial shells for both phases are again an indication of disorder around U(VI).

Although two equatorial distances were fit for the subsequent Ca/Si ratios of 0.8, 1.2 and 1.6, this is an indication of the lower resolution further out in k-space for these spectra, in comparison to the previously discussed phases, rather than an increase in order around U(VI).

As well as being more akin to the O_{ax} distance for soddyite, the lower O_{ax} distances obtained for the 10 mM U(VI) systems could also be indicative of a haiweeite-type coordination (**Table 5.21**). The distance for U-U obtained in the aged CSH(0.6) phase was $3.99 \pm 0.04 \text{ \AA}$, which is also closer to the U-U value obtained for haiweeite ($4.02 \pm 0.02 \text{ \AA}$) than soddyite ($3.90 \pm 0.03 \text{ \AA}$).

5.4.1.5 Formation of calcium uranates

Further to the formation of uranyl silicate phases, *Macé et al.* also reported the formation of a coexistent hydrous calcium uranate-type phase ($\text{CaUO}_4 \cdot \text{H}_2\text{O}$ -type) at U(VI) loadings of ~13 000 to ~45 000 ppm on C-S-H phases. *Tits et al.* also noted that at higher Ca/Si ratios the formation of a U(VI)-silanol coordinated species was likely present in C-S-H phases, for U(VI) loadings of ~700 ppm, but that at increased loadings of ~200 000 ppm, a calcium uranate phase was also observed, due to oversaturation of this phase [69]. It has already been reported that calcium uranate phases will be solubility limiting for U(VI) in cementitious waters with high calcium content [53,62,63].

Geochemical modelling also identified the formation of calcium uranate in all the U(VI) / C-S-H systems studied here and the results from XANES linear combination were indicative of signal contributions from calcium uranate phases (CaUO_4 or Ca_3UO_6). The O_{ax} distance of the CaUO_4 phase was determined to be 1.953 ± 0.006 in **Chapter 4**. Given that the O_{ax} distances obtained for the U(VI)-contacted C-S-H phases were nominally ~1.8 Å, as discussed in the previous sections, the largest contribution to the EXAFS signal appears to be uranyl silicate phases.

Nevertheless, an additional experiment conducted in this work whereby CaO and SiO_2 were mixed stoichiometrically to achieve a Ca/Si ratio of 1.0 using the direct synthesis method (**Chapter 3**), with a 0.1 M uranyl nitrate solution in replacement of UHQ (the pH was not measured), resulted in a solid phase (a “C-U(VI)-S-H” phase) that was shown to be amorphous by XRD. The phase C-U(VI)-S-H was sequentially heat treated to induce crystallisation of the

components formed. The XRD patterns of this heat-treated phase at 600, 800 and 1000 °C and pure phase C-S-H (Ca/Si = 1.0) treated at 1000 °C are given in **Figure 5.38**.

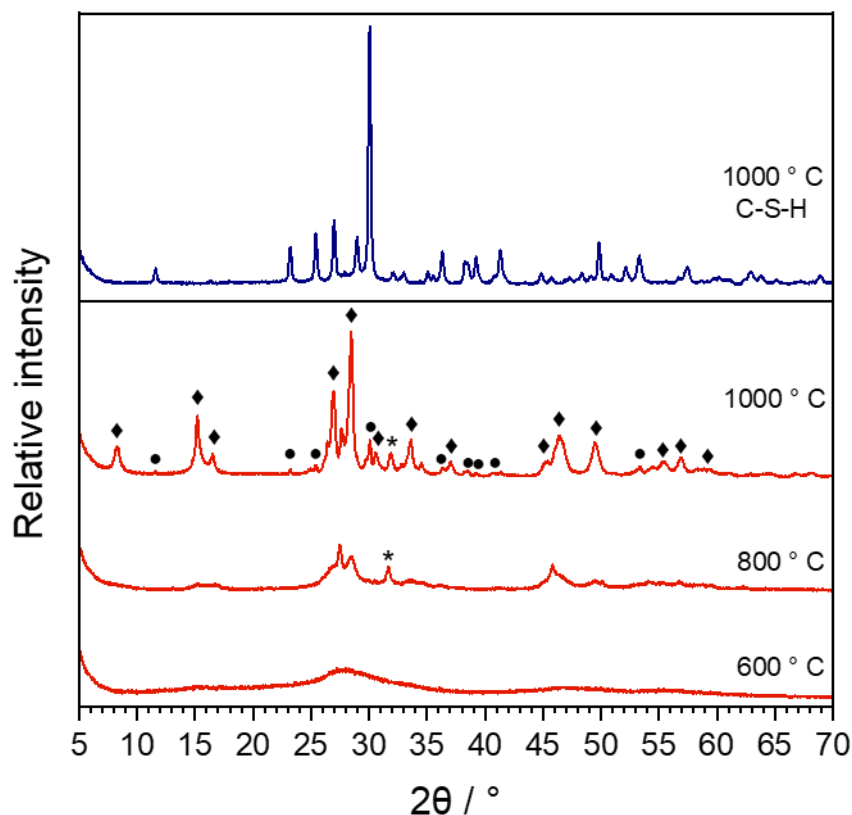


Figure 5.38: XRD patterns of heat-treated C-U(VI)-S-H phase (bottom, red) and heat-treated C-S-H(I) as a comparison (top, blue) i.e. β -wollastonite (PDF card no. 00-043-1460 [271,272]). Temperatures used are indicated on the figure. ● = wollastonite; ◆ = calcium uranate (PDF card no. 01-084-8399 [273]); * = unidentified phase.

The C-U(VI)-S-H phase was still amorphous after heating at 600 °C, but from 800 °C the formation of peaks pertaining to calcium uranate (PDF card no. 01-084-8399 [273]) were apparent. The high temperature degradation product of C-S-H, wollastonite (β -CaSiO₃; PDF card no. 00-043-1460 [271,272]) [274] was observed for the pure C-S-H phase heated at 1000 °C. Heating of the C-U(VI)-S-H phase at 1000 °C resulted in a mixed wollastonite / calcium uranate phase and any silicon that was initially associated with U(VI) was subsequently partitioned into the wollastonite phase. Although this high temperature is not relevant for cementitious environments, the formation of hydrous calcium uranate phases that limit the solubility of U(VI) at alkaline pH values is still an important factor to consider for the immobilisation of U(VI) in cementitious wastefoms.

5.4.1.6 Mineral ageing

In agreement with the current study whereby the Ca-weeksite appeared to become more crystalline with time, *Sutton* (1999) observed the same phenomenon for schoepite ($(\text{UO}_2)_8\text{O}_2(\text{OH})_{12}\cdot 12(\text{H}_2\text{O})$) and hydrous calcium uranate phases [63]. Solutions of uranyl nitrate were added to $\text{Ca}(\text{OH})_2$ which formed mixed schoepite and calcium uranate precipitates, which increased in calcium uranate content with increasing pH. The precipitate formed at pH 11 was analysed by XRD and initially displayed diffuse scattering, but after ageing for 3, 6 and 9 weeks under anaerobic conditions (ambient temperature) an additional small, broad peak pertaining to either schoepite or calcium diuranate (CaU_2O_7) was observed.

Sutton described the formation of a metastable state whereby the initial U(VI) phase formed is not the most thermodynamically stable but changes over time to a more stable phase, which is the case for precipitates that form when solutions are oversaturated with respect to U(VI), and are therefore inherently disordered. This study again highlights the importance of U(VI) solubility limiting calcium uranate phases that can form in cementitious environments, and how their behaviour may change overtime.

However, the indexing of the $\text{Ca}_2(\text{UO}_2)_2\text{Si}_6\text{O}_{15}\cdot 10\text{H}_2\text{O}$ (Ca-weeksite) diffraction peaks in both the young and aged samples in this study, albeit with different intensity, indicates the role that silicon has on the ageing effect of U(VI) / C-S-H systems. This is also in line with Ostwald's step rule which states that crystallisation from a solution will occur in a process such that thermodynamically unstable phases form first, followed by a thermodynamically stable step, or steps [63,275], and can be related to the process of "Ostwald ripening". **Figure 5.39** shows this process, relative to this study, whereby at pH 7-10 in the presence of flocculating salts (i.e. uranyl nitrate), silicon will undergo polymerisation to form a three-dimensional gel network [231].

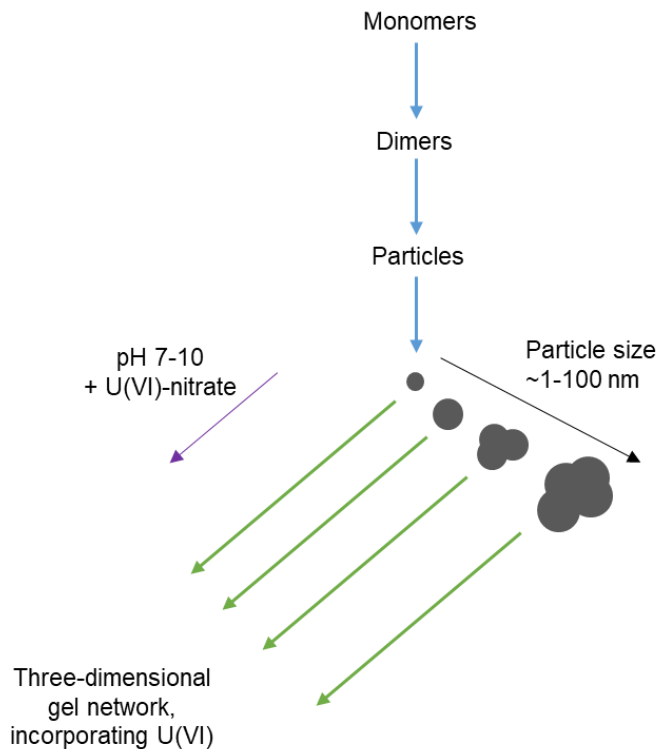


Figure 5.39: The polymerisation behaviour of silica in basic solution in the presence of uranyl nitrate where particles aggregate into three-dimension gel networks. Figure made with reference to [231].

5.4.2 U(VI)-ettringite systems

The lack of XAFS data for the U(VI)-contacted ettringite systems makes the identification of the U(VI) coordination environment difficult. However, the identification of an amorphous region in the XRD pattern could be the result of a poorly crystalline U(VI)-bearing phase. The geochemical modelling results elude to the formation of a calcium uranate phase, due to the abundance of calcium released into solution.

From the ^{27}Al NMR data, the presence of an AFm ($\text{Ca}_4(\text{Al}_2\text{O}_6)(\text{SO}_4)\cdot x\text{H}_2\text{O}$) impurity in the ettringite phase was indicated by the shoulder on the main ettringite aluminium peak; a second peak at ~ 10 ppm. This peak was shown to diminish on addition of 0.5 mM U(VI) to the ettringite phase, but the emergence of a peak within the same region was observed on addition of 10 mM U(VI), coinciding with the relative increase and decrease of aluminium release into solution, respectively. This peak could therefore be tentatively assigned to the formation of an AFm-U(VI) incorporated phase. AFm- SO_4 phases have previously been shown to have capacity for the uptake of anionic species (and / or radionuclides). *Aimoz et al.* determined that iodate (I^-) was incorporated into the interlayer of AFm- SO_4 to form an AFm phase with mixed SO_4^{2-} and I^- interlayer anions [157]. Further to this, the results from geochemical modelling indicated the presence of uranyl hydroxide / sulfate anions in solution at the pH values of the ettringite solutions (pH ~ 10) (Table 5.24). The precipitation of an AFm-U(VI)

phase could therefore be plausible, with the higher concentration of U(VI) in the 10 mM solution required for formation and / or detection of this phase by NMR. From the species identified in **Table 5.24**, the $\text{UO}_2(\text{OH})_4^{2-}$ and $\text{UO}_2(\text{SO}_4)_2^{2-}$ anions are the most likely candidates that would directly incorporate into an AFm- SO_4 interlayer, forming $\text{Ca}_4(\text{Al}_2\text{O}_6)\text{UO}_2(\text{OH})_4 \cdot x\text{H}_2\text{O}$ and $\text{Ca}_4(\text{Al}_2\text{O}_6)\text{UO}_2(\text{SO}_4)_2 \cdot x\text{H}_2\text{O}$ type phases, respectively, taking into account the charge balance.

Table 5.24: Anionic U(VI) species identified by geochemical modelling in the 10 mM U(VI)-contacted ettringite system at pH = 9.9.

Anionic U(VI) species
$(\text{UO}_2)_3(\text{OH})_7^-$
$\text{UO}_2(\text{OH})_3^-$
$\text{UO}_2(\text{OH})_4^{2-}$
$\text{UO}_2(\text{SO}_4)_2^{2-}$

However, direct identification of such a phase is inconclusive without further evidence such as XAFS measurements and analysis of a U(VI)-contacted pure phase AFm- SO_4 phase.

5.4.3 U(VI)-hydrotalcite systems

For the U(VI)-contacted hydrotalcite systems, no significant change in the XRD pattern was observed. However, approximately 30 % of $[\text{U}]_{t=0}$ was taken up by the hydrotalcite phase. The results from the EXAFS fitting of the U(VI)-contacted hydrotalcite phases are given again in **Table 5.25** for reference. The results indicate that the coordination of U(VI) was largely unchanged as a function of U(VI) concentration.

Table 5.25: U-X distances and coordination numbers obtained by EXAFS fitting of U(VI)-contacted hydrotalcite phases.

Scatterer	0.5 mM		10 mM	
O_{ax}	1.817(9) Å	N = 2.4(2)	1.819(9) Å	N = 2.8(2)
O_{eq}	2.44(1) Å	N = 4	2.44(1) Å	N = 4
C	2.93(2) Å	N = 3	2.93 (1) Å	N = 3
U	3.40(3) Å	N = 2	3.39(2) Å	N = 2
Mg	3.83(3) Å	N = 4	3.84(2) Å	N = 6

The O_{ax} , O_{eq} and carbon distances are fairly typical of a uranyl carbonate phase, such as those obtained for the bayleyite / andersonite phase in **Chapter 4**, which is also consistent with the identification of a bayleyite / andersonite signal in the XANES LCF results. The distances are given in **Table 5.26** along with the values obtained for 2 mM uranyl nitrate solutions contacted onto brucite ($Mg(OH)_2$), hydromagnesite ($Mg_5(CO_3)_4(OH)_2 \cdot 4H_2O$) and nesquehonite ($MgCO_3 \cdot 3H_2O$) at $\sim 34 \text{ g L}^{-1}$ by *van Veelen et al.* [276].

Table 5.26: U-X distances obtained by EXAFS fitting of bayleyite / andersonite (**Chapter 4**) and U(VI)-contacted magnesium and / or carbonate mineral phases from *van Veelen et al.* Note that errors were not quoted in [276].

Phase	$O_{ax} / \text{\AA}$	$O_{eq} / \text{\AA}$	C / \AA	Mg / \AA	U / \AA
Bayleyite / andersonite	1.796(9)	2.43(12)	2.91(2)	-	-
Brucite + U(VI)	1.80	2.38, 2.48	2.90 *	3.60	3.88
Hydromagnesite + U(VI)	1.81	2.43	2.90	3.62	3.90
Nesquehonite + U(V)	1.81	2.40, 2.50	2.90	3.59	3.89

*present due to the formation of $UO_2(CO_3)_3^{4-}$ in solution under the ambient experimental conditions adopted [276].

In the results obtained by *van Veelen et al.*, magnesium and uranium scatterers were also fitted at distances of $\sim 3.6 \text{ \AA}$ and $\sim 3.9 \text{ \AA}$, respectively. This is in contrast to the result obtained here whereby magnesium and uranium were fitted retrogradely at ~ 3.8 and $\sim 3.4 \text{ \AA}$, respectively. This could be a result of the U(VI) coordination having mixed magnesium uranate character in this study, whereby uranium is at a closer distance [203].

Additionally, no change was observed in the ^{27}Al NMR spectra as a result of U(VI) addition to hydrotalcite, which indicates that aluminium did not play a role in the uptake and coordination of U(VI). This is consistent with the formation of a Mg,C-containing surface U(VI) precipitate or U(VI) surface sorbed species, rather than anion-exchange into the hydrotalcite interlayer. The absence of a secondary U(VI) precipitate was not evidenced in the XRD pattern which would suggest that U(VI) was sorbed to the outer surface of hydrotalcite, which was also concluded in [276] as an outer-sphere complex on the surface of the studied minerals.

5.5 Conclusions and Further Work

5.5.1 Conclusions

The formation of uranyl-silicate phases and, potentially, hydrous calcium uranate phases has been evidenced in U(VI)-contacted C-S-H systems through XRD, XAFS and ^{29}Si NMR. The formation of these phases is in line with literature findings [67–70]. However, the results

obtained here build on previous knowledge of uranyl silicate formation in these systems by considering other analogous minerals, such as haiweeite ($\text{Ca}(\text{UO}_2)_2(\text{Si}_5\text{O}_{12})(\text{OH})_2 \cdot 6\text{H}_2\text{O}$) and weeksite-type ($\text{K}_2(\text{UO}_2)_2(\text{Si}_5\text{O}_{12})(\text{OH}) \cdot 4\text{H}_2\text{O}$), rather than comparison to the relatively commonly studied uranophane ($\text{Ca}[(\text{UO}_2)(\text{SiO}_3\text{OH})]_2 \cdot 5\text{H}_2\text{O}$) and soddyite ($(\text{UO}_2)_2\text{SiO}_4 \cdot 2\text{H}_2\text{O}$) minerals only. The use of XAS, NMR and XRD has highlighted the minor differences in molecular scale interactions in these mineral phases. This is particularly important to consider for a cementitious repository, as different mineral structures, such as weeksite or uranophane, will have different solubilities (and rates of dissolution) in varying pore water and groundwater compositions. This is also inferred by the differences in saturation indices calculated by geochemical modelling. Further to this, the effect of Ostwald ripening of the uranyl silicate phases over time has not previously been considered in this context, and the ageing of these U(VI)-bearing phases could have important implications for the bulk cement matrix surrounding ILW streams that contain uranium contamination. These are important factors to consider when assessing the controlled release of uranium isotopes from a geological repository.

The application of minor cement hydrate phases for sequestration of uranium in cement matrices has also not been widely considered. For the ettringite systems, uptake of U(VI) directly by the ettringite phase was not apparent. Rather, the formation of a poorly crystalline hydrous calcium uranate phase or uptake by the AFm impurity seemed more likely. AFm-SO₄ phases are still important layered double hydroxides (LDHs) present in cement matrices, particularly for blast-furnace slag containing blends, that should also be considered for the uptake of uranium. The LDH hydrotalcite phases also displayed uptake of U(VI) through formation of what was concluded to be a surface sorbed uranyl magnesium carbonate phases. These findings could be prominent if Magnox sludge wastes are to be immobilised using a cement grout in the future. However, it should also be noted that the hydrotalcite phases displayed ~30 % uptake of U(VI) from solution, compared to >99 % in the ettringite systems, which could indicate that precipitation of calcium uranate phases or formation of AFm-U(VI) phases are more effective for immobilising U(VI) in a solid phase.

5.5.2 Further work

In order to finalise this work for publication, the following experiments are required:

- X-ray diffraction and absorption analysis of a uranophane phase.
- ²⁹Si NMR data of C-S-H and U(VI)-contacted C-S-H phases, as a function of time, to develop a detailed understanding the U(VI) induced Ostwald ripening process, as well as ²⁹Si NMR of uranyl-silicate mineral standards.

- Principal component analysis of the U(VI)-contacted C-S-H EXAFS spectra to differentiate between the spectral features of uranyl silicates and calcium uranate phases.
- Application of the Hamilton R-factor test to the LCF combinations to determine the best fit, statistically.
- XAFS measurements of U(VI)-contacted ettringite phases.
- Synthesis of single phase AFm-SO₄ and repetition of the U(VI) experiments with this phase.

Chapter 6 – Effect of high plutonium loading on C-S-H phases

6.1 Introduction

The aim of this Chapter is to elucidate the behaviour of plutonium (Pu) in cementitious systems, relevant to waste management and disposal of plutonium contaminated materials (PCM). The approach used was to understand how plutonium and its surrogate, uranium (U), behave in a simplified cement system, using actinide loadings that are higher than may be expected in a wasteform. The research was primarily performed at the Joint Research Centre (JRC), Karlsruhe, where plutonium and uranium were contacted with C-S-H phases of differing Ca/Si ratio; both non-carbonated and pre-carbonated.

The experimental section is split into two main parts; **Part 1** relates to experiments conducted during the first period of work carried out at JRC. The work described in **Chapter 5**, where the interaction of U(VI) with cement hydrate minerals was performed, was used as a basis to plan pseudo-analogous experiments, using Pu(VI). Due to the behaviour observed, a return visit to JRC, described in **Part 2**, details experiments conducted using U(IV) as a Pu(IV) surrogate. The synthesis and pre-carbonation of all C-S-H phases used in both parts is discussed in **Chapter 4**.

Also discussed, in part, is a collaborative study between the University of Sheffield (TUoS) and the National Nuclear Laboratory (NNL), focused on characterisation of cement-encapsulated Pu(IV)O₂ particles [131].

6.2 Experimental methods

6.2.1 Part 1 – U(VI) as a Pu(VI) surrogate

6.2.1.1 U(VI) / C-S-H hydrothermal ageing

Due to the observed ageing behaviour of U(VI) in the presence of C-S-H (Ca/Si = 0.6) discussed in **Chapter 5**, it was planned to investigate whether such behaviour also occurred for Pu(VI) in the presence of C-S-H phases, given that uranyl nitrate (U(VI)O₂(NO₃)₂) and plutonyl nitrate (Pu(VI)O₂(NO₃)₂) are isostructural in aqueous solution [91,277]. Since the time scale available for work at JRC was shorter than the time taken to observe the transformation described in **Chapter 5**, an initial investigation of a more rapid, hydrothermal ageing procedure was carried out to the same effect. U(VI)_(aq) was added in the form of uranyl nitrate to CSH(0.6) and heated in an autoclave at 200 °C and 100 % RH for 16 hours at JRC. The resulting solid was washed with 2 mL ethanol and 2 mL acetone prior to measurement by XRD (parameters used described in **Chapter 5**).

The XRD patterns of the aged and hydrothermally treated U(VI) / CSH(0.6) phases are given in **Figure 6.1**, along with hydrothermally treated pure CSH(0.6) for comparison. The heating process appeared to replicate a “C-U-S-H” phase with XRD peaks also attributable to the same Ca-wecksite / haiweeite mineral phase that was identified in **Chapter 5** for the aged sample [211,249]. There are some slight differences observed in the peak positions, whereby peaks are shifted to slightly higher 2θ values for the hydrothermally aged sample, notably, the reflection at $\sim 9^\circ 2\theta$. This could be a result of discrepancies in the amount of water present in the framework channels of the mineral structure; an increased water content leading to a decrease in the d-spacing [238]. It is difficult to directly compare the intensities of the peaks from both XRD patterns due to the difference in background signals and different XRD instruments used.

The pure CSH(0.6) phase did not appear to change significantly, structurally, as a result of analogous hydrothermal treatment in UHQ water. The XRD pattern showed a slight increase in peak intensity and sharpness, which indicates increased crystallinity of the C-S-H structure [185], and the presence of small amounts of vaterite (PDF card no. 04-017-8634 [191]) and calcite (PDF card no. 01-078-4614 [187]) polymorphs of calcium carbonate resulting from carbonation.

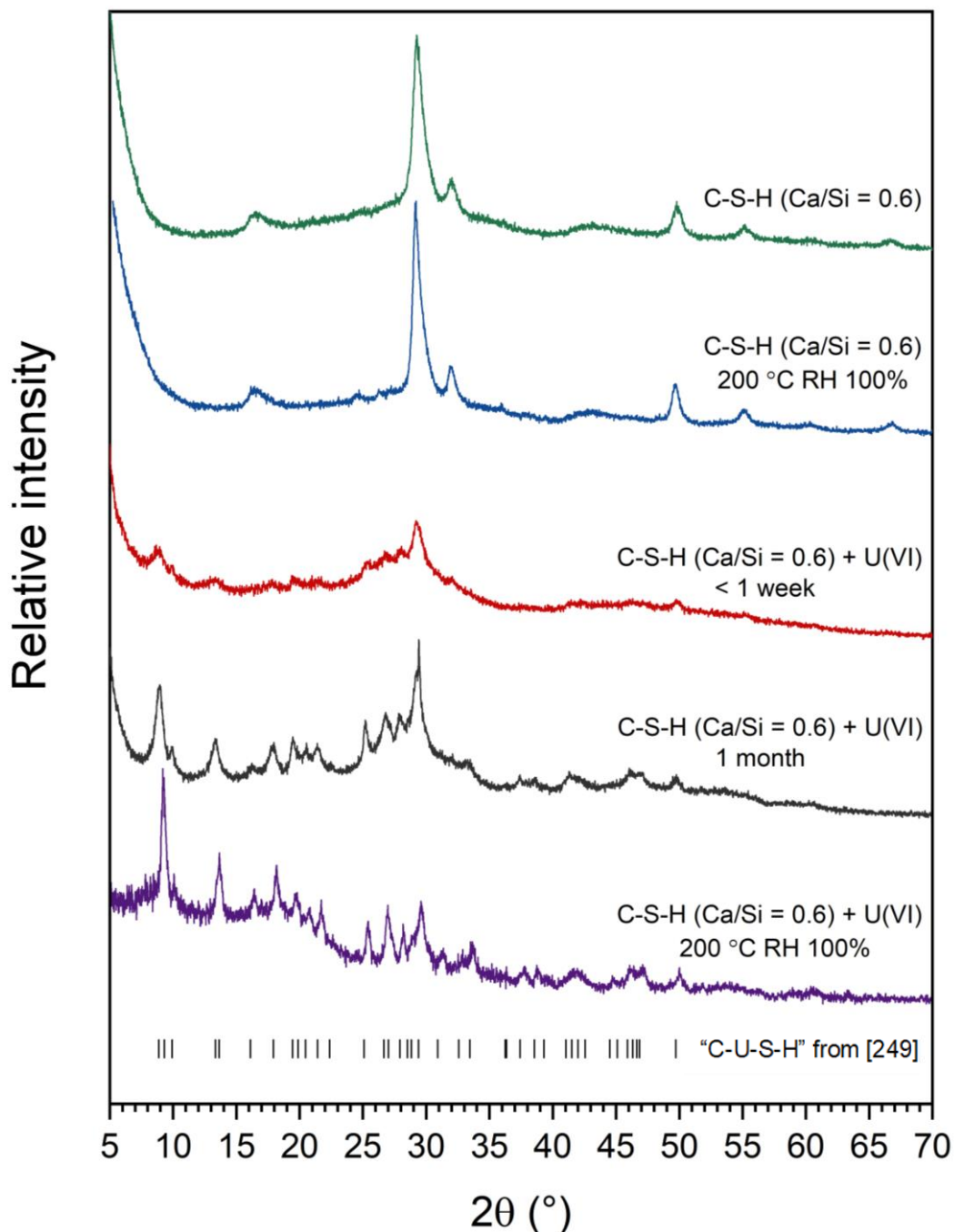


Figure 6.1: XRD patterns of C-S-H (Ca/Si = 0.6) from top to bottom: **1**) as synthesised and **2**) thermally treated (identified as tobermorite, PDF card no. 00-045-1480 [184]) compared to the U(VI) contacted CSH(0.6) phase after **3**) <1 week and **4**) 1 month ageing times (synthesised at TUoS) and **5**) thermally treated U(VI) contacted CSH(0.6) (synthesised at JRC). The peak positions for the **6**) $\text{Ca}_2(\text{UO}_2)_2(\text{Si}_2\text{O}_5)_3 \cdot 10(\text{H}_2\text{O})$ phase (“C-U-S-H”, PDF card no. 00-047-0497 [249]) are also given. All heating referred to was carried out at 200 °C and 100% RH in distilled non-degassed water.

6.2.1.2 Pu(VI) / C-S-H contact studies

The first part of the plutonium-directed work at JRC was aimed at understanding the efficacy of uranyl nitrate ($\text{U(VI)}_{(\text{aq})}$) as a surrogate for plutonyl nitrate ($\text{Pu(VI)}_{(\text{aq})}$) in C-S-H contact

experiments, and to determine if the same structural effects on C-S-H phases are observed as with U(VI). A Pu(VI) nitrate solution was produced by oxidation of a stock Pu(IV) nitrate solution, using double evaporation, similar to methods reported elsewhere [278,279]. An aliquot of Pu(IV) nitrate solution was heated to 200 °C until only solid remained. Concentrated nitric acid was added and heating was repeated until a dark-brown coloured solid was left. The oxidation state was not spectroscopically determined, but the presence of Pu(VI) was inferred from the solution colour [100,280]. Photographic evidence to show this colour change was not possible due to security restrictions on site. The isotopic composition of the plutonium used is given in **Table 6.1**.

Table 6.1: Plutonium isotopic composition (JRC).

Isotope percentages (wt %)					
²³⁸ Pu	²³⁹ Pu	²⁴⁰ Pu	²⁴¹ Pu	²⁴² Pu	²⁴¹ Am
0.01430 ± 0.00086	90.87 ± 1.8	8.95 ± 0.26	0.0804 ± 0.0019	0.0826 ± 0.0017	0.748 ± 0.002

Table 6.2 details the C-S-H samples that were contacted with aqueous Pu(VI). The pre-carbonated C-S-H samples, as described in **Chapters 3** and **4**, were subjected to 1 % CO₂ (10 000 ppm) atmosphere for 48 hours. The powders were sealed under an inert nitrogen atmosphere at TUoS before transport to JRC and were stored under argon when not in use at JRC. Aqueous Pu(VI) nitrate solution was added to 40 mg of C-S-H with a range of Ca/Si ratios (as stated in **Table 6.2**), to achieve the same absolute amount of actinide addition to C-S-H as with U(VI) experiments performed in **Chapter 5**. In this case, the S/L of C-S-H/water was 40 g L⁻¹ (unless stated otherwise in **Table 6.2**). The pH of the starting solution was not measured but was assumed to be << pH 3 due to the presence of nitrates. The resulting Pu / C-S-H suspensions were shaken well and left to equilibrate for 2 hours; the C-S-H solids were observed to turn from white to an orange-brown colour instantly after mixing with the Pu(VI) nitrate solution, and the pre-carbonated C-S-H solids appeared to be darker in colour than the non-carbonated C-S-H phases. The supernatant solution was collected, and the solids washed with 2 mL ethanol and 2 mL acetone. After Pu(VI) contact, all samples were unavoidably stored in air due to the setup of alpha glove box containment.

The Pu / C-S-H solids were then heated at 200°C and 100 % RH for 16 hours in an autoclave under non-degassed, distilled water. The supernatant solution was collected, and the solids washed as previously described. The solids turned from orange-brown to green and the supernatant solution was also green. Ideally, the resulting supernatant solutions would have been measured for their plutonium, calcium and silicon content (to assess the amount of

plutonium uptake and calcium and silicon release), however, it was not possible to obtain the data.

Table 6.2: C-S-H samples contacted with Pu(VI) as plutonyl nitrate. CSH(X) denotes a C-S-H phase where X = Ca/Si ratio. The “_C” suffix denotes C-S-H phases that were pre-carbonated in a 1 % CO₂ atmosphere for 48 hours prior to transport to JRC.

Sample name	C-S-H / mg	Pu / mg	H ₂ O / mL	Pu:C-S-H	Resulting pH*
CSH(0.6)	40	15	1	0.38:1	3-4
CSH(1.2)	40	15	1	0.38:1	8
CSH(0.6)_C	40	15	1	0.38:1	8
CSH(1.2)_C	40	15	1.6**	0.38:1	8

*determined approximately using indicator paper

**S/L = 25 g L⁻¹

6.2.2 Part 2 – U(IV) as a Pu(IV) surrogate: a lower concentration study

Experiments in this part were performed under an inert argon atmosphere using Schlenk apparatus, where possible, and the experimental procedure for addition of actinide solutions to C-S-H, and subsequent washing, drying and characterisation were followed as in **Part 1**.

Initially, additions of a stock U(IV) nitrate solution to aqueous suspended C-S-H phases were trialled to be analogous in pH and relative amount of actinide/C-S-H as with the plutonyl nitrate experiments. XRD measurements of the phases after addition of uranium nitrate were shown to be almost completely amorphous and, together with visible observations, it was determined that the pH was too acidic for further experiments; particularly for the CSH(0.6) phases where most of the phase was observed to have dissolved (**Table 6.3**).

Table 6.3: C-S-H samples contacted with U(IV) as uranium nitrate. CSH(x) denotes a C-S-H phase where $x = \text{Ca/Si}$ ratio. The “_C” suffix denotes C-S-H phases that were pre-carbonated in a 1 % CO₂ atmosphere for 48 hours prior to transport to JRC.

Sample name	C-S-H / mg	U / mg	H ₂ O / mL	U:C-S-H	Resulting pH*	Observations by eye
CSH(0.6)	200	75	8	0.38:1	0	Light green solution, most C-S-H dissolved
CSH(1.2)	200	75	8	0.38:1	7	Colourless solution, some C-S-H remaining
CSH(0.6)_C	200	75	8	0.38:1	0	Light green solution, most C-S-H dissolved
CSH(1.2)_C	200	75	8	0.38:1	7	Colourless solution, some C-S-H remaining

*determined approximately using indicator paper

From these findings, it was decided that a more diluted aqueous uranium tetrachloride (U(IV)Cl₄) stock solution should be used, to allow greater control over the pH (starting solution pH = ~5). A S/L ratio of 25 g L⁻¹ for C-S-H/solution was used, which was later reduced to ~12 g L⁻¹ by dilution with water (unless stated otherwise in **Table 6.4**) for an actinide/C-S-H ratio of 0.05:1 by weight (**Table 6.4**). The washed phases were heated at 200°C and 100 % RH for 16 hours in an autoclave under non degassed water, as with the plutonium-containing phases described in **Part 1**. No obvious colour change was noted after heating.

Table 6.4: C-S-H samples contacted with U(IV) as uranium tetrachloride. CSH(x) denotes a C-S-H phase where $x = \text{Ca/Si}$ ratio. The “_C” suffix denotes C-S-H phases that were pre-carbonated in a 1 % CO₂ atmosphere for 48 hours prior to transport to JRC.

Sample name	C-S-H / mg	U / mg	H ₂ O / mL	U:C-S-H	Resulting pH*
CSH(0.6)	200	10.75	10**	0.05:1	9-10
CSH(1.2)	200	10.75	17	0.05:1	11
CSH(0.6)_C	200	10.75	17	0.05:1	9-10
CSH(1.2)_C	200	10.75	17	0.05:1	10-11

*determined approximately using indicator paper

**S/L = 20 g L⁻¹

XRD patterns for all actinide contacted C-S-H phases were measured before and after heating. Samples were prepared by dropping a suspension of the phase in acetone onto a low background Si(111) plate holder which was left to dry before covering with a small drop of liquid paraffin.

6.2.3 Geochemical modelling

Geochemical modelling was performed using the Phreeqc Interactive 3.4.0-12927 software [248] and the Lawrence Livermore National Laboratory thermodynamic database, to determine the saturation index (SI) of mineral phases likely to form in aqueous solution under experimental conditions in both **Parts 1** and **2**. The saturation index of a phase determines whether an aqueous system is saturated with respect to the given phase, such that: SI = 0 means the phase is in equilibrium (i.e. saturated); SI < 0 means the phase is undersaturated and SI > 0 means the phase is supersaturated.

As ICP analyses of the solutions were not able to be measured at JRC, the concentrations of calcium and silicon released from C-S-H phases in contact with acidic 10 mM uranyl nitrate (initial pH ~3) from **Chapter 5** were used for the model input. Similarly, the concentration of carbonate in solution could not be determined, therefore, the model was generated (i) in the absence of HCO₃⁻; (ii) at the equilibrium HCO₃⁻ concentration required to achieve plutonium-carbonate precipitation [100]; and (iii) at elevated carbonate concentrations (**Table 6.5**). The plutonium and uranium concentrations input to the model were calculated from the experimental concentrations used, already discussed in **Tables 6.2** and **6.4**, for plutonium and uranium, respectively. Results from geochemical modelling of U(VI) in C-S-H systems has already been discussed in **Chapter 5** and the results are not reproduced here, but are discussed where relevant.

Table 6.5: Geochemical modelling inputs.

	Ca / ppm	Si / ppm	Pu / ppm	U(IV) / ppm	HCO ₃ ⁻ / ppm
CSH(0.6)	360	48	15 000	1 000	0
					0.015
					1 000
CSH(1.2)	460	8	15 000	1 000	0
					0.015
					1 000

Given that the oxidation state of the plutonium was not spectroscopically confirmed, in the geochemical model, both Pu(VI) and Pu(IV) were accounted for. This also allows for consideration of changes in the plutonium oxidation state during the course of the experiment, which is explained in further detail as this Chapter progresses.

6.2.4 PuO₂ encapsulation in Portland cement blends

In a further study between TUoS and NNL, the implications of cementitious encapsulation of PuO₂ in cement blends commonly used for radioactive waste immobilisation was described

[131]. Portland cement grouts of BFS/OPC 3.44:1 (w/s = 0.35) and PFA/OPC 3:1 (w/s = 0.43), respectively, were prepared at the NNL Central Lab facility at the Sellafield site. PuO₂, obtained from Magnox fuel reprocessing, was encapsulated in the grout at 0.5 wt % and the blends were cured under a saturated-lime solution for over a year, as well as analogous non-PuO₂ containing control cement blends; the full experimental protocol is detailed in *Kearney, Yorkshire et al.* [131] (see **Appendix 1**) The isotopic composition of the plutonium used is given in **Table 6.6**.

Table 6.6: Plutonium isotopic composition (NNL).

Isotope percentages (wt %)					
²³⁸ Pu	²³⁹ Pu	²⁴⁰ Pu	²⁴¹ Pu	²⁴² Pu	²⁴¹ Am
0.27	72	23	3.2	0.11	0.49

The results from XRD and SEM/EDX results reported by *Kearney, Yorkshire et al.* are discussed. Further to this, the storage solutions of the cements were also analysed. The solutions were filtered through a 0.45 µm filter and the pH was measured before acidification and analysis by alpha spectrometry and ICP-MS. The control storage solutions were also analysed by ICP-OES.

6.3 Results

The experimentally determined pH values of the pure non-carbonated C-S-H phases equilibrated in UHQ water at TUoS, from **Chapter 4**, are given in **Table 6.7** for reference.

Table 6.7: pH values of C-S-H phases in UHQ water at 25 g L⁻¹.

Ca/Si	pH
0.6	10.0 ± 0.1
1.2	11.7 ± 0.1

6.3.1 Plutonium (VI) contacted with C-S-H

The XRD patterns for each of the Pu(VI)-contacted C-S-H samples before and after heating are shown in **Figure 6.2-5**. Diffraction patterns were collected from 10-70 ° 2θ but only the 20-70 ° 2θ range is shown here due to the high background interference at low angles. The formation of calcite was common in most of the C-S-H samples and did not show a particular

trend, suggesting that this was due to carbonation from different levels of ambient CO₂ exposure during the time that the samples spent at JRC. Vaterite and aragonite polymorphs, however, were only observed in the pre-carbonated phases CSH(1.2) and CSH(0.6), respectively.

6.3.1.1 Plutonium contacted C-S-H(0.6)

The low pH of the Pu(VI) solution resulted in complete dissolution of the C-S-H structure for CSH(0.6) which is inferred from the absence of C-S-H peaks in the XRD pattern (**Figure 6.2**) and the resulting pH of 3. Similar behaviour was observed for C-S-H contacted with uranyl nitrate at low pH (**Chapter 5**) and, as determined for the U(VI) / C-S-H system, it is also likely that significant leaching of calcium from the C-S-H occurred in this experiment. If plutonium was removed from solution, it may have done so as a colloidal species, amorphous in nature, possibly sorbed to the outside of the silica phase [281].

After heating of this sample there were no peaks observable for calcium- or silicon-containing species, however, it was possible to index peaks identifiable as a hydrous Pu(IV)O₂ phase (PuO₂·xH₂O; PDF card no. 01-073-7903 [282]) (**Figure 6.2**) which agrees with the green colour of the solid observed [100] and supports the hypothesis that plutonium from solution was sorbed to the outer-surface of the C-S-H. The peaks were diffuse, indicating the nano-crystalline nature of PuO₂·xH₂O [100]. The presence of the +4 oxidation state of plutonium is thought to be due to self-irradiation-induced reduction of Pu(VI) to Pu(IV) [91], which is discussed in further detail in *Sections 6.4.1* and *6.4.2*.

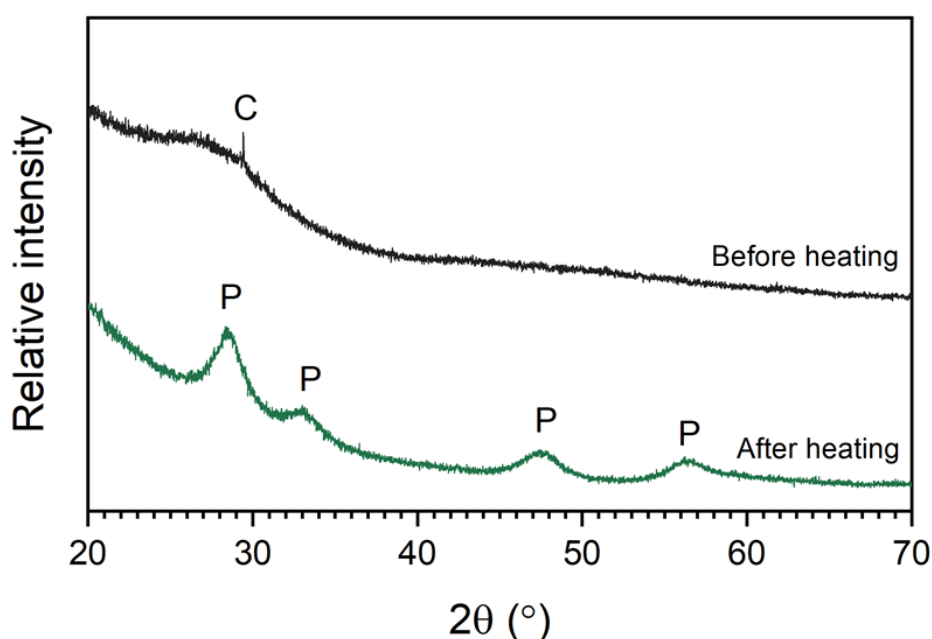


Figure 6.2: XRD patterns of C-S-H(0.6) after contact with Pu(VI) before and after heating
C = calcite (PDF card no. 01-078-4614 [187]); P = PuO₂·xH₂O (PDF card no. 01-073-7903 [282])

6.3.1.2 Plutonium contacted CSH(0.6): pre-carbonated

For pre-carbonated CSH(0.6) it was not possible to index any peaks for a C-S-H mineral phase (**Figure 6.3**), as with the non-carbonated CSH(0.6) sample, both before and after heating. The pH of the supernatant solution was pH 8, suggesting some calcium release. Pre-carbonation would have also led to de-calcification of the C-S-H structure and formation of carbonates; dissolution of which would also generate a pH of ~8 [253]. $\text{PuO}_2 \cdot x\text{H}_2\text{O}$ was tentatively indexed in the XRD pattern acquired after heating.

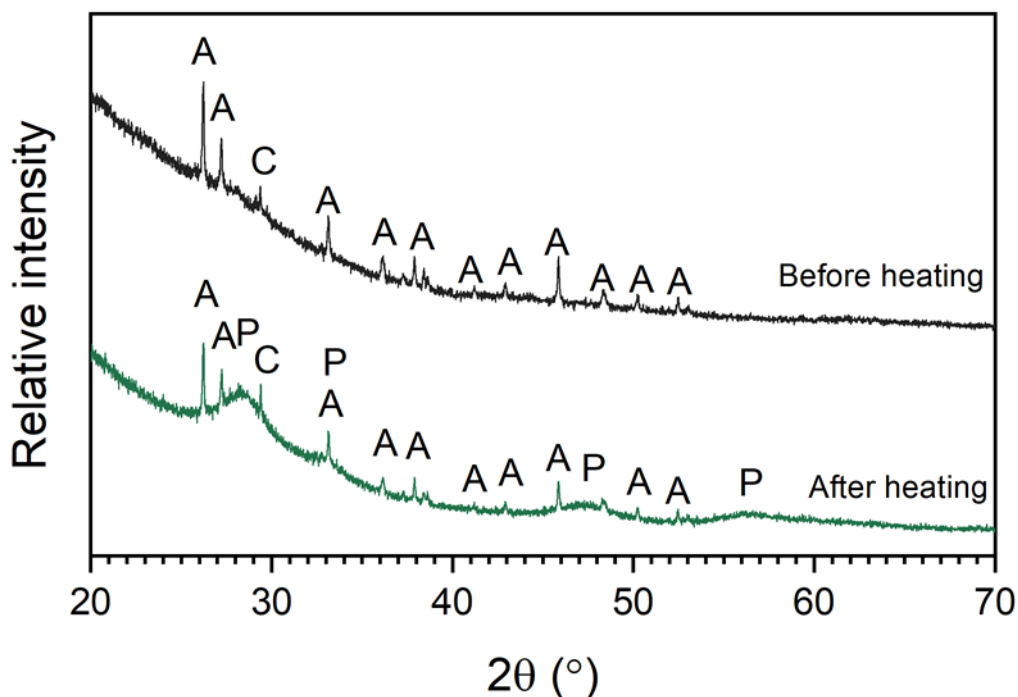


Figure 6.3: XRD patterns of C-S-H(0.6) carbonated after contact with Pu(VI) before and after heating
A = aragonite (PDF card no. 01-085-6703 [190]); C = calcite (PDF card no. 01-078-4614 [187]); P = $\text{PuO}_2 \cdot x\text{H}_2\text{O}$ (PDF card no. 01-073-7903 [282])

6.3.1.3 Plutonium contacted CSH(1.2)

As for CSH(0.6), prior to heating there was no evidence in the XRD pattern of plutonium containing phases, again suggesting that either plutonium remained in solution or that it was incorporated into, or sorbed via silica onto, the solid C-S-H phase as colloids or another amorphous phase. As for CSH(0.6), after heating, peaks indexed to $\text{PuO}_2 \cdot x\text{H}_2\text{O}$ were identified. The higher calcium content of the phase resulted in better retention of the C-S-H structure, as can be seen in **Figure 6.4**. Calcium leaching would have occurred to some extent to cause an increase from the acidic starting pH to the final pH of 8. The presence of calcite in CSH(1.2) after heating was likely a result of storing the samples in air and using non-degassed water for the heating stage, leading to CO_2 ingress and carbonation.

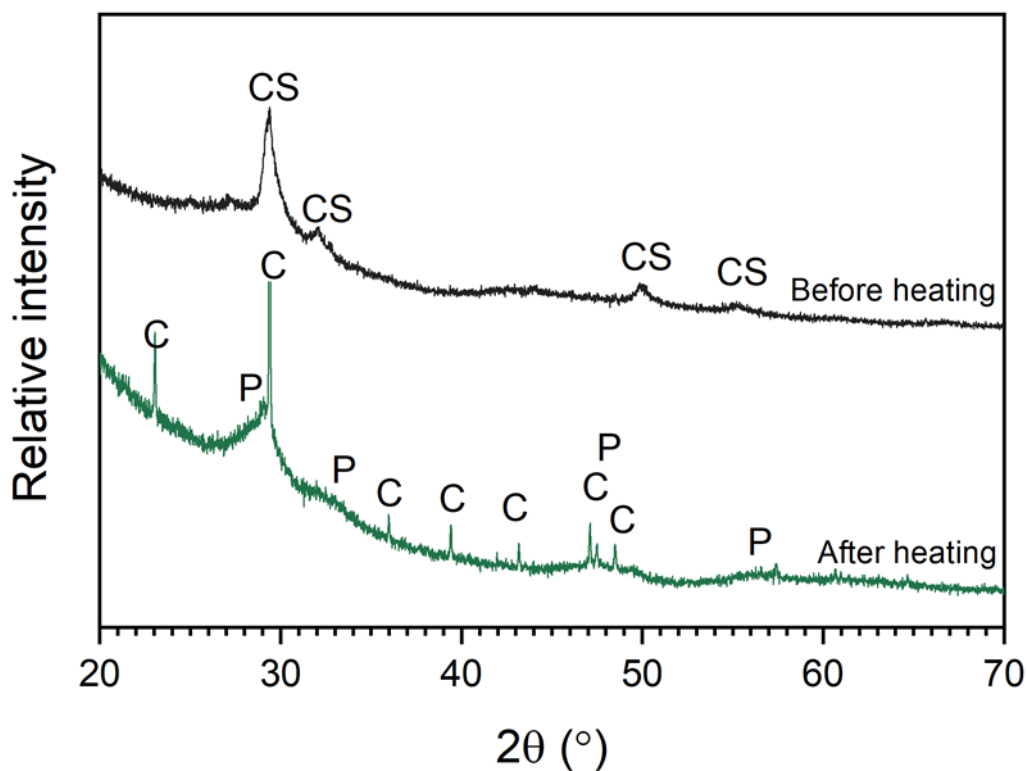


Figure 6.4: XRD patterns of C-S-H(1.2) after contact with Pu(VI) before and after heating
 C = calcite (PDF card no. 01-078-4614 [187]) ; CS = C-S-H(I) (tobermorite, PDF card no. 00-045-1480 [184]); P = $\text{PuO}_2 \cdot x\text{H}_2\text{O}$ (PDF card no. 01-073-7903 [282])

6.3.1.4 Plutonium contacted CSH (1.2): pre-carbonated

In the pre-carbonated CSH(1.2) sample a small amount of C-S-H was identifiable prior to heating, which was subsequently lost after heating. Calcium leaching was again indicated by the increased pH of the supernatant solution, which reached pH 8. However, as calcium leaching also occurred in the non-carbonated CSH(1.2) sample where the C-S-H structure was retained, the cause of significant decalcification in this case could also be related to pre-carbonation effects [233,256]. The vaterite polymorph of calcium carbonate was identified both before and after heating, which does suggest calcium decalcification from the C-S-H phase due to the pre-carbonation process. Once again, $\text{PuO}_2 \cdot x\text{H}_2\text{O}$ was tentatively indexed in the XRD pattern acquired after heating.

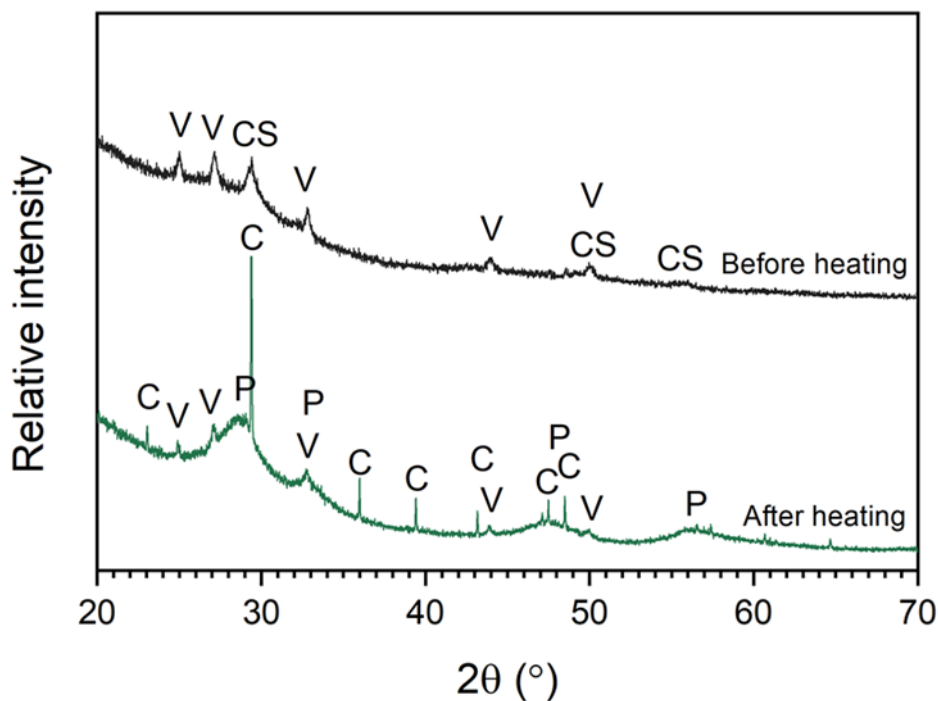


Figure 6.5: XRD patterns of C-S-H(1.2) after contact with Pu(VI) before and after heating
 C = calcite (PDF card no. 01-078-4614 [187]); CS = C-S-H(I) (tobermorite PDF card no. 00-045-1480 [184]); P = PuO₂·xH₂O (PDF card no. 01-073-7903 [282]); V = vaterite (PDF card no. 04-017-8634 [191]).

6.3.2 Uranium(IV) contacted with C-S-H

The results from the uranium nitrate-contacted C-S-H phases are not discussed here as it was previously concluded that the low pH caused dissolution of the C-S-H structure. The focus instead is on U(IV) interactions with C-S-H in a uranium tetrachloride solution, for comparison with the results of the plutonium experiments, which yielded Pu(IV) as PuO₂·xH₂O. The pH values obtained were more favourable to maintaining the C-S-H structure compared to the highly acidic initial nitrate solution used, however, given that the relative amount of uranium to C-S-H (0.05:1 by weight) was low, identification of uranium-containing phases by the XRD patterns proved difficult.

Aragonite and vaterite were identified in the pre-carbonated CSH(0.6) and CSH(1.2) samples, respectively, as with the plutonium experiments. However, vaterite and a small amount of calcite were also identified in the CSH(0.6) sample after heating. This is likely a result of the storage conditions of the C-S-H samples between the time-frame of the plutonium and uranium experiments (~2 months).

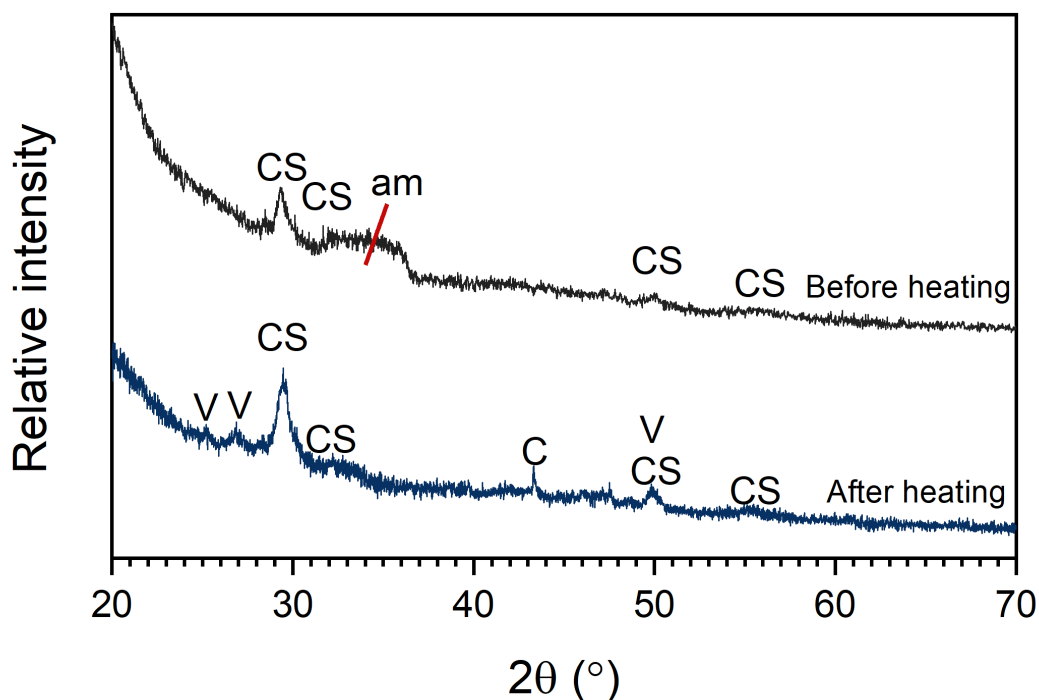


Figure 6.6: XRD patterns of CSH(0.6) after contact with U(IV) before and after heating. am = amorphous region; C = calcite (PDF card no. 01-078-4614 [187]); CS = C-S-H(I) (tobermorite PDF card no. 00-045-1480 [184]); V = vaterite (PDF card no. 04-017-8634 [191]).

6.3.2.1 Uranium contacted CSH(0.6)

For the CSH(0.6) phase, the retention of the C-S-H structure can be seen from the XRD reflections that were previously assigned in **Part 1 (Figure 6.6)** which suggests that there was a lower calcium release from the C-S-H structure when compared to the higher concentration (i.e. lower pH) Pu(VI) / CSH(0.6) studies. This indicates the detrimental effect of localised concentrations of acidic radionuclides on the stability of low Ca/Si C-S-H phases.

The pH of 9-10 for the resulting solution does indicate some calcium release, however this is comparatively minimal given that C-S-H is still identifiable by XRD. A large diffuse contribution to the diffraction pattern was also observed between $\sim 33\text{-}38^\circ 2\theta$, possibly resulting from the precipitation of an amorphous silica phase. There are no obvious peaks indicative of carbonation, however these could be masked by the large noise contribution to the signal. After heating of this phase, the diffuse contribution decreased but the C-S-H reflections remained. In addition, calcite peaks were identified, likely introduced from carbonation that occurred during the heating step or while the phases could not be stored under argon.

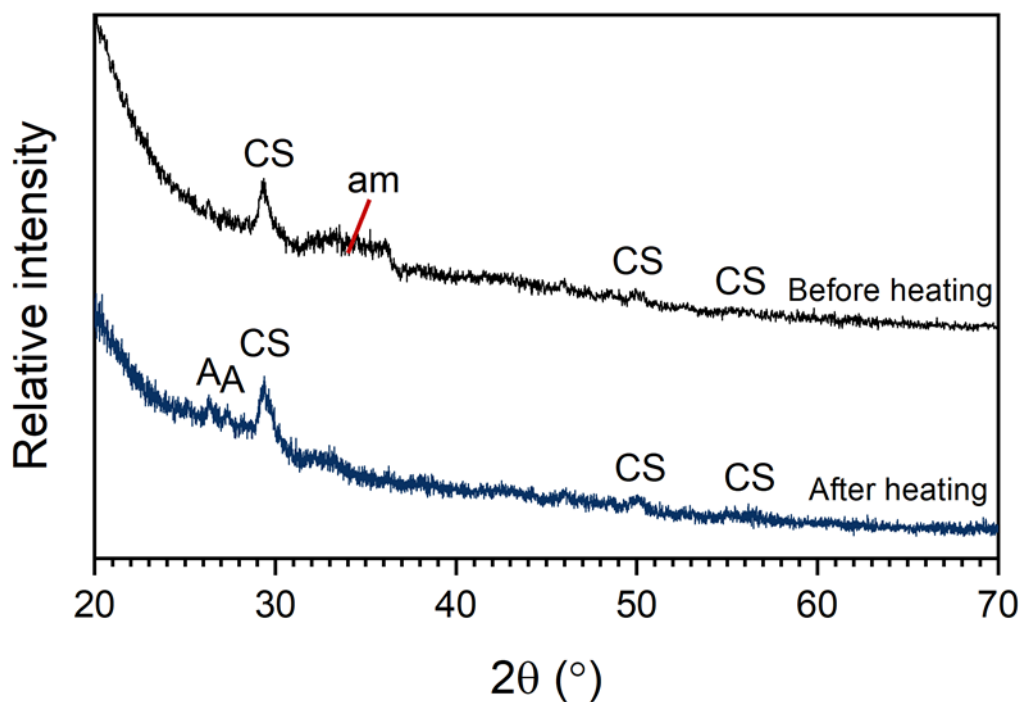


Figure 6.7: XRD patterns of CSH(0.6) carbonated after contact with U(IV) before and after heating. am = amorphous region; A = aragonite (PDF card no. 01-085-6703 [190]); CS = C-S-H(I) (tobermorite PDF card no. 00-045-1480 [184]).

6.3.2.2 Uranium contacted CSH(0.6): pre-carbonated

The carbonated CSH(0.6) sample showed little change before and after heating when analysed by XRD (**Figure 6.7**). The C-S-H structure was maintained and peaks for calcite were identifiable in both cases. An amorphous region, between $\sim 33\text{--}38^\circ 2\theta$, which appears to diminish after heating, was observed; this was the major observable difference between samples before and after heating. As for the non-carbonated phase, the resulting pH after U(IV) addition was between 9 and 10.

6.3.2.3 Uranium contacted CSH(1.2)

The CSH(1.2) sample showed retention of the C-S-H structure both after U(IV) addition and after heating (**Figure 6.8**). The resulting pH of 11 suggests that release of calcium from the C-S-H occurred, but not a significant amount to cause full dissolution of C-S-H. Before heating, CSH(1.2) showed increased amorphicity compared to after heating (as evidenced by regions of diffuse scattering between $\sim 23\text{--}29^\circ$ and $\sim 33\text{--}38^\circ 2\theta$). There did not appear to be any observable carbonation before or after heating. The major difference observed for this phase was the emergence of a peak at $\sim 15.2^\circ 2\theta$ after U(IV) addition which then disappeared after heating. This peak could be attributed to the highest intensity reflection (011) of UCl_4 (PDF card no. 01-078-1413 [283]) (**Figure 6.9**) [284], however, the peak better corresponds to the

high intensity reflection (003) of a hydrous calcium-uranyl phase; Ca-bearing clarkeite ($\text{Ca}(\text{UO}_2)\text{O}(\text{OH}) \cdot 0.1(\text{H}_2\text{O})$; PDF card no. 00-050-1586 [73]), at $15.03^\circ 2\theta$. This would indicate oxidation of U(IV) to U(VI).

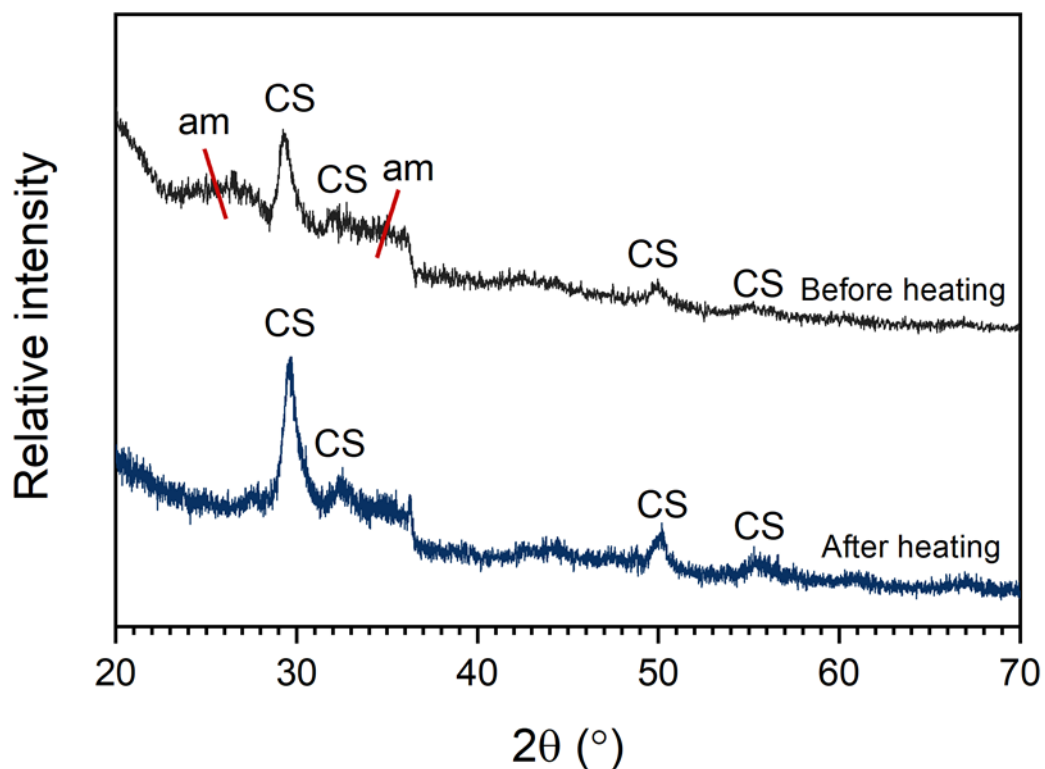


Figure 6.8: XRD patterns of CSH(1.2) after contact with U(IV) before and after heating. am = amorphous region; CS = C-S-H(I) (tobermorite, PDF card no. 00-045-1480 [184]).

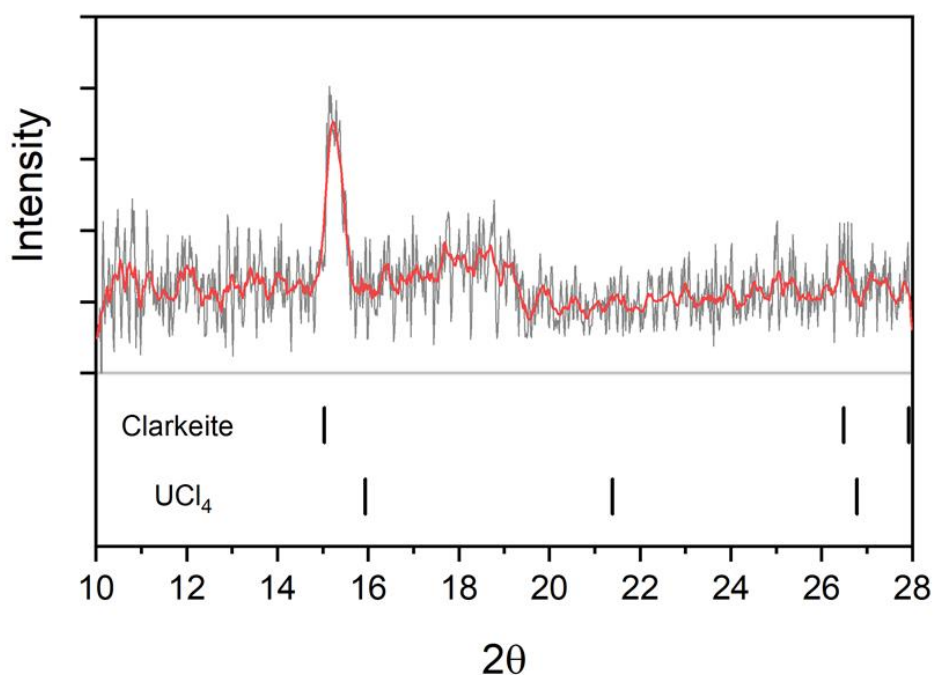


Figure 6.9: XRD pattern of C-S-H(1.2) contacted with UCl_4 before heating. The raw data (grey) are accompanied by an adjacent average smoothing of 10 points (red). Peak positions for clarkeite (PDF card no. 00-050-1586 [73]) and UCl_4 (PDF card no. 01-078-1413 [283]) are shown.

6.3.2.4 Uranium contacted CSH(1.2): pre-carbonated

Carbonated CSH(1.2) samples showed XRD peaks attributable to C-S-H, calcite and vaterite both before and after heating. Before heating, the strongest calcite peak was possibly masked by the main C-S-H reflection (**Figure 6.10**). The resulting pH of the solution after the contact experiment was between pH 10 and 11 which is slightly lower than for non-carbonated CSH(1.2) (which had a pH of 11), which is consistent with the presence of calcium carbonates [285]. The major differences, before and after heating, for the CSH(1.2) carbonated sample were observed in the background region of the XRD pattern between 10-28 °2 θ . After heating additional peaks were present in this region, notably at ~ 11.4, 13.5 and 18.5 °2 θ (**Figure 6.11**) that were not present before heating. No possible uranium, silicon, calcium, chlorine or carbon containing phases that were available in the PDF 4+ and HighScore Plus software databases could be definitively identified as potential candidates. The presence of soddyite ((UO₂)₂SiO₄·2H₂O; PDF card 01-077-0604 [286]) could be plausible, with a slight shift in the peak position that could be attributable to the water content of the phase formed.

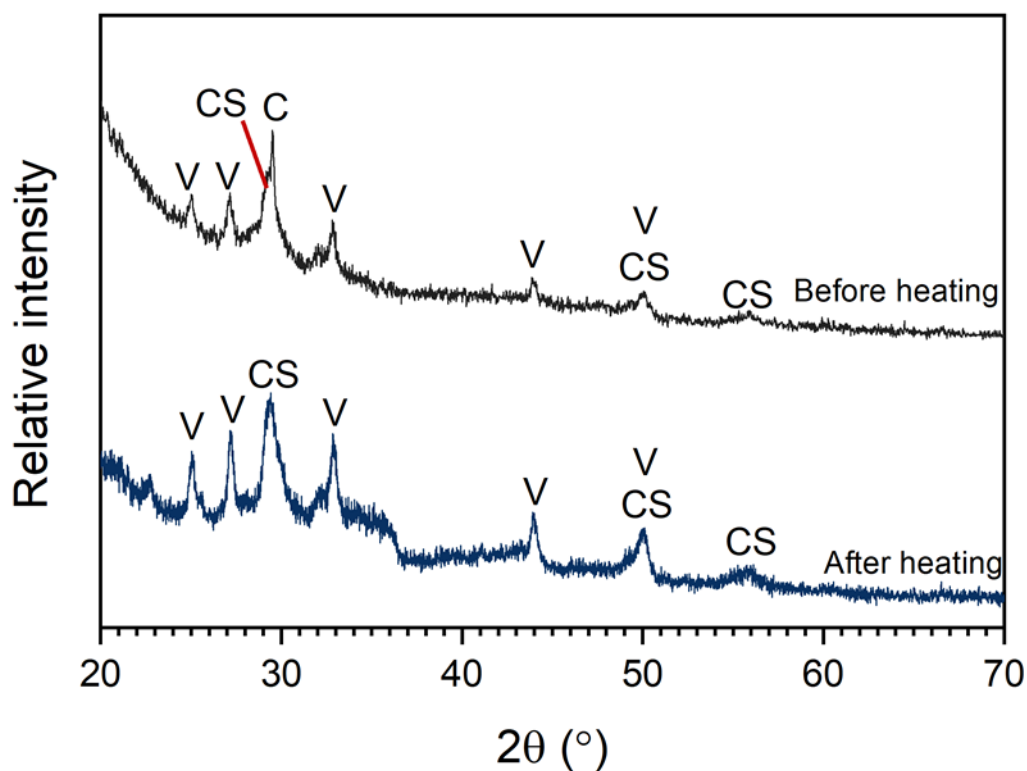


Figure 6.10: XRD patterns of CSH(1.2) carbonated after contact with U(IV) before and after heating. CS = C-S-H(I) (tobermorite, PDF card no. 00-045-1480 [184]); V = vaterite (PDF card no. 04-017-8634 [191]).

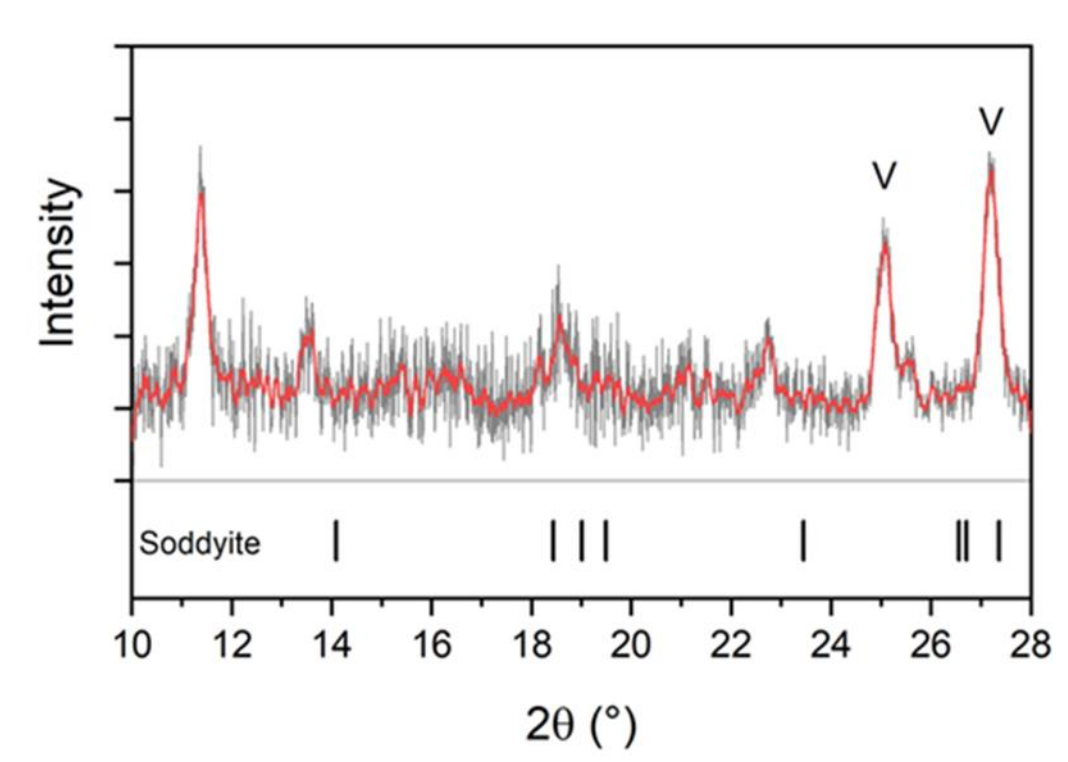


Figure 6.11: XRD patterns of carbonated C-S-H(1.2) after heating. The raw data (grey) are accompanied by an adjacent average smoothing of 10 points (red). The peak positions for soddyite (PDF card 01-077-0604 [286]) are shown. V = vaterite (PDF card no. 04-017-8634 [191]).

6.3.3 Geochemical modelling results

The results for geochemical modelling of plutonium and uranium solid phase formation in C-S-H suspensions are shown in **Figures 6.12** and **6.13**, respectively, to cover the experimental pH ranges and the 'ideal' pH to maintain C-S-H in solution.

For plutonium, the results did not vary significantly with Ca/Si ratio. $\text{PuO}_2(\text{s})$ was identified as the most saturated phase in both cases at the experimentally measured values of pH 3/4 and 8. The hydrous oxide, as $\text{PuO}_2 \cdot 2\text{H}_2\text{O}(\text{am})$, was also shown to be saturated from pH 4-12. At pH 3 for Ca/Si = 0.6, only $\text{PuO}_2(\text{s})$ and SiO_2 were shown to be saturated, which is in agreement with the identification of only $\text{PuO}_2 / \text{PuO}_2 \cdot x\text{H}_2\text{O}$ in the X-ray diffraction pattern for CSH(0.6) and the hypothesis that plutonium was sorbed, physically or chemically, to an amorphous silica phase [281]. Above pH ~10 the calculated SI of amorphous silica decreased due to increased silicon solubility at high pH [231].

Tobermorite, only shown to be saturated from pH ~10 onwards at both Ca/Si ratios, is the calcium silicate mineral with the closest structure to that of C-S-H(I) phases [170]. This does not agree with the XRD patterns for CSH(1.2) and CSH(1.2) C where at least the most intense diffraction peak of C-S-H(I) was still identified at ~29 ° 2θ. *Dickson et al.* observed the equilibrium pH of synthetic tobermorite to be 9.48 ± 0.45 [287] and, taking into account the

error associated with the pH determination in this study using indicator paper, the tobermorite phase was assumed to be in equilibrium with the solid phase at pH ~8-9 (SI = ~0).

Calcite was shown to be saturated in the system at 1000 ppm for both Ca/Si ratios. As calcium carbonates were identified in the XRD patterns for all of the samples, this indicates that the dissolved carbonate concentration was at least 1000 ppm in the solutions to achieve calcium carbonate precipitation.

As for plutonium-carbonate complexation, the $\text{Pu}(\text{OH})_2\text{CO}_3$ phase was calculated to be saturated at both the lower carbonate concentration (0.015 ppm) and elevated concentration (1000 ppm) for both Ca/Si ratios. Although no plutonium hydroxy-carbonate complexes were identified by XRD, their formation seems very likely at the elevated concentrations of carbonate assumed here [100,288] and their formation may be masked by co-precipitation with the nano-crystalline $\text{PuO}_2 \cdot x\text{H}_2\text{O}$ phase.

In the case of the U(IV) model, the uranium phases identified were UO_2 , UO_2 (am) and coffinite (USiO_4) at both Ca/Si ratios. Both UO_2 phases maintained a steady SI in the pH range 8-12, whereas the SI of coffinite started to decrease from pH 9 in both cases. The generation of tobermorite and calcite phases showed similar behaviour as in the plutonium model. The mineral phase rutherfordine (UO_2CO_3) was identified by the model, but the SI was largely negative at the pH range plotted for both concentrations of HCO_3^- .

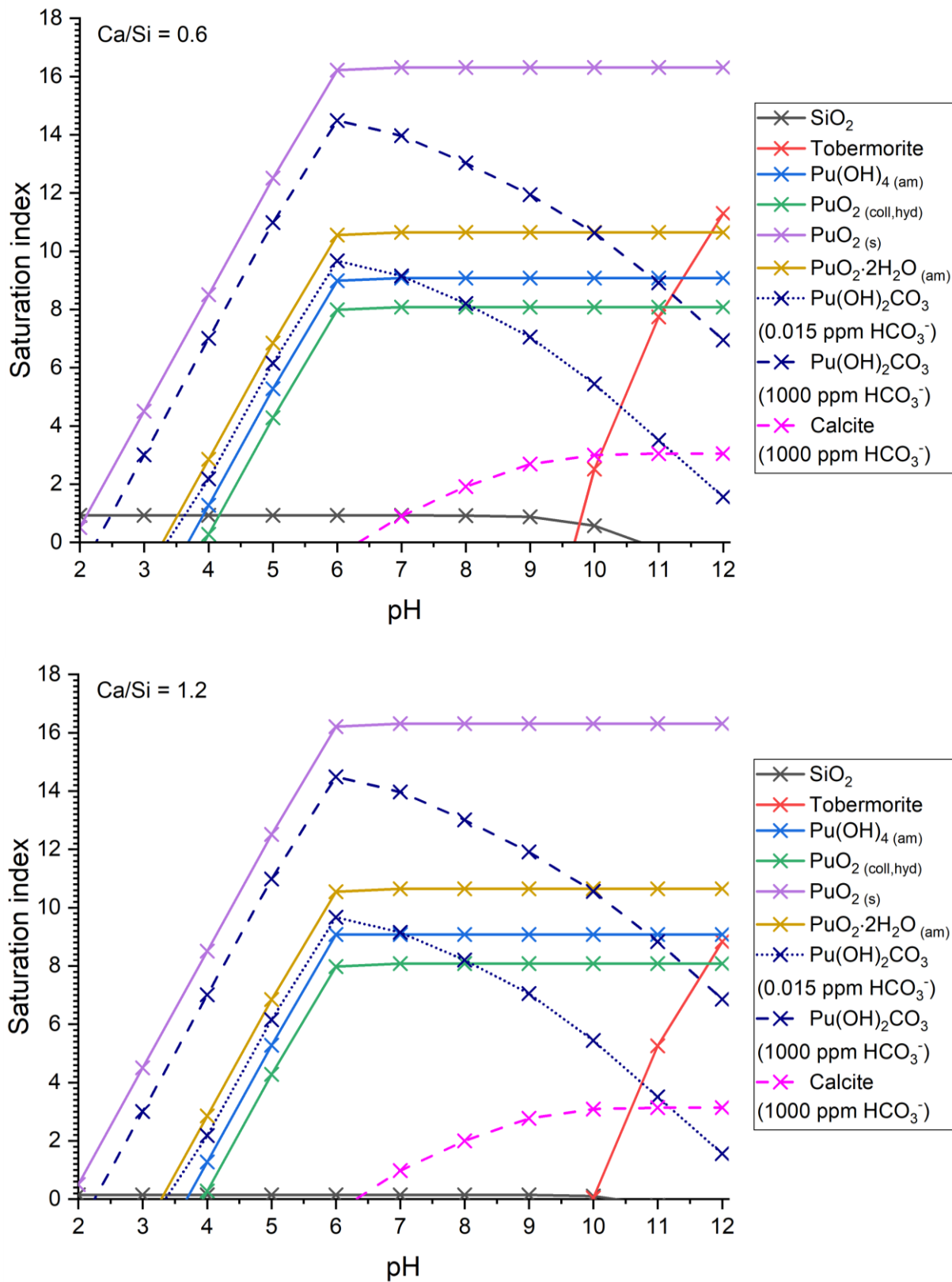


Figure 6.12: Geochemical modelling results showing saturated phases over the pH range 2-12 for Pu in contact with C-S-H at Ca/Si = 0.6 (top) and Ca/Si = 1.2 (bottom).

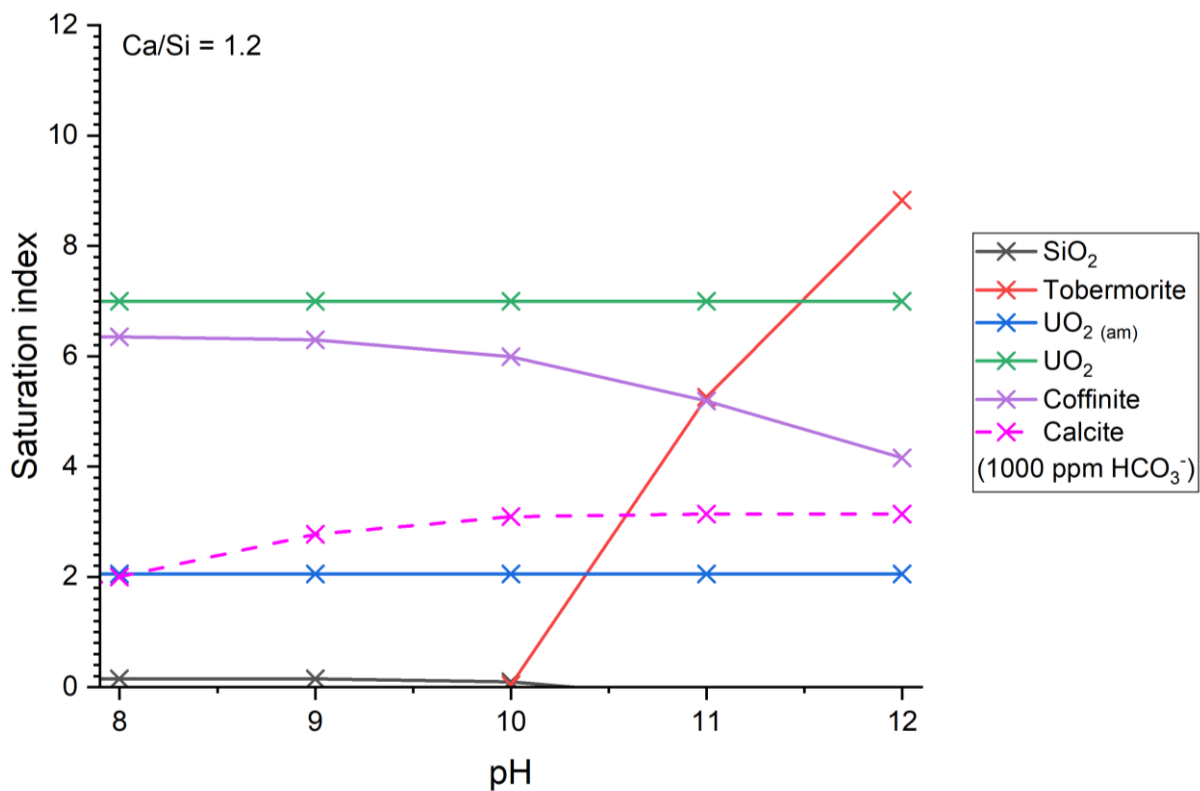
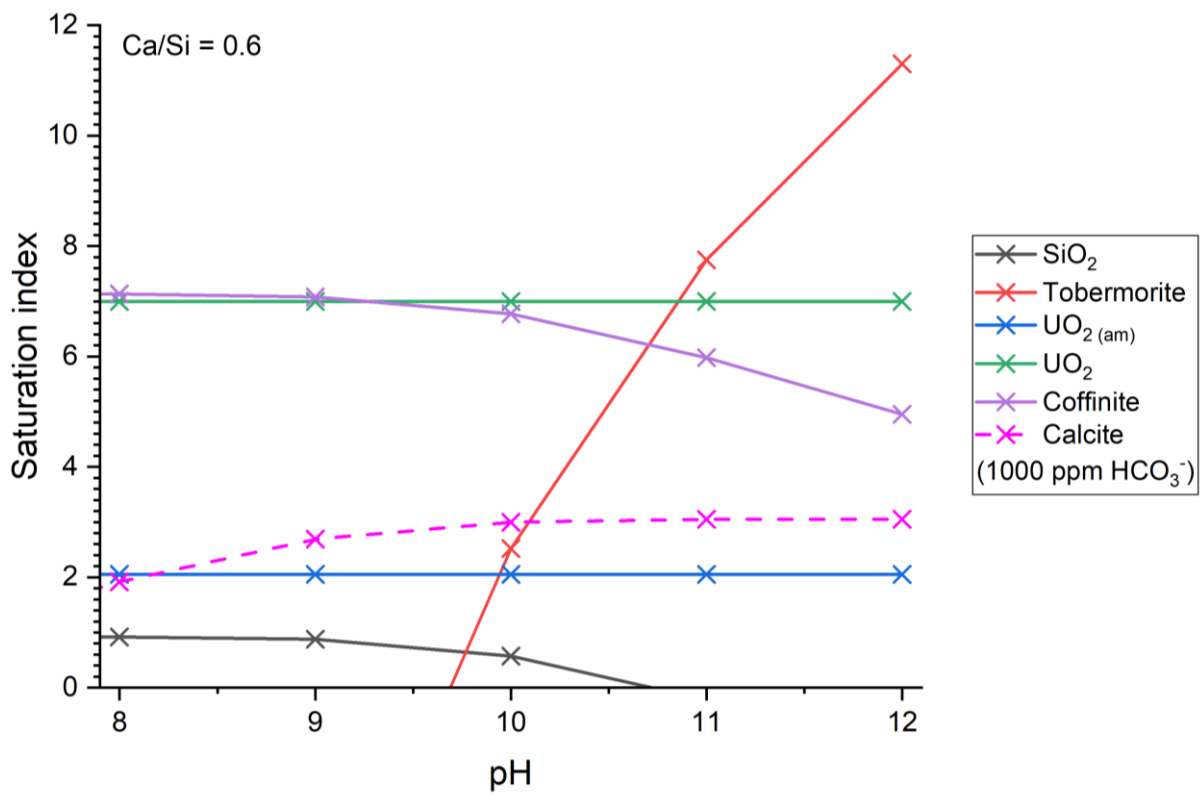


Figure 6.13: Geochemical modelling results showing saturated phases over the pH range 8-12 for U(IV) in contact with C-S-H at Ca/Si = 0.6 (top) and Ca/Si = 1.2 (bottom).

6.3.4 PuO₂ encapsulation in Portland cement blends

6.3.4.1 Solid-phase analyses

The XRD results for the PFA/OPC and BFS/OPC blends encapsulating PuO₂ particles are shown in **Figures 6.14**. It was difficult to establish differences in phase assemblage between control and active samples, respectively, as different instruments were used in both cases. Sample preparation for active samples required mounting of the cement powder into an epoxy resin which led to a large background contribution, and subsequently a background subtraction was performed. This hindered peak assignment at angles below 30° 2θ. Expected PuO₂ reflections were marked; no obvious effect of plutonium incorporation was seen to changes in hydrate phases by XRD alone and peaks for isolated PuO₂ are identifiable (PDF card no. 01-073-7903 [282]). From assigned peaks it is clear that pozzolanic reactivity of fly ash resulted in a lower portlandite fraction in the PFA/OPC sample after ~1 year curing, in comparison to the BFS/OPC blend [289]. Diffuse scattering was observed for both cement blends between 20-40° 2θ, indicating the C-S-H phase [184,185], however this diffuse scattering was less identifiable in the active samples due to the effect of background subtraction.

The corresponding SEM/EDX analyses for the PFA/OPC and BFS/PC blends taken from [131] are also shown in **Figure 6.15**. In addition to the typical features of BFS and PFA blends, including large angular Calumite™ (coarse-ground slag) particles and spherical fly ash particles, respectively, the EDX spot analysis also distinguishes between areas of PuO₂ (**Spot 1**) and areas containing no PuO₂ inclusions (**Spot 2**) for both cement blends (**Table 6.8**).

For the BFS/OPC cement, the visibly bright PuO₂ particle is an agglomerate of smaller particles with darker areas of lower density, possibly including calcium and silicon. This suggests that cement clinker and supplementary cementitious materials have hydrated around the textured morphology of the PuO₂ particles. The detection of calcium and silicon by EDX corresponding with the PuO₂ particle shown in the PFA/OPC blend also suggests the same effect.

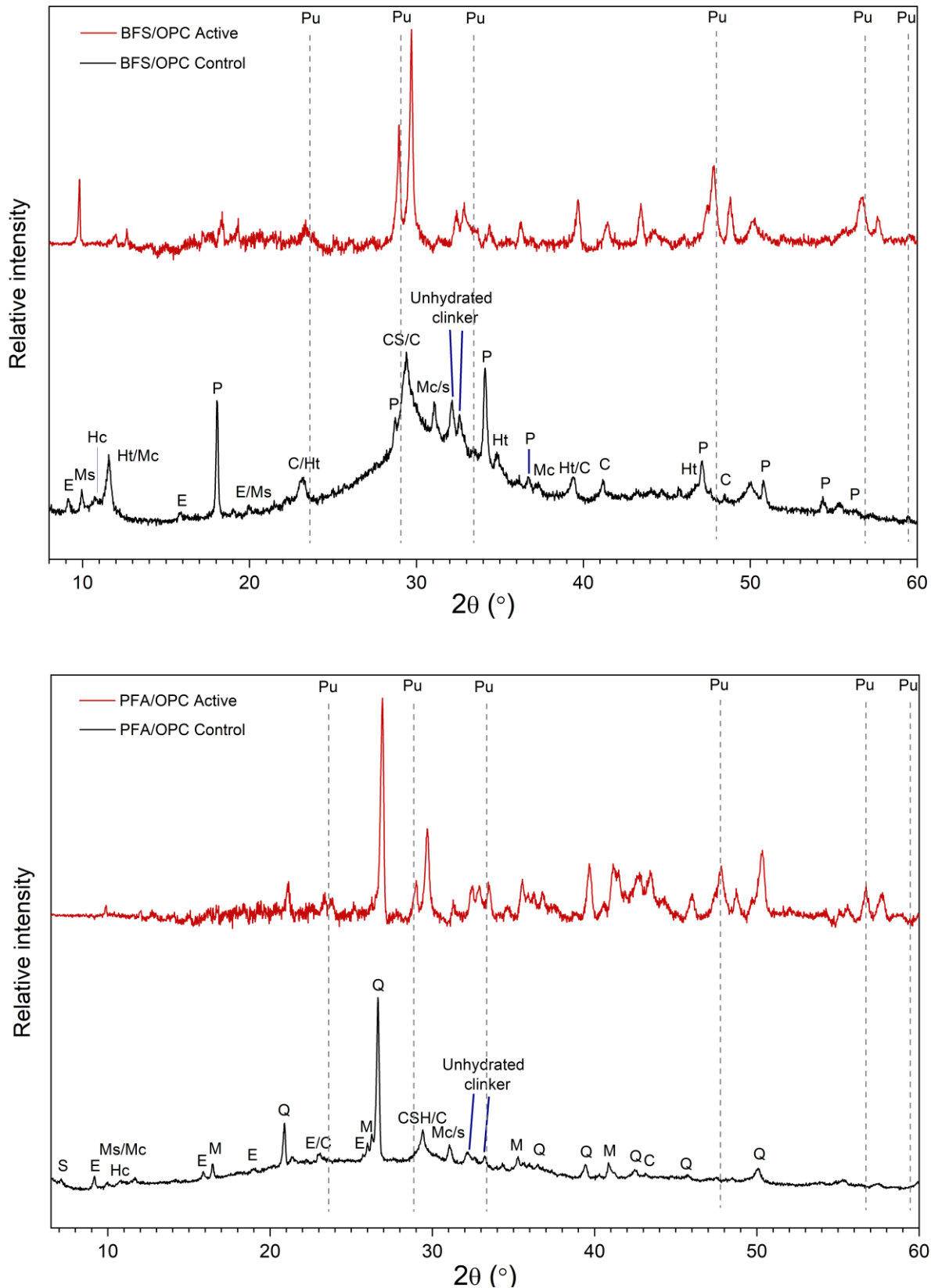


Figure 6.14: XRD patterns for PuO₂ containing and control PC samples. Top: BFS/OPC. Bottom: PFA/OPC. The OPC and BFS used were of UK nuclear specification sourced from Hanson Cement as Ketton coarse ground OPC, and Scunthorpe GGBS blended with Calumite™ (70:30), respectively. PFA was also of UK nuclear specification, supplied by the CEMEX Drax plant. C = calcite; CS = C-S-H; E = ettringite; Hc = hemihydrate; Ht = hydrotalcite; M = mullite; Mc = monocarbonate; Ms = monosulfate; P = portlandite; Q = quartz; S = stratingite. See *Kearney et al.* for full analyses and PDF card no. references.

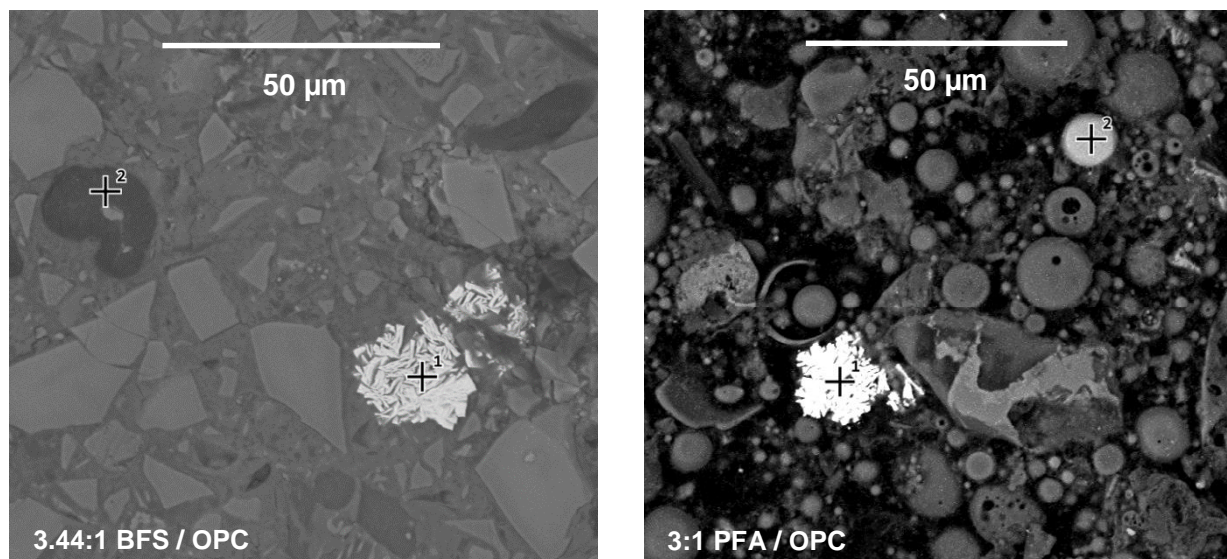


Figure 6.15: SEM micrographs of 3.44:1 BFS/OPC (left) and 3:1 PFA/OPC (right) PuO₂ cement blends.

Table 6.8: Weight percentage of elements from EDX mapping.

	BFS/OPC		PFA/OPC	
	Spot 1	Spot 2	Spot 1	Spot 2
Pu	76.2 ± 0.7	-	76.2 ± 0.5	-
O	12.5 ± 0.0	80.2 ± 0.2	9.7 ± 0.4	58.9 ± 0.0
Ca	2.8 ± 0.3	14.3 ± 0.2	4.4 ± 0.9	4.4 ± 0.3
Si	1.8 ± 0.2	5.5 ± 0.3	2.1 ± 0.3	17.3 ± 0.1
Al	-	-	-	12.2 ± 0.0

Overall it was concluded in [131] that there was no observable microstructural damage to surrounding cement hydrate phases as a result of alpha-radiation damage and, concurrently, no change in the integrity of the PuO₂ particles encapsulated by a highly alkaline cement grout.

6.3.4.2 Solution analyses

In addition to the results analysed by *Kearney, Yorkshire et al.*, additional alpha spectrometry analysis was conducted on the cement storage solutions to calculate the concentration of

^{239}Pu and ^{240}Pu at 5.1 MeV (accounting for 95 wt % of the total Pu). The results are given in **Table 6.9** along with the pH values of the storage solutions.

Table 6.9: Plutonium concentrations and pH values of BFS/OPC and PFA/OPC lime-saturated storage solutions.

	$^{239}\text{Pu}/^{240}\text{Pu}$ concentration / M	pH	pH (control)
BFS/OPC	$1 \pm 0.5 \times 10^{-9}$	9.9 ± 0.1	13.5 ± 0.0
PFA/OPC	$2 \pm 0.5 \times 10^{-9}$	8.3 ± 0.1	12.7 ± 0.0

The $^{239}\text{Pu}/^{240}\text{Pu}$ concentration in the storage solutions of the cements was of the order of 10^{-9} M for both the BFS and PFA blends which account for 95 % of the total actinide content. Assuming that the leached amount of plutonium from the cements maintained the same isotopic weight fraction as the initial plutonium added, the total concentration of plutonium would not be expected to exceed more than the $\sim 10^{-9}$ M range measured for $^{239}\text{Pu}/^{240}\text{Pu}$.

As established in a review of the literature in **Chapter 2**, the solubility of plutonium in cement equilibrated waters of PFA and BFS blends can reach the order of 10^{-8} M which is reduced to 10^{-9} M in the presence of carbonate [119]. The pH values of the active samples, 9.9 for BFS and 8.3 for PFA, are lower than expected for a cement water and in comparison, to the controls, 13.5 for BFS and 12.7 for PFA, which is indicative of carbonation.

Carbonation of the solutions may have occurred during storage of these samples in the $\text{Ca}(\text{OH})_2$ saturated solution for the purpose maintaining alkaline conditions as the samples were stored with loose fitting lids to allow escape of radiolytic hydrogen. Alternatively, carbonation of the solutions may have also occurred during the extended period between filtration and analysis.

The plutonium concentrations obtained here, therefore reflect the effects of carbonation, i.e. plutonium-carbonate complexation likely occurred [100]. According to calculations performed in **Figure 6.12**, the measured species may have been $\text{Pu}(\text{OH})_2\text{CO}_3$, indicating that oxidation of Pu(IV) had occurred, either within the cement pore water or in the aliquot of solution prior to measurement. The measurable concentrations of plutonium could suggest that the cement matrix is not a robust encapsulant to prevent plutonium release into solution at such high plutonium/cement loadings, however it is not envisaged that such high levels of plutonium will be present in ILW streams and direct encapsulation of PuO_2 particles in a cement matrix seems unlikely. Given that the cements had been aged for ~ 3 years prior to the solution analyses, the plutonium had sufficient time to dissolve and equilibrate to the expected solubility levels. These results provide evidence that the PuO_2 behaviour is much as expected under alkaline conditions.

The results from ICP-MS analysis of the cement storage solutions and ICP-OES analysis of the control cement storage solutions are also given in **Figures 6.16** and **6.17**.

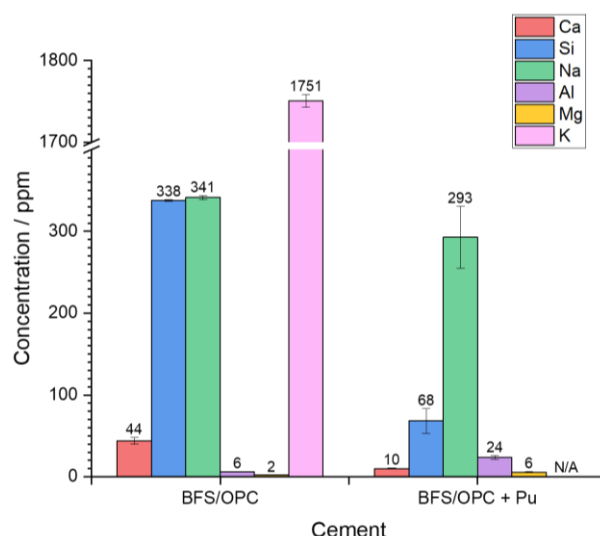


Figure 6.16: Concentration of cations in cement storage solutions for BFS/OPC control (left, ICP-OES) and PuO₂-containing (right, ICP-MS). Note that K was outside of the calibration range for ICP-OES measurements and Na was outside of the calibration range for ICP-MS measurements. K was not measured for the PuO₂-containing sample (N/A).

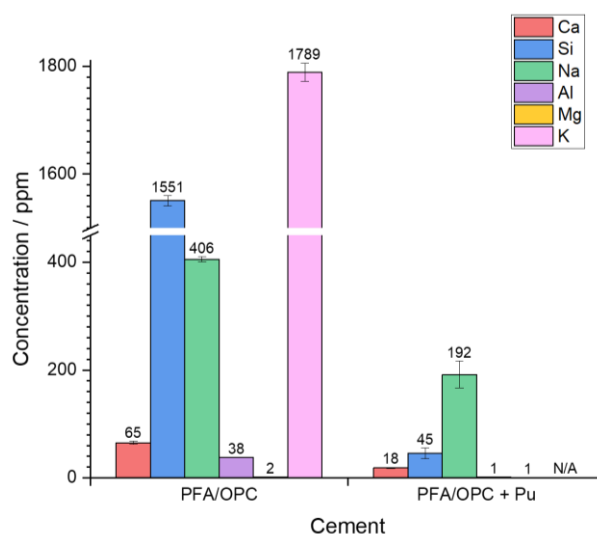


Figure 6.17: Concentration of cations in cement storage solutions for PFA/OPC control (left, ICP-OES) and PuO₂-containing (right, ICP-MS). Note that K and Si were outside of the calibration range for ICP-OES measurements and Na was outside of the calibration range for ICP-MS measurements. K was not measured for the PuO₂-containing sample (N/A).

The ratio of cement per volume of solution was not accurately recorded and therefore the results for the cation compositions cannot be directly compared between the control and PuO₂-containing samples. However, some general observations can be made:

- (i) The calcium concentrations are extremely low compared to the expected value for a $\text{Ca}(\text{OH})_2$ -saturated solution ($[\text{Ca}]_{\text{saturated}} \gg 1000$ ppm) in all samples, which can potentially be explained by the common ion effect (see **Section 6.4.3**)
- (ii) The sodium and potassium concentrations are high relative to calcium concentrations. Sodium concentrations were measured at ~300 ppm (BFS) and ~200 / ~400 ppm (PFA / control) and potassium concentrations at $\gg 1000$ ppm (controls only). *Mann et al.* reported the concentrations of sodium and potassium to be ~1500 ppm and ~14000 ppm, respectively, for a synthetic young cement water which are significantly higher than the concentrations observed here [290]. The alkali oxide content of the anhydrous raw materials for the cement blends analysed here were 1, 1.1 and 4.3 wt % for PC, BFS and PFA, respectively [131]. *Sutton et al.* measured concentrations of ~900 ppm and ~3000 ppm for sodium and potassium, respectively, for a fresh leachate obtained from 3:1 PFA/OPC cement in deionised water. Comparatively, that cement had an alkali oxide dry wt % after LOI (850 ° C) of 2.5 % [53]. This therefore goes some way in explaining the concentration ranges obtained for sodium and potassium.
- (iii) The silicon concentrations appeared much lower in the PuO_2 -containing samples relative to the concentrations for the control samples (again, however, these cannot be directly compared) at ~70 ppm / ~300 ppm (BFS / control) and ~45 ppm / $\gg 1000$ ppm (PFA / control). *Mann et al.* and *Sutton et al.* reported silicon concentrations of ~7 ppm and ~6 ppm, respectively and so the concentrations in the control samples in particular are elevated. These high concentrations cannot be explained by disparity in the silicon oxide content, as *Sutton et al.* reported a dry wt % of 42.3 % compared to 21.6, 36.1 and 52.9 wt % for the PC, BFS and PFA anhydrous materials, respectively.

Given that the cements were stored in the $\text{Ca}(\text{OH})_2$ solution under static conditions for the duration of the curing process (~3 years), it is not unreasonable to compare the equilibrium concentrations of these elements with those for a 'fresh' leachate or cement water as an approximate guide.

6.4 Discussion

6.4.1 Pu(VI)/(VI) behaviour in C-S-H suspension

Although plutonium-containing calcium silicate phase was not directly identifiable by XRD, the nanoscale crystallisation of Pu(IV) as $\text{PuO}_2 \cdot x\text{H}_2\text{O}$ after washing and heating indicates that plutonium was initially associated with the surface of the C-S-H in some form [97,281]. Pu(VI) may have been physically or chemically sorbed to the outside of the C-S-H or silica phases or

else precipitated as an amorphous solid during the initial contacting stage, with hydrous PuO₂ nano-crystallisation induced by heating, which is explained in further detail later.

A calcium-plutonyl-silicate phase analogous to that observed for U(VI) (see *Section 6.2.1.1* and **Chapter 5**) was not observed after heating. The limitation of plutonium to form +6 compounds analogous to those of uranium may arise from the lower range of coordination that plutonium displays. While plutonium can only exhibit N = 6 coordination in the +6 oxidation state, uranium ranges from N = 2-8 [291]. As the coordination of U(VI) in the calcium-silicate mineral formed previously is hypothesised to be square-based pyramidal (N = 5), based on the weeksite or haiweeite mineral structures, then the formation of a direct plutonium analogue would not be possible in this case [237,249]. There are no single-valence minerals of calcium-uranyl-silicate with a uranium(VI) coordination of N = 6 reported in the literature. Nevertheless, no other plutonium phases of a calcium or silicate type were directly identifiable by XRD.

It has been reported that Pu(IV) can complex Ca²⁺, by the formation of a ternary Ca_x[Pu(IV)O₂(OH)_n]^{2x+1-n} complex in solutions of 4-5 M CaCl₂ above pH 11, likely as Ca₄[Pu(OH)₈]⁴⁺ [292]. One condition of the formation of this complex is high ionic strength. The measured pH values of the supernatant solutions in the plutonium contact experiments were therefore approximately converted into ionic strength (I) using **Equations 7.1** and **7.2** for an aqueous system at 25°C:

$$\text{pH} + \text{pOH} = 14 \quad (7.1)$$

$$\text{pOH} = -\log[\text{OH}^-] \quad (7.2)$$

based on the assumption that I = [OH⁻] with complete dissociation of Ca²⁺ and 2OH⁻ in aqueous solution.

Given that the approximate ionic strengths calculated in **Table 6.10** are low compared to the CaCl₂ solutions in which the ternary Ca_x[Pu(VI)O₂(OH)_n]^{2x+1-n} complex has been isolated (4-5 M [39]), formation of such a complex seems unlikely in this study.

Table 6.10: Approximately calculated pOH values and ionic strengths for pH values relevant to plutonium experiments.

pH (measured)	pOH	I ([OH ⁻] concentration) / mM
3	11	10 ⁻⁸
4	10	10 ⁻⁷
8	6	10 ⁻³

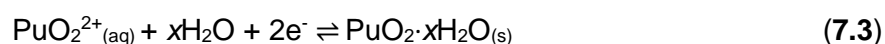
6.4.1.1 Effect of carbonation

Due to the diffuse nature of the XRD patterns, the effect of either pre-carbonation and / or carbonation in air is difficult to distinguish. It was previously reported that in alkaline systems, the solubility of plutonium is unaffected by carbonate until its dissolved content exceeds 0.25 M (reported for 3-5 M NaOH solution, with the assumption that NaOH activity is equal to OH⁻ activity) [100]. Given that the identification of calcium carbonates is evident in the XRD patterns for the samples at pH 8, it is believed that the dissolved carbonate content is very likely to exceed this value. Whether the effect of carbonates in the C-S-H system at pH 8 can compare to that of carbonates in a concentrated NaOH solution is debatable. However, it does appear that carbonation had little or no effect on the precipitation of plutonium in this system as the only plutonium phase observed by XRD was PuO₂·xH₂O. For the CSH(0.6) sample (pH 3) the story is slightly different. Although calcite was evident in the XRD pattern before heating, the pH and geochemical modelling results suggests that most carbonate present would have dissolved. However, after heating, PuO₂·xH₂O was still the only phase identifiable by XRD, which suggests that the dissolved carbonate content did not exceed the concentration required to form solid plutonium carbonate complexes.

6.4.2 Origin of PuO₂·xH₂O

The PuO₂·xH₂O phase identified is thought to be formed during the reductive precipitation of aqueous Pu(VI). Previous literature has reported the behaviour of crystalline PuO₂ in aqueous media, showing that it can undergo dissolution and re-precipitation into a less-ordered hydrous PuO₂ phase overtime (referred to as PuO₂·xH₂O_(am)) [99,100,112,113,117]. Furthermore, it has been determined that this hydrous phase still displays the same cubic Fm-3m structure as crystalline PuO₂ [112,113].

The re-precipitation process need only be considered here given that plutonium was added to the C-S-H system as Pu(VI)_(aq). On initial contact with C-S-H a Pu(VI) intermediate was precipitated and observed as the orange-brown solid. The conversion of Pu(VI), assumed to be present as PuO₂²⁺ in solution [91,99], into solid / amorphous PuO₂·xH₂O proceeded via the reductive precipitation process described by **Equation 7.3**, which was accelerated by the heating process. Reducing species (such as hydrated electrons) are assumed to be present in aqueous solution due to alpha-radiolysis of water, substantiating the idea of a reductive precipitation process [117].



Equation 7.3 is described as being reversible in [99]. The ongoing redox dissolution-precipitation process of crystalline PuO₂ and PuO₂·xH₂O_(am) is thought to occur in a range of aqueous media at various pH values until equilibrium is reached. For example, *Neck et al.*

demonstrated that equilibrium was achieved for the process between 77-104 days of ageing at pH 2.5-13, with plutonium concentrations on the order of 0.4 g L⁻¹ (compared to 9.38 g L⁻¹ used in this study) [99]. However, the lack of solution analysis and the fact that the solid phases were removed from solution promptly in this study means that it was not possible to determine the redox speciation of aqueous plutonium, or whether a steady state for PuO₂·xH₂O_(am) formation was reached.

It should be noted that most previous studies discussing PuO₂ hydrous oxide stability in alkaline systems are generally conducted at ionic strengths exceeding those predicted here [99,100,293]. Despite the 'low' pH values measured experimentally (pH 3 - 4, 8) and the modest ionic strength, the formation of the PuO₂ hydrous oxide was observed in this system. Even in a solution more akin to a high pH cement system, it seems unlikely that at these elevated concentrations of plutonium the formation of a calcium-silicon containing plutonium complex would occur. Rather, it seems that Pu(IV) prefers to precipitate as a hydrous oxide that co-exists with C-S-H phases in the system at pH 8. Given that for the CSH(0.6) sample at pH 3-4 we can assume almost full dissolution of the C-S-H phase, the observation of PuO₂·xH₂O by XRD indicates the stability of this phase at a wide range of pH values and in the presence of dissolved calcium and silicon.

Further to this, in a study by *Haußler et al.*, the uptake of Pu(III) onto C-S-H phases at µM to nM concentrations was very recently investigated. Despite the lower concentrations studied, the authors still concluded that Pu(III) underwent an oxidative precipitation process to form Pu(IV)O₂, rather than being chemically incorporated by the C-S-H phase [97]. This suggests that even at trace levels of plutonium, the PuO₂ precipitation process dominates and plutonium will not be incorporated by the C-S-H structure.

6.4.2.1 PuO₂·xH₂O crystallite size

The crystallite size of the PuO₂·xH₂O formed in the CSH(0.6) sample after heating was estimated using the Scherrer equation, **Equation 7.4**:

$$D = \frac{K\lambda}{FWHM \cdot \cos\theta} \quad (7.4)$$

where D is the crystallite size in Å, K is a constant described as the crystallite shape factor, λ is the wavelength in Å, FWHM is the full width at half maximum of the diffraction peak in radians (determined by eye in the Origin 2018b (9.55) software) and θ is diffraction angle in radians. The (1 1 1) and (1 1 3) reflections of the phase identified as PuO₂·xH₂O in the CSH(0.6) material were used. The results are shown in **Table 6.11** and indicate that the material was nano-crystalline with a crystallite size of approximately 5 nm.

Table 6.11: Input values for the Scherrer equation to calculate crystallite size of $\text{PuO}_2 \cdot x\text{H}_2\text{O}$ formed in CSH(0.6). The values of K used are taken from [294] for cubic crystallites.

Reflection	K	FWHM / radians	θ / radians	D / nm
(1 1 1)	0.8551	0.0297	0.248	4.6
(1 1 3)	0.9082	0.0272	0.491	5.8

Crystallite size for $\text{PuO}_2 \cdot x\text{H}_2\text{O}$ in all of the heated samples was also calculated using Rietveld refinement in the Topas 4.2 software (Fm-3m space group, PuO_2 , PDF card no. 01-073-7903 [282]), shown in **Table 6.12**.

Table 6.12: Average crystallite size of $\text{PuO}_2 \cdot x\text{H}_2\text{O}$ calculated by Rietveld refinement.

Sample	Hydrous PuO_2 %	Crystallite size (nm)	Aragonite %	Crystallite size (nm)	Calcite %	Crystallite size (nm)	Vaterite %	Crystallite size (nm)
CSH(0.6) Rwp = 60	100	4.6 ± 0.1	-	-	-	-	-	-
CSH(0.6) C Rwp = 60	12.28 ± 1.75	5.1 ± 0.3	87.72 ± 1.75	147.2 ± 16.9	*	*	-	-
CSH(1.2) Rwp = 76	19.91 ± 3.47	5.4 ± 0.4	-	-	80.10 ± 3.47	315.3 ± 63.8	-	-
CSH(1.2) C Rwp = 51	18.49 ± 2.32	5.9 ± 0.3	-	-	30.06 ± 4.26	214.2 ± 53.5	51.49 ± 5.37	32.9 ± 16.2

*not identified

The crystallite size of the CSH(0.6) sample, where only $\text{PuO}_2 \cdot x\text{H}_2\text{O}$ was identified, was the lowest, at 4.6 nm, and is in good agreement with the value determined by *Tasi et al.* (4 ± 1 nm) for $\text{PuO}_2(\text{s})$ aged in 0.1 m NaCl solution for ~8 years at pH ~6 [26]. For the other three samples, the crystallite size was ~5-6 nm, which suggests that at a higher pH, the precipitation of $\text{PuO}_2 \cdot x\text{H}_2\text{O}$ after heating generates moderately larger crystals.

Neck et al. established that the size of Pu(VI) oxyhydroxide colloids were directly related to pH; at low pH colloids formed are larger (> 5 nm) than those formed at neutral or higher pH (~1.5 to 2 nm) [99]. The opposite trend is seen here for the crystallite size of $\text{PuO}_2 \cdot x\text{H}_2\text{O}$, however, given that these are solid precipitates rather than colloidal suspended material, the varied crystallite sizes are probably related to differing nucleation processes [295,296]. Investigations on the effect of the processing conditions on the formation of $\text{PuO}_2 \cdot x\text{H}_2\text{O}$ precipitates would be required to conclude anything further at this point.

6.4.3 PuO₂ encapsulated in cement matrices

The most informative comparison to be drawn from the experiments conducted at JRC and the study of cement encapsulated PuO₂ by *Kearney, Yorkshire et al.* is the ability of PuO₂ to co-exist in a cementitious system with little structural interaction with cement hydrate phases. This shows the importance of plutonium residing in the +4 oxidation state to potentially allow for decreased plutonium mobility in cementitious systems. The observation of plutonium concentrations at 10⁻⁹ M in the cement storage solutions does, however, show an equilibrated release of plutonium from the cement matrix.

The low concentrations of calcium measured in the cement storage solutions can perhaps be explained by the common-ion effect. It has been reported that the addition of alkali-hydroxides to a solution will reduce the solubility of Ca(OH)₂ [297,298]. Given that the sodium and potassium concentrations (latter measured for controls only) in the solution were appreciable, this effect could be prominent.

6.4.4 U(IV) behaviour in C-S-H suspension

As in the plutonium studies, there is potential for U(IV) to show precipitation into an amorphous hydrous oxide over time [49,299], which is also indicated in the identification of an amorphous UO₂ phase using geochemical modelling. However, unlike the experiments for plutonium described in this Chapter, the process of U(IV) oxide precipitation is not controlled by radiolytic processes, due to the lower specific activity of depleted uranium utilised in the study (1.85 x 10⁴ Bq vs 2.294 x 10⁹ MBq for ²³⁹Pu). Rather, it requires uranium to be maintained in the +4 state via reducing conditions [49]. However, if the different isotopes of uranium that will be present as a result of plutonium decay are also considered, the same phenomenon might be observed for the formation of UO₂ for isotopes of uranium with higher specific activities. **Table 6.13** lists the primary isotopes of plutonium involved in this study (see also **Table 6.1**) and their resultant decay products. ²³⁵U also displays a specific activity on the order of 10⁴ Bq, but for ²³⁶U is higher at 2.33 x 10⁶ Bq. Although this alpha activity is still many magnitudes lower than that for ²³⁹Pu, the possibility that ²³⁶U isotopes may also undergo radiolytic self-reduction in these systems cannot be overlooked, but further investigation would be required. The coexistence of plutonium isotopes, capable of radiolytic reduction, with uranium isotopes in cementitious wastefoms could also be a potential trigger for the reduction of U(VI) to U(IV) and formation of poorly crystalline UO₂ phases, and therefore decreased solubility of uranium in these systems.

Table 6.13: Specific activities of uranium decay products of plutonium isotopes.

Isotope	Half-life / y	Decay product	Specific activity / Bq	Decay mode
²³⁹ Pu	24 100	²³⁵ U	7.77 x 10 ⁴	Alpha
²⁴⁰ Pu	6 560	²³⁶ U	2.33 x 10 ⁶	Alpha

Given that the exclusion of air during the course of uranium experiments could not be guaranteed, it is expected that U(IV) underwent oxidation to U(VI) [51]. The potential identification of the Ca-bearing clarkeite mineral phase (calcium uranate) in the XRD pattern for the CSH(1.2) phase is suggestive of this [57,58]. Geochemical modelling of U(VI) in C-S-H systems previously in this Thesis (**Chapter 5**) has also yielded a calcium uranate phase with $SI > 0$ and there have been several studies that confirm, using X-ray absorption techniques, the presence of calcium uranates or calcium-uranyl-silicates, after contact of C-S-H phases with U(VI) [53,67,68]. This suggests that the presence of a fast-precipitating calcium uranate phase cannot be ruled out, however the quality of the XRD data is not sufficient to identify such phases in this study. The aforementioned studies are not discussed here but are detailed previously in **Chapter 2** and **Chapter 5**.

6.5 Conclusions and Further Work

6.5.1 Conclusions

Plutonyl nitrate did not show the same behaviour as uranyl nitrate in contact with C-S-H phases. The +6 oxidation state of plutonium was shown to be unstable during the ageing experiment and underwent reduction. Further to this, as the starting oxidation state of plutonium could not be spectroscopically determined, there is no certainty that plutonium was added to the system as Pu(VI) in the first instance. With reference to the release of U(VI) and Pu(VI) from a cementitious system (e.g. a geological repository), U(VI) does not therefore appear to be a useful surrogate for Pu(VI). U(VI) will readily precipitate as calcium-silicate hydrate phases in the presence of calcium and silicon to form relatively stable mineral and / or sorbed mineral, however, plutonium preferentially forms a hydrous PuO₂ phase rather than combining with calcium and silicon. The solubility of plutonium will therefore be dictated by the transformation of other plutonium oxidations states into Pu(IV). This is also indicated by the equilibrated concentrations of plutonium measured in the PuO₂-containing cement storage solutions.

Due to the limitations of instrument sensitivity at JRC (XRD) high actinide loading had to be used; however, the high acidity associated with this had a detrimental effect on the solubility of the C-S-H phases, particularly at lower Ca/Si. Further to this, ²⁹Si NMR analysis was also attempted and was unsuccessful due to the large contribution from plutonium paramagnetic effects, making a significant silicon signal unobtainable [300]. Regardless of this, for the CSH(1.2) samples whereby the C-S-H phase was identifiable there was still no clear indication of an additional plutonium-calcium-silicon containing phase by XRD. It was inconclusive as to

whether the regions of diffuse scattering seen by XRD were a result of such a phase, or a plutonium sorbed silica phase.

In accordance with the study by *Kearney, Yorkshire et al.*, the importance of solid or incorporated PuO_2 cannot be overlooked when investigating the immobilisation of plutonium in cements. Even subjected to aqueous alkaline solutions, plutonium preferentially appears to precipitate in the +4 oxidation state, overtime, which could render cements at least as a chemically stable environment for Pu(IV)O_2 immobilisation.

6.5.2 Further work

To fully understand the effect that cementitious conditions impose on the stability of Pu(IV) , further experiments are required and include:

- X-ray absorption spectroscopy of the hydrous nano-crystalline PuO_2 phases formed in C-S-H systems to identify short range interactions with calcium, silicon or carbon.
- A full sorption study of plutonium onto C-S-H and other minor cement hydrate phases under controlled redox conditions to differentiate the behaviour of +4, +5 and +6 plutonium oxidation states where possible.
- A controlled leaching study on PuO_2 encapsulating cement blends to determine the true leachability of plutonium from cement matrices.

Chapter 7 – Rhenium and technetium uptake and coordination in cementitious environments

7.1 Introduction

This Chapter describes an investigation of rhenium (Re) uptake by C-S-H and other minor cement phases in order to evaluate the potential of rhenium as a surrogate for technetium (Tc) in cementitious systems. Rhenium is often used as a surrogate for technetium, since the perrhenate anion (ReO_4^-) is isostructural with the pertechnetate anion (TcO_4^-) [301]; the Re(VII) and Tc(VII) oxyanions that are the focus of this study.

Technetium-99 (^{99}Tc) is a beta emitting fission product of uranium-235 or plutonium-239 with a half-life of 210 000 years [137]. The radionuclide has the potential to accumulate in the sub-surface around nuclear power or disposal facilities and is a major constituent of concern at historic plutonium reprocessing sites. For example, at the Sellafield site in the UK, ^{99}Tc has already been detected in groundwater [302] and at the Hanford site in the USA, large Tc-salt containing tanks are leaking into the ground. There is clear requirement for safe treatment and disposal of technetium-contaminated land and groundwater, and also to safely immobilise technetium from modern spent nuclear fuel reprocessing [23]. Given that the predominant form of technetium is the +7 oxidation state as the aqueous, mobile pertechnetate anion (TcO_4^-), much work has been focused on immobilisation of ^{99}Tc in solid materials, including glass wastefoms and cementitious-based materials [24,152,303]. The focus of this Chapter is to investigate the individual cement hydrate phases or components in a cementitious matrix that may be responsible for rhenium and / or technetium coordination or complexation.

7.2 Experimental methods

The synthesis and characterisation of all pre-cursor cement phases in this section are detailed in **Chapter 3** and **Chapter 4** of this Thesis.

7.2.1 Rhenium sorption experiments

All parts of the experiment in this section were carried out under a N_2 atmosphere in an anaerobic chamber, unless otherwise specified.

7.2.1.1 C-S-H phases

Rhenium batch sorption experiments were carried out for C-S-H phases with theoretical Ca/Si ratios of 0.6, 0.8, 1.0, 1.2, 1.4 and 1.6. Suspensions of C-S-H were synthesised using the

solution reaction method and samples of the reaction mixtures were analysed by ICP-OES to determine the Ca/Si ratio of the C-S-H phases (procedure outlined in **Chapter 3** and **4**).

Aliquots of the C-S-H suspensions (~8 mL) were removed in triplicate and spiked with an amount (~1 mL) of ammonium perrhenate (NH_4ReO_4) solution (0.1 mM) to achieve μM concentrations of Re(VII), with a Re(VII) loading on the C-S-H phases between ~150-300 ppm (**Table 7.1**). The batch Re(VII) / C-S-H suspensions were left to equilibrate for 48 hours on a rotary shaker.

Table 7.1: Experimental parameters for Re(VII) batch sorption onto C-S-H phases. Note that masses are based on the weight of reacted CaO and SiO_2 .

Sample	Ca/Si	S/L / g L^{-1}	Re(VII) concentration / μM	Re(VII) loading / ppm
CSH(0.6)	0.65	6	10	267
CSH(0.8)	0.86	7	10	230
CSH(1.0)	1.06	8	10	200
CSH(1.2)	1.25	9	10	180
CSH(1.4)	1.40	10	10	333
CSH(1.6)	1.58	11	10	154

7.2.1.2 Minor cement phases

Batch sorption experiments were also conducted for rhenium with minor cement phases: ettringite ($\text{Ca}_6\text{Al}_2(\text{SO}_2)_3(\text{OH})_{12}\cdot x(\text{H}_2\text{O})$), hydrotalcite ($\text{Mg}_6\text{Al}_2(\text{CO}_3)(\text{OH})_{16}\cdot x(\text{H}_2\text{O})$), portlandite ($\text{Ca}(\text{OH})_2$), calcite (CaCO_3) and gypsum ($\text{CaSO}_4\cdot 2\text{H}_2\text{O}$) (syntheses and characterisation described in **Chapter 3** and **Chapter 4**, respectively). The powders were transferred out of the anaerobic chamber briefly to be weighed out accurately, before being immediately transferred back into the N_2 atmosphere. The phases were suspended in degassed NH_4ReO_4 solution (0.1 mM) to achieve a Re(VII) loading of ~800 ppm for each phase (**Table 7.2**). Note that the associated decrease in pH from ~7, for UHQ, to 4.8 by use of higher concentrations of NH_4ReO_4 , was accounted for when performing control measurements in UHQ by addition of appropriate volumes of nitric acid. The suspensions were left to equilibrate on a rotary shaker for 2 weeks.

Table 7.2: Experimental parameters for Re(VII) batch sorption onto minor phases.

Sample	S/L / gL ⁻¹	Re(VII) concentration / μM	Re(VII) loading / ppm	Comments
Portlandite	25	100	792	added as CaO
Gypsum	25	100	792	
Calcite	25	100	792	
Ettringite	25	100	792	~24 wt% anhydrite, ~0.4 wt% gypsum ^a
Ettringite	10*	100	1980	~30 wt% anhydrite, ~2 wt% gypsum ^a
Hydrotalcite	25	100	792	

*denoted with an asterisk hereafter

^a as determined by Rietveld refinement of XRD data

7.2.1.3 Solution and solid phase analyses

After equilibration, all batch rhenium sorption suspensions were filtered through a 0.22 μm cellulose filter and the pH of the supernatant solution was measured before being acidified and prepared for ICP-OES and / or ICP-MS analysis for determination of Ca, S, Al, Mg and Re concentrations. The solid phases were left to dry for a minimum of 24 hours and XRD measurements were performed using the same parameters as for the initially synthesised phases (determined in **Chapter 3** and **4**). Control samples of the rhenium solution with no cement phases present were also filtered in the same way to account for any sorption to the cellulose filter. The concentrations of rhenium in the control samples did not appear to be significantly reduced in ICP measurements, indicating no or minimal sorption of rhenium to the filters.

7.2.2 Technetium sorption experiments

7.2.2.1 C-S-H phases

Technetium batch sorption experiments were carried out in a similar way to rhenium experiments. Aliquots of the C-S-H suspensions were removed in triplicate and spiked with a small volume (~40 μL) of ammonium pertechnetate (NH_4TcO_4) solution (2 mM) to achieve μM concentrations of Tc(VII), with a Tc(VII) loading on the C-S-H phases between ~90-160 ppm (**Table 7.3**). Due to the high sensitivity of the C-S-H phases to carbonation, aliquot collection in vials was carried out in the anaerobic chamber before being sealed with Parafilm and transferred immediately to a separate N_2 environment for Tc-specific manipulations. The batch Tc(VII) / C-S-H suspensions were left to equilibrate for 48 hours on a plate shaker.

Table 7.3: Experimental parameters for Tc(VII) batch sorption onto C-S-H phases. Note that masses are based on the weight of reacted CaO and SiO₂.

Sample	Ca/Si	S/L / g L ⁻¹	Tc(VII) concentration / μM	Tc(VII) loading / ppm
CSH(0.6)	0.65	6	10	159
CSH(0.8)	0.86	7	10	137
CSH(1.0)	1.06	8	10	119
CSH(1.2)	1.26	9	10	106
CSH(1.4)	1.42	10	10	99
CSH(1.6)	1.58	11	10	91

7.2.2.2 Minor cement phases

Batch technetium sorption experiments of the minor cement phases were also carried out in triplicate (**Table 7.4**). The powders were transferred out of the anaerobic chamber in Parafilm sealed vials and weighed out accurately, before being immediately transferred into the N₂ environment for Tc-specific manipulations. The phases were suspended in degassed UHQ water and spiked with NH₄TcO₄ solution to achieve μM concentrations of Tc(VII) and a Tc(VII) loading of ~150 ppm for each phase (**Table 7.4**).

Table 7.4: Experimental parameters for Tc(VII) batch sorption onto minor phases.

Sample	S/L / gL ⁻¹	Tc(VII) concentration / μM	Tc(VII) loading / ppm	Comments
Portlandite	25	20	158	added as CaO
Gypsum	25	20	158	
Calcite	25	20	158	
Ettringite	25	20	158	~6 wt% anhydrite, ~7 wt% gypsum ^a
Ettringite	10*	20	396	~39 wt% anhydrite, ~2 wt% gypsum ^a
Hydrotalcite	25	20	158	

*denoted with an asterisk hereafter

^a as determined by Rietveld refinement of XRD data

7.2.2.3 Solution and solid phase analyses

After equilibration, all technetium batch sorption suspensions were filtered through a 0.22 μm cellulose filter. Samples of the supernatant solutions were mixed with EcoScint A scintillation cocktail (2 mL solution to 18 mL scintillant) for measurement by beta liquid scintillation counting to determine the concentration of technetium remaining in solution and measured to technetium percentage uptake. Control samples of the technetium solution with no cement

phases present were also filtered in the same way to account for any sorption to the cellulose filter. The concentrations of technetium in the control samples were not significantly reduced in LSC measurements, indicating no or minimal sorption of technetium to the filters.

The solid phases were left to dry for a minimum of 24 hours before being measured by XRD. The powders were suspended in IPA and dropped onto a low-background Si(111) plate, left to dry, and capped with a PMMA dome for measurement (dictated by beta-activity protocol). The XRD parameters used were the same as for the initially synthesised phases described in **Chapter 4** and background contribution from the sample holder was subtracted during data processing.

7.2.3 Calculation of mass changes

7.2.3.1 R_d values

The R_d value is the ratio of a sorbate partitioned onto / into a sorbent, compared to the solution phase [127]. The rhenium concentrations remaining in solution were taken directly from ICP-OES measurements and for technetium the average decays per minute (DPM) outputted from LSC were converted into concentrations using the specific activity of ^{99}Tc . Each were converted into concentrations for the amount of rhenium or technetium partitioned into a solid phase. The R_d values for each cement phase (sorbent) with rhenium or technetium (sorbate) were calculated using **Equation 7.1**:

$$R_d = \frac{V}{m} \cdot \frac{[X]_{\text{sorbed}}}{[X]_{\text{equilibration}}} \quad (7.1)$$

where V is the volume of the suspension in L; m is the mass of the sorbent in g; $[X]_{\text{sorbed}}$ is the concentration of technetium or rhenium partitioned onto the sorbent and $[X]_{\text{equilibration}}$ is the concentration of technetium or rhenium remaining in solution. The units of R_d are L g^{-1} .

7.2.3.2 Percentage mass loss of Re-contacted minor phases and controls

The percentage mass loss of each cation (Ca, S, Al or Mg) released from the Re-contacted minor cement phases and control experiment phases, as a percentage of the starting mass, was calculated using **Equation 7.2**:

$$\text{Percentage mass loss} = \frac{\text{Mass of cation released (mg L}^{-1}\text{)}}{\text{Initial mass of phase added (mg L}^{-1}\text{)}} \times 100 \% \quad (7.2)$$

where the 'initial mass of phase added' is the triplicate average of the pre-weighed mass before suspension (~ 0.1 g converted to mg L^{-1}) and the 'mass of the cation released' is outputted from the ICP-OES analysis of the solutions after equilibration.

7.2.4 X-ray absorption / fluorescence measurements

7.2.4.1 Preparation of Re L_{III} -edge XAFS samples

Supplementary samples with higher rhenium loadings, to allow for increased rhenium signal during measurement, were prepared for XAFS analysis. Approximately 30 mg of CSH(0.8), CSH(1.2), CSH(1.6), calcium oxide (CaO) and calcite (CaCO_3) were contacted with 40 μL NH_4ReO_4 solution (20 mM), to achieve a Re(VII) loading of $\sim 5\,000$ ppm, and left to for 24 hours. For C-S-H phases, “pre-carbonated” versions were also prepared and measured (see procedure in **Chapter 3**), denoted with a “C” suffix hereafter.

Additional samples of CSH(0.6) (both “non-carbonated” and “pre-carbonated”), ettringite and hydrotalcite were also prepared for measurement with a Re(VII) loading of $\sim 3\,700$ ppm. In the case of ettringite and hydrotalcite, carbonated versions were also prepared in the presence of a 1 % CO_2 atmosphere, denoted with a “C” suffix hereafter. The powders were pressed into 6 mm pellets and placed into a Perspex® sample holder backed with Kapton® tape on either side. The holder and samples were heat sealed in a polythene bag under N_2 to minimise carbonation during transport and measurement.

Rhenium L_{III} -edge (10 535 eV) data were primarily acquired from beamline B18 at DLS and beamline BL-27B at KEK. Samples were measured in fluorescence mode due to the dilute nature of the absorbing atom, whereby the sample was orientated at 45° to the incidence X-ray beam and adjacent fluorescence detector. Standard samples that were considered relevant for the coordination of rhenium in the cementitious phases were also measured, in transmission mode (see **Table 7.5**).

Table 7.5: Re standards for XAFS.

Standard	Oxidation state	Beamline(s)
Re metal (for E_0 alignment)	0	BL-27B (KEK), BMM (NSLS-II) and B18 (DLS)
Ca-perrhenate ($\text{Ca}_{x/2}(\text{ReO}_4)_2 \cdot z\text{H}_2\text{O}$)	7	NSLS-II (BMM)
NH_4ReO_4	7	BL-27B (KEK)
ReS_2	4	BL-27B (KEK)
ReO_3	6	BL-27B (KEK)

7.2.4.2 Preparation of Tc K-edge XAFS samples

Supplementary samples in pellet form were prepared for technetium analysis by XAFS for CSH(0.8), CSH(1.2), CSH(1.6), calcite and ettringite. For the C-S-H phases, ettringite and hydrotalcite, “pre-carbonated” versions were also prepared and measured (see procedure in **Chapter 3**), denoted with a “C” suffix hereafter. Approximately 25 mg of each phase was

pressed into a 6 mm pellet and placed into a Perspex® holder backed with Kapton® tape. A 20 µL volume of the 2 mM NH₄TcO₄ solution was placed directly onto the pellets which was allowed to dry for 24 hours, to achieve a Tc(VII) loading of 158 ppm. A layer of Kapton® tape was placed over the pellets and the holder and pellets were heat sealed in a polythene bag under N₂ to minimise carbonation during transport and measurement.

Technetium K-edge (21 044 eV) data were primarily acquired from beamline B18 at DLS. Samples were measured in fluorescence mode due to the dilute nature of the absorbing atom, whereby the sample was orientated at 45° to the incidence X-ray beam and adjacent fluorescence detector. Standard samples that were considered relevant for the coordination of technetium in the cementitious phases were also measured in transmission mode. Additional technetium standard data were measured at NSLS-II on beamline BMM or acquired from other sources (see **Table 7.6**).

The Re- and Tc-contacted cement phases measured are also summarised in **Table 7.7**.

Table 7.6: Tc standards for XAFS.

Standard	Oxidation state	Beamline
Tc metal (for E ₀ alignment)	0	B18 (DLS)
Ca-pertechnetate (Ca _{x/2} (TcO ₄) ₂ .zH ₂ O)	7	B18 (DLS)
NH ₄ TcO ₄	7	B18 (DLS)
TcS _x (Tc ₂ S ₇)	~7	Stanford Synchrotron Radiation Laboratory, courtesy of W. Lukens [152]

Table 7.7: All Re- or Tc-contacted cement phase samples measured.

Sample	Beamline	Transmission / fluorescence	Re(VII) / Tc(VII) loading / ppm	Standards of relevance
Re-CSH(0.6)	BL-27B (KEK)	F	~3 700	NH ₄ ReO ₄ and Ca-perrhenate
Re-CSH(0.8)	B18 (DLS)	T	~5 000	
Re-CSH(1.2)	B18 (DLS)	F	~5 000	
Re-CSH(1.6)	B18 (DLS)	T	~5 000	
Re-CaO	B18 (DLS)	T	~5 000	
Re-CSH(0.6) C	BL-27B (KEK)	F	~3 700	
Re-CSH(0.8) C	B18 (DLS)	T	~5 000	
Re-CSH(1.2) C	B18 (DLS)	T	~5 000	
Re-CSH(1.6) C	B18 (DLS)	T	~5 000	
Re-calcite	B18 (DLS)	T	~5 000	
Re-Ettringite	BL-27B (KEK)	F	~3 700	NH ₄ ReO ₄ ,
Re-Ettringite C	BL-27B (KEK)	F	~3 700	Ca-perrhenate, ReS ₂ and ReO ₃
Re-Hydrotalcite	BL-27B (KEK)	F	~3 700	NH ₄ ReO ₄ , Ca-perrhenate and ReO ₃
Re-Hydrotalcite C	BL-27B (KEK)	F	~3 700	
Tc-CSH(0.8)	B18 (DLS)	F	158	NH ₄ TcO ₄ and Ca-pertechnetate
Tc-CSH(1.2)	B18 (DLS)	F	158	
Tc-CSH(1.6)	B18 (DLS)	F	158	
Tc-CSH(0.8) C	B18 (DLS)	F	158	
Tc-CSH(1.2) C	B18 (DLS)	F	158	
Tc-CSH(1.6) C	B18 (DLS)	F	158	
Tc-calcite	B18 (DLS)	F	158	
Tc-Ettringite	B18 (DLS)	F	158	NH ₄ TcO ₄ , Ca-pertechnetate and TcS _x
Tc-Ettringite C	B18 (DLS)	F	158	

7.3 Results I: Sorption / Uptake

7.3.1 Rhenium uptake by C-S-H phases

All C-S-H phases showed an uptake of rhenium of ~40-50 % compared to the initial rhenium concentration ($[Re]_{t=0}$). There was an overall increase of percentage uptake with increasing Ca/Si which is shown in **Figure 7.1**. The R_d values of the uptake are also given in **Table 7.8**.

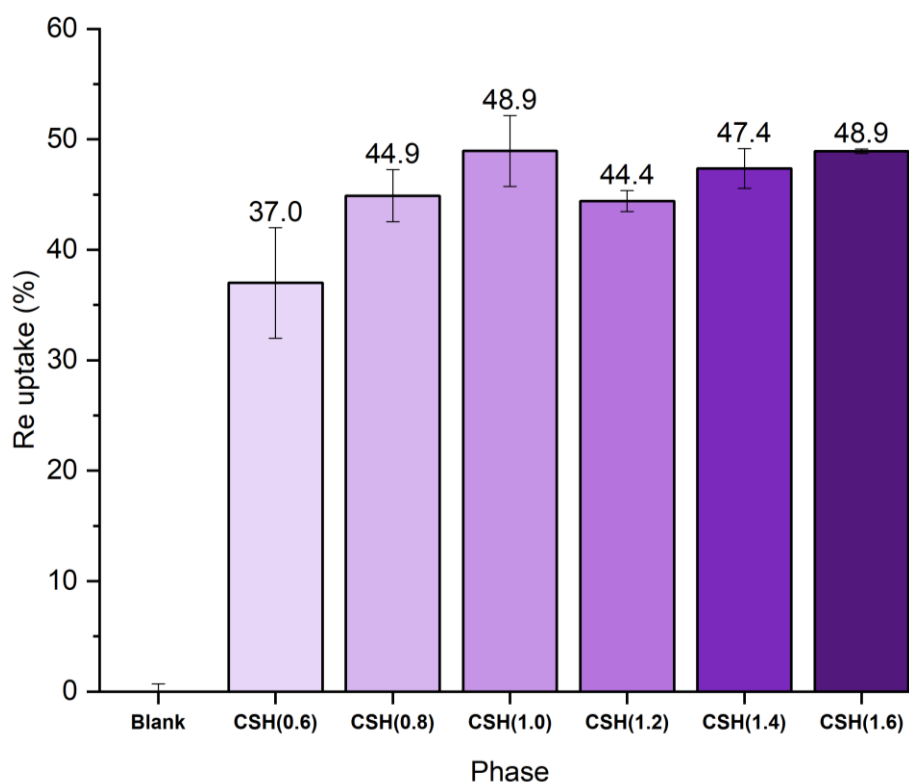


Figure 7.1: Uptake of Re by C-S-H phases as a percentage of $[Re]_{t=0}$.

The R_d values for rhenium uptake by C-S-H show an increase of uptake from CSH(0.6) to CSH(1.0), which then decreases at CSH(1.2). Rhenium uptake appears to approximately plateau within error between CSH(1.2) and CSH(1.6). As the R_d values (**Table 7.8**) are normalised to take into account the mass of the C-S-H phase in the suspension, these values are perhaps a better indication of the trend of rhenium uptake with increasing Ca/Si ratio than the percentage uptake relative to $[Re]_{t=0}$. The R_d values suggest that rhenium partitioned on the C-S-H phases was essentially the same irrespective of the Ca/Si ratio, but that the R_d values for the CSH(0.8) and CSH(1.6) phase were anomalously high.

Table 7.8: R_d values for Re uptake by C-S-H phases for given Ca/Si ratios.

Ca/Si ratio (Calculated Ca/Si ratio)	$R_d / L \text{ kg}^{-1}$
0.6 (0.65)	96 ± 20
0.8 (0.86)	113 ± 11
1.0 (1.06)	116 ± 15
1.2 (1.25)	86 ± 3
1.4 (1.40)	91 ± 7
1.6 (1.58)	88 ± 1

The pH values for the Re-contacted C-S-H phases demonstrate that the addition of NH_4ReO_4 did not cause a decrease in the pH and, in fact, the pH values for the solutions for the C-S-H controls are slightly lower which could indicate carbonation of the control samples [11,253] (**Table 7.9**).

Table 7.9: pH values for Re-contacted C-S-H phases and controls.

Sample	Re-contacted		Controls (as synthesised)	
	pH	Standard deviation	pH	Standard deviation
NH_4ReO_4 solution ([Re] _{t=0} = 10 μM)	6.3	0.09	-	-
CSH(0.6)	9.8	0.00	9.7	0.00
CSH(0.8)	9.8	0.05	9.7	0.00
CSH(1.0)	11.2	0.00	10.4	0.00
CSH(1.2)	11.9	0.05	11.7	0.00
CSH(1.4)	12.4	0.00	12.1	0.00
CSH(1.6)	12.4	0.05	12.3	0.00

7.3.1.1 X-ray diffraction

The X-ray diffraction patterns for the Re-contacted C-S-H phases are shown in **Figure 7.2**. There is no obvious change observed for the C-S-H phases, at all Ca/Si ratios, before and after Re-contact. The pure phase XRD patterns for all C-S-H phases can be viewed in **Chapter 4** and C-S-H(l) peaks [185] can be assigned for each Re-contacted C-S-H phase (tobermorite, PDF card no. 00-045-1480 [184]). Carbonation is observable for samples with Ca/Si ratios of 1.0, 1.2, 1.4, and 1.6 by the identification of diffraction peaks for calcite (Ca/Si = 1.6, 1.4, 1.2) (PDF card no. 01-078-4614 [187]) and vaterite (Ca/Si = 1.4, 1.2 and 1.0) (PDF card no. = 04-017-8634 [191]).

Although every attempt was made to exclude CO₂ during the course of the experiment, it is still possible that this carbonation process could have occurred during the sorption experiments as a result of mild CO₂ ingress into the anaerobic chamber; this would account for the presence of vaterite and / or calcite in the C-S-H phases from Ca/Si = 1.0.

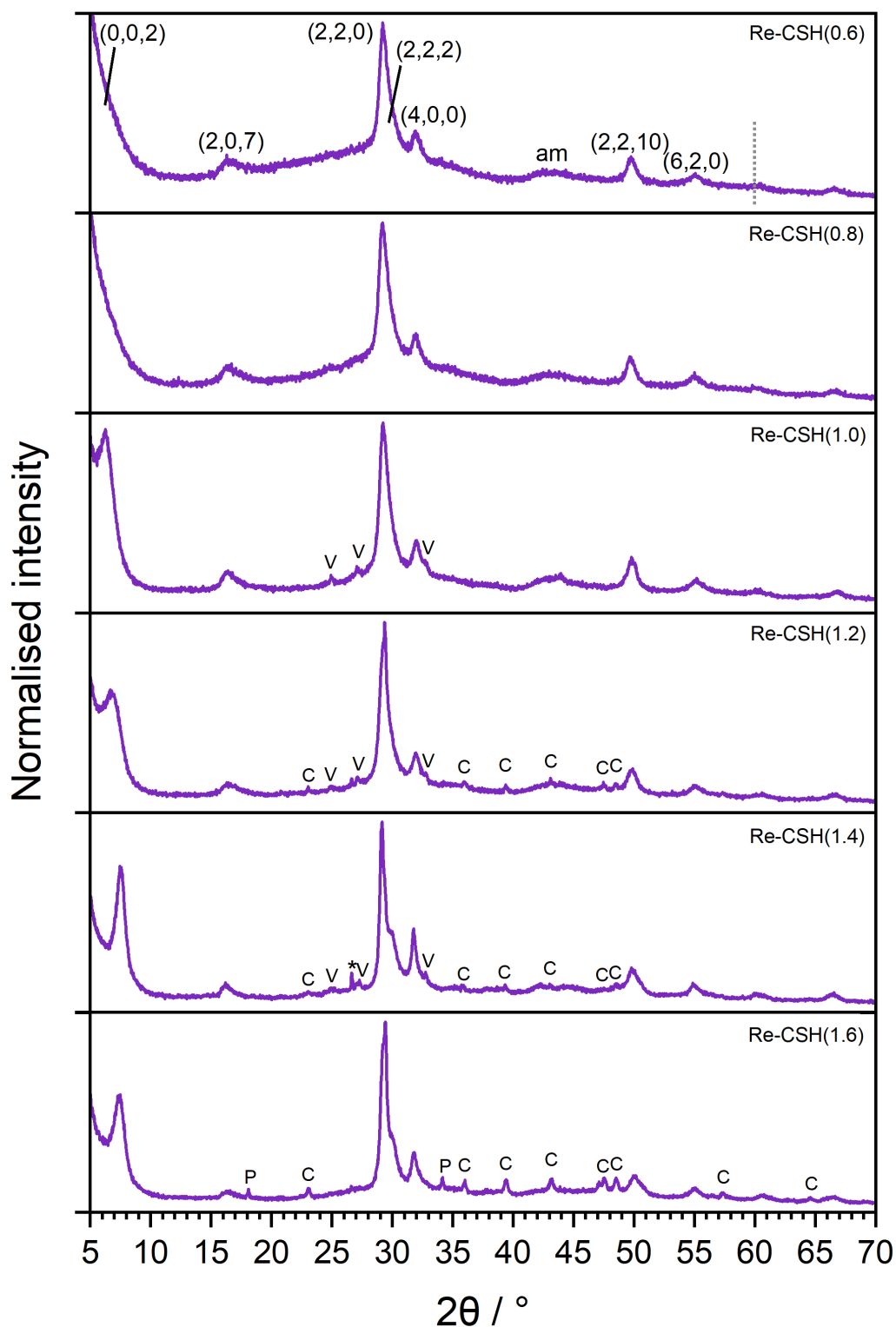


Figure 7.2: XRD patterns for C-S-H phases after contact with Re. Miller indices for C-S-H(I) [185] are given (tobermorite, PDF card no. 00-045-1480 [184]) and the dashed grey line indicates where indexing for the PDF card ceases. “am” = amorphous SiO₂; “C” = calcite (PDF card no. 01-078-4614[187]); “P” = portlandite (COD no. 1001768); “V” = vaterite (PDF card no. = 04-017-8634[191]); * = quartz impurity from post experimental preparation.

7.3.2 Rhenium uptake by minor cement phases

Figure 7.3 shows the percentage decrease of rhenium in solution compared to the initial starting concentration, $[\text{Re}]_{t=0}$. The minor cement phase suspensions all showed a decrease of rhenium concentration in solution, suggesting that uptake had occurred. However, it should be noted that the determination of rhenium concentrations by ICP-OES was not possible due to the high dilutions required to accommodate for the relatively high concentrations of Ca, S, Al and Mg released from the cement phases. ICP-MS analysis was therefore adopted to determine the rhenium concentrations in solution, unfortunately resulting in large errors still arising from the 100-fold dilution required; the value of $[\text{Re}]_{t=0}$ had a 50 % standard deviation of triplicate measurements.

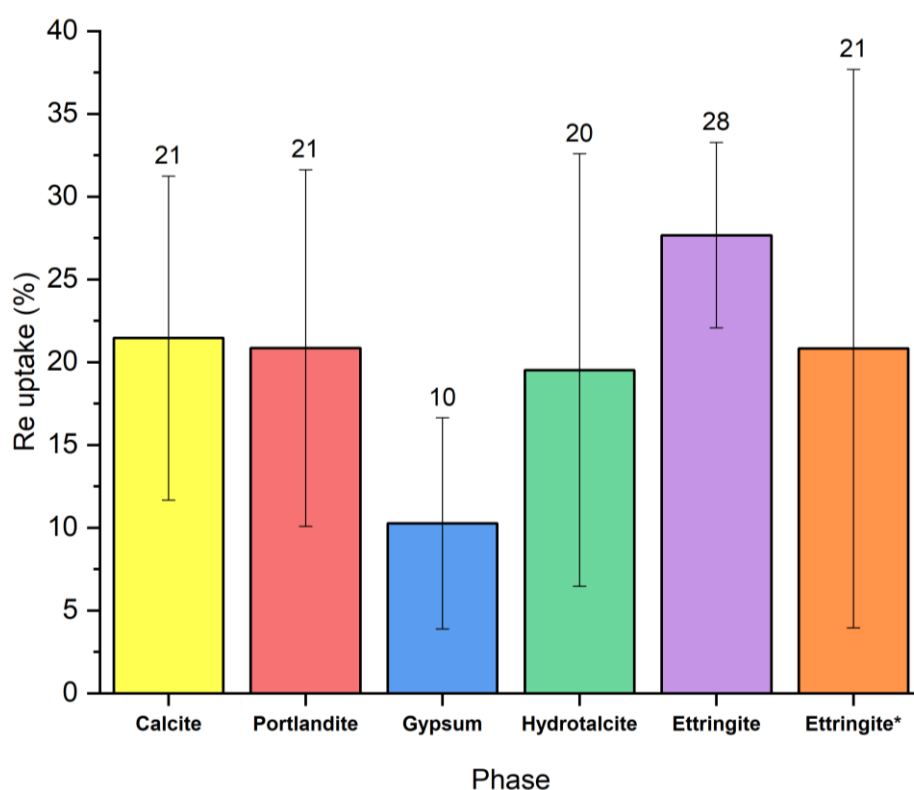


Figure 7.3: Percentage concentration decrease of Re in contact with minor cement phases.

By assuming that the decrease in rhenium concentration was attributed to rhenium sorption or incorporation by the solid phase, the formal order of rhenium uptake at 25 g L^{-1} was ettringite calcite > hydrotalcite > portlandite > gypsum as demonstrated by the R_d values in **Table 7.10**, but not taking into the large associated errors.

Table 7.10: R_d values for Re uptake on minor phases at 25 g L⁻¹.

Minor cement phase	$R_d / \text{L kg}^{-1}$
Calcite	285 ± 88
Portlandite	86 ± 38
Gypsum	74 ± 27
Hydrotalcite	239 ± 200
Ettringite	361 ± 176

The pH values for the Re-contacted phases and controls are also given in **Table 7.11**. There appeared to be at least a slight decrease in the pH for all of the phases, except for portlandite, in comparison to the controls. Given that the pH of the UHQ used for the control samples was adjusted to the pH of the NH_4ReO_4 solution (pH = 4.8) using nitric acid prior to equilibration with phases, it is not obvious why the pH was generally markedly higher in the control samples.

Table 7.11: pH measurements for Re-contacted minor cement phases and controls.

Sample	Re-contacted		Controls	
	pH	Standard deviation	pH	Standard deviation
NH_4ReO_4 solution ($[\text{Re}]_{t=0} = 100 \mu\text{M}$)	4.8	0.00	-	-
NH_4ReO_4 blank	4.8	0.00	-	-
Calcite	8.7	0.19	9.7	0.09
Portlandite	12.4	0.00	12.7	0.00
Gypsum	7.9	0.08	7.5	0.08
Hydrotalcite	9.7	0.00	9.6	0.00
Ettringite	9.9	0.05	9.8	0.00
Ettringite*	9.7	0.12	-	-

7.3.2.1 Percentage mass change

The graphs in **Figures 7.4 to 7.7** show the percentage mass release of Ca, S, Al or Mg from each of the Re-contacted minor cement phases and the corresponding control samples.

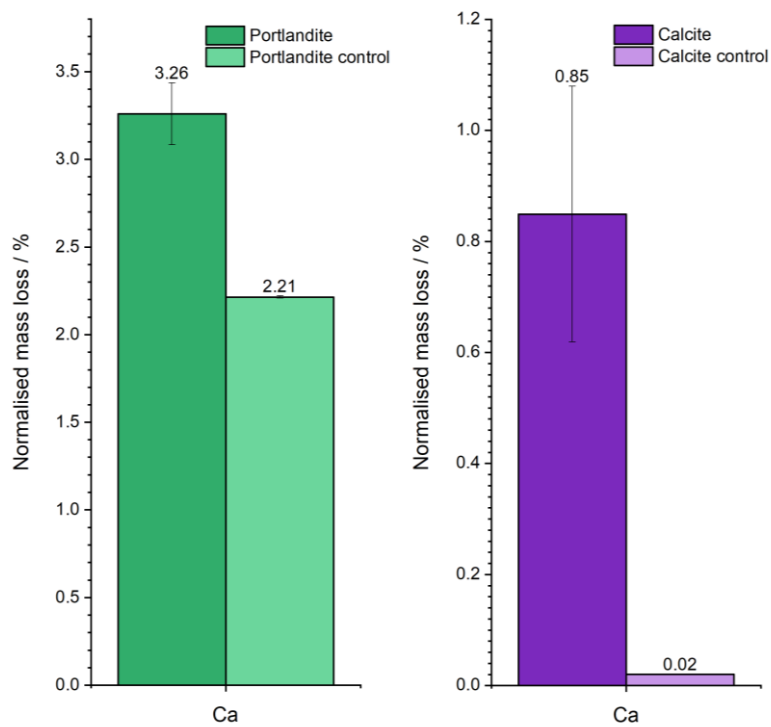


Figure 7.4: Ca percentage mass release from portlandite and calcite.

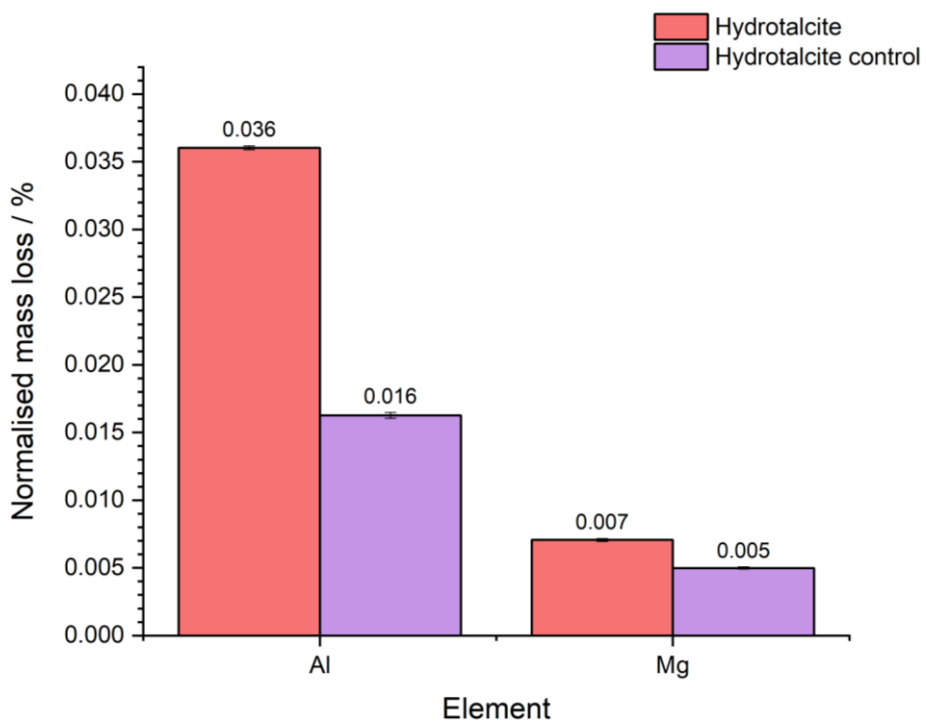


Figure 7.5: Al and Mg percentage mass release from hydrotalcite.

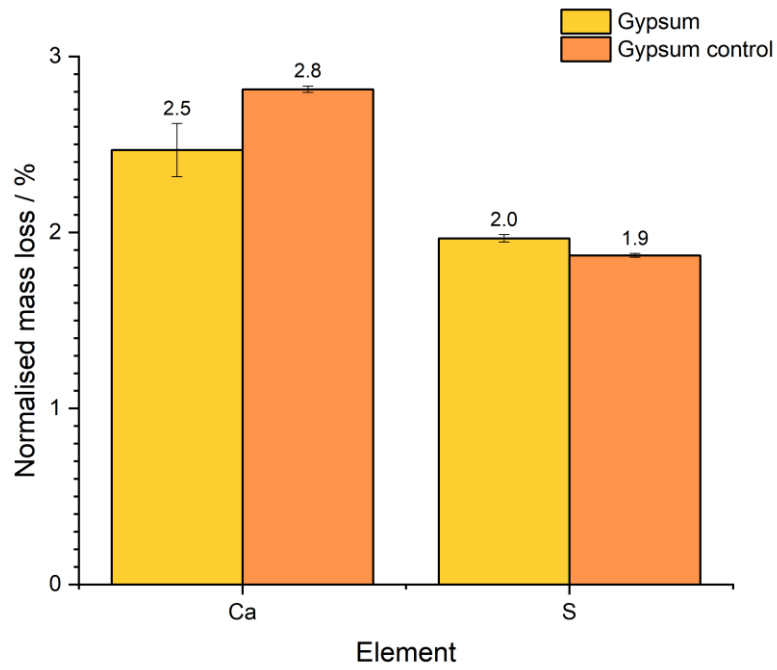


Figure 7.6: Ca and S percentage mass release from gypsum.

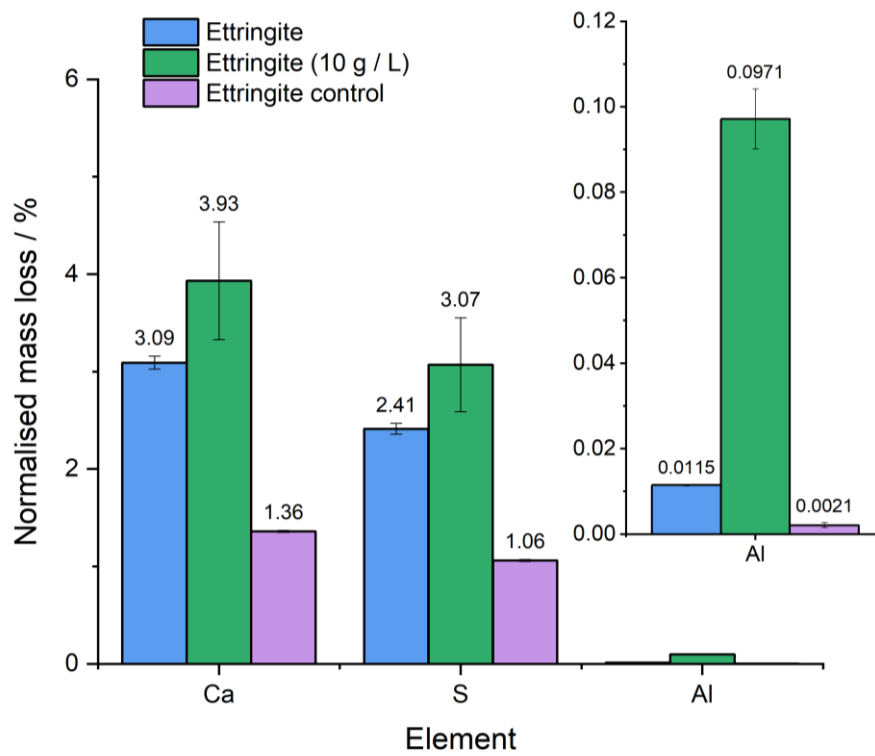


Figure 7.7: Ca, S and Al percentage mass release from ettringite.

Portlandite showed a ~3 % release of calcium compared to ~0.9 % for calcite, in the presence of rhenium (**Figure 7.4**). For the control sample, portlandite showed a calcium release of ~2.2 % (~1.1 % less than when Re-contacted) compared to ~0.02 % for calcite (~0.8 % less than when Re-contacted) which is expected due to the higher aqueous solubility of portlandite compared to calcite [254,255]. This increased release of calcium in the presence of rhenium for both phases could be an indication of favourable Ca-perrhenate complex formation [223,224] in solution, which is discussed further in *Section 7.5.1.1*. For gypsum, the percentage calcium and sulfur release from the Re-contacted and control samples were similar at ~2.5-2.8 % for calcium, and ~2 % for sulfur, respectively (**Figure 7.6**). In the hydrotalcite suspensions, magnesium and aluminium showed a low percentage release overall (<1 %) (**Figure 7.5**).

For ettringite, calcium, sulfur and aluminium release into solution was observed which is expected below pH = 10.7 (measured pH = 9.7 to 9.9) [304]. In general, there was an increased percentage release of calcium, sulfur and aluminium in the 10 g L⁻¹ Re-contacted sample compared to the 25 g L⁻¹ Re-contacted sample, which is attributed to the lower S/L ratio and, thus, the increased surface area to volume ratio for the 10 g L⁻¹ sample. The release of calcium, aluminium and, in particular, sulfur (as SO₄²⁻) in the presence of rhenium could imply mechanisms of rhenium uptake such as anion exchange between ReO₄⁻ and SO₄²⁻ [159,160,305], or the formation of Ca- and/or Al-perrhenate complexes [223,224,306].

Both of the Re-contacted ettringite samples (at both S/L) showed an increased percentage release of calcium, sulfur and aluminium compared to the control (measured for S/L = 25 g L⁻¹ only) (**Figure 7.7**). The results can, in part, be rationalised by the results from Rietveld refinement of the ettringite starting phases, shown in **Table 7.12**, which show that the Re-contacted ettringite samples were initially made up of ~75 wt % ettringite compared to only ~66 wt % in the control ettringite sample. The remainder of the phases were made up of calcium sulfate impurities.

Table 7.12: Percentage composition of ettringite phases determined by Rietveld refinement using CIF files for ettringite, anhydrite (orthorhombic) and gypsum [194,197,198].

	Rwp	GOF	Ettringite / %	Anhydrite / %	Gypsum / %
Re-Ettringite (25 g L ⁻¹)	18.44	5.14	76.7 ±13.6	24.0 ±13.5	0.4 ±0.3
Re-Ettringite* (10 g L ⁻¹)	17.62	5.14	75.2 ±7.6	22.9 ±7.6	2.0 ±0.8
Ettringite control (25 g L ⁻¹)	20.88	5.94	66.0 ±10.9	32.6 ±10.7	1.5 ±0.6

Due to the presence of calcium sulfate impurities in all of the ettringite phases, the calcium, sulfur and aluminium release data shown in **Figure 7.7** must be considered in terms of dissolution of both ettringite and calcium sulfate. Of the impurity phases, anhydrite is considered to be the primary phase responsible for the release of calcium and sulfur because anhydrous / dehydrated calcium sulfate phases are much more soluble than the corresponding hydrated calcium sulfate phases [307–309], and there is much less gypsum present in the ettringite samples (<2 wt %) compared to anhydrite (~25%). In the following discussion, therefore, the elemental release of calcium and sulfur is considered for the presence of anhydrite only, for simplification.

For each of the Re-contacted ettringite phases, at both S/L ratios, and the control at 25 gL⁻¹, the average molar ratios of Ca/S, S/Al and Ca/Al ratios calculated for the ions present in solution are given in **Table 7.13**, as well as the expected ratios for congruent dissolution of single-phase ettringite in aqueous solution outlined by *Constantiner et al.* and given by the stoichiometric equation, **Equation 7.3** [310]:



Table 7.13: Molar ratios of cations present in ettringite solutions.

	Ca/S	S/Al	Ca/Al
Ettringite [310]	2	1.5	3
Re-ettringite (25 g L ⁻¹)	1.03	180	180
Re-ettringite* (10 g L ⁻¹)	1.03	27	27
Ettringite control (25 g L ⁻¹)	1.03	>400	>400

Together with the composition values from **Table 7.12**, the following observations can be made:

- (i) The Ca/Al (and S/Al) ratios for both Re-contacted phases are higher than the ideal ratios for pure-phase ettringite, at 180 and 27 for Re-ettringite and Re-ettringite*, respectively. This is an indication of the presence of higher calcium and sulfur release from the phases due to the presence of ~24 wt % anhydrite. The ratios are lower in the Re-ettringite* sample due to the lower S/L ratio.
- (ii) The very high Ca/Al (and S/Al) ratio(s) of the control sample (> 400) is an indication of the higher amount of anhydrite present in this phase compared to that of the Re-contacted phases (~33 wt %).
- (iii) The Ca/S ratios calculated for all three of the ettringite phases are closer to unity than would be expected for dissolution of pure-phase ettringite (1.03 compared

to 2). This indicates that anhydrite is preferentially dissolved over ettringite, given that the Ca/S molar ratio of anhydrite is 1.

7.3.2.2 X-ray diffraction

The X-ray diffraction patterns for the minor cement phases after rhenium contact are shown in **Figure 7.8** and the lattice parameters are given in **Table 7.14** for the control and Re-contacted phases.

The X-ray diffraction pattern for Re-contacted portlandite (PDF card no 00-044-1481 [186]) showed signs of carbonation by the presence of calcite (denoted by “C”). There was also the observation of an additional peak at $\sim 20.9^\circ$ 2θ , (denoted by “♦”) which potentially corresponds to the highest intensity (202) reflection of $\text{Ca}(\text{ReO}_4)_2 \cdot 2\text{H}_2\text{O}$ (ICSD collection codes 41049 and 65417 [222,223]), which was not observed in the control sample.

Calcite (PDF card no. 01-078-4614 [187]) appeared to show no immediately obvious change after rhenium contact. A peak at $\sim 11.7^\circ$ 2θ was assigned to the (020) reflection of gypsum (PDF card no. 00-033-0311 [196]), (denoted by “♠”) indicating gypsum impurities were present in both the control and rhenium contacted sample (also indicated by a small sulfur release in ICP-OES measurements, but not discussed in detail here). On further investigation there was an additional peak observed at $\sim 20.7^\circ$ 2θ , that could potentially be assigned to the (021) reflection of gypsum, and which is only present in the Re-contacted sample, (denoted by “♠?”). However, given that this peak is not observed in either the calcite starting material or in the calcite control sample, this peak could also be assigned to the (202) reflection of $\text{Ca}(\text{ReO}_4)_2 \cdot 2\text{H}_2\text{O}$, as in the portlandite sample.

In the case of ettringite (PDF card no. 04-013-3691 [194]), the intensity of the anhydrite peak at $\sim 25.5^\circ$ 2θ (denoted by “♣”) (PDF card no. 00-037-1496 [195]) decreased in intensity for both ettringite samples, confirming preferential anhydrite dissolution. The cell volume of ettringite also showed a $\sim 1.8 \text{ \AA}^3$ decrease after Re-contact compared to the control sample, which could indicate re-sizing of the lattice structure to accommodate ReO_4^- , potentially in place of SO_4^{2-} (**Table 7.14**) [159], in agreement with elemental release data. There were no additional peaks that evidenced the formation of a Ca- or Al-perrhenate type phase.

Hydrotalcite (PDF card no. 01-082-8041 [192]) maintained its nano-scale crystallinity after contact with rhenium and additional peaks were observed at $\sim 18.5^\circ$ and $\sim 20.4^\circ$ 2θ , in both the control and Re-contacted sample (“●”). These peaks were assigned to the nordstrandite polymorph of $\text{Al}(\text{OH})_3$ (PDF card no. 00-024-0006 [311]) and were also present in the control sample.

Gypsum did not appear to show any change after rhenium contact, apart from a slight decrease in peak intensity, but the phase still maintained a gypsum crystal structure.

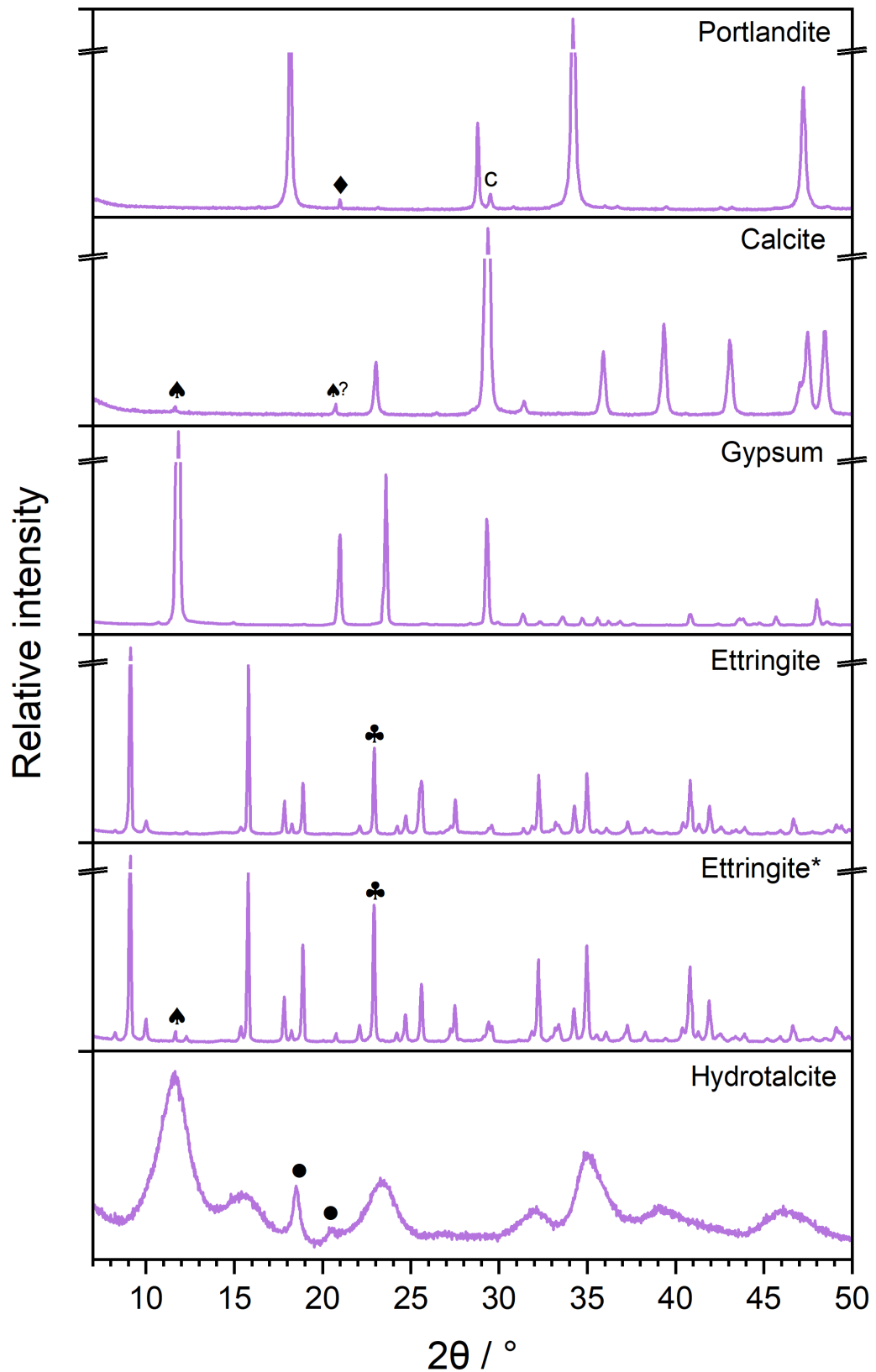


Figure 7.8: XRD patterns for Re-contacted minor cement phases portlandite (PDF card no 00-044-1481 [186]), calcite (C; PDF card no. 01-078-4614 [187]), gypsum (♠; PDF card no. 00-033-0311 [196]), ettringite (PDF card no. 04-013-3691 [194]) and hydrotalcite (PDF card no. 01-082-8041 [192]). ♦ = $\text{Ca}(\text{ReO}_4)_2 \cdot 2\text{H}_2\text{O}$ (ICSD collection codes 41049 and 65417 [222,223]); ♠ = anhydrite (PDF card no. 00-037-1496 [195]); ● = nordstrandite (PDF card no. 00-024-0006 [311]).

Table 7.14: Lattice parameters for control (top) and Re-contacted (middle) samples and the observed difference (bottom), established using Rietveld refinement and LaB₆ as an internal standard (~1-3 wt %).

	Space group	Rwp	GOF	Volume / Å ³	a / Å	b / Å	c / Å	β / °
Portlandite	P3m1	10.61	2.56	54.915(10)	3.59291(27)	-	4.91211(53)	-
Calcite	R3c	6.78	1.67	368.752(41)	4.99646(25)	-	17.05610(88)	-
Gypsum	C2/c	22.45	8.30	496.63(15)	6.2888(14)	15.2222(16)	5.68271(79)	114.089(12)
Ettringite	P31c	9.78	2.98	2346.73(24)	11.23275(48)	-	21.4763(12)	-
Hydrotalcite	R3m	5.97	2.12	183.0(19)	3.031(16)	-	23.008(16)	-

	Space group	Rwp	GOF	Volume / Å ³	a / Å	b / Å	c / Å	β / °
Portlandite	P3m1	9.73	2.29	54.829(12)	3.59122(33)	-	4.90905(59)	-
Calcite	R3c	7.17	1.79	368.613(43)	4.99528(26)	-	17.05765(93)	-
Gypsum	C2/c	18.69	6.37	496.16(12)	6.2875(11)	15.2225(15)	5.67940(69)	114.1099(97)
Ettringite	P31c	9.33	2.68	2344.90(31)	11.22833(63)	-	21.4765(14)	-
Hydrotalcite	R3m	5.89	2.09	182.4(22)	3.024(18)	-	23.035(16)	-

	Δ Volume / Å ³	Δ a / Å	Δ b / Å	Δ c / Å	Δ β / °
Portlandite	-0.086	-0.00169	-	-0.00306	-
Calcite	-0.139	-0.00118	-	0.00155	-
Gypsum	-0.47	-0.0013	0.0003	-0.00331	0.0209
Ettringite	-1.83	-0.00442	-	0.0002	-
Hydrotalcite	-0.6	-0.007	-	0.027	-

7.3.3 Technetium uptake by C-S-H phases

As was observed for counterpart rhenium experiments, C-S-H phases showed uptake of technetium. For CSH(0.6) ~3 % technetium uptake was measured, which increased to ~9 % for CSH(1.4), compared to the initial technetium concentration ($[Tc]_{t=0}$) (**Figure 7.9**). CSH(1.6) did not follow the overall trend, showing a decrease to 3.4 %.

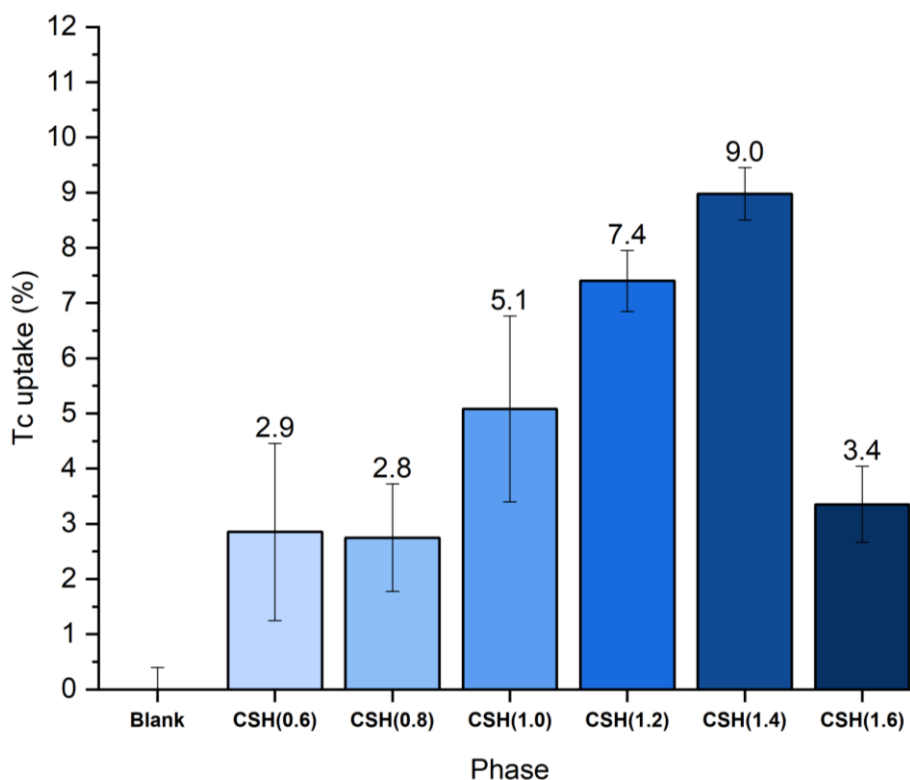


Figure 7.9: Uptake of Tc by C-S-H phases as a percentage of $[Tc]_{t=0}$.

The R_d values of technetium uptake by C-S-H are also given in **Table 7.15**, which indicate that there was a general increase in technetium uptake with increasing Ca/Si from CSH(0.6) ($R_d = 4.8 \pm 2.7$) up to CSH(1.4) ($R_d = 9.8 \pm 0.6$). These data also highlight the anomalous behaviour for CSH(1.6) ($R_d = 3.2 \pm 0.7$).

Table 7.15: R_d value for Tc uptake by C-S-H phases at given Ca/Si ratios.

Ca/Si ratio (Calculated Ca/Si ratio)	$R_d / L \text{ kg}^{-1}$
0.6 (0.65)	4.8 ± 2.7
0.8 (0.86)	3.9 ± 1.4
1.0 (1.06)	6.5 ± 2.3
1.2 (1.26)	8.6 ± 0.7
1.4 (1.42)	9.8 ± 0.6
1.6 (1.58)	3.2 ± 0.7

The pH values for the Tc-contacted C-S-H phases were determined approximately using indicator paper (**Table 7.16**). Given that control samples were measured more accurately using a pH probe, the lower pH values measured for the technetium contacted C-S-H samples are likely a result of less accurate pH measurement methods necessitated by radioactive material handling protocols.

Table 7.16: pH values for C-S-H phases in contact with Tc and controls.

Sample	Tc-contacted		Controls	
	pH	Standard deviation	pH	Standard deviation
NH₄TcO₄ solution ([Tc] _{t=0} = 10 μM)	7	0.0	-	-
CSH(0.6)	~8.5	0.0	9.7	0.00
CSH(0.8)	9	0.0	9.7	0.00
CSH(1.0)	9.5	0.0	10.4	0.00
CSH(1.2)	10	0.0	11.7	0.00
CSH(1.4)	~11.5	0.0	12.1	0.00
CSH(1.6)	12	0.0	12.3	0.00

7.3.3.1 X-ray diffraction

The X-ray diffraction patterns for the Tc-contacted C-S-H phases are shown in **Figure 7.10**. Peaks for the C-S-H phases [185] were observable (tobermorite, PDF card no. 00-045-1480[184]), however, calcite (PDF card no. 01-078-4614[187]) was also present at all Ca/Si ratios. No additional reflections were observed.

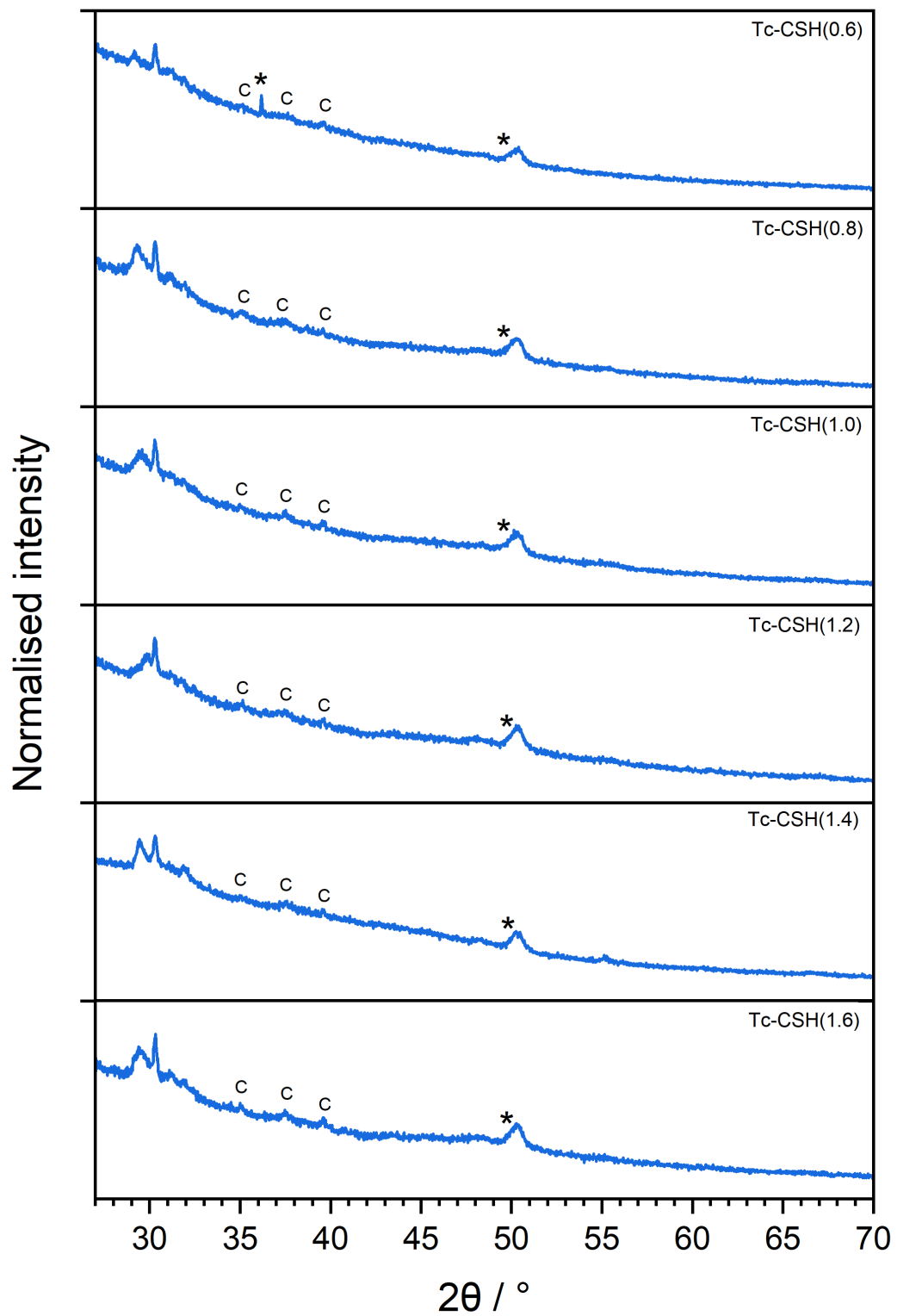


Figure 7.10: XRD patterns for C-S-H phases (tobermorite, PDF card no. 00-045-1480[184]) after contact with Tc. "C" = calcite (PDF card no. 01-078-4614[187]); * = sample holder interference.

7.3.4 Technetium uptake by minor cement phases

Technetium uptake by minor cement phases was not observed on the timescale of the sorption experiments performed. The results from pH measurements are given in **Table 7.17** for reference.

Table 7.17: pH values for Tc-contacted minor cement phases and controls.

Sample	Tc-contacted		Controls (ICP-OES / LSC)	
	pH	Standard deviation	pH	Standard deviation
NH₄TcO₄ solution ([Tc]_{t=0} = 20 μM)	~7.5	0.0	-	-
NH₄TcO₄ blank	~7.5	0.0	-	-
Calcite	8	0.0	9.6 / 9.7	0.14 / 0.05
Portlandite	12	0.0	12.9 / 12.9	0.00 / 0.00
Gypsum	6	0.0	8.0 / 7.6	0.08 / 0.08
Hydrotalcite	9	0.0	9.7 / 9.6	0.05 / 0.05
Ettringite	8	0.0	8.7 / 8.7	0.0 / 0.0
Ettringite*	~6.5	0.0	8.6 / 9.1	0.0 / 0.0

As for the C-S-H phases, the pH values for technetium contacted minor phases were determined approximately using indicator paper, and so any discrepancies between those and the controls must be treated with some uncertainty.

7.3.4.1 Percentage mass loss of controls

The percentage mass loss of the control samples for the minor phases in UHQ are given in **Figures 7.11 to 7.14**. Due to limitations for measuring ⁹⁹Tc containing solutions using ICP-OES or ICP-MS, the results for the percentage mass loss of technetium contacted samples could not be determined. The main observation to make from the percentage mass loss for the control samples is that there is very little difference observed between the controls for the rhenium experiments (starting pH 4.8) and the controls for the technetium experiments (starting pH ~7).

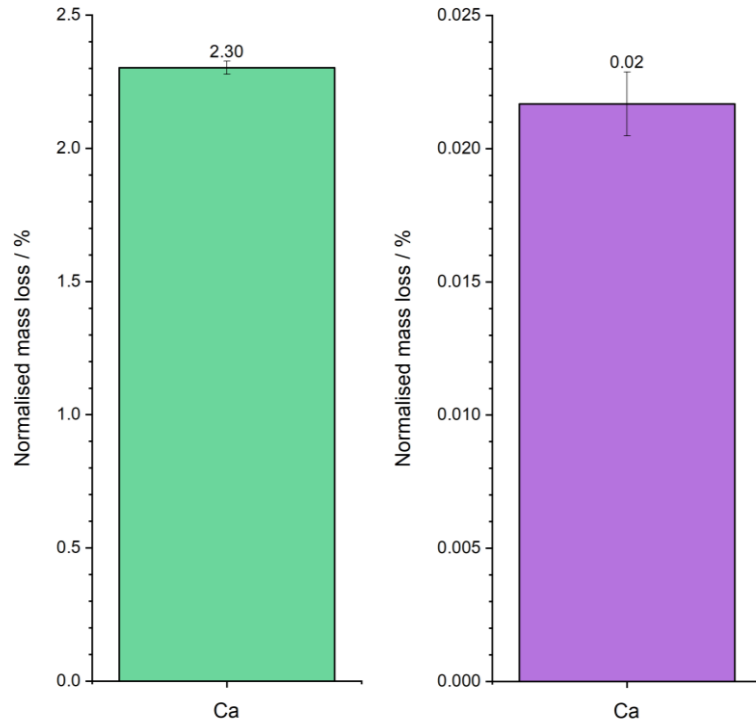


Figure 7.11: Ca percentage mass release from portlandite (left) and calcite (right) controls.

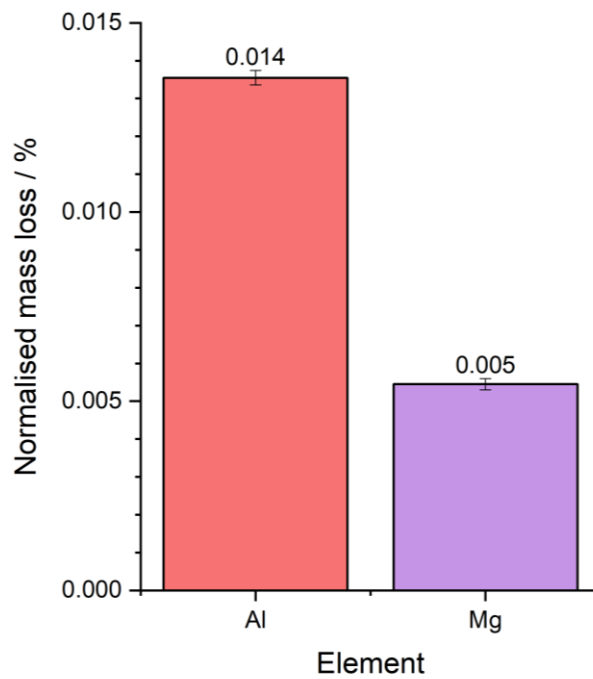


Figure 7.12: Al and Mg percentage mass release from hydrothermal control.

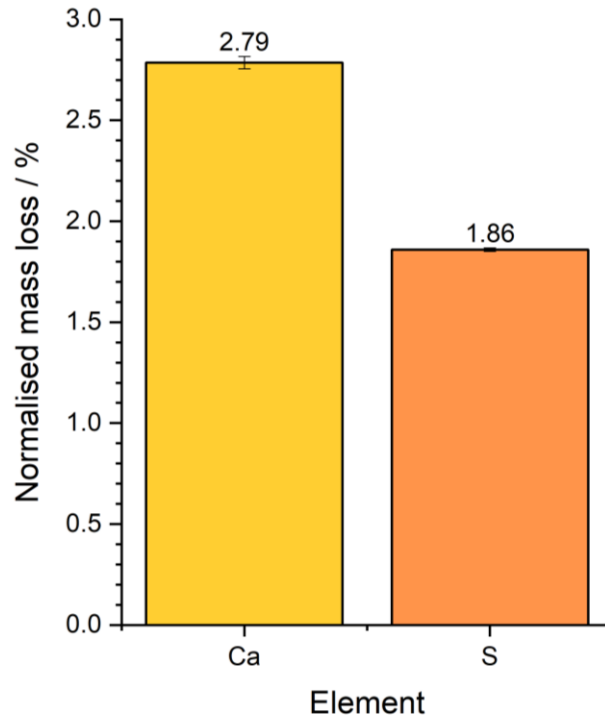


Figure 7.13: Ca and S percentage mass release from gypsum control.

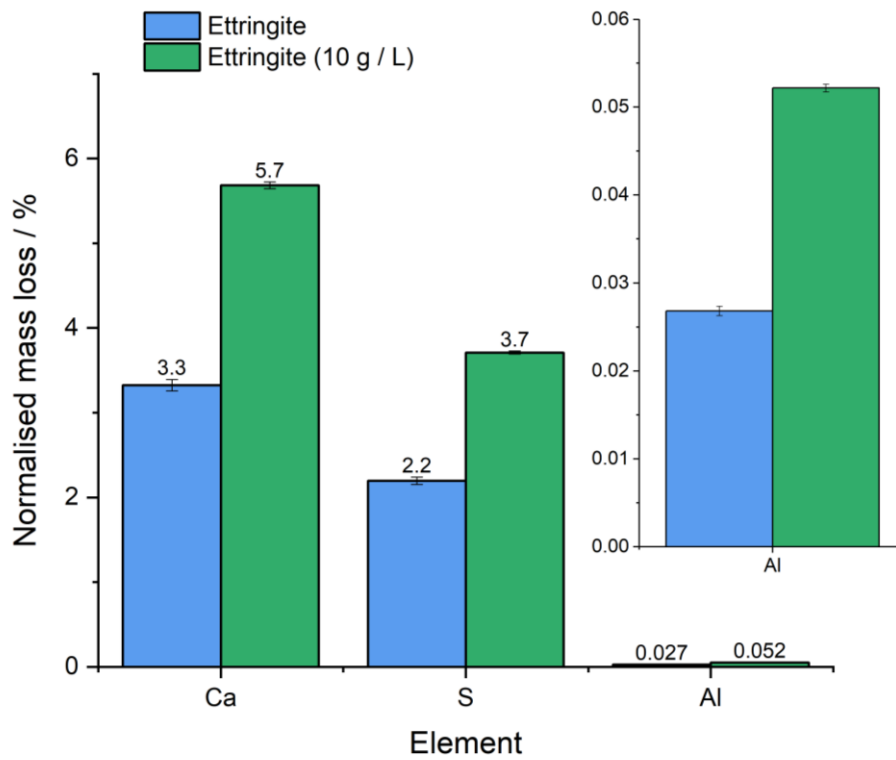


Figure 7.14: Ca, S and Al percentage mass release from ettringite controls.

The ettringite controls for the 25 g L⁻¹ and 10 g L⁻¹ samples show similar behaviour to the Re-contacted ettringite samples at the same corresponding S/L. The percentage composition of the starting ettringite phases are given in **Table 7.18** for completeness.

Table 7.18: Percentage composition of ettringite phases determined by Rietveld refinement using CIF files for ettringite, anhydrite (orthorhombic) and gypsum [194,197,198].

	Rwp	GOF	Ettringite / %	Anhydrite / %	Gypsum / %
Tc-Ettringite (25 g L⁻¹)	14.81	4.14	86.6 ± 4.7	6.1 ± 2.5	7.3 ± 3.1
Ettringite control (25 g L⁻¹)	18.44	5.14	76.7 ± 13.6	24.0 ± 13.5	0.4 ± 0.3
Tc-Ettringite* (10 g L⁻¹)	19.81	6.25	58.7 ± 24.9	39.1 ± 23.6	2.2 ± 1.4
Ettringite* control (10 g L⁻¹)	18.37	5.03	65.5 ± 15.0	31.8 ± 14.1	2.5 ± 1.3

The Ca/Si, S/Al and Ca/Al ratios of the (Tc) ettringite controls, in solution, are given in **Table 7.19** and compared to the expected ratios for congruent dissolution of ettringite [310].

Table 7.19: Molar ratios of cations present in ettringite solutions.

	Ca/S	S/Al	Ca/Al
Ettringite [310]	2	1.5	3
<u>Ettringite control</u> (25 g L⁻¹)	1.21	68.8	83.3
<u>Ettringite* control</u> (10 g L⁻¹)	1.22	59.8	73.2

The Ca/S ratios for the control for technetium samples are slightly higher than for the control samples for rhenium. This indicates that the release of calcium was slightly higher relative to the sulfur release. The S/Al and Ca/Al ratios are slightly lower for the 10 g L⁻¹ control compared to the 25 g L⁻¹ control which is consistent with a lower percentage of ettringite present (66 wt % ettringite compared to 76 wt %, by Rietveld).

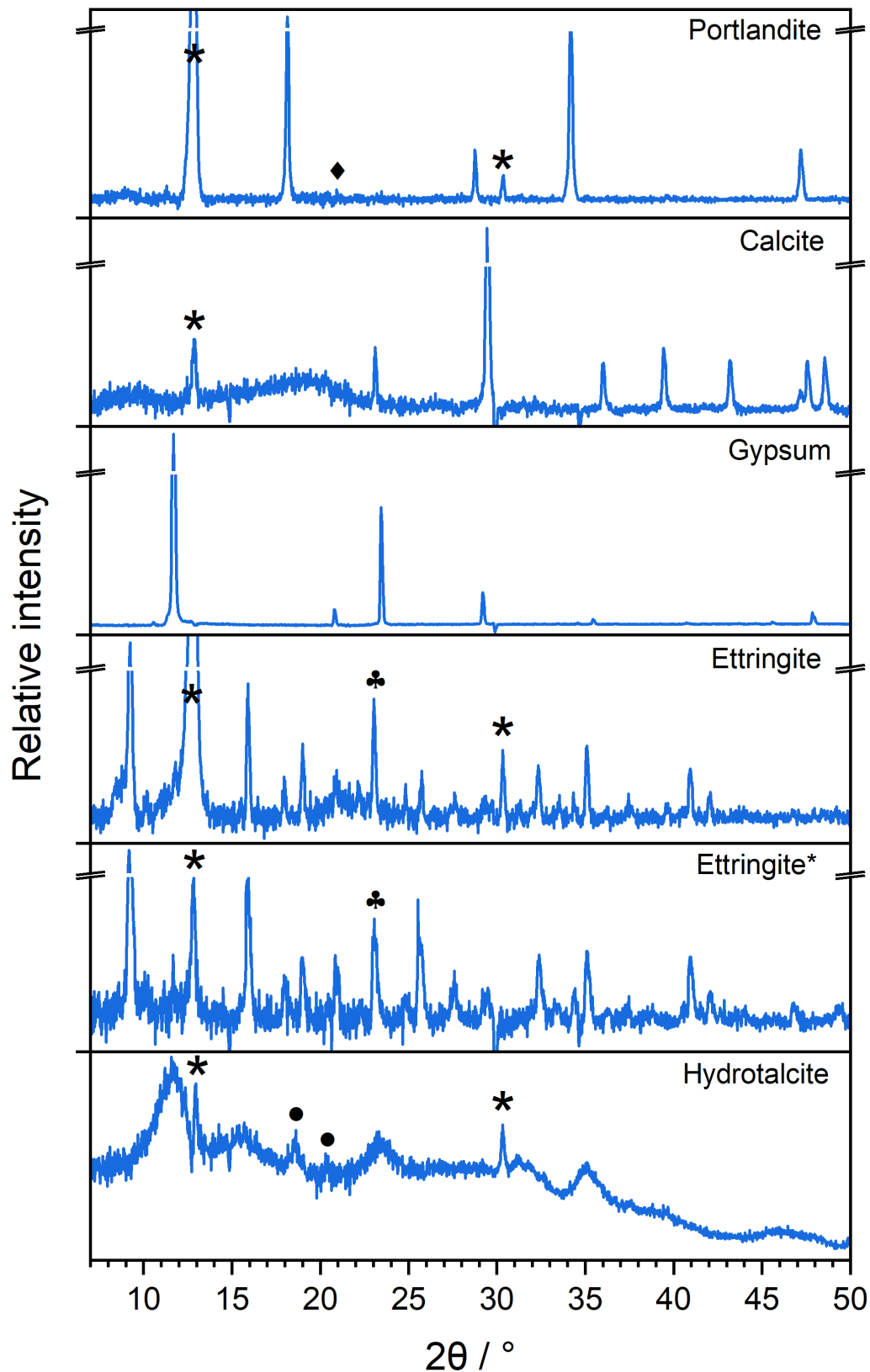


Figure 7.15: XRD patterns for Tc-contacted minor cement phases portlandite (PDF card no 00-044-1481 [186]), calcite (C; PDF card no. 01-078-4614 [187]), gypsum (PDF card no. 00-033-0311 [196]), ettringite (PDF card no. 04-013-3691 [194]) and hydrotalcite (PDF card no. 01-082-8041 [192]). \blacklozenge = $\text{Ca}(\text{ReO}_4)_2 \cdot 2\text{H}_2\text{O}$ (ICSD collection codes 41049 and 65417 [222,223]); \clubsuit = anhydrite (PDF card no. 00-037-1496 [195]); \bullet = nordstrandite (PDF card no. 00-024-0006 [311]). The asterisk indicates contributions from the sample containment.

7.3.4.2 X-ray diffraction

The X-ray diffraction patterns for the Tc-contacted minor phases, that did not display any technetium uptake, are shown in **Figure 7.15** for reference.

In the portlandite sample, a small diffraction peak (denoted by “♦”) was identified, which could correlate to $\text{Ca}(\text{TcO}_4)_2 \cdot 2\text{H}_2\text{O}$, under the assumption that this phase has the same crystal structure as $\text{Ca}(\text{ReO}_4)_2 \cdot 2\text{H}_2\text{O}$ [222,223]. Even though technetium uptake was not observed by the solid phase (i.e. a change in technetium concentration in solution), the observation of this peak in the diffraction pattern could suggest the formation of an aqueous Ca-pertechetate complex in solution which precipitates out onto the surface of the solid phase during the drying process, given that the solid phases were not washed after the experiment. This would not necessarily affect the concentration of technetium in solution at the time of sampling and therefore not elude to an “uptake” process by the solid portlandite phase. This is discussed in more detail in *Section 7.5.2.1*.

For the other phases, there was little observable change in the diffraction patterns before and after technetium contact. For hydrotalcite, the presence of peaks for $\text{Al}(\text{OH})_3$ were also observed as with Re-contacted phases, in both the control and Tc-contacted samples (denoted by “●”). This is also in agreement with the higher release of Mg from the control sample, compared to Al release. A decrease in intensity for the anhydrite peak (denoted by “♣”) in the ettringite samples is difficult to determine due to background interference. Gypsum and calcite show no additional peaks and minor gypsum impurities are not observable in the calcite sample which is likely a result of high background interference.

7.4 Results II: X-ray absorption spectroscopy

7.4.1 XANES

The XANES spectra at the rhenium L_{III} -edge and the technetium K-edge for the selected Re- and Tc-contacted samples are shown in **Figure 7.16** and **Figure 7.17**, respectively. Additional Re-contacted calcium oxide (Re-CaO) and calcite (Re-calcite) and Tc-contacted calcite (Tc-calcite) were also measured for comparison to the C-S-H phases. The XAFS of Tc-contacted hydrotalcite or calcium oxide were unfortunately not measured, due to constraints on available experimental time at Diamond Light Source. The Athena application from the Demeter 0.9.26 software package was used for post-processing and normalisation of XAFS data. The value of E_0 was assigned to the first inflection point of the derivative of the energy spectrum.

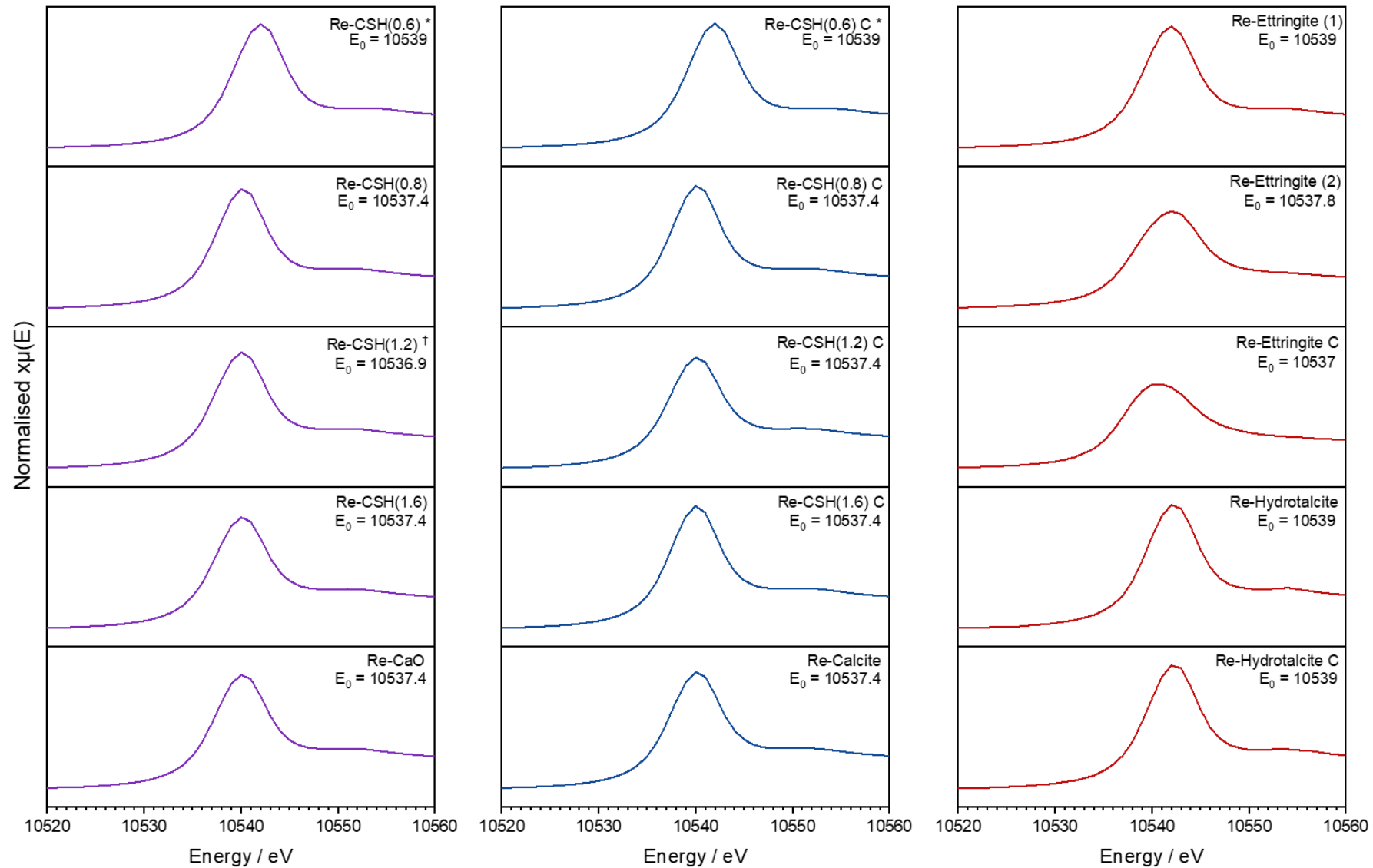


Figure 7.16: XANES spectra of Re-contacted phases. * Re-CSH(0.6) samples were measured at KEK rather than DLS, unlike the rest of the C-S-H series. † sample measured in fluorescence mode, the rest of the C-S-H series were measured in transmission mode.

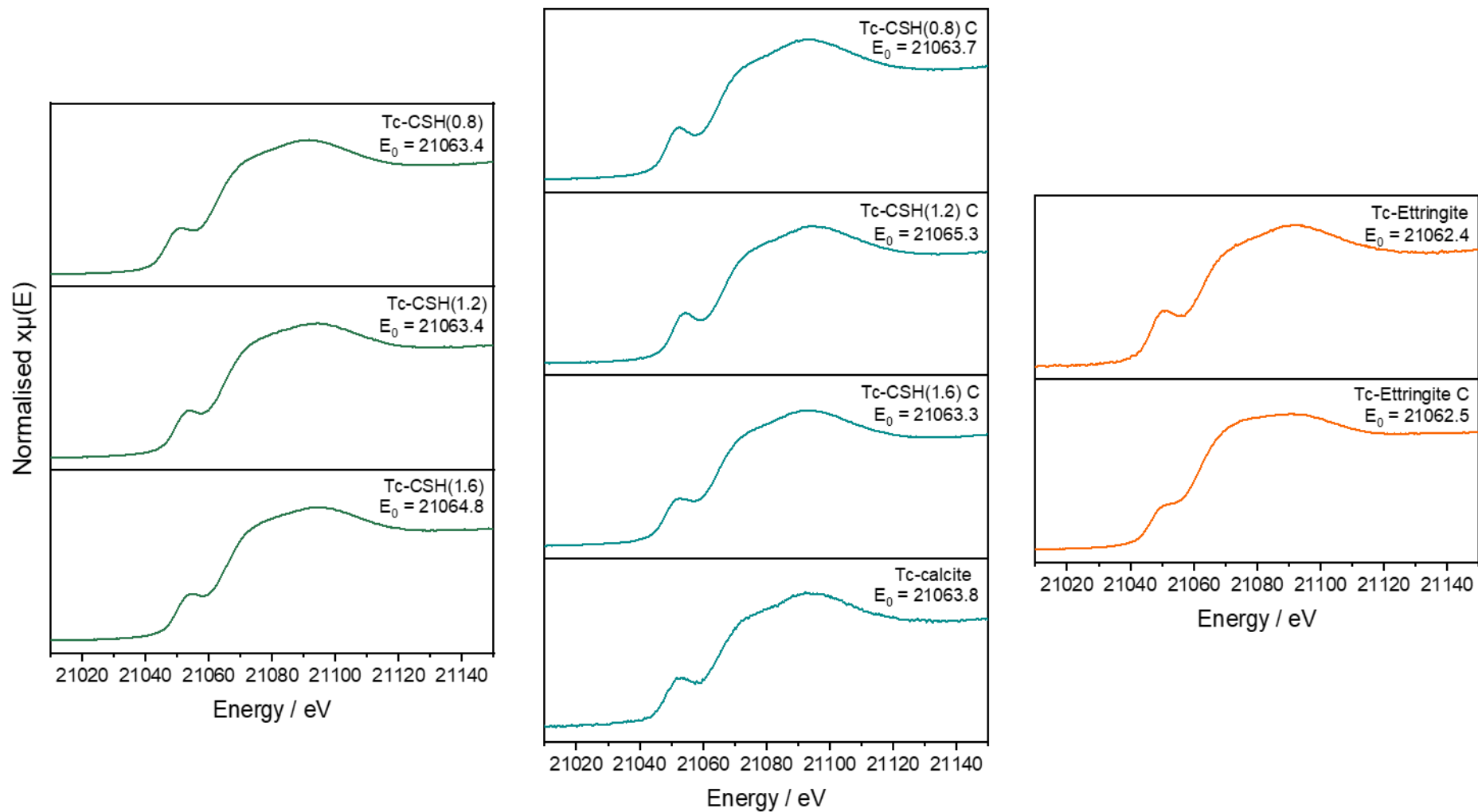


Figure 7.17: XANES spectra of Tc-contacted phases. All samples measured in fluorescence mode.

On first inspection of the XANES spectra, all Re-contacted CSH(X) and hydrotalcite phases displayed a XANES profile that was similar to that of NH_4ReO_4 or Ca-perrhenate (see **Chapter 4**), regardless of whether or not they were pre-carbonated. For the Re-contacted ettringite sample (denoted (1)), the XANES spectra also appeared perrhenate-like. However, the second measurement of the Re-ettringite phase (denoted (2)) displayed a dampening of the post-edge signal which was more typical of the spectrum obtained for the Re-ettringite phase prepared under 1 % CO_2 (denoted C).

The XANES spectra of the Tc-contacted phases all displayed a pre-edge feature typical of a pertechnetate phase [227]. However, the feature was generally dampened in all the spectra in comparison to NH_4TcO_4 and was more comparable to that observed for the Ca-pertechnetate phase (see **Chapter 4**). The Tc-ettringite phase, that was pre-carbonated before technetium addition, shows the most notable dampening of the pre-edge feature, as well as dampening in the post-edge region.

7.4.1.1 Linear combination fitting

XANES linear combination fitting of the Re- and Tc-contacted phases to the XANES spectra of Re- and Tc-bearing phases, used as standards (described in **Tables 7.5** and **7.6** and **Chapter 4**), was also performed in the Athena application.

For the Re-contacted phases, the standards fitted were as follows:

- C-S-H: NH_4ReO_4 , Ca-perrhenate and Re-CaO (Re-CaO and Re-calcite were also fitted separately to NH_4ReO_4 and Ca-perrhenate). The results are given in **Figure 7.18** (percentages) and **Table 7.20** (weighted fractions).
- Ettringite: NH_4ReO_4 , Ca-perrhenate, ReO_3 and ReS_2 . The results are given in **Figure 7.19** (percentages) and **Table 7.21** (weighted fractions)
- Hydrotalcite: NH_4ReO_4 and ReO_3 . The results are given in **Figure 7.19** (percentages) and **Table 7.22** (weighted fractions).

All fitting was performed between -20 and +30 eV from the position of E_0 and the value of ΔE for each standard fitted was recorded.

For the Tc-contacted phases, the standards were fitted as follows:

- C-S-H: NH_4TcO_4 and Ca-pertechnetate (Tc-calcite was also fitted separately to NH_4TcO_4 and Ca-pertechnetate). The results are given in **Figure 7.20** (percentages) and **Table 7.23** (weighted fractions).

- Ettringite: NH_4TcO_4 , Ca-perrhenate and TcS_x . The results are given in **Figure 7.21** (percentages) and **Table 7.24** (weighted fractions).

All fitting was performed between -30 and +40 eV from the position of E_0 , to encompass the pre-edge feature of the perrhenate group, and the value of ΔE for each standard fitted was recorded.

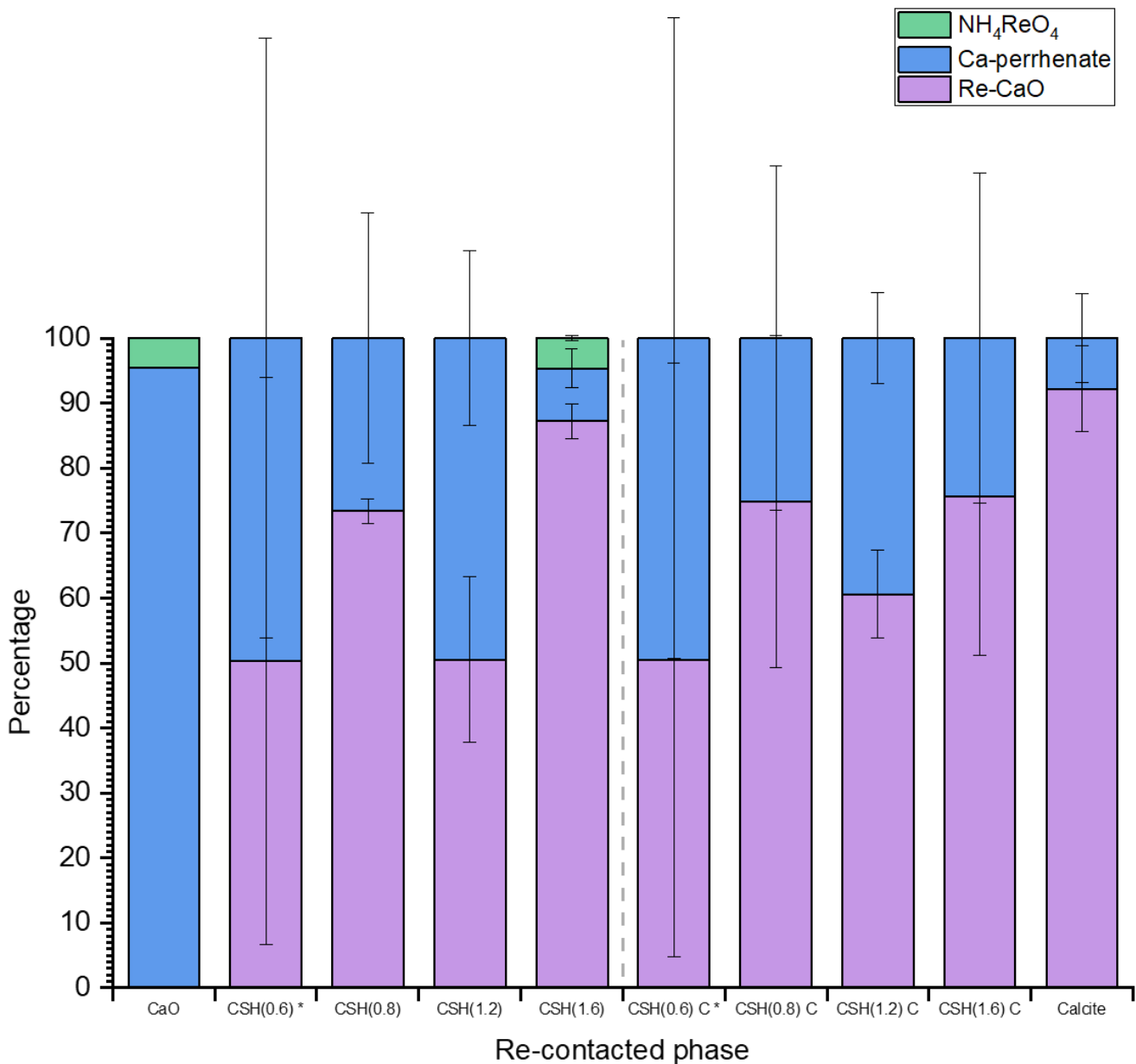


Figure 7.18: Linear combination fitting of Re-contacted C-S-H and related phases.

Table 7.20: Weighted LCF results for Re-CSH series.

Sample	R-factor	Total weighting	NH ₄ ReO ₄		Ca-perrhenate		Re-CaO	
			Wt.	ΔE	Wt.	ΔE	Wt.	ΔE
Re-CaO	5 x 10 ⁻⁴	1.047	0.047(0)	-0.5(0)	1.000(0)	-1.4(0)	N/A	N/A
Re-CSH(0.6) *	0.003	1.073	0.000(65)	-	0.533(496)	0.5(8)	0.540(469)	1.8(9)
Re-CSH(0.8)	0.001	1.027	-	-	0.273(198)	-1.3(7)	0.753(190)	0.02(24)
Re-CSH(1.2)	5 x 10 ⁻⁴	1.027	0.000(15)	-	0.508(138)	-1.4(3)	0.519(131)	-0.1(3)
Re-CSH(1.6)	2 x 10 ⁻⁵	0.994	0.046(4)	-0.3(4)	0.081(30)	-1.4(4)	0.867(27)	-0.03(4)
Re-CSH(0.6) C *	0.003	1.078	0.000(77)	-	0.534(532)	0.3(6)	0.544(493)	1.9(6)
Re-CSH(0.8) C	0.002	1.041	-	-	0.262(276)	-1.4(1.0)	0.779(266)	0.02(33)
Re-CSH(1.2) C	2 x 10 ⁻⁴	1.000	-	-	0.394(70)	-1.89(8)	0.606(67)	0.28(6)
Re-CSH(1.6) C	0.002	1.041	-	-	0.254(264)	-1.4(1.0)	0.787(254)	-0.06(33)
Re-Calcite	2 x 10 ⁻⁴	1.015	-	-	0.079(70)	-1.4(0.8)	0.936(67)	0.01(7)

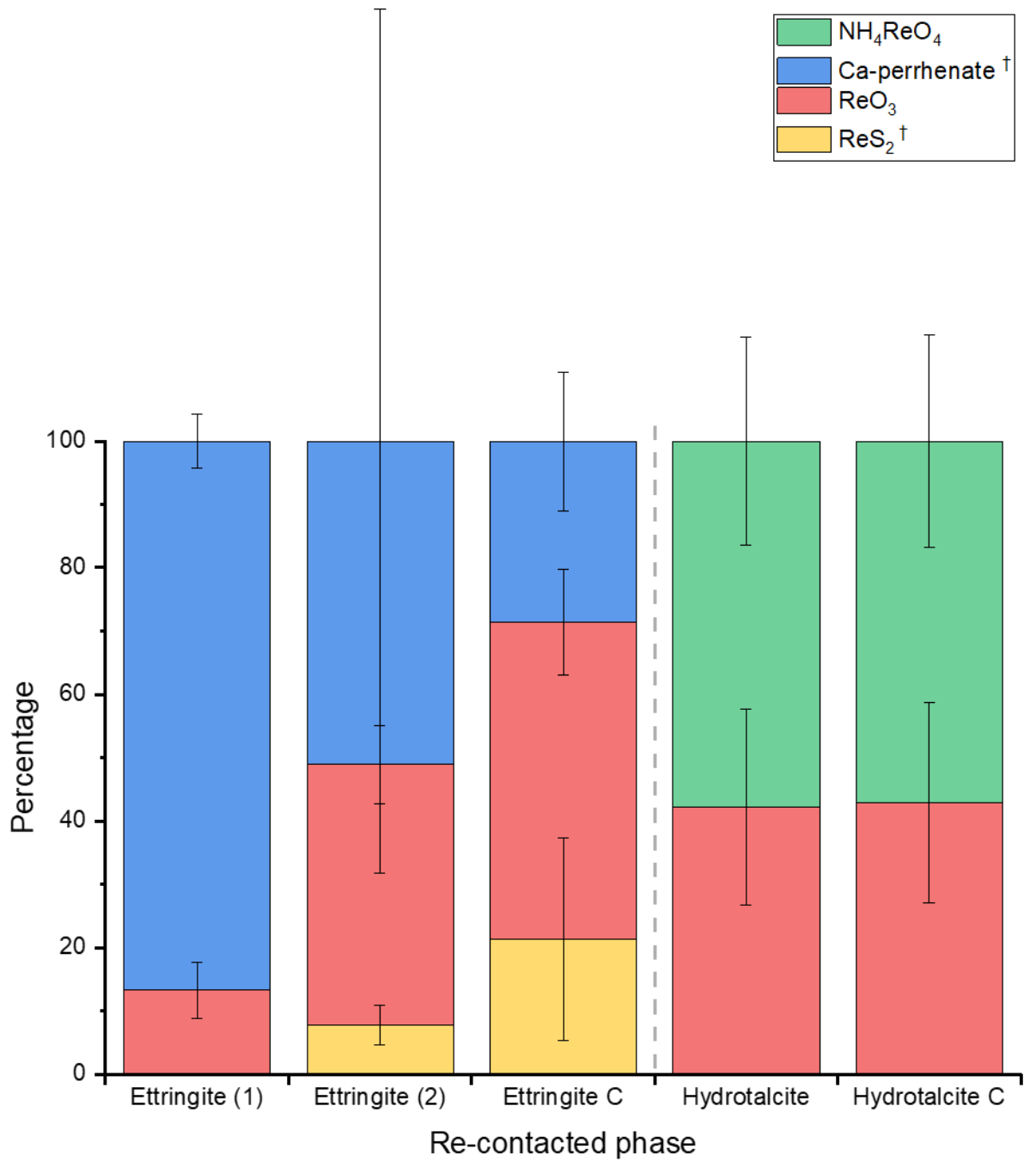


Figure 7.19: Linear combination fitting of Re-contacted ettringite and hydrotalcite phases. † not included in the fit for hydrotalcite.

Table 7.21: Weighted LCF results for Re-ettringite series.

Sample	R-factor	Total weighting	NH ₄ ReO ₄		Ca-perrhenate		ReO ₃		ReS ₂	
			Wt.	ΔE	Wt.	ΔE			Wt.	ΔE
Re-Ettringite (1)	0.003	1.107	0.000(62)	-	0.960(48)	0.4(2)	0.157(49)	0.2(1.2)	-	-
Re-Ettringite (2)	8 x 10 ⁻⁴	1.055	-	-	0.539(72)	0.7(1)	0.434(65)	0.09(46)	0.082(33)	2.1(3.2)
Re-Ettringite C	9 x 10 ⁻⁴	1.005	0.000(143)	-	0.288(110)	-0.5(5)	0.503(84)	-0.3(8)	0.214(161)	1.5(2.0)

Table 7.22: Weighted LCF results for Re-hydroxalcite series.

Sample	R-factor	Total weighting	NH ₄ ReO ₄		ReO ₃	
			Wt.	ΔE	Wt.	ΔE
Re-Hydroxalcite	0.06	1.264	0.730(208)	1.3(8)	0.533(196)	0.9(1.1)
Re-Hydroxalcite C	0.06	1.255	0.717(210)	1.4(8)	0.538(198)	0.9(1.1)

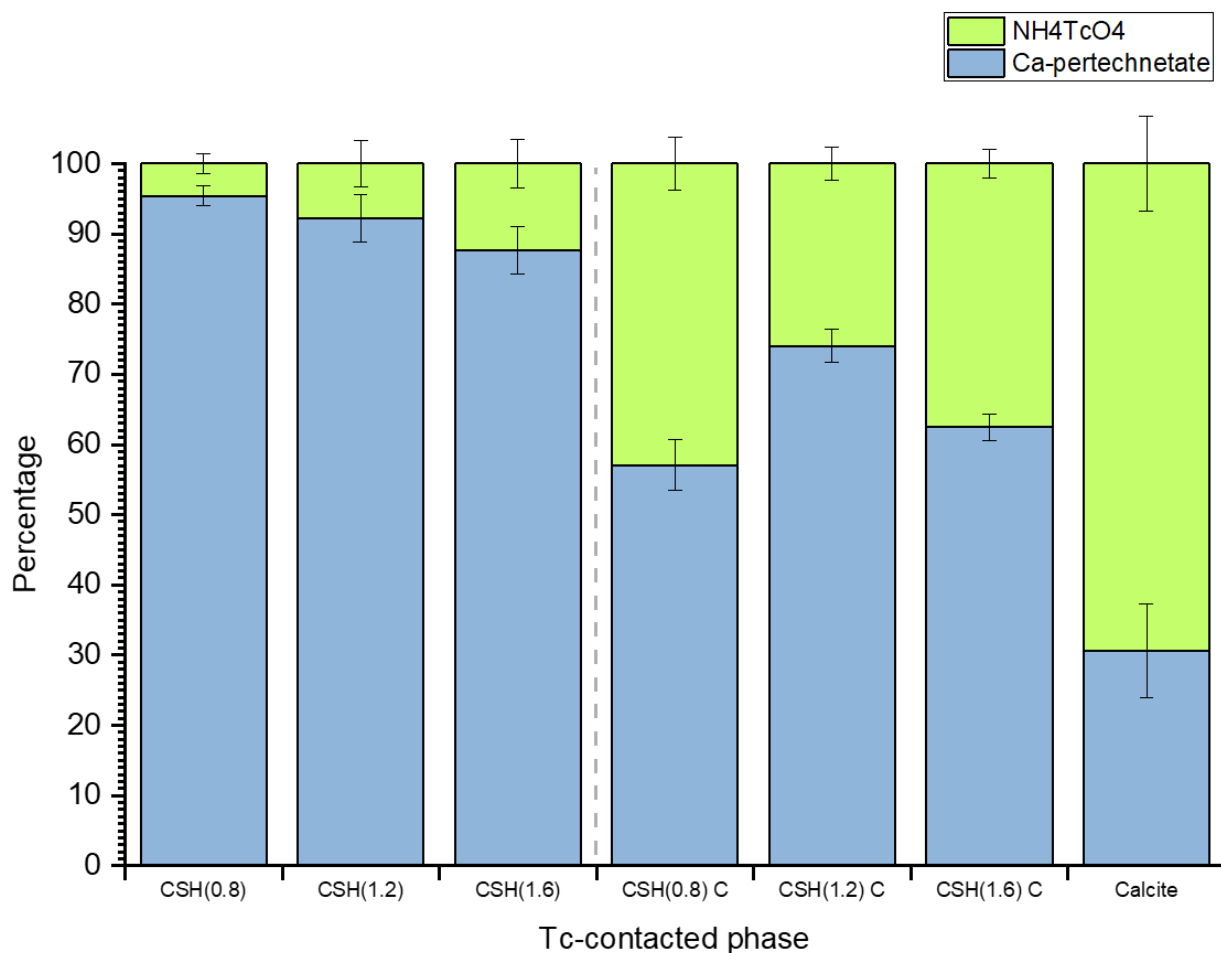


Figure 7.20: Linear combination fitting of Tc-contacted C-S-H and related phases.

Table 7.23: Weighted LCF results for Tc-CSH series

Sample	R-factor	Total weighting	NH ₄ TcO ₄		Ca-pertechnetate	
			Wt.	ΔE	Wt.	ΔE
Tc-CSH(0.8)	2×10^{-4}	1.000	0.046(14)	2.8(7)	0.954(14)	-0.05(4)
Tc-CSH(1.2)	7×10^{-4}	1.005	0.078(34)	4.1(7)	0.927(34)	2.24(9)
Tc-CSH(1.6)	7×10^{-4}	1.002	0.124(34)	4.5(5)	0.878(34)	2.62(9)
Tc-CSH(0.8) C	6×10^{-4}	1.035	0.444(39)	0.07(14)	0.591(38)	3.3(2)
Tc-CSH(1.2) C	2×10^{-4}	1.010	0.262(24)	2.0(2)	0.747(24)	4.3(1)
Tc-CSH(1.6) C	2×10^{-4}	1.010	0.379(20)	-1.08(9)	0.631(19)	3.4(1)
Tc-Calcite	0.003	1.008	0.699(68)	1.8(2)	0.309(67)	0.5(5)

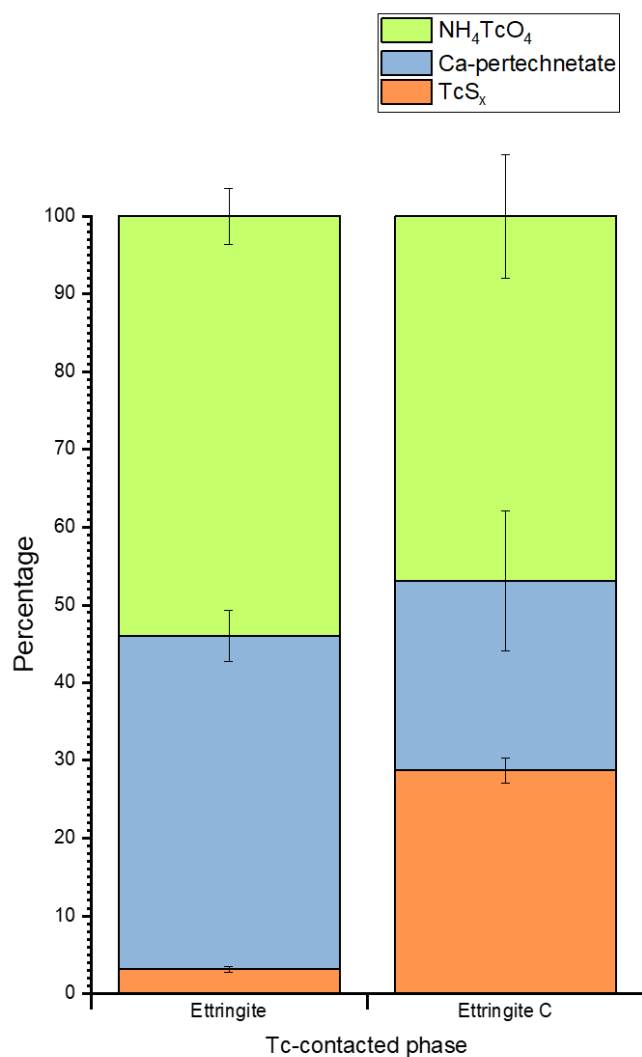


Figure 7.21: Linear combination fitting of Tc-contacted ettringite phases.

Table 7.24: Weighted LCF results for Tc-ettringite series

Sample	R-factor	Total weighting	NH ₄ TcO ₄		Ca-pertechnetate		TcS _x	
			Wt.	ΔE	Wt.	ΔE	Wt.	ΔE
Tc-Ettringite	2 x 10 ⁻⁴	1.059	0.572(38)	-1.8(67)	0.455(35)	1.6(2)	0.033(4)	-9.8(8)
Tc-Ettringite C	0.001	1.065	0.499(85)	-0.5(2)	0.260(96)	-1.6(7)	0.306(17)	7.0(3)

7.4.1.2 Re-contacted phases

Re-CaO: ~95 % of the XANES signal from this phase was attributed to Ca-perrhenate, with ~5 % from NH₄ReO₄. This could indicate that rhenium displayed local coordination to calcium, preferentially over ammonium (NH₄⁺), on contact with calcium oxide.

Re-CSH(X): The Re-contacted C-S-H phases (and Re-calcite) displayed signal contributions predominantly from Ca-perrhenate and the Re-CaO phase, regardless of whether they were pre-carbonated. This could also be indicative of a Ca-perrhenate type local coordination on contact with C-S-H phases. The Re-CSH(1.6) phase additionally displayed a small signal from NH_4ReO_4 (~5 %).

It should be noted that fitting of all the Re-CSH(X) phases with only NH_4ReO_4 and Ca-perrhenate (i.e. in the absence of the Re-CaO 'standard') resulted in Ca-perrhenate being attributed to 100 % of the XANES signal.

Re-ettringite: The first measurement of Re-ettringite resulted in a XANES fit of ~85 % Ca-perrhenate and ~15 % ReO_3 . The second measurement resulted in a fit of ~50 % Ca-perrhenate, ~45 % ReO_3 and ~5 % ReS_2 . In the presence of 1 % CO_2 , the contribution from ReS_2 further increased to ~20 % and Ca-perrhenate contribution decreased to ~25 %. This suggests that rhenium initially shows a local coordination environment similar to Ca-perrhenate, but that the environment evolves with mixed sulfur and oxygen character as a result of carbonation effects and / or time spent in the X-ray beam. This is discussed further in *Section 7.5.1.3*.

Re-hydrotalcite: Hydrotalcite displayed ~60 % signal from NH_4ReO_4 and ~40 % signal from ReO_3 , regardless of the presence of 1 % CO_2 . This could suggest that the rhenium coordination environment did not change significantly as a result of contact with hydrotalcite. However, the total weightings of the fits were high (> 1.2) with R-factors of 6 %. This indicates that the NH_4ReO_4 and ReO_3 standards were not sufficient to obtain a good fit and that additional Mg- and Al-containing standards would be beneficial.

7.4.1.3 Tc-contacted phases

Tc-CSH(X): The Tc-contacted C-S-H phases showed a XANES Ca-pertechetate signal of ~95-90 % which showed a very small decrease with increasing Ca/Si ratio. The pre-carbonated C-S-H phases had an increased signal from NH_4TcO_4 (~30-45 %) and this was increased further still for Re-calcite (~70 %). This could indicate that carbonation (i.e. calcium carbonate formation) of C-S-H phases decreases the availability of calcium in the system for coordination with technetium in a Ca-pertechetate-type moiety.

Tc-ettringite: Ettringite displayed a XANES signal attributable to ~55 % NH_4TcO_4 , ~40 % Ca-pertechetate and < 5 % TcS_x . The signal from TcS_x was shown to increase to nearly 30 % for the pre-carbonated ettringite phase. Again, this could be a result of carbonation effects that change the coordination environment of technetium to the effect of increased coordination with sulfur, as detailed further below.

7.4.2 EXAFS

Scattering paths for EXAFS fitting were generated from FEFF calculations using appropriately selected CIF files as the input. In the first instance, models for the fitting of X-ray scatterers to the rhenium and technetium standards were devised. The value of the amplitude reduction factor (S_0^2) for the specific absorber measured on each beamline (B18 or BL-27B) was refined in the model for the perrhenate or pertechnetate phases (see **Chapter 4**) and was thereafter set in the model for the fitting of all other samples. The k^3 -weighted spectra, Fourier transform radial plots and EXAFS models for all of the rhenium and technetium standards have already been given in **Chapter 4**.

The k^3 -weighted spectra of the Re- and Tc-contacted phases are given in **Figures 7.22** to **7.27** with corresponding Fourier transform radial plots.

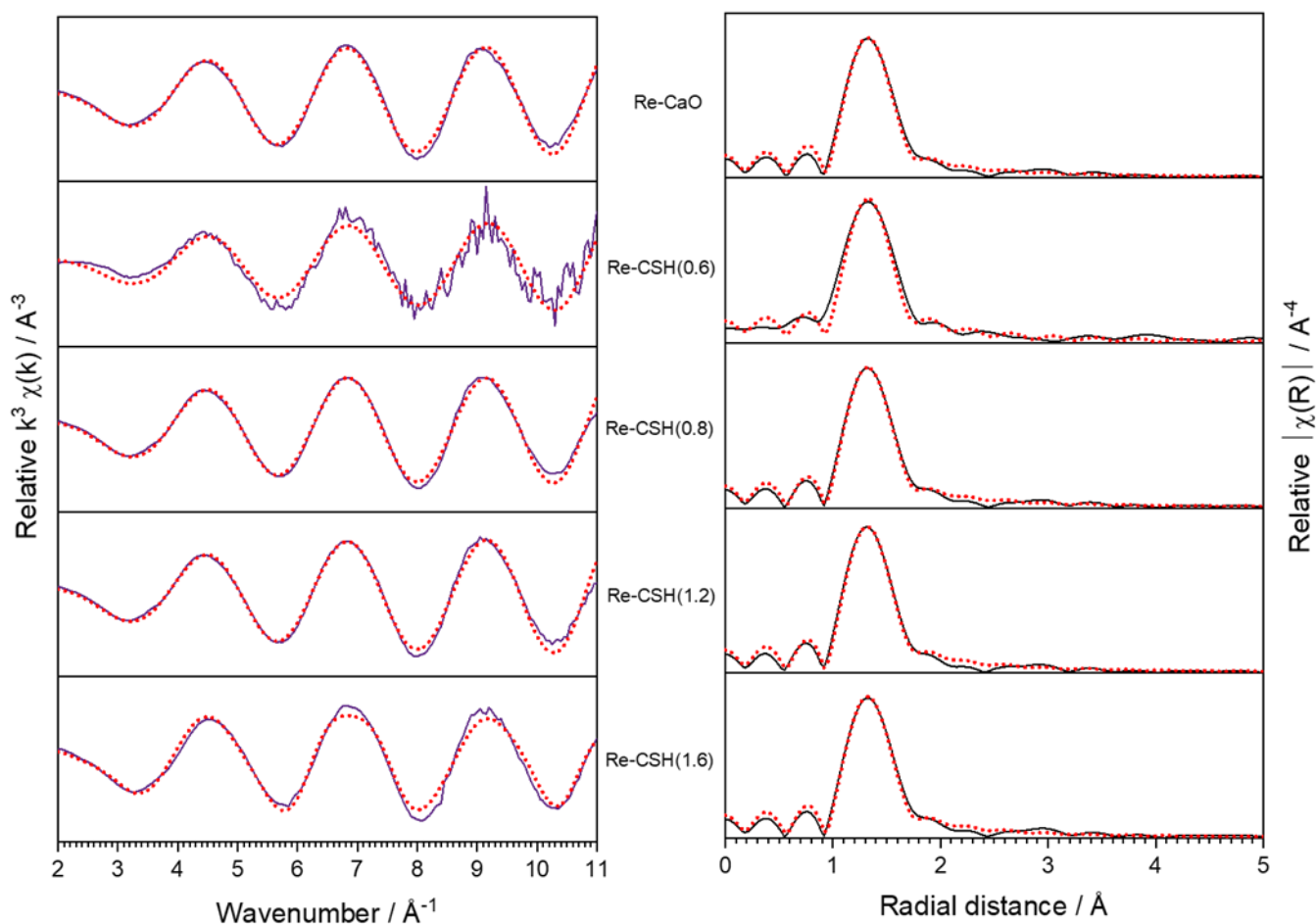


Figure 7.22: k^3 -weighted spectra and Fourier transform radial plots for Re-CSH(X) phases and Re-CaO.

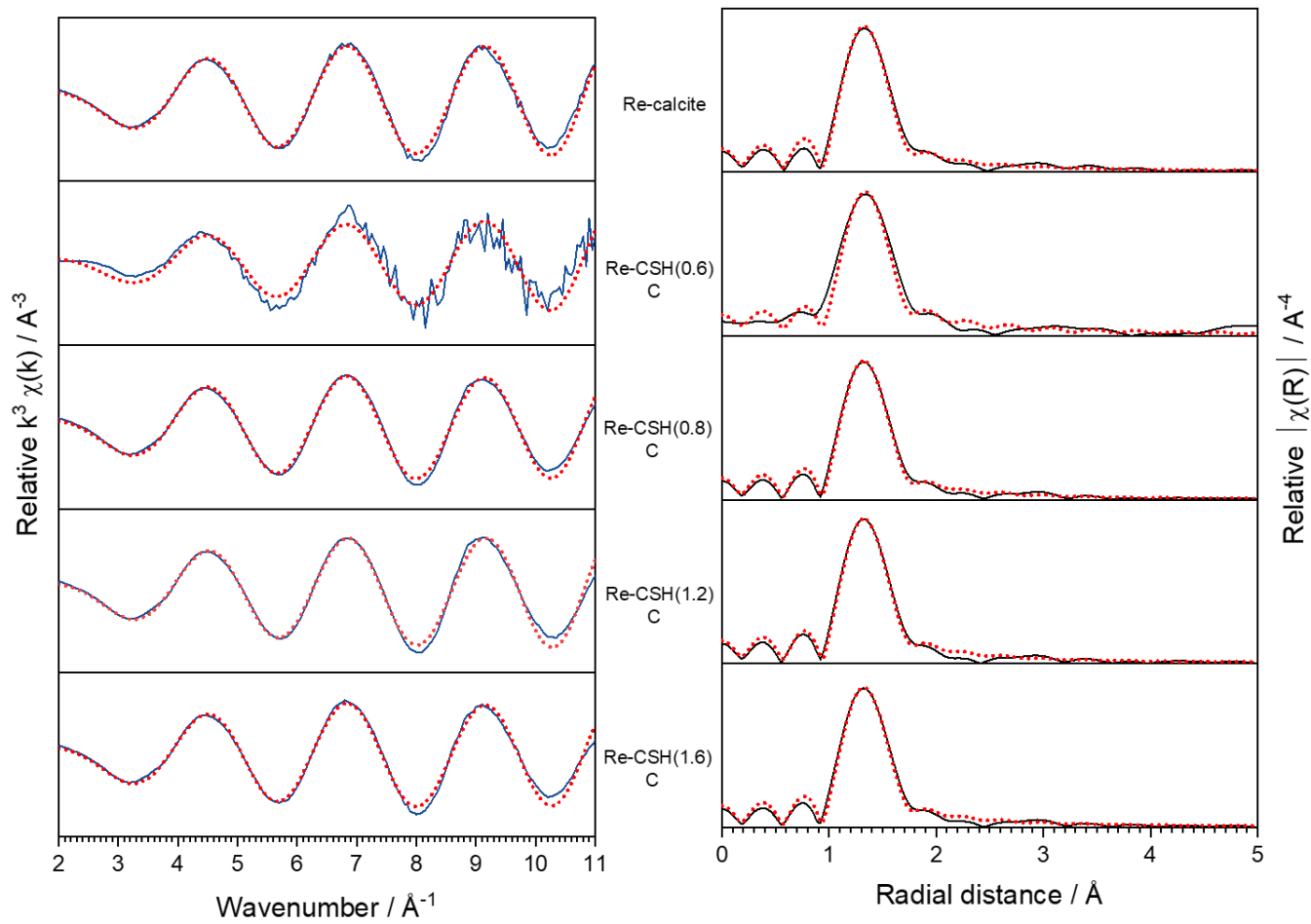


Figure 7.23: k^3 -weighted spectra and Fourier transform radial plots for pre-carbonated Re-CSH(X) phases and Re-calcite.

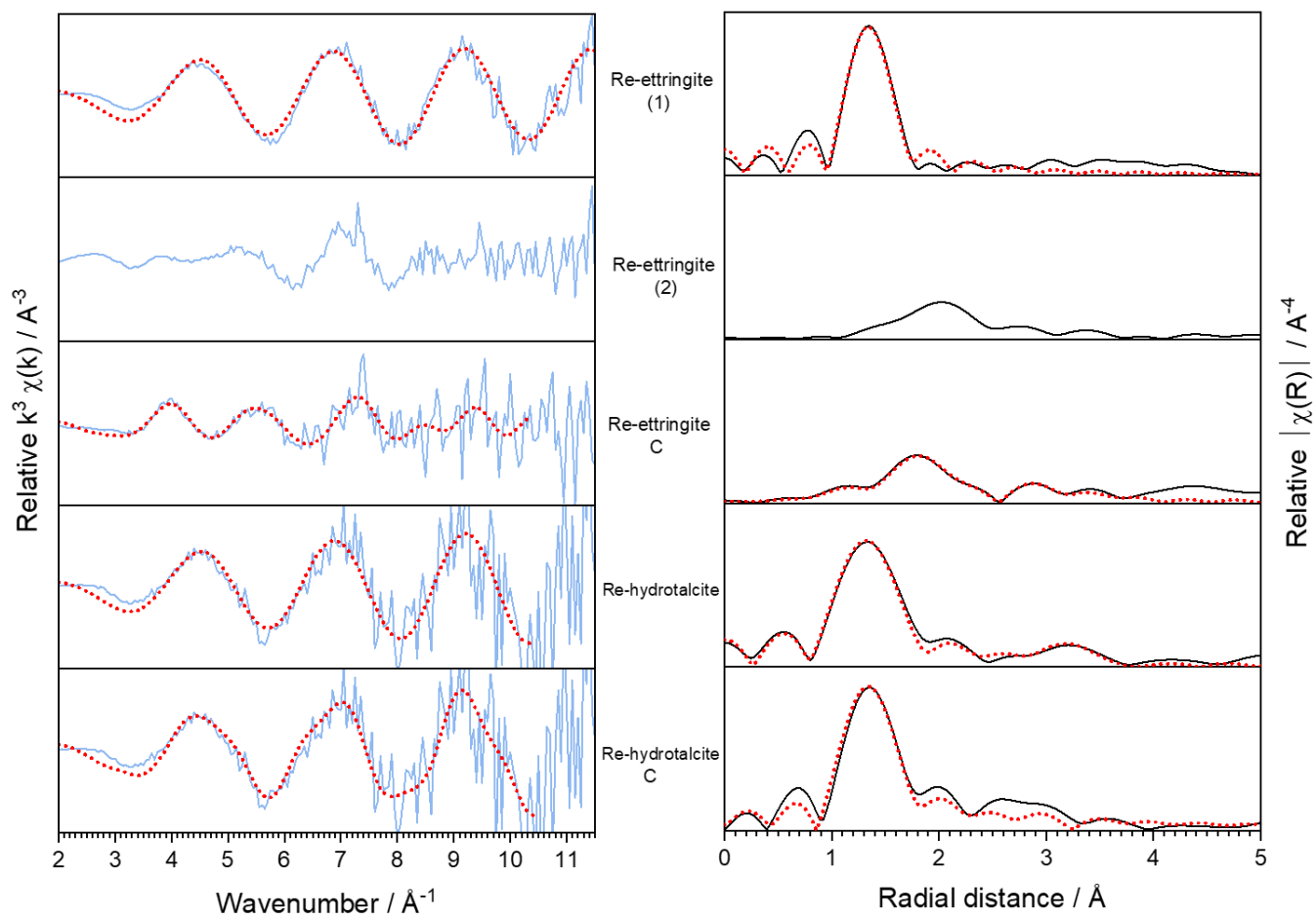


Figure 7.24: k^3 -weighted spectra and Fourier transform radial plots for Re-contacted ettringite and hydrotalcite phases. The (1) and (2) refer to first and second measurements of the Re-ettringite phase. The fits shown for the hydrotalcite phases also include a Mg/Al distance at ~ 3.6 Å.

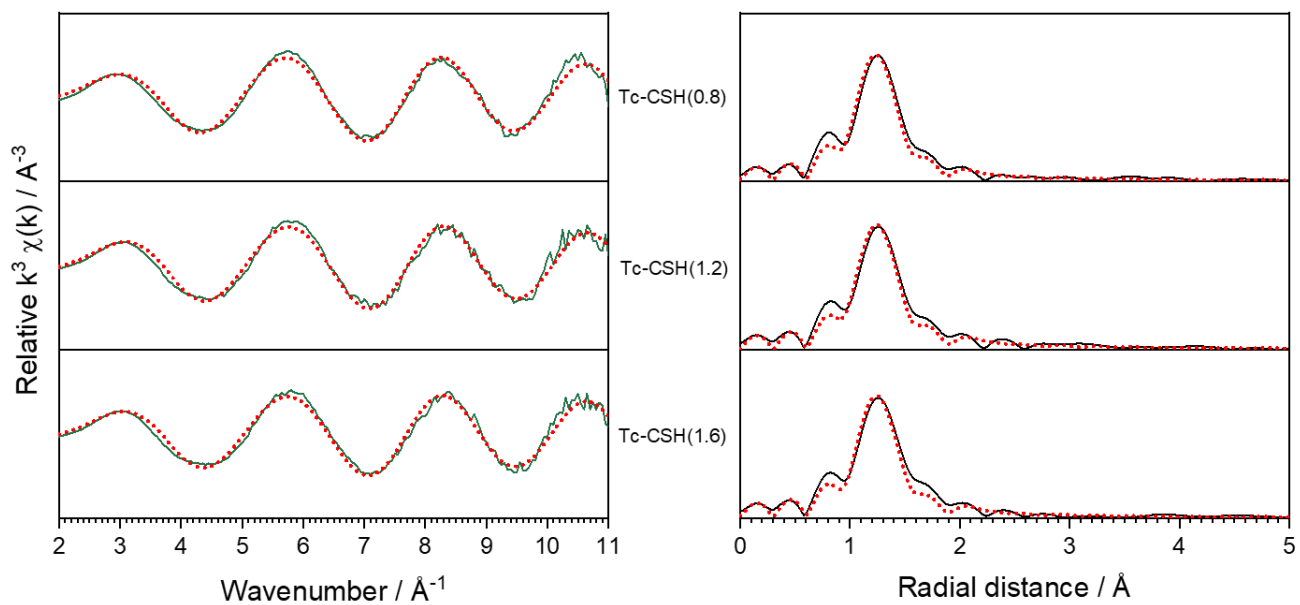


Figure 7.25: k^3 -weighted spectra and Fourier transform radial plots for Tc-CSH(X) phases.

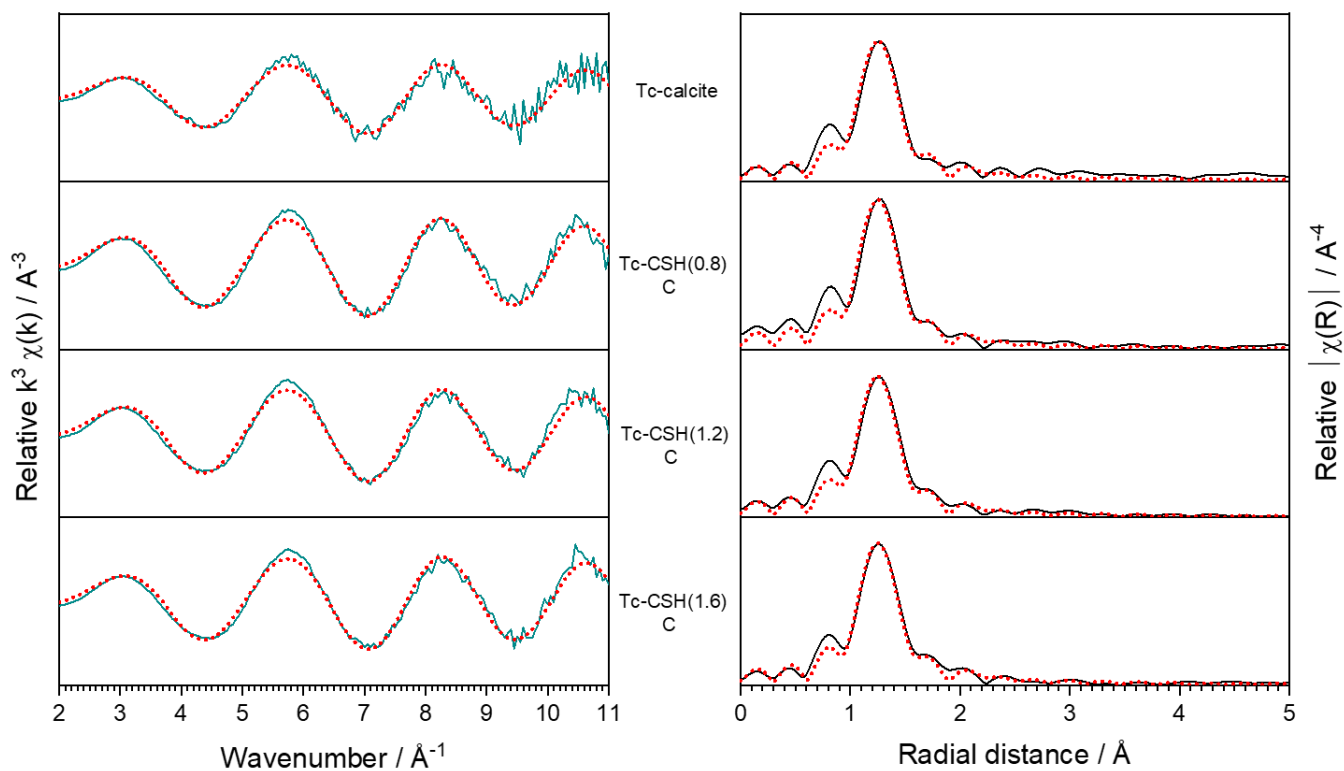


Figure 7.26: k^3 -weighted spectra and Fourier transform radial plots for pre-carbonated Tc-CSH(X) phases.

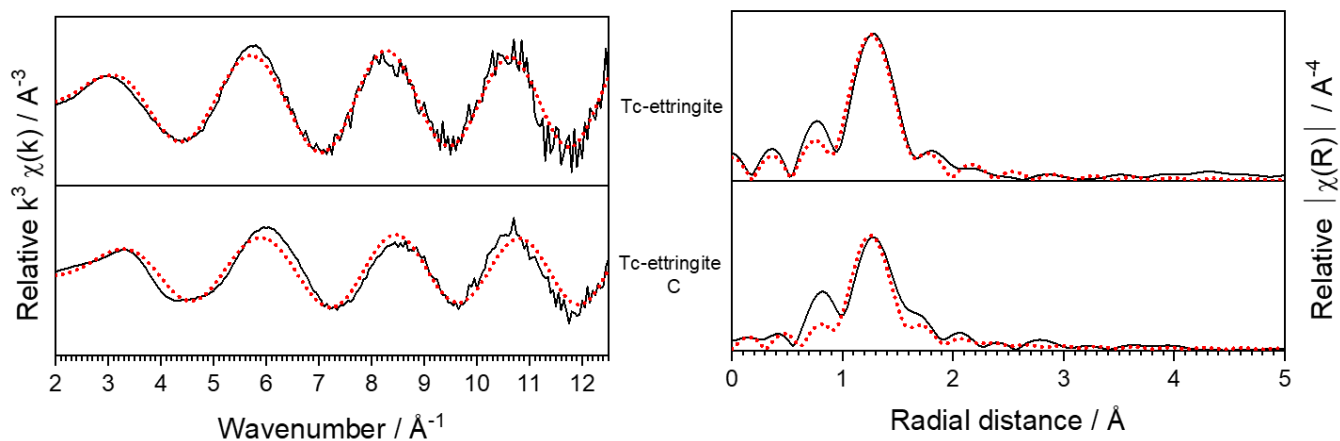


Figure 7.27: k^3 -weighted spectra and Fourier transform radial plots for Tc-ettringite phases.

7.4.2.1 EXAFS fitting of Re-contacted phases

The k -range of the fits were selected where the signal was equal to 0 using a $dk = 0$ Hanning window. Pathways were generated and fitted up to 4 \AA in R -space using a $dR = 1$ Hanning window. ΔE was allowed to vary as a global parameter. The majority of fits yielded σ^2 values for O1 that were negative, but these were close to zero within error.

Re-CSH(X) and Re-CaO: One perrhenate oxygen pathway was fitted in the Re-contacted C-S-H phases, as well as for Re-CaO, all at $\sim 1.73 \text{ \AA}$. For CSH(0.8) to CSH(1.6) there was a slight general decrease in N_{O1} from ~ 4.3 to ~ 4.1 , albeit within error (± 2). The value of N_{O1} for the CSH(0.6) phase was determined to be 3.9 ± 5 , but was measured on a different beamline and so cannot be considered in the same trend. The value of N_{O1} for Re-CaO was also determined to be 4.2 ± 2 . This indicates that rhenium displays a similar oxygen coordination when contacted with C-S-H phases or calcium oxide. The results are given in **Table 7.25**.

Re-CSH(X) C and Re-calcite: One perrhenate oxygen pathway was also fitted for the pre-carbonated C-S-H phases and Re-calcite at $\sim 1.73 \text{ \AA}$. For CSH(0.8) to CSH(1.6) (increasing Ca/Si) there was no particular trend observed for the value of N_{O1} , which was between ~ 4.3 and ~ 4.5 ; slightly higher than for the non-carbonated phases. For CSH(0.6), N_{O1} was determined to be 3.9 ± 0.5 as with the non-carbonated phase. The value of N_{O1} for Re-calcite was also determined to be 4.4 ± 0.2 which again suggests that rhenium displays a similar oxygen coordination when in contact with all the Ca-bearing phases studied here, regardless of the presence of calcium carbonates. The results are given in **Table 7.26**.

Re-ettringite: The Re-ettringite phase (first measurement, denoted "(1)") was fitted with a perrhenate oxygen pathway at distance of $1.721 \pm 0.005 \text{ \AA}$ with $N_{O1} = 5.2 \pm 0.4$, slightly higher

than the expected coordination of a perrhenate ($N = 4$). The results are given in **Table 7.27**. For the Re-ettringite phase prepared under a 1 % CO_2 atmosphere (denoted with “C”), the Fourier transform obtained a radial plot that was notably different by eye from that expected for perrhenate coordination. The best EXAFS fit was achieved with a first mixed oxygen and sulfur shell. The oxygen distance was refined at $1.66 \pm 0.02 \text{ \AA}$ with N_{O_1} fixed at 2 and the sulfur distance was refined at 2.27 ± 0.002 with N_{S_1} fixed at 6 (Re-S pathway taken from the CIF file for ReS_2 [226]). The results are given in **Table 7.28**. This was an indication of a loss of perrhenate type coordination and increase in a coordination environment of rhenium bonded to sulfur. There was also a decrease in the value of E_0 from 10539 eV for Re-ettringite to 10537 eV for the Re-ettringite C phase, towards the value of 10535 eV for ReS_2 measured on the same beamline (at KEK) (see **Chapter 4**). Additional rhenium and sulfur scatterers taken from the ReS_2 CIF file could also be fitted in the model, and improved the fit, but must be treated with caution taking into consideration the background noise of the Re-ettringite C spectrum. In addition to this, the second measurement of the Re-ettringite phase (“(2)”) resembled a combination of both Re-ettringite (1) and Re-ettringite C by eye in the Fourier transform, however a reasonable EXAFS fit could not be achieved.

Re-hydrotalcite: Both Re-contacted hydrotalcite phases were fitted with a perrhenate oxygen distance of $1.72 \pm 0.01 \text{ \AA}$. The value of N_{O_1} was refined at ~ 4.6 , within error, for both the phases prepared under N_2 or under 1 % CO_2 , which is not unexpected given that hydrotalcite is a stable carbonate phase. The results are given in **Table 7.27**. It should be noted that the addition of a magnesium or aluminium pathway at $\sim 3.6 \text{ \AA}$ also improved the R-factor of the fits to 0.02, however these pathways must be treated tentatively within the noise of the data.

7.4.2.2 EXAFS fitting of Tc-contacted phases

The k-range of the fits were selected where the signal was equal to 0 using a $dk = 0$ Hanning window. Pathways were generated and fitted up to 4 \AA in R-space using a $dR = 1$ Hanning window. ΔE was allowed to vary as a global parameter.

Tc-CSH(X): One pertechnetate oxygen pathway was fitted for the Tc-contacted C-S-H phases at $\sim 1.72 \text{ \AA}$. Technetium therefore appeared to show a similar oxygen coordination environment to pertechnetate on contact with C-S-H. There was a trend of slight decreasing N_{O_1} value with increasing Ca/Si ratio from 4.5 ± 0.3 for CSH(0.8) to 4.1 ± 0.3 for CSH(1.6), within error, which tentatively coincides with an increase in the NH_4TcO_4 signal for the XANES LCF of these phases. The results are given in **Table 7.29**.

Tc-CSH(X) C and Tc-calcite: One pertechnetate oxygen pathway was also fitted for the Tc-contacted pre-carbonated C-S-H phases and Tc-calcite at $\sim 1.72 \text{ \AA}$, within error. The N_{O_1} values obtained were higher than for the non-carbonated phases, closer to ~ 5 (than ~ 4.3) but there was no particular trend observed with increasing Ca/Si ratio. The value of N_{O_1} for Tc-

calcite was also 4.9 ± 0.3 which could indicate that calcium carbonates have a small influence on the local oxygen coordination of technetium on contact with C-S-H phases. The results are given in **Table 7.30**.

Tc-ettringite: Both Tc-contacted ettringite phases were fitted with a pertechnetate oxygen distance. In the Tc-ettringite phase, the distance was refined at 1.711 ± 0.007 Å with $N_{O1} = 4.9 \pm 0.05$. For the pre-carbonated Tc-ettringite phase, the pertechnetate oxygen distance and N_{O1} value were decreased to 1.700 ± 0.008 Å and 3.2 ± 0.3 , respectively. This could be an indication of loss of pertechnetate-type coordination as a result of carbonation effects on the ettringite phase. No additional scattering paths improved the fits. The results are given in **Table 7.31**.

Table 7.25: EXAFS fits of Re-CSH(X) phases performed between k-range ~ 2.5 - ~ 11 Å⁻¹ and R-range 1 - 4 Å.

Sample	R-factor	ΔE	R_{Tc-O1}	N_{O1}	σ^2_{O1}
Re-CSH(0.6) * $S_0^2 = 0.68$	0.04	8(2)	1.725(10)	3.93(47)	-0.002(1)
Re-CSH(0.8) $S_0^2 = 0.7$	0.006	8.6(6)	1.730(3)	4.31(17)	-0.0008(4)
Re-CSH(1.2) $S_0^2 = 0.7$	0.007	7.8(6)	1.728(3)	4.27(18)	-0.0012(4)
Re-CSH(1.6) $S_0^2 = 0.7$	0.007	8.6(6)	1.730(3)	4.11(17)	-0.0012(4)
Re-CaO $S_0^2 = 0.7$	0.007	8.6(6)	1.732(3)	4.19(18)	-0.0011(4)

Table 7.26: EXAFS fits of Re-CSH(X) C phases performed between k-range ~ 2.5 - $\sim 11 \text{ \AA}^{-1}$ and R-range 1 - 4 \AA .

Sample	R-factor	ΔE	R_{Tc-O1}	N_{O1}	σ^2_{O1}
Re-CSH(0.6) C * $S_0^2 = 0.68$	0.05	9(2)	1.732(12)	3.92(49)	-0.002(1)
Re-CSH(0.8) C $S_0^2 = 0.7$	0.005	8.9(5)	1.732(3)	4.46(17)	-0.0005(4)
Re-CSH(1.2) C $S_0^2 = 0.7$	0.007	9.3(6)	1.729(3)	4.32(18)	-0.0011(4)
Re-CSH(1.6) C $S_0^2 = 0.7$	0.006	9.1(6)	1.731(3)	4.53(19)	-0.0004(4)
Re-calcite $S_0^2 = 0.7$	0.007	9.4(5)	1.733(3)	4.44(18)	-0.0009(4)

* measured at KEK rather than DLS.

Table 7.27: EXAFS fits of Re-hydroxalcite and Re-ettringite phases performed between k-range ~ 3.8 - $\sim 10 \text{ \AA}^{-1}$ for hydroxalcite and up to 12 \AA^{-1} for ettringite between R-range 1 - 4 \AA .

Sample	R-factor	ΔE	R_{Tc-O1}	N_{O1}	σ^2_{O1}
Re-hydroxalcite † $S_0^2 = 0.68$	0.03	9(2)	1.721(10)	4.76(82)	-0.002(2)
Re-hydroxalcite C † $S_0^2 = 0.68$	0.04	8(2)	1.719(10)	4.59(66)	-0.002(1)
Re-ettringite (1) $S_0^2 = 0.68$	0.02	9(1)	1.721(5)	5.20(41)	-0.0004(7)

† the addition of a Mg or Al pathway at $\sim 3.6 \text{ \AA}$ improved the R-factor of the fits to ~ 0.02 but this was treated with caution due to the large noise associated with the data.

Table 7.28: EXAFS fit of Re-ettringite C performed between k-range 3 - 10 Å⁻¹ and R-range 1 - 4 Å.

Sample	R-factor	ΔE	R _{Tc-O1}	N _{O1}	σ ² _{O1}	R _{Tc-S}	N _S	σ ² _S	R _{Tc-Re}	N _{Re}	σ ² _{Re}
Re-ettringite C S ₀ ² = 0.68	0.04	2(2)	1.656(24)	2	0.007(4)	2.27(2)	6	0.013(2)	2.72(4)	2	0.006(3)
						3.65(8)	4		3.42(4)	4	

Table 7.29: EXAFS fits of Tc-CSH(X) phases performed between k-range ~2.2 - ~12.2 Å⁻¹ for and R-range 1 - 4 Å.

Sample	R-factor	ΔE	R _{Tc-O1}	N _{O1}	σ ² _{O1}
Tc-CSH(0.8) S ₀ ² = 0.8	0.02	0.7(1.0)	1.722(6)	4.54(30)	0.0018(8)
Tc-CSH(1.2) S ₀ ² = 0.8	0.02	2(1)	1.718(6)	4.30(29)	0.0016(7)
Tc-CSH(1.6) S ₀ ² = 0.8	0.03	2(1)	1.718(7)	4.14(32)	0.0015(8)

Table 7.30: EXAFS fits of Tc-CSH(X) C phases performed between k-range ~2.2 - ~12.2 Å⁻¹ for and R-range 1 - 4 Å.

Sample	R-factor	ΔE	R _{Tc-O1}	N _{O1}	σ ² _{O1}
Tc-CSH(0.8) C S ₀ ² = 0.8	0.02	3(1)	1.726(5)	5.13(29)	0.0016(6)
Tc-CSH(1.2) C S ₀ ² = 0.8	0.02	2(1)	1.722(5)	4.87(27)	0.0016(6)
Tc-CSH(1.6) C S ₀ ² = 0.8	0.01	2.4(9)	1.720(4)	4.62(23)	0.0012(5)
Tc-calcite S ₀ ² = 0.8	0.02	3(1)	1.725(6)	4.87(31)	0.0016(7)

Table 7.31: EXAFS fits of Tc-ettringite phases performed between k-range 2.6 - 12.3 Å⁻¹ and R-range 1 - 4 Å.

Sample	R-factor	ΔE	$R_{\text{Tc-O1}}$	N_{O1}	σ^2_{O1}
Tc-ettringite $S_0^2 = 0.8$	0.03	1(1)	1.713(6)	4.70(30)	0.0006(6)
Tc-ettringite C $S_0^2 = 0.8$	0.06	0.5(1.9)	1.700(8)	3.15(34)	0.0006(9)

7.5 Discussion

Since the surface charge of the cement mineral phase may have an influence on the observed uptake behaviour of rhenium and technetium, the relative zeta potentials of the ettringite, hydrotalcite, portlandite, calcite and gypsum phases are given in **Figure 7.28** (the addition of small volumes of NH_4ReO_4 or NHTcO_4 did not alter the final pH of the cement phase suspensions). Gypsum and hydrotalcite demonstrated negative surface zeta potentials, while ettringite, portlandite and calcite each displayed a positive surface zeta potential. Calcium sulfate impurities present in the ettringite phase were not significant enough to reduce the zeta potential to a negative value [236].

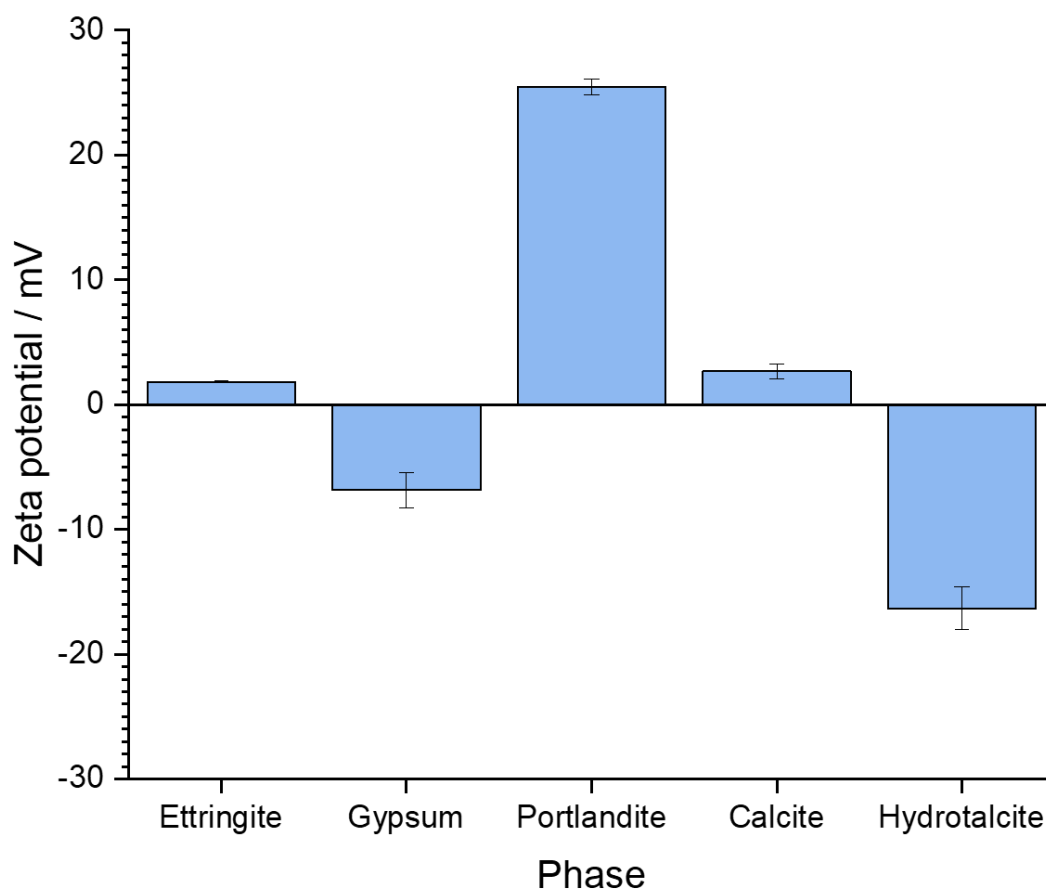


Figure 7.28: Zeta potentials of selected cement phases in UHQ.

Further to this, the zeta potentials of the C-S-H phase are given in **Figure 7.29**, as also shown in **Chapter 4**, as a function of Ca/Si ratio of the solid phase in contact with UHQ or C-S-H equilibrated solution. The C-S-H surfaces equilibrated in UHQ all display a negative zeta potential regardless of Ca/Si ratio, however in C-S-H equilibrated solutions the zeta potentials all display a decrease in negativity. This is consistent with the effect of increased Ca^{2+} in

solution in C-S-H equilibrated solutions, which sorbs Si-O⁻ sites on the C-S-H surface, creating an electrical double layer to the effect of increasing the positivity of the zeta potential [130,232,312]. *Viallis-Terrise et al.* determined that the potential of zero charge for C-S-H, in relation to Ca²⁺ ions in solution, was achieved at [Ca²⁺] = 80 ppm [130]. In this study, the potential of zero charge was achieved between Ca/Si = 1.2 and Ca/Si = 1.4 and therefore somewhere close to a Ca²⁺ concentration of ~120 ppm.

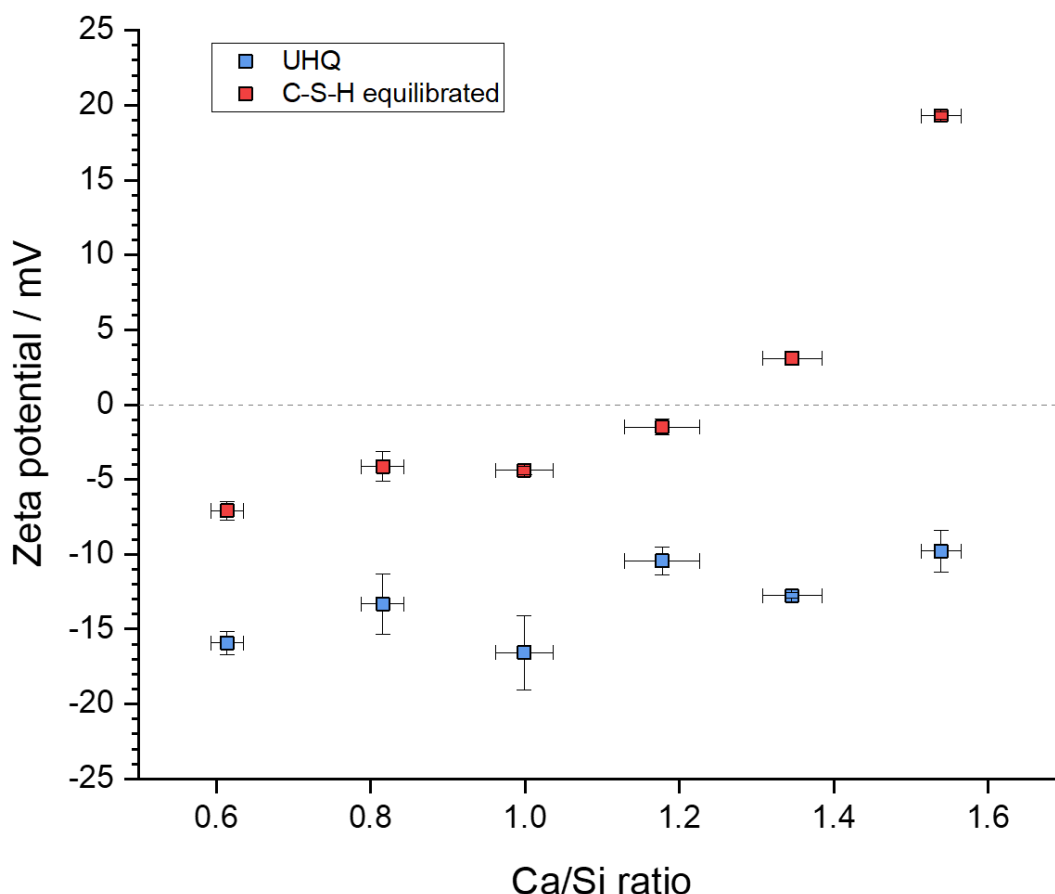


Figure 7.29: Zeta potential measurements of C-S-H phases in UHQ (blue) and C-S-H equilibrated solutions (red).

7.5.1 Rhenium uptake and coordination in cement phases

7.5.1.1 C-S-H, portlandite and calcite

The evidence for formation of a Ca-perrhenate phase was observed in the sorption experiments in the XRD pattern for portlandite (~800 ppm [Ca²⁺]), and potentially calcite (~200 ppm [Ca²⁺]), by the emergence of a small diffraction peak at ~20.9 °2θ. This peak corresponds to the highest intensity peak of the Ca-perrhenate (Ca_{x/2}(ReO₄)_x·zH₂O) phase synthesised and

used as a standard for X-ray absorption measurements (see **Chapter 4**) and the highest intensity peak expected for the $\text{Ca}(\text{ReO}_4)_2 \cdot 2\text{H}_2\text{O}$ phase reported by *Picard et al.* [222]. The formation of this phase could be attributed to the available Ca^{2+} present in the aqueous Re-Portlandite and Re-calcite systems able to favourably complex the perrhenate anion (ReO_4^-) and precipitate as a solid phase during the drying process. The results from EXAFS fitting of Re-contacted calcium oxide and calcite also indicated that a perrhenate-type coordination was maintained in these phases, with the Re-CaO phase also showing a XANES signal similar to that for the Ca-perrhenate ($\text{Ca}_{x/2}(\text{ReO}_4)_x \cdot z\text{H}_2\text{O}$) phase.

In the case of ReO_4^- sorption to single phase portlandite and calcite, both phases displayed a ~20 % decrease in the rhenium concentration in solution which coincides with a positive zeta potential for both phases and therefore suggests an affinity for negatively charged ReO_4^- via physi-sorption. However, as addressed previously the error associated with measuring rhenium concentrations for these phases by ICP-OES and ICP-MS means that these results must be treated with some uncertainty.

A decrease in the rhenium concentration in the C-S-H equilibrated solutions was observed in the sorption experiment, indicating a transition of aqueous rhenium into a solid or sorbed phase. The amount of Ca^{2+} present in solution was lower in the Re / C-S-H suspensions compared with that of Re-Portlandite, ranging from ~47 ppm for $\text{Ca}/\text{Si} = 0.6$ to ~590 ppm for $\text{Ca}/\text{Si} = 1.6$ (and ~800 ppm for Portlandite). As a Ca-perrhenate phase was not identified in the XRD patterns for Re-contacted C-S-H phases, this could indicate two possible scenarios: 1) there was not a high enough concentration of Ca^{2+} present to form sufficient quantities of Ca-perrhenate to precipitate out during the drying process to be detectable by XRD; and / or 2) the electrical double layer of Ca^{2+} ions on the C-S-H surface facilitated the uptake the negatively charged perrhenate ions via physi-sorption [232]. This is also consistent with retention of a perrhenate-type coordination, as indicated by EXAFS fitting of the Re-contacted C-S-H phases, which may be further coordinated by calcium, indicated by XANES linear combination fitting.

7.5.1.2 Ettringite and calcium sulfate

Ettringite and gypsum both showed an extent of rhenium uptake, at ~21-28 % and ~10 %, respectively. For ettringite, this is in good agreement with a positive zeta potential and an affinity of the surface for negatively charged ReO_4^- . However, the zeta potential of gypsum was measured to be negative and, although rhenium uptake was observed to be lower than for than ettringite, the negative zeta potential would suggest that ReO_4^- by physi-sorption is unfavourable. However, the results for the percentage uptake have large errors and must again be treated with uncertainty.

The retention of a perrhenate-type coordination for rhenium contacted with ettringite was indicated by the fitting of a perrhenate oxygen pathway in the EXAFS spectrum of the Re-contacted ettringite phase. This in itself could be suggestive of two scenarios: 1) there was no association of rhenium with ettringite and the ReO_4^- moiety was maintained in solution or as an ammonium, a calcium, aluminium or magnesium perrhenate surface precipitate [222–224,306]; and / or 2) ReO_4^- was taken up into the ettringite structure via anion exchange with SO_4^{2-} .

The results for the XANES linear combination fitting of this phase suggest that a Ca-perrhenate type coordination could be possible, with fitting of ~85 % of the signal to the $\text{Ca}_{x/2}(\text{ReO}_4)_x \cdot z\text{H}_2\text{O}$ phase in conjunction with a high release of calcium into solution in the sorption experiment (~780 ppm). However, considering that rhenium uptake was also observed in the sorption experiments (albeit with large errors), the latter situation is plausible. The ionic radius of the perrhenate anion is 2.60 Å [305], compared to 2.42 Å for SO_4^{2-} [161], suggesting that a 1:1 exchange could be possible. This however, would lead to a negative charge balance deficiency in the ettringite structure.

A collaborative study with the current author, led by *Saslow et al.* at the Pacific Northwest National Laboratory (see **Appendix 2**), has investigated the incorporation of TcO_4^- into ettringite via SO_4^{2-} substitution in the channel structure of ettringite [159]. In this case, the charge balance deficiency was rationalised by the simultaneous incorporation of an OH^- anion with TcO_4^- , in place of ($\text{SO}_4^{2-} + \text{H}_2\text{O}$). Given the similarity in ionic radius of TcO_4^- (2.52 Å [160]) with ReO_4^- , it is plausible that this anion-exchange mechanism could also occur for $\text{ReO}_4^- / \text{SO}_4^{2-}$ anion-exchange.

7.5.1.3 Ettringite and Re-sulfate formation

The presence of a 1% CO_2 atmosphere appeared to significantly change the coordination environment of rhenium in contact with ettringite. The presence of elevated CO_2 levels would suggest destabilisation of ettringite with respect to monocarboaluminate (AFm- CO_3) formation, due to increased dissolved CO_2 in solution [157,256]. This in turn would cause an increased release of SO_4^{2-} anions into solution which could complex rhenium, potentially in a $\text{Re}-[(\text{SO}_4)_3(\text{OH})]$ -type coordination.

Alternatively, increased dissolved CO_2 content would also increase the presence of HCO_3^- anions in solution which could act as a reducing agent. The decrease in E_0 by 2 eV (relative to Re-ettringite prepared under N_2) could therefore be an indication of the reduction of rhenium +7 to rhenium +6, with a coordination more akin to rhenium sulfate ($\text{Re}(\text{SO}_4)_3$ -type). However, with lack of a rhenium sulfate standard, this is speculative.

7.5.1.4 Hydrotalcite

Hydrotalcite displayed a rhenium uptake of ~20 % (with a large error of ± 13). The negative surface potential of the hydrotalcite phase measured here is generally not considered favourable for ReO_4^- uptake via physi-sorption, however, a previous study by *Tanaka et al.* has eluded to the uptake of ReO_4^- by outer-sphere complexation on hydrotalcite surfaces [313]. The K_d values of rhenium were shown to decrease between pH ~11 to ~12 in aqueous, salt-free solution which is consistent with an increase in negativity of the hydrotalcite zeta potential with increasing pH [84].

The tentative fitting of a magnesium or aluminium scattering pathway in the EXAFS fits could also suggest the formation of magnesium or aluminium perrhenate precipitates, however further investigation with relevant standards is required here to conclude the formation of such phases.

7.5.2 Technetium uptake and coordination with cement phases

7.5.2.1 C-S-H, portlandite and calcite

The formation of a Ca-pertechnetate hydrate phase was also potentially evidenced by a small peak in the XRD pattern for the portlandite phase in technetium sorption experiments at $\sim 20.9^\circ 2\theta$, consistent with the highest intensity peak of the synthesised $\text{Ca}_{x/2}(\text{TcO}_4)_x \cdot z\text{H}_2\text{O}$ phase used as a standard for X-ray absorption measurements (see **Chapter 4**).

The C-S-H phases displayed increased uptake of technetium with increasing Ca/Si which is explained by the increased concentration of Ca^{2+} in solution, to the effect of electrical double layer formation, and thus increased positivity of the zeta potential. This is also consistent with the retention of a pertechnetate-type coordination, as indicated by EXAFS fitting of the Tc-contacted C-S-H phases, which may be further coordinated by calcium, indicated by XANES linear combination fitting. The anomalously low result for the C-S-H phase with a Ca/Si ratio of 1.6 could be a result of calcium carbonate formation during the synthesis process of C-S-H. As discussed in **Chapter 4**, the C-S-H phase with Ca/Si ratio of 1.6 was particularly prone to carbonation during synthesis due to its high calcium content, despite efforts to minimise CO_2 ingress. The presence of unavoidable calcium carbonates present in this C-S-H phase prior to sorption experiments could result in a slight decrease of the local surface charge, given that calcite has a more negative zeta potential than portlandite (**Figure 7.28**) and therefore a decrease in rhenium uptake. This is also consistent with the Tc-contacted pre-carbonated C-S-H and calcite phases displaying a decreased XANES signal from the Ca-pertechnetate phase (<75 %), relative to the Tc-contacted non-carbonated C-S-H phases (>95 %). Nevertheless, this anomalous result requires further investigation.

Technetium uptake by the portlandite and calcite single solid phases was not evidenced by a detected decrease in technetium concentration by liquid scintillation counting at the concentration range and timescale studied.

7.5.2.2 Ettringite and calcium sulfate

Technetium uptake by ettringite and gypsum (consistent with negative zeta potential for the latter) was not evidenced by a detected decrease in technetium concentration by liquid scintillation counting at the concentration range and timescale studied. Although TcO_4^- incorporation by ettringite was observed by *Saslow, Yorkshire et al.*, that study differed in that a co-precipitation method was used to partition technetium into ettringite phases, rather than sorption onto pre-formed ettringite phases used in this study.

The fitting of a pertechnetate oxygen distance in the EXAFS region of the Tc-contacted ettringite phase was apparent with $N_{\text{O}1} = \sim 4.7$ ($\sim 1.71 \text{ \AA}$), and for the pre-carbonated ettringite phase, the value of $N_{\text{O}1}$ was reduced to ~ 3.2 as well as a decreased distance of $\sim 1.70 \text{ \AA}$. There was also a dampening of the pre-edge feature observed in the XANES spectrum of the latter sample. The $N_{\text{O}1}$ and bond distance decreases are synonymous to those observed for the change in perrhenate coordination for the Re-contacted ettringite phase prepared under a 1 % CO_2 atmosphere ($\sim 1.7 \text{ \AA}$ with $N_{\text{O}1}$). A mixed oxygen-sulfur shell was not obtained for the Tc-contacted sample (as was seen for rhenium) however this probably arises from the different preparation methods of the two samples (see **Section 7.2.4**). In **Chapter 4**, the synthesised ettringite phases were shown not to display any change in the XRD pattern as a result of exposure to a 1 % CO_2 atmosphere for 48 hours, to the effect of AFm- CO_3 formation (or otherwise). However, it still appears that there is some carbonation effect on the ettringite phase that is reducing the pertechnetate-type coordination of technetium in contact with the phase.

7.5.2.3 Hydrotalcite

Technetium uptake by hydrotalcite was not evidenced by a detected decrease in technetium concentration by liquid scintillation counting at the concentration range and timescale studied, however this is consistent with the measured negative zeta potential of the hydrotalcite phase.

7.6 Conclusions and Further Work

7.6.1 Rhenium as a technetium surrogate

Re(VII) and Tc(VII) appear to show similar behaviour in aqueous solution in the presence of Ca^{2+} by displaying uptake by C-S-H, portlandite and calcite via formation of Ca-[Re,Tc] physiosorbed species and potentially the formation of Ca-perrhenate/pertechnetate precipitates.

The behaviour of rhenium in the presence of ettringite (under a 1 % CO₂ atmosphere) and technetium in the presence of pre-carbonated ettringite is difficult to directly compare, given the different preparation conditions. However, the effect of carbonation shows some importance for the differing coordination environments of rhenium or technetium associated with ettringite phases.

The spectroscopic features of the different X-ray absorption edges studied cannot, however, be directly compared. The Tc K-edge displays a pre-edge feature, unlike the Re L_{III}-edge, and has distinctive post-edge features that may be used for fingerprinting of the different coordination environments of pertechnetates [227]. This has resulted in a further collaboration with the Pacific Northwest National Laboratory whereby pre- and post-edge fitting techniques are being trialled to infer structural differences in the synthesised Ca-pertechnetate phase, at different stages of hydration, and in comparison with other pertechnetate phases, as a result of varying energy contributions from different electronic orbitals.

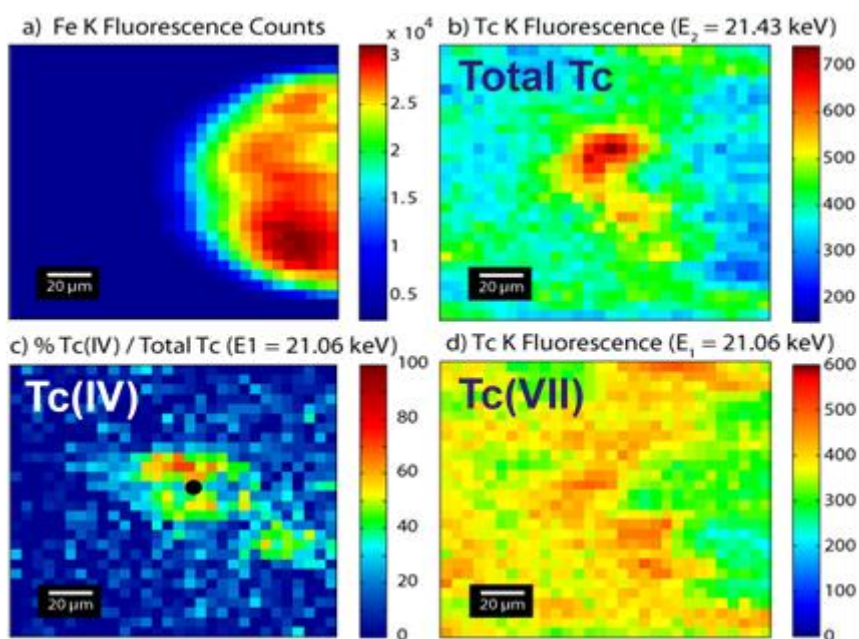


Figure 7.30: XRF map of blast-furnace slag-containing cement whereby pertechnetate has been reduced to Tc(IV) by association with a slag particle (particle position indicated by iron map). Image courtesy of Dr. C. Corkhill.

The importance of sulfide-bearing phases has already been previously demonstrated as an important consideration for pertechnetate sequestration in cements, via reductive precipitation [152]. In reference to this, **Figure 7.30** shows the association of reduced technetium species with blast-furnace slag particles (inherently sulfide-containing) in a cement matrix (image courtesy of Dr. C. Corkhill). As this figure shows, much of the work regarding Tc-S

sequestration in cements has therefore been focused on electrochemical means. The potential for sulfate species to sorb technetium by physical or chemical means however, in a non-redox role, has been indicated in this work by the removal of the rhenium (as a chemical surrogate) in solution, by ettringite phases. In conjunction with the study by *Saslow et al.*, this could indicate the importance for competition between pertechnetate and sulfate ions for incorporation into ettringite phases [159], which may render them a useful cement former for immobilisation purposes. Further exploration is required here.

7.6.2 Implications for waste disposal

For the consideration of waste disposal in a cementitious repository, the behaviour of Tc(VII) in the presence of C-S-H phases is of particular importance. Given the high abundance of portlandite and C-S-H in Portland cements (~50 %) [11], the ability of these phases to partially retain technetium as a Ca²⁺-facilitated sorbed phase is beneficial to understanding how technetium mobility may be temporarily retarded in cementitious systems. The previous studies discussed in **Chapter 2**, which describe only partial or very low retention of technetium in non-reducing cements [146,155,156], may not have considered the role of pertechnetate counter ions. In the study by *Corkhill et al.*, the “lag time” displayed by technetium elution through an NRVB column was attributed to the high internal porosity of the cement; given that NRVB is a particularly high calcium-content cement, counter ion sorption processes could also be an assisting factor in this case.

As technetium sorption has been observed in this work for C-S-H equilibrated, high Ca²⁺ containing solutions, the age of the repository could therefore have an impact on the efficacy of the cement to delay technetium transport. Higher Ca/Si ratios will be observed for fresh cement at an early stage in the repository. On initial contact of groundwater with cement, the dissolution of alkali earth elements will occur, such as sodium and potassium. After this time, high calcium concentrations will prevail in cement pore solutions which may promote the physi-sorption of pertechnetate. Considering this, early sodium and potassium concentrations may also have the potential to physi-sorb pertechnetate, to the same effect, given that soluble alkali earth pertechnetate species have also been reported [227]. Over the timescale of tens of thousands of years, calcium (and alkali earth elements) will be leached and transported away from the cement into the groundwater, leading to the predominance of negatively charged Si-O⁻ sites which will result in the release of Tc(VII) as the mobile pertechnetate species.

7.6.3 Further work

To further build a case study for the efficacy of rhenium as a technetium surrogate, the following experiments should also be performed:

- Sorption and desorption experiments with Re(VII) and Tc(VII) onto pre-carbonated C-S-H phases.

- Extensive sorption studies of Re(VII) and Tc(VII) onto ettringite phases under the same 1 % CO₂ atmosphere.
- XAFS measurements of portlandite / perrhenate (or pertechnetate) suspension solutions to confirm the presence of a Ca-perrhenate (or -pertechnetate) complex.

Chapter 8 – Concluding remarks

The objectives of this Thesis, as outlined in **Chapter 1**, were to:

- 1) Understand how the actinides U(VI) and Pu(VI) behave in cementitious environments, in terms of their speciation, and how their behaviour differs from one another.
- 2) Understand the sorption and uptake behaviour of Re(VII) and Tc(VII) in cementitious environments and evaluate the usefulness of rhenium as a surrogate for ^{99}Tc .

In **Chapter 5** the speciation of aqueous U(VI) contacted with C-S-H phases, ettringite ($\text{Ca}_6\text{Al}_2(\text{SO}_4)_3(\text{OH})_{12}\cdot 26\text{H}_2\text{O}$) and hydrotalcite ($\text{Mg}_6\text{Al}_2(\text{CO}_3)(\text{OH})_{16}\cdot 4\text{H}_2\text{O}$) was evaluated using X-ray diffraction (XRD), X-ray absorption / fluorescence spectroscopy (XAFS) and solid-state nuclear magnetic resonance (SS-NMR) spectroscopy.

Firstly, the coordination environment of U(VI) on C-S-H was shown to predominantly adopt a mixed uranyl-silicate-type and calcium uranate-type coordination, apparent from X-ray absorption near edge spectroscopy (XANES) linear combination fitting and extended X-ray absorption fine structure (EXAFS) results. This is in line with reported U(VI) coordination in the literature [67–70]. However, this was the first instance, to the best of the author's knowledge, of the use of haiweeite ($\text{Ca}(\text{UO}_2)_2(\text{Si}_5\text{O}_{12})(\text{OH})_2\cdot 6\text{H}_2\text{O}$) and weeksite ($\text{K}_2(\text{UO}_2)_2(\text{Si}_5\text{O}_{12})(\text{OH})_4\cdot 4\text{H}_2\text{O}$) natural mineral analogues to determine the local, and to some extent, extended coordination of uranyl silicate phases formed in C-S-H phases.

XRD revealed that a $\text{Ca}_2(\text{UO}_2)_2\text{Si}_6\text{O}_{15}\cdot x\text{H}_2\text{O}$ -type phase at relatively high loadings of U(VI) (~95 000 ppm) can form at low Ca/Si ratios of C-S-H (Ca/Si = 0.6) which is related to the weeksite mineral group [249]. The formation of this phase is important to consider for high silica-content cements or an aged cementitious repository whereby the Ca/Si ratio will be lower, especially as its crystallinity was observed to increase overtime as a result of Ostwald ripening effects.

Further to this, this is the first reported use of SS-NMR to probe the coordination of silicon (^{29}Si) and aluminium (^{27}Al) in cement phases in contact with U(VI). In the case of C-S-H, the silicon environment (at low Ca/Si) was shown to shift from predominantly Q^1 and Q^2 species for single phase C-S-H, to a silicon environment with mixed C-S-H and uranyl-silicate character, after contact with U(VI). The latter was evidenced by the emergence of additional Q^3 and Q^4 species coupled with an increase in Ca/Si of the whole system.

In the ^{27}Al NMR spectra of ettringite phases, a decrease and re-emergence in the peak assigned to a low yield AFm-SO₄ ($\text{Ca}_4(\text{Al}_2\text{O}_6)(\text{SO}_4)12\text{H}_2\text{O}$) impurity was observed on addition of low (~5 000 ppm) and high (~95 000 ppm) loadings of U(VI), respectively. This was tentatively attributed to the formation of an AFm-U(VI) phase that was only formed or detected

at higher U(VI) loadings, highlighting the importance of further investigation into AFm phases for U(VI) retention in cement matrices.

Hydrotalcite did not display a change in the ^{27}Al NMR on addition of U(VI). This suggests that U(VI) uptake was not observed to occur via anion-exchange in the interlayer, which is not surprising given the stability of the hydrotalcite- CO_3 phase. Rather, the formation of a magnesium uranyl carbonate-type moiety was evidenced by EXAFS fitting, likely as a surface sorbed outer-sphere complex [276].

Chapter 6 was an attempt to understand the speciation of aqueous Pu(VI) on C-S-H phases, relative to that observed for U(VI). Although the concentrations of plutonium used were similar to those for uranium used in **Chapter 5**, the acidic solutions required to maintain plutonium as aqueous Pu(VI) resulted in significant dissolution of the C-S-H phases. Regardless, Pu(VI) displayed radiolytically-induced reduction to Pu(IV), accelerated by heating at 200 °C at 100 % RH, precipitating as a nano-crystalline hydrous PuO_2 -type phase. Without further analysis, e.g. by XAFS, it was not possible to ascertain whether plutonium was chemically or physically sorbed to the surface of C-S-H, however, it was considered highly unlikely that plutonium was incorporated into the C-S-H structure. In conjunction with the results from the collaborative study between TUoS and NNL on Magnox PuO_2 immobilised in Portland cement blends, the findings from this Thesis indicate the chemical stability of PuO_2 in cement matrices / in contact with cement hydrate phases.

The use of acidic plutonium nitrate solutions (and to some extent use of uranyl nitrate solutions in **Chapter 5**) and high temperatures are undoubtedly detrimental for the retention of the ideal structure of cement phases. However, low pH values generated from corrosion of steel and heat generation from adjacently placed ILW and / or HLW waste canisters in a cementitious repository are important issues to consider upon closure of a geological disposal facility. This study has therefore highlighted the prevalence of plutonium to reside as Pu(IV) oxide under pseudo-related conditions.

In **Chapter 7**, the sorption and speciation of Tc(VII), and Re(VII) as a surrogate, in contact with C-S-H, ettringite, hydrotalcite and other minor cement phases was investigated using XRD and XAFS.

The role of calcium was considered to be vital for the uptake and coordination of technetium (and rhenium) by C-S-H phases. In C-S-H equilibrated waters, C-S-H phases displayed an increase in the positivity of their surface zeta potential as a result of Ca^{2+} sorption onto SiO^- sites, forming an electrical double layer. This double layer acted to facilitate the uptake of the negatively charged pertechnetate (and perrhenate) anions from solution.

Further to this, XANES linear combination fitting of the Tc K-edge spectra for technetium on C-S-H phases eluded to a Ca-pertechnetate type coordination environment due to a strong

signal contribution attributed to a $\text{Ca}_{x/2}(\text{TcO}_4)_x \cdot z\text{H}_2\text{O}$ phase. This phase has not before been reported in the literature, thus never before considered as a potential technetium species in cement phases. This was also analogous to the observed coordination of rhenium on C-S-H phases as the corresponding $\text{Ca}_{x/2}(\text{ReO}_4)_x \cdot z\text{H}_2\text{O}$ phase, which indicates that rhenium is an effective surrogate for technetium in simplified cementitious systems.

These findings indicate that uptake of pertechnetate by the bulk of a cement matrix requires an abundance of calcium. The age of a cementitious repository is important to consider for the retention of pertechnetate in cementitious wasteforms; after the dissolution of alkali elements from the cement (e.g. Na, K), which occurs soon after initial contact of groundwater with cement, high calcium concentrations will be prevalent in pore solutions after some estimated several tens of thousands of years. Until this time, therefore, this high content of calcium in the cement will promote sorption of technetium as a physi-sorbed Ca-pertechnetate species. Over time, as groundwater ingresses and calcium is dissolved from the cement into groundwater, negatively charged Si-O⁻ sites are expected to dominate the surface chemistry of the cement, resulting in a release of aqueous pertechnetate species.

Ettringite phases could, however, be considered for medium-term retention of pertechnetate species. The study by *Saslow, Yorkshire et. al* (see **Appendix 2**) has demonstrated that technetium is capable of co-precipitating with ettringite phases, taking the place of sulfate anions within the ettringite structure [159]. In this Thesis, the importance of carbonation of the ettringite phase, and by default, formation of AFm-CO₃ phases, has been shown to affect the local coordination of rhenium, with respect to a decrease in perrhenate type-coordination and an increase in what is assumed to be rhenium-sulfate type coordination. However, further investigation into the formation of such phases, including with technetium rather than rhenium, is required here.

Finally, this Thesis has demonstrated that U(VI) and Pu(VI) do not display synonymous behaviour in cementitious environments, reiterating the complex chemistry of aqueous plutonium. However, Re(VII) can be considered as an effect surrogate for Tc(VII) in aqueous, calcium bearing solutions relevant to the early stages of a cementitious repository.

Appendix 1

The following is the title page of peer-reviewed journal publication by *Kearney, Yorkshire et al.*
Article at: <https://doi.org/10.1016/j.jnucmat.2019.151960>

Journal of Nuclear Materials 530 (2020) 151960



Contents lists available at ScienceDirect

Journal of Nuclear Materials

journal homepage: www.elsevier.com/locate/jnucmat



Effects of plutonium dioxide encapsulation on the physico-chemical development of Portland cement blended grouts



Sarah A. Kearney ^a, Bliss McLuckie ^b, Kevin Webb ^b, Robin Orr ^b, Ian A. Vatter ^b,
Antonia S. Yorkshire ^a, Claire L. Corkhill ^a, Martin Hayes ^b, Michael J. Angus ^b,
John L. Provis ^{a,*}

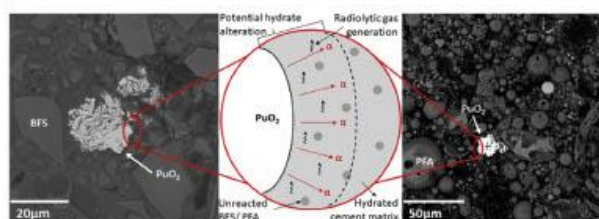
^a NucleUS Immobilisation Science Laboratory, Department of Materials Science and Engineering, University of Sheffield, Sheffield, S1 3JD, United Kingdom

^b National Nuclear Laboratory, Sellafield, Seascale, Cumbria, CA20 1PG, United Kingdom

HIGHLIGHTS

- PuO₂ was encapsulated in BFS/PFA blended cements used for nuclear waste disposal.
- Cellulose was added to the systems to investigate the effects of organics.
- No large scale microstructural defects were observed and good physical contact between the PuO₂ and grout was seen.
- Changes to the phase assemblage were noted in BFS containing grouts.
- Radiolytic gas evolution was consistent with expectations, with increased values observed for samples containing cellulose.

GRAPHICAL ABSTRACT



ARTICLE INFO

Article history:

Received 10 July 2019
Received in revised form
19 November 2019
Accepted 15 December 2019
Available online 17 December 2019

Keywords:

Cement encapsulation
Plutonium
Radiolysis
Microstructural and phase assemblage changes

ABSTRACT

The effects of alpha radiation on cementitious systems used for nuclear waste encapsulation, and the subsequent physico-chemical properties, have been subject to limited investigation comparative to the effects of gamma and neutron irradiations. This paper outlines an assessment of the impact of PuO₂ incorporation on the bulk characteristics of BFS and PFA blended Portland cements, with specific focus on the microstructure, phase assemblage and the radiolysis of pore water. Cellulose was also added to the cements to investigate the effects of organics on these systems. Characterisation of the bulk phase assemblage and microstructure were completed using optical and scanning electron microscopy (SEM), x-ray diffraction (XRD), and thermogravimetric analysis (TGA). Gas evolution was measured to determine the radiolytic breakdown of pore solution. In all samples the PuO₂ appeared well encapsulated, with good physical contact to the cement grout and no large scale defects observed. Pu-containing hydrates were not observed, but PuO₂ containing BFS based systems showed variations in the ratio of sulfate-containing phases, with increased ettringite observed. Gas evolution results were consistent with expectations based on likely radiation deposition, and increased G(H₂) values were observed for cellulose containing samples. The findings of this study suggest the investigated cements are suitable encapsulants matrices for wastes containing PuO₂.

© 2019 Elsevier B.V. All rights reserved.

* Corresponding author.
E-mail address: j.provis@sheffield.ac.uk (J.L. Provis).

Appendix 2

The following is the abstract of “Just Accepted” peer-reviewed journal publication by *Saslow, Yorkshire et al.*

Article at: <https://doi.org/10.1021/acs.est.0c03119>

Immobilizing Pertechnetate in Ettringite via Sulfate Substitution

Technetium-99 immobilization in low-temperature nuclear waste forms often relies on additives that reduce environmentally mobile pertechnetate (TcO_4^-) to insoluble Tc(IV) species. However, this is a short-lived solution unless reducing conditions are maintained over the hazardous life cycle of radioactive wastes (some ~10,000 years). Considering recent experimental observations, this work explores how rapid formation of ettringite [$\text{Ca}_6\text{Al}_2(\text{SO}_4)_3(\text{OH})_{12}\cdot 26(\text{H}_2\text{O})$], a common mineral formed in cementitious waste forms, may be used to directly immobilize TcO_4^- . Results from ab initio molecular dynamics (AIMD) simulations and solid-phase characterization techniques, including synchrotron X-ray absorption, fluorescence, and diffraction methods, support successful incorporation of TcO_4^- into the ettringite crystal structure via sulfate substitution when synthesized by aqueous precipitation methods. One sulfate and one water are replaced with one TcO_4^- and one OH^- during substitution, where Ca^{2+} -coordinated water near the substitution site is deprotonated to form OH^- for charge compensation upon TcO_4^- substitution. Furthermore, AIMD calculations support favorable TcO_4^- substitution at the SO_4^{2-} site in ettringite rather than gypsum ($\text{CaSO}_4\cdot 2\text{H}_2\text{O}$, formed as a secondary mineral phase) by at least 0.76 eV at 298 K. These results are the first of their kind to suggest that ettringite may contribute to TcO_4^- immobilization and the overall lifetime performance of cementitious waste forms.

References

- [1] DECC, Nuclear Power in the UK, HC 511, 2017.
- [2] C.L. Corkhill, N.C. Hyatt, Nuclear Waste Management, IOP Publishing Ltd., 2018.
- [3] NDA, 2019 UK Radioactive Waste Inventory, 2019.
- [4] NDA, 2019 UK Radioactive Waste Detailed Data, 2019.
- [5] B. Batchelor, Overview of waste stabilization with cement, *Waste Manage.* 26 (2006) 689–698.
- [6] P. Bamforth, G. Baston, F. Glasser, T. Heath, Cement materials for use as backfill, sealing and structural materials in geological disposal concepts. A review of current status, SERCO/005125/001 Issue 3, 2012.
- [7] M. Atkins, F.P. Glasser, Application of portland cement-based materials to radioactive waste immobilization, *Waste Manage.* 12 (1992) 105–131.
- [8] P.C. Basu, P. Labbe, D.J. Naus, Nuclear Power Plant Concrete Structures, SMiRT-22 Trans. VI (2013).
- [9] DECC, Implementing Geological Disposal, 14D/235, 2014.
- [10] K. Scrivener, R. Snellings, B. Lothenbach, A Practical Guide to Microstructural Analysis of Cementitious Materials, Taylor & Francis, CRC Press, 2016.
- [11] H.F.W. Taylor, Cement chemistry, 2nd ed., Thomas Telford, London, 1997.
- [12] B. Lothenbach, K. Scrivener, R.D. Hooton, Supplementary cementitious materials, *Cem. Concr. Res.* 41 (2011) 1244–1256.
- [13] I.G. Richardson, G.W. Groves, Microstructure and microanalysis of hardened cement pastes involving ground granulated blast-furnace slag, *J. Mater. Sci.* 27 (1992) 6204–6212.
- [14] Nirex, Why a cementitious repository?, N/034, 2001.
- [15] RWM, Geological Disposal. The 2013 Derived Inventory, NDA/RWM/120, 2015.
- [16] RWM, Geological Disposal. Waste Package Evolution Status, DSSC/451/01, 2016.
- [17] RWM, Geological Disposal: Guidance on the production of encapsulated wasteforms, WPS/502/01, 2015.
- [18] NDA, Waste stream 2D24 Magnox Cladding and Miscellaneous Solid Waste, 2013.
- [19] M.J. Angus, I.H. Godfrey, M. Hayes, S. Foster, Managing Change in the Supply of Cement Powders for Radioactive Waste Encapsulation - Twenty Years of Operational Experience, WM 2010. (2010).
- [20] NDA, Waste Stream 2D03 Plutonium Contaminated Materials; Drums, 2019.
- [21] NDA, Packaging of Plutonium Contaminated Material at the Waste Treatment Complex (Extension to Final stage and Periodic Review) Summary of Assessment Report, 2013.
- [22] M. Egan, Treatment of Plutonium Contaminated Material at Sellafield. Best Practicable Environmental Option Study, QRS-1372A-1, 2008.
- [23] ANL, Technetium, Human Health Fact Sheet, (2001).
- [24] D. Kim, A.A. Kruger, Volatile species of technetium and rhenium during waste vitrification, *J. No. Cryst. Solids.* 481 (2018) 41–50.
- [25] C.A. Langton, S.B. Oblath, D.W. Pepper, E.L. Wilhite, Waste salt disposal at the savannah river plant, *Chem. Eng. Commun.* 66 (1988) 189–199.
- [26] P.C. Hewlett, M. Liska, Lea's Chemistry of Cement and Concrete, 5th ed., Butterworth-Heinemann, Elsevier, 2019.
- [27] J. Bensted, P. Barnes, Structure and Performance of Cements, 2nd ed., Spon Press, Taylor &

Francis, 2008.

- [28] B. Lothenbach, E. Wieland, A thermodynamic approach to the hydration of sulphate-resisting Portland cement, *Waste Manage.* 26 (2006) 706–719.
- [29] R.J. Myers, S.A. Bernal, R.S. Nicolas, J.L. Provis, Generalized Structural Description of Calcium–Sodium Aluminosilicate Hydrate Gels: The Cross-Linked Substituted Tobermorite Model, *Langmuir.* 29 (2013) 5294–5306.
- [30] E. L’Hopital, B. Lothenbach, G. Le Saout, D. Kulik, K. Scrivener, Incorporation of aluminium in calcium-silicate-hydrates, *Cem. Concr. Res.* 75 (2015) 91–103.
- [31] C. Taviot-Gueho, Y. Feng, A. Faour, F. Leroux, Intercalation chemistry in a LDH system: anion exchange process and staging phenomenon investigated by means of time-resolved, in situ X-ray diffraction, *Dalton Trans.* 39 (2010) 5994–6005.
- [32] T. Matschei, B. Lothenbach, F.P. Glasser, The AFm phase in Portland cement, *Cem. Concr. Res.* 37 (2007) 118–130.
- [33] R. Wijitwongwan, S. Intasa-ard, M. Ogawa, Preparation of Layered Double Hydroxides toward Precisely Designed Hierarchical Organization, *ChemEngineering.* 3 (2019) 68.
- [34] F. Goetz-Neunhoffer, J. Neubauer, P. Schwesig, Mineralogical characteristics of Ettringites synthesized from solutions and suspensions, *Cem. Concr. Compos.* 36 (2006) 65–70.
- [35] S.M. Clark, B. Colas, M. Kunz, S. Speziale, P.J.M. Monteiro, Effect of pressure on the crystal structure of ettringite, *Cem. Concr. Res.* 38 (2008) 19–26.
- [36] M. Ojovan, W. Lee, Immobilisation of Radioactive Wastes in Cement, in: *An Introduction to Nuclear Waste Immobilisation*, 1st ed., Elsevier, 2005: pp. 179–200.
- [37] R. Snellings, G. Mertens, J. Elsen, Supplementary Cementitious Materials, *Rev. Mineral. Geochem.* 74 (2012) 211–278.
- [38] R. Siddique, M.I. Khan, *Supplementary Cementing Materials*, Engineering Materials, Springer, 2011.
- [39] C.I. Pearce, J.P. Icenhower, R.M. Asmussen, P.G. Tratnyek, K.M. Rosso, W.W. Lukens, N.P. Qafoku, Technetium Stabilization in Low-Solubility Sulfide Phases: A Review, *ACS Earth Space Chem.* 2 (2018) 532–547.
- [40] IAEA, *The Long Term Storage of Radioactive waste: Safety and Sustainability*, IAEA-LTS/RW, 2003.
- [41] NDA, *Geological Disposal. How the world is dealing with its radioactive wastes*, (2013).
- [42] NDA, *Geological Disposal. An overview of the generic Disposal System Safety Case*, NDA/RWMD/010, 2010.
- [43] RWM, *Geological Disposal. Geosphere Status Report*, DSSC/453/01, 2016.
- [44] NDA, *Geological Disposal. Near-field evolution status report*, NDA/RWMD/033, 2010.
- [45] J. Selbin, J.D. Ortego, Chemistry of uranium (V), *Chem. Rev.* 69 (1969) 657–671.
- [46] K. Fujiwara, H. Yamana, T. Fujii, K. Kawamoto, T. Sasaki, H. Moriyama, Solubility of uranium(IV) hydrous oxide in high pH solution under reducing condition, *Radiochim. Acta.* 93 (2005) 347–350.
- [47] J.L. Ryan, D. Rai, The solubility of uranium(IV) hydrous oxide in sodium hydroxide solutions under reducing conditions, *Polyhedron.* 2 (1983) 947–952.
- [48] P.R. Tremaine, J.D. Chen, G.J. Wallace, W.A. Boivin, Solubility of uranium (IV) oxide in alkaline aqueous solutions to 300°C, *J. Solution Chem.* 10 (1981) 221–230.
- [49] N. Çevirim-Papaioannou, E. Yalçintaş, X. Gaona, K. Dardenne, M. Altmaier, H. Geckeis, Redox chemistry of uranium in reducing, dilute to concentrated NaCl solutions, *Appl. Geochemistry.* 98 (2018) 286–300.
- [50] V. Neck, J.I. Kim, Solubility and hydrolysis of tetravalent actinides, *Radiochim. Acta.* 89 (2001)

1–16.

- [51] D.W. Shoemsmith, Used Fuel and Uranium Dioxide Dissolution Studies - A Review, NWMO TR-2007-03, 2007.
- [52] K.W. Kim, D.Y. Chung, H.B. Yang, J.K. Lim, E.H. Lee, K.C. Song, K. Song, A conceptual process study for recovery of uranium alone from spent nuclear fuel by using high-alkaline carbonate media, *Nucl. Technol.* 166 (2009) 170–179.
- [53] M. Sutton, P. Warwick, A. Hall, Uranium(VI) interactions with OPC/PFA grout, *J. Environ. Monit.* 5 (2003) 922–928.
- [54] A. Martínez-Torrents, S. Meca, N. Baumann, V. Martí, J. Giménez, J. De Pablo, I. Casas, Uranium speciation studies at alkaline pH and in the presence of hydrogen peroxide using time-resolved laser-induced fluorescence spectroscopy, *Polyhedron*. 55 (2013) 92–101.
- [55] G.R. Choppin, Solution Chemistry of the Actinides, *Radiochim. Acta.* 32 (1983) 43–54.
- [56] B. Drobot, A. Bauer, R. Steudtner, S. Tsushima, F. Bok, M. Patzschke, J. Raff, V. Brendler, Speciation Studies of Metals in Trace Concentrations: The Mononuclear Uranyl(VI) Hydroxo Complexes, *Anal. Chem.* 88 (2016) 3548–3555.
- [57] M. Altmaier, E. Yalçintaş, X. Gaona, V. Neck, R. Müller, M. Schlieker, T. Fanghänel, Solubility of U(VI) in chloride solutions. I. The stable oxides/hydroxides in NaCl systems, solubility products, hydrolysis constants and SIT coefficients, *J. Chem. Thermodyn.* 114 (2017) 2–13.
- [58] N. Çevirim-Papaioannou, E. Yalçintaş, X. Gaona, M. Altmaier, H. Geckeis, Solubility of U(VI) in chloride solutions. II. The stable oxides/hydroxides in alkaline KCl solutions: Thermodynamic description and relevance in cementitious systems, *Appl. Geochemistry*. 98 (2018) 237–246.
- [59] E. Yalçintaş, N. Çevirim-Papaioannou, X. Gaona, D. Fellhauer, V. Neck, M. Altmaier, Solubility of U(VI) in chloride solutions. III. The stable oxides/hydroxides in MgCl₂ systems: Pitzer activity model for the system UO₂²⁺–Na⁺–K⁺–Mg²⁺–H⁺–OH[–]–Cl[–]–H₂O(l), *J. Chem. Thermodyn.* 131 (2019) 375–386.
- [60] F. Endrizzi, X. Gaona, Z. Zhang, C. Xu, L. Rao, C. Garcia-Perez, M. Altmaier, Thermodynamic description of U(VI) solubility and hydrolysis in dilute to concentrated NaCl solutions at T = 25, 55 and 80°C, *Radiochim. Acta.* 107 (2019) 663–678.
- [61] E. Valsami-Jones, K.V. Ragnarsdóttir, Solubility of Uranium Oxide and Calcium Uranate in Water, and Ca(OH)₂-bearing Solutions, *Radiochim. Acta.* 79 (1997) 249–257.
- [62] W. Ding, J.A. Botha, B.C. Hanson, I.T. Burke, Aqueous hydroxylation mediated synthesis of crystalline calcium uranate particles, *J. Alloys Compd.* 688 (2016) 260–269.
- [63] M. Sutton, Uranium solubility, speciation and complexation at high pH, PhD Thesis, 1999.
- [64] M. Felipe-Sotelo, J. Hinchliff, L.P. Field, A.E. Milodowski, O. Preedy, D. Read, Retardation of uranium and thorium by a cementitious backfill developed for radioactive waste disposal, *Chemosphere*. 179 (2017) 127–138.
- [65] A.S. Saleh, J. Il Yun, Equilibrium and kinetics of calcium–uranyl–carbonate adsorption on silica nanoparticles, *J. Radioanal. Nucl. Chem.* 314 (2017) 93–103.
- [66] I. Pointeau, C. Landesman, E. Giffaut, P. Reiller, Reproducibility of the uptake of U(VI) onto degraded cement pastes and calcium silicate hydrate phases, *Radiochim. Acta.* 92 (2004) 645–650.
- [67] M. Harfouche, E. Wieland, R. Dähn, T. Fujita, J. Tits, D. Kunz, M. Tsukamoto, EXAFS study of U(VI) uptake by calcium silicate hydrates, *J. Colloid Interface Sci.* 303 (2006) 195–204.
- [68] E. Wieland, N. Mace, R. Dähn, D. Kunz, J. Tits, Macro- and micro-scale studies on U(VI) immobilization in hardened cement paste, *J. Radioanal. Nucl. Chem.* 286 (2010) 793–800.
- [69] J. Tits, G. Geipel, N. Macé, M. Eilzer, E. Wieland, Determination of uranium(VI) sorbed species in calcium silicate hydrate phases: A laser-induced luminescence spectroscopy and batch sorption study, *J. Colloid Interface Sci.* 359 (2011) 248–256.

- [70] N. Macé, E. Wieland, R. Dähn, J. Tits, A.C. Scheinost, EXAFS investigation on U(VI) immobilization in hardened cement paste: Influence of experimental conditions on speciation, *Radiochim. Acta.* 101 (2013) 379–389.
- [71] X. Gaona, D.A. Kulik, N. Macé, E. Wieland, Aqueous-solid solution thermodynamic model of U(VI) uptake in C-S-H phases, *Appl. Geochem.* 27 (2012) 81–95.
- [72] D.A. Kulik, Improving the structural consistency of C-S-H solid solution thermodynamic models, *Cem. Concr. Res.* 41 (2011) 477–495.
- [73] R.J. Finch, R.C. Ewing, Clarkeite: New chemical and structural data, *Am. Mineral.* 82 (1997) 607–619.
- [74] R.J. Finch, J. Suksi, K. Rasilainen, R.C. Ewing, Uranium-series ages of secondary uranium minerals with applications to the long-term evolution of spent nuclear fuel, *Mater. Res. Soc. Symp.* 412 (1996) 823–830.
- [75] K. Štamberg, K.A. Venkatesan, P.R. Vasudeva Rao, Surface complexation modeling of uranyl ion sorption on mesoporous silica, *Colloids Surf A: Physicochem. Eng. Aspects.* 221 (2003) 149–162.
- [76] J.A. Davis, D.E. Meece, M. Kohler, G.P. Curtis, Approaches to surface complexation modeling of Uranium(VI) adsorption on aquifer sediments, *Geochim. Cosmochim. Acta.* 68 (2004) 3621–3641.
- [77] P.M. Fox, J.A. Davis, J.M. Zachara, The effect of calcium on aqueous uranium(VI) speciation and adsorption to ferrihydrite and quartz, *Geochim. Cosmochim. Acta.* 70 (2006) 1379–1387.
- [78] J.D. Prikryl, A. Jain, D.R. Turner, R.T. Pabalan, Uranium(VI) sorption behavior on silicate mineral mixtures, *J. Contam. Hydrol.* 47 (2001) 241–253.
- [79] A.S. Saleh, J.Y. Lee, Y. Jo, J. Il Yun, Uranium(VI) sorption complexes on silica in the presence of calcium and carbonate, *J. Environ. Radioact.* 182 (2018) 63–69.
- [80] S. Nair, B.J. Merkel, Impact of Alkaline Earth Metals on Aqueous Speciation of Uranium(VI) and Sorption on Quartz, *Aquat. Geochem.* 17 (2011) 209–219.
- [81] G.N. Pshinko, Layered double hydroxides as effective adsorbents for U(VI) and toxic heavy metals removal from aqueous media, *J. Chem.* 2013 (2013) 1–9.
- [82] G.N. Pshinko, A.A. Kosorukov, L.N. Puzyrnaya, S.A. Kobets, Recovery of U(VI) from aqueous media with layered double hydroxides of Zn and Al, intercalated with complexones, *Radiochemistry.* 55 (2013) 601–604.
- [83] S.A. Kulyukhin, E.P. Krasavina, Sorption of U(VI) onto layered double hydroxides and oxides of Mg and Al, prepared using microwave radiation, *Radiochemistry.* 58 (2016) 405–408.
- [84] K. Ralla, U. Sohling, K. Suck, F. Sander, C. Kasper, F. Ruf, T. Scheper, Adsorption and separation of proteins by a synthetic hydrotalcite, *Colloids Surf. B: Biointerfaces.* 87 (2011) 217–225.
- [85] T.G. Timoshenko, A.A. Kosorukov, G.N. Pshinko, V. V. Goncharuk, Calcinated hydrotalcite-a sorbent for purifying uraniferous waters, *J. Water Chem. Technol.* 31 (2009) 250–255.
- [86] J.M. Durán-Blanco, B.E. López-Muñoz, M.T. Olguín, Influence of pH on U(VI) Adsorption using a Thermally-Treated Mg-Al Hydrotalcite and a Natural Zeolite in a Batch System, *Sep. Sci. Technol.* 48 (2013) 797–804.
- [87] C. Altenhein-Haese, H. Bischoff, L. Fu, J. Mao, G. Marx, Adsorption of actinides on cement compounds, *J. Alloys Compd.* 213–214 (1994) 554–556.
- [88] NDA, Introduction to plutonium contaminated material (PCM) issues, W&NM/PP/008, 2008.
- [89] NDA, Progress on Plutonium Consolidation, Storage and Disposition, (2019).
- [90] V. Neck, M. Altmaier, T. Fanghänel, Solubility of plutonium hydroxides/hydrous oxides under reducing conditions and in the presence of oxygen, *C. R. Chim.* 10 (2007) 959–977.
- [91] S. Cotton, Coordination Chemistry of the Actinides, in: *Lanthanide and Actinide Chemistry*,

John Wiley & Sons, 2006: pp. 173–199.

- [92] H.R. Cho, Y.S. Youn, E.C. Jung, W. Cha, Hydrolysis of trivalent plutonium and solubility of Pu(OH)₃ (am) under electrolytic reducing conditions, *Dalton Trans.* 45 (2016) 19449–19457.
- [93] M. Altmaier, V. Neck, J. Ltützenkirchen, T. Fanghänel, Solubility of plutonium in MgCl₂ and CaCl₂ solutions in contact with metallic iron, *Radiochim. Acta.* 97 (2009) 187–192.
- [94] A. Tasi, X. Gaona, D. Fellhauer, M. Böttle, J. Rothe, K. Dardenne, D. Schild, M. Grivé, E. Colàs, J. Bruno, K. Källström, M. Altmaier, H. Geckeis, Redox behavior and solubility of plutonium under alkaline, reducing conditions, *Radiochim. Acta.* (2018) 1–21.
- [95] A. Felmy, D. Rai, J.A. Schramke, J.L. Ryan, The solubility of Plutonium Hydroxide in Dilute Solution and in High-Ionic-Strength Chloride Brines, *Radiochim. Acta.* 48 (1989) 29–35.
- [96] D. Rai, Y.A. Gorby, J.K. Fredrickson, D.A. Moore, M. Yui, Reductive dissolution of PuO₂ (am): The effect of Fe(II) and hydroquinone, *J. Solution Chem.* 31 (2002) 433–453.
- [97] V. Häußler, S. Amayri, A. Beck, T. Platte, T.A. Stern, T. Vitova, T. Reich, Uptake of actinides by calcium silicate hydrate (C-S-H) phases, *Appl. Geochemistry.* 98 (2018) 426–434.
- [98] S.O. Odoh, E.J. Bylaska, W.A. De Jong, Coordination and hydrolysis of plutonium ions in aqueous solution using car-parrinello molecular dynamics free energy simulations, *J. Phys. Chem. A.* 117 (2013) 12256–12267.
- [99] V. Neck, M. Altmaier, A. Seibert, J.I. Yun, C.M. Marquardt, T. Fanghänel, Solubility and redox reactions of Pu(IV) hydrous oxide: Evidence for the formation of PuO₂+x (s,hyd), *Radiochim. Acta.* 95 (2007) 193–207.
- [100] C.H. Delegard, Solubility of PuO₂.xH₂O in alkaline hanford high-level waste solution, *Radiochim. Acta.* 41 (1987) 11–21.
- [101] V. Neck, M. Altmaier, T. Fanghänel, Thermodynamic data for hydrous and anhydrous PuO₂+x (s), *J. Alloys Compd.* 444–445 (2007) 464–469.
- [102] S.D. Conradson, B.D. Begg, D.L. Clark, C. Den Auwer, F.J. Espinosa-Faller, P.L. Gordon, N.J. Hess, R. Hess, D.W. Keogh, L.A. Morales, M.P. Neu, W. Runde, C.D. Tait, D.K. Veirs, P.M. Villella, Speciation and unusual reactivity in PuO₂+x, *Inorg. Chem.* 42 (2003) 3715–3717.
- [103] J.M. Haschke, T.H. Allen, L.A. Morales, Reaction of plutonium dioxide with water: Formation and properties of PuO₂+x, *Science.* 287 (2000) 285–287.
- [104] M.R. Antonio, C.W. Williams, J.A. Sullivan, S. Skanthakumar, Y.J. Hu, L. Soderholm, Preparation, stability, and structural characterization of plutonium(VII) in alkaline aqueous solution, *Inorg. Chem.* 51 (2012) 5274–5281.
- [105] Y.M. Kiselev, M. V. Nikonov, V.D. Dolzhenko, A.Y. Ermilov, I.G. Tananaev, B.F. Myasoedov, On existence and properties of plutonium(VIII) derivatives, *Radiochim. Acta.* 102 (2014) 227–237.
- [106] M. V. Nikonov, A. V. Gogolev, I.G. Tananaev, B.F. Myasoedov, Experimental data points to the existence of plutonium(VIII) in alkaline solutions, *Mendeleev Commun.* 15 (2005) 50–52.
- [107] M. V. Nikonov, Y.M. Kiselev, I.G. Tananaev, B.F. Myasoedov, Plutonium volatility in ozonization of alkaline solutions of Pu(VI) hydroxo complexes, *Dokl. Chem.* 437 (2011) 69–71.
- [108] M. V. Nikonov, B.F. Myasoedov, A spectrophotometric study of the reduction of Pu(VIII) and Pu(VII) in alkaline solutions, *Radiochemistry.* 56 (2014) 227–234.
- [109] V.P. Shilov, A. V. Gogolev, A.M. Fedoseev, Estimation of the rate constants of the Pu(VI) + O₃- Reaction in alkaline solutions, *Radiochemistry.* 57 (2015) 395–397.
- [110] I.G. Tananaev, M. V. Nikonov, B.F. Myasoedov, D.L. Clark, Plutonium in higher oxidation states in alkaline media, *J. Alloys Compd.* 444–445 (2007) 668–672.
- [111] A. V. Gogolev, A.M. Fedosseev, P. Moisy, The influence of f-elements' oxidizing potential and ion charge on their stability in aqueous alkaline solution, *Radiochim. Acta.* 100 (2012) 809–811.

- [112] C. Ekberg, K. Larsson, G. Skarnemark, A. Ödegaard-Jensen, I. Persson, The structure of plutonium(IV) oxide as hydrolysed clusters in aqueous suspensions, *Dalton Trans.* 42 (2013) 2035–2040.
- [113] A.Y. Romanchuk, T. V. Plakhova, A. V. Egorov, T.B. Egorova, P. V. Dorovatovskii, Y. V. Zubavichus, A.A. Shiryaev, S.N. Kalmykov, Redox-mediated formation of plutonium oxide nanoparticles, *Dalton Trans.* 47 (2018) 11239–11244.
- [114] K. Fujiwara, H. Yamana, T. Fujii, H. Moriyama, Solubility product of plutonium hydrous oxide and its ionic strength dependence, *Radiochim. Acta.* 90 (2002) 857–861.
- [115] K. Fujiwara, H. Yamana, T. Fujii, H. Moriyama, Solubility product of Pu(VI) hydrous oxide, *Radiochim. Acta.* 91 (2003) 81–85.
- [116] C.R. Gregson, J.J. Hastings, H.E. Sims, H.M. Steele, R.J. Taylor, Characterisation of plutonium species in alkaline liquors sampled from a UK legacy nuclear fuel storage pond, *Anal. Methods.* 3 (2011) 1957–1968.
- [117] D. Rai, J.L. Ryan, Crystallinity and Solubility of Pu(IV) Oxide and Hydrous Oxide in Aged Aqueous Suspensions, *Radiochim. Acta.* 30 (1982) 213–216.
- [118] F.T. Ewart, R.M. Howse, H.P. Thomason, S.J. Williams, J.E. Cross, Solubility of Actinides in the Near-Field, *Mater. Res. Soc. Symp. Proc.* 50 (1986) 701–708.
- [119] D.C. Pryke, J.H. Rees, Influence on Actinide Solubilities of Candidate Materials for Use in Repositories for Low and Intermediate Level Nuclear Wastes., *J. Less Common Met.* 121 (1986) 519–524.
- [120] D.C. Pryke, J.H. Rees, R.J.W. Streeton, Determination of the solubilities and degrees of sorption of uranium, plutonium, americium and neptunium under nearfield conditions for disposal, AERPRI1391, 1984.
- [121] N.N. Krot, V.P. Shilov, A.B. Yusov, I.G. Tananaev, M.S. Grigoriev, A.Y. Garnov, V.P. Perminov, L.N. Astafurova, Plutonium(IV) Precipitates Formed in Alkaline Media in the Presence of Various Anions, PNNL-11901, UC-2030, 1998.
- [122] F.T. Ewart, J.L. Smith-Briggs, H.P. Thomason, S.J. Williams, The solubility of actinides in a cementitious near-field environment, *Waste Manage.* 12 (1992) 241–252.
- [123] M. Ochs, D. Mallants, L. Wang, Sorption Values for Thorium, Uranium, Plutonium, Neptunium, and Protactinium Abstract, in: *Radionuclide and Metal Sorption on Cement and Concrete*, 2016: pp. 5–17.
- [124] S. Hoglund, L. Eliasson, B. Allard, K. Andersson, B. Torstenfelt, Sorption of Some Fission Products and Actinides in Concrete Systems., *Mater. Res. Soc. Symp. Proc.* 50 (1986) 683–690.
- [125] R.B. Heimann, Interaction of Cement and Radioactive Waste Forms in Multicomponent Systems Tests at 200°C. Part 1: Leaching and Sorption of Cesium, Strontium and Actinides, *Cem. Concr. Res.* 18 (1988) 389–400.
- [126] S. Aggarwal, M.J. Angus, J. Ketchen, Sorption of radionuclides onto specific mineral phases present in repository cements, NSS/R312, AEA-D&R-0395, 2000.
- [127] Standard Test Method for Distribution Coefficients of Inorganic Species by the Batch Method ASTM C1733-10, 2012.
- [128] T.G. Heath, D.J. Ilett, C.J. Tweed, Thermodynamic modelling of the sorption of radioelements onto cementitious materials, *Mater. Res. Soc. Symp. Proc.* 412 (1996) 443–449.
- [129] D. Sugiyama, T. Fujita, A thermodynamic model of dissolution and precipitation of calcium silicate hydrates, *Cem. Concr. Res.* 36 (2006) 227–237.
- [130] H. Viallis-Terrise, A. Nonat, J.C. Petit, Zeta-Potential Study of Calcium-Silicate Hydrates Interacting with Alkaline Cations, *J. Colloid Interface Sci.* 244 (2001) 58–65.
- [131] S.A. Kearney, B. McLuckie, K. Webb, R. Orr, I.A. Vatter, A.S. Yorkshire, C.L. Corkhill, M. Hayes, M.J. Angus, J.P. Provis, Effects of plutonium dioxide encapsulation on the physico-chemical development of Portland cement blended grouts, *J. Nucl. Mater.* 530 (2020) 151960.

- [132] I.G. Richardson, G.W. Groves, C.R. Wilding, Effect of gamma radiation on the microstructure and microchemistry of GGBFS/OPC cement blends, *Mater. Res. Soc. Symp. Proc.* 176 (1989) 31.
- [133] A. Bernard, J.C. Nomine, G. Cornec, A. Bonnet, L. Farges, Long-term leaching tests on full-scale blocks of radioactive wastes, *Nucl. Chem. Waste Manage.* 3 (1982) 161–168.
- [134] K.A. Law, S. Parry, N.D. Bryan, S.L. Heath, S.M. Heald, D. Knight, L. O'Brien, A.J. Fuller, W.R. Bower, G.T.W. Law, F.R. Livens, Plutonium Migration during the Leaching of Cemented Radioactive Waste Sludges, *Geosciences J.* 9 (2019) 31.
- [135] J.A. Berry, K.A. Bond, A. Green, C.M. Linklater, A.J. Smith, An experimental study of actinide sorption onto calcite, aluminium oxide and hematite, *AEAT/R/ENV/0205*, 2000.
- [136] J.J.W. Higgo, L.V.C. Rees, Adsorption of Actinides by Marine Sediments: Effect of the Sediment/Seawater Ratio on the Measured Distribution Ratio, *Environ. Sci. Technol.* 20 (1986) 483–490.
- [137] A.H. Meena, Y. Arai, Environmental geochemistry of technetium, *Environ. Chem. Lett.* 15 (2017) 241–263.
- [138] R.J. Serne, B.M. Rapko, Technetium Inventory, Distribution, and Speciation in Hanford Tanks, *PNNL-23319, EMSP-RPT-022*, 2014.
- [139] P. Warwick, S. Aldridge, N. Evans, S. Vines, The solubility of technetium(IV) at high pH, *Radiochim. Acta.* 95 (2007) 709–716.
- [140] E. Yalcintas, Redox, solubility and sorption chemistry of technetium in dilute to concentrated saline systems, PhD Thesis, 2015.
- [141] E. Yalçintaş, X. Gaona, M. Altmaier, K. Dardenne, R. Polly, H. Geckeis, Thermodynamic description of Tc(IV) solubility and hydrolysis in dilute to concentrated NaCl, MgCl₂ and CaCl₂ solutions, *Dalton Trans.* 45 (2016) 8916–8936.
- [142] T.E. Eriksen, P. Ndalamba, J. Bruno, M. Caceci, The Solubility of TcO₂·nH₂O in Neutral to Alkaline Solutions under Constant pCO₂, *Radiochim. Acta.* 58 (1992) 67–70.
- [143] R.E. Meyer, W.D. Arnold, F.I. Case, Valence Effects on Solubility and Sorption. The solubility of Tc(IV) Oxides, *NUREG/CR-4309, ORNL-6199*, 1986.
- [144] B.R.E. Meyer, W.D. Arnold, F.I. Case, G.D.O. Kelley, Solubilities of Tc(IV) Oxides, *Radiochim. Acta.* 55 (1990) 11–18.
- [145] N.J. Pilkington, the Solubility of Technetium, *J. Less Common Met.* (1990) 203–212.
- [146] B.G. Brodda, Leachability of technetium from concrete, *Sci. Total Environ.* 69 (1988) 319–345.
- [147] T.M. Gilliam, R.D. Spence, W.D. Bostick, J.L. Shoemaker, Solidification/stabilization of technetium in cement-based grouts, *J. Hazard. Mater.* 24 (1990) 189–197.
- [148] K.J. Cantrell, B.D. Williams, Solubility control of technetium release from Saltstone by TcO₂·xH₂O, *J. Nucl. Mater.* 437 (2013) 424–431.
- [149] R.T. Pabalan, G.W. Alexander, D.J. Waiting, C.S. Barr, Experimental study of contaminant release from reducing grout, *EPJ Web Conf.* 56 (2013) 01010.
- [150] E. Deutsch, W.R. Heineman, R. Hurst, J.C. Sullivan, W.A. Mulac, S. Gordon, Production, detection, and characterization of transient hexavalent technetium in aqueous alkaline media by pulse radiolysis and very fast scan cyclic voltammetry, *J. Chem. Soc. Chem. Commun.* 23 (1978) 1038–1040.
- [151] M. Chotkowski, M. Grdeń, B. Wrzosek, Intermediate oxidation states of technetium in alkaline solutions, *J. Electroanal. Chem.* 829 (2018) 148–156.
- [152] W.W. Lukens, J.J. Bucher, D.K. Shuh, N.M. Edelstein, Evolution of technetium speciation in reducing grout, *Environ. Sci. Technol.* 39 (2005) 8064–8070.
- [153] Y. Arai, B.A. Powell, D.I. Kaplan, Residence time effects on technetium reduction in slag-based cementitious materials, *J. Hazard. Mater.* 342 (2018) 510–518.

- [154] R.M. Asmussen, C.I. Pearce, B.W. Miller, A.R. Lawter, J.J. Neeway, W.W. Lukens, M.E. Bowden, M.A. Miller, E.C. Buck, R.J. Serne, N.P. Qafoku, Getters for improved technetium containment in cementitious waste forms, *J. Hazard. Mater.* 341 (2018) 238–247.
- [155] C.L. Corkhill, J.W. Bridge, X.C. Chen, P. Hillel, S.F. Thornton, M.E. Romero-Gonzalez, S.A. Banwart, N.C. Hyatt, Real-time gamma imaging of technetium transport through natural and engineered porous materials for radioactive waste disposal, *Environ. Sci. Technol.* 47 (2013) 13857–13864.
- [156] R. Druteikienė, J. Šapolaitė, Ž. Ežerinskis, L. Juodis, Batch-type study of Cs, Co, and Tc binding with hydrated cement under hyperalkaline conditions, *J. Radioanal. Nucl. Chem.* 313 (2017) 299–307.
- [157] L. Aimoz, E. Wieland, M. Vespa, S. V Churakov, Structural Insight into Iodide Uptake by AFm Phases, *Environ. Sci. Technol.* 46 (2012) 3874–3881.
- [158] I. Baur, C.A. Johnson, Sorption of selenite and selenate to cement minerals, *Environ. Sci. Technol.* 37 (2003) 3442–3447.
- [159] S.A. Saslow, S.N. Kerisit, T. Varga, S.T. Mergelsberg, C. Corkhill, M.V. Michelle, V. Snyder, N. Avalos, A.S. Yorkshire, D.J. Bailey, J. Crum, R.M. Asmussen, Immobilizing Per technetate in Ettringite via Sulfate Substitution (Just Accepted), *Environ. Sci. Technol.* (2020).
- [160] J.O. Dickson, J.B. Harsh, W.W. Lukens, E.M. Pierce, Perrhenate incorporation into binary mixed sodalites: The role of anion size and implications for technetium-99 sequestration, *Chem. Geol.* 395 (2015) 138–143.
- [161] Y. Marcus, Ionic Radii in Aqueous Solutions, *Chem. Rev.* 88 (1988) 1475–1498.
- [162] D.Y. Yang, R. Guo, Experimental study on modulus and hardness of ettringite, *Exp. Tech.* 38 (2014) 6–12.
- [163] J. Als-Nielsen, D. McMorrow, *Elements of modern X-ray physics*, 2nd ed., Wiley, 2002.
- [164] H.M. Rietveld, A profile refinement method for nuclear and magnetic structures, *J. Appl. Crystallogr.* 2 (1969) 65–71.
- [165] Beckman Coulter, Mie and Fraunhofer Diffraction Theories, <https://www.mybeckman.uk/resources/technologies/laser-diffraction/mie-fraunhofer-theories> (accessed March 2020), (2020).
- [166] C.F. Ferraris, V.A. Hackley, A.I. Avilés, Measurement of particle size distribution in portland cement powder: Analysis of ASTM round robin studies, *Cem. Concr. Aggregates.* 26 (2004) 71–81.
- [167] R.J. Hunter, *Zeta Potential in Colloid Science: Principles and Applications*, Academic Press, 1981.
- [168] B. Walkley, J.L. Provis, Solid-state nuclear magnetic resonance spectroscopy of cements, *Mater. Today Adv.* 1 (2019) 100007.
- [169] K.J.D. Mackenzie, M.E. Smith, *Multinuclear Solid-State NMR of Inorganic Materials*, Pergamon, Elsevier, 2002.
- [170] S. Calvin, *XAFS for everyone*, Taylor & Francis, CRC Press, 2013.
- [171] B. Ravel, M. Newville, ATHENA, ARTEMIS, HEPHAESTUS: data analysis for X-ray absorption spectroscopy using IFEFFIT, *J. Synchrotron Radiat.* 12 (2005) 537–541.
- [172] S. Diaz-Moreno, M. Amboage, M. Basham, R. Boada, N.E. Bricknell, G. Cibin, T.M. Cobb, J. Filik, A. Freeman, G. Kalotina, D. Gianolio, S. Hayama, K. Ignatyev, L. Keenan, I. Mikulska, J.F.W. Mosselmans, J.J. Mudd, S.A. Parry, The Spectroscopy Village at Diamond Light Source, *J. Synchrotron Radiat.* 25 (2018) 998–1009.
- [173] C. Weiland, C. Jaye, N.F. Quackenbush, E. Gann, Z. Fu, J.P. Kirkland, B.A. Karlin, B. Ravel, J.C. Woicik, D.A. Fischer, NIST HAXPES at NSLS and NSLS-II, *Synchrotron Radiat. News.* 31 (2018) 23–28.
- [174] H. Konishi, A. Yokoya, H. Shiwaku, H. Motohashi, T. Makita, Y. Kashihara, S. Hashimoto, T.

- Harami, T.A. Sasaki, H. Maeta, H. Ohno, H. Maezawa, S. Asaoka, N. Kanaya, K. Ito, N. Usami, K. Kobayashi, Synchrotron radiation beamline to study radioactive materials at the Photon Factory, *Nucl. Instruments Methods Phys. Res. A.* 372 (1996) 322–332.
- [175] IUCr, Online Dictionary of Crystallography, Extended X-ray absorption fine structure (EXAFS), [https://dictionary.iucr.org/Extended_X-ray_absorption_fine_structure_\(EXAFS\)](https://dictionary.iucr.org/Extended_X-ray_absorption_fine_structure_(EXAFS)) (accessed March 2020), (2017).
- [176] J.J. Rehr, R.C. Albers, Theoretical Approaches to X-ray Absorption Fine Structure, *Rev. Mod. Phys.* 72 (2000) 621.
- [177] J.J. Rehr, J.J. Kas, M.P. Prange, A.P. Sorini, Y. Takimoto, F.D. Vila, Ab initio theory and calculations of X-ray spectra, *C. R. Phys.* 10 (2009) 548–559.
- [178] S.J. Hill, *Inductively Coupled Plasma Spectrometry and its Applications*, Blackwell, 2007.
- [179] K.D. Neame, C.A. Homewood, *Introduction to Liquid Scintillation Counting*, Butterworth & Co, 1974.
- [180] K. Siegbahn, *Alpha-, Beta- and Gamma-Ray Spectroscopy*, North-Holland, 1979.
- [181] S.R. Charlton, D.L. Parkhurst, Modules based on the geochemical model PHREEQC for use in scripting and programming languages, *Comput. Geosci.* 37 (2011) 1653–1663.
- [182] Aqion, Mineral Solubility and Saturation Index, <https://www.aqion.de/site/168> (accessed March 2020), (2012).
- [183] N. Clavier, S. Szenknect, D.T. Costin, A. Mesbah, C. Poinssot, N. Dacheux, From thorite to coffinite: A spectroscopic study of Th_{1-x}U_xSiO₄ solid solutions, *Spectrochim. Acta A.* 118 (2014) 302–307.
- [184] C. Henmi, I. Kusachi, Monoclinic tobermorite from Fuka, Bitchu-cho, Okayama Prefecture, Japan, *J. Mineral. Petrol. Econ. Geol.* 84 (1989) 374–379.
- [185] E. Tajuelo Rodriguez, K. Garbev, D. Merz, L. Black, I.G. Richardson, Thermal stability of C-S-H phases and applicability of Richardson and Groves' and Richardson C-(A)-S-H(I) models to synthetic C-S-H, *Cem. Concr. Res.* 93 (2017) 45–56.
- [186] K. Martin, G. McCarthy, PDF card no 00-044-1481 (Portlandite), (1992).
- [187] H. Sitepu, Texture and structural refinement using neutron diffraction data from molybdate (MoO₃) and calcite (CaCO₃) powders and a Ni-rich Ni_{50.7}Ti_{49.30} alloy, *Powder Diffr.* 24 (2009) 315–326.
- [188] M. Martín-Garrido, M. Teresa Molina-Delgado, S. Martínez-Ramírez, A comparison between experimental and theoretical Ca/Si ratios in C–S–H and C–S(A)–H gels, *J. Sol-Gel Sci. Technol.* (2019).
- [189] L. Black, C. Breen, J. Yarwood, Structural Features of C–S–H(I) and Its Carbonation in Air—A Raman Spectroscopic Study. Part II: Carbonated Phases, *J. Am. Ceram. Soc.* 90 (2007) 908–917.
- [190] E.M. Palaich, H.R. A., M. Hanfland, A. Lausi, A. Kavner, C.E. Manning, M. Merlini, High-Pressure Compressibility and Thermal Expansion of aragonite, *Am. Mineral.* 101 (2016) 1651–1658.
- [191] A. Le Bail, S. Ouhenia, D. Chateigner, Microtwinning hypothesis for a more ordered vaterite model, *Powder Diffr.* 26 (2011) 16–21.
- [192] H.W.F. Taylor, Crystal structures of some double hydroxide minerals, *Miner. Mag.* 30 (1973) 377.
- [193] M. Bellotto, B. Rebours, O. Clause, J. Lynch, R.M. Cedex, D. Bazin, E. Elkaim, A Reexamination of Hydrotalcite Crystal Chemistry, *J. Phys. Chem.* 100 (1996) 8527–8534.
- [194] F. Goetz-Neunhoffer, J. Neubauer, Refined ettringite (Ca₆Al₂(SO₄)₃(OH)_{12.26}(H₂O)) structure for quantitative X-ray diffraction analysis, *Powder Diffr.* 21 (2006) 4–11.
- [195] H. McMurdie, M. Morris, E. Evans, B. Paretzkin, W. Wong-Ng, C. Hubbard, Standard X-ray

diffraction powder patterns from the JCPDS research associateship, Powder Diffr. 1 (1986) 265–275.

- [196] Standard X-ray diffraction patterns, National Bureau of Standards, Volume 17, (1980).
- [197] A. Kirfel, G. Will, Charge density in anhydrite, CaSO_4 , from X-ray and neutron diffraction measurements, Acta Crystallogr. B. 36 (1980) 2881–2890.
- [198] T. Fukami, S. Tahara, K. Najasone, C. Yasuda, Synthesis, crystal structure, and thermal properties of $\text{CaSO}_4 \cdot 2\text{H}_2\text{O}$ single crystals, Int. J. Chem. 7 (2015) 12–20.
- [199] S. Greaux, L. Gautron, D. Andrault, N. Bolfan Casanova, N. Guignot, J. Haines, Structural characterization of natural UO_2 at pressures up to 82 GPa and temperatures up to 2200 K, Am. Mineral. 93 (2008) 1090–1098.
- [200] B.O. Loopstra, J.C. Taylor, A.B. Waugh, Neutron powder profile studies of the gamma uranium trioxide phases, J. Solid State Chem. 20 (1977) 9–19.
- [201] J.C. Taylor, M.H. Mueller, A Neutron Diffraction Study of Uranyl Nitrate Hexahydrate., Acta Crystallogr. 19 (1965) 536–543.
- [202] J. Holc, L. Golic, The synthesis and crystal structure of $\alpha\text{-Ca}_3\text{UO}_6$, J. Solid State Chem. 48 (1983) 396–400.
- [203] W.H. Zachariasen, Crystal chemical studies of the 5f-series of elements. XXI. The crystal structure of magnesium orthouranate, Acta Crystallogr. 7 (1954) 788–791.
- [204] P.D. Ginderow, Structure de l'Uranophane Alpha, $\text{Ca}(\text{UO}_2)_2(\text{SiO}_3\text{OH})_2 \cdot 5\text{H}_2\text{O}$, Acta Crystallogr. C. 44 (1988) 421–424.
- [205] A.V. Barinova, R.K. Rastsvetaeva, G.A. Sidorenko, I. Verin, Crystal structure of beta uranophane from the Transbaikal region and its relation to the alpha modification, Kristallografiya. 48 (2003) 17–20.
- [206] R.J. Finch, P.C. Burns, F.C. Hawthorne, R.C. Ewing, Refinement of the crystal structure of billietite, $\text{Ba}((\text{UO}_2)_6\text{O}_4(\text{OH})_6)(\text{H}_2\text{O})_8$, Can. Mineral. 44 (2006) 1197–1205.
- [207] A.L. Klingensmith, K.M. Deely, W.S. Kinman, V. Kelly, P.C. Burns, Neptunium incorporation in sodium-substituted metaschoepite, Am. Mineral. 92 (2007) 662–669.
- [208] K. Kihara, An X-ray study of the temperature dependence of the quartz structure, Eur. J. Miner. 2 (1990) 63.
- [209] R.J. Finch, R.C. Ewing, Alteration of Natural UO_2 under Oxidizing Conditions from Shinkolobwe, Katanga, Zaire: A Natural Analogue for the Corrosion of Spent Fuel, Radiochim. Acta. 52–53 (1991) 395–402.
- [210] T. McBurney, J. Murdoch, Haiweeite, a new uranium mineral from California, Am. Mineral. 44 (1959) 839–843.
- [211] J. Plasil, K. Fejfarova, J. Cejka, M. Dusek, R. Skoda, R. Sejkora, Revision of the crystal structure and chemical formula of haiweeite, $\text{Ca}(\text{UO}_2)_2(\text{Si}_5\text{O}_{12})(\text{OH})_2 \cdot 6\text{H}_2\text{O}$, Am. Mineral. 98 (2013) 718–723.
- [212] R. Vochten, N. Blaton, O. Peeters, Synthesis of sodium weeksite and its transformation into weeksite, Neues Jahrb. Für Mineral. 12 (1997) 569.
- [213] S.V. Baturin, G.A. Sidorenko, Crystal structure of weeksite $(\text{K}_{0.62}\text{Na}_{0.38})_2(\text{UO}_2)_2(\text{Si}_5\text{O}_{13})(\text{H}_2\text{O})_3$, Sov. Phys. Dokl. 30 (1985) 435–437.
- [214] C.L. Christ, J.R. Clark, H.T. Evans Jr, Crystal structure of rutherfordine, UO_2CO_3 , Science. 121 (1955) 472–473.
- [215] F. Demartin, C.M. Gramaccioli, T. Pilati, The importance of accurate crystal structure determination of uranium minerals. II. Soddyite $(\text{UO}_2)_2(\text{SiO}_4)(\text{H}_2\text{O})_2$, Acta Crystallogr. C. 48 (1992) 1–4.
- [216] H. Mayer, K. Mereiter, Synthetic bayleyite, $\text{Mg}_2\text{UO}_2(\text{CO}_3)_3(\text{H}_2\text{O})_{18}$, Thermochem. Crystallogr. Cryst. Struct. 35 (1986) 133–146.

- [217] J. Li, A preliminary study on andersonite, *Uranium Geol.* 4 (1988) 235–239.
- [218] A. Coda, A.D. Giusta, V. Tazzoli, The structure of synthetic andersonite, $\text{Na}_2\text{Ca}(\text{UO}_2)(\text{CO}_3)_3(\text{H}_2\text{O})_x$ ($x \sim 5.6$), *Acta Crystallogr. B.* 37 (1981) 1496–1500.
- [219] L.H. Fuchs, E. Gebert, X-ray studies of synthetic coffinite, thorite and uranothorites, *Am. Mineral.* 43 (1958) 243–248.
- [220] J.D. Bauer, S. Labs, S. Weiss, L. Bayarjargal, W. Morgenroth, V. Milman, A. Perlov, H. Curtius, D. Bosbach, H. Zaenker, B. Winkler, High-pressure phase transition of coffinite, USiO_4 , *J. Phys. Chem. C.* 118 (2014) 25141–25149.
- [221] M.K. Pagoaga, D.E. Appleman, J.M. Stewart, Crystal structures and crystal chemistry of the uranyl oxide hydrates becquerelite, billietite, and protasite, *Am. Mineral.* 72 (1987) 1230–1238.
- [222] R. Picard, J.P. Besse, J.P. Chevalier, M. Gasperin, Structure cristalline de $\text{Ca}(\text{ReO}_4)_2(\text{H}_2\text{O})_2$, *J. Solid State Chem.* 69 (1987) 380–384.
- [223] W.H. Baur, D. Kassner, The Crystal Structure of $\text{Ca}(\text{ReO}_4)_2 \cdot 2\text{H}_2\text{O}$, *J. Solid State Chem.* 100 (1992) 166–169.
- [224] J. Hetmańczyk, Ł. Hetmańczyk, W. Nitek, Crystal structure, phase transitions and vibrations of H_2O molecules in $[\text{Ca}(\text{H}_2\text{O})_2](\text{ReO}_4)_2$, *J. Therm. Anal. Calorim.* 131 (2018) 479–489.
- [225] G.J. Kruger, E.C. Reynhardt, Ammonium perrhenate at 295 and 135 K, *Acta Crystallogr. B.* 34 (1978) 259–261.
- [226] H.H. Murray, S.P. Kelty, R.R. Chianellie, C.S. Day, Structure of Rhenium Disulfide, *Inorg. Chem.* 33 (1994) 4418–4420.
- [227] J. Weaver, C.Z. Soderquist, N.M. Washton, A.S. Lipton, P.L. Gassman, W.W. Lukens, A.A. Kruger, N.A. Wall, J.S. McCloy, Chemical Trends in Solid Alkali Pertechnetates, *Inorg. Chem.* 56 (2017) 2533–2544.
- [228] R. Faggiani, C.J.L. Lock, J. Poce, The structure of ammonium pertechnetate at 295, 208 and 141K, *Acta Crystallogr. B.* 36 (1980) 231–233.
- [229] I.G. Richardson, Model structures for C-(A)-S-H(I), *Acta Crystallogr. B.* 70 (2014) 903–923.
- [230] I.G. Richardson, G.W. Groves, Models for the composition and structure of calcium-silicate-hydrate (C-S-H) gel in hardened tricalcium silicate pastes, *Cem. Concr. Res.* 22 (1992) 1001–1010.
- [231] R.K. Iler, *The Chemistry of Silica. Solubility, Polymerization, Colloid and Surface Properties, and Biochemistry*, John Wiley & Sons, 1979.
- [232] D. Pletcher, *A First Course in Electrode Processes*, RSC, 2009.
- [233] Y. Li, W. Liu, F. Xing, S. Wang, L. Tang, S. Lin, Z. Dong, Carbonation of the synthetic calcium silicate hydrate (C-S-H) under different concentrations of CO_2 : Chemical phases analysis and kinetics, *J. CO₂ Util.* 35 (2020) 303–313.
- [234] D.J. Wan, H.J. Liu, X. Zhao, J.H. Qu, S.H. Xiao, Y.N. Hou, Role of the Mg/Al atomic ratio in hydrotalcite-supported Pd/Sn catalysts for nitrate adsorption and hydrogenation reduction, *J. Colloid Interface Sci.* 332 (2009) 151–157.
- [235] P.J. Sideris, U.G. Nielson, Z. Gan, C.P. Grey, Mg/Al Ordering in Layered Double Hydroxides Revealed by Multinuclear NMR Spectroscopy, *Science*, 321 (2008) 113–117.
- [236] M. Medala, C. Labbez, I. Pochard, A. Nonat, Ettringite surface chemistry: Interplay of electrostatic and ion specificity, *J. Colloid Interface Sci.* 354 (2011) 765–770.
- [237] F. V Stohl, D.K. Sunh, The crystal chemistry of the uranyl silicate minerals, *Am. Miner.* 66 (1980).
- [238] J.M. Jackson, P.C. Burns, A re-evaluation of the structure of weeksite, a uranyl silicate framework mineral, *Can. Mineral.* 39 (2001) 187–195.
- [239] P.C. Burns, A new uranyl silicate sheet in the structure of haiweeite and comparison to other uranyl silicates, *Can. Mineral.* 39 (2001) 1153–1160.

- [240] J. Plasil, *Mineralogy, Crystallography and Structural Complexity of Natural Uranyl Silicates*, *Minerals*. 8 (2018) 1–15.
- [241] H.A. Thompson, G.E. Brown, G.A. Parks, XAFS spectroscopic study of uranyl coordination in solids and aqueous solution, *Am. Mineral.* 82 (1997) 483–496.
- [242] J.G. Catalano, G.E. Brown Jr, Analysis of uranyl-bearing phases by EXAFS spectroscopy: Interferences, multiple scattering, accuracy of structural parameters and spectral differences, *Am. Mineral.* 89 (2004) 1004–1021.
- [243] P.G. Allen, D.K. Shuh, J.J. Bucher, N.M. Edelstein, C.E.A. Palmer, R.J. Silva, S.N. Nguyen, L.N. Marquez, E.A. Hudson, Determinations of Uranium Structures by EXAFS: Schoepite and Other U(VI) Oxide Precipitates, *Radiochim. Acta.* 75 (1996) 47–53.
- [244] D.C. Burciaga-Valencia, C.G. Mendez, H. Esparza-Ponce, A.M. Beesley, M.T. Crespo, Synchrotron radiation study of the uranium chemical species electrodeposited for alpha spectrometry sources, *Rev. Mex. Física.* 57 (2011) 21–29.
- [245] D.I. Brown, What is the best way to determine bond-valence parameters?, *IUCrJ.* 4 (2017) 514–515.
- [246] O.C. Gagné, F.C. Hawthorne, Comprehensive derivation of bond-valence parameters for ion pairs involving oxygen, *Acta Crystallogr. B.* 71 (2015) 562–578.
- [247] D.W. Wester, N.J. Hess, Bond-valence sums for Tc-O systems from EXAFS data, *Inorganica Chim. Acta.* 358 (2005) 865–874.
- [248] USGS, Phreeqc Interactive 3.4.0-12927, https://wwwbrr.cr.usgs.gov/projects/GWC_coupled/phreeqc.v1/ (accessed March 2020), (2020).
- [249] J.M.S. Skakle, L.P. Moroni, F.P. Glasser, X-ray diffraction data for two new calcium uranium (VI) hydrates, *Powder Diffr.* 12 (1997) 81–86.
- [250] W.F. Outerbridge, M.H. Staats, R. Meyrowitz, A.M. Pommer, Weeksite, a new uranium silicate from the Thomas Range, Juab County, Utah, *Am. Mineral.* 45 (1960) 39–52.
- [251] J. Plášil, K. Fejfarová, J. Cejka, M. Dušek, R. Škoda, J. Sejkora, Revision of the crystal structure and chemical formula of weeksite, $K_2(UO_2)_2(Si_5O_{12})(OH)_2 \cdot 4H_2O$, *Am. Mineral.* 97 (2012) 750–754.
- [252] I.G. Richardson, The calcium silicate hydrates, *Cem. Concr. Compos.* 38 (2008) 137–158.
- [253] E. Ruiz-Agudo, C. V. Putnis, C. Rodriguez-Navarro, A. Putnis, Effect of pH on calcite growth at constant $a_{Ca^{2+}}/a_{CO_3^{2-}}$ ratio and supersaturation, *Geochim. Cosmochim. Acta.* 75 (2011) 284–296.
- [254] F.W. Tegethoff, J. Rohleder, E. Kroker, *Calcium Carbonate: From the Cretaceous Period Into the 21st Century*, Birkhäuser, 2001.
- [255] R.T. Haslam, G. Calingaert, C.M. Taylor, The Hydrates of Lime, *J. Am. Chem. Soc.* 46 (1924) 308–311.
- [256] T.F. Sevelsted, J. Skibsted, Carbonation of C-S-H and C-A-S-H samples studied by ^{13}C , ^{27}Al and ^{29}Si MAS NMR spectroscopy, *Cem. Concr. Res.* 71 (2015) 56–65.
- [257] K. Takahashi, F. Takeo, L.R. Morss, Crystal Chemical and Thermodynamic Study on $CaUO_4-x$, $(Ca_{0.5}Sr_{0.5})UO_4-x$, and $\alpha-SrUO_4-x$ ($x = 0 \sim 0.5$), *J. Solid State Chem.* 105 (1993) 234–246.
- [258] H.C. van Duivenboden, D.J.W. IJdo, Redetermination of Tricalcium Uranate(VI). A Rietveld Refinement of Neutron Powder Diffraction Data, *Acta Crystallogr. C.* 42 (1986) 523–525.
- [259] X. Cong, R. James Kirkpatrick, ^{29}Si MAS NMR study of the structure of calcium silicate hydrate, *Adv. Cem. Based Mater.* 3 (1996) 144–156.
- [260] W. Kunther, S. Ferreira, J. Skibsted, Influence of the Ca/Si ratio on the compressive strength of cementitious calcium-silicate-hydrate binders, *J. Mater. Chem. A.* 5 (2017) 17401–17412.
- [261] A. Cuesta, J.D. Zea-Garcia, D. Londono-Zuluaga, A.G. De La Torre, I. Santacruz, O.

- Vallcorba, M. Dapiaggi, S.G. Sanf elix, M.A.G. Aranda, Multiscale understanding of tricalcium silicate hydration reactions, *Sci. Rep.* 8 (2018) 1–11.
- [262] R.L. Santos, R.B. Horta, J. Pereira, T.G. Nunes, P. Rocha, J.N.C. Lopes, R. Colaço, Novel high-resistance clinkers with $1.10 < \text{CaO}/\text{SiO}_2 < 1.25$: production route and preliminary hydration characterization, *Cem. Concr. Res.* 85 (2016) 39–47.
- [263] A. Kumar, B.J. Walder, A. Kunhi Mohamed, A. Hofstetter, B. Srinivasan, A.J. Rossini, K. Scrivener, L. Emsley, P. Bowen, The Atomic-Level Structure of Cementitious Calcium Silicate Hydrate, *J. Phys. Chem. C.* 121 (2017) 17188–17196.
- [264] G. Zhu, H. Li, X. Wang, S. Li, X. Hou, W. Wu, Q. Tang, G. Scherer, Synthesis of Calcium Silicate Hydrate in Highly Alkaline System, *J. Am. Ceram. Soc.* 99 (2016) 2778–2785.
- [265] J. Skibsted, M.T. Pedersen, J. Holzinger, Resolution of the Two Aluminum Sites in Ettringite by ^{27}Al MAS and MQMAS NMR at Very High Magnetic Field (22.3 T), *J. Phys. Chem. C.* 121 (2017) 4011–4017.
- [266] J. Skibsted, E. Henderson, H.J. Jakobsen, Characterization of Calcium Aluminate Phases in Cements by ^{27}Al MAS NMR Spectroscopy, *Inorg. Chem.* 32 (1993) 1013–1027.
- [267] L. Lu, J. He, M. Wei, D.G. Evans, X. Duan, Uptake of chloride ion from aqueous solution by calcined layered double hydroxides: Equilibrium and kinetic studies, *Water Res.* 40 (2006) 735–743.
- [268] P.J. Sideris, F. Blanc, Z. Gan, C.P. Grey, Identification of cation clustering in Mg-Al layered double hydroxides using multinuclear solid state nuclear magnetic resonance spectroscopy, *Chem. Mater.* 24 (2012) 2449–2461.
- [269] F. Colmenero, J. Pl ařil, J. Sejkora, The layered uranyl silicate mineral uranophane- β : crystal structure, mechanical properties, Raman spectrum and comparison with the α -polymorph, *Dalton Trans.* 48 (2019) 16722–16736.
- [270] W. Hunnicutt, L. Struble, P. Mondal, Effect of synthesis procedure on carbonation of calcium-silicate-hydrate, *J. Am. Ceram. Soc.* 100 (2017) 3736–3745.
- [271] W.Z. Baur, L. Keller, J. Rask, P. Buseck, PDF card no. 00-043-1460 (Wollastonite), (1986).
- [272] R. Shamsudin, F.A.A. Azam, M.A.A. Hamid, H. Ismail, Bioactivity and Cell Compatibility of β -Wollastonite Derived from Rice Husk Ash and Limestone, *Materials (Basel)*. 10 (2017) 1188.
- [273] M. Murphy, Gabriel, Kennedy, Brendan J., Johannessen, Bernt, Kimpton, Justin A., Avdeev, Z. Griffith, Christopher S., Thorogood, Gordon J., Zhang, Structural studies of the rhombohedral and orthorhombic monouranates: CaUO_4 , $\alpha\text{-SrUO}_4$, $\beta\text{-SrUO}_4$ and BaUO_4 , *J. Solid State Chem.* 237 (2016) 86–92.
- [274] Y. He, X. Zheng, L. L u, S. Yu, G. Deng, S. Hu, Dehydration Characteristics of C-S-H with Ca/Si Ratio 1.0 Prepared Via Precipitation, *Journal Wuhan University of Technology Mater. Sci. Ed.* 33 (2018) 619–624.
- [275] R.A. van Santen, The Ostwald Step Rule, *J. Phys. Chem.* 88 (1984) 5768–5769.
- [276] A. van Veelen, R. Copping, G.T.W. Law, A.J. Smith, J.R. Bargar, J. Rogers, D.K. Shuh, R.A. Wogelius, Uranium uptake onto Magnox sludge minerals studied using EXAFS, *Mineral. Mag.* 76 (2012) 3095–3104.
- [277] A.J. Gaunt, I. May, M.P. Neu, S.D. Reilly, B.L. Scott, Structural and Spectroscopic Characterization of Plutonyl(VI) Nitrate under Acidic Conditions, *Inorg. Chem.* 2 (2011) 4244–4246.
- [278] H.R. Cho, E.C. Jung, K.K. Park, K. Song, J. Yun, Effect of reduction on the stability of Pu(VI) hydrolysis species, *Radiochim. Acta.* 98 (2010) 555–561.
- [279] E. Dalodi ere, M. Virost, T. Dumas, D. Guillaumont, M.-C. Illy, C. Berthon, L. Guerin, A. Rossberg, L. Venault, P. Moisy, S.I. Nikitenki, Structural and magnetic susceptibility characterization of Pu(V) aqua ion using sonochemistry as a facile synthesis method, *Inorg. Chem. Front.* 5 (2018) 100–111.
- [280] D.L. Clark, The Chemical Complexities of Plutonium, *Los Alamos Sci.* 26 (2000) 366–381.

- [281] J.M. Schwantes, P.H. Santschi, Mechanisms of plutonium sorption to mineral oxide surfaces: new insights with implications for colloid-enhanced migration, *Radiochim. Acta.* 98 (2010) 737–742.
- [282] P.E. Raison, M.A. Reynaud, P.J. Valenza, R.C. Belin, New hermetic sample holder for radioactive materials fitting to Siemens D5000 and Bruker D8 X-ray diffractometers: application to the Rietveld analysis of plutonium dioxide, *J. Appl. Crystallogr.* 37 (2004) 1034–1037.
- [283] J.P. Bros, M. Gaune Escard, W. Szczepaniak, A. Bogacz, H.A. W., Structural transitions in UCl₄ anticipating melting, *Acta Crystallogr. B.* 43 (1987) 113.
- [284] L.R. Schleid, T., Meyer, G., Morss, Facile synthesis of UCl₄ and ThCl₄, metallothermic reductions of UCl₄ with alkali metals and crystal structure refinements of UCl₃, UCl₄ and Cs₂UCl₆, *J. Less Common Met.* 132 (1987) 69–77.
- [285] V. Rostami, Y. Shao, A.J. Boyd, Z. He, Microstructure of cement paste subject to early carbonation curing, *Cem. Concr. Res.* 42 (2012) 186–193.
- [286] Y.Z. Nozik, L.M. Kuznetsov, Neutron diffraction study of synthetic Soddyite by the full-profile analysis technique, *Kristallografiya.* 35 (1990) 1563.
- [287] C.L. Dickson, D.R.M. Brew, F.P. Glasser, Solubilities of CaO-SiO₂-H₂O phases at 25°, 55° and 85°C, *Adv. Cem. Res.* 16 (2004) 35–43.
- [288] D.L. Clark, S.D. Conradson, D. Webster Keogh, P.D. Palmer, B.L. Scott, C.D. Tait, Identification of the Limiting Species in the Plutonium(IV) Carbonate System. Solid State and Solution Molecular Structure of the [Pu(CO₃)₅]⁶⁻ Ion, *Inorg. Chem.* 37 (1998) 2893–2899.
- [289] J. Duchesne, M.A. Berube, The effectiveness of supplementary cementing materials in suppressing expansion due to ASR: Another look at the reaction mechanisms part 1: Concrete expansion and portlandite depletion, *Cem. Concr. Res.* 24 (1994) 73–82.
- [290] C. Mann, J.R. Eskelsen, D.N. Leonard, E. Pierce, C.L. Corkhill, The dissolution of simulant vitrified intermediate level nuclear waste in young cement water, *MRS Adv.* 5 (2020) 131–140.
- [291] R.D. Shannon, Revised Effective Ionic Radii and Systematic Studies of Interatomic Distances in Halides and Chalcogenides, *Acta Crystallogr. A.* 32 (1976) 751–767.
- [292] M. Altmaier, V. Neck, T. Fanghänel, Solubility of Zr(IV), Th(IV) and Pu(IV) hydrous oxides in CaCl₂ solutions and the formation of ternary Ca-M(IV)-OH complexes, *Radiochim. Acta.* 96 (2008) 541–550.
- [293] D.T. Hobbs, D.G. Karraker, Recent Results on the Solubility of Uranium and Plutonium in Savannah River Site Waste Supernate, *Nucl. Technol.* 114 (1995) 318–324.
- [294] J.I. Langford, A.J.C. Wilson, Seherer after Sixty Years: A Survey and Some New Results in the Determination of Crystallite Size, *J. Appl. Crystallogr.* 11 (1978) 102–113.
- [295] D.M. Wayne, L.G. Peppers, D.S. Schwartz, P.C. DeBurgomaster, Surface area and particle size distribution of plutonium oxides derived from the direct oxidation of Pu metal, *J. Nucl. Mater.* 511 (2018) 242–263.
- [296] B.L. Scott, A.L. Pugmire, J.T. Stritzinger, D.K. Veirs, L.E. Wolfsberg, M.P. Wilkerson, Relationships between experimental signatures and processing history for a variety of PuO₂ materials, *J. Nucl. Mater.* 521 (2019) 155–160.
- [297] J. Jain, N. Neithalath, Analysis of calcium leaching behavior of plain and modified cement pastes in pure water, *Cem. Concr. Compos.* 31 (2009) 176–185.
- [298] J. Duchesne, E. J. Reardon, Measurement and prediction of portlandite solubility in alkali solutions, *Cem. Concr. Res.* 25 (1995) 1043–1053.
- [299] K. Fujiwara, H. Yamana, T. Fujii, K. Kawamoto, T. Sasaki, H. Moriyama, Solubility product of hexavalent uranium hydrous oxide, *J. Nucl. Sci. Technol.* 42 (2005) 289–294.
- [300] H. Nakamura, M. Machida, M. Kato, Effects of spin-orbit coupling and strong correlation on the paramagnetic insulating state in plutonium dioxides, *Phys. Rev. B.* 82 (2010) 155131.

- [301] K. Tanaka, N. Kozai, S. Yamasaki, T. Ohnuki, D.I. Kaplan, B. Grambow, Adsorption mechanism of ReO_4^- on Ni–Zn layered hydroxide salt and its application to removal of ReO_4^- as a surrogate of TcO_4^- , *Appl. Clay Sci.* 182 (2019) 1–8.
- [302] Sellafield Ltd., Monitoring our Environment. Discharges and Environmental Monitoring, Annual Report, 2017.
- [303] P.G. Allen, Technetium Speciation in Cement Waste Forms Determined by X-ray Absorption Fine Structure Spectroscopy, LBNL-38887, UC-401, 1996.
- [304] A. Gabrisová, J. Havlica, S. Sahu, Stability of calcium sulphoaluminate hydrates in water solutions with various pH values, *Cem. Concr. Res.* 21 (1991) 1023–1027.
- [305] J.O. Dickson, J.B. Harsh, M. Flury, W.W. Lukens, E.M. Pierce, Competitive incorporation of perrhenate and nitrate into sodalite, *Environ. Sci. Technol.* 48 (2014) 12851–12857.
- [306] M.B. Varfolomeev, V.N. Krustalev, N.B. Shamrai, A.Y. Vol'fkovich, D. V. Drobot, Crystal Structures of Aqua Complexes with Octahedral $\text{M}(\text{H}_2\text{O})_6^{3+}$ Groups: Aluminium and Gallium Perrehnate Octahydrates $\text{M}(\text{ReO}_4)_3 \cdot 8\text{H}_2\text{O}$ ($\text{M} = \text{Al}, \text{Ga}$), *Russ. J. Inorg. Chem.* 42 (1996) 1605–1609.
- [307] G.A. Hulett, The solubility of gypsum as affected by size of particles and by different crystallographic surfaces, *J. Am. Chem. Soc.* 27 (1905) 49–56.
- [308] M.L. Dundon, F. Mack, The solubility and surface energy of calcium sulfate, *J. Am. Chem. Soc.* 45 (1923) 2479–2485.
- [309] G.A. Hulett, L.E. Allen, The solubility of gypsum, *J. Am. Chem. Soc.* 24 (1902) 667–679.
- [310] D. Constantiner, S.A. Farrington, Review of the thermodynamic stability of ettringite, *Cem. Concr. Aggregates.* 21 (1999) 39–42.
- [311] H. Bosmans, Unit cell and crystal structure of nordstrandite, $\text{Al}(\text{OH})_3$, *Acta Crystallogr. B.* 26 (1970) 649–652.
- [312] E. Yogarajah, N. Toyoharu, K. Kiyofumi, Influence of Surface Electrical Properties of C-S-H on Chloride Binding in Slag-Blended Cementitious Materials, *J. Mater. Civ. Eng.* 30 (2018) 04018064.
- [313] K. Tanaka, N. Kozai, T. Ohnuki, B. Grambow, Study on coordination structure of Re adsorbed on Mg–Al layered double hydroxide using X-ray absorption fine structure, *J. Porous Mater.* 26 (2019) 505–511.